

Wrocław University of Technology
Centre of Advanced Materials and Nanotechnology

Materials Science-Poland

Vol. 27



No. 3



2009



Oficyna Wydawnicza Politechniki Wrocławskiej

Materials Science-Poland is an interdisciplinary journal devoted to experimental and theoretical research into the synthesis, structure, properties and applications of materials.

Among the materials of interest are:

- glasses and ceramics
- sol-gel materials
- photoactive materials (including materials for nonlinear optics)
- laser materials
- photonic crystals
- semiconductor micro- and nanostructures
- piezo-, pyro- and ferroelectric materials
- high- T_c superconductors
- magnetic materials
- molecular materials (including polymers) for use in electronics and photonics
- novel solid phases
- other novel and unconventional materials

The broad spectrum of the areas of interest reflects the interdisciplinary nature of materials research. Papers covering the modelling of materials, their synthesis and characterisation, physicochemical aspects of their fabrication, properties and applications are welcome. In addition to regular papers, the journal features issues containing conference papers, as well as special issues on key topics in materials science.

Materials Science-Poland is published under the auspices of the Centre of Advanced Materials and Nanotechnology of the Wrocław University of Technology, in collaboration with the Institute of Low Temperatures and Structural Research of the Polish Academy of Sciences and the Wrocław University of Economics.

All accepted manuscripts are placed on the Web page of the journal and are available at the address:
<http://MaterialsScience.pwr.wroc.pl>

All published papers are placed on the Web page of the journal and are **freely accessible** at the address:
<http://MaterialsScience.pwr.wroc.pl>

Materials Science-Poland is abstracted/indexed in: **Chemical Abstracts, Materials Science Citation Index, Science Citation Index Expanded, Scopus.**

Editor-in-Chief

Juliusz Sworakowski

Institute of Physical and Theoretical Chemistry
Wrocław University of Technology
Wyrbrzeże Wyspiańskiego 27
50-370 Wrocław, Poland
sworakowski@pwr.wroc.pl

Deputy Editor

Faculty of Microsystem Electronics and Photonics
Wrocław University of Technology
Wyrbrzeże Wyspiańskiego 27
50-370 Wrocław, Poland
jan.felba@pwr.wroc.pl

Associate Editors

Wiesław Stręk

Institute of Low Temperature
and Structure Research
Polish Academy of Sciences
P. O. Box 1410
50-950 Wrocław 2, Poland
strek@int.pan.wroc.pl

Jerzy Hanuza

Department of Bioorganic Chemistry
Faculty of Industry and Economics
Wrocław University of Economics
Komandorska 118/120
53-345 Wrocław, Poland
hanuza@credit.ae.wroc.pl

Advisory Editorial Board

Frédéric Bernard, Dijon, France
Mikhaylo S. Brodyn, Kyiv, Ukraine
Alexander Bulinski, Ottawa, Canada
J. Paulo Davim, Aveiro, Portugal
Roberto M. Faria, São Carlos, Brazil
Andrzej Gałęski, Łódź, Poland
Reimund Gerhard, Potsdam, Germany
Paweł Hawrylak, Ottawa, Canada
Andrzej Kłonkowski, Gdańsk, Poland
Shin-ya Koshihara, Tokyo, Japan
Krzysztof J. Kurzydłowski, Warsaw, Poland
Janina Legendziewicz, Wrocław, Poland
Benedykt Licznerski, Wrocław, Poland

Jerzy Lis, Cracow, Poland
Tadeusz Luty, Wrocław, Poland
Bolesław Mazurek, Wrocław, Poland
Ram M. Mehra, New Delhi
Jan Misiewicz, Wrocław, Poland
Jerzy Mroziński, Wrocław, Poland
Krzysztof Nauka, Palo Alto, CA, U.S.A.
Stanislav Nešpůrek, Prague, Czech Republic
Marek Samoć, Wrocław, Poland
Jan Stankowski, Poznań, Poland
Jacek Ulański, Łódź, Poland
Vladislav Zolin, Moscow, Russia

The Journal is supported by the State Committee for Scientific Research

Editorial Office

Daniel Davies
Marek Łata

Printed in Poland

© Copyright by Oficyna Wydawnicza Politechniki Wrocławskiej, Wrocław 2009

From the Guest Editor

This special issue of the *Materials Science-Poland* contains selected papers based on lectures, communications and poster presentations contributed to the 11th International Conference on Electrical and Related Properties of Organic Solids (ERPOS-11). The Conference took place in Piechowice, Poland on 13–17 July 2008 under the auspices of the Wrocław University of Technology (WUT).

The ERPOS conferences started in 1974 in Karpacz (Poland) as a Summer School and was initiated at WUT by a group of physical chemists from the Institute of Organic and Physical Chemistry (now, the Institute of Physical and Theoretical Chemistry). The present conference is eleventh in the series of international events devoted to electrical and related properties of organic solids. Around 110 researchers from 17 countries participated in ERPOS-11. The major topics covered by the plenary and poster sessions of the ERPOS-11 conference include electrical and optical properties of materials, nonlinear optics, nanophotonics and structure of biomaterials. The papers published in these proceedings relate to some of these subjects. It should be noticed that the papers have been subject to the normal refereeing procedures of *Materials Science-Poland*.

As Guest Editor, I would like to express my sincere appreciation to all the authors for their contributions. Especially, I extend my gratitude to all the reviewers who have kindly collaborated in selecting the papers and improving their quality.

Wojciech Bartkowiak

Institute of Physical and Theoretical Chemistry
Wrocław University of Technology

Optical study of β'' -(bis(ethylenedithio)tetrathiafulvalene)₂SF₅CH₂SO₃ Activation of intramolecular modes*

I. OLEJNICZAK^{1**}, B. BARSZCZ¹, A. GRAJA¹, J.A. SCHLUETER²

¹Institute of Molecular Physics, Polish Academy of Sciences,
Smoluchowskiego 17, 60-179 Poznań, Poland

²Materials Science Divisions, Argonne National Laboratory, Argonne, Illinois 60439-4831, USA

We report on the temperature dependences of polarized reflectance spectra of β'' -(bis(ethylenedithio)tetrathiafulvalene)₂SF₅CH₂SO₃. The material remains in the charge-ordered state over the whole temperature range. Room temperature infrared spectra display the response characteristic of a quasi-two-dimensional organic conductor, with a broad mid-infrared electronic excitation and a number of vibrational features related to intramolecular modes of both the bis(ethylenedithio)tetrathiafulvalene (ET) donor molecule and the SF₅CH₂SO₃ anion. Upon lowering the temperature, unusual activation of intramolecular modes of ET is observed. We suggest that this effect is connected with electron-molecular vibration coupling within a dimerized lattice.

Key words: *BEDT-TTF; organic conductor; reflectance spectra; electron-phonon interactions; charge ordering*

1. Introduction

Quasi-two-dimensional organic conductors based on the organic donor molecule of bis(ethylenedithio)tetrathiafulvalene (ET) are widely regarded as good model compounds to study broken symmetry ground states [1]. Extensive experimental studies of these materials have been stimulated by the discovery of superconductivity and other competing ground states that are related to a complex interplay of charge, spin and vibrational degrees of freedom. In particular, the procedure of incorporating large, discrete, chemically tunable anions within an ET framework resulted in the family

*The paper presented at the 11th International Conference on Electrical and Related Properties of Organic Solids (ERPOS-11), July 13–17, 2008, Piechowice, Poland.

**Corresponding author, e-mail: ywy@ifmpan.poznan.pl

β'' -(ET)₂SF₅RSO₃ (R = CH₂CF₂, CHF₂CF₂, or CHF), where superconducting, semiconducting, or metallic ground states have been realized depending on R [2, 3]. β'' -(ET)₂SF₅CH₂SO₃ is another example of a salt synthesized based on ET and pentafluorothiomethylsulfonate anions being of interest here.

The crystal structure of β'' -(ET)₂SF₅CH₂SO₃ consists of alternating layers of ET cations and SF₅CH₂SO₃⁻ anions [4]. ET molecules in the donor layer form stacks along the *a* direction. Short intermolecular S...S contacts* are found between adjacent donor stacks but not within stacks. F and O atoms of the anion make numerous contacts with ethylene hydrogen atoms of donor molecules. Also, C-H...O hydrogen bond interactions occur between anions. The unit cell is composed of four ETs, forming one conducting plane, and has an inversion centre, therefore there are two pairs of equivalent ETs. Non-equivalent ET molecules are characterized by different patterns of short contacts with the anion layer, and also different charge, which was estimated 0.6 and 0.4, based on the structure [4]. Such a charge localization results in semiconducting properties, although typical β'' -type quarter-filled systems are usually two-dimensional metals.

In this paper, we present polarized reflectance spectra of β'' -(ET)₂SF₅CH₂SO₃, measured as a function of temperature in order to gain further information on the nature of electronic processes in the β'' -phase materials with highly tunable organic anions. In our experiment, we concentrate on intramolecular vibrational modes of the ET molecule, which strongly appear in the spectra upon lowering the temperature.

2. Experimental

High-quality single crystals of β'' -(ET)₂SF₅CH₂SO₃ were grown using electrochemical techniques in an H-cell [4]. For infrared measurements we used a 3.5×2×0.4 mm³ plate sample. Optical axes were defined as those displaying the largest anisotropy at 300 K. Two directions within the conducting plane were probed; the *||b* direction of maximum reflectance, and the *⊥b* direction, which is close to the ET stack of the *a* direction. Polarized infrared reflectance measurements (600–7000 cm⁻¹) were performed using a Perkin Elmer 1725 X Fourier-transform infrared spectrometer, equipped with an Olympus infrared microscope and a polarized gold grid. The sample was cooled from room temperature down to 10 K using an Oxford Instruments continuous-flow cryostat. Additionally, the 300 K polarized reflectance spectra were recorded using a Bruker Equinox 55 FT-IR spectrometer equipped with a Bruker IRScope II infrared microscope (7000–15000 cm⁻¹). The room temperature infrared absorption spectrum of LiSO₃CH₂SF₅ was recorded as a reference.

The frequency-dependent optical conductivity was calculated by means of the Kramers-Krönig analysis of the measured reflectance. The range of data outside the

*Intermolecular contacts shorter than the sum of the sulfur van der Waals radii.

middle infrared was extended using 300 K spectra, for all the temperatures. The high frequency data were extrapolated as ω^{-2} , where ω is the frequency, and the low frequency data were extrapolated as a constant appropriate for semiconducting materials [5]. Complex vibrational bands were analysed using standard peak fitting techniques to extract centre peak frequencies and integral areas (oscillator strengths). Oscillators were fitted using the Voigt function*.

3. Results and discussion

Figure 1 displays the optical conductivity spectra of β' -(ET) $_2\text{SF}_5\text{CH}_2\text{SO}_3$ recorded at 10 and 300 K, together with the 300 K polarized reflectance (inset in Fig. 1a).

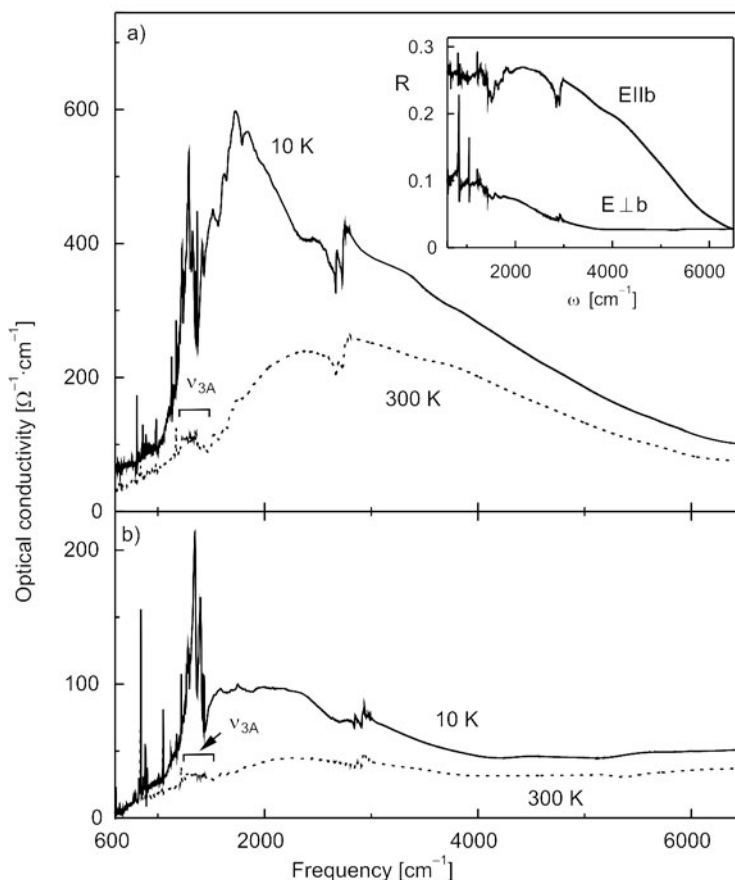


Fig. 1. Optical conductivity spectra of β' -(ET) $_2\text{SF}_5\text{CH}_2\text{SO}_3$ polarized in the $E \parallel b$ (a) and $E \perp b$ (b) directions, recorded at 10 and 300 K. The inset in Fig. 1a displays the polarized infrared reflectance at 300 K

*The Voigt function is a four-parameter model spectral line that includes two types of broadening, characteristic of both the Gaussian and Lorentzian shape.

The reflectance in the interstack direction ($E \parallel b$) is significantly greater than the reflectance in the stack direction ($E \perp b$) and displays a drop between 3000 and 6500 cm^{-1} . The reflectance spectrum polarized in the $\perp b$ direction is similar to the $E \parallel b$ response but is characterized by overdamping. Such a type of anisotropy is characteristic of a β'' -phase quasi-two-dimensional conductor [1]. In fact, a similar behaviour is observed in the infrared spectra of β'' -(ET) $_2\text{SF}_5\text{CH}_2\text{CF}_2\text{SO}_3$ superconductor and β'' -(ET) $_2\text{SF}_5\text{CHFSO}_3$ metallic sample [3]. In the optical conductivity spectra of β'' -(ET) $_2\text{SF}_5\text{CH}_2\text{SO}_3$, in both the $E \parallel b$ and $E \perp b$ polarizations (Fig. 1), one can observe at 300 K a broad electronic band centred near 2200 cm^{-1} . Upon lowering the temperature, this electronic excitation grows monotonically, slightly moves toward lower frequencies and displays a gap-like, low-frequency edge, probably related to the charge gap. Overall temperature changes in electronic excitation are modest, unlike vibrational structure.

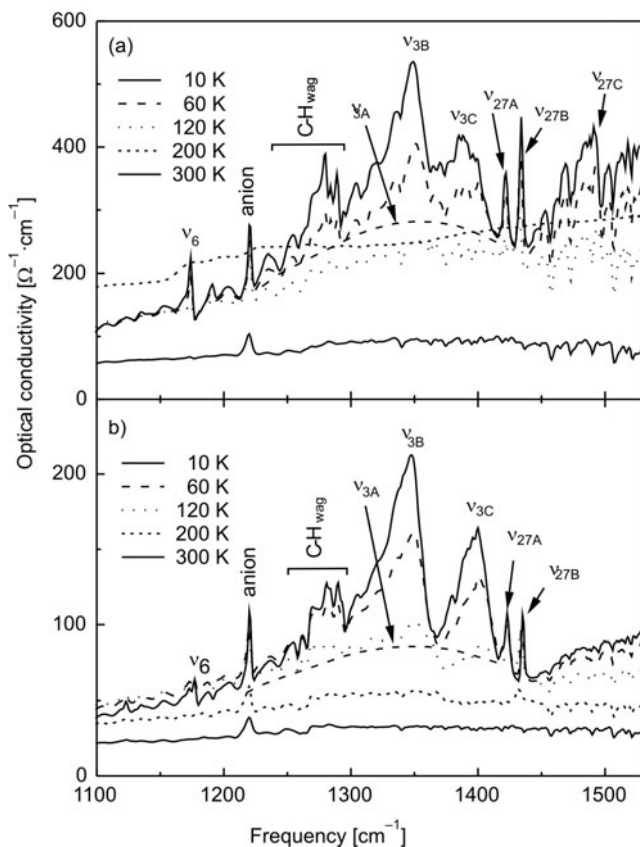


Fig. 2. Optical conductivity spectra of β'' -(ET) $_2\text{SF}_5\text{CH}_2\text{SO}_3$ in the frequency range of the prominent vibrational features for $E \parallel b$ (a) and $E \perp b$ (b), measured at various temperatures

Figure 2 displays the optical conductivity spectra of β'' -(ET) $_2\text{SF}_5\text{CH}_2\text{SO}_3$ in the range of the most prominent vibrational modes at various temperatures. In general, the

infrared spectra of ET-based materials mostly display intramolecular modes of the ET molecule, and the strongest features appear as a result of electron-molecular vibration (EMV) coupling of totally symmetric modes with electrons [6–8]. These so-called vibronic modes are infrared active in the presence of symmetry breaking, usually dimerization [9]. Unlike most ET-based solids, the spectra of β'' -(ET)₂SF₅CH₂SO₃, at 300 K in the frequency range corresponding to vibrational features, are characterized by relatively strong modes of the SF₅CH₂SO₃ anion. For example, in the $E \perp b$ polarization, the anion modes are found at 841, 1050 and 1220 cm⁻¹ (the 1220 cm⁻¹ mode is shown in Fig. 2 for both polarizations). These modes do not change much upon lowering temperature. On the other hand, very strong ET-related modes grow upon lowering the temperature below about 250 K in both the polarizations (Fig. 2). In particular, the largest effect is observed in the frequency range 1300–1410 cm⁻¹ for the totally symmetric bridge C=C stretching mode labelled $\nu_3(A_g)$ in the D_{2h} point group symmetry representation we use here for isolated molecule [7]. This mode having a large coupling constant [8] is known for its sensitivity to both structural as well as charge modifications [10]. Other prominent EMV-related effects observed in the spectra include C–H wagging vibrations (1250–1300 cm⁻¹), C–S stretching vibrations (870–910 cm⁻¹, see Fig. 3), and the $\nu_6(A_g)$ mode at about 1174 cm⁻¹. In addition, the out-of-phase stretching C=C mode $\nu_{27}(B_{1u})$ displays a similar behaviour although it is normally infrared active and not coupled based on the symmetry considerations. Most of the above mentioned features appear as multiple peaks. Another C=C stretching mode $\nu_2(A_g)$, which can appear in the infrared spectra as a result of coupling with electrons, is characterized by a small coupling constant [7], and for this reason it is absent in the infrared spectra of β'' -(ET)₂SF₅CH₂SO₃.

The unit cell of the β'' -(ET)₂SF₅CH₂SO₃ system is triclinic (space group $P\bar{1}$) and accommodates four ET donor molecules. Therefore, every internal ET vibration splits into four components, forming unit-cell modes. These modes should be fourfold degenerated in the case if four molecules in the unit cell are almost equivalent. In the β'' -(ET)₂SF₅CH₂SO₃ material, there are molecules with two different values of charge present over the whole temperature range. As a result, we could expect at least two separate peaks to appear in the infrared spectra for each charge-sensitive mode, including $\nu_3(A_g)$ and also $\nu_{27}(B_{1u})$ [11]. To discuss vibrational features in a more detailed way, we use factor-group analysis, taking into account these two modes. In the factor-group symmetry C_i , four crystalline modes for both the $\nu_3(A_g)$ and $\nu_{27}(B_{1u})$ are split into two pairs of A_g and A_u modes, the two former being Raman active and the two latter being infrared active. This mutual exclusion rule is related to the inversion centre present in the $P\bar{1}$ space group. The $\nu_3(A_g)$ mode appears in the $E \parallel b$ and $E \perp b$ spectra of β'' -(ET)₂SF₅CH₂SO₃ below 250 K, mainly as two very strong features (ν_{3B} and ν_{3C} in Fig. 2) centred at about 1348 and 1400 cm⁻¹ at the lowest temperature. We assign these modes to two EMV-activated ungerade crystalline modes (A_u). Another very broad ν_3 component, labelled as ν_{3A} , appears in the frequency range 1200–1450 cm⁻¹ (the dashed line marked in Fig. 2 for the lowest temperature 10 K) over the whole

temperature range (see spectra at 300 K in Fig. 1 for comparison). Such a broad but substantially stronger vibronic ν_3 feature is characteristic of infrared spectra of the β'' -(ET)₂SF₅RSO₃ (R = CH₂CF₂, CHF₂CF₂, and CHF) family of materials including a superconductor (R = CH₂CF₂), a material with the metal/insulator phase transition (R = CHF₂CF₂) and a metallic sample (R = CHF) [3]. We suggest that this is the crystalline mode of the A_g symmetry that is supposed to be Raman active only. In fact, a strong low-frequency component of ν_3 was found at about 1330 cm⁻¹, in the 80 K Raman spectrum of the analogue material β'' -(ET)₂CF₃CH₂SO₃ [12], and both in Raman and infrared spectra of the charge-ordered phase of θ -(ET)₂RbZn(SCN)₃ [10]. That it appears in the infrared spectra means that the inversion symmetry is broken in the β'' -(ET)₂SF₅CH₂SO₃ material.

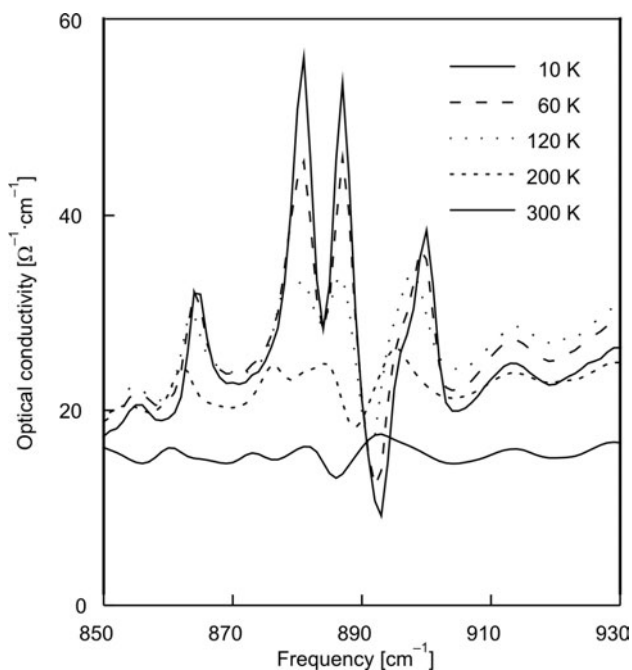


Fig. 3. Temperature dependence of intensity of selected vibrational C=C modes normalized by the 10 K values for β'' -(ET)₂SF₅CH₂SO₃ (lines between points are intended to guide the eye)

Similarly to ν_3 , the ν_{27} mode also displays three components: 1423, 1435, and ca. 1497 cm⁻¹ at low temperatures, labelled as ν_{27A} , ν_{27B} , and ν_{27C} in Fig. 2, respectively. This mode is considered to be the best probe of the local charge on the molecule [11]. Here we assign the ν_{27A} and ν_{27B} components as related to the hole-rich molecules, and ν_{27C} as the mode belonging to the hole-poor molecules in the structure. When lowering the temperature, the ν_{27B} and ν_{27C} components appear in the infrared spectra at about 200 K, and the ν_{27A} mode is displayed at about 120 K. Using the linear relationship between the frequency and charge ρ on the molecule [11]

$$\nu_{27}(\rho) = 1398 + 140(1 - \rho) [\text{cm}^{-1}]$$

and taking into account the ν_{27B}^* and ν_{27C} components, we estimate the fractional charge in β'' -(ET)₂SF₅CH₂SO₃ to be $0.3e$ and $0.7e$. Our result is different from the values $0.4e$ and $0.6e$ calculated based on the bond lengths [4]. Other EMV coupling-related effects accompanied by mode splitting are observed for the C–H wagging vibrations in the frequency range 1250–1300 cm⁻¹ (Fig. 2) and for the C–S stretching mode (ca. 880 cm⁻¹, Fig. 3) which is known to be strongly temperature dependent in the infrared spectra of ET-based organic conductors [13].

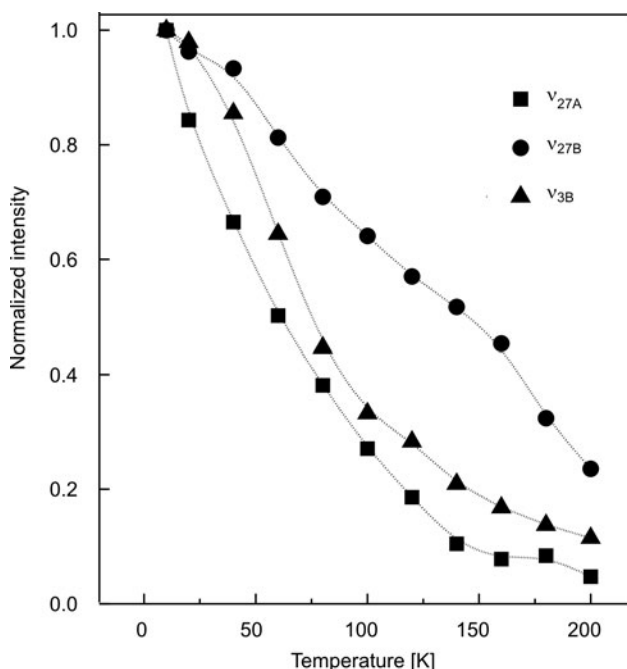


Fig. 4. Optical conductivity spectra of β'' -(ET)₂SF₅CH₂SO₃ in the frequency range of the stretching C–S mode for polarization $E \perp b$, measured at selected temperatures

To discuss the temperature dependence of the ν_3 and ν_{27} mode components, we calculated the integral intensities (oscillator strengths) of ν_{27A} , ν_{27B} and ν_{3B} for the infrared spectra polarized in the $E \parallel b$ direction. Figure 4 displays the temperature dependence of the selected mode intensities, normalized by the 10 K values. We have chosen these components because they are relatively strong and are not disturbed by an excessive noise. In the case of vibronic modes (i.e. modes activated through EMV coupling), the infrared oscillator strength is related to stack dimerization amplitude

*We have chosen ν_{27B} out of two low frequency ν_{27} components because it appears in broader temperature range than ν_{27A} .

[14, 15]. In fact, a very strong temperature dependence of the integral intensity of the ν_{3B} mode is observed for $\beta''\text{-(ET)}_2\text{SF}_5\text{CH}_2\text{SO}_3$. Such a behaviour suggests that the material undergoes apparent dimerization upon a lowering of temperature. Surprisingly, both the ν_{27} components grow proportionally to ν_3 , and temperature dependence of integral intensity of ν_{27A} is even more steep than in the case of ν_3 (Fig. 4). The ν_{27B} mode is characterized by a weaker temperature dependence but it is still much stronger than in case of other normally infrared-active vibrations (see the anion mode in Fig. 2 for comparison). To explain this unusual behaviour, we suggest that EMV coupling is also involved in activation of the ν_{27} mode components. Probably, due to local symmetry of the ET donor molecule and factor-group splitting, the ν_{27} mode partly gains a new identity as a totally symmetric mode and hence is available for coupling with electrons.

Although $\beta''\text{-(ET)}_2\text{SF}_5\text{CH}_2\text{SO}_3$ does not undergo any phase transition in the studied temperature range, the vibronic signatures of dimerization observed in this material are very strong and include factor-group splitting. We suggest that hydrogen bonding between anion layer and ET donor layer takes part in dimerization providing a mechanism for strong interaction between ET molecules.

4. Conclusions

The polarized infrared spectra of $\beta''\text{-(ET)}_2\text{SF}_5\text{CH}_2\text{SO}_3$ were recorded at various temperatures. The material is a two-dimensional semiconductor, with an electronic response similar to that of the $\beta''\text{-(ET)}_2\text{SF}_5\text{RSO}_3$ ($R = \text{CH}_2\text{CF}_2$, CHFCF_2 , and CHF) family of materials. The vibrational study reveals a very strong activation and splitting of the ν_3 and ν_{27} modes as the temperature is lowered. We suggest that these effects are related both to EMV coupling within the dimerized structure and to the presence of two different charges on ET molecules in the donor layer. Unusually strong temperature dependence of all the vibronic signatures of dimerization indicates that hydrogen bonding between anions and donor molecules facilitates stabilization of ET dimers at low temperature.

Acknowledgement

This work was supported by the Ministry of Science and Higher Education of Poland as the research project in the years 2008–2010.

References

- [1] SEO H., HOTTA C., FUKUYAMA H., *Chem. Rev.*, 104 (2004), 5005.
- [2] OLEJNICZAK I., JONES B.R., ZHU Z., DONG J., MUSFELDT J.L., SCHLUETER J.A., MORALES E., GEISER U., NIXON P.G., WINTER R.W., GARD G.L., *Chem. Mater.*, 11 (1999), 3160.
- [3] JONES B.R., OLEJNICZAK I., DONG J., PIGOS J.M., ZHU Z.T., GARLACH A.D., MUSFELDT J.L., KOO H.-J., WHANGBO M.-H., SCHLUETER J.A., WARD B.H., MORALES E., KINI A.M., WINTER R.W., MOHTASHAM J., GARD G.L., *Chem. Mater.*, 12 (2000), 2490.

- [4] WARD B.H., SCHLUETER J.A., GEISER U., WANG H.H., MORALES E., PARAKKA J.P., THOMAS S.Y., WILLIAMS J.M., NIXON P.G., WINTER R.W., GARD G.L., KOO H.-J., WHANGBO M.-H., *Chem. Mater.*, 12 (2000), 343.
- [5] WOOTEN, F., *Optical Properties of Solids*, Academic Press, New York, 1972.
- [6] RICE M.J., *Phys. Rev. Lett.*, 37 (1976), 36.
- [7] KOZLOV M.E., POKHODNIA K.I., YURCHENKO A.A., *Spectrochim. Acta*, 43A (1987), 323.
- [8] GIRLANDO A., MASINO M., BRILLANTE A., DELLA VALLE R.G., VENUTI E., *Pairing mechanism in organic superconductors: the entangled role of phonons*, [in:] Ross W. Stevens (Ed.), *New Developments in Superconductivity Research*, Nova Science Publishers, New York 2003, p. 15.
- [9] MENEGHETTI M., BOZIO R., PECILE C., *J. Physique (France)*, 47 (1986), 1377.
- [10] YAMAMOTO K., YAKUSHI K., MIYAGAWA K., KANODA K., KAWAMOTO A., *Phys. Rev. B*, 65 (2002), 085110.
- [11] YAMAMOTO T., URUICHI M., YAMAMOTO K., YAKUSHI K., KAWAMOTO A., TANIGUCHI H., *J. Phys. Chem. B*, 109 (2005), 15226.
- [12] WOJCIECHOWSKI R., unpublished results.
- [13] MUSFELDT J.L., ŚWIETLIK R., OLEJNICZAK I., ELDRIDGE J.E., GEISER U., *Phys. Rev. B*, 72 (2005), 014516.
- [14] RANZIERI P., MASINO M., GIRLANDO A., LEMÉE-CAILLEAU M.-H., *Phys. Rev. B*, 76 (2007), 134115.
- [15] PAINELLI A., DEL FREO L., SOOS Z.G., *Synth. Met.*, 133-134 (2003), 619.

Received 10 July 2008
Revised 15 September 2008

Stabilization energies in charged tetracene clusters Quantum chemical and microelectrostatic calculations *

A. EILMES **

Jagiellonian University, Department of Computational Methods in Chemistry,
Ingardena 3, 30-060 Cracow, Poland

Theoretical calculations of the stabilization energy for an excess electron in tetracene clusters are presented. Vertical detachment energies were calculated for small clusters (up to 7 tetracene molecules) using the quantum-chemical DFT method. For larger clusters and an infinite 2D layer of tetracene molecules, the self-consistent polarization field (SCPF) method was used to calculate the polarization energy for a tetracene anion. Both DFT and SCPF results show that the charge stabilization energy increases rapidly with the cluster size and, even for clusters of less than 10 tetracene molecules, amounts to more than 50% of the bulk crystal value, which is in agreement with the conclusions of a recent experimental work.

Key words: *tetracene; polarization energy; electron detachment energy*

1. Introduction

Linear oligoacenes (anthracene, tetracene or pentacene) are commonly used in research on fundamental physical properties of organic molecular crystals. Studies on charge-carrier localization and transport in such systems attract significant attention owing to possible applications in molecular electronics. The major research effort is focused on crystals, while small aggregates are of lesser interest. Molecular clusters, however, offer new possibilities for the study of microscopic charge localization phenomena and allow one to trace the evolution of physical properties of aggregates towards bulk crystals.

Recently, a study on tetracene cluster anions has been reported [1]. Photoelectron spectroscopy (PE) combined with mass spectrometry was used to measure the values

*The paper presented at the 11th International Conference on Electrical and Related Properties of Organic Solids (ERPOS-11), July 13–17, 2008, Piechowice, Poland.

**E-mail: eilmes@chemia.uj.edu.pl

of electron vertical detachment energy (VDE) for a series of clusters (tetracene) $_n^-$, ($n = 1-100$). It has been found that for $n > 50$, two bands of almost constant VDE were observed. One band appeared at about 1.8 eV; its intensity gradually decreased with the cluster size, and for $n > 60$ the other band, at 2.0 eV, was more prominent. The former band was attributed to a 2-dimensional cluster of tetracene molecules, while it was argued that the higher-energy band originates from a double- or multilayered structure. The authors of [1] concluded that a large part of the polarization energy of bulk tetracene crystal is reached in surprisingly small clusters.

In this paper, a theoretical study of electron binding energy in small tetracene aggregates is presented. Two complementary approaches are used to estimate the electron detachment energies from charged tetracene aggregates. For small clusters, the detachment energy may be obtained from standard quantum-chemical calculations as the difference between energies of electrically neutral and negatively charged clusters. As the computational cost increases rapidly with the number of tetracene molecules, this method is feasible only for the smallest aggregates. The other approach is the self consistent method of microelectrostatic calculations easily capable of computing the polarization energy for an excess charge in a cluster consisting of thousands of molecules. Polarization energy calculations will therefore provide information about the increase in the charge stabilization energy in large clusters.

2. Quantum chemical calculations

The Gaussian 03 program [2] was used for the density functional theory calculations with B3LYP functional. Single point energy calculations were performed for input geometries of tetracene clusters taken from the crystallographic data [3]. To reduce the time of calculations, the basis set was limited to 3-21G. The calculated detachment energies are therefore significantly underestimated, however, the energy change upon increasing cluster size should be less affected by the basis set size.

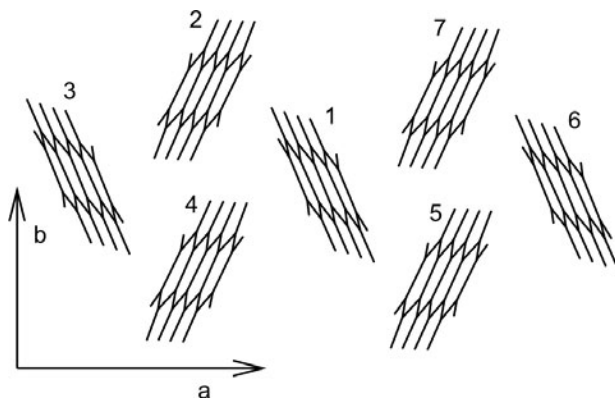


Fig. 1. Geometry of the largest tetracene cluster used in calculations

The DFT calculations were performed for clusters of up to seven tetracene molecules cut from the *ab* plane of the crystal. Figure 1 presents the geometry of the largest aggregate, the numbers give the sequence in which the molecules were added to the cluster. The geometries measured for two molecules [3] at the (0,0,0) and (1/2,1/2,0) crystallographic positions differ slightly, which leads to differences in the calculated energies. Results were therefore averaged over two choices of cluster position in the tetracene lattice.

The electron detachment energy VDE was calculated as a difference of two single-point energies:

$$\text{VDE} = E^0 - E^- \quad (1)$$

where E^0 and E^- are the energies of clusters with charge 0 and -1 , respectively.

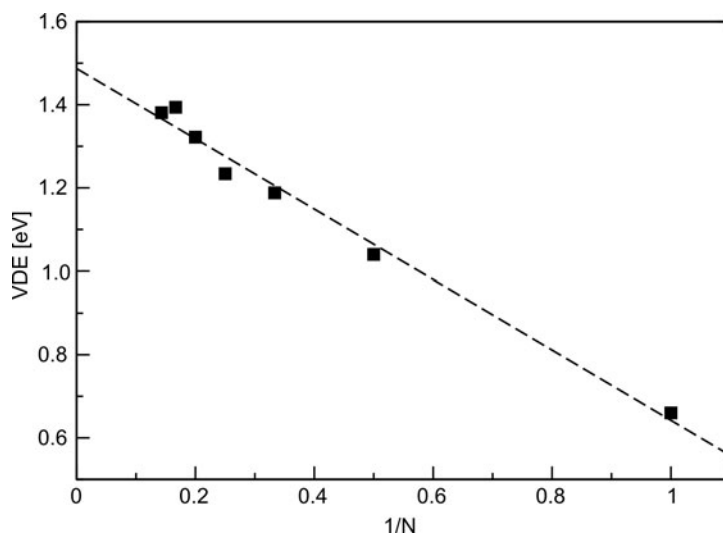


Fig. 2. Vertical detachment energy for electrons in tetracene clusters calculated at the B3LYP/3-21G level vs. reciprocal of the number of tetracene molecules in the cluster. The line is the linear fit to the data

Electron detachment energy calculated at the B3LYP/3-21G level for a single tetracene molecule at the crystal geometry is 0.66 eV, i.e. ca. 0.4 eV lower than the electron affinity of tetracene (1.06 eV) [1]. The dependence of the calculated VDE values on the reciprocal value of cluster size is shown in Fig. 2. Linear data fitting provides an estimate of 1.49 eV for the detachment energy corresponding to an infinite number of molecules. The increase in the VDE from one tetracene molecule to the infinite *ab* plane amounts, therefore, to 0.83 eV. This value can be compared with the experimental data. Assuming (as in [1]) that the peak at 1.8 eV in the photoelectron spectra of tetracene clusters corresponds to the limit of an infinite monomolecular layer, we obtain 0.74 eV as the experimentally determined estimate for the increase in VDE if the number of tetracene molecules increases from 1 to infinity. In spite of the low level of

theory applied in calculations, the quantum-chemically computed value is in good agreement with measurements. It should be noted that preliminary results of calculations employing a larger basis set suggest that with increase in the cluster size, the VDE values change more slowly than at the 3-21G level, which opens up prospect of an even better agreement with the experimental data.

Although the VDE of 0.66 eV calculated for a single molecule is only 44% of the value extrapolated for an infinite system, for a cluster consisting of only seven tetracene molecules about 93% of the electron detachment energy for the *ab* crystallographic plane is reached. This agrees with the PE spectra of tetracene clusters (Fig. 3 of Ref. 1), indicating increase of the detachment energy for small clusters which saturates for about 10 molecules. The results of DFT calculations support, therefore, the conclusions of Ref. 1, namely that for a relatively small tetracene cluster the detachment energy approaches the bulk crystal value.

3. Microelectrostatic calculations

The self-consistent polarization field (SCPF) method [4] was used to calculate polarization energies for an excess charge in tetracene clusters. The SCPF method solves iteratively the problem of local fields and induced dipoles. Given a system of polarizable points (which may be molecules or parts of molecules in submolecule treatment [5]) and external charges, the first approximation of induced dipoles is calculated and used to update local fields. Local fields are then used to obtain a better approximation of the induced dipoles and these steps are repeated until a satisfactory convergence is reached. Final estimates of the induced dipoles are used to calculate the polarization energy. Calculations are performed for systems of increasing size. Such procedure has been applied in the past for calculations of the polarization energy in fullerene microcrystals and polymers [6–9]. It differs from the method described in [4] by omitting the contribution to the polarization energy arising from the dielectric continuum surrounding the system. It is therefore applicable to calculations for microclusters but the polarization energy for bulk crystal may also be estimated by data extrapolation [6]. Microelectrostatic SCPF calculations are also useful for imperfect crystals, as demonstrated by recent calculations on energies of electronic states at grain boundaries in pentacene [10].

The input data necessary for SCPF calculations are the positions of polarizable points (molecules or submolecules) and their polarizabilities.

Polarizability of the tetracene molecule was obtained from quantum-chemical B3LYP/6-31+G** calculations. The polarizability tensor is diagonal in the (*L*, *M*, *N*) molecular axis system* and its α_{LL} , α_{MM} and α_{NN} components read 66.12, 31.03 and

**L* and *M* are the long and middle axis of the molecule, respectively and *N* is the axis normal to the molecular plane.

15.05 Å³, respectively. These values may be compared with the tetracene polarizability tensor extrapolated by Eisenstein and Munn [11] from effective (in crystal environment) molecular polarizabilities of shorter oligoacenes. Quantum chemical calculations predict a larger α_{LL}/α_{NN} ratio (4.39 compared with 2.88 from Ref. [11]), nevertheless the calculated value of the mean isotropic polarizability, i.e. 37.4 Å³, is only a little higher than the value of 36.25 Å³ obtained for the extrapolated effective tensor [11]. The anisotropy of the polarizability is therefore more pronounced for the quantum-chemically computed tensor.

Geometries of the systems (positions and orientations of tetracene molecules) were constructed based on the crystallographic data [3]. Each tetracene molecule was represented as four polarizable points (submolecules) located at the centres of benzene rings. Accordingly, the total molecular polarizability and the excess charge on the molecular ion were equally distributed over the four points, with the standard assumption that the submolecule does not polarize other submolecules belonging to the same molecule [5]. Without such polarizability partitioning, SCPF calculations would not converge. Such problems are related to the large anisotropy of the molecule and the submolecule treatment is necessary for longer oligoacenes, in order to avoid physically unrealistic results [12].

Two series of SCPF calculations were performed. In each series an excess charge was located at the tetracene molecule located in the centre of the cluster. The cluster size was increased either in all three dimensions (3D clusters) or in the *ab* plane only (2D clusters).

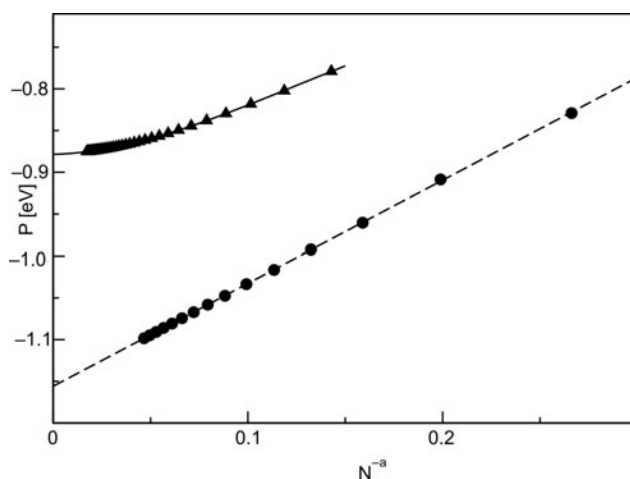


Fig. 3. Dependence of the polarization energy P on the number of tetracene molecules N . Circles – 3D clusters ($a = 1/3$), triangles – 2D clusters ($a = 1/2$). Lines are the best fits to the data (3D – linear, 2D – cubic)

The resulting dependence of the polarization energy P on the number of tetracene molecules N is displayed in Fig. 3. Apparently, the dependence of P on $N^{-1/3}$ is linear and the extrapolation to infinitely large N yields -1.156 eV. As shown in [6], this

value corresponds to the polarization energy for the charge in the bulk crystal. The polarization energy calculated by the Fourier transform method [11] was -1.144 eV; the difference reflects mainly a slight difference in the mean polarizability used in calculations.

Similar extrapolation of P versus $N^{-1/2}$ by cubic regression gives -0.88 eV as the polarization energy for a charge in the infinite ab plane of tetracene crystal. This means that a single layer of tetracene molecules gives rise to about 76% of the polarization energy for the infinite 3D crystal. Such a result is a consequence of crystal structure: the distances between planes are larger than within a plane, which weakens the electrostatic interactions, and although the largest component of the polarizability tensor is oriented roughly perpendicular to the plane, the first effect prevails.

Additional SCPF calculations were performed for a planar cluster of 30 tetracene molecules (as proposed in Ref. 1 Fig. 2b) as well as for such a cluster “sandwiched” between two smaller clusters of 14 molecules, each located in the neighbouring crystal ab planes. For the planar 30-mer, the polarization energy is -0.72 eV, i.e. ca. 82% of the value for an infinite layer and more than 60% of the polarization energy for the bulk crystal. For the system of 14–30–14 molecules, the P value of -0.84 eV was obtained (about 70% of the bulk value). The above results show that in the aggregate of several tens of molecules, a major part of the electrostatic stabilization corresponding to charged molecules in the bulk crystal is reached.

5. Conclusions

Quantum-chemical and microelectrostatic calculations of the stabilization energy for a charge in a tetracene cluster were performed. Both methods show that even in relatively small clusters the stabilization may exceed half the stabilization experienced by a charged molecule in bulk crystal.

The “vertical” total charge stabilization energies obtained in [1] from the photoelectron spectra are -0.74 and -0.94 eV for an infinite 2D layer and an infinite 3D crystal, respectively. SCPF microelectrostatic calculations yield -0.88 eV for the 2D system and -1.16 eV for the bulk crystal. Quantum-chemical calculations of the electron detachment energy provide an estimate of the electron stabilization in a planar layer ca. -0.83 eV. Although the computed values of the stabilization energy are larger than the experimental values, they are of the same order of magnitude and the agreement is surprisingly good taking into account all the approximations made in the calculations.

Theoretical predictions will be supposedly improved at the cost of more detailed or applying higher level of theory calculations. Increase of the basis set in the quantum-chemical calculations will greatly reduce the underestimation of the absolute values of electron detachment energies and, as suggested by some test calculations, will yield a better agreement between the computed and the measured dependence of VDE on the cluster size. In addition, some kind of analysis of the relative stability of tetracene clusters would be desirable. However, as the weak dispersion interactions play an important role in the stabilization of oligoacene molecular crystals, such an analysis

will require a higher level of theory (MP2 calculations) and the computational time will become prohibitive.

In the electrostatic calculations reported in this paper, the charge–quadrupole energy was not taken into account. It has been shown [11] that this interaction reduces the stabilization energy for negative charges in tetracene crystals, therefore when it is included in the SCPF calculations (e.g., by introducing permanent charges located on the atoms) the agreement with experimental estimates is likely to improve. Similar, although not so significant, may be the effect of spreading the polarizability onto more points (e.g. assigning polarizability tensors to individual atoms in the molecule).

To conclude, it has been shown that even approximate theoretical methods can provide a reasonable estimate of changes in the electron stabilization energy upon increase in the tetracene cluster size, and thereby confirm the experimental findings [1]. For a better description more computational effort has to be invested in the calculations.

Acknowledgement

The Gaussian 03 calculations were performed in the ACK Cyfronet Computing Centre (grant No. MNiSW/SGI3700/UJ/043/2008).

References

- [1] MITSUI M., ANDO N., NAKAJIMA A., *J. Phys. Chem. A*, 111 (2007), 9644.
- [2] FRISCH M.J., TRUCKS G.W., SCHLEGEL H.B., SCUSERIA G.E., ROBB M.A., CHEESEMAN J.R., MONTGOMERY J.A. Jr., VREVEN T., KUDIN K.N., BURANT J.C., MILLAM J.M., IYENGAR S.S., TOMASI J., BARONE V., MENNUECCI B., COSSI M., SCALMANI G., REGA N., PETERSSON G.A., NAKATSUJI H., HADA M., EHARA M., TOYOTA K., FUKUDA R., HASEGAWA J., ISHIDA M., NAKAJIMA T., HONDA Y., KITAO O., NAKAI H., KLENE M., LI X., KNOX J.E., HRATCHIAN H.P., CROSS J.B., BAKKEN V., ADAMO C., JARAMILLO J., GOMPERS R., STRATMANN R.E., YAZYEV O., AUSTIN A.J., CAMMI R., POMELLI C., OCHTERSKI J.W., AYALA P.Y., MOROKUMA K., VOTH G.A., SALVADOR P., DANNENBERG J.J., ZAKRZEWSKI V.G., DAPPRICH S., DANIELS A.D., STRAIN M.C., FARKAS O., MALICK D.K., RABUCK A.D., RAGHAVACHARI K., FORESMAN J.B., ORTIZ J.V., CUI Q., BABOUL A.G., CLIFFORD S., CIOSLOWSKI J., STEFANOV B.B., LIU G., LIASHENKO A., PISKORZ P., KOMAROMI I., MARTIN R.L., FOX D.J., KEITH T., AL-LAHAM M.A., PENG C.Y., NANAYAKKARA A., CHALLACOMBE M., GILL P.M.W., JOHNSON B., CHEN W., WONG M.W., GONZALEZ C., POPLE J.A., *Gaussian 03*, Gaussian, Inc., Wallingford CT, 2004.
- [3] ROBERTSON J. M., SINCLAIR V. C., TROTTER J., *Acta Cryst.*, 14 (1961), 697.
- [4] KNOWLES D. B., MUNN R. W., *J. Mater. Sci.: Mat. Electr.*, 5 (1994), 89.
- [5] BOUNDS P. J., MUNN R. W., *Chem. Phys.*, 59 (1981), 47.
- [6] EILMES A., *Synth. Metals*, 109 (2000), 129.
- [7] EILMES A., *Chem. Phys. Lett.*, 326 (2000), 580.
- [8] EILMES A., MUNN R. W., GÓRA A., *J. Chem. Phys.*, 119 (2003), 11467.
- [9] EILMES A., MUNN R. W., *J. Chem. Phys.*, 120 (2004), 7779.
- [10] VERLAAK S., HEREMANS P., *Phys. Rev. B*, 75 (2007), 115127.
- [11] EISENSTEIN I., MUNN R. W., *Chem. Phys.*, 77 (1983), 47.
- [12] BOUNDS P.J., MUNN R.W., *Chem. Phys.*, 44 (1979), 103.

Simulation of ion transport through poly(ethylene oxide) loaded with lithium perchlorate *

R. W. MUNN^{1**}, A. EILMES², S. SCARLE³, M. STERZEL⁴

¹School of Chemistry, University of Manchester, Manchester M13 9PL, U.K.

²Faculty of Chemistry, Jagiellonian University, Ingardena 3, 30-060 Cracow, Poland

³International Digital Laboratory, WMG, University of Warwick, Coventry CV4 7AL, U.K.

⁴Academic Computer Centre CYFRONET AGH, Nawojki 11, 30-950 Cracow, Poland

A hierarchical approach is used to simulate lithium ion motion through poly(ethylene oxide) loaded with lithium perchlorate, alone and with a tungsten oxide (WO_3) interface to model an electrochromic smart window assembly. The structure of the polymer is simulated using commercial software. Relaxation of the polymer is allowed on a lattice on which the lithium ions move as a lattice gas. Polarization and van der Waals energy changes are calculated for an added lithium ion at each lattice point. The structure and energy are also calculated in the presence of the WO_3 interface. Ion transport is simulated in a kinetic Monte Carlo method, with and without an electric field. During runs at 300 K without the WO_3 interface, with a field the lithium ions move 35 Å along it and 3–7 Å across it but without a field they move 2–5 Å; these distances vary with temperature as expected for activated hopping. Ions explore their immediate neighbourhood, occasionally jumping to an adjacent neighbourhood along, across or sometimes against the field, thus circumventing regions where transport is hindered. With the WO_3 , the lithium ions tend to accumulate at the interface, producing a repulsive potential that reduces ion movement.

Key words: *ion transport simulation; lithium perchlorate; poly(ethylene oxide); tungsten oxide; electrochromism*

1. Introduction

Windows are important contributors to the comfort of the occupants of a building but also to the cost of operating the building. Windows admit natural light, which is usually found preferable to artificial light and saves on cost. However, natural light

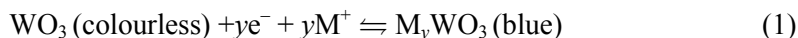
*The paper presented at the 11th International Conference on Electrical and Related Properties of Organic Solids (ERPOS-11), July 13–17, 2008, Piechowice, Poland.

** Corresponding author, e-mail: bob.munn@manchester.ac.uk

may cause glare, and may add significantly to the thermal load on a building, depending on the latitude, climate and season, so increasing the cost of air conditioning. In order to admit maximum light, windows need to be large and thin, but they then provide poor thermal insulation that adds to the cost of heating or cooling to maintain a comfortable temperature inside the building when the temperature outside is much lower or higher.

Advanced glazing improves the balance between cost and comfort [1]. Modern glass can be made with reduced thermal conductivity and coated for high infrared reflectivity. Sealed-unit evacuated double glazing using such glass reduces heat transfer. Significant improvement then requires 'smart windows', with control of the optical behaviour of the glazing which can be achieved by adding an electrochromic thin film confined between transparent electrodes [2]. Changing the electric potential across the electrodes changes the optical transmission through the glazing. For this purpose, the electrochromic material needs to have a large difference in absorption between the colourless and coloured states. It needs to change colour quickly, remain coloured stably, and remain effective over many colouration cycles.

A standard electrochromic material such as tungsten oxide (WO_3) changes colour because the electronic state of the tungsten changes [3]. When this happens, electrical neutrality requires the reduction of the tungsten oxidation state to be balanced by an influx of cations M^+ according to



Commonly lithium ions are the cations, supplied by a polymer electrolyte acting as an ion-storage layer with a suitable counter-anion. The transport of lithium ions through the polymer electrolyte material to the interface with the electrochromic material is then an important factor in the performance of the electrochromic component.

Since it was found that poly(ethylene oxide) (PEO) containing alkali metal salts displayed high ionic conductivity [4], solid polymer electrolytes have been extensively studied. Usually made by dissolving a 1:1 electrolyte in a host polymer, they can be regarded as ionic solutions in a basically immobile solvent. If the lattice energy of the salt is low enough and solvating power of the polymeric solvent is high enough (e.g., via complexation of the alkali cation by oxygen lone pairs on the ether subunits) then a thermodynamically well-defined homogeneous and stable phase can be produced. Such materials have potential applications that include all-polymer high energy batteries, artificial muscles, smart windows and biosensors.

Although classified as solids, these materials can have charge transport mechanisms that are more like those in liquids, and very different from those in inorganic crystals because the polymer host is not rigid, so that chain motion can make an essential contribution to the ion transport. Ion-conducting polymers can therefore be thought of as electrolytes that are intermediate between solids (defect crystals) and liquids (solutions and melts) [5]. Studies of processes in such systems must therefore look at the interplay between the observed properties and the polymer structure. For

example, it was originally thought that the ions moved primarily through the crystalline regions of these polymers [6] but later it became clear that the ion transport was primarily through the amorphous regions [7], where dynamic pathways for Li^+ transport are created [8]. Even crystalline polymers exhibit extensive disorder, and in a non-crystalline phase there is quite well defined short-range order and primary chemical structure but a typical radial distribution becomes featureless after a few repeat distances. Moreover, if the polymer is above its glass temperature, even the average order evolves as the structure relaxes. Hence one need to consider transport of charge in a host medium that undergoes microscopic structural reorganization as the carriers move [9].

Such consideration is complicated by the interaction between the polymer and the mobile lithium ions. The phase is stabilized by the attraction between the lithium ions and the coordinating oxygen atoms, but local segment motion can facilitate ion motion via 'Red Sea events': the polymer moves, opening a void adjacent to an ion, which quickly moves into the void, leaving an equivalent void that closes by further polymer movement [10]. Because amorphous regions of the polymer contain more easily redistributed free volume than crystalline regions, conductivity should be much higher in amorphous regions, and so increasing chain mobility generally increases conductivity [8, 11]. However, coordination with Li^+ tends to reduce the motion of the associated polymer segment, leading to two segment relaxation processes, a slower one for such coordinating segments and a faster one for other segments, as observed [12] in the system poly(vinyl methyl ether)- LiClO_4 . The polymer may also be more actively involved in ion transport if a segment moves carrying with it a coordinated ion, which then transfers to coordinate to another segment or chain, a process we describe as 'octopus football'.

The work reported here forms a part of a project to develop electrochromic evacuated advanced glazing. As explained above, this offers control of solar radiation and high thermal insulation, thereby improving lighting levels and thermal comfort while reducing space heating and cooling loads, electricity demand and carbon dioxide emissions. Our work simulates lithium ion transport through a PEO electrolyte loaded with lithium perchlorate, LiClO_4 . This material exhibits multiple phases: a salt-rich crystalline phase with conductivity appreciable only above 65 °C [13], a pure PEO spherulite crystalline phase, and an amorphous phase with dissolved salt, where the ion conduction primarily takes place [7, 14]. We also study the effect of an interface between the polymer electrolyte and tungsten oxide. For present purposes, the key physical process is transport of a lithium ion to the tungsten oxide interface. Once there, it can be transported into the bulk and participate in the electrochromic colour change, a process being studied separately as another part of this project [15]. However, the tungsten oxide does affect transport of the lithium ion by changing the energetics in the vicinity of the interface.

Our approach is to model all aspects of the system theoretically: the structure, the energetics of the ions in this structure, and the motion of the ions in this energy land-

scape. We adopt a hierarchical approach whereby more phenomenological methods are validated by comparison with methods that are closer to first principles. This makes the treatment relatively economical in terms of computer time, and makes it simple enough to be practicable for screening new candidate electrolyte systems. Even so, we need complicated potentials to model the interactions in our system, and a particular issue is the hierarchy of relaxation processes, from local processes such as changes in bond angle to the movements of whole segments already alluded to. Molecular dynamics (MD) is a preferred method for providing an atomic description of dynamical behaviour, and has been applied to Li^+ in PEO [16], but even with very long computer simulation runs, MD models time periods much shorter than realistic ion transit times. We therefore use a lattice polymer model [17], in which the atoms of the polymer are allowed to move, but only on a relatively coarse grid of points, with the ions moving as a lattice gas on the same grid. The time evolution of the system is then determined by the Monte Carlo (MC) method. For a single atom at site i with energy E_i moving to a neighbouring site j the dwell time t_{ij} is calculated as

$$t_{ij} = -\ln R \exp\left(\frac{E_j - E_i}{kT}\right) \quad (2)$$

where R is a random number uniformly distributed between 0 and 1. The move with lowest dwell time for the atom is carried out, this dwell time is subtracted from all other dwell times, and the energy differences are recalculated.

This paper is organized as follows. We first describe the calculations of the background structure and energetics, which have been presented in detail elsewhere [18]. We then explain how we model the interface between the polymer electrolyte and the tungsten oxide electrochromic material. We simulate the lithium ion transport in this energy landscape and finally draw conclusions from the work.

2. Polymer electrolyte structure

We simulate background polymer electrolyte structures using the Cerius² software package from Accelrys Inc. We have previously shown that for calculating dielectric response [19] and polarization energies [20] in poly(ethylene), this package gives structures equivalent to those given by advanced MD simulations. Here the PEO simulation cell comprised five polymer chains each of 200 ethylene oxide segments, plus 50 lithium ions and 50 perchlorate ions at the density of 1.125 g/cm^3 . This corresponds to loadings in practical electrolyte systems. The structures prepared using the software are relaxed by energy minimization (4000 iterations with the Cerius² Minimizer) and then an MD run (4 ps with a time step 1 fs at constant NVT for $T = 300 \text{ K}$).

The simulation requires a suitable energy function to describe the conformational energy of the polymer, its interactions with the ions, and the interactions among the ions. For the polymer, we have explored the potentials due to Smith et al. [21] and to

Lin et al. [22] but eventually use a slightly extended form of the universal force field (UFF) [23] because it provides a potential that can also be used to model tungsten oxide. The UFF comprises a Morse potential bond stretch term, cosine bond bend and torsional terms, and a Lennard–Jones nonbonding term. In order to keep the tetrahedral geometry of the perchlorate ions with the Cl–O bond length about 1.45 Å, consistent with a study [24] of the ion pairing in LiClO₄, we modify the valence bond radius r_l and angle q^0 in the potential for Cl from the published values (the second and third columns of Table I in Ref. [23]) to 0.792 Å and 109.47° respectively; the obvious alternative of imposing a rigid geometry is not practicable in the approach we adopt. Finally, because our calculation of the motion of a mobile lithium ion depends in an essential way on its energy of which its electrostatic energy is an important component, we supplement the UFF parameters with the partial charges on the atoms shown in Table 1, taken from a previous study of the PEO–LiClO₄ system [25]. To speed up the calculations, we impose a cut-off radius of 6 Å beyond which all long-range potential terms are neglected. However, if during the calculation of the energy differences $E_j - E_i$ an atom initially within this cut-off radius moves outside it, then we retain the atom in the calculation so as to minimize any discontinuity.

Table 1. Atomic partial charges used with the UFF

Atom	Li	Cl	O in ClO ₄	O in PEO	C	H	W	O in WO ₃
Partial charge	1	1.0092	-0.5023	-0.326	0.163	0	2.6	-0.9

The structures show a variety of environments for lithium ions, from an isolated ion surrounded by polymer to small clusters of ions and perchlorate counter-ions in a polymer matrix. The calculated static structure factors are in satisfactory agreement with those obtained from full molecular dynamics simulations and in reasonable agreement with these from experiments on perdeuterated PEO. A lithium ion is typically coordinated to 3–6 atoms on a single PEO chain, close to the cation coordination in crown ethers [26].

3. Energetics of a mobile lithium ion

A key component of the energetics of the ions in the material is their electrostatic energy. This comprises two components. One is the Coulomb energy of interaction between the ion and the other ions and between the ion and the permanent charge distributions of the polymer molecules modelled by the atomic partial charges. The other is the polarization energy between the ion and the changes it induces in the charge distributions of the surrounding molecules. We have described the calculation of the electrostatic energy in detail elsewhere [18]. For present purposes, we require the change in the electrostatic energy on adding a lithium ion, which is in effect the chemical potential.

For the purposes of calculating the ion transport, we superimpose a $100 \times 100 \times 100$ cubic lattice on the simulation cell, corresponding to a lattice spacing of 0.42 \AA . We then calculate the energy of the added lithium ion at every position on this lattice, subject only to the condition that points on the lattice are forbidden if they lie too close to another atom. This amounts to imposing a hard-core repulsive potential. During the simulation the atoms of the polymer are allowed to move on the same lattice to adjust to the ion movement.

4. Effect of interface with WO_3

The tungsten oxide affects the energy of an ion in its vicinity and thereby affects the transport of ions to the interface, through which they must travel as a part of the electrochromic colour change process. There are again two contributions to the energetic difference near the interface. One is the change in the force field near the interface. In order to model this, we use the UFF, because it is capable of describing any element, although we do have to derive some parameters. We add terms to the UFF for W and for O in WO_3 , including the partial charges as shown in Table 1. These are taken from Mulliken analysis of electronic structure calculations for a WO_3 cluster containing 12 W atoms using ADF with BP functionals and a TDZ basis set, taking the atoms nearest the centre of the cluster as best representative of bulk WO_3 .

The other contribution to the energetic difference near the interface is the change in the dielectric properties that govern the electrostatic energy. We have shown previously [27] that this is accurately reproduced up to a few atom spacings from the interface by an image-charge mechanism, taking account of the difference in static electric permittivity between the polymer material and the tungsten oxide. However, it proves inconvenient to use this approach with our method for simulation of the ion motion, and so we model the same contribution by a polarization energy term. To lowest order, the polarization energy between two atoms i and j with polarizabilities α_i and α_j separated by a distance r is given by

$$U_{ij} = -\frac{q_i^2 \alpha_j + q_j^2 \alpha_i}{r} \quad (3)$$

The atomic partial charges and low-frequency polarizabilities for the species in PEO are available in the literature, as is the polarizability of O^{2-} [28], taken as the anion species in WO_3 . By analysing polarizabilities for a series of complex crystalline oxide and fluoride species containing tungsten [29], assuming that their mean polarizability is a simple sum of the polarizabilities of the constituent ions, we derive an average polarizability volume of 4.24 \AA^3 for the cation species W^{6+} .

We break the periodic boundary conditions of our model system along the x direction, and split the system into three regions, the oxide, the real polymer and the ghost polymer, as shown in Fig. 1. The oxide is a WO_3 structure tiled over $x > 0$ with all

atoms fixed as the lithium ion moves. The real polymer extends in the yz plane for a depth of one simulation cell below $x = 0$; its atoms are allowed to move during the simulation, but not into the other regions. Finally, the ghost polymer is a semi-infinite layer of fixed polymer below the real polymer for $x < 0$. Thus we freeze in the bulk configuration of the system except for the layer of polymer adjacent to the interface.

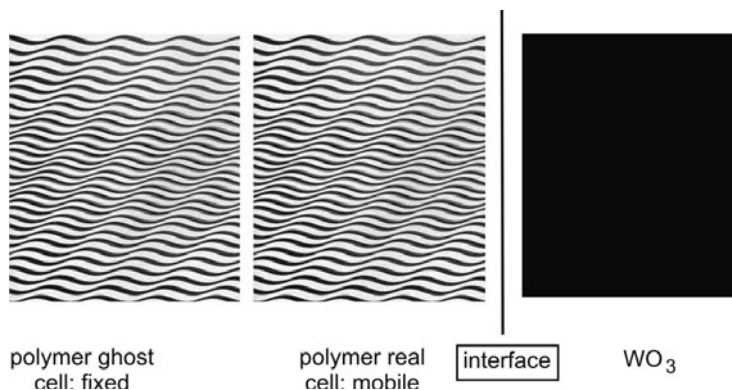


Fig. 1. A scheme showing three regions used in simulating the polymer and the interface to tungsten oxide

5. Simulation of transport

We simulate transport using an n -fold way kinetic Monte Carlo method described in detail elsewhere [30]. Each run comprises 20 000 steps, i.e. 400 for each of the 50 Li^+ ions in the simulation cell, with the structure of the real cell allowed to relax on the superimposed lattice after each move. Simulations are run at temperatures of 250 K, 300 K and 350 K, in zero field or in a field of 100 GV/m in the x direction; such a large field is used in order to achieve significant net motion of the ion during a simulation run of this relatively short duration, but we have verified that the transport remains linear up to this value. We perform simulations for the polymer alone and for the polymer with a tungsten oxide interface.

We find that during runs in the polymer alone, at 300 K in zero field Li^+ ions move 2–5 Å but in the field the ions move 35 Å along the direction of the field and 3–7 Å across it; these distances are higher at 350 K and lower at 250 K, as expected for an activated hopping process. Figures 2 and 3 show plots of the ion mean-square displacement during individual runs for fields in two perpendicular directions. These plots show spikes as an ion moves around exploring its immediate neighbourhood, interspersed with jumps as the ion moves to an adjacent neighbourhood. Jumps along the field are naturally favoured, though jumps across it can also be seen, and Figure 3 shows that jumps against the field are also possible. We have produced movies of ion trajectories that confirm this observation and show how moving against the field al-

lows an ion to circumvent a region where transport is hindered in order to move to a nearby region where transport along the field is easier.

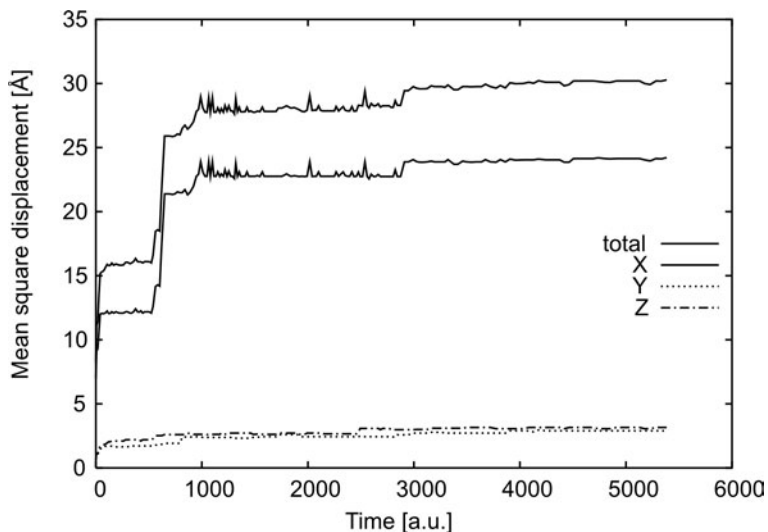


Fig. 2. Mean-square displacement of lithium ions in the polymer alone for a field in the x direction

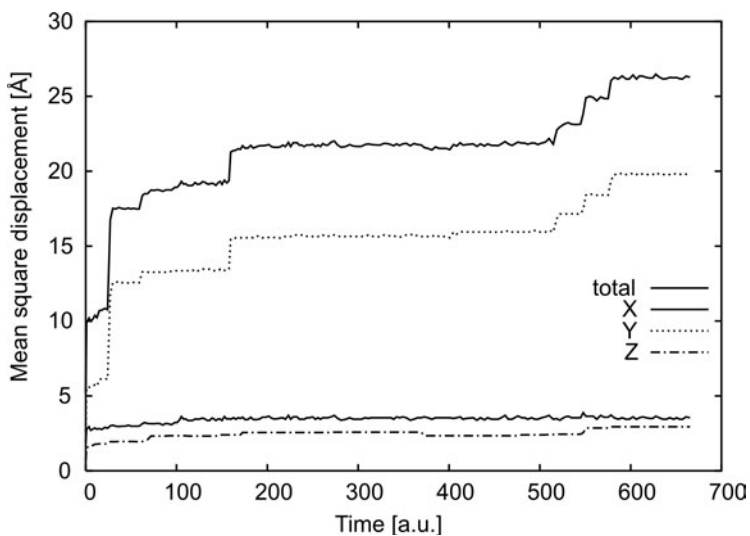


Fig. 3. Mean-square displacement of lithium ions in the polymer alone for a field in the y direction

During runs in the polymer with the tungsten oxide interface, the ions tend to accumulate at the interface. This produces a repulsive potential for lithium ions at the interface, and significantly reduces their overall movement, with mean-square dis-

placements of only 5–6 Å, as shown in Figs. 4 and 5. This finding is consistent with calculations that model the process of lithium insertion into WO_3 films [15], which show that there are energy minima for a lithium ion on either side of the interface, which are of comparable depths when the polymer dielectric constant is included. Depth profiling measurements [31] also show that Li^+ does not readily penetrate into bulk WO_3 .

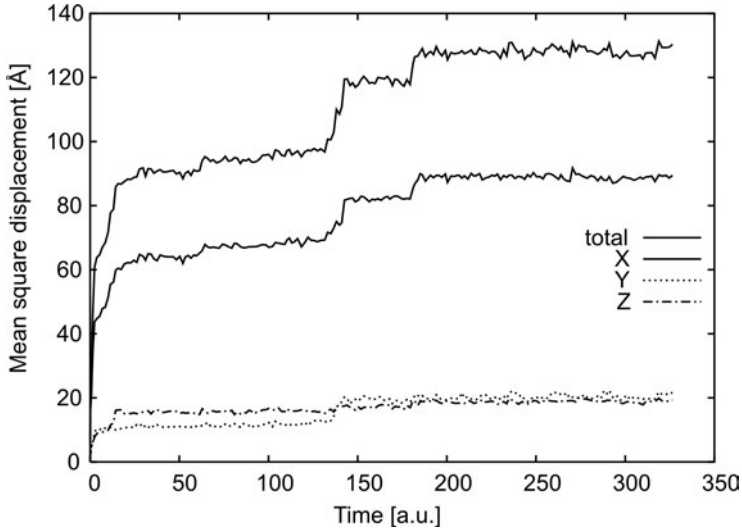


Fig. 4. Mean-square displacement of lithium ions in the polymer with the tungsten oxide interface for a field in the x direction, normal to the interface

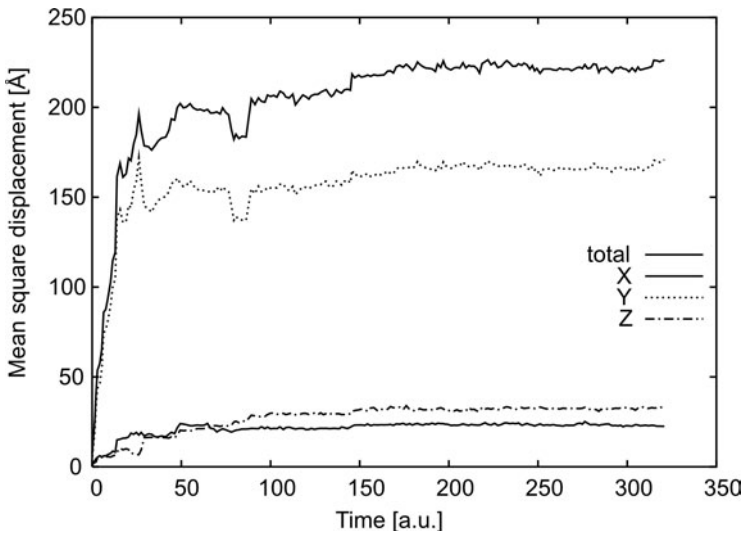


Fig. 5. Mean-square displacement of lithium ions in the polymer with the tungsten oxide interface for a field in the y direction, parallel to the interface

6. Conclusions

We have conducted Monte Carlo simulations of lithium ion transport in the polymer electrolyte system PEO–LiClO₄ both as the bulk material and with an interface to tungsten oxide. The simulations rely on a detailed model of the energetics including the Coulomb and polarization energies of the ions in the material. The picture that emerges is that ions ‘rattle’ in their local energy well, which is allowed to relax on a lattice to accommodate the ion motion, and occasionally ‘hop’ between adjacent wells. The same processes occur in an electric field, where ions may occasionally move against the field.

This shows that two timescales are involved in the motion, consistent with observations of two relaxation times in dielectric relaxation studies on poly(vinyl methyl ether)–LiClO₄ [12]. However, we also expect that ions ‘slide’ between wells on an even longer time scale as the polymer structure deforms; this is essentially the ‘Red Sea event’ mentioned in the Introduction, and corresponds to the microscopic process that underlies the dynamic bond percolation model [32]. Our simulation times are not long enough to show this behaviour, which is a standard problem that arises from the widely differing timescales of different processes in polymer materials. Our approach could be modified to explore these events by fixing the ions in position and allowing the polymer structure to evolve for a number of time steps, after which the ions are again allowed to respond to the new structure, and then repeating the sequence.

Overall, we have provided microscopic insights into the process of lithium ion transport on a realistic model of a practical polymer electrolyte–electrochromic system suitable for applications in glazing. The simulation process is kept simple in order to be practical for relatively routine use, but its various features have been validated against more detailed treatments. The approach is simple enough to be extended to other materials by relatively simple adjustments or computations of input parameters; for example, we have used it to explore the behaviour of systems in which PEO is replaced by variants with short side-chains designed to lower the glass temperature and enhance the ion mobility, and it could be used similarly to investigate the behaviour of systems with enhanced performance in which boronate esters replace PEO [33].

Acknowledgements

This work was funded under the EU FP5 project ELEVAG, reference ENK6-CT-2001-00547.

References

- [1] GRIFFITHS P.W., DI LEO M., CARTWRIGHT P., EAMES P.C., YIANOULIS P., LEFTHERIOTIS G., NORTON B., *Solar Energy* 63 (1998), 243.
- [2] AZENS A., GRANQVIST C.G., *J. Solid State Electrochem.*, 7 (2003), 64.
- [3] PAPAETHIMIOU S., LEFTHERIOTIS G., YIANOULIS P., *Electrochim. Acta*, 46 (2001), 2145; SIOKOU A., NTAIS S., PAPAETHIMIOU S., LEFTHERIOTIS G., YIANOULIS P., *Surf. Sci.*, 566 (2004), 1168.
- [4] FENTON D.E., PARKER J.M., WRIGHT V., *Polymer*, 14 (1973), 589.

- [5] RATNER M.A., *Mater. Forum* 15 (1991), 1, BARIL D., MICHOTT C., ARMAND M.B., *Solid State Ionics* 94 (1997), 35.
- [6] WATSON J.E., STEELE B.C.H., *Solid State Ionics*, 2 (1981), 347.
- [7] BERTHIER C., GORECKI W., MINIER M., ARMAND M.B., CHABAGNO J.M., GIGAUD P., *Solid State Ionics*, 11 (1983), 91; MINIER M., BERTHIER C., GORECKI W., *J. Phys. Chem.*, 45 (1984), 739.
- [8] GRAY F.M., *Polymer Electrolytes*, Roy. Soc. Chem., Cambridge, 1997.
- [9] VINCENT C.A., *Prog. Solid State Chem.* 17 (1987), 145.
- [10] MÜLLER-PLATHE F., LAAKSONEN L., VAN GUNSTEREN W.F., *J. Mol. Graphics*, 11 (1993), 118; SOK R.M., BERENDSEN H.J.C., VAN GUNSTEREN W.F., *J. Chem. Phys.*, 96 (1992), 4699; TAKEUCHI H., *J. Chem. Phys.*, 93 (1990), 2062.
- [11] MEYER K., *Adv. Mater.*, 10 (1998), 439.
- [12] ZHANG S., RUNT J., *J. Phys. Chem. B*, 108 (2004), 6295.
- [13] BRUCE P.G., (Ed.), *Solid State Electrochemistry*, Cambridge Univ. Press, Cambridge, 1997, p. 106.
- [14] *Polymer Electrolyte Reviews*, J. R. MacCallum, C. A. Vincent (Eds.), Vols. 1–2, Elsevier, London, 1987–1989; FAUTEUX D., PRUDHOMME J., HARVEY P.E., *Solid State Ionics*, 28 (1988), 923.
- [15] BROCLAWIK E., GÓRA A., LIGUZINSKI P., PETELENY P., SLAWIK M., *Catalysis Today*, 101 (2005), 155.
- [16] FERREIRA B.A., MÜLLER-PLATHE F., BERNARDES A.T., DEALMEIDA W.B., *Solid State Ionics*, 147 (2002), 361; AABLOO A., THOMAS J., *Solid State Ionics*, 143 (2001), 83.
- [17] DURR O., VOLZ T., DIETERICH W., *J. Chem. Phys.*, 117 (2002), 441; PAUL W., BINDER K., *Polym. Prepr. (Am. Chem. Soc. Polym. Chem. Div.)*, 33 (1992), 535; PAUL W., BINDER K., KREMER K., HEERMANN D.W., *Macromolecules*, 24 (1991), 6332; BASCHNAGEL J., BINDER K., PAUL W., LASO M., SUTER U.W., BATOULIS I., JILGE W., BURGER T. J., *Chem. Phys.*, 95 (1991), 604.
- [18] EILMES A., MUNN R.W., *Solid State Ionics*, 176 (2005), 1861.
- [19] EILMES A., MUNN R.W., MAVRANTZAS V.G., THEODOROU D.N., GÓRA A., *J. Chem. Phys.*, 119 (2003), 11458.
- [20] EILMES A., MUNN R.W., GÓRA A., *J. Chem. Phys.*, 119 (2003), 11467.
- [21] SMITH G.D., JAFFE R.L., YOON D.Y., *J. Phys. Chem.*, 97 (1993), 12752; BORODIN O., SMITH G.D., *J. Phys. Chem. B*, 107 (2003), 6801.
- [22] LIN B.J., HALLEY W., BOINSKE R.T., *J. Chem. Phys.*, 105 (1996), 1668.
- [23] RAPPÉ A.K., CASEWIT C.J., COLWELL K.S., GODDARD III W.A., SKIFF W.M., *J. Am. Chem. Soc.*, 114 (1992), 10024.
- [24] KLASSEN B., AROCA R., NAZRI G.A., *J. Phys. Chem.* 100 (1996), 9334.
- [25] HALLEY J.W., DUAN Y., CURTISS L.A., BABOUL A.G., *J. Chem. Phys.* 111 (1999), 3302.
- [26] BORODIN O., SMITH G.D., *Macromolecules* 31 (1998), 8396; LONDONO J.D., ANNIS B.K., HABEN-SCHUSS A., BORODIN O., SMITH G.D., TURNER J.Z., SOPER A.K., *Macromolecules* 30 (1997), 7151.
- [27] EILMES A., MUNN R.W., *J. Chem. Phys.* 120 (2004), 3887.
- [28] GRIMES N.W., GRIMES R.W., *J. Phys.: Condens. Matter* 9 (1997), 6737.
- [29] SHANNON R.D., *J. Appl. Phys.* 73 (1993), 348.
- [30] SCARLE S., STERZEL M., EILMES A., MUNN R.W., *J. Chem. Phys.* 123 (2005), 154909.
- [31] SIOKOU A., private communication.
- [32] DRUGER S.D., NITZAN A., RATNER M.A., *J. Chem. Phys.* 79 (1983), 3133; DRUGER S.D., RATNER M.A., NITZAN A., *Phys. Rev.* 31 (1985), 3939; RATNER M.A., SHRIVER D.F., *Chem. Rev.*, 88 (1988), 109.
- [33] PENNARUN P.-Y., JANNASCH P., *Solid State Ionics*, 176 (2005), 1849.

Sensoric properties of aromatic and heterocyclic compounds with conjugated bonds^{*}

O. SALYK^{1**}, P. BEDNÁŘ¹, M. VALA¹, J. VYŇUCHAL²

¹Brno University of Technology, Faculty of Chemistry, Purkyňova 118, Brno

²Research Institute of Organic Syntheses, Rybitvi 296, Rybitvi, 533 54, Czech Republic

Dipyridyldiketopyrrolopyrrole and phenylpyridyldiketopyrrolopyrrole were investigated in terms of the effect of acid vapour on their properties, in comparison with diphenyldiketopyrrolopyrrole. Materials were deposited by vacuum evaporation in the form of thin films ca. 100 nm thick. Reversible changes of UV-VIS absorption spectra as well as those of IR absorption spectra when treated with acid vapour were tested. The explanation for the protonation of the ternary nitrogen atom in the pyridyl ring was found. The conductivity measured in a gap electrode arrangement increased by 5 to 6 orders of magnitude. All changes remained stable, unless the sample was regenerated by annealing at 170 °C and the entire process was fully reversible. The compounds exhibit good thermal and chemical stability and are suitable as detector materials in sensors of acids, vapours, and hydrogen.

Key words: *dipyridyldiketopyrrolopyrrole; UV-VIS spectra; IR spectra; conductivity*

1. Introduction

The future expectation of the hydrogen based economy will necessitate a vast demand for devices that operate on hydrogen, including new sensors. The main drawback of modern sensors is the need for extra energy for hydrogen dissociation.

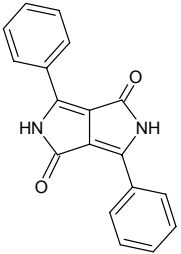
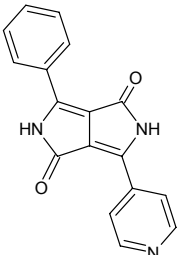
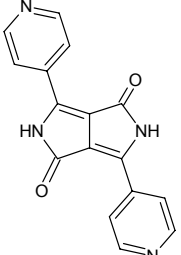
A comparative study of acid protonation of three diketopyrrolopyrrole (DPP) derivatives shown in Table 1 was performed. Derivatives of DPP compounds are widely used as colorants in the paint industry, especially as red pigments for automobile top-coat paints of various tones. The compound 1,4 diketo-3,6-bis phenyl-pyrrolo-[3,4-c]pyrrole (U4), specified also as DPP Scarlet EK (manufacturer Ciba-Geigy, name

^{*}The paper presented at the 11th International Conference on Electrical and Related Properties of Organic Solids (ERPOS-11), July 13–17, 2008, Piechowice, Poland.

^{**}Corresponding author, e-mail: salyk@fch.vutbr.cz

– Iragazin DPP Scarlet EK) [1] or as the pigment Red255, is the simplest, from which the other compounds are derived.

Table 1. Series of investigated compounds with maximum thermal stability T_m

	<p>U4 1,4 diketo-3,6-bis phenyl-pyrrolo-[3,4-c]pyrrole (DPP) diphenyldiketopyrrolopyrrole $T_m > 300$ °C</p>
	<p>U34 1,4 diketo-3-phenyl-6-(4'-pyridyl) pyrrolo-[3,4-c]pyrrole $T_m > 300$ °C</p>
	<p>U35 1,4 diketo-3,6-bis (4' -dipyridyl) pyrrolo-[3,4-c]pyrrole (DPPP) dipyridyldiketopyrrolopyrrole $T_m > 220$ °C</p>

In 1993, Mizuguchi [2] noticed a colour change in the colorant diketo-dipyridylpyrrolopyrrole (DPPP) when the pigment dispersed layer in polymer was prepared at higher temperatures. It was found that traces of protons evolving from the polymer matrix were captured by three-valent nitrogen. A range of organic molecules exist containing three-valent nitrogen atoms with a high proton affinity. In the case of diketopyrrolopyrrole derivatives with pyridyl, piperidyl or a morpholinyl ring, we obtain a pigment that can change colour after protonation [2]. These materials are also semiconductive, thus protonation can influence their conductivity. It has already been observed in the case of a pyridyl derivative [3]. The protonation itself is tested in acid vapours, because in an acid water solvent the shielding effect of water molecules prevents proton penetration to active centres in the DPP film. Protonation in real hydrogen gas is possible only after dissociation of hydrogen molecules. It proceeds on the catalyst surface of a noble metal such as platinum or palladium [3]. The presence of an

electric field promotes hydrogen dissociation, so the clusters of non-conductive catalyst layer between gap electrodes have to be fabricated. The catalyst can be sputtered, evaporated or galvanically electrodeposited using anodic alumina templates [4] or simply spread by Pd nanoparticle suspension.

The mechanism of enhancement of the material conductivity is based on the donor function of a protonated quaternary nitrogen in a pyridyl ring. The electron contributes to the conductivity after hydrogen capture. The process is reversible; thermal hydrogen evolution brings the conductivity back to a low value [5].

2. Experimental

A comparative study of acid protonation of three DPP derivatives shown in Table 1 was performed. The compound U04 (3,6-diphenyl-2,5-dihydro-pyrrolo[3,4-c]pyrrole-1,4-dione) is a commercial pigment. This sample was prepared according to previous work [6]. Synthesis of the derivative U35 (3,6-di-pyridin-4-yl-2,5-dihydro-pyrrolo[3,4-c]pyrrole-1,4-dione) was carried out in compliance with the patent literature [7].

Synthesis of 3-phenyl-6-pyridine-4-yl-2,5-dihydro-pyrrolo[3,4-c]pyrrole-1,4-dione [8–10] (U34 derivative) was carried out as follows: *tert*-amyl alcohol (165 ml) and 3 g (0.13 mol) of metallic sodium were charged into a 500 cm³ flask equipped with a stirrer, a reflux condenser, a thermometer and a nitrogen inlet. Metallic sodium was dissolved under the reflux in the presence of a catalytic amount of FeCl₃ (it takes approximately 2 h), whereupon 6.7 g (0.064 mol) of 4-cyanopyridine was added. After that, 15 g (0.064 mol) of pyrrolinone ester [11] (in small portions) was continuously added over a total time of 15 min. This mixture was stirred and refluxed for 2 h. The reaction suspension of U34 sodium salt was cooled to 60 °C, and 100 cm³ of methanol together with 10 cm³ of acetic acid were added to protolyze it. The dark red suspension was again refluxed for 1 h and then filtrated after cooling to room temperature. The filtrate cake was dispersed in 300 cm³ of methanol and refluxed again for 1 h. The final product was filtrated off, washed with 100 ml of methanol and hot water. Yield: 5.15 g (28%) compound U34. MS analysis of U34 gave $M = 289$; negative ion MS: $m/z = 288 [M + H]^+$, 100%. NMR: ¹H chemical shifts: 11.15 (2H, br. s, NH); 8.84 (2H, m, H-orto Py); 8.55 (2H, m, H-orto Ar); 8.35 (2H, m, H-meta Py); 7.65 (3H, m, H-meta + H-para Ar) ¹³C chemical shifts were not determined, due to a very low solubility of the sample.

Thin films of DPP derivative materials were prepared by vacuum evaporation. The compounds were available in a powder form. Products composed of heterocyclic rings without alkyl chains bonded to the molecule appear to be poorly soluble in organic solvents and they cannot be deposited from solutions. They exhibit, however, good thermal resistance against pyrolysis and can be sublimed. Substrates were selected in the following way: high resistivity silicon wafers were used for FTIR spectroscopy, quartz glass for optical measurement, and glazed alumina plates for electrical gap arrangement. The deposition of the active DPP layer was carried out in a vacuum coat-

ing facility with the ultimate pressure of 1×10^{-4} Pa pumped by a diffusion oil pump. A crystal thin film thickness monitor was used for the deposition control. Thin films of 100 nm thickness were deposited on the selected substrates. The material was pressed into pellets 5.8 mm in diameter and about 1 mm high, typically having the mass of about 30 mg, which was the proper amount for producing a 200–300 nm thick layer without excess waste. The evaporator was home-designed in order to minimize possible decomposition, droplet creation, cluster sputtering, wastage and irradiation damage of the fabricated film. The shape of the molybdenum boat was optimized to focus the irradiation onto the pellet, thus it reduced the required heating power (Fig. 1). This procedure allowed a steady sublimation and deposition rate, without sputtering of bigger clusters or drops, in the case of non-melting material. It also improved ease of manipulation and general cleanliness—no powder was sputtered into a vacuum chamber. The thickness, checked by ellipsometry, was typically 100 nm. The deposition rate was typically 0.2–0.5 nm/s. The 10 μ m gap was fabricated by aluminium contacts deposited by evaporation through a 10 μ m tungsten wire mask. (Fig. 2). Glazed corundum prefabricated substrates with firm gold contact layers for wire soldering and electrical shielding were used.

The samples were then analyzed using a scanning electron microscope (SEM) FEI QUANTA 200. No grain structure was observed at a scale of 50 nm resolution, so the surface appeared uniform. A NICOLET IMPACT 400 FTIR spectrometer was used for scanning IR spectra, and a Varian UV-VIS-NIR spectrometer was used for scanning UV-VIS spectra.

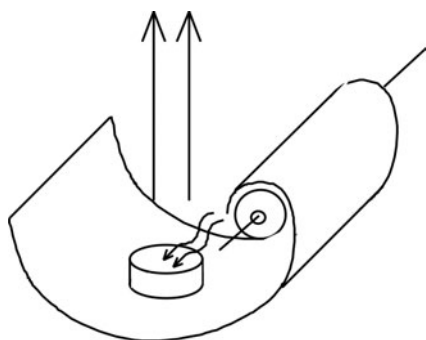


Fig. 1. Vacuum evaporation by radiative heating of the material pressed into a pellet

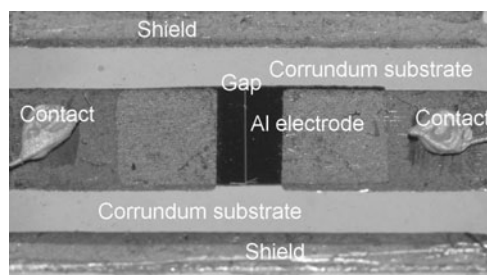


Fig. 2. Samples of DPP gap structure (10 μ m) on a glazed alumina plate with aluminium deposited contacts

3. Results and discussion

The effect of HNO_3 vapour treatment on thin film material was observed in changes of UV-VIS spectra, IR spectra and gap electrical conductivity. The investigated compounds (Table 1) in layers were first placed in a quartz cell and their absorbances in hydrochloric acid were measured. The attempt with acid aqueous solu-

tions of various pH brought only a weak spectral shift in the case of the U35 sample. It is explained by water molecules shielding protons, which means that the protons cannot penetrate into active centres of the film where they could be captured by quaternary nitrogen. Only acid vapours had a significant effect. Nitric and hydrochloric acids produced a very similar effect. Vapours of organic acids such as acetic acid and formic acid were tested and the results were similar but they damaged the layers by dissolving them quickly.

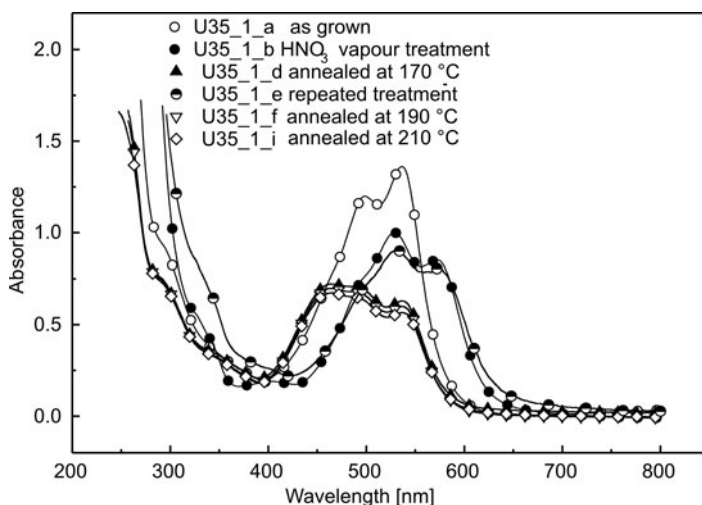


Fig. 3. Layer U-35. Absorption affected by vapour of nitric acid treatment and subsequent annealing

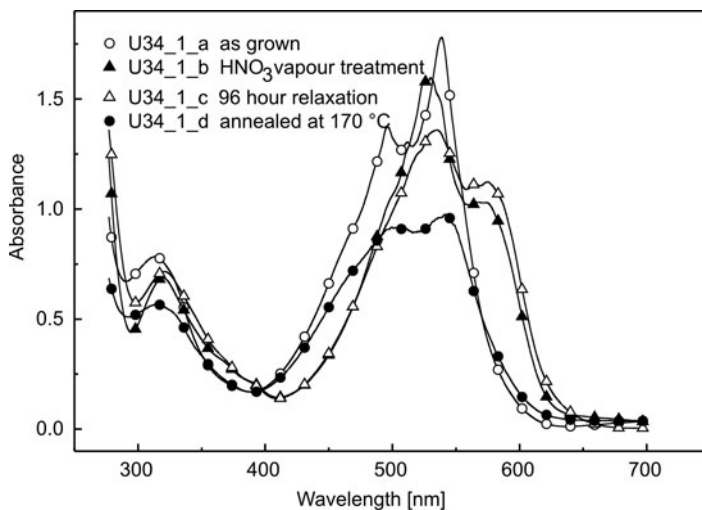


Fig. 4. Sample U34. Absorption affected by vapour of nitric acid treatment and subsequent annealing

Thin film samples of U34 and U35 react, in an etching dish, with HNO_3 vapour by changing their colour from vivid red to violet under the same conditions. A very similar reaction was observed in hydrochloric acid vapour. A U4 sample was taken as a reference with a similar absorption spectrum, where no detectable changes were observed.

Absorption spectra of thin film samples of U4, U34 and U35 on quartz glass substrates in the UV-VIS region were recorded. The results are presented in Figs. 3 and 4. The spectra of U4 sample are not presented, as they did not change in the presence of acid vapour. The effect proves that the quaternary nitrogen in the pyridyl ring is responsible for the absorbance variation. The nitric acid vapour treatment causes irreversible changes in the spectrum, which cannot be removed by the subsequent exposition to air – spectrum (b) in Fig. 3. This means that the acid vapour is firmly bonded and cannot be released at room temperature. Weak absorption decrease can be caused by pinhole damage in the layer or scratching. The annealing to $170\text{ }^\circ\text{C}$ leads to spectrum (d). A certain initial formation is present because the initial, as-grown layer spectrum (a) was not recovered. By repeated treatment and annealing, the recovered spectra switch between (b, d) and (e, f, i) regions and the effect is fully reversible if damages are negligible. Also the shape of the recovered spectrum differs from the initial one (a). This can be explained only by a structure change. The qualitative, permanent change in the U35 case (curves a–i) can be due to crystallographic dimorphism of the compound, as described by Mizuguchi et al. [3] and a change of the ratio of the amounts of the two phases by annealing. All thin films were also observed under a scanning electron microscope. The grain structure of $0.1\text{--}1\text{ }\mu\text{m}$ with regular shapes as well as X-ray diffractograms are the evidence of crystallinity. These results will be presented elsewhere.

Sample U34 (Fig. 4) behaved very similarly, with the exception of a qualitative permanent change: the initial forming equivalent to thinning is observable but does not change the character of the spectrum. The acid treatment represents spectrum (b), the relaxation confirming stability for four days spectrum (c) and annealing change spectrum (d). It was then fully reversible and switched between curve (c) and (d) in Fig. 4 similarly as in the case of U35. X-ray diffractograms as well as the scanning electron microscopy show unimorphism.

The HNO_3 treatment also caused some changes in the IR absorption spectra. First, the U4, U34 and U35 samples were deposited with a thickness of $300\text{--}500\text{ nm}$ on high resistivity silicon substrates. The comparison of their absorbances was related to maximum equal to 1 at 1640 cm^{-1} corresponding to keto-oxygen bond and 1610 cm^{-1} corresponding to N–H bond, which is also called amide II band [12]. These are the strongest absorption bands due to the largest electrical dipole moment in the molecule (Fig. 5). Substitution of the phenyl ring with the pyridyl ring has a slight effect on amide II band shift – single substitution in compound U34 from 1610 to 1595 cm^{-1} and double substitution in compound U35 further to 1585 cm^{-1} . Other bands in the fingerprint region are weak due to smaller dipole moments and do not differ much for all three compounds. Only a small shift to lower energy oscillations with pyridyl substitution is apparent.

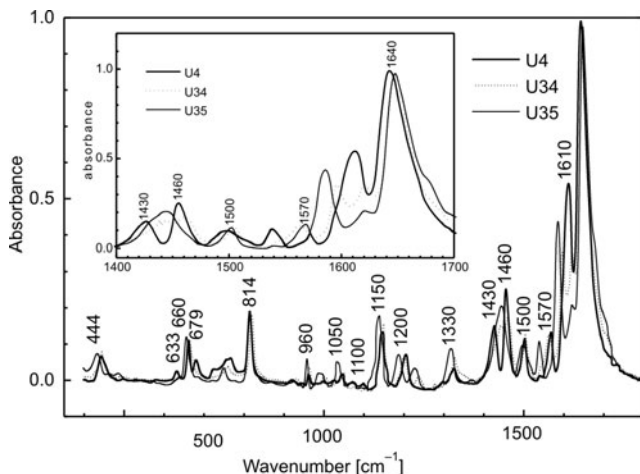


Fig. 5. IR spectra of compounds U4, U34 and U35

HNO_3 treatment of the U4 layer as a reference did not bring any visible changes in the IR spectrum. U34 layer showed significant increase of intensities of vibrational modes at 1320, 1460, 1500, 1530, 1630, and 1680 cm^{-1} as well as layer U35 even more considerable. This is explained by the higher dipole moment of the molecule when an N atom is charged by a proton and the remaining electron is captured in the central part of the molecule. A detailed analysis did not show any shift in the absorbance peak, as is apparent from Figs. 6, 7 but only their growth. This means that the oscillations are strengthened by charge redistribution and hence increase the electrical dipole moment in the molecule. In U35 case there appeared two strong new peaks at 1630 and 1680 cm^{-1} related to protonation which might have included weak peaks or shoulders at U34. This effect is not understood. The protonation – annealing process was fully reversible, as can be seen from the third spectrum scanned after recovery by annealing at 170 $^\circ\text{C}$.

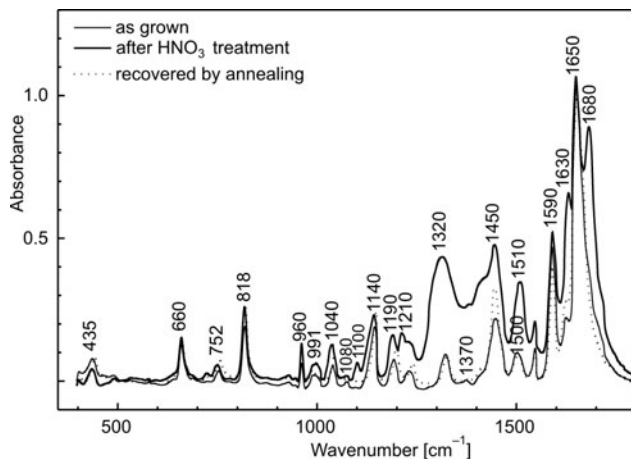


Fig. 6. Influence of HNO_3 treatment on IR absorption of U35 sample

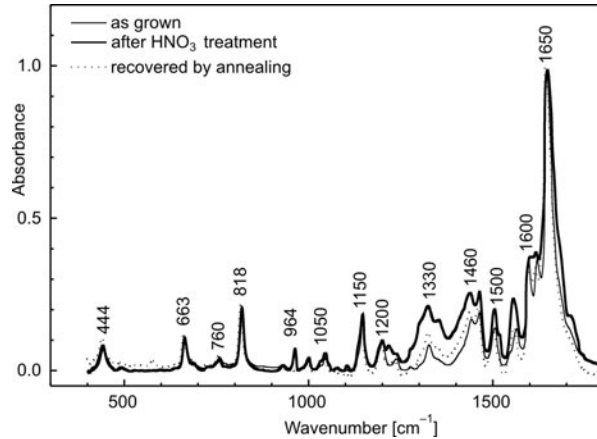


Fig. 7. Influence of HNO₃ treatment on IR absorption of U34 sample

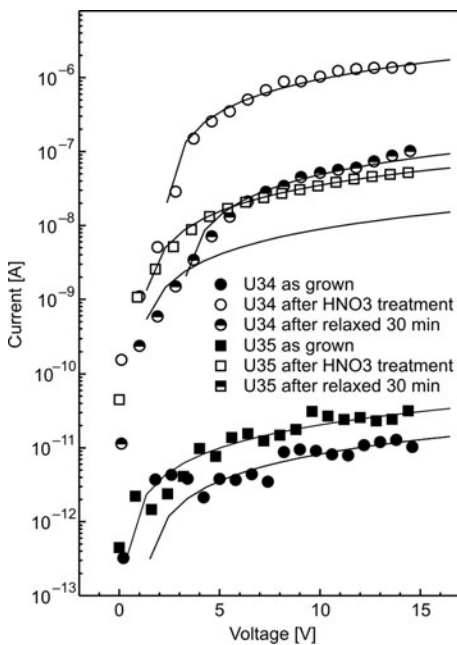


Fig. 8. Effect of HNO₃ treatment on conductivity of U34 and U35 samples

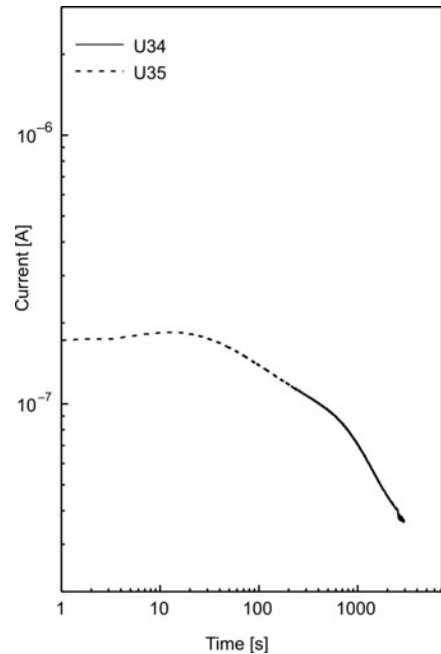


Fig. 9. Relaxation after acid vapour treatment under 4 V of voltage load

The conductivity and photoconductivity of thin films was tested as well since its changes under acid vapour treatment are expected. The measurements were carried out in the surface arrangement of electrodes, the inter-electrode distance amounting to 10 μm and the electrode lengths to 4 mm. The film thicknesses were equal to 100 nm. Voltages up to 15 V have been applied; the resulting current–voltage characteristics

were linear yielding the currents of the order of a few pA in the case of as grown films (cf. Fig. 8). This translates into specific conductivities of the order of $10^{-10} \Omega^{-1} \cdot \text{m}^{-1}$.

Repeated measurements after acid treatment proved irreproducible. The current permanently decreases as can be seen from the curves measured after 30 min relaxation. That is why the current was scanned at a constant applied voltage for a period of 3600 s. The current was found to decrease slow at first, as the carrier would be permanently supplied until exhaustion, and then a more rapid decrease is observed (Fig. 9). It gives evidence of more processes, affecting the current, such as decomposition of NO_3^- ion or quaternary nitrogen in pyridyl. The process is again reversible although small permanent forming changes appeared. No effect of the applied voltage on the relaxation process was observed.

The conductivity of U34 is higher than that of U35. We find it surprising as the U34 molecule has only one functional group. But full bonding saturation in the solid samples can play the role of some ternary nitrogen atoms. The latter could be already saturated by intermolecular interactions and not available for protons.

The explanation of reversible variations of properties proposed by Takahashi and Mizuguchi [2] may have the following explanation: one hydrogen ion from the acid is captured by the nitrogen atom in the pyridyl ring, and the complex salt $(\text{R}-\text{N}-\text{H})^+(\text{NO}_3)^-$ undergoes colour and structure change. The evolution of NO_2 and O_2 is possible as well, while the free electron remains in the material. In the case of dissociated hydrogen, it is presumed the reaction, where instead of $(\text{NO}_3)^-$ ion free electron is created, which contributes to material conductivity.

4. Conclusions

DPP pyridyl derivatives semiconductive organic pigments are able to capture protons in amine groups. HNO_3 vapour treatment offering protons leads to significant optical and electrical changes that are reversible. The dipole moment of the molecule is enhanced and increases the infrared absorption in the region $1230\text{--}1500 \text{ cm}^{-1}$. UV-VIS absorption exhibits significant growth of the absorption at 580 nm and decrease at 470 nm that results in a colour shift from red to violet. Absorption spectrum of the derivatives undergo hypsochromic shift. The protonation releases conductive electrons, thereby enhancing conductivity by orders of 10^{-10} to $10^{-6} \Omega^{-1} \cdot \text{cm}^{-1}$. Other side effect as conductivity, anomalous voltage-current characteristics and time relaxations were observed and will be further investigated. All processes described are reversible; the material can be recovered by annealing at 170°C and repeatedly tested. Relaxation tests indicate the presence of at least two processes with different time constants. It is believed that the studied derivatives can be exploited for the development of new sensing material, especially hydrogen sensing.

Acknowledgement

This work has been supported by the Czech Science Foundation in the projects GACR 203/08/1594 and by the Ministry of Industry and Trade of the Czech Republic via Tandem project No. FT-TA3/048).

References

- [1] SUZUKI E.M., *J. Forensic Sci.*, 44 (1999), 297.
- [2] MIZUGUCHI J., *Ber. Bunsenges Phys. Chem.*, 97 (1993), 684.
- [3] MIZUGUCHI J., TOMOHIKO I., TAKAHASHI H., YAMAMAKI H., *Dyes Pigm.*, 68 (2006), 47.
- [4] KLOSOVÁ K., HUBÁLEK J., *phys. stat. sol. (a)*, 205 (2008), 1435.
- [5] TAKAHASHI H., MIZUGUCHI J., *J. Appl. Phys.*, 100 (2006), 034908.
- [6] VALA M., WEITER M., VYŇUCHAL J., TOMAN P., LUŇÁK S.JR., *J. Fluoresc.*, 18 (2008), 1181.
- [7] ROCHAT A.C., CASSAR L., IQBAL A., US Pat. 4,579,949, (Ciba – Geigy Corporation 1983).
- [8] TAKAHASHI R., YAMAMOTO K., IQBAL A., HAO Z., *Electrophotographic photoreceptor*. Eur. Pat. Appl. (1996), 46 pp. CODEN: EPXXDW EP 718697 A2 19960626 CAN 125:181169 AN 1996:527278 CAPLUS.
- [9] MIZUGUCHI J., IQBAL A., GILLER G., *Preparation of electrochromic diketopyrroles for electrochromic display devices*. Ger. Offen. (1995), 10 pp. CODEN: GWXXBX DE 4435211 A1 19950427 CAN 123:83351 AN 1995:667261 CAPLUS.
- [10] ROCHAT A.C., CASSAR L., IQBAL A., 1, 4-Dioxopyrrolo [3,4-c] pyrroles. Eur. Pat. Appl. (1983), 32 pp. CODEN: EPXXDW EP 94911 A2 19831123 CAN 100:87260 AN 1984:87260 CAPLUS.
- [11] VYŇUCHAL J., LUŇÁK S.JR., HATLAPATKOVÁ A., HRDINA R., LYČKA A., HAVEL L., VYŇUCHALOVÁ K., JIRÁSKO R., *Dyes Pigm.*, 77 (2008), 266.
- [12] WILLIAMS D.H., FLEMING I., *Spectroscopic Methods in Organic Chemistry*, McGraw-Hill, Maidenhead, Berks., UK, 1995.

Received 14 July 2008

Revised 28 November 2008

Modification of gold nanoparticle surfaces with pyrenedisulfide in ligand-protected exchange reactions*

P. UZNAŃSKI**, J. KURJATA, E. BRYZIEWSKA

Centre for Molecular and Macromolecular Studies, Polish Academy of Sciences,
Sienkiewicza 112, 90-363 Łódź, Poland

We provide a study of ligand place-exchange reaction on Au nanoparticles. Nanoparticles of the dimensions of 7–9 nm were fabricated by high-temperature anhydrous route in the presence of primary aliphatic amine. The advantage of weak coordination to gold, through the nonbonding electrons of the amino group, was to use in an exchange of an initial protective ligand. Therefore, among other stabilizing agents, photoactive dialkyldisulfide molecules functionalized with fluorescent pyrene moieties were attached. The photophysical properties of such a stabilized gold system were investigated during place-exchange reaction. Fluorescence studies show that the excimeric band, characteristic of bispyrene, disappears in the spectrum after binding to the gold NPs, indicating that pyrene molecules are adsorbed separately on the surface. Efficient quenching of monomeric emission suggests that deactivation of the fluorescent excited state occurs through a radiationless transition, probably a charge transfer one, formed due to prior electron transfer from pyrene moiety to gold. Kinetics of chemisorption of pyrene disulfide and its desorption in the presence of thiols was also studied, revealing that both processes comprise a fast and a slow component with an overall rate higher for the desorption.

Key words: *gold nanoparticles; ligand exchange; pyrene; functionalization*

1. Introduction

Since the important paper by Brust et al. [1], extensive studies have been carried out on ligand-protected noble metal particles. These investigations include alternative methods for the syntheses of gold nanoparticles (NPs) [2], introduction of chemical functional groups to the particle surface [3], in-place exchange reaction of an original ligand [4–8], controllable NPs arrangements [9], etc. We have recently described a new anhydrous method for the synthesis of gold NPs from triphosphinogold oxon-

*The paper presented at the 11th International Conference on Electrical and Related Properties of Organic Solids (ERPOS-11), July 13–17, 2008, Piechowice, Poland.

**Corresponding author, e-mail: puznanski@cbmm.lodz.pl

ium salt $[O(AuPPh_3)_3]BF_4$ in the presence of amine [10]. This precursor was found to be a versatile gold atom source in mesitylene in the presence of primary amine which, apart from playing a stabilizing role, takes part in the reduction of gold(I) atom. One of the advantages of this route is that primary amines containing long aliphatic chains would be easily exchanged for other functionalized ligands. It is a fundamentally and technologically important aspect as the composition of the stabilizing shell of parent nanoparticles can be modified, hence allowing controllable synthesis of stable nanoparticles with different chemical properties such as solubility or reactivity. Functionalized nanoparticles maintain the dimensions of the original particles and exhibit enhanced resistance to decomposition and aggregation.

For a better understanding of the properties of nanoparticles obtained from gold oxonium salt, we have studied a colloidal stabilization by various ligands and dynamics of ligand exchange on the nanoparticle surface. HDA-protected particles were functionalized by various capping agents being not exposed to the reaction conditions under which the metal particles themselves are formed. We have also employed fluorescence of pyrene as a probe for electronic interactions of the surface-bound organic group with the metal core, due to its special photophysical properties exemplified by a structured emission band sensitive to the polarity of its environment and concentration dependent excimer emission [11].

Luminescence properties of gold–chromophore systems attract increasing attention because of their potential in applications. However, only a few examples of studies have been reported on arrangements, interactions, and photophysical behaviour of ligands with gold core using the fluorescence probe method [7, 8, 12–15]. We have to emphasize that the molecular probe method, apparently, is extremely helpful in studies of ligand motion on nanoparticle surfaces [6, 16].

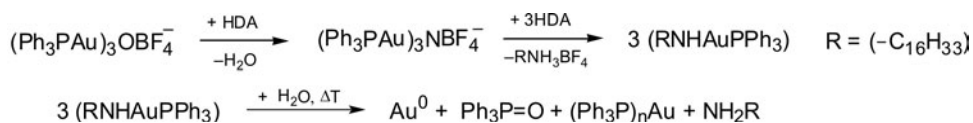
2. Experimental

Materials. 1-Hexadecanethiol (HDT), 1-Hexadecylamine (HDA), 1,8-diaminooctane (diAO), and tetraoctylammonium bromide (TOABr) purchased from Aldrich were used as received. Dichloromethane and toluene, prior to use, were distilled over CaH_2 . Gold oxonium salt $[O(AuPPh_3)_3]BF_4$ was prepared according to previously published methods [17]. Symmetric bispyrene disulfide (diSPy) was synthesized by pyrene bromoalkylation according to the method described in [4], followed by thiol substitution *via* the procedure worked out in [12]. The corresponding thiol was converted to disulphide using the oxidation of thiol, as proposed in [18]. 1H NMR ($CDCl_3$, 200Mz) δ 8.27 (d, 1H, $J = 9.27$ Hz); 8.01 (m, 7H); 7.85 (d, 1H, $J = 6.83$ Hz); 3.32 (t, 2H, $J = 7.53$ Hz), 2.67 (t, 2H, $J = 7.30$ Hz); 1.85 (m, 2H); 1.65 (m, 2H), 1.27 (m, 14H). All other reagents and solvents were used as-received from Aldrich.

Characterization techniques. 1H NMR spectra were recorded with a Bruker Avance AV 200 MHz spectrometer. Absorption measurements were made on a Hew-

lett Packard HP8453 photodiode array instrument and fluorescence spectra were collected with a Perkin-Elmer LS50 luminescence spectrometer in a 1 cm quartz cell.

Synthesis. Gold nanoparticles stabilized with hexadecylamine (HDA) AuNPs-HDA were synthesized in a monophasic system which employs triphosphinogold oxonium salt $[\text{O}(\text{AuPPh}_3)_3]\text{BF}_4$ as a gold atom source (Scheme 1). With a large excess of amine in mesitylene, oxonium salt transforms to gold ammonium salt, which at elevated temperatures and under aerated conditions decomposes into gold neutral atoms and phosphine-gold clusters. Initially, HDA plays the role of a reducing agent but finally the excess amine molecules act as a stabilizing ligand, tightly covering the NPs surface. This propriety of AuNPs-HDA nanoparticles was exploited in in-place ligand exchange reactions. The average size of the NPs is in the range of 7–9 nm. Details of the synthesis and characterization of AuNPs-HDA are given in our previous communication [10].



Scheme 1. Synthesis of hexadecylamine protected gold nanoparticles

Disulfide coated gold nanoparticles AuNPs-diSPy were synthesized by a ligand exchange reaction, with the parent AuNPs-HDA particles at an excess of disulfide. A solution of 5 mg of AuNPs-HDA in toluene (2 cm^3) was mixed with a dichloromethane solution of 2.5 mg of pyrenedisulfide. The reaction mixture was stirred rapidly at $45\text{ }^\circ\text{C}$ for 3 h. Upon completion of the ligand exchange, the solvent was removed under a rotary evaporator. Crude NPs were dissolved in a minimum amount of toluene and purified by repeated precipitation with ethanol ($3\times 6\text{ cm}^3$). The dark blue powder was further characterized by spectroscopic techniques. We have found that the reaction time for diSPy is longer than that for HDT molecules. The obtained NPs were redispersed in dichloromethane for further studies.

3. Results and discussion

3.1. Binding of diamine and ammonium salt to HDA-protected gold nanoparticles

The binding of aliphatic diamine and charged aliphatic ammonium salt to HDA protected gold nanoparticles was studied by UV-vis spectroscopy, taking advantage of the enhanced optical absorption associated with surface plasmon resonance of gold. The plasmon peak of colloidal nanoparticles results from resonant excitations of collective oscillations of conductive electrons in metal with incident light. The position of

this peak depends on the particle size, shape, solvent, and the distance between particles. A solution of the parent AuNPs-HDA nanoparticles was mixed with equivalent amounts of 1,8-diaminooctane or tetraoctylammonium bromide. The temporal evolution of the plasmon band of NPs in CH_2Cl_2 after the addition of diAOc or TOABr is presented in Fig. 1.

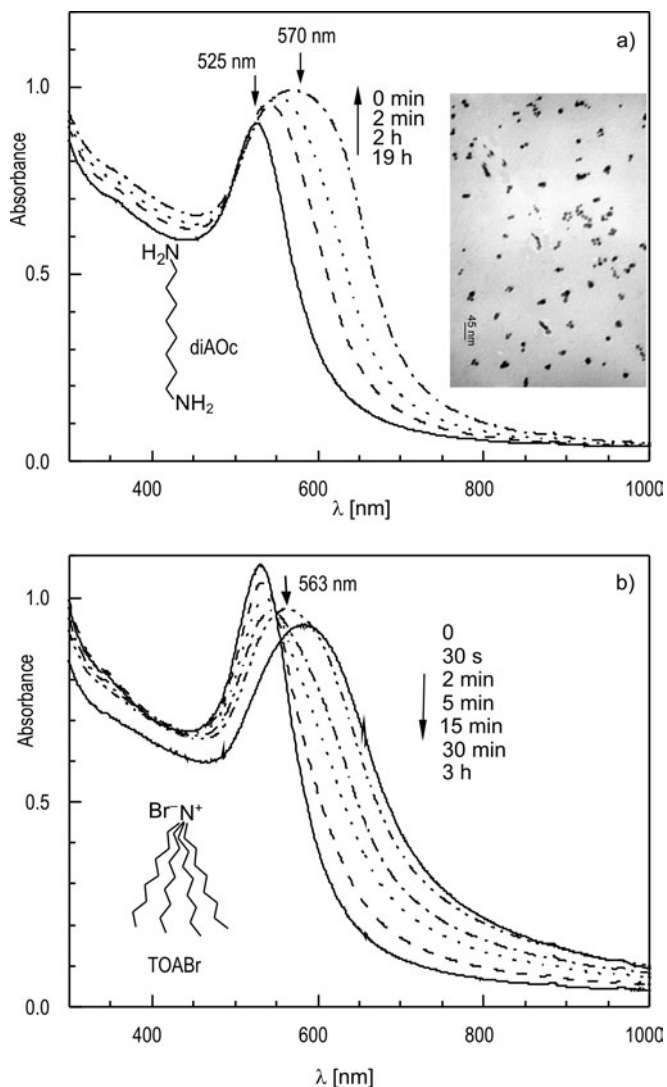


Fig. 1. Temporal evolution of the plasmon band of AuNPs-HDA in CH_2Cl_2 after addition of diAOc (a) and TOABr (b) to gold nanoparticles. The inset shows TEM microphotograph of gold nanoparticles 19 h after addition of 1,8-diaminooctane

The plasmon absorption peak shifts from 525 nm to 570 nm for diAOc and to 563 nm for TOABr, upon ligand exchange. The presence of an isosbestic point on the

blue side of the absorption band (496 nm) for diAOc and at the red side (549 nm) for TOABr indicates that at the early stage of the ligand exchange at least two spectral individuals exist in the colloidal solutions. The quick formation of a second band, which progressively red-shifts while the initial band either remains unchanged (Fig. 1a) or slightly drops in intensity (Fig. 1b) accounts for the aggregation of the starting gold colloid. The observed shift of the plasmon resonance maximum is attributed to near field coupling occurring when the interparticle distance decreases [19]. The smaller the interparticle distance, the larger the red shift is. In fact, in both cases the original long aliphatic chain ligand is replaced by twice as short capping agents. The evolution of absorption bands indicates that exchange of HDA by diAOc is far slower than that of TOABr. It requires at least 15 h and 1 h, respectively, to reach a state where changes in the spectra are negligible.

The time evolution of the plasmon band shows that positively charged groups easily replace amine ligand. This is consistent with the observed trend in reactivity, which reveals that charged ligands generally require considerably shorter reaction times than uncharged ones. On the other hand, an increase in extinction for AuNPs-HDA/diAOc mixture is intriguing. The explanation is provided by a TEM micrograph (inset in Fig. 1a) which indicates that diAOc promotes a special shape of aggregates, in the form of chains consisting of 2-4 linearly ordered gold particles. Unfortunately, the aggregates are not stable enough and after few days finally precipitate from the solution. It means that, upon desorption of HDA, the steric stability of nanoparticles is disturbed and causes irreversible aggregation of colloidal nanoparticles.

3.2. Binding of disulfides and thiols to HDA-protected gold nanoparticles

High stability against aggregation of AuNPs-HDA nanoparticles was observed when amine ligand was exchanged for thiol. Thus HDA-protected gold nanoparticles enable investigations of such a reaction. For its examination, we applied a fluorescence method. As a photofunctionalized dopant for protecting monolayers, we synthesized fluorescent disulfide using commercially available pyrene. The system of HDA capped nanoparticles and the fluorophore offers the possibility to probe the binding of disulfides to nanoparticles through its fluorescence emission. The symmetric pyrene-disulfide molecule itself shows a structured monomer emission band and a distinct intramolecular excimer band in its fluorescence spectrum. This excimer band is evident even at very low concentrations and results from the fixed connection of the two pyrenyl groups.

First, we studied the binding of pyrene disulfide to the particle surface by observing the quenching of pyrene fluorescence. To the solution of diSPy (Fig. 2, curves a) in dichloromethane ($[\text{pyrene}] = 3 \times 10^{-6} \text{ M}$) a drop of concentrated colloid of AuNPs-HDA was added. An instantaneous fluorescence drop was observed due to an inner filter effect (Fig. 2A, dotted line). During the next few hours, a continuous diminution of fluorescence was observed, as was evidenced by a series of emission spectra

and changes in fluorescence intensity at 377 nm. Moreover, we have noticed that the excimer emission peak at 476 nm decreases faster than the monomer one.

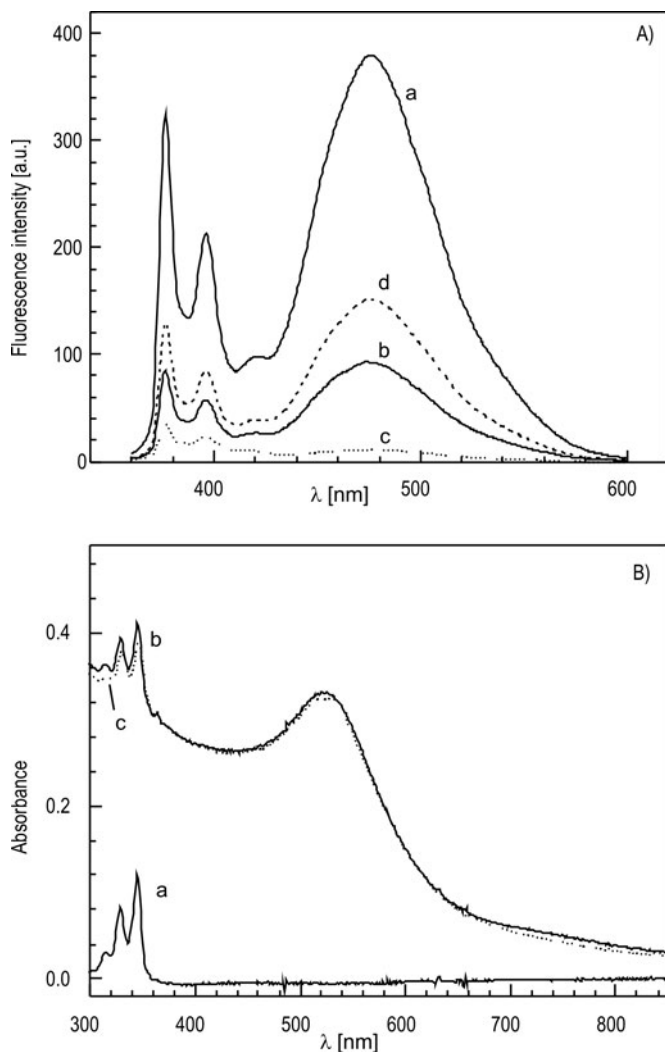


Fig. 2. Fluorescence (A) ($\lambda_{\text{ex}} = 346 \text{ nm}$) and absorption (B) spectra of diSPy in dichloromethane recorded before (a) and after addition of AuNPs-HDA: b – 80 min and c – 22 h. Dashed line (d) represents the spectrum immediately upon AuNPs-HDA addition and shows dropping in fluorescence intensity due to the inner filter effect originating from the gold nanoparticles. Both monomer and broad excimer bands decrease vs. time; $[\text{pyrene}] = 3 \times 10^{-6} \text{ M}$

Initially the intensity ratio I_{476}/I_{377} amounts to 1.18 while after 22 h it drops to 0.33. This result suggests that the two parts of disulfide mainly adsorb independently from each other on the Au particle surface. Similar separation of disulfide moiety was noticed in the EPR study on the nitroxide diradical probe [6]. The reaction of

AuNPs-HDA with diSPy at low concentration produces a similar coverage of the gold surface as the exchange reaction with an excess of pyrene disulfide ($I_{476}/I_{377} = 0.32$, *vide infra*). The absorption spectrum after 1 h of reaction does not superimpose on the absorption spectra of diSPy and AuNPs-HDA nanoparticles and during the exchange reaction it red-shifts and reduces its absorbance by 1.8 times (from 0.127 to 0.071). This indicates an enhancement of interactions between pyrene moieties and the gold core.

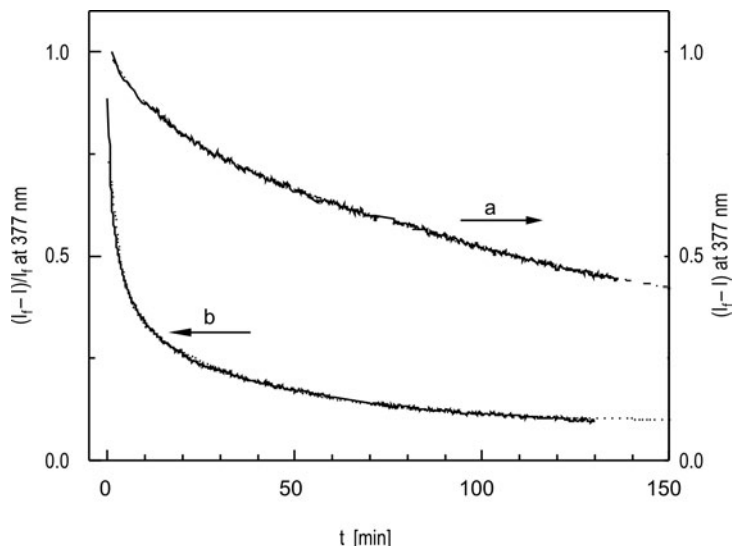


Fig. 3. Kinetics of chemisorption (a) of diSPy to AuNPs-HDA gold surface and its desorption (b) after the injection of 10^{-3} M HDT measured by changes in the fluorescence intensity at 377 nm.

The dotted lines represent fitting with two exponentials

Time dependences of changes of fluorescence intensity at 377 nm normalized to final intensity after complete binding of diSPy to the surface of the NPs are shown in Fig. 3. The exchange reaction, where amine is replaced for disulphide, involves a slow and a fast step. This behaviour can be ascribed to different spots on the NP surface. The fast step takes place at the edges or vertexes, where disulfides can reach gold quite easily. The kinetics slows down in flat domains, where molecules are tightly packed and functionalization takes more time. A similar trend in kinetic exchange processes was previously observed for flat gold substrates [20] and gold nanoparticles [8]. The monomer emission data were analyzed by a double-exponential function. The empirically determined values of characteristic decay times obtained by fitting the fluorescence intensity profiles with a sum of two exponentials

$$I(t) = A_1 \exp(-t/\tau_1) + A_2 \exp(-t/\tau_2)$$

upon chemisorption of diSPy and desorption of SPy from the gold nanoparticles surface are given in Table 1.

Table 1. Characteristic decay times

Observed phenomenon	τ_1 [min]	τ_2 [min]	r_2
Chemisorption of diSPy to Au core ^a	10.7±2	133.5±0.8	0.999
Desorption of SPy from Au core ^a	2.93±0.04	36.40±0.40	0.997
Desorption of SPy from Au core ^b	1.63±0.13	34.40±5.76	0.998

^aPlace exchange reaction on HDA-protected gold nanoparticles.

^bPlace exchange reaction on diSPy-protected gold nanoparticles

On the same sample, we were able to conduct an opposite experiment, namely desorption of pyrene from the gold surface. In the presence of hexadecanethiol, another exchange reaction occurs in colloidal solution, setting pyrene free from gold [8]. As a result, a recovery of fluorescence against time is observed (Fig. 4). However, only the monomeric band undergoes enhancement while the intensity of excimer emission stays at the level before the HDT injection. Two kinetic processes occur with changes in fluorescence intensity with different rates of fluorescence recovery (Table 1). Interestingly, although desorption is faster than chemisorption, there exists a relationship between the time parameters τ_1 and τ_2 for chemisorption and desorption. The ratio τ_2/τ_1 (equal to 12.4) is the same for both samples, similarly as the ratio $\tau_1(\text{chemisorption})/\tau_1(\text{desorption})$, equal to the ratio $\tau_2(\text{chemisorption})/\tau_2(\text{desorption})$ (amounting to 3.7).

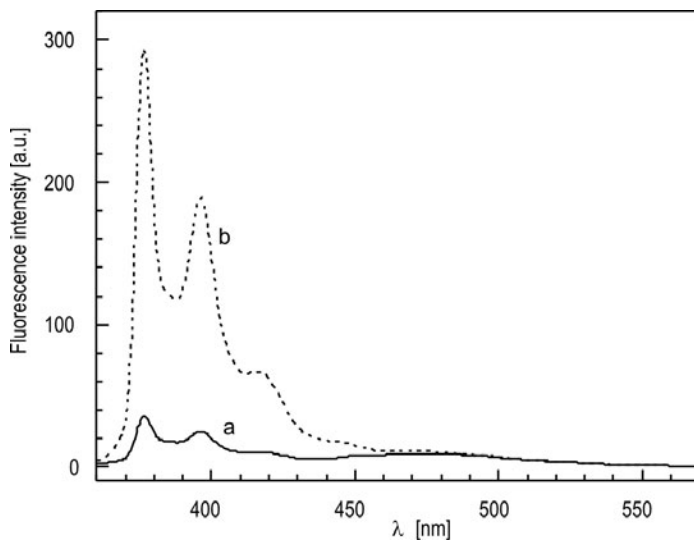
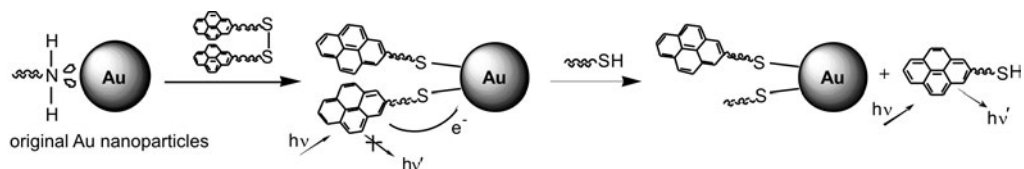


Fig. 4. Time evolution of the emission spectrum ($\lambda_{\text{ex}} = 346$ nm) of a solution of AuNPs-Py in CH_2Cl_2 (a) and after injection of HDT (b). The monomer band increases upon time whereas the excimer band remains fixed

The discussed place exchange reaction of pyrene disulfide on Au nanoparticles directly illustrates S–S bond cleavage on gold, followed by formation of Au–S bonds and finally Au–S dissociation in the presence of a stronger thiolate ligand.



Scheme 2. Mechanism explaining the observed fluorescence from bispyrene disulfide molecules chemisorbed and desorbed from gold NPs surface

The overall mechanism of the fluorescence quenching and enhancement consistent with our observations is schematically presented in Scheme 2. The fluorescence of the pyrene probe gradually diminishes upon its binding and arrangement on the gold surface. Several mechanisms have been considered [21, 22], however for gold particles of dimensions around 10 nm and molecules having more than 4 carbon atoms in the linking chain, fluorescence quenching occurs mainly by electron transfer to the gold NP [12, 15], with the formation of a pyrene radical cation. Upon subsequent HDT addition, fast release of pyrene takes place, which is manifested by the fluorescence enhancement of gold colloid.

3.3. Place exchange reaction on diSPy-protected gold nanoparticles

Starting from purified HDA-capped gold particles in toluene, we synthesized NPs coated with a monolayer of pyrenesulfide by adding an excess of diSPy at elevated

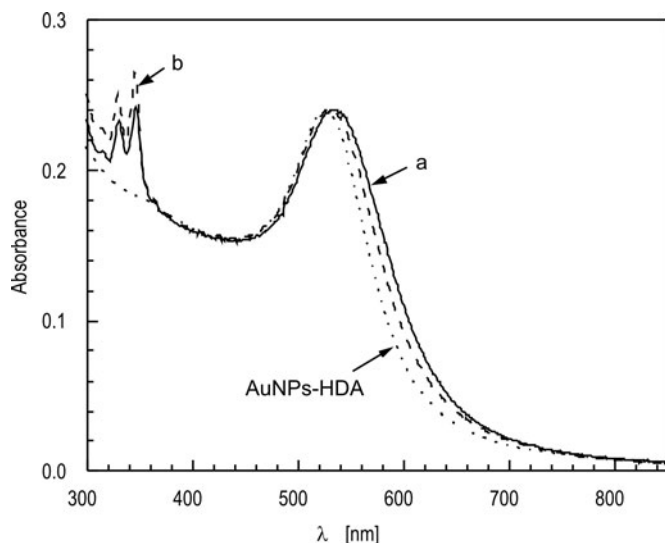


Fig. 5. UV-Vis absorption spectra of AuNPs-diSPy in dichloromethane before (a) and 80 min after (b) addition of 10^{-3} M HDT. The dotted line represents absorption of HDA-stabilized gold nanoparticles

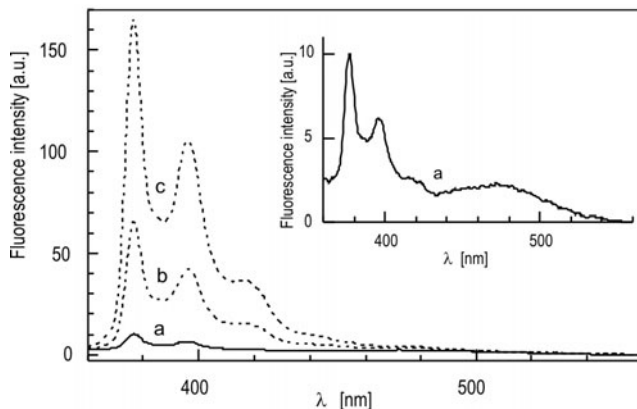


Fig. 6. Fluorescence spectra of pure AuNPs-diSPy nanoparticles (a), and 80 min (b) and 2 days (c) after addition of 10^{-3} M HDT. The inset shows the magnified fluorescence spectrum (a) of the initial colloidal solution

temperature. Such functionalized particles were purified by precipitation using ethanol. The UV-vis spectra of AuNPs-HDA and AuNPs-Py redispersed in dichloromethane are presented in Fig. 5. They display typical pyrene related peaks at 313, 328 and 346 nm, which are slightly broadened and red shifted in comparison with a free pyrene chromophore. The surface plasmon resonance absorption band of thiol-passivated gold nanoparticles has a maximum located at noticeably longer wavelength ($\lambda_{\max} = 534$ nm) as compared to that of the HDA-stabilized particles ($\lambda_{\max} = 525$ nm). This observation is in accordance with the presence of thiols on the gold particle surface. The fluorescence emission spectrum of AuNPs-Py shows similar excimer-to-monomer intensity ratio ($I_{476}/I_{377} = 0.32$), as pyrene modified nanoparticles obtained from AuNPs-HDA and diSPy at 25 °C in CH_2Cl_2 (the inset in Fig. 6.).

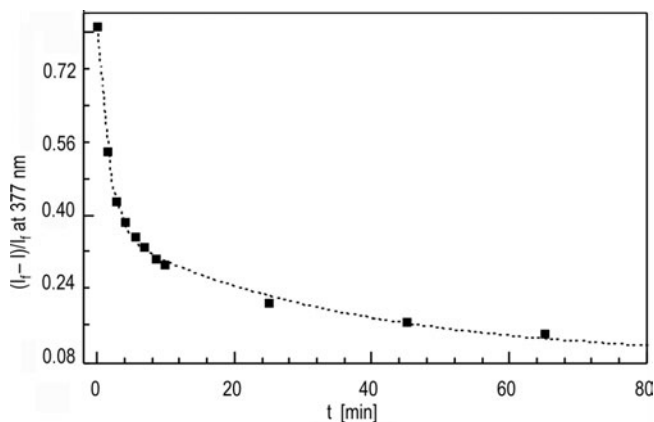


Fig. 7. Kinetics of the relative changes of fluorescence intensity at 377 nm for AuNPs-diSPy colloid after the injection of 10^{-3} M HDT. The dotted line represents fitting with two exponentials

We also attempted to verify whether sample preparation conditions influence the kinetics of ligand exchange reaction [8]. Immediately after the addition of HDT to a colloidal AuNPs-Py solution, similarly as in the previously studied system, an increase in monomer fluorescence intensity is observed. There are no accompanying changes to the intensity of the excimer (Fig. 6). While the monomer fluorescence profile keeps its shape, pyrene absorption peak blue-shifts and increases its absorbance by 1.9 times. Simultaneously the plasmon band shifts to $\lambda_{\text{max}} = 528$ nm, indicating changes in ligand–gold nanoparticle interactions. The kinetics of the ligand exchange reaction is also described by a two step process, as was discussed earlier (Fig. 7). The fast desorption process τ_1 is characterized by slightly faster kinetics, while the slow one has the same decay time τ_2 (Table 1).

4. Conclusions

We have studied place exchange reactions of aliphatic disulfides and thiols on two types of gold colloids. We were able to compare kinetic processes of binding and detachment of pyrene disulfide from a gold surface. First, starting with HDA-protected nanoparticles, we monitored the adsorption of bis-functionalized disulfides by fluorescence quenching of pyrene. After completion of the HDA for diSPy ligand exchange reaction, we studied the kinetics of diSPy for HDT replacing reaction on the same sample. The second colloid were gold nanoparticles, capped with pyrene disulfide prepared in the ligand excess at elevated temperatures. In both cases fluorescence intensity as well as absorption were significantly attenuated upon bonding to NPs as compared with the solution of free diSPy. When pyrene sulfide was displaced by HDT, the opposite effect took place as was evident from the fluorescence enhancement and absorption increase. Another observation was a fixed low efficiency excimer emission of pyrene linked to gold nanoparticles as compared to the bulk solvent. We ascribed this residual emission to a very small fraction of diSPy which may be not subject to S–S bond cleavage on gold.

In the literature, the accepted mechanism for the main deactivation channel of the singlet excited state of pyrene linked to gold with a longer spacer is electron transfer to the gold core [12, 15]. This unexpected result is ascribed to chain flexibility, enabling appropriate arrangement of pyrene moiety and interaction with gold surface. Significant changes in gold plasmon band position cannot be simply explained based on the sulphide for thiol exchange, since the interfacial sulfur and carbon atoms remain the same in both ligands. Our hypothesis is that ω -functionalized sulfides form, opposite to alkanethiolate monolayers, loosely-packed coverage enabling short-distance pyrene–gold interactions through an appropriate geometrical arrangement. This would also explain the attenuated absorbance of pyrene on gold NPs.

Acknowledgement

This work is financed by the Polish Ministry of Scientific Research and Information Technology project No. 3T08E 02228.

References

- [1] BRUST M., WALKER M., BETHELL D., SCHIFFRIN D.J., WHYMAN R., Chem. Comm. (1994), 801.
- [2] LEFF D.V., OHARA P.C., HEATH J.R., LANGMUIR, 12 (1996), 4723; HIRAMATSU H., OSTERLOH F.E., Chem. Mat., 16 (2004), 2509; FLEMING D.A., WILLIAMS M.E., Langmuir, 20 (2004), 3021.
- [3] HOSTETLER M.J., TEMPLETON A.C., MURRAY R.W., LANGMUIR, 15 (1999), 3782; PETROSKI J., CHOU M.H., CREUTZ C., Inorg. Chem., 43 (2004), 1597.
- [4] BOAL A.K., ROTELLO V.M., J. Am. Chem. Soc., 122 (2000), 734.
- [5] WOHRLE G.H., BROWN L.O., HUTCHISON J.E., J. Am. Chem. Soc., 127 (2005), 2172.
- [6] IONITA P., CARAGHEORGHEPOL A., GILBERT B.C., CHECHIK V., J. Am. Chem. Soc., 124, (2002) 9048.
- [7] WERTS M.H.V., ZAIM H., BLANCHARD-DESCE M., Photochem. Photobiol. Sci., (2004), 29.
- [8] MONTALTI M., PRODI L., ZACCHERONI N., BAXTER R., TEOBALDI G., ZERBETTO F., Langmuir, 19 (2003), 5172.
- [9] WRIGHT A., GABALDON J., BURCKEL D.B., JIANG Y.-B., TIAN Z.R., LIU J., BRINKER C.J., FAN H., Chem. Mater., 18 (2006), 183034; UNG T., LIZ-MARZAN L.M., MULVANEY P., J. Phys. Chem. B., 105 (2001), 3441.
- [10] UZNANSKI P., AMIENS A., CHAUDRET B., BRYSEWSKA E., Polish J. Chem., 80 (2006), 1845.
- [11] REYNDEERS P., KUEHNLE W., ZACHARIASSE K.A., J. Phys. Chem., 94 (1990), 4073.
- [12] THOMAS K.G., KAMAT P.V., Acc. Chem. Res., 36 (2003), 888; IPE B.I., THOMAS K.G., BARAZZOUK S., HOTCHANDANI S., KAMAT, P.V., J. Phys. Chem. B, 106 (2002), 18.
- [13] CANEPA M., FOX M.A., WHITESSELL J.K., Photochem. Photobiol. Sci., (2003), 1177
- [14] WANG T., ZHANG D., XU W., YANG J., HAN R., ZHU D., Langmuir, 18 (2002), 1840.
- [15] BATTISTINI G., COZZI P.G., JALKANEN J.-P., MONTALTI M., PRODI L., ZACCHERONI N., ZERBETTO F., ACS Nano, 2 (2008), 77.
- [16] IONITA P., VOLKOV A., JESCHKE G., CHECHIK V., Anal. Chem., 80 (2008), 95.
- [17] BARDAJI M., UZNANSKI P., ANIENS C., CHAUDRET B., LAGUNA A., Chem. Comm. (2002), 598.
- [18] DRABOWICZ J., MIKOŁAJCZYK M., Synthesis, (1980), 32.
- [19] MULVANEY P., Langmuir, 12 (1996), 788.
- [20] LOVE J.C., ESTROFF L.A., KRIEBEL J.K., NUZZO R.G., WHITESIDES G.M., Chem. Rev., 105 (2005), 1103.
- [21] DULKEITH E., RINGLER M., KLAR, T.A., FELDMANN, J., MUÑOZ, JAVIER A., PARAK W.J., Nano Lett., 5 (2005), 585.
- [22] YUN C.S., JAVIER A., JENNINGS T., FISHER M., HIRA S., PETERSON S., HOPKINS, B.; REICC N.O., STROUSE, G.F., J. Am. Chem. Soc., 127 (2005), 3115.

Received 13 July 2008

Revised 26 September 2008

Nonradiative electron and energy transfer. Explicit estimation of the influence of coherent and dephasing processes in a vibrational bath on electronic dynamics*

M. MENŠÍK^{1**}, K. L. KRÁL²

¹Institute of Macromolecular Chemistry, Academy of Sciences of the Czech Republic,
Heyrovský Sq. 2, 162 06 Prague 6, Czech Republic

²Institute of Physics, Academy of Sciences of the Czech Republic,
Na Slovance 2, 182 21 Prague 8, Czech Republic

A theoretical model is studied of the coupling of several electronic states to a vibrational manifold. In this approach, the vibrational manifold is divided into two subbaths. The first one, a coherent subbath, interacts coherently with electronic states. The second one, a thermalizing subbath, is responsible for relaxation of vibronic energy. In the first step, the thermalizing subbath is projected out, under the assumption of a standard (Markovian) approximation in the interaction picture and the effective dissipative Liouville equation for a coherent vibronic system (electronic states + coherent bath modes) is thus obtained. Next, “coherent bath modes” are also projected out and irreversible master equations for electronic degrees of freedom are obtained, even without the Markovian approximation. Analytical expressions based on the double projection technique are compared with numerical simulations of a two-level electronic systems interacting with a single vibrational mode embedded in the dissipative environment. We show that the double projection technique can be applied to predict spikes of resonant amplification of electron (vibronic) energy transfer, as well as to analytically test various models of kinetic theories.

Key words: *electron-vibrational interaction; non-adiabatic coupling; resonant energy transfer; vibrational coherence; excited state decay*

1. Introduction

In the standard theoretical studies of the electronic transitions, vibrational degrees of freedom are projected out and obtained kinetic equations are closed with respect to

*The paper presented at the 11th International Conference on Electrical and Related Properties of Organic Solids (ERPOS-11), July 13–17, 2008, Piechowice, Poland.

**Corresponding author, e-mail: mensik@imc.cas.cz

the relevant degrees of freedom (e.g., electronic states) [1–4]. The influence of the degrees of freedom projected out (e.g., vibrational modes) on the system of interest (e.g., electrons) is mathematically expressed through effective spectral functions controlling rate constants (memory functions) in kinetic equations. If these spectral functions are exact up to second-order in the system–bath coupling, their analytical forms explicitly consist of a weighted sum of delta functions in the frequency domain. Practically, on the other hand, they are alternatively replaced by phenomenological expressions, like Debye’s, Ohmic spectral functions and etc. Physically, it is argued that a vibrational manifold behaves like a heat bath with an implicit auto-thermalization process.

Time-resolved experiments proved, on the other hand, that among vibrational manifolds only a few vibrational modes can retain their coherent character for a longer time, even in the donor-acceptor complexes [5] containing a relatively large number of vibrational modes. Indeed, quantum chemical calculations really proved that often only a few modes have non-zero values of the Huang–Rhys factor or contribute more to the non-adiabatic couplings. Therefore, they keep their coherent character longer than the rest of the modes of a vibrational manifold. Moreover, it was calculated that even in QaAS quantum dot systems, consisting of tens of repeating units, the electronic transfer should be resonantly amplified due to the interaction with longitudinal optical phonons [6]. It seems natural to expect that vibrational modes coupled coherently to electrons should be separated from those that are responsible for the dephasing process due to the anharmonic or Duschinsky couplings.

In the paper, we outline in brief the basics of the so-called double-projection technique where, first, dephasing modes are projected out by means of the standard projection technique and coherent modes are let to develop due to their interactions with electrons and being dephased by the bath of dephasing modes. The obtained kinetic equations for electrons and coherent modes are time irreversible and, in the second step, also coherent modes are projected out. We show that rate constants of electronic transfer thus obtained are directly expressed via parameters of coherent couplings between electrons and vibrational modes (Huang–Rhys factor, non-adiabatic couplings) and relaxation rates of coherent vibrational modes. Consequently, the model thus introduces explicit dependences of the relaxation process, not only with respect to the system–bath coupling but also with respect to the dephasing process in the heat bath. A similar approach may be found, e.g., in Ref. 7. Alternatively, it enables the prediction of critical estimates for various kinetic relaxation theories.

2. The double projection technique

We assume that the systems consisting of electrons and coherent vibrational modes is fully described by the density matrix (statistical) operator $\rho(t)$ that is controlled by the following Liouville equation:

$$\frac{\partial}{\partial t} \rho(t) = -i(L_0 + L^1 + L^{\text{dis}}) \rho(t) = -i \frac{(H_0 + H^1, \rho(t))}{\hbar} - iL^{\text{dis}} \rho(t) \equiv -i(L_{\text{eff}}) \rho(t) \quad (1)$$

Here, $L_0(H_0)$ is the Liouville superoperator (Hamiltonian) of free electrons and vibrations, $L^1(H^1)$ describes their interactions, while L^{dis} controls the impact of the vibrational modes being previously projected out. Formally, we can assume various forms of the dissipative tensors which can be found in the literature (e.g., the Redfield form or diabatic damping approximation (DDA) [8]). The coupling between coherent and dephasing modes may be assumed to be either the Duschinsky coupling or anharmonic coupling, but the Hamiltonian of the system consisting of electrons and coherent vibrational modes is defined as follows

$$H = \sum_j |j\rangle \langle j| (\epsilon_j + \sum_n \hbar \omega_n \left(\frac{Q_n^2}{2} + \frac{P_n^2}{2} \right) + \sum_n \hbar \omega_n D_n^j Q_n) + \sum_{j,k} |j\rangle \langle k| H_{jk}^1(Q) \quad (2)$$

Here, $|j\rangle$ denotes the j -th electronic diabatic state, with local energy ϵ_j . $\hbar \omega_n$ is the vibrational energy quantum of the n -th mode, while Q_n and P_n correspond to the normal vibrational coordinates and momenta of the n -th mode, respectively. D_n^j is the diagonal coupling constant of the n -th mode in the j -th PES. Consequently, the corresponding Huang–Rhys factor is $(D_n^j)^2/2$, and the vibrational binding energy of the n -th mode in the j -th PES equals $\hbar \omega_n (D_n^j)/2$. The interstate interaction (between various PESs) $H_{jk}^1(Q)$ is assumed to be a general function of vibrational coordinates. It is straightforward that the vibronic potential of respective PESs in the Hamiltonian (2) are connected by the following unitary transformation

$$S_j \equiv \exp \left(i \sum_n D_n^j P_n \right) \quad (3)$$

corresponding to the shift of equilibrium positions $Q_n \rightarrow Q_n + D_n^j$. Now, the Hamiltonian (2) can be rewritten to the form

$$H \equiv H_0 + \sum_{j,k} |j\rangle \langle k| H_{jk}^1(Q) = \sum_j |j\rangle \langle j| S_j (\epsilon_j^{\text{R}} + H^{\text{v}}) S_j^+ + \sum_{j,k} |j\rangle \langle k| H_{jk}^1(Q) \quad (4)$$

where ϵ_j^{R} are “relaxed” electronic energies and the vibrational Hamiltonian

$$H^{\text{v}} = \sum_n \hbar \omega_n \left(\frac{Q_n^2}{2} + \frac{P_n^2}{2} \right) \quad (5)$$

corresponds to the unshifted oscillators.

In the following, we will be interested in the occupation probabilities $p_i(t)$ of the i -th potential energy surfaces (PES). Here, $p_i(t)$ is defined as follows:

$$p_i(t) \equiv \text{Tr}_{\text{vib}} \left(\langle i | \rho(t) | i \rangle \right) \quad (6)$$

where $\text{Tr}_{\text{vib}} \left(\langle i | \rho(t) | i \rangle \right)$ means the trace over the vibrational states of the electronic diagonal elements of the total density matrix $\rho(t)$. Probabilities $p_i(t)$ can also be written in the form

$$p_i(t) = \text{Tr}_{\text{vib}} \left(\langle i | P \rho(t) | i \rangle \right) \quad (7)$$

utilizing the projector P defined as

$$P \dots = \sum_i |i\rangle \langle i| \otimes S_i \rho_{\text{vib}} S_i^+ \text{Tr}_{\text{vib}} \left(\langle i | \dots | i \rangle \right) \quad (8)$$

It can be checked by straightforward algebra that the projector P in Eq. (8) also has the following properties

$$P^2 = P \quad (9)$$

$$PL_0 = L_0P = 0 \quad (10)$$

$$PL^1P = 0 \quad (11)$$

Additionally, we assume that the projector P also satisfies the relation

$$PL^{\text{dis}}P = 0 \quad (12)$$

indicating that during the dissipation process the system thermalizes within a given PES. Now, by also projecting out the coherent modes in Eq. (1) we come to the standard Nakajima–Zwanzig equation to get

$$\begin{aligned} \frac{\partial}{\partial t} P \rho(t) = & -iPL_{\text{eff}}P \rho(t) - \int_0^t d\tau PL_{\text{eff}} \exp(-i(1-P)L_{\text{eff}}(t-\tau))(1-P)L_{\text{eff}}P \rho(\tau) \\ & -iPL_{\text{eff}} \exp(-i(1-P)L_{\text{eff}}t)(1-P)\rho(0) \end{aligned} \quad (13)$$

Equation (13) is quite general, but we can simplify it if we utilize Eqs. (9)–(12).

Also, if for the initial condition term we can assume that $\rho(0) = |1\rangle \langle 1| \otimes \rho_{\text{vib}}$, we get

$$P \rho(0) = \rho(0) \quad (14)$$

Then, Eq. (13) will be simplified to the form

$$\frac{\partial}{\partial t} P \rho(t) = - \int_0^t d\tau P (L^1 + L^{\text{dis}}) \exp \left((-i(1-P)(L_0 + L^1 + L^{\text{dis}})(t-\tau)) (L^1 + L^{\text{dis}}) P \rho(\tau) \right) \quad (15)$$

The kinetic equation (15), as it stands, is time-irreversible. The relaxation in the memory function is not introduced assumption based on the thermodynamic limit, as it is done in standard approaches but it is based on the influence of dephasing modes (expressed by L^{dis}) which were projected out earlier, i.e., before constructing the master equation (1). The dissipative tensor L^{dis} can be formally taken in the Redfield form [9] but for the internal summation in the tensor we can approximate the vibronic eigenstates by those of non-interacting diabatic PESs (e.g. [8]). The corresponding dissipative tensor will be then denoted as $L^{\text{dis}(0)}$. Alternatively, we can take a perturbative solution of vibronic states to the first order in the interstate coupling $H_{jk}^1(Q)$ and the corresponding first-order correction in the dissipative tensor would be $L^{\text{dis}(1)}$ [10]. Whence, we would get the following equations

$$PL^{\text{dis}(0)} = L^{\text{dis}(0)}P = 0 \quad (16)$$

$$PL^{\text{dis}(1)}P = 0 \quad (17)$$

Equation (15) can be thus rewritten in the form

$$\frac{\partial}{\partial t} P\rho(t) = -\int_0^t d\tau P(L^1 + L^{\text{dis}(1)}) \exp(-i(L_0 + L^1 + L^{\text{dis}})(t - \tau))(L^1 + L^{\text{dis}(1)})P\rho(\tau) \quad (18)$$

The memory kernel in the last equation is, at least, a second-order one in the interstate coupling. Consequently, if we restrict the kinetic rates just to the second-order in the interstate coupling, we can immediately perform the Markovian approximation because deviations from it would just affect terms of higher order in the expression for the interstate coupling.

An open question here is the convergence of the iteration series in Eq. (18). As will be seen from below, neither the assumption of weak interstate coupling (with respect to the electronic transition energies, i.e., $\langle H_{jk}^1 \rangle \ll |\mathcal{E}_j^R - \mathcal{E}_k^R|$) nor fast decay of the memory kernel is a sufficient condition for the ‘‘second order’’ approach. According to our numerical simulations introduced below, the interstate coupling must be weak with respect to the vibronic transition energies of the active mode, i.e., the system must be in the ‘‘off-resonant limit’’. The analytical expressions below, exact up to the second order in the interstate coupling equation/expression, will be thus derived on the assumption of the ‘‘off-resonant limit’’.

After making the Markovian approximation, we can perform a formal integration of the memory kernel, thus by considering second-order terms in the interstate coupling equation, we directly get:

$$\begin{aligned} \frac{\partial}{\partial t} P\rho(t) \approx & -P(L^1 + L^{\text{dis}(1)}) \left(-i(L_0 + L^{\text{dis}(0)}) \right)^{-1} \\ & \left(\exp(-i(L_0 + L^{\text{dis}(0)})t) - 1 \right) (L^1 + L^{\text{dis}(1)}) P\rho(t) \end{aligned} \quad (19)$$

In the next step, we perform the resolvent expansion of the superoperator $(L^0 + L^{\text{dis}(0)})^{-1}$ and in the total expression we only keep first order terms in the expression for the dissipation

$$\begin{aligned} \frac{\partial}{\partial t} P\rho(t) \approx & -iPL^1(L_0)^{-1} \left(\exp(-i(L_0 + L^{\text{dis}(0)})t) - 1 \right) L^1 P\rho(t) \\ & + iPL^1 L_0^{-1} L^{\text{dis}(0)} L_0^{-1} \left(\exp(-i(L_0 + L^{\text{dis}(0)})t) - 1 \right) L^1 P\rho(t) \\ & - iPL^{\text{dis}(1)} L_0^{-1} \left(\exp(-i(L_0 + L^{\text{dis}(0)})t) - 1 \right) L^1 P\rho(t) \\ & - iPL^1 L_0^{-1} \left(\exp(-i(L_0 + L^{\text{dis}(0)})t) - 1 \right) L^{\text{dis}(1)} P\rho(t) \end{aligned} \quad (20)$$

The master equation (20) contains a contribution from formally different processes. The first term corresponds to gradually decaying coherent Rabi oscillation. The second term is related to the dissipation process controlled due to the DDA [8]. The third and fourth terms correspond to the dissipation process, which incorporates the first order terms of the interstate coupling [10]. If we are finally interested in the decay of the population $p_m(t)$ of the m -th PES we arrive at the equation

$$\frac{\partial}{\partial t} p_m(t) \approx - \sum_k \left((W_{km}^{\text{Rabi}})(t) + W_{km}^{\text{dis}}(t) \right) p_k(t) \quad (21)$$

The rate of the decay of the population $p_m(t)$ is controlled by the rate constant $W_{mm}^{\text{dis}}(t)$, which after time corresponding to the vibrational relaxation in the respective PES can be expressed as

$$W_{mm}^{\text{dis}} = W_{mm}^{\text{dis}}(t \rightarrow \infty) = W_{mm}^{\text{dis}(0)}(t \rightarrow \infty) + W_{mm}^{\text{dis}(1)}(t \rightarrow \infty) \quad (22)$$

with

$$W_{mm}^{\text{dis}(0)}(t \rightarrow \infty) = \text{Tr}_{\text{vib}} \left(\langle m | (L^1 [L_0]^{-1}; iL^{\text{dis}(0)}(L_0)^{-1} L^1) (|m\rangle\langle m| \otimes S_m \rho_{\text{vib}} S_m^+) | m \rangle \right) \quad (23)$$

$$\begin{aligned} W_{mm}^{\text{dis}(1)}(t \rightarrow \infty) = & -\text{Tr}_{\text{vib}} \left(\langle m | (iL^{\text{dis}(1)} L_0^{-1} L^1 (|m\rangle\langle m| \otimes S_m \rho_{\text{vib}} S_m^+) | m \rangle) \right) \\ & -i\text{Tr}_{\text{vib}} \left(\langle m | (L^1 L_0^{-1} L^{\text{dis}(1)} (|m\rangle\langle m| \otimes S_m \rho_{\text{vib}} S_m^+) | m \rangle) \right) \end{aligned} \quad (24)$$

3. Model of two electronic levels coupled to a single vibrational mode

The double-projection technique will be tested on a simple model consisting of coupled two electronic levels with a single vibrational mode. The vibrational mode is also assumed to be embedded in the dephasing bath, so that the system of two electronic levels with a single vibrational mode satisfies Eq. (1). We will solve Eq. (1)

numerically and we get estimates of time dependences of the excited state population $p_1(t)$ by Eq. (6). The dependences of the occupation probabilities are approximated by the following relation

$$p_1(t) \approx A_0 + A_1 \exp(-\Gamma_1 t) + A_2 \exp(-\Gamma_2 t) \cos(\omega_2 t) + A_3 \exp(-\Gamma_3 t) \cos(\omega_3 t) \quad (25)$$

which consists of two decaying Rabi oscillations and a central excited state decay. Formally the Rabi oscillations should include more components but, except for regions having resonant amplification, it can be proved that the approximation with two oscillating components is sufficiently good.

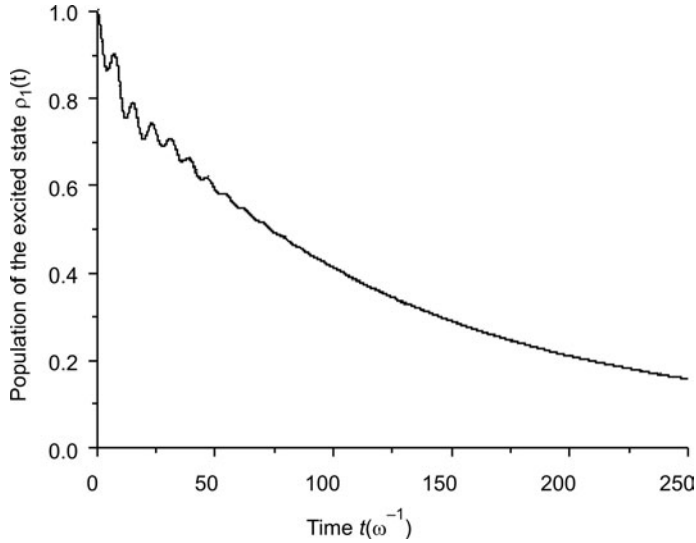


Fig. 1. Time evolution of excited state population $p_1(t)$ for the rate of vibrational relaxation $k = 0.05\omega$ and ratio $r = \varepsilon / \hbar\omega = 1.8$. Calculated values are depicted by the solid curve, while fitted values are depicted by the dotted curve

In Figure 1, the time dependences obtained from the solution to Eqs. (1), (6) cannot be distinguished from those obtained according to Eq. (25). Nevertheless, as we are interested in the decay dynamics, we mainly need to know the parameter Γ_1 , i.e., the rate of decay of the excited state. Numerical estimates obtained from data fitting (Eq. (25)) will be compared with the analytically obtained Eq. (23).

The model Hamiltonian of the relevant electronic-vibrational system is defined as

$$H = |1\rangle\langle 1| \left(\varepsilon + \hbar\omega DQ + \hbar\omega \left(\frac{Q^2}{2} + \frac{P^2}{2} \right) \right) + |2\rangle\langle 2| \hbar\omega \left(\frac{Q^2}{2} + \frac{P^2}{2} \right) + (|1\rangle\langle 2| + |2\rangle\langle 1|) H_{12}^1(Q) \quad (26)$$

The parameters of the Hamiltonian (26) have the same meaning as in Eq. (2). For the interstate coupling, we will assume two cases: constant coupling, i.e., $H_{12}^1(Q) = V$ (a) and linear coupling, i.e., $H_{12}^1 = \Delta Q$ (b). The dephasing mechanism in Eq. (1) will be chosen according to the DDA approach of Ref. [8]. For simplicity, we will parametrize it by the rate of vibrational dephasing k (corresponding to $\gamma(\omega_m)/(4a_m)$ in Ref. 8).

3.1. Numerical solution

The numerical values will be taken from the model of QD in GaAs as in Ref. 6, where the strong coherent coupling of longitudinal optical phonons in the resonant regions was theoretically predicted. Besides that, these parameters are suitable for the illustration of resonant properties in the weak coupling limit. The limiting value of a small Huang–Rhys factor below is taken for the sake of formal analytic simplicity and also to show that strong resonant amplification of the decay of the excited state is also present for small Huang–Rhys factors. However, it is not too difficult to prove analytically that Eqs. (23), (24) can be used for arbitrary values of Huang–Rhys factors if, in particular, a given dependence of the relaxation tensor and interstate coupling with respect to the vibrational displacement, is used. The last statement can be easily understood if we realize that unitary operators (3), formally appearing in Eqs. (23), (24), shift the equilibrium position $Q_n \rightarrow Q_n + D_n^j$ for arbitrary values of the Huang–Rhys factor.

The vibrational energy $\hbar\omega$ will be 36 meV. The electronic separation energy ranges in the interval 25–120 meV. The diagonal coupling constant $\hbar\omega_1 D^1$ ranges from 0 to 11.3 meV. The limiting value 11.3 meV corresponds to the Huang–Rhys factor of 4/81. For the case of constant interstate coupling we set $V = 5.6$ meV, and for the linear model we set $\Delta = 5.6$ meV. We also fixed the room temperature to be $T = 300$ K. The rate of vibrational dephasing k is taken from the weak damping limit up to the limit of the strongly damped oscillator model: $k = 0.03\omega$, $k = 0.05\omega$, $k = 0.1\omega$, $k = 0.2\omega$.

Constant interstate coupling $H_{12}^1 = V$. The numerically calculated dependences of the rate constant Γ_1 on the ratio $r = \varepsilon / \hbar\omega$ of the electronic separation energy ε and vibrational quantum $\hbar\omega$ are shown in Fig. 2. Here we can observe a strong resonant amplification for the resonant condition $\varepsilon = \hbar\omega$ and also weak amplification for the second resonant condition $\varepsilon = 2\hbar\omega$. In this figure, we assumed a very small value for the Huang–Rhys factor $S = 1/50$ (For $S = 0$ we generally get very slow decay, thus we rather took this asymptotically small value of 1/50). The dependences for the increased value of the Huang–Rhys factor $S = 4/81$ are shown in Fig. 3. Again we observe a strong resonant amplification for the first resonant condition $\varepsilon = \hbar\omega$ but also a more pronounced, but still weak, resonant amplification for $\varepsilon = 2\hbar\omega$. In the off-resonant conditions in both figures we observe that the rate Γ_1 linearly increases with the rate of vibrational relaxation k .

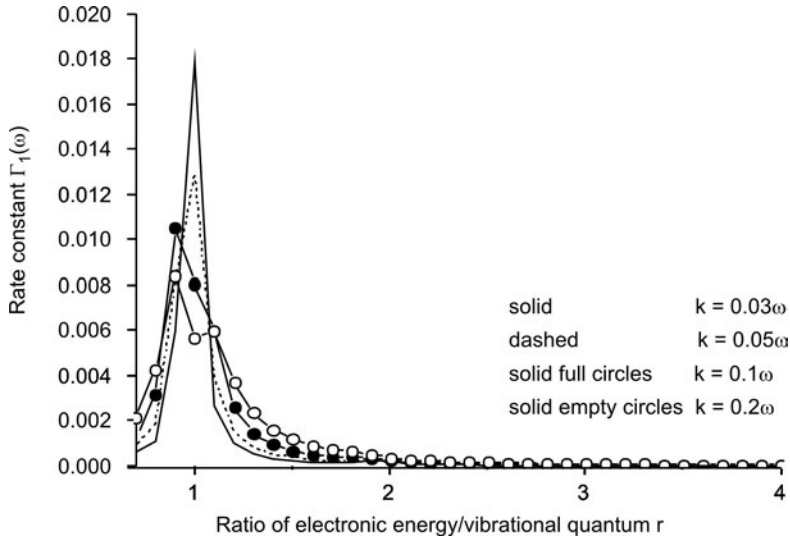


Fig. 2. Dependence of the rate constant Γ_1 of the excited state decay on the ratio $r = \varepsilon/\hbar\omega$ of the electronic excitation energy ε and vibrational quantum $\hbar\omega$. Various rates of vibrational dephasing k are used, while the value of the Huang–Rhys factor $S = 1/50$. The interstate coupling is constant with respect to the vibrational coordinate

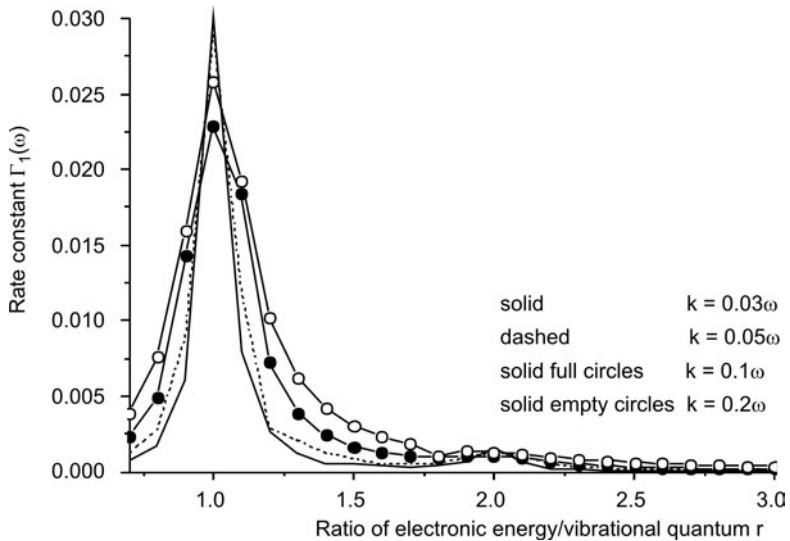


Fig. 3. Dependence of the rate constant Γ_1 of the excited state decay on the ratio $r = \varepsilon/\hbar\omega$ of the electronic excitation energy ε and vibrational quantum $\hbar\omega$. Various rates of vibrational dephasing k are used, while the value of the Huang–Rhys factor $S = 4/81$. The interstate coupling is constant with respect to the vibrational coordinate

Linear interstate coupling $H_{12}^1 = \Delta Q$. In the case of interstate coupling, linear with respect to vibrational coordinate, we get even more interesting dependences. In Fig-

ure 4, we also find a strong resonant peak for $\varepsilon = \hbar\omega$ for the Huang–Rhys factor $S = 0$. Besides that we see that in the region of the first resonant pole $\Gamma_1 \approx k$, i.e. the rate of electronic decay equals the rate of vibrational relaxation.

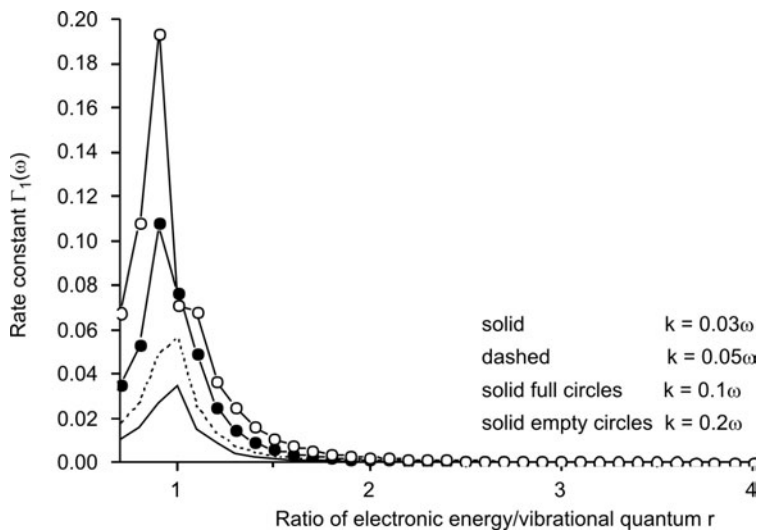


Fig. 4. Dependence of the rate constant Γ_1 of the excited state decay on the ratio $r = \varepsilon/\hbar\omega$ of the electronic excitation energy ε and vibrational quantum $\hbar\omega$. Various rates of vibrational dephasing k are used, while the value of the Huang–Rhys factor $S = 0$.

The interstate coupling is linear with respect to the vibrational coordinate

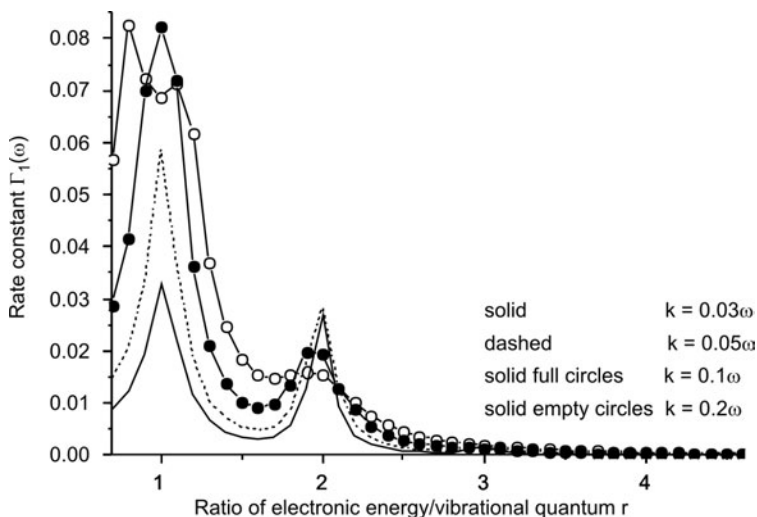


Fig. 5. Dependence of the rate constant Γ_1 of the excited state decay on the ratio $r = \varepsilon/\hbar\omega$ of the electronic excitation energy ε and vibrational quantum $\hbar\omega$. Various rates of vibrational dephasing k are used, while the value of the Huang–Rhys factor $S = 4/81$.

The interstate coupling is linear with respect to the vibrational coordinate

If we increase the Huang–Rhys factor S to the value $4/81$ (Fig. 5), we again find a strong resonant peak for $\varepsilon = \hbar\omega$ and that at this pole $\Gamma_1 \approx k$ (only for $k = 0.2\omega$ peak is broader due to the overdamped oscillator). Furthermore, we find a very strong resonant peak for $\varepsilon = 2\hbar\omega$.

3.2. Analytical results

In this part, we show results of analytical estimates of the rate of electronic decay Γ_1 . It should correspond to the value $W_{mm}^{\text{dis}(0)}$ in Eq. (23). Below we show our results based on the application of the DDA model [8] for the dissipation of the coherent vibrational mode and therefore we utilize Eq. (23). The results taking into account the role of the electronic interstate coupling on the dephasing process in the vibrational manifold will be published elsewhere.

Constant coupling $H_{12}^1 = V$. In the analytical calculation, we perform expansion up to the first order in the Huang–Rhys factor $S = D^2/2$. If we insert the constant interstate coupling and the relaxation tensor [8] into Eq. (23), we get after some algebra

$$\Gamma_1 = (VD^1)^2 k \left[\frac{1}{(\omega_{12} - \omega)^2} + \frac{1}{\omega_{12}^2 - \omega^2} \frac{1 + 2n(\omega)}{1 + n(\omega)} + \frac{1}{(\omega_{12} + \omega)^2} \frac{n(\omega)}{1 + n(\omega)} \right] \quad (27)$$

where $n(\omega) = 1/(e^{\hbar\omega/k_B T} - 1)$ is the Bose-Einstein distribution and $\omega_{12} = \varepsilon/\hbar$ is the transition frequency. Equation (27) confirms our numerical results that in the limit of a small Huang–Rhys factor S there is only one resonant pole at $\varepsilon \approx \hbar\omega$. In the case of strict resonance, Eq. (27) may not be correct because in the case of strong amplification we cannot restrict ourselves just to the second order terms in the interstate coupling. On the other hand, Eq. (27) correctly (in agreement with numerical simulations) predicts the region of the pole $\omega_{12} \sim \omega$ and that it is controlled by the Huang–Rhys factor. For the off-resonant condition, we can expect, on the other hand, a good correspondence at least qualitatively. From Figs. 2 and 3 we directly see the linear increase of Γ_1 with respect to k and $(D^1)^2/2$. Because of the limited scope of this paper, we do not show that in the regions $\hbar\omega_{12} \gg \hbar\omega \gg k_B T$ the dependence $\Gamma_1 \sim 2(VD^1/\omega_{12})^2 k$, stemming directly from Eq. (27), can also be obtained numerically.

Linear coupling $H_{12}^1 = \Delta Q$. Limiting again our calculation just to the first order terms in the Huang–Rhys factor $(D^1)^2/2$ we find that we also get a non-zero electronic decay rate $\Gamma_1^{(0)}$ for the zero values of the Huang–Rhys factor. Namely, we obtain

$$\Gamma_1^{(0)} = \frac{2\Delta^2\omega}{\omega_{12}^2 - \omega^2} \frac{k}{1 + n(\omega)} \left[n(\omega) \frac{2\omega}{\omega_{12}^2 - \omega^2} + \frac{1}{\omega_{12} - \omega} \right] \quad (28)$$

that there is just one pole of resonant amplification $\varepsilon = \hbar\omega$ (cf. Fig. 4). The linear increase with the rate of vibrational relaxation k can be also directly checked in Fig. 4, for the off-resonant condition. In the case of resonance, we cannot conclude from Eq. (28) that $\Gamma_1^{(0)} \approx k$, which confirms again that a finite-series perturbation expansion of the interstate coupling is not acceptable, but rather an appropriate self-energy effects in the denominator could be expected. Besides, we see that for zero values of the Huang–Rhys factor only high frequency modes will contribute to the non-radiative decay of the excited state. In agreement with the numerical simulation, we can see that Eq. (28) correctly predicts the region of the resonant pole $\omega_{12} \sim \omega$ and that it is not necessarily controlled by the Huang–Rhys factor.

Keeping just the linear terms in the Huang–Rhys factor for the rate constant $\Gamma_1^{(1)}$ we arrive at the expression

$$\begin{aligned} \Gamma_1^{(1)} = & \frac{(\Delta D^1)^2}{2} \frac{k}{1+n(\omega)} \left[\frac{1}{\omega_{12}^2 - \omega^2} + \frac{1}{(\omega_{12} - \omega)^2} + \frac{4}{(\omega_{12} - 2\omega)^2} \right. \\ & + n(\omega) \left(\frac{1}{\omega_{12}^2 - \omega^2} + \frac{3(\omega_{12}^2 + 3\omega^2)}{(\omega_{12}^2 - \omega^2)(\omega_{12}^2 - 9\omega^2)} + \frac{2\omega\omega_{12}}{(\omega_{12}^2 - \omega^2)^2} \right) \\ & + \langle n^2 \rangle(\omega) \left(\frac{3}{\omega_{12}^2 - \omega^2} - \frac{3(\omega_{12}^2 + 3\omega^2)}{(\omega_{12}^2 - \omega^2)(\omega_{12}^2 - 9\omega^2)} - \frac{4(\omega_{12}^2 + \omega^2)}{(\omega_{12}^2 - \omega^2)^2} \right) \\ & \left. + \frac{4(\omega_{12}^2 + 4\omega^2)}{(\omega_{12}^2 - 4\omega^2)^2} + n(\omega)^2 \left(\frac{6(\omega_{12}^2 + 3\omega^2)}{(\omega_{12}^2 - \omega^2)(\omega_{12}^2 - 9\omega^2)} - \frac{2}{\omega_{12}^2 - \omega^2} + \frac{4(\omega_{12}^2 + \omega^2)}{(\omega_{12}^2 - \omega^2)^2} \right) \right] \end{aligned} \quad (29)$$

with the second moment of phonon occupation $\langle n^2 \rangle(\omega) = \tanh(\hbar\omega/k_B T)n(\omega)$. In comparison with the previous case, we see a richer structure of resonant poles. Here, we recognize also a strong resonant amplification even for $\varepsilon = 2\hbar\omega$, as is also numerically confirmed in Fig. 5. In the case of the first resonance ($\varepsilon = \hbar\omega$), we again cannot confirm the relation $\Gamma_1^{(1)} \approx k$ directly from Eq. (29). On the other hand, we see that if the self-energy of order $(\Delta D^1)^2/2$ were added to the denominator, we would obtain, for the first resonance, the numerically obtained relation $\Gamma_1^{(1)} \approx k$. Again we can observe that analytical formulae can correctly predict the regions of resonant poles and that in the case of linear interstate coupling, the Huang–Rhys factor can also induce the second resonant pole $\varepsilon = 2\hbar\omega$.

Because of the limited scope of this paper, we do not show that in the limit $\hbar\omega_{12} \gg \hbar\omega \gg k_B T$ the analytical formula (29) corresponds fairly well to numerical simulations. Namely, $\Gamma_1 \sim 3(\Delta D^1 / \omega_{12})^2 k$.

4. Conclusion

The vibrational manifold has been separated into two subbaths. The first one, interacting with electronic states via non-adiabatic coupling and the Huang–Rhys factors, was left in the coherent state. The second one, responsible for the dephasing and relaxation of coherent vibrational modes due to the Duschinsky mixing, was projected out. The resulting equations for the system consisting of electrons and coherent vibrational subbath were time irreversible. In the next step, the coherent subbath has also been projected out and finally equations for the occupation probabilities of electronic states were obtained. In the case of weak interstate coupling and in the off-resonant limit, explicit analytical expressions of the electronic decay rates were found. The latter formulae were expressed through the parameters of coherent electronic-vibrational couplings and the relaxation rates of coherent vibrational modes.

The derived analytical formulae were compared with the numerical solutions of the time evolution of a simple two-level electronic system, coupled to a single vibrational mode attached to the thermalizing subbath. We have found that in comparison with numerical simulations analytical expressions correctly predicted the poles of resonant amplification of electronic transfer.

In the case of the off-resonant limit and a weak interstate coupling, the analytical expressions based on the perturbative approach up to the second-order in the interstate coupling corresponded qualitatively to the numerical results. The agreement between the numerical and analytical second order approach was found for transition electronic frequencies. The latter frequencies were larger by an order of magnitude than the vibrational frequency.

We have also shown that the double projection technique provides an analytic expression for the internal relaxation processes in the bath, i.e. the transfer of excess vibrational energy of coherent modes to the dephasing subbath. It will be published elsewhere that we can even predict analytically whether the interstate coupling should be taken into account in the relaxation process in the vibrational manifold. Or, in other words, under which condition the diabatic damping approximation, or its extension to the first order in the interstate coupling or other models like, e.g. the Lindblad model, are correct.

Numerical simulations in the resonant regions proved that in the case of first resonance, the rate of electronic decay equals the dephasing rate of the coupled vibrational mode.

In the near future, we plan to estimate the cooperative and/or competing of more vibrational modes, particularly in the regions of resonant conditions.

An open problem is the analytical estimation of resonant decay rates and also for a stronger interstate coupling. Here, the theory would have to go beyond the standard approach.

The double projection technique presented here can be utilized for arbitrary values of the Huang–Rhys factors, although the analytical formulae presented here, for the sake of simplicity, were shown just up to the first order in the Huang–Rhys factors.

We conjecture that the theoretical background presented in the paper is applicable for systems like quantum dots, molecular transistors, molecular wires and other systems where charge transfer and excited state decay are important. In particular, in the field of molecular transistors, the subject of non-adiabatic couplings have been almost totally neglected. Our simulations showed that under specific conditions of resonant transfer, the non-radiative decay of electronic states can be of the same order as vibrational dephasing. In future, molecular systems embedded between two contacts should take into account the vertical electronic transfer.

Acknowledgement

This work was supported by the grant No. 202/07/0643 of the Czech Science Foundation, and also by the grant KAN401770651 of the Grant Agency of the Academy of Sciences of the Czech Republic and by the institutional project AVOZ10100520.

References

- [1] NAKAJIMA S., *Progr. Theor. Phys.*, 20 (1958).
- [2] ZWANZIG R., *J. Chem. Phys.*, 33 (1960), 1338.
- [3] HASHITSUME N., SHIBATA F., SHINGU M., *J. Stat. Phys.*, 17 (1977), 155.
- [4] TAKAHASHI Y., SHIBATA F., HASHITSUME N., *J. Stat. Phys.*, 17 (1977), 171.
- [5] RUBTSOV I.V., YOSHIHARA K., *J. Phys. Chem.*, 103 (1999), 10202.
- [6] KRÁL K., ZDENĚK P., *Physica E* 29, (2005), 341.
- [7] MAY V., *Physical Rev. B*, 6 (2002), 245411.
- [8] KÜHN O., MAY V., SCHREIBER M., *Chem. Phys.*, 101 (1994), 10404.
- [9] REDFIELD A.G., *Magn. Res.*, 1 (1965), 1.
- [10] KLEINEKATHÖFER U., KONDOV I., SCHREIBER M., *Chem. Phys.*, 268 (2001), 121.

Received 14 July 2008

Revised 19 September 2008

Thin protein LB films as functional components within biosensors *

J. CABAJ^{1**}, A. CHYLA², J. SOŁODUCHO¹

¹Faculty of Chemistry, Wrocław University of Technology,
Wybrzeże Wyspiańskiego 27, 50-370 Wrocław, Poland

²Institute of Physical and Theoretical Chemistry, Wrocław University of Technology,
Wybrzeże Wyspiańskiego 27, 50-370 Wrocław, Poland

Biomolecules can often be incorporated and immobilized into Langmuir–Blodgett (LB) films by using covalent immobilization of proteins with glutaraldehyde. Laccase from *Cerrena Unicolor* was incorporated into an LB film deposited on a glass substrate. The samples fabricated in such a way can be used for the detection of phenolic compounds. The function of enzyme immobilization was carried out by glutaraldehyde added to a film of stearic acid and laccase. The sensor sensitization was achieved by an amphiphilic *N*-alkyl-bis(thiophene)diphenylamine admixed into the film. The interlaced diphenylamine derivative was expected to facilitate the electron transfer thereby enhancing the sensor sensitivity.

Key words: *Langmuir–Blodgett films; laccase; diphenylamine derivatives; biosensor; AFM*

1. Introduction

For years Langmuir monolayers and Langmuir–Blodgett films of pure molecules or biomolecules embedded into organic matrices have been used to investigate molecular processes as well as to facilitate biosensing [1–5].

An effective use of enzymes widely applied for this purpose may be hampered by some peculiar properties of enzymatic proteins such as their non-reuseability, high sensitivity to denaturing processes, and the presence of agents blocking active centres of proteins. Many of these undesirable constraints may be avoided by the immobilization of enzymes. Immobilized enzymes appeared to be more useful in all catalytic processes than unbounded proteins. In measurements of electrical properties of enzymes exhibiting direct electron transfer to electrode surface, the orientation, organisation are parameters of utmost relevance. Several strategies have been employed to

*The paper presented at the 11th International Conference on Electrical and Related Properties of Organic Solids (ERPOS-11), July 13–17, 2008, Piechowice, Poland.

**Corresponding author, e-mail: joanna.cabaj@pwr.wroc.pl

immobilize biological compounds such as physical adsorption on graphite or on polymer matrices, covalent or electrostatic attachment to a electrochemically modified carbon surface and to self-assembled monolayers [6]. Here, advantage can be taken of the molecular control provided by the Langmuir–Blodgett (LB) technique, in which suitable orientations of biomolecules are possible to achieve.

The LB technique allows control of the thickness of the film deposited on a surface and is therefore well suited for the fabrication of both mono- and multilayer structured films. Such films could provide a simple foundation for the construction of various types of chemical, electrochemical and biological sensors. Few reports appeared on this subject; an ordered arrangement of glucose oxidase and ferrocene on a platinum electrode has been obtained by the LB technique [7]. In this paper, the fabrication of a biosensing LB layer is described built of laccase, cross-linked with glutaraldehyde.

Laccases (EC 1.10.3.2) are multicopper oxidases widely distributed in plant and fungal species. They have received particular attention due to their rather low substrate specificity and due to ability to oxidise phenols, anilines, benzenethiols, phenothiazines with the concomitant reduction of molecular oxygen to water. Laccases are mainly used in the paper and textile industries, for wastewater treatment, delignification and dye bleaching [8]. They also found application in biofuel cell technology. Laccase-based biosensors, in the absence or in the presence of mediators, have been applied for the determination of a broad range of phenolic species [9].

Generally, a mediator could be a sort of ‘electron shuttle’ that, after being oxidised by the enzyme, diffuses away from an active site to oxidise any molecule that, because of its size, cannot enter the enzymatic pocket directly. In addition, the oxidised form of the mediator, being structurally ‘diverse’ from the enzyme, might undergo a different mechanism of oxidation, thereby extending the range of substrates susceptible to the enzymatic action [10, 11]. Also, another type of the mediating agent, especially easily incorporated into LB film conducting polymers and monomers has been extensively studied due to its improving sensing effect of the sensor. For example, poly-3-dodecyl thiophene which, when mixed with stearic acid, is a suitable matrix for the deposition of glucose oxidase, retains its electroactivity and detects glucose [12].

Continuing our interest in the of precursors of conducting and sensing materials [4], we covalently immobilized laccase from *Cerrena Uicolor* into LB film deposited on a substrate. The system can be used for detection of phenolic compounds. The function of enzyme cross-linking was carried by glutaraldehyde (GA). Moreover, sensor sensitisation was achieved by an amphiphilic, conducting *N*-alkyl-bis(thiophene)-diphenylamine [13] admixed into the film. The interlaced diphenylamine derivative as expected facilitates the electron transfer and therefore enhances the sensor sensitivity.

2. Materials and methods

Materials. Prior to the deposition of LB films, the substrates were washed according to a standard procedure, followed by sonication in detergent (1% solution of DE-

CON 90), rinsing with deionized water, etching in an ethanolic solution of KOH (Yirayama solution) to make them hydrophilic. An amphiphilic 4,4'-bis(thiophene)-*N*-nonyldiphenylamine (DFTA9, Fig. 1) was synthesized according to the procedure described earlier, using a multi step method, in which the main point was the Stille coupling reaction [13]. Laccase (from *Cerrena unicolor*) was isolated and purified by the standard method [14, 15], whereas 2,2'-azino-bis(3-ethylbenzthiazoline-6-sulphonate, ABTS), catechol (all supplied by Aldrich) were used as- received.

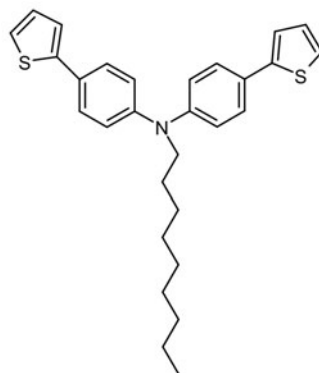


Fig. 1. The structure of 4,4'-bis(thiophene)-*N*-nonyldiphenylamine

Method. The Langmuir and Langmuir–Blodgett films were obtained with a commercial LB trough (KSV, System 5000). The amphiphilic 4,4'-bis(thiophene)-*N*-nonyldiphenylamine (DFTA9) and stearic acid were dissolved in chloroform (Aldrich, HPLC grade) and mixed in equimolar proportions, then laccase was dissolved in the obtained solution. The concentration of each solution was maintained at ca. $1 \text{ mg}\cdot\text{ml}^{-1}$. About $50 \mu\text{l}$ of the mixture was spread on a water subphase ($22 \text{ }^\circ\text{C}$) of the trough and the monolayer was compressed with a movable barrier at $50 \text{ mm}\cdot\text{min}^{-1}$. The deposition was Y-type with the transfer ratio very close to unity, and the π - A isotherms were recorded. The layers were transferred at a dipping rate of $20 \text{ mm}\cdot\text{min}^{-1}$ and removed at the drainage rate of $3.5 \text{ mm}\cdot\text{min}^{-1}$ at the transfer pressure of $25 \text{ mN}\cdot\text{m}^{-1}$. Between dipping cycles, the samples were dried for 15 min in the open air. All LB films were built up on the hydrophilic quartz microscopic slides.

For a covalent cross-linking of laccase on a modified surface, an obtained LB film was sprinkled with one millilitre of glutaraldehyde (GA) [16]. In each case, immediately after applying the protein to the thin LB layers, the substrates were placed in a desiccator. The process of immobilization was carried out for 12 hours, at $4 \text{ }^\circ\text{C}$ in a humid environment. Figure 2 shows a simplified scheme for fabricating LB type film with immobilized proteins.

For determination of laccase activity, the substrates were immersed in 25 cm^3 of 2,2'-azino-bis(3-ethylbenzthiazoline-6-sulphonate) ABTS ($0.228 \text{ mmol}\cdot\text{dm}^{-3}$, pH 5.25) or catechol ($10 \text{ mmol}\cdot\text{dm}^{-3}$, pH 5.25) and incubated at $30 \text{ }^\circ\text{C}$, under continuous stirring. The laccase catalyzed oxidation of reagent (ABTS or catechol) was carried out for 30 min.

ABTS is commonly used as a standard reagent with a laccase enzyme. This compound has been chosen because the enzyme facilitates the oxidation process, turning it into a green and soluble end-product. The fungal laccase oxidises ABTS to green-coloured radical cation (ABTS^+) and colour changes of ABTS solution can be measured.

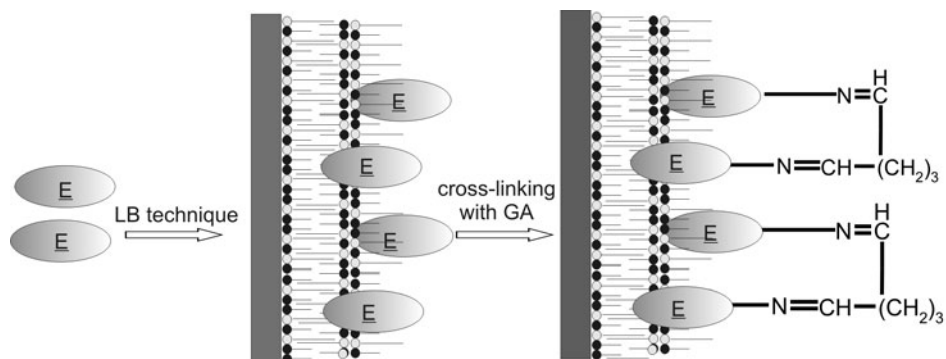


Fig. 2. The possible scheme of fabricating biological active layers; grey ellipses – laccase

After washing off the oxidized reagent (with buffer, pH 5.25), the regenerated substrate (immobilized laccase) was ready to react repeatedly, and the reaction was repeated up to 25 times. The activity of the immobilized laccase was monitored by continuous recording changes of the absorbance at the wavelength characteristic for the maximum for the green oxidation product of ABTS – 420 nm or 410 nm for catechol by means of the spectrometer Unicam Helios during 30 min incubating cycle with reagent.

The specific activity was calculated from the measured absorbance value and one activity unit (1 U) was defined as the quantity of protein, which in test conditions changes the absorbance by 0.0001 per minute. This specific activity is related to the surface area of LB film, its unit of dimension is ($\text{U}\cdot\text{cm}^{-2}$), and it expresses the activity of an immobilized enzyme. Enzyme activity could be also expressed in relative units (%); 100% activity could be defined as the change of absorbance (compared with the absorbance at the first measurement), equivalent to 1 U.

AFM studies of SA/DFTA9/laccase cross-linked LB films were carried out using an AFM Dimension V Veeco.

3. Results and discussion

3.1. The surface pressure–area isotherms of laccase

The surface pressure–area isotherms of films a and b on pure water, at 22 °C, are presented in Fig. 3. The isotherms indicate that both, a and b films, at high surface pressure behave as a 2D solids. The surface per molecule area (calculated for a mole-

cule of SA) for the film a is 33 \AA^2 , whereas for the film b it is 183 \AA^2 . The low area per molecule for film a, only a little higher than for pure SA and steeply isotherm, suggests that protein molecules may be partly squeezed off the film. This situation is even more

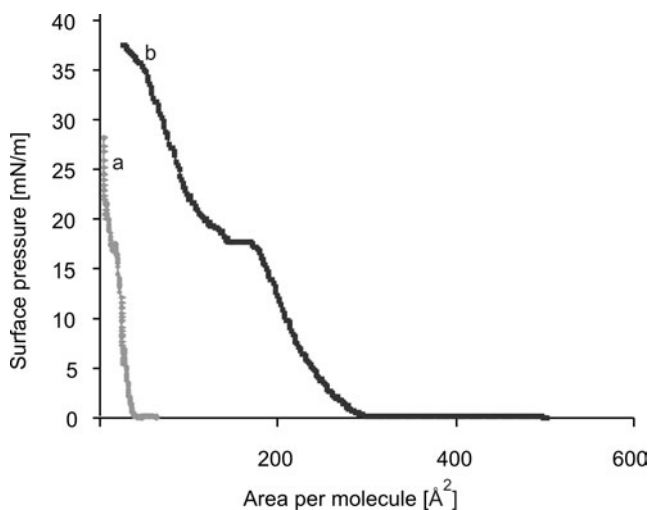


Fig. 3. Surface pressure – area isotherms of layer built of laccase – SA with (a) or without (b) DFTA9 incorporated into the film, at 22 °C on pure water

pronounced in the case of the film of laccase mixed with SA and DFTA9. A short plateau visible in an isotherm b above $18 \text{ mN}\cdot\text{m}^{-1}$ does not provide evidence of the collapse of the film but rather of the process of partial squeezing because the transfer ratio observed above $18 \text{ mN}\cdot\text{m}^{-1}$ was close to unity and the obtained films were tougher and more elastic.

3.2. Characterization of immobilized protein

Since the immobilization of laccase in LB films occurs through the cross-linking reaction with glutaraldehyde, we use it in an excess amount. In our case, the laccase incorporated into the obtained film had an initial enzyme activity of $743 \text{ U}\cdot\text{cm}^{-2}$ (Fig. 4). This activity, however, makes merely 10% of the activity of the native laccase.

As one can see from Fig. 5, the sensing activity of the laccase, covalently immobilized onto LB films via glutaraldehyde, is rather stable up to 25 incubation cycles (repeated reaction of oxidizing reagent catalyzed by immobilized laccase). The observed decrease in the enzyme activity is rather small, and the cross-linked protein is active for a few months. If the DFTA9 molecules, acting as an electron mediator are present in the system they significantly enhance an ABTS mediating efficiency. We have found the effect of equimolar addition of DFTA9 into protein; an enzyme activity increased almost three times, and it retained ca. 70% of its initial activity for as long as 4 months (stored in the buffer, at 4 °C).

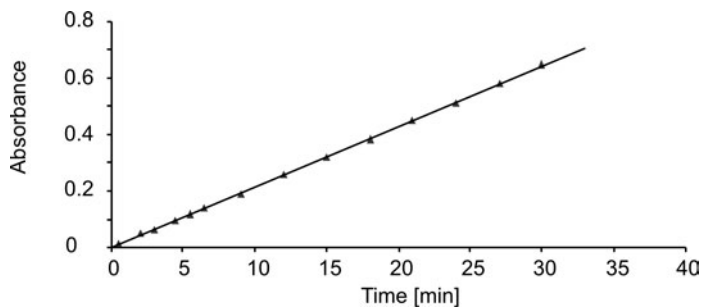


Fig. 4. Time dependence of absorbance (A) at 420 nm as a measure of enzyme activity (U) during the first oxidation of ABTS catalyzed by immobilized laccase

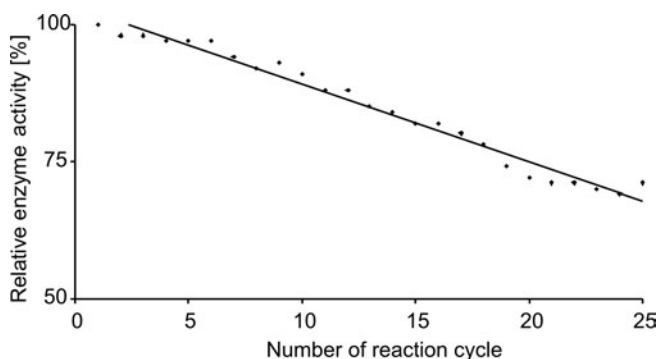


Fig. 5. Immobilized laccase activity during repeated incubation of immobilized laccase with ABTS dependent on number of reaction cycle. The line serves to guide the eye only

In the case of natural reagents like catechol, the laccase efficiency in the film followed the same number of measurement runs, proving the system was stable and reproducible, although the activity itself was as low as 20–30% of the activity of laccase in solution.

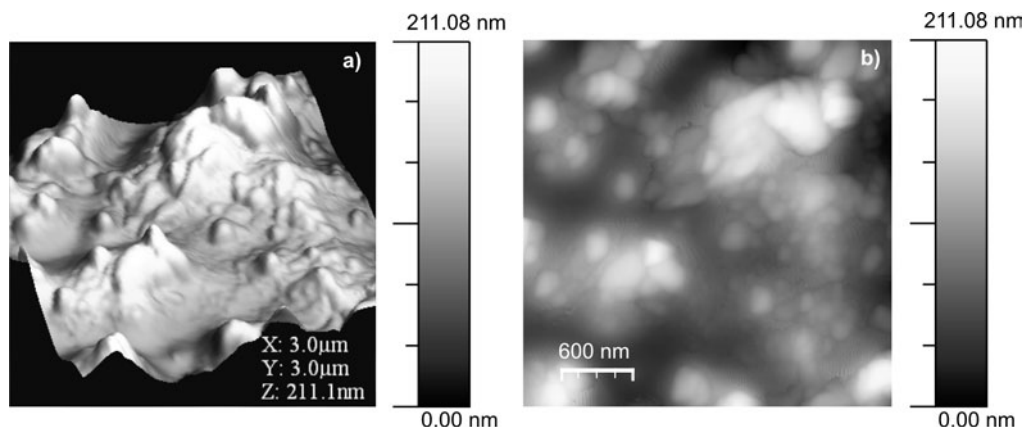


Fig. 6. AFM images of SA/DFTA9/laccase LB film. All images are $3 \times 3 \mu\text{m}^2$

ABTS as a standard enzyme activity indicator use for reaction catalyzed by laccase causes much higher activity of the protein compared with natural reagents like catechol. The enzyme activity in the presence of catechol ($24.65 \text{ U}\cdot\text{cm}^{-2}$) as a reagent is a few times lower than in the case of ABTS ($195.95 \text{ U}\cdot\text{cm}^{-2}$) but the results are stable and the sensing film is able to catalyze catechol oxidation for a few months.

Atomic force microscopy was used for the topographic characterisation of the laccase LB films deposited on the quartz microscopic slides (Fig. 6). Laccase was observed as characteristic islands (aggregates, grain size 10–200 nm). The roughness of the film SA/DFTA9/laccase (38.2 nm) confirms the presence of protein, at least partly, out of the film in the form of comparatively large aggregates of immobilized enzyme, cross-linked by glutaraldehyde molecules. Moreover, one cannot also exclude the changes of the surface density of during the formation of the film of the aggregates of laccase or the enzyme conformation.

4. Conclusions

It is possible to achieve successful immobilization of laccase by using heterogeneous LB film consisting of laccase cross-linked with glutaraldehyde, amphiphilic *N*-nonyl-bis(thiophene)diphenylamine (DFTA9) and stearic acid. This type of sensing system retains specific enzyme activity equal to 10% of that of native laccase. Enzyme immobilized by this technique is active and stable for at least 25 reaction cycles (ABTS). Catalytical activity of immobilized laccase was observed also for the catechol potentially present in most wastewaters.

The use of this electroactive nanohybrid material as a host matrix for enzyme immobilization prevents the protein leaking and enhances specific interactions. This biosensor offers a fast and a sensitive response in the presence of dissolved oxygen and can be used to detect phenolic compounds. Moreover, based on its good electrocatalysis for oxygen reduction, this system can be applied as the cathodic catalyst to fabrication of biofuel cells.

Acknowledgements

The authors are grateful to the Wrocław University of Technology and acknowledge the financial support provided by MNiI Grant No. NN 204 24493. The authors thank also Dr. J. Bryjak of the Wrocław University of Technology for providing the laccase samples.

The AFM data were visualized by WSxM software (Horcas I., Fernandez R., Gomez-Rodriguez J. M., Colchero J., Gomez-Herrero J., Baro A. M., *Rev. Sci. Instrum.*, 78 (2007), 013705).

References

- [1] GIRARD-EGROT A.P., GODOY S., BLUM L.J., *Adv. Colloid Interface Sci.*, 116 (2005), 205.
- [2] LEBLANC R.M., *Curr. Opin. Chem. Biol.*, 10 (2006), 529.
- [3] LEHN J.M., *Angew. Chem. Int. Edit.*, 29 (1990), 1304.

- [4] BROCKMAN H., *Curr. Opin. Struc. Biol.*, 9 (1999), 438.
- [5] NICOLINI C., PECHKOVA E.C., *J. Nanosci. Nanotechnol.*, 6 (2006), 2209.
- [6] CABRITA J.F., ABRANTES L.M., VIANA A.S., *Electrochim. Acta*, 50 (2005), 2117.
- [7] SINGHAL R., CHAUBEY A., SRIKHIRIN T., APHIWANTRAKUL S., PANDEY S.S., MALHOTRA B.D., *Curr. Appl. Phys.*, 3 (2003), 275.
- [8] FARNETH W.E., D'AMORE M.B., *J. Electroanal. Chem.*, 581 (2005), 197.
- [9] MOUSTY C., VIEILLE L., COSNIER S., *Biosensors Bioelectr.*, 22 (2007) 1733.
- [10] BAIOTTO P., BARRECA A.M., FABBRINI M., GALLI C., GENTILI P., *Org. Biomol. Chem.*, 1 (2003), 191.
- [11] BRANDI P., D'ANNIBALE A., GALLI C., GENTILI P., NUNES PONTES A.S., *J. Mol. Catal. B*, 41 (2006), 61.
- [12] DAVIS F., HIGSON S.P.J., *Biosensors Bioelectr.*, 21 (2005), 1.
- [13] IDZIK K., SOŁODUCHO J., CABAJ J., MOSIĄDZ M., ŁAPKOWSKI M., GOLBA S., *Helv. Chim. Acta*, 91 (2008), 618.
- [14] BRYJAK J., *Wiad. Chem.*, 58 (2004), 691.
- [15] ROGALSKI J., DAWIDOWICZ A., JÓŻWIK E., LEONOWICZ A., *J. Mol. Catal. B*, 6 (1999), 29.
- [16] CABAJ J., IDZIK K., SOŁODUCHO J., CHYŁA A., BRYJAK J., DOSKOCZ J., *Thin Solid Films*, 516 (2008), 1171.

Received 16 July 2008

Revised 3 March 2009

Gold nanoparticles grown on multiwall carbon nanotubes^{*}

Ł. PIETRZAK, J. K. JESZKA^{**}

Centre of Molecular and Macromolecular Studies, Polish Academy of Sciences,
90-363 Łódź, ul. Sienkiewicza 112, Poland

A new method of decorating carbon nanotubes (CNTs) with metal nanoparticles (NPs) is proposed. It consists in evaporating a metal layer on CNT deposited on a substrate and subsequent annealing at 400 °C. It is shown that after annealing the Au layer is reshaped and metal nanoparticles are formed. The size of NPs depends mostly on the initial thickness of the metal layer and the thickness of the nanotubes. The Au layers are not detached when decorated CNTs are redispersed in a solvent and deposited again on a support. Au NPs on CNT can be functionalised by well known methods of thiol adsorption and used e.g., in sensors.

Key words: *gold nanoparticles; carbon nanotubes; reshaping*

1. Introduction

Recently, a renewal of interest in gold nanoparticles (NPs) has been observed since the discovery of their catalytic activity towards low temperature CO oxidation [1]. There is also a considerable interest in the deposition of metal nanoparticles on carbon nanotubes (CNTs) using various methods (see e.g., [2]). In most cases, the NPs were synthesized in solution and attached or covalently bound to CNTs. It was also shown that nanotubes with deposits of Au [3], Pt [4], or Ag [3] NPs can act as low pressure gas sensors. Metal nanoparticles on solid supports, including CNTs, can be obtained by metal evaporation. The size and shape of the NPs formed depend on evaporation conditions and eventually on subsequent annealing. The most studied was deposition of gold [5–7] and silver [8]. For Au, the influence of support temperature and purity was also investigated [9, 10]. It was found that annealing conditions depend on the thickness of the Au layer and on the surface energy of the support. Thin, non-

^{*}The paper presented at the 11th International Conference on Electrical and Related Properties of Organic Solids (ERPOS-11), July 13–17, 2008, Piechowice, Poland.

^{**}Corresponding author, e-mail: jkjeszka@cbmm.lodz.pl

continuous layers reshape by coalescence of Au aggregates. This process leads to a decrease of surface energy of the metal but, to be observed in a reasonable time, it requires a sufficiently high temperature, so that the clusters are mobile. Warmack [11] observed coalescence of 2 nm Au films on SiO₂ in the temperature range 200–800 °C. After 4 min at 200 °C some coalescence was already visible, and after the same heating time at 400 °C the effect was pronounced – a twofold increase in the particle size was observed. A thicker, continuous layer was found to reshape at much higher temperatures. Heyraud [12] studied dewetting of thick (300 nm) gold layer on graphite and found that annealing at 1000 °C for 50 h is necessary to obtain an equilibrium shape of Au crystals (few microns in diameter).

In this paper, we present the results of decorating multiwall carbon nanotubes (MWCNT) with gold nanoparticles by vacuum evaporation of continuous layers and subsequent annealing. We discuss the effect of the thickness of the evaporated layer, and the effect of annealing conditions on the size and form of Au NPs.

2. Experimental

Aligned multiwall carbon nanotubes were synthesized by aerosol-assisted catalytic chemical vapour deposition (CCVD) from toluene/ferrocene solution in the laboratory of Dr. M. Mayne-L'Hermite (CEA Saclay, France). CNT come from the synthesis in the form of a carpet, the nanotubes being aligned nearly perpendicularly to the carpet base. The purity of this material is high; it contains only a small amount of by-products [13].

Carbon nanotubes were dispersed in trichloromethane in an ultrasonic bath for 1.5 h. The solution was cast on Si wafer and after the solvent evaporation it was left for half an hour in an oven, heated up to 400 °C to remove residual impurities. At this temperature, the nanotubes are not oxidized, but residues of amorphous carbon or solvent impurities are removed. Then Au was deposited on the surface of the specimen, using Jeol JFC – 1200 Fine Coater. In most experiments, the Au layer was deposited twice from two sides, at an angle of 45°. Such a procedure should assure a more uniform covering of the nanotube surface. However, no significant difference was observed in NPs formation on CNTs oriented parallel or perpendicular to the evaporation direction. The initial Au layer thickness given in the text was determined using atomic force microscopy (Nanoscope IIIa, Veeco Instruments) on a flat support. In the next step, the specimens were annealed at 400 °C in air in a home-made oven, which resulted in reshaping of the Au layer. The samples were investigated using a Jeol JSM – 5500LV scanning electron microscope.

3. Results and discussion

Figure 1 presents a SEM image of CNTs deposited from CHCl₃ solution on Si wafer after evaporation of gold. The thickness of the Au layer on a flat Si surface is

11 nm, and that is much smaller than the average thickness of the nanotubes. These images of the CNTs prior to Au evaporation and after evaporation are very similar, only the contrast is slightly increased. No individual nanoparticles can be seen, which proves that the nanotubes are uniformly covered with gold.

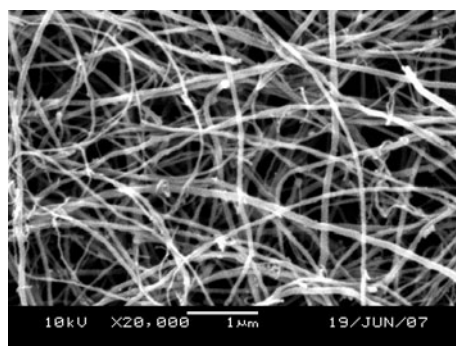


Fig. 1. SEM image MWCNTs dispersed in CHCl_3 and deposited on Si, covered by an 11 nm thick layer of Au

The image of such a sample after annealing at $400\text{ }^\circ\text{C}$ is shown in Fig. 2. It can be seen that the gold layer on the nanotubes and on the Si support undergoes reshaping (dewetting) and Au nanoparticles are formed. The size of nanoparticles decorating the nanotubes depends on the thickness of the nanotubes. In the case of thinner nanotubes, the maximum size is limited by the nanotube thickness. On thicker nanotubes one can see bigger and smaller NPs. Few NPs (like those indicated by an arrow in Fig. 2) have oblate shapes and are longer than the CNT thickness. The NPs formed on Si are smaller as compared with these formed on thicker CNTs and their size is more uniform. The difference can be explained by different surface energy of CNTs and Si. Similar effect was observed also comparing reshaping of Au on HOPG with other supports [14].

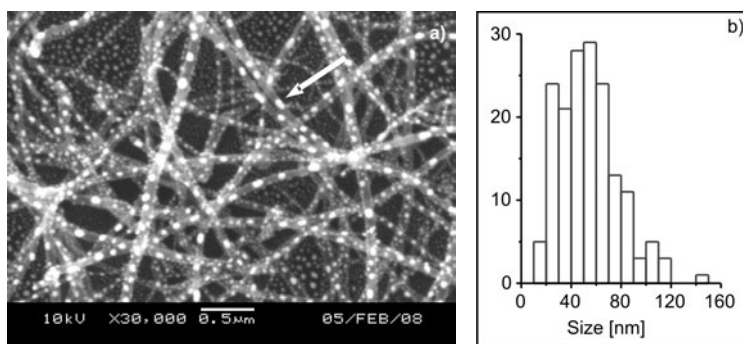


Fig. 2. SEM image of Au nanoparticles (a) formed on MWCNTs and on Si support by annealing a 11 nm gold layer for 10 min at $400\text{ }^\circ\text{C}$ (mean size of NPs on CNTs is 55 nm), and the size distribution (b) of the NPs on 4 images of different regions of the same sample. In the case of oblate particles, the longest axis is taken as the NP size

Figure 3 shows an image of the MWCNTs with Au NPs formed by reshaping of an evaporated, 15 nm thick Au layer. It can be seen that, in this case, the nanoparticles

are much bigger (mean size increases from 60 to 130 nm and many of them have oblate shapes). Thus the thickness of the deposited gold layer is a very important factor. Also, the difference in size of the NPs on thinner and thicker CNTs (Fig. 2) can be attributed to the Au layer thickness, because the amount of Au deposited on the curved surface of the CNT is smaller than that on the corresponding flat surface. Thicker Au layers require more time for reshaping.

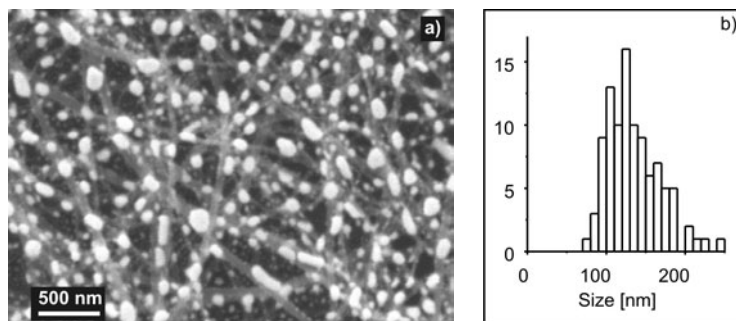


Fig. 3. SEM image of Au nanoparticles (a) formed on MWCNTs by annealing a 15 nm gold layer for 15 min at 400 °C. Mean size of NPs on CNTs is 135 nm and the size distribution (b) of the NPs on 4 images of different regions of the same sample. In the case of oblate particles, the longest axis is taken as the NP size

The size of the nanoparticles can be also controlled to some extent by the annealing time and the temperature but only at the initial stage. After some time the NPs are formed and the effect of longer annealing at the same temperature becomes negligible. The images shown in Figs. 2 and 3 correspond to such an “equilibrium” NPs size after annealing at 400 °C. At higher temperatures the annealing time sufficient to obtain NPs is much shorter, and for instance for a 11 nm Au layer at 600 °C it is only 10 s.

The evaporated layers adhere well to the nanotubes, thus they can be redispersed in solvents and deposited again on a support. A SEM image of such redeposited CNTs is practically the same as that shown in Fig. 1. Such a sample can also be annealed and the image of such a redispersed sample is shown in Fig. 4.

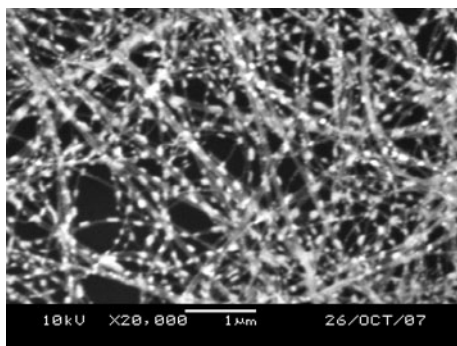


Fig. 4. SEM image of Au nanoparticles formed on MWCNTs after evaporation of Au layer (15 nm), redispersion in CH_2Cl_2 , deposition on Si and annealing for 15 min at 400 °C

It seems that in the case of the layers deposited on CNTs, the process of reshaping is easier than on flat surfaces because the metal is deposited on CNTs in a form of stripes with thin edges on the sides of CNTs. Such structures can more easily separate into smaller particles starting from these thin edges (Fig. 5).

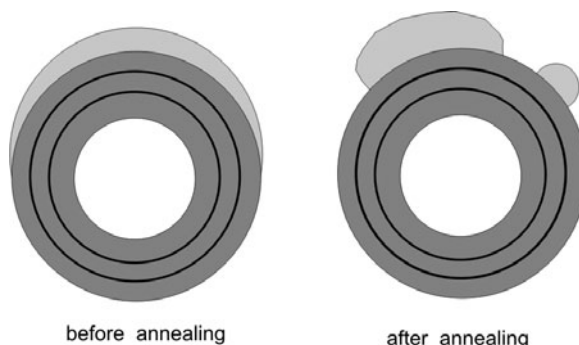


Fig. 5. Schematic representation of Au layer on a MWCNT after evaporation and after reshaping

4. Conclusions

One can obtain CNT decorated with Au nanoparticles by vacuum evaporation of gold and subsequent annealing. The size of the nanoparticles can be controlled by changing the thickness of the deposited gold layer and the annealing conditions. Such gold-decorated carbon nanotubes can be redispersed in a solvent and used e.g., to produce nanocomposites. They can be functionalised by taking advantage of strong thiol adsorption on gold.

References

- [1] HARUTA M., YAMADA N., KOBAYASHI T., IJIMA S., *J. Catal.*, 115 (1989), 301.
- [2] GEORGAKILAS V., GOURNIS D., TZITZIOS V., PASQUATO L., GULDI D.M., PRATO M., *J. Mater. Chem.*, 17 (2007), 2679.
- [3] ESPINOSA E.H., LONESCU R., BITTENCOURT C., FELTEN A., ERNI R., VAN TENDELOO G., PIREAUX J.J., LLOBET E., *Thin Solid Films*, 515 (2007), 8322.
- [4] KONG J., CHAPLINE M.G., DAI H.J., *Adv. Mater.*, 13 (2001), 1384.
- [5] BERTHIER S., PEIRO J., FAGNENT S., GADENNE P., *Physica A*, 241 (1997), 1.
- [6] DARBY T.P., WAYMAN C.M., *J. Cryst. Growth.*, 28 (1975), 41.
- [7] LEVLIN M., LAAKSO A., NIEMI H.E.M., HAUTOJARVI P., *Appl. Surf. Sci.*, 115 (1997), 31.
- [8] LEVLIN, M., LAAKSO A., *Appl. Surf. Sci.*, 171 (2001), 257.
- [9] VANDAMME, N., JANSSENS E., VANHOUTTE F., LIEVENS P., VAN HAESENDONCK C., *J. Phys.C: Cond. Mat.*, 15 (2003), S2983.
- [10] WAYMAN, C.M., T.P. DARBY, *J. Cryst. Growth*, 28 (1975), 53.
- [11] WARMACK R.J., HUMPHREY S.L., *Phys. Rev. B*, 34 (1986), 2246.

- [12] HEYRAUD J.C., METOIS J.J., *J. Cryst. Growth*, 50 (1980), 571.
- [13] PINAULT M., MAYNE-L'HERMITE M., REYNAUD C., PICHOT V., LAUNOIS P., BALLUTAUD D., *Carbon*, 43 (2005), 2968.
- [14] TRACZ A., KUCINSKA I., WOSTEK-WOJCIECHOWSKA D., JESZKA J.K., *Eur. Polym. J.*, 41 (2005), 501.

Received 3 September 2008

Revised 20 November 2008

Synthesis and photochromic properties of poly[*N*-vinyl-2-(phenylazo)-imidazole] derivatives in the near UV range*

M. KOSZYKOWSKA**, M. TOKAREK, S. KUCHARSKI

Wrocław University of Technology, Faculty of Chemistry,
Wybrzeże Wyspiańskiego 50-370 Wrocław, Poland

The following novel photochromic poly(*N*-vinylimidazole) polymers have been synthesized: poly[*N*-vinyl-2-(4-cyano-phenylazo)imidazole] (PV-4-CBAI), poly[*N*-vinyl-2-(3-cyano-phenylazo)imidazole] (PV-3-CBAI) and poly[*N*-vinyl-2-(4-methoxy-phenylazo)imidazole] (PV-4-MBAI). Quantum chemical calculations of monomeric chromophores were carried out to foresee their linear and nonlinear optical properties. The polymeric materials were characterized by UV-vis spectroscopy and ellipsometry to determine changes in their properties during illumination. It was found that the stable *trans* form of polymeric chromophores absorbed in the range of 360–380 nm (absorption band maximum) and underwent *trans-cis* isomerization on illumination with 395 nm light. The ellipsometric measurement showed a change of the refractive index of polymer films during illumination, which was in the range of 0.010 to 0.014, depending on chromophore type.

Key words: *photochromic polymers; 2-(phenylazo)imidazole; trans-cis photoisomerization; ellipsometry*

1. Introduction

The polymers containing azobenzene groups have been widely studied due to their potential applications in optical data storage, surface relief grating formation and as optoelectronics switches [1–3]. The photochromic azo compounds show reversible *trans-cis* isomerization upon irradiation with light. The reverse *cis-trans* process is realized thermally (thermal relaxation) or on illumination with light. During illumination, the chromophores show reversible changes in their molecular properties such as geometrical structures, electric permittivities, absorption and fluorescence spectra, and refractive indices. The changes in chemical and physical properties during irradiation have been widely employed in optics and optoelectronics [4–9].

*The paper presented at the 11th International Conference on Electrical and Related Properties of Organic Solids (ERPOS-11), July 13–17, 2008, Piechowice, Poland.

**Corresponding author, e-mail: maria.koszykowska@pwr.wroc.pl

The papers dealing with isomerization of azo compounds mainly referred to the compounds containing six-member aromatic rings on both sides of the diazo group and distinct electron donor functional group on one side of the molecule, and a strong electron acceptor group on its opposite side. Such chromophores, particularly those containing $-\text{NO}_2$ or $-\text{CN}$ acceptor groups, showed an absorption maximum at ca. 460–485 nm.

In this work, the main attention was focused on the synthesis of novel poly[*N*-vinyl-2-(phenylazo)imidazole] derivatives. Phenylazoimidazoles belong to analogues of azobenzene which have a heterocyclic ring instead of the phenyl group. The presence of the five-member heterocyclic ring has an effect on photochromic properties of the material, shifting the maximum of the absorption band to shorter wavelengths [8–13]. The main goal of this work was to obtain chromophoric polymers having the maximum of the absorption band in the near UV range. The presence of a five-member ring in the chromophore fragment was expected to be helpful in this context. The change in the properties of poly[*N*-vinyl-2-(benzoazo)imidazoles] on *trans*–*cis* photoisomerization were to be evaluated with the help of UV-vis spectroscopy and ellipsometry.

2. Materials and methods

Materials. *N*-vinylimidazole monomer (Aldrich) was distilled under vacuum before use. 2,2'-Azobisisobutyronitrile, AIBN, (Fluka) initiator was recrystallized twice from methanol. Benzene (POCH, Gliwice) as a solvent was dried over metallic sodium chips and distilled before use. 4-Aminobenzonitrile, 3-aminobenzonitrile, 4-methoxyaniline (Aldrich) were reagent grade quality and were used as received. Poly(*N*-vinylimidazole) was prepared by a reported procedure [14, 15]. The route of synthesis is shown in Fig. 1. Polymerization was carried out in benzene solution at 70 °C with AIBN as an initiator in nitrogen atmosphere. After 24 h of polymerization, the product was separated by filtration and dried. Yield: 87%. T_g : 171.7 °C. $^1\text{H NMR}$ (DMSO- d_6): 1.93 (s, 2H, $-\text{CH}_2-$), 2.46 (d, 1H, $-\text{CH}-$), 6.95 (m, 2H, in imidazole ring, $-\text{CH}=\text{CH}-$), 7.09 (m, 1H, in imidazole ring, $-\text{N}=\text{CH}-$).

The synthesis of poly[*N*-vinyl-2-(4-cyano-phenylazo)imidazole] (PV-4-CBAI) was carried out according to the route shown in Fig. 1 [16–18]. To the HCl solution (15 cm³, 1 M) of 4-aminobenzonitrile (1.30 g, 0.011 mol) under ice-cold conditions (0–5 °C) the aqueous solution of NaNO₂ (0.80 g, 0.012 mol) was added dropwise under stirring. This mixture was stirred at low temperature for a period of 1 h. Then diazotized solution was added in drops to a solution of poly(*N*-vinylimidazole) (1.30 g, 0.011 mol) in methanol (15 cm³) and aqueous solution of Na₂CO₃ (2.00 g in 15 cm³ water) at 0–5 °C. This solution was stirred for 2 h and then was kept at low temperature for several hours. The solution was basic in nature. Cold HCl (1 M) was added in drops to reach pH = 7. The precipitate was filtered off, washed and dried. Yield: 92%. T_g : 131.8 °C. $^1\text{H NMR}$ (DMSO- d_6): 1.85 (s, 2H, CH₂), 2.90 (s, 1H, CH), 6.83 (s, 2H,

CH in imidazole ring, $-\text{CH}=\text{CH}-$), 7.63 (d, 2H, $-\text{CH}-$, in benzene ring), 7.94 (d, 2H, $-\text{CH}-$, in benzene ring).

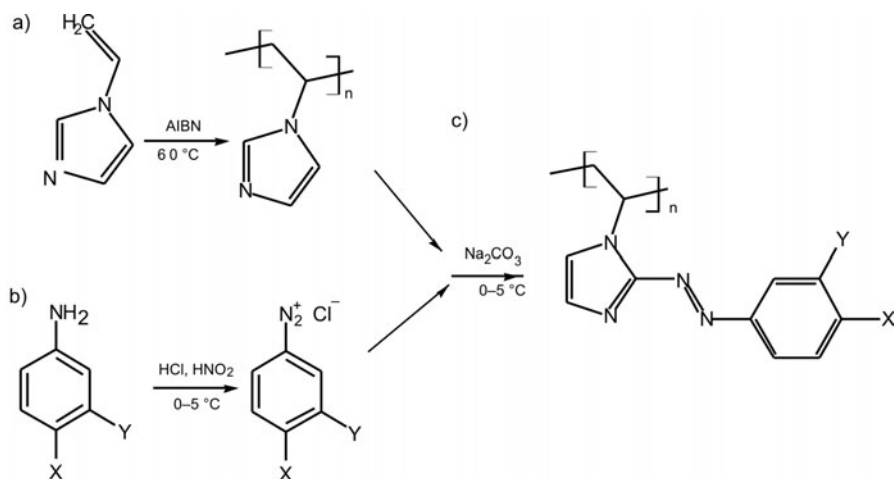


Fig. 1. Radical polymerization of *N*-vinylimidazole (a), diazo reaction of aniline derivatives (b), coupling a phenyldiazonium ion with poly(*N*-vinylimidazole) (c), PV-4-CBAI: X = CN, Y = H; PV-3-CBAI: X = H, Y = CN; PV-4-MBAI: X = OCH₃, Y = H

Poly[*N*-vinyl-2-(3-cyano-phenylazo)imidazole] (PV-3-CBAI) was prepared following an identical reaction procedure. Yield: 89%. T_g : 164.3 °C. ¹HNMR (DMSO-*d*₆): 1.85 (s, 2H, CH₂), 3.00 (s, 1H, CH), 6.84 (s, 2H, CH in imidazole ring, $-\text{CH}=\text{CH}-$), 7.68 (m, 1H, $-\text{CH}-$, in benzene ring), 7.80 (m, 2H, $-\text{CH}-$, in benzene ring), 7.94 (m, 1H, $-\text{CH}-$, in benzene ring).

Poly[*N*-vinyl-2-(4-methoxy-phenylazo)imidazole] (PV-4-MBAI) was prepared following an identical reaction procedure. Yield: 76%. T_g : 120.0 °C. ¹HNMR (DMSO-*d*₆): 2.49 (s, 2H, $-\text{CH}_2-$), 3.67 (q, 1H, CH), 3.74 (s, 3H, $-\text{OCH}_3$), 6.88 (d, 2H, $-\text{CH}-$, in benzene ring), 6.95 (s, 2H, CH in imidazole ring, $-\text{CH}=\text{CH}-$), 7.33 (s, 2H, $-\text{CH}-$, in benzene ring).

Methods. Quantum chemical calculations were carried out at the Wrocław Supercomputer Centre using the Gaussian03 program [19] by the *ab initio* method at the RHF/3-21g level of theory. The UV-vis spectra were calculated with ZINDO method using optimized molecular coordinates from the RHF calculation. Glass transition temperatures (T_g) of polymers were measured by the differential scanning calorimetry (DSC) with a Mettler Toledo device. The rate of heating was 10 °C/min. UV-vis spectra were recorded with a Diode Array Hewlett Packard Spectrophotometer 8452A. Measurements were carried out using polymer films deposited on glass substrates before and during illumination with a diode light of 395 nm.

Ellipsometry measurements were carried out with an EL X-02C Ellipsometer, DRE-Ellipsometerbau GmbH (Germany), to characterize thin polymer film deposited on glass substrates before and during illumination with a diode light of 395 nm.

3. Results and discussion

3.1. Quantum-chemical calculations

Quantum chemical calculations were carried out with the Gaussian03 program by *ab initio* method at RHF/3-21g level of theory to foresee linear and nonlinear optical properties of the chromophores [20,21]. The calculations were performed for monomeric [*N*-ethyl-2-(phenylazo)imidazole] derivatives. Using vinyl derivatives for these purposes would be inadequate due to a possible electron conjugation of the vinyl group with the rest of the dye molecule. In polymers, the vinyl group disappears, giving a sequence of saturated (polyvinyl) chain units. As the *cis* form of the azo dye molecule is unstable and re-isomerises to the *trans* form in ambient conditions, it is impossible to determine experimentally its spectral and other physicochemical properties. Optimization of the geometry of the molecule makes it possible to characterize the difference of potential energy between the *trans* and *cis* isomers (ΔE), volume of the molecule (V) and the dipole moment (μ). Calculated values are presented in Table 1. The difference in shape of chromophoric molecule fragments between *trans* and *cis* isomer is shown in Fig. 2, based on the example of the PV-4-MBAI polymer. The molecules of the chromophores in question are rather short and on isomerization the change in the molecular shape is evidenced by small differences in the dipole moment. The potential energy difference between the *trans* and *cis* form, being in the range of ca. 51–60 kJ/mol, is low compared with that calculated for analogous azo chromophores containing two phenyl groups on both sides of the diazo group, if the same basis set is used [22].

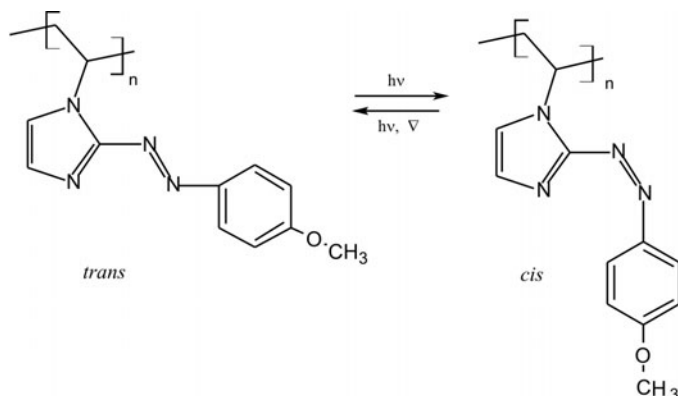


Fig. 2. Molecular shapes of *trans* and *cis* forms of the chromophore fragment of PV-4-MBAI polymer

The simulated UV-vis spectrum for monomer corresponding to PV-4-MBAI is shown in Fig. 3. The results of simulation of UV-vis spectra are presented in Table 2.

The calculated maxima of absorption bands for *trans* forms of monomers are located in the near UV range (373–380 nm). Analogous absorption bands corresponding

to the *cis* form are shifted towards shorter wavelengths, and consequently, the intensities of the bands, expressed by the oscillator strengths, are lower for the *cis* forms. The most significant difference between the *trans* and *cis* form can be observed in methoxyphenyl derivatives that varied in the maximum absorption wavelength as well as in the oscillator strength.

Table 1. The calculated properties of monomeric chromophores [19]

Monomer corresponding to	ΔE^a [kJ/mol]	Volume of molecule ^b V [cm ³ /mol]		Dipole moment $\mu/10^{-30}$ [C·m]	
		<i>trans</i>	<i>cis</i>	<i>trans</i>	<i>cis</i>
PV-4-MBAI	52.138	190.72	186.75	9.56	11.05
PV-3-CBAI	51.481	183.66	169.87	27.87	25.21
PV-4-CBAI	60.274	159.23	148.28	20.46	25.50

^aDifference of potential energies *cis* and *trans* isomers.

^bCalculated by Gaussian using the Monte Carlo method.

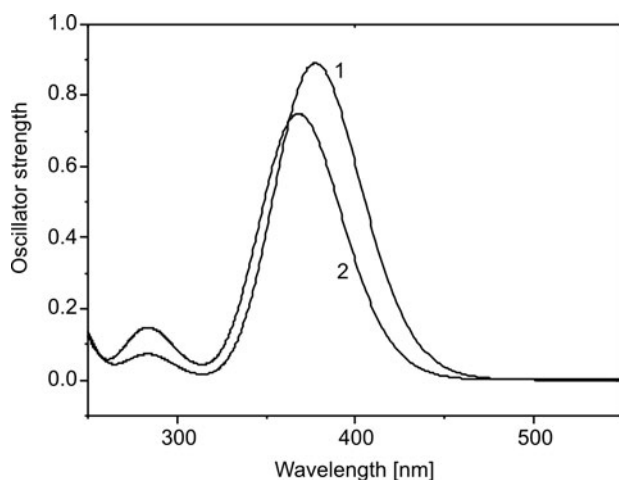


Fig. 3. UV-vis spectrum of the monomer corresponding to PV-4-MBAI (*N*-ethyl-2-(4-methoxy-phenylazo)imidazole): 1 – *trans* form, 2 – *cis* form

Table 2. Spectral properties of monomeric chromophores calculated with ZINDO method of Gaussian program [19]

Monomer corresponding to	Maximum of absorption band [nm]		Oscillator strength	
	<i>trans</i>	<i>cis</i>	<i>trans</i>	<i>cis</i>
PV-4-MBAI	377	368	0.8896	0.7481
PV-3-CBAI	373	359	0.8034	0.6890
PV-4-CBAI	380	329	0.8963	0.4864

The calculations of linear and nonlinear optical properties were carried out for isolated molecules which had been optimized before by Gaussian. The calculated values of polarizability and hyperpolarizability for monomeric species are presented in Table 3. In the *trans* form, the polarizability was slightly higher than in the *cis* form and, as polarizability is correlated with molecular volume, the same tendency was observed in the case of the latter parameter (Table 2).

Table 3. Polarizability and first hyperpolarizability of monomeric chromophores

Monomer corresponding to	Polarizability α $\alpha^\circ/10^{-30}$ [m ³]		Hyperpolarizability β $\beta^\circ/10^{-40}$ [m ⁴ /V]	
	<i>trans</i>	<i>cis</i>	<i>trans</i>	<i>cis</i>
PV-4-MBAI	22.29	21.85	2.52	32.97
PV-3-CBAI	21.79	21.47	42.21	20.74
PV-4-CBAI	22.35	20.05	54.91	24.04

There was an observed difference in the first hyperpolarizability (β) data between *trans* and *cis* isomers, although the absolute values of β for long *trans* forms and short *cis* forms are rather small. The chromophore corresponding to the PV-4-MBAI polymer, contrary to the other two chromophores, contains a relatively weak electron acceptor (methoxy group). This is manifested in the higher value of the dipole moment and the first hyperpolarizability of its *cis* form, in comparison with the *trans* form. And this is analogous fact to that observed in the case of unsubstituted azobenzene. The dyes with stronger cyano acceptor group behave, one may say normally, showing higher values of dipole moment and first hyperpolarizability value in the case of *trans* forms. The difference in the first hyperpolarizability value of the border structures is distinct for all three chromophores. This fact could eventually be utilized at the macromolecular scale, by forcing a change in the value of β during illumination of the polymers with UV light, however the second order nonlinear susceptibility of the materials is expected to be rather moderate.

3.2. Characteristics of photochromic polymer films

The polymers were deposited on glass substrates in the form of thin transparent films by the spin coating technique. The solutions of poly[*N*-vinyl-2-(phenylazo)-imidazole] derivatives were prepared in 2-methoxyethanol in the presence of polyvinylpyrrolidone. The concentration of the photochromic poly(*N*-vinylimidazole) derivatives in solution was ca. 3 wt. %. Poly(*N*-vinylimidazole) derivatives and polyvinylpyrrolidone were used in the ratio of two to three.

The measurements of UV-vis spectra were carried out using thin films of polymers on glass plates. The polymers containing chromophoric fragments showed an absorption peak with the maximum in the range of ca. 362–376 nm, depending on

the polymer type. The changes in UV-vis spectra occurred during illumination with light. The materials showed a reversible *trans*–*cis*–*trans* photoisomerization of the chromophoric fragments; the route from *cis* to *trans* took place as a thermal relaxation, however, by using a light source emitting at the wavelength absorbed by the *cis* isomer would considerably accelerate this process. The UV-vis spectra were recorded before and after illumination with a diode light of 395 nm and the spectral parameters are presented in Table 4. Among the polymers tested, the cyano derivatives showed a certain resistance to isomerization and required longer illumination time to observe distinct changes in the spectra. The PV-4-MBAI whose UV-vis spectrum is shown in Figure 4, occurred to be the best material to show a reverse run of *trans*–*cis*–*trans* transformations, and its spectra before and after illumination with a 395 nm diode showed maximum difference in absorption intensity, although nearly no shift towards shorter wavelengths was observed.

Table 4. Spectral properties of polymeric chromophores

Polymer	Before illumination		After illumination		Time of illumination [s]
	Maximum of absorption band [nm]	Absorbance [a.u.]	Maximum of absorption band [nm]	Absorbance [a.u.]	
PV-4-MBAI	376	0.9263	370	0.6697	30
PV-3-CBAI	362	0.5576	360	0.5045	75
PV-4-CBAI	376	0.8411	372	0.7747	120

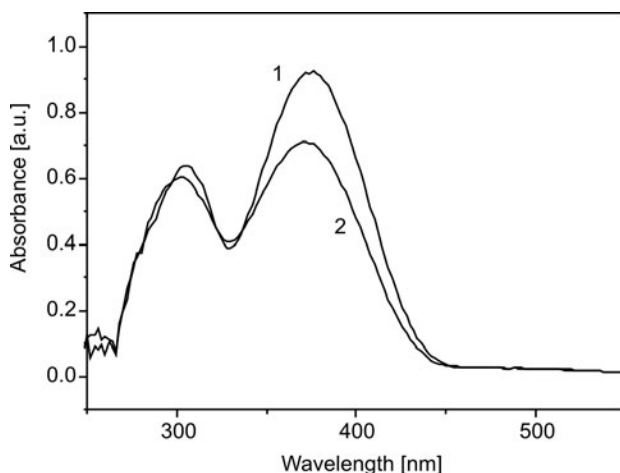


Fig. 4. The UV-vis spectrum of PV-4-MBAI: 1 – before illumination, 2 – after illumination

Comparison of data in Table 2 and 4 leads to the conclusion that the wavelengths of maximum absorption bands calculated for monomeric chromophores are close to those determined for respective polymers.

Ellipsometry is an optical method which makes it possible to determine the reversible changes in the refractive index of a given material after repeated illumination cycles with absorbed light [23]. This technique was used to investigate changes in ellipsometric parameters of the polymer films deposited on glass plates.

The light interacting with the sample undergoes a polarization change to elliptically polarized light. The change in the polarization is measured as a ratio of the complex Fresnel reflection coefficients, R_p and R_s , for p- and s-polarized light, respectively. The fundamental equation of ellipsometry is:

$$\rho = e^{i\Delta} \tan \Psi = \frac{R_p}{R_s} \quad (1)$$

where Ψ denotes the intensity ratio and Δ is the phase difference of the reflected p- and s-polarized light. From these measured values, it is possible to calculate the film thickness and complex dielectric function expressed by the complex refractive index:

$$n = n_r + ik, \quad i^2 = -1 \quad (2)$$

The measurements were carried out during illumination with a diode light of the wavelength of 395 nm and the change in the ellipsometric parameter Ψ was measured, dependent on the illumination time (first stage) and relaxation time (second stage) resulting in a change of refractive index, as shown for PV-4-MBAI in Fig. 5. The change in the real part of the refractive index n_r , measured for polymer thin films deposited on glass substrates was 0.011, 0.012 and 0.014 for PV-3-CBAI, PV-4-CBAI and PV-4-MBAI, respectively.

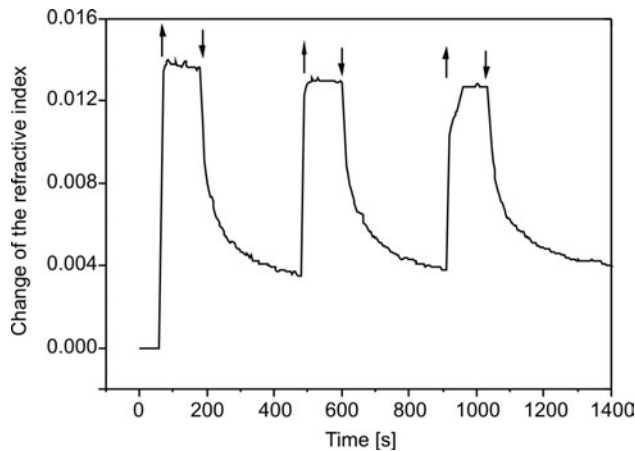


Fig. 5. Changes of the refractive index of PV-4-MBAI on illumination and thermal relaxation determined by the ellipsometry method: arrow up – light on, arrow down – light off

The periodic change in the refractive index on illumination and thermal relaxation is reversible, however the thermal relaxation needs a longer time for the sample to

recover its previous state. During illumination not only relatively fast photochemical isomerization takes place but also changes in the macroscopic properties of the material are observed being much slower. Thus, to recover the primary value of the refractive index, the time expressed in hours would be necessary. As the illuminating diode emitted unpolarized light, no formation of surface relief grating was expected.

4. Conclusions

Novel photochromic polymers, specifically poly[*N*-vinyl-2-(phenylazo)imidazole] derivatives, were obtained. The polymers showed a maximum absorption peak in the near UV range. The photoisomerization and thermal relaxation of poly(*N*-vinylimidazole) containing chromophores, as examined by ellipsometry, showed reversible changes in refractive indices in the range of 0.010 to 0.014, during illumination. The reverse *cis*–*trans* transformation run due to thermal relaxation and it was slower as compared with the previous step induced by light action. These photo-induced transformations resulted in a change in physicochemical properties of the materials in question, and could be interesting for practical applications in reversible optical data storage in the near UV range.

Acknowledgements

This work was supported by Grant No. NN507 3269 33 of the Polish Ministry of Science and Higher Education.

References

- [1] BOUAS-LAURENT H., DÜRR H., *Pure Appl. Chem.*, 73 (2001), 639.
- [2] NATANSOHN A., ROCHON P., *Chem. Rev.*, 102 (2002), 4139.
- [3] MATEE V., MARKOVSKY P., NIKOLOVA L., TODOROV T., *J. Phys. Chem.*, 96 (1992), 3055.
- [4] TAMAI N., MIYASAKA H., *Chem. Rev.*, 100 (2000), 1875.
- [5] WANG Y., ZHAN J., SI J., YE P., FU X., QIU L., SHEN Y., *J. Chem. Phys.*, 103 (1995), 5357.
- [6] RANGELO-ROJO R., YAMADA S., MATSUDA H., YANKELEVICH D., *Appl. Phys. Lett.*, 72 (1998), 1021.
- [7] CHIMURA K., *Chem. Rev.*, 100 (2000), 1847.
- [8] OTSUKI J., SUWA K., NARYTAKI K., SINHA C., YOSHIKAWA I., ARAKI K., *J. Phys. Chem. A.*, 109 (2005), 8064.
- [9] OTSUKI J., SUWA K., SARKER K.K., SINHA C., *J. Phys. Chem. A.*, 111 (2007), 1403.
- [10] ENDO M., NAKAYAMA K., KAIDA Y., MAJIMA T., *Tetrahedron Lett.*, 44 (2003), 6903.
- [11] FUKUDA N., KIM J.Y., USHIJIMA H., TAMADA K., *Jpn. J. Appl. Phys.*, 45 (2006), 460.
- [12] SCHULZ-EKLOFF G., WÖHRLE D., VAN DUFFEL B., SCHOONHEYDT R.A., *Microporous Mesoporous Mater.*, 51 (2002), 91.
- [13] KATSONIS N., LUBOMSKA M., POLLARD M.M., FERGINGA B.L., RUDOLF P., *Prog. Surf. Sci.*, 82 (2007), 407.
- [14] OZYALCIN M., KUCUKYAVUZ Z., *Synth. Met.*, 87 (1997), 123.
- [15] PEKEL N., SAHINER N., GUVEN O., RZAEV Z.M.O., *Eur. Polym. J.*, 37 (2001), 2443.
- [16] RAY U.S., MOSTAFA G., LU T.H., SINHA C., *Cryst. Eng.*, 5 (2002), 95.

- [17] SENAPOTI S., SARKER K.K., MONDA T.K.L., SINHA C., *Transition Met. Chem.*, 31 (2006), 293.
- [18] PAL S., DAS D., CHATTOPADHYAY P., SINHA C., PANNEERSELVAM K., LU T.H., *Polyhedron*, 19 (2000), 1263.
- [19] FRISCH M. J., TRUCKS G. W., SCHLEGEL H.B., SCUSERIA G.E., ROBB M.A., CHEESEMAN J.R., MONTGOMERY JR., J. A., VREVEN T., KUDIN K.N., BURANT J.C., MILLAM J.M., IYENGAR S.S., TOMASI J., BARONE V., MENNUCCI B., COSSI M., SCALMANI G., REGA N., PETERSSON G.A., NAKATSUJI H., HADA M., EHARA M., TOYOTA K., FUKUDA R., HASEGAWA J., ISHIDA M., NAKAJIMA T., HONDA Y., KITAO O., NAKAI H., KLENE M., LI X., KNOX J.E., HRATCHIAN H.P., CROSS J.B., BAKKEN V., ADAMO C., JARAMILLO J., GOMPERS R., STRATMANN R.E., YAZYEV O., AUSTIN A.J., CAMMI R., POMELLI C., OCHTERSKI J.W., AYALA P.Y., MOROKUMA K., VOTH G.A., SALVADOR P., DANNENBERG J.J., ZAKRZEWSKI V.G., DAPPRICH S., DANIELS A.D., STRAIN M.C., FARKAS O., MALICK D.K., RABUCK A.D., RAGHAVACHARI K., FORESMAN J.B., ORTIZ J.V., CUI Q., BABOUL A.G., CLIFFORD S., CIOŚLOWSKI J., STEFANOV B.B., LIU G., LIASHENKO A., PISKORZ P., KOMAROMI I., MARTIN R.L., FOX D.J., KEITH T., AL-LAHAM M.A., PENG C.Y., NANAYAKKARA A., CHALLACOMBE M., GILL P.M.W., JOHNSON B., CHEN W., WONG M.W., GONZALEZ C., POPLE J. A., Gaussian 03, Revision C.02, Gaussian, Inc., Wallingford CT, 2004.
- [20] HAKEN H., WOLF H.C., *Molecular Physics and Elements of Quantum Chemistry*, Springer Verlag, Berlin, 1995.
- [21] FORESMAN J.B., FRISCH A., *Exploring Chemistry with Electronic Structure Methods*, 2nd Ed., Gaussian, Inc. Pittsburg, PA, 1996.
- [22] HEHRE W.J., *Computational Chemistry in Quantum Chemistry and Spectroscopy*, T. Engel, P. Reid (Eds.), Prentice Hall, San Francisco, 2006.
- [23] AZZAM R.M.A., BASHARA N.M., *Ellipsometry and Polarized Light*, North-Holland, New York, 1997.

Received September 2008

Revised 8 April 2009

Ambipolar injection into pentacene field effect transistor observed by time-resolved optical second harmonic generation imaging*

T. MANAKA **, M. NAKAO, E. LIM, M. IWAMOTO

Department of Physical Electronics, Graduate School of Science and Engineering,
Tokyo Institute of Technology, 2-12-1 Ookayama, Meguro-ku, Tokyo 152-8552, Japan

Ambipolar carrier injection from gold electrode into pentacene was investigated by time-resolved optical second harmonic generation (TRM-SHG) imaging. Smooth hole injection is verified by rapid decrease of the SHG intensity at the electrode edge, indicating the absence of an injection barrier. In contrast, TRM-SHG results clearly indicated the presence of electron injection from the high-work function metal into the electrode, though after injection electrons were trapped in the channel and could not contribute to the conduction. Transient electric field distribution due to the injected holes and electrons were evaluated based on the SHG intensity distribution.

Key words: optical second harmonic generation (SHG); organic field effect transistor; carrier injection

1. Introduction

For organic electronic devices such as organic field effect transistors (OFETs), device operation is ruled by the injection, accumulation and transport processes of a carrier. In this sense, metal–semiconductor contacts play an important role in organic electronic devices, because injected carriers dominate the device operation [1]. For instance, ambipolar behaviour in OFETs was observed upon using appropriate electrode metals: electrons and holes are selectively injected from the electrode with a low and a high work function, respectively [2–4], clearly showing the significance of electrode contact. In contrast, for Si and other inorganic semiconductors, intentional doping precisely determines the type of majority carrier and carrier density in the semiconductors, and thus the injection and transport processes can be fully controlled.

*The paper presented at the 11th International Conference on Electrical and Related Properties of Organic Solids (ERPOS-11), July 13–17, 2008, Piechowice, Poland.

**Corresponding author, e-mail: manaka@ome.pe.titech.ac.jp

Owing to the irregularities of the metal–organic interface, the situation becomes more complicated for organic devices, and adequate control of injection and transport processes is not satisfactory at present. It was reported that the preparation process of a metal electrode significantly affects properties of the device [5]. Therefore, an adequate evaluation and control of injection processes is of great importance to improve device performance effectively.

For pentacene FETs, holes inject smoothly from Au electrode because the energy level of the highest occupied molecular orbital (HOMO) in pentacene [6] is close to the work function of Au [7]. On the other hand, since an electron should be injected into the lowest unoccupied molecular orbital (LUMO), the metal with a low work function such as Ca and Mg is suitable for electron injection into pentacene [2]. In this way, use of an appropriate electrode is a general way to realize the ambipolar operation in OFET. Nevertheless, we reported the presence of the electron injection from Au electrode into pentacene FET observed by the electric field induced optical second harmonic generation (EFISHG) [8]. In the present paper, ambipolar carrier behaviour in pentacene FET is reported based on results of time resolved, optical second harmonic generation (TRM-SHG). In our previous paper, TRM-SHG measurement was introduced for visualizing carrier motion in OFETs based on the EFISHG [9]. Since the SHG signal is activated by an electric field applied to organic materials [10, 11], carrier motion can be observed by following the time evolution of the electric field distribution in the devices because charges are the source of a local electric field. One of the important advantages of the TRM-SHG method is the capacity to discriminate the injection and transport processes in devices. By using this technique, injection of an electron from noble metals such as Au into pentacene is revealed, and the motion of both carriers in pentacene FET is visualized with a high spatial resolution lower than 1 μm . Furthermore, we introduce the method of evaluation of transient electric field distribution in OFET by analyzing the TRM-SHG results. Quantitative analysis of the time-dependent electric field distribution would be helpful for subsequent discussion regarding the device operation mechanism.

2. Experimental

The samples used in the experiments were top-contact pentacene FETs. Heavily doped Si wafers covered with a 500 nm thick oxide (SiO_2) layer were used as the base substrate. Before the pentacene deposition, a 100 nm thick poly(methyl methacrylate) layer (PMMA) was spin-coated in order to improve the on-off ratio of the devices. Then, the pentacene layer, approximately 100 nm thick, was deposited on a surface. The process pressure during deposition of pentacene was kept at less than 1×10^{-4} Pa, and the deposition rate was controlled at approximately 3 nm/min. After the deposition of pentacene, top-Au electrodes (source and drain electrodes) 100 nm thick were deposited. The designed channel length (L) and width (W) were 50 μm and 3 μm ,

respectively. Pentacene FETs were operated with the application of pulse voltages using a function generator (NF Corp., WF1947) and a high speed bipolar amplifier (NF Corp., HSA4101). All measurements were performed in laboratory ambient atmosphere.

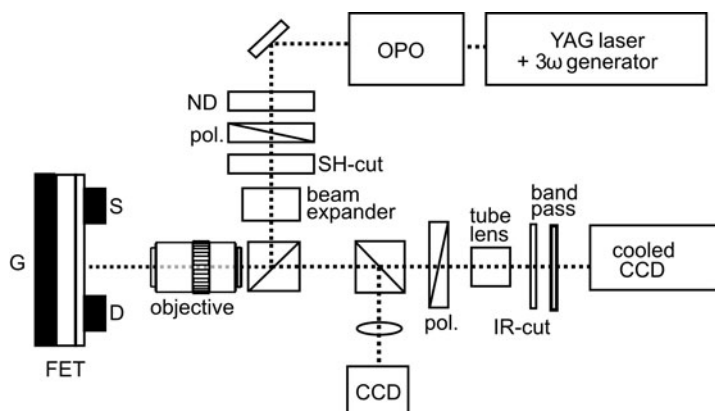


Fig. 1. Optical configuration of the TRM-SHG measurement. Wavelength of the SHG measurement can be changed using OPO, and fundamental light with the wavelength of 1120 nm was chosen in this experiment [12]. The fundamental light is focused on the device using a microscopic objective lens

The light source for the TRM-SHG measurement was an optical parametric oscillator (OPO: Continuum Surelite OPO) pumped by the third-harmonic light of a Q-switched Nd-YAG laser (Continuum: Surelite II-10). An external Q-switch signal from a YAG laser was also supplied from a function generator to synchronize the voltage pulse applied to the OFET with the laser pulse. A timing chart of the voltage pulse applied to the OFET and of the laser pulse is presented in [10]. Fundamental light was focused onto the channel region of OFET with normal incidence using a long working distance objective lens (Mitutoyo: M Plan Apo SL20 \times , NA = 0.28, W.D. = 30.5 mm). The fundamental light irradiated a large area (spot size was approximately 150 μm) of the channel region for taking SHG image by using a beam expander (Fig. 1). SH light generated from the FET was filtered by a fundamental-cut filter and an interference filter to remove fundamental and other unnecessary light. Finally, SH light generated was detected by a cooled CCD camera (Andor technology: DU420-BV). In this configuration, the polarization direction of the fundamental light was chosen in the direction corresponding to the channel direction (source-drain direction).

3. Results and discussion

3.1. Hole injection

Figure 2 represents the SHG images from an OFET channel captured with various delay times. To take these images, positive pulses were applied to the source elec-

trode. Here, a source electrode is defined as an electrode from which carriers are injected by the applied voltage pulse. As shown, the SHG peak moves rapidly from the source to the drain electrode with an increase of delay time. It should be noted that no SHG signal was observed from the FET without the pentacene layer. Needless to say, such a device does not show any FET characteristics, though the SiO₂ insulator is subjected to an external electric field. Thus the SHG signal from the gate insulator is negligibly small and the SHG signal from the pentacene layer was selectively observed. In our previous paper, it was shown that migration of the peak position of the SHG intensity follows a novel, diffusion-like behaviour; namely, the square of the peak position of \bar{x} is proportional to time t [13]. As just described, the time-resolved measurement successfully demonstrated the emission band movement of the SHG.

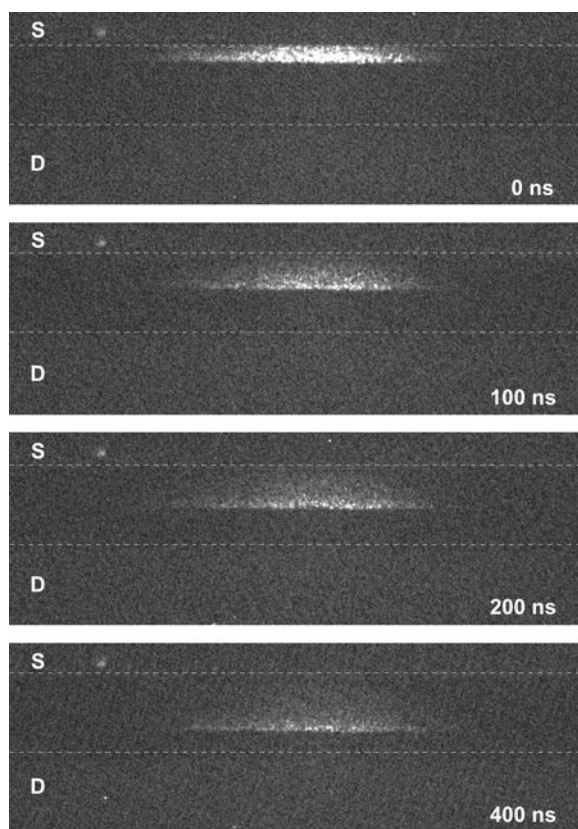


Fig. 2. SHG images from OFET channel with various delay times under the application of positive pulse to the source electrode. These images are top-view of pentacene OFET, the region between two dashed lines corresponds to the channel of the FET. Actual channel length was 45 μm . S and D represent the source and drain electrode, respectively

For hole injection, the injected holes from the source electrode spread immediately over the FET channel. It should be noted that SH intensity immediately disappears

(actually it takes less than 100 ns) at the electrode edge: this indicates a low injection barrier for holes between the Au and the pentacene. After carrier injection, carriers adequately accumulate in the channel. Sufficiently accumulated charges in the channel form the space charge field that cancels out the source field, so that no SHG signal is generated from the edge of the source electrode. Disappearance of the SHG signal around the electrode clearly supports this assertion, that is, no electric field is concentrated at the edge of the electrode. Under our experimental condition, vacuum evaporated pentacene film is composed of a number of small-size domains (domain size was less than 1 μm), and the *a*- and *b*-axis of pentacene crystals align parallel to the substrate surface [14], that is the *c*-axis almost aligns normally to the surface. In that case, electronic conduction is dominated along in-plane direction [15], reflecting strong intermolecular interaction along the *ab* direction. Therefore, it is reasonable to consider that $\chi^{(3)}$ components of pentacene film along the *c*-axis are small compared with that along the in-plane direction. Consequently, the SHG signal is sensitive to the in-plane components of the electric field in pentacene film under the normal incidence condition.

3.2. Electron injection

Figure 3 shows the SHG images from an OFET channel with various delay times associated with an applied negative pulse. To capture these images, negative pulses were applied to the source electrode. It was found that the emission band of the SHG slightly moved away from the source electrode, as shown in the figure. This result indicates that electron injection from the Au electrode to pentacene film was actually possible. Since the energy difference between the LUMO of pentacene and the Fermi level of Au is approximately 2.0 eV [6], electron injection is quite difficult and it is reasonable to consider that electron injection from Au into pentacene is not possible. Metal deposition onto the pentacene layer leads to the penetration of metal atoms into the pentacene layer [5]. Such penetration of metal results in appearance of the interfacial states near the pentacene–Au interface. For hole injection with negligible injection barrier, such interfacial states must prevent the injection, and lead to the degradation of device parameters, such as field effect mobility. However, these interfacial states presumably accept electrons via a tunnelling process from the Au surface. Electron injection, which is strongly inhibited by the energy difference between the LUMO of pentacene and the Fermi level of Au, is presumably promoted under the presence of such states.

Another possible mechanism for the electron injection is the interface dipole layer at the pentacene–Au interface. Formation of the interface dipole layer at the pentacene–Au interface was revealed using UPS measurement in [16], and such an interface dipole supposedly promotes electron injection. As well as at the pentacene–Au interface, UPS measurement also confirmed the presence of the interface dipole at the pentacene–Ag interface. For the Ag electrode, the work function of an Ag surface is lower than that of a Au surface, leading to a more efficient injection of electrons from the Ag

electrode. It should be noted that such electron injection was not observed in the devices using an Ag electrode by the TRM-SHG measurement obtained within the constraints of our experiments. In this sense, penetration of metal atoms into the pentacene layer is more possible for the electron injection. However, at the present stage, the true mechanism of electron injection is not clear. To reveal the details of electron injection such as the mechanisms is our future task.

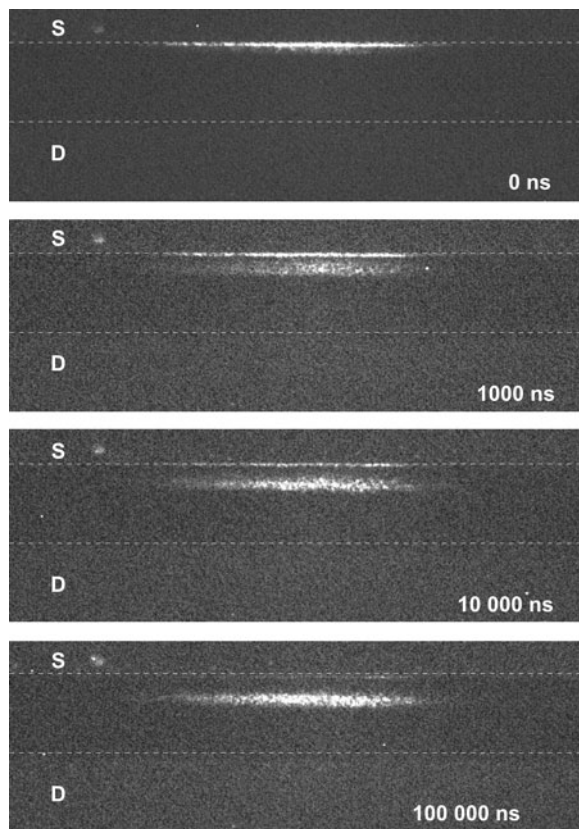


Fig. 3. SHG images from OFET channel with different delay times under the application of a negative pulse to the source electrode. At the edge of source electrode, SH signal still remains at a delay time of 10 μ s, though it disappears at the delay time of 100 μ s

Interestingly, after the electron injection, motion of the emission band of the SHG stopped immediately near the source electrode (see Fig. 3). Needless to say, it moved smoothly and continuously along the channel for hole injection as a positive pulse was applied (see Fig. 2). These results imply that injected electrons were trapped near the electrode in the FET channel. Benzocyclobutene (BCB) and PMMA layer inserted between organic semiconductor and insulator is frequently used to prevent the electron entrapment [3]. In the present study, PMMA was coated on the SiO₂ surface but the trapping of electrons is actually observed, presumably owing to the presence of oxy-

gen [17, 18] and moisture. Although the electron trapping at the organic semiconductor/insulator interface has been commonly discussed, there is as yet no detailed understanding of such traps. This is the first time to directly observe the interruption of the electron transport. Such observation certainly might help with solving the problem of carrier transport inhibition.

3.3. Electric field distribution

Quantitative evaluation of the transient electric field distribution is introduced, based on the analysis of the SH intensity distribution. For the discussion of the device mechanisms of OFET with the TRM-SHG measurement, some of the most important information which can be extracted from the TRM-SHG results is the time evolution of the electric field and the carrier distribution along the FET channel.

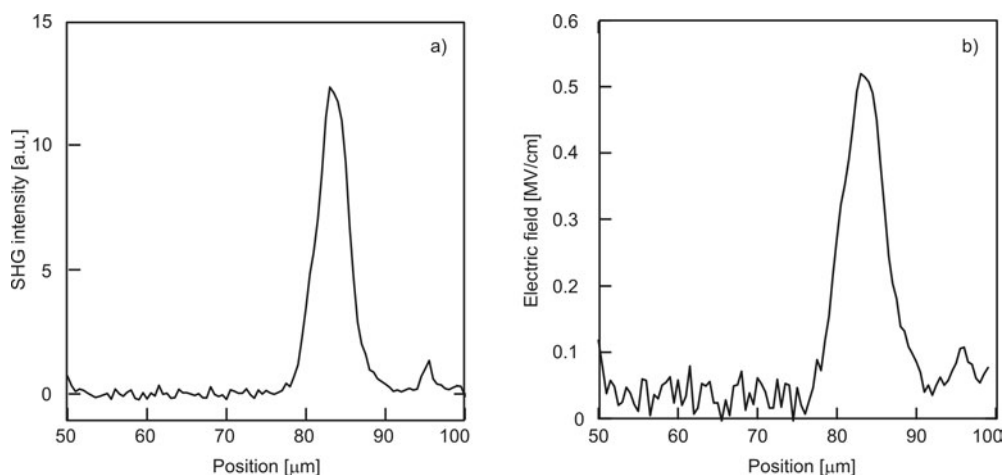


Fig. 4. Typical example of the SH intensity distribution along the FET channel (a) obtained by taking a cross section of an SH image shown in Fig. 3. SH intensity distribution under the electron injection at the delay time of 100 μs is indicated, and electric field distribution along the FET channel (b) evaluated from an SH intensity distribution

In Figure 4, an exemplary SH intensity distribution along the FET channel obtained by taking a cross section of an SH image shown in Fig. 3 (for electron injection, at the delay time of 100 μs), and the distribution of the lateral component of the electric field in the FET channel, respectively. Since SHG intensity is proportional to the square of the local electric field for the EFISHG process, electric field distribution can be obtained with a high spatial resolution by only taking the square root of the SHG distribution. Note that the absolute value of the electric field strength cannot be obtained directly from the SHG intensity. Nevertheless, we can evaluate the electric field strength by comparing it with the result of a reference measurement. Without carrier injection, a Laplace electric field is formed in the devices under the voltage applied to

the electrode. In that case, electric field distribution can be calculated based on the classical electromagnetic theory, taking into account the device geometry [19]. Thus, comparing the theoretical electric field strength with the SHG intensity, the electric field distribution in the devices can be experimentally evaluated.

In a Laplace electric field, the electric field is concentrated between source and gate electrodes, and, accordingly, the peak position of the electric field is located at the edge of the source electrode. In contrast, the peak position of the electric field moves away from the source electrode and is located between the source and drain electrodes after electron injection (see Fig. 4b). This fact clearly indicates that the electric field, after electron injection, is dominated by the space charge field due to the injected electrons. The TRM-SHG measurement can evaluate the transient electric field in devices at high spatial (approximately 1 μm) and temporal (10 ns) resolutions.

4. Conclusion

Ambipolar carrier injection from gold electrode into pentacene was investigated by time-resolved, optical second harmonic generation (TRM-SHG) imaging. Although electron injection from Au into pentacene is quite difficult, because the energy difference between the LUMO of pentacene and the Fermi level of Au is approximately 2.0 eV, TRM-SHG results clearly indicated the electron injection from high-work function metal into pentacene. For this electron injection, motion of the emission band of the SHG stopped in the channel, indicating that the injected electrons were trapped in the OFET channel. A transient electric field, due to injected electrons, was evaluated based on the SHG intensity distribution.

Acknowledgement

This work is supported by the New Energy and Industrial Technology Development Organization (NEDO). Support by the Grants-in-Aid for Scientific Research (Grants Nos.18686029 and 15206032) is also gratefully acknowledged.

References

- [1] OGAWA S., KIMURA Y., ISHII H., NIWANO M., *Jpn. J. Appl. Phys.*, 42 (2003), L1275.
- [2] YASUDA T., GOTO T., FUJITA K., TSUTSUI T., *Appl. Phys. Lett.*, 85 (2004), 2098.
- [3] CHUA L.L., ZAUMSEIL J., CHANG J.F., OU E. C.W., HO P.K.H., SIRRINGHAUS H., FRIEND R.H., *Nature*, 434 (2005), 194.
- [4] ZAUMSEIL J., FRIEND R.H., SIRRINGHAUS H., *Nat. Mater.*, 5 (2006), 69.
- [5] CHO J.H., KIM D.H., JANG Y., LEE W. H., IHM K., HAN J.-H., CHUNG S., *Appl. Phys. Lett.*, 89 (2006), 132101.
- [6] KARL N., [In:] *Organic Electronic Materials*, R. Farchioni, G. Grosso (Eds.), Springer, Berlin, 2001, p. 231.
- [7] MICHAELSON H.B., *J. Appl. Phys.*, 48 (1977), 4729.
- [8] LIM E., MANAKA T., IWAMOTO M., *J. Appl. Phys.*, 101 (2007), 024515.

- [9] MANAKA T., LIM E., TAMURA R., IWAMOTO M., *Nat. Photonics*, 1 (2007), 581.
- [10] MANAKA T., LIM E., TAMURA R., YAMADA D., IWAMOTO M., *Appl. Phys. Lett.*, 89 (2006), 072113.
- [11] MANAKA T., NAKAO M., YAMADA D., LIM E., IWAMOTO M., *Opt. Express*, 15 (2007), 15964.
- [12] MANAKA T., SUZUE Y., IWAMOTO M., *Jpn. J. Appl. Phys.*, 44 (2005), 2818.
- [13] MANAKA T., LIU F., MARTIN W., IWAMOTO M., *Phys. Rev. B*, 78 (2008), 121302(R).
- [14] MINAKATA T., IMAI H., OZAKI M., SACO K., *J. Appl. Phys.*, 72 (1992), 5220.
- [15] CHENG Y.C., SILBEY R.J., Da SILVA FILHO D.A., CALBERT J.P., CORNIL J., BREDAS J.L., *J. Chem. Phys.*, 118 (2003), 3764.
- [16] WATKINS N.J., YAN L., GAO Y., *Appl. Phys. Lett.*, 80 (2002), 4384.
- [17] HADDON R.C., PEREL A.S., MORRIS R.C., PALSTRA T.T.M., HEBARD A.F., FLEMING R.M., *Appl. Phys. Lett.*, 67 (1995), 121.
- [18] LAQUINDANUM J.G., KATZ H.E., DODABALAPUR A., LOVINGER A.J., *J. Am. Chem. Soc.*, 118 (1996), 11331.
- [19] YAMADA D., MANAKA T., LIM E., TAMURA R., IWAMOTO M., *J. Appl. Phys.*, 103 (2008), 084118.

Received 28 August 2008

Revised 7 February 2009

Observation of electron injection in an organic field-effect transistor with electroluminescence*

Y. OHSHIMA**, H. KOHN, E. LIM, T. MANAKA, M. IWAMOTO

Department of Physical Electronics, Graduate School of Science and Engineering,
Tokyo Institute of Technology, 2-12-1 Ookayama, Meguro-ku, Tokyo 152-8552, Japan

A tetracene field-effect transistor (FET) with Au source and drain electrodes showed p-channel type behaviour, where the injected holes were the main carriers. Application of an ac electric field to the source electrode, while drain and gate electrodes were grounded, induced electroluminescence (EL) around the source electrode that was caused by alternating electron and hole injection. This result indicated that electron injection into tetracene was possible from a metal with a high work function such as Au. The application of an ac voltage superposed on a dc voltage showed that electron injection was assisted by the space-charge field that originated from holes accumulated around the source electrode.

Key words: *electroluminescence; field-effect transistor; tetracene; space charge field*

1. Introduction

Organic materials have been used as electrical insulators because of their mechanical flexibility and high insulating performance which is why they are suitable for power cables, for example [1]. In order to use organic materials as insulators, we should always pay attention to dielectric breakdown phenomena, where charge injection from metal into insulator leads to electrical treeing and subsequently to dielectric breakdown [2]. Under an applied ac voltage, electrons and holes inject into an insulator alternately, and light emission is induced during their recombination process [3–5]. This light emission is known as electroluminescence (EL), and is utilized as one of the diagnostic methods for detecting dielectric pre-breakdown of an electrical insulator.

On the other hand, the recent discovery of organic semiconducting materials has opened a new way to use organic materials for electronic devices such as an organic

*The paper presented at the 11th International Conference on Electrical and Related Properties of Organic Solids (ERPOS-11), July 13–17, 2008, Piechowice, Poland.

**Corresponding author, e-mail: ohshima.y.aa@m.titech.ac.jp

field-effect transistor (OFET) and an organic light-emitting diode (OLED) [6]. In OLEDs operating under an applied dc voltage, electrons and holes are injected from cathode and anode, respectively, and they recombine, leading to the EL phenomenon [7, 8]. Here efficient charge injection is one of the key parameters for practical applications such as displays and light sources.

As mentioned above, organic EL is considered to be a phenomenon triggered by charge injection but it has two aspects; as a dielectric pre-breakdown phenomenon under ac electric field and as a light-emitting source of devices under a dc electric field. Therefore we consider two EL modes for discussing the EL mechanism, that is, an ac excited mode and a dc excited mode. For understanding the difference in the mechanisms of the two EL modes, we need to know the electric field distribution in organic devices because electrons and holes might be along the electric field, and carrier injection is ruled by the electric field formed at the electrode. However, injected charges are excess charges, and generate a space-charge electric field. This complicates the electric field distribution in organic devices and the carrier injection mechanism. Note that the determination of an electric field in OLED at the nanometer scale is generally difficult because active organic layers are installed as a metal–organic multilayer–metal systems.

OFETs have drawn our attention along with the discovery of high-mobility organic materials where injected carriers mainly contribute to a device performance [6], where carrier injection is a key parameter. Hepp et al. reported the enhancement of green light emitted from tetracene FET [9]. They argued that holes injected from the source electrode moved to the drain electrode, and then they recombined with electrons injected from the drain electrode via tunnelling. Interestingly, the use of three electrodes as in OFET provides a way to control hole and electron injection, because we can choose the drain and gate voltages independently. We can see such examples in recent experiments on organic EL using OFET structure [10, 11]. That is, light-emitting OFET can be used as one of the model systems to study physics of EL devices.

In our previous study, we observed EL from tetracene FET under an ac electric field, and concluded that the EL under an ac electric field is helpful for investigating the carrier injection process [12, 13]. In this study, we focused on the effect of space charge field caused by injected carriers under an ac electric field.

2. Experimental

Sample preparation. Tetracene was purchased from Tokyo Kasei Kogyo and was used without further purification. It is well known as an active material in OFET and OLED because of its high carrier mobility and intrinsic, visible luminescent emission [14, 15]. Therefore, tetracene is one of the most appropriate materials for observing the EL enhanced in an OFET structure. Tetracene thin films show absorption with the maximum at ca. 520 nm and photoluminescence (PL) at ca. 532 nm [16].

Figure 1 illustrates the structure of the tetracene FET employed. High-doped Si substrate, coated with a thermally grown SiO_2 layer (500 nm thick) was used for the OFET substrate. Interdigital Au electrodes were deposited on the SiO_2 as source and drain electrodes, using the photolithography technique. The channel length and width were 50 μm and 11 μm , respectively. High-doped Si was used as a gate electrode. The substrate was cleaned, in an ultrasonic cleaning system, with acetone, ethanol, and distilled water, and then it was subject to UV/ozone treatment for 30 min. After that, tetracene was deposited on the substrate by thermal evaporation in a vacuum at the pressure lower than 2×10^{-6} Torr. The deposition rate and the film thickness were adjusted to about 0.6–1.1 $\text{\AA}/\text{s}$ and 200 nm, respectively, using a quartz crystal microbalance.

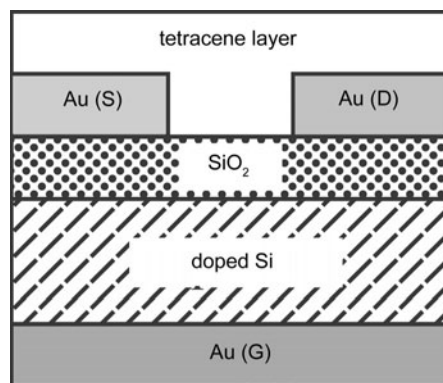


Fig. 1. Device structure of tetracene FET

Measurement. Figure 2 shows the experimental setup for EL measurement. A square wave voltage was applied between the source (S) and gate (G) electrodes

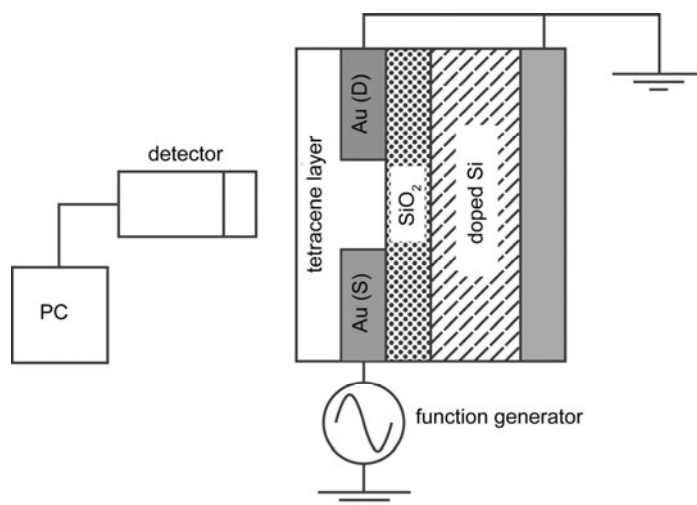


Fig. 2. Experimental setup for the observation of EL under ac electric field. This setup was located in the chamber and the measurement was carried out in vacuum or in Ar gas atmosphere

using a function generator (NF WF1944) and a high-speed amplifier (NF 4005), while the drain (D) and gate electrodes were grounded. Hereafter, we refer to this square wave voltage as “ac voltage”. By applying the ac voltage, electron and hole injection take place alternately from the source electrode. The spatial distribution of the EL intensity in tetracene FET was monitored using a charge-coupled device (CCD) imaging sensor (Andor DU420-BV), where a 40 V ac voltage at 300 kHz was applied in an Ar gas atmosphere. The EL spectrum from tetracene FET was obtained by using a multi-channel spectrometer (Andor SR163 with Newton 920-BV) in a vacuum of less than 10^{-6} Torr. Here, the EL was measured by applying a 50 V ac voltage at 500 kHz. Photoluminescence (PL) spectrum was obtained by using the spectrometer (BWtek BTC112E) where the ultraviolet light emitting diode (LED) at the wavelength of 400 nm was used for the excitation of tetracene thin film. In addition, EL intensity was measured in a vacuum using a photomultiplier tube (PMT; Hamamatsu R3869) by changing the ac voltage amplitude from 10 V to 60 V. EL intensity was monitored as a PMT current, I_{photo} , by using a digital picoammeter (Keithley 6487). In this measurement, the applied voltage was always positive, in order to examine the effect of space charge field.

3. Results and discussion

3.1. Current-voltage characteristics

The output and transfer characteristics of tetracene FET are shown in Fig. 3a, b, respectively. Tetracene FET operated as a p-channel type OFET, where holes injected from an Au electrode made the main contribution to the drain current. The hole mobility, calculated from the slope of the transfer characteristics, was about $5 \times 10^{-4} \text{ cm}^2 \cdot \text{V}^{-1} \cdot \text{s}^{-1}$.

3.2. Observation of EL

Figure 4 shows the spatial distribution of EL intensity in the channel region of tetracene FET. The enhancement of EL was observed around the edge of the source electrode, because holes and electrons injected into the tetracene alternately, and recombined in the same region. Note that the light emitted in this process could be seen in the dark with the naked eye.

The result suggested that EL was enhanced only around the edge of the source electrode, not in the channel region of the FET. The following reasons were considered:

1. ac frequency was too high and injected carriers did not spread over the channel.
2. Nearly all injected electrons were trapped at the interface between the tetracene and the source electrode, and they did not enter into the channel region.
3. Carrier injection was only possible from the source electrode, and injected electrons and holes recombined only around the edge of the electrode.

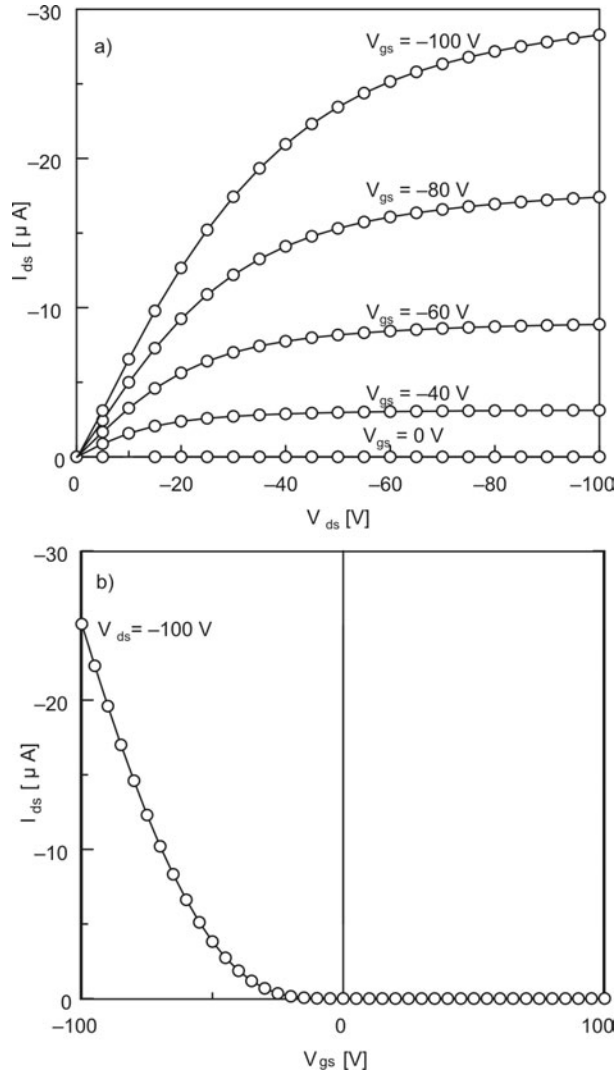


Fig. 3. Output characteristic (a), and transfer characteristics (b) of tetracene FET. Digital source meter (Keithley 2400) was used for voltage source and measurement of the drain current. V_{ds} was set at -100 V in transfer characteristics

Here it is instructive to calculate the hole transport distance, L_{drift} , within a half cycle of ac voltage. L_{drift} is given by

$$L_{\text{drift}} = \mu_h E_{\text{ext}} \frac{1}{2f} \quad (1)$$

where μ_h is the hole mobility, E_{ext} is the external electric field from the source to drain direction, f is the ac frequency. From Eq. (1) with $\mu_h = 5 \times 10^{-4} \text{ cm}^2 \cdot \text{V}^{-1} \cdot \text{s}^{-1}$, $E = 8 \times 10^3 \text{ V} \cdot \text{cm}^{-1}$, and $f = 300 \text{ kHz}$, L_{drift} is calculated to be about 67 nm from the source elec-

trode. Therefore, the first explanation (i.e. reason 1 above) accounts for the local light-emission around the source electrode. However, we cannot exclude the other reasons (2 and 3) from the experimental results obtained here, and further investigation is needed.

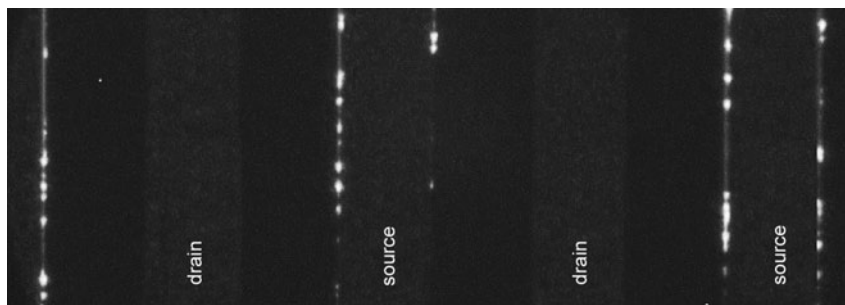


Fig. 4. Spatial distribution of EL intensity in tetracene FET

In summary, electron injection was detected using the EL under an ac electric field, even when this electron injection was undetectable from the FET characteristics.

3.3. EL spectrum

EL and PL spectra are shown in Fig. 5. There is an EL spectrum peak at the wavelength of ca. 540 nm, corresponding to the position of the PL spectrum peak. This

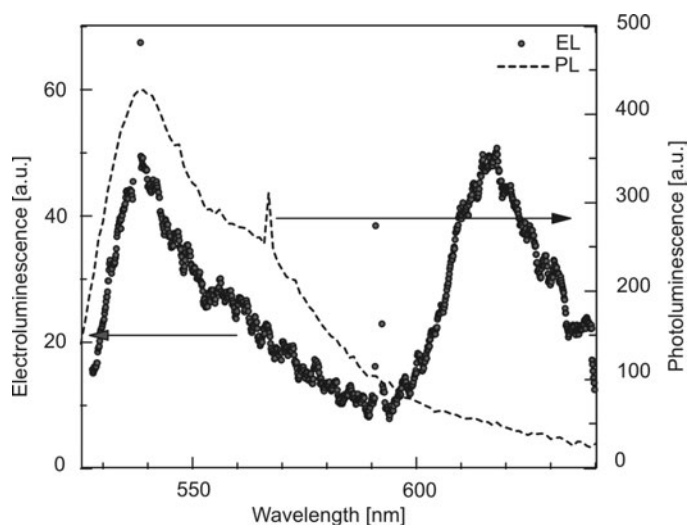


Fig. 5. EL and PL spectra of tetracene FET

peak indicates that this emission originates from the intrinsic luminescence of tetracene thin film [9, 13]. On the other hand, another EL peak appeared at a longer wavelength of ca. 620 nm, possibly due to the presence of an interfacial trapping state be-

tween the metal electrode and the tetracene thin film [17]. The average depth of the trapping state, calculated from the peak separation, was estimated to be about 0.29 eV from the highest occupied molecular orbital (HOMO) state, for a hole, or -0.29 eV from the lowest unoccupied molecular orbital (LUMO) state, for an electron. However, we should consider a possible presence of electron traps, because holes inject and transport very smoothly in comparison with electrons (see Fig. 3).

3.4. Electron injection process from Au electrode

From the current–voltage characteristics, we could not detect the presence of electron injection. However, the EL measurement under an ac electric field suggested that alternating carrier injection from the electrodes did indeed occur. Two reasons were considered; one is that injected electrons do not move in the material; the other is that electron injection is assisted by the space-charge field formed by accumulated holes in the FET channel region. To clarify the electron injection process assisted by the space charge field, a square-wave voltage, having the form illustrated in Fig. 6, was applied to the source electrode. Note that the voltage applied to the source electrode changed in a positive region. That is, electrons could not inject into tetracene by an external electric field. Voltage amplitude was defined V_p , as given in Fig. 6, and the V_p dependence of EL intensity was measured.

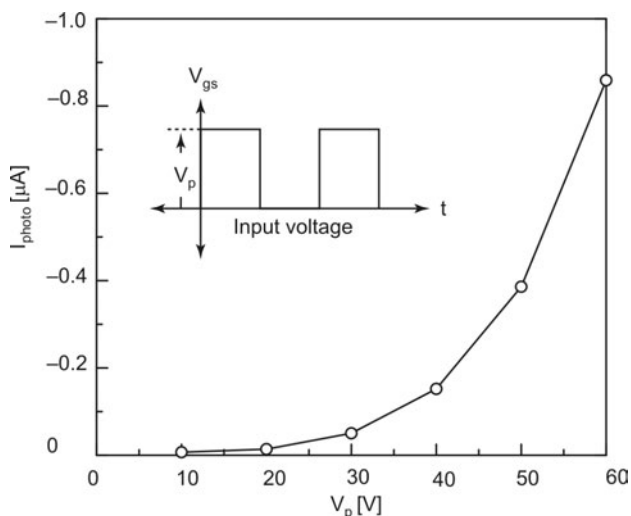


Fig. 6. V_p dependence of EL intensity. The voltage waveform illustrated in the graph was applied to the source electrode in this measurement

Figure 6 shows that EL intensity increased as the V_p increased, though the applied voltage was always in a positive region. This indicates that electrons were injected not only by an external electric field but also by the space charge field. Injected electrons recombined with holes which were injected and accumulated in tetracene by an exter-

nal electric field V_p . That is, the accumulated holes form a space charge field that assists electron injection. As mentioned above, the space charge field plays a significant and important role in the charge injection process under an ac electric field.

Furthermore, the light emission initiated at the voltage V_p of about 20 V, where the electric field is about $4 \times 10^5 \text{ V} \cdot \text{cm}^{-1}$. This field reasonably accounts for charge injection from metal into organic materials.

4. Conclusion

We investigated the charge injection from an Au electrode into tetracene in an OFET structure using EL under an ac electric field. We detected the existence of EL under an ac electric field using a CCD imaging sensor and a multichannel spectrometer. We observed EL from the edge of the source electrode of tetracene FET by applying an ac voltage to the source electrode. This EL had a spectrum peak at a wavelength corresponding to the PL spectrum peak. We confirmed the electron injection without the external electric field by using the EL. The effect of a space charge field formed by accumulated holes is important in the charge injection process under an ac electric field.

References

- [1] SESSLER G. M., *Electrets*, Springer, New York, 1987. (2nd Ed.)
- [2] KOSAKI N., SHIMIZU N., HORII K., *IEEE. Electr. Insul.*, Ei-12 (1977), 40.
- [3] SHIMIZU N., KOSAKI M., HORII K., *J. Appl. Phys.*, 48 (1977), 2191.
- [4] LEBEY T., LAURENT C., *J. Appl. Phys.*, 68 (1990), 275.
- [5] LIU Y. S., MIZUNO T., YASUOKA K., ISHII S., *Jpn. J. Appl. Phys.*, 37 (1998), 146.
- [6] BRUTTING W., *Physics Of Organic Semiconductors*, Wiley, Weinheim, 2005.
- [7] TANG C. W., VANSLYKE S. A., *Appl. Phys. Lett.*, 51 (1987), 913.
- [8] HELFRICH W., SCHNEIDER W. G., *Phys. Rev. Lett.*, 14 (1965), 229.
- [9] HEPP A., HEIL H., WEISE W., AHLES M., SCHMECHEL R., VON SEGGERN H., *Phys. Rev. Lett.*, 91 (2003), 157406.
- [10] ZAUMSEIL J., FRIEND R. H., SIRRINGHAUS H., *Nature Mater.*, 5 (2006), 69.
- [11] TAKAHASHI T., TAKENOBU T., TAKEYA J., IWASA Y., *Adv. Funct. Mater.*, 17 (2007), 1623.
- [12] OHSHIMA Y., KOHN H., LIM E., MANAKA T., IWAMOTO M., *Jpn. J. Appl. Phys.*, 47 (2008), 1297.
- [13] OHSHIMA Y., KOHN H., LIM E., MANAKA T., IWAMOTO M., *Jpn. J. Appl. Phys.*, 47 (2008), 3200.
- [14] DE BOER R. W. I., KLAPWIJK T. M., MORPURGO A. F., *Appl. Phys. Lett.*, 83 (2003), 4345.
- [15] YOU E. A., HA Y. G., CHOI Y. S., CHOI J. H., *Synth. Met.*, 153 (2005), 209.
- [16] WAPPELT A., BERGMANN A., NAPIWOTZKI A., EICHLER H. J., JUPNER H. J., KUMMROW A., LAU A., WOGGON S., *J. Appl. Phys.*, 78 (1995), 5192.
- [17] SALANECK W. R., SEKI K., KHAN A., PIREAUX J. J., *Conjugated Polymer and Molecular Interfaces*, Marcel Dekker, New York, 2002.

Received 1 September 2008

Revised 26 January 2009

Circular dichroism and electroluminescence of poly(diacetylene) film with chirality*

H. KOHN, M. FUKADA, Y. OHSHIMA, T. MANAKA, M. IWAMOTO**

Department of Physical Electronics, Graduate School of Science and Engineering,
Tokyo Institute of Technology, 2-12-1 Ookayama, Meguro-ku, Tokyo 152-8552, Japan

By applying only circularly polarized light (CPL) irradiation to evaporated achiral diacetylene (DA) monomer film during its photopolymerization process, we prepared poly(diacetylene) (PDA) films that show circular dichroism (CD). The left- or right-handed chirality was induced in the polymerized PDA films by the left- and right-CPL irradiation. We studied physical properties of the prepared PDA films, including their electrical and optical properties. The induced chirality in PDA films was not destroyed after annealing at 353 K for 10 min, whilst their blue-phase was changed into a red one. The intensity of the CD signal was dependent on the substrate temperature employed for the monomer deposition. Electroluminescence was found to be enhanced with the polymerized PDA films installed as an active layer of organic field-effect transistors.

Key words: *poly(diacetylene); circularly polarized light; chirality; electroluminescence*

1. Introduction

Recently, chiral conjugated polymer with helical structure has drawn attention in electronics, e.g., as a source material of inductor, as an active layer of polarized luminescence devices, etc., and a variety of preparation techniques have been proposed [1]. Among them, the most well-known preparation method is to use a chiral dopant. Akagi et al. prepared helical polyacetylene (PA) from acetylene monomers mixed with chiral liquid crystal [2, 3]. A method without using dopant has also been proposed. Wu et al. introduced chirality into an achiral liquid crystal polymer by using a conformational change of azobenzene by photoisomerization [4]. However, so prepared conjugated polymers contain impurities of a chiral dopant or photofunctional

*The paper presented at the 11th International Conference on Electrical and Related Properties of Organic Solids (ERPOS-11), July 13–17, 2008, Piechowice, Poland.

**Corresponding author, e-mail: iwamoto@pe.titech.ac.jp

moiety used in their fabrication. We found a way, without using chiral dopant or photofunctional moiety, for the fabrication of pure chiral poly(diacetylene) (PDA) films by only applying circularly polarized light (CPL) to precursor achiral diacetylene (DA) monomer film in its photopolymerization process [5]. By the use of this technique, we could prepare chiral PDA Langmuir–Blodgett (LB) films as well as chiral PDA evaporated films. However, the details of the induced chirality are still not clear. It is necessary to understand the relationship between the induced chirality and the conditions under which films are prepared, e.g. annealing temperature, irradiation time of CPL, etc. Furthermore, we have not yet studied the physical properties of the prepared chiral PDA films, e.g., their electrical transport property. In this paper, we study the induced chirality in PDA films prepared at various substrate temperatures, and then investigate the electrical transport property and electroluminescence (EL) of the prepared PDA films that were installed as an active layer of organic field-effect transistor (FET) with gate-SiO₂ insulator.

2. Sample preparation

10,12-Tricosadiynoic acid (TDA), CH₃(CH₂)₉C≡C–C≡C(CH₂)₈COOH, was purchased from Tokyo Chemical Industry Co., Ltd., and used without further purification. The TDA monomers were deposited on a glass substrate by the vacuum evaporation. The evaporation rate was set to 0.8 Å/s, and the film thickness of deposited TDA was approximately 100 nm. The pressure was lower than 2.3×10⁻⁴ Pa during deposition, and the substrate temperature was 313 K. After the TDA deposition, the substrate temperature was kept at 293 K, and the substrate was immediately removed from the vacuum system for photoirradiation. Photopolymerization of TDA films was carried out using 314 nm UV light from a high-pressure Hg lamp (Hamamatsu L-8333), where the UV light was irradiated onto the samples perpendicularly.

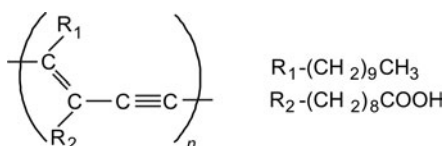


Fig. 1. Chemical structure of PDA

The intensity of each left- and right-CPL was approximately 19.4 mW/cm², and the irradiation time was 25 min. After photoirradiation, blue-phase PDA was polymerized from TDA monomers (Fig. 1). Finally, red-phase PDAs were prepared by annealing (353 K, 10 min). For the study of the carrier transport property, chiral red-phase PDA films polymerized using left- and right-CPL were prepared on the SiO₂ (500 nm)/n-Si substrate, and it was installed as an active layer of the bottom contact FET (Fig. 2). EL was measured using the FET under alternating current (ac) voltage.

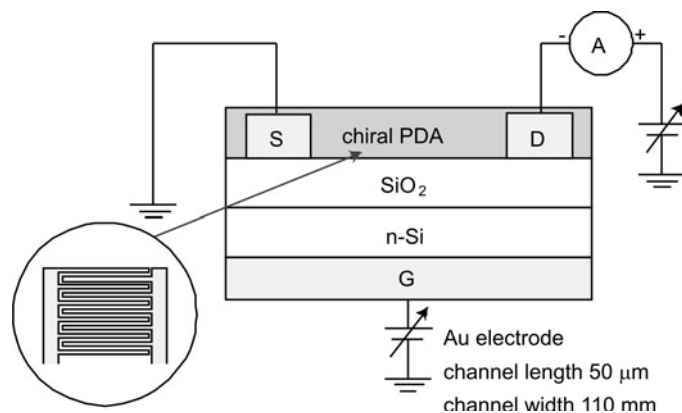


Fig. 2. Measurement set up for the chiral red phase PDA-FET (bottom contact type)

3. Results and discussion

3.1. Chiral PDA and optical properties

The circular dichroism (CD) spectra of red-phase PDAs polymerized by left- and right-CPL are shown in Fig. 3 (for the CD measurement, the spot area of incident light was $7 \times 7 \text{ mm}^2$).

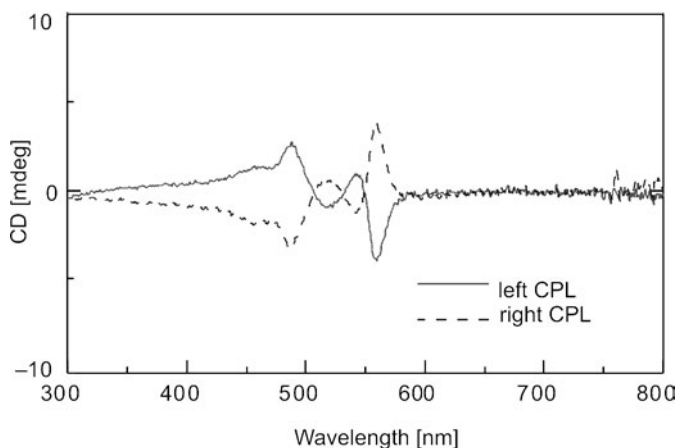


Fig. 3. CD spectra of evaporated PDA films. The samples were fabricated at 313 K. Solid and dashed lines represent the spectra for the films polymerized with left (solid line) and right (dashed line) CPL irradiation

In our previous study, achiral TDA monomers were deposited by evaporation on the glass substrate, and then transformed into chiral blue-phase PDA by irradiating

CPL. The induced chirality withstood for a long time after the phase transition from blue-phase to a red one [5]. It was considered that the phase transition of PDA was caused by the distortion of the backbone [6], that is, single-bond of the backbone rotated in accordance with the reorientation of the side chains during annealing. On the other hand, the surface morphology was strongly dependent on the substrate temperature employed for the evaporation. Tanaka et al. reported that crystallinity of an *n*-paraffin film changed with respect to the substrate temperature [7]. The vacuum-deposited TDA film is composed of a large number of domains, and each domain consists of the rod-like TDA monomers resembling an *n*-paraffin chain. Polymerization of TDA monomers proceeds on keeping the original crystal structure (i.e., topochemical reaction) [8, 9]. Therefore, a large conjugated system is formed perpendicularly to the long axis of monomers, and crystallinity of PDA film prepared by UV light irradiation can change, depending on the packing structure. Furthermore, when CPL irradiation was introduced into the polymerization process after controlling the substrate temperature, a stronger CD signal was observed, accompanied by larger domains on the surface at high substrate temperature (313 K) [10, 11].

3.2. Electrical transport property of chiral PDA

Figure 4 shows typical current–voltage (I_{DS} – V_{DS}) characteristics of chiral PDA-FET at various gate voltages V_G (from 0 to ca. -100 V), measured under the pressure lower than 1×10^{-4} Pa. As shown in the figure, I_{DS} increased when a negative gate voltage was applied, and p-channel type FET behaviour was confirmed.

In contrast, no n-channel FET behaviour was observed when a positive gate voltage was applied. Under the gradual channel approximation, I_{DS} in a saturated region is expressed as

$$I_{DS} = \frac{1}{2} \frac{W}{L} \mu C_{OX} (V_G - V_{Th})^2 \quad (3.1)$$

where L and W are the channel length and width, respectively, and C_{OX} is the capacitance per unit area of the SiO_2 gate insulator [12]. Mobility (μ) of left- and right-handed chiral PDAs was nearly the same ($\approx 10^{-6}$ $\text{cm}^2/\text{V}\cdot\text{sec}$; $V_{DS} = -60$ V). p-Channel behaviour was also reported using bottom and top contact type FET with blue-phase PDA, polymerized by unpolarized light [13, 14], where I_{DS} saturated. For chiral red-phase PDA, I_{DS} reached a maximum, and then decreased with the increase in V_{DS} . Similar behaviour was observed for top contact FET with chiral blue-phase PDA polymerized by CPL. Carrier trapping during the device operation presumably was responsible for such I – V characteristics [15]. Detailed experiments and analysis are now proceeding to reveal the origin of the observed behaviour. It should be noted that no clear difference between left- and right-CPL was recorded in the I – V characteristics, and the results showed good reproducibility.

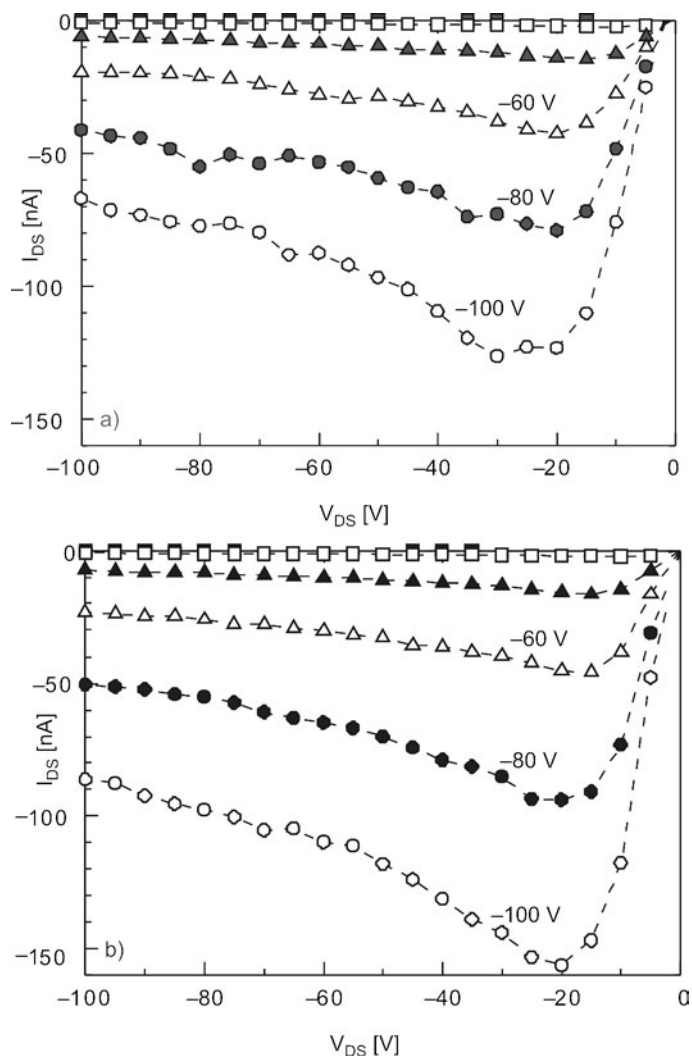


Fig. 4. Typical I_{DS} - V_{DS} characteristics of chiral red-phase PDA-FET. The films were polymerized by using left- (a) and right-CPL (b) irradiation, respectively

These results are reasonable, because the chirality of molecules has no influence on the electrical characteristics of the direct current (dc) e.g., I - V characteristics.

3.3. Electroluminescence for chiral PDA

The possibility of EL enhancement from chiral PDA was investigated. There are many papers about EL using organic materials [16]. To observe EL from organic materials effectively under an applied dc current, the relationship between the HOMO and the LUMO gap of organic material and the work function of the metal electrode

should be known. Nevertheless, our group reported EL enhanced from tetracene-FET with Au electrode under an applied ac voltage. That EL was caused by alternating injection of hole and electron from the same electrode [17, 18]. In this paper, EL from the bottom contact type FET structure was investigated under the pressure lower than 1×10^{-4} Pa, where source and drain electrodes were connected to each other and a square wave was applied (frequency 50 kHz).

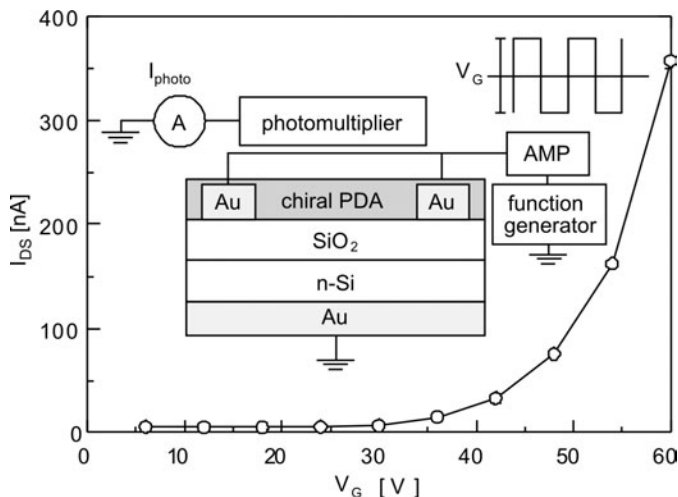


Fig. 5. ac voltage (V_G) dependence of EL intensity from chiral red-phase PDA-FET

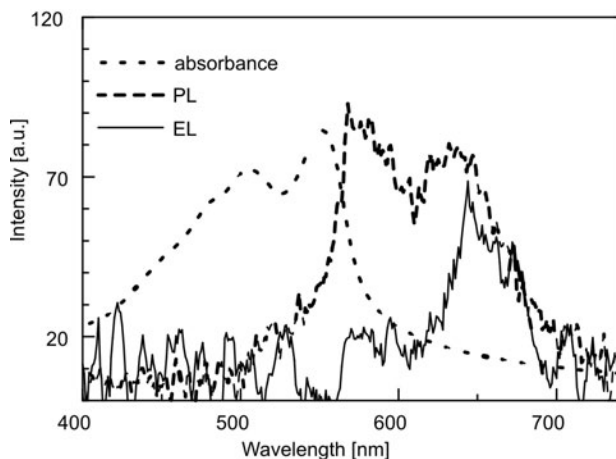


Fig. 6. Absorption and luminescence spectra of chiral red-phase PDA film. ac amplitude and measuring pressure are $120 V_{p-p}$ and ambient atmosphere, respectively

Figure 5 shows the V_G dependence of the EL intensity (recorded as photocurrent using the photomultiplier tube) from the chiral red-phase PDA-FET. The increase in the EL intensity was observed upon applying V_G in chiral red-phase PDAs, polymer-

ized by left- and right-CPL, respectively. For the measurement, the detector was a photomultiplier tube (Hamamatsu R-3896), capable of detecting extremely weak signals in the visible region. As shown in Fig. 6, the EL signal was observed at a longer wavelength of the absorption band of red-phase PDA, and the peak position of the EL spectrum was coincident with that of photoluminescence (PL). Accordingly, EL from chiral PDA was observed. In the past, EL enhanced from red-phase PDA, sandwiched between ITO and Al electrodes, was reported [19]. However, to the best of the author's knowledge, there has been no report concerning EL using FET under an ac voltage. These results obtained in the present paper testify to the novel functionality of the chiral PDA.

4. Conclusion

The strength of induced chirality of PDA was dependent on the substrate temperature. Substrate temperature was set to 313 K during the evaporation process, and both chiral blue-phase PDAs, polymerized by left- and right-CPL, were prepared on the glass substrate. The prepared blue-phase PDAs were annealed and changed into the chiral red-phase PDAs which showed good stability. In the same way, chiral red-phase PDA was prepared on the SiO₂ substrate as an active layer of contact type FET. In the I - V measurement, both chiral red-phase PDA-FETs showed p-channel behaviour. On the other hand, in the study of EL, an increase in the current was recorded, under the applied ac voltage, by using a photomultiplier.

Acknowledgements

The authors thank Professors H. Takezoe and F. Araoka (Tokyo Institute of Technology) for supporting our experiment. Support by Grants-in-Aid for Scientific Research (Grant No. 19206034) and Global Centers of Excellence Program (Photonics Integration-Core Electronics) from the Ministry of Education, Culture, Sports, Science and Technology is also gratefully acknowledged.

References

- [1] YASHIMA E., MAEDA K., OKAMOTO Y., *Nature*, 399 (1999), 449.
- [2] AKAGI K., PIAO G., KANEKO S., HIGUCHI I., SHIRAKAWA H., KYOTANI M., *Synth. Met.*, 102 (1999), 1406.
- [3] AKAGI K., GUO S., MORI T., GOH M., PIAO G., KYOTANI M., *J. Am. Chem. Soc.*, 127 (2005), 14647.
- [4] WU Y., NATANSOHN A., ROCHON P., *Macromolecules*, 37 (2004), 6801.
- [5] MANAKA T., KON H., OHSHIMA Y., ZOU G., IWAMOTO M., *Chem. Lett.*, 35 (2006), 1028.
- [6] LEE D. C., SAHOO S. K., CHOLLI A. L., SANDMAN D. J., *Macromolecules*, 35 (2002), 4347.
- [7] TANAKA K., OKUI N., SAKAI T., *Thin Solid Films*, 196 (1991), 137.
- [8] ENKELMANN V., WEGNER G., *Angew. Chem., Int. Ed. Engl.*, 16 (1977), 416.
- [9] ENKELMANN V., *Structural Aspects of the Topochemical Polymerization of Diacetylenes*, [in:] H. J. Cantow (Eds.), *Advances in Polymer Science*, Vol. 63, Springer, Berlin, 1984, p. 91.
- [10] KOHN H., OHSHIMA Y., MANAKA T., IWAMOTO M., *Jpn. J. Appl. Phys.*, 47 (2008), 1359.
- [11] KOHN H., OHSHIMA Y., MANAKA T., IWAMOTO M., *Macromol. Symp.*, 268 (2008), 77.

- [12] SZE S. M., *Physics of Semiconductor Devices*, John Wiley & Sons, New York, 1981.
- [13] KOYANAGI T., MURATSUBAKI M., HOSOI Y., SHIBATA T., TSUTSUI K., WADA Y., FURUKAWA Y., *Chem. Lett.*, 35 (2006), 20.
- [14] ZOU G., LIM E., KAJIMOTO N., KOHN H., OHSHIMA Y., MANAKA T., IWAMOTO M., *Jpn. J. Appl. Phys.*, 46 (2007), 3071.
- [15] LINDNER TH., PAASCH G., SCHEINERT S., *J. Appl. Phys.*, 98 (2005), 114505.
- [16] ZAUMSEIL J., FRIEND R. H., SIRRINGHAUS H., *Nat. Mater.*, 5 (2006), 69.
- [17] OHSHIMA Y., KOHN H., LIM E., MANAKA T., IWAMOTO M., *Jpn. J. Appl. Phys.*, 47 (2008), 1297.
- [18] OHSHIMA Y., KOHN H., LIM E., MANAKA T., IWAMOTO M., *Jpn. J. Appl. Phys.*, 47 (2008), 3200.
- [19] GIORGETTI E., SOTTINI S., DEL ROSSO T., MARGHERI G., ALLOISIO M., DELLEPIANE G., *Synth. Met.*, 147 (2004), 271.

Received 1 September 2008

Revised 17 October 2008

Excimers and exciplexes in organic electroluminescence*

J. KALINOWSKI**

Department of Molecular Physics, Gdańsk University of Technology, 80-952 Gdańsk, Poland

In organic light emitting devices (LEDs) various types of emissive states are created: (i) molecular excited states (localized excitons), or bimolecular (B-M) species: excimers, electromers, exciplexes and electroplexes. The consequences of the formation of B-M excited species for optical and electrical characteristics of organic LEDs are discussed and illustrated by various examples. While molecular excitons can be viewed in some sense as correlated electron-hole (e-h) pairs with the inter-charge mean separation less than an intermolecular spacing, the size of B-M excited states amounts usually to one or two intermolecular spacings. The B-M species can be classified as electrically balanced states, formed under energy and charge exchange between neighbour molecules, and have either a singlet or a triplet character. The focus of the paper is on excimer and exciplex forming single phosphorescent dopant blends-based emitting layers but characteristic features of other B-M excited species (electromers and electroplexes) and their emissions are also mentioned. Of particular interest in modern optoelectronics are white and infrared organic LEDs. It is shown how excimer and exciplex emissions can be employed in manufacturing such devices. Examples include efficient white and near-infrared LEDs, based on single dopant emitters of an efficient N-C-N-coordinated platinum(II) complex phosphor, and their improved versions, obtained by modification of the emitter matrix materials and electron injecting electrodes.

Key words: *organic electroluminescence; organic LEDs; bimolecular excited states; near-infrared; white light emitting diodes*

1. Introduction

Excited states of molecular solids are traceable to properties of individual molecules. However, the energy of weak van der Waals interactions between molecules impose a notable, communal response upon the behaviour of the molecular condensed phase (see e.g., [1, 2]). The collective response is embodied in an entity called an *exci-*

*The paper presented at the 11th International Conference on Electrical and Related Properties of Organic Solids (ERPOS-11), July 13–17, 2008, Piechowice, Poland.

**Corresponding author, e-mail: kalino@polnet.cc

ton (see Sect. 2). In single component organic solids composed of chemically identical molecules which do not aggregate in the ground state, bimolecular (B-M) excited states are possible due to resonance interactions of a *molecular exciton* with neighbour non-excited molecules (M). They are called *excimers* [3]. Exciton and charge-transfer resonance can be defined by intermolecular exchange of the singlet or triplet excitation energy and/or charge. The first process leads to the so called ‘locally-excited excimers’ (local excimers), the second to ‘charge-transfer excimers’ (CT excimers). In general, mixed excimers are formed with different contributions of local and CT excimer structures (see Sect. 3). In bicomponent and multicomponent molecular solids (chemically different molecular mixtures – molecular blends), especially for electron donor (D) and electron acceptor (A) molecules, the formation of bimolecular excited states by electron transfer from donor to acceptor is highly facilitated, in analogy to single-component systems: they are called *exciplexes* [4]. The molecular and B-M excited states can be generated either optically, by light, or electrically, by electron–hole recombination, that is they appear in both photoluminescence (PL) and electroluminescence (EL). An interesting combination of these two emissions has recently been observed and called *electrophotoluminescence* (EL-PL) [5]. In EL, electrons and holes introduced at suitable electrodes approach each other, being able to form excimer, exciplex and molecular emissive states. However, by definition, they have to pass an intermediate stage of coulombically-correlated electron–hole pairs. Radiative ‘cross transitions’ between closely spaced, but different, molecules may then be observed, modifying the effective EL emission spectrum. Such “prepared” emissive electron–hole pairs have been named *electromers* and *electroplexes*, respectively [2].

In the present paper, the emission features of B-M excited states will be identified and demonstrated in all luminescence phenomena with particular attention to those occurring in organic light emitting devices (LEDs).

2. Types of excitons

A collision of a photon with an electrically neutral atom or a molecule can transfer an electron from it to another site situated at various distances. Depending on the strength of the inter-atom (inter-molecular) interactions, the electrons and holes created in this way become either free carriers (we observe the intrinsic photoconductivity) or become coupled charge pairs called *excitons*. As shown in Fig. 1, these are large-radius Mott–Wannier excitons, small-radius (Frenkel or molecular) excitons and intermediate (one or two-molecular distances in size) charge-transfer excitons. While large-radius excitons are formed in tightly-bonded inorganic semiconductors, the latter two are characteristic of weakly-bonded organic solids. Also, it is worthy to note that Mott–Wannier excitons, being weakly-bonded, and therefore easily dissociating, are usually observed at low temperature. For organic solids, the emission, as a rule, originates from excitons, even at room temperature, as band-to-band transitions are very inefficient in them.

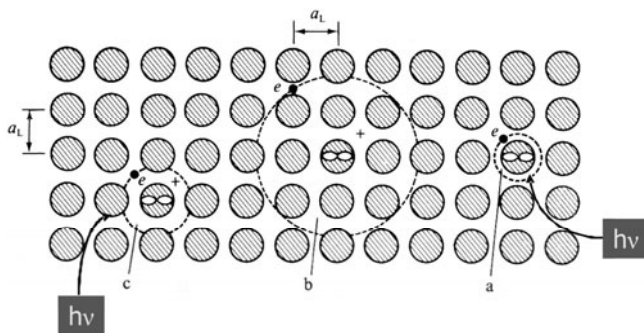


Fig. 1. General classification of excitons in solids: a) localized excited state: Frenkel or small radius exciton, b) Mott–Wannier or large radius exciton, c) charge pair (one or two intermolecular distances) intermediate size exciton. Excitation by a photon is indicated as $h\nu$. For explanations see text

3. Excimers and electromers in PL and EL

In single-component organic solids composed of chemically identical molecules which do not aggregate in their ground states (do not form dimers or larger aggregates), the formation of B–M excited states is possible, due to resonance interactions of a molecular exciton with neighbour non-excited molecules. They are called ‘excimers’ [2, 4] or ‘electromers’ [2, 6, 7]. Exciton and charge-transfer resonance can be defined by intermolecular exchange of the singlet or triplet excitation energy and/or charge. The first process leads to the so called ‘locally-excited excimers’ (local excimers), the second to ‘charge-transfer excimers’ (CT excimers). In general, mixed excimers are formed and described by local (‘loc’) and ‘CT’ eigenfunctions of the Hamiltonian pair, with different amplitudes c_1 and c_2 (see Fig. 2).

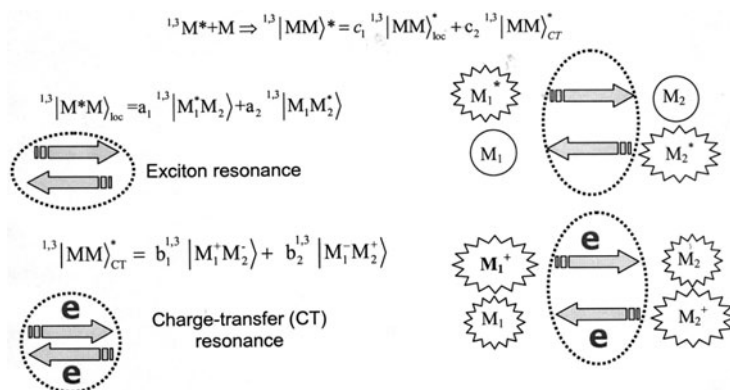


Fig. 2. Quantum mechanical description of the excimer state (either singlet, 1, or triplet, 3) composed of a locally excited (loc) and charge-transfer (CT) components of this B–M excited state formed in the exciton and CT resonance interactions as illustrated by block arrows coupling two molecules

The eigenvalues of the Hamiltonian determine the energy of excimer:

$${}^{1,3}E_{(MM^*)} = \left(\left[{}^{1,3}E_{M^*} \mp \frac{\mu^2}{r^3} (\cos \alpha - 3 \cos^2 \theta) \right] \mp E_{M^+M^-} \right) \quad (1)$$

It is a function of the energy of the molecular exciton (${}^{1,3}E_{M^*}$) and isotropic Coulombic interaction energy ($E_{M^+M^-}$). Equation (1) shows the interaction energy dependence on the intermolecular distance (r) and the mutual orientation of the interacting molecules given by two angles defined by the directions between their transition moments (μ), as shown in Fig. 3.

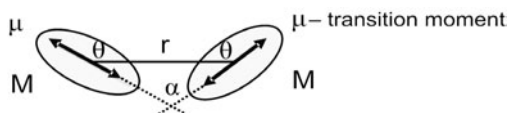


Fig. 3. The parameters determining the excimer energy (see Eq. (1))

Of the two energy levels, usually the lower one is responsible for the radiative transitions. In Figure 4, the lack of dimers in the ground state molecules is apparent, through the monotonically decreasing repulsive potential, and a shallow minimum on the potential curve of the excimer.

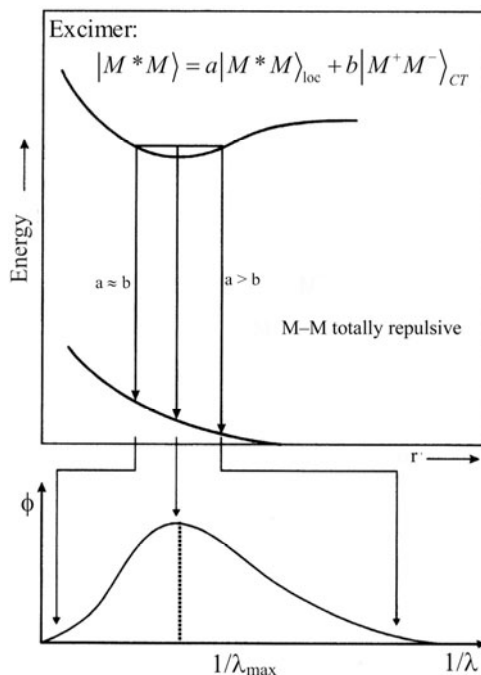


Fig. 4. Excimer energetics: potential energy diagram (upper part), and emission spectrum (bottom part). For discussion see the text

We note that the shape of the emission spectrum depends on the composition of the mixed excimer. Lower energy transitions correspond to a substantial contribution of the CT excimer ($a \approx b$), and higher energy transitions correspond to a larger contribution of the loc excimer. From quantum mechanical calculations, it follows that no pure loc and CT excimers can exist. Moreover, at distances exceeding 0.4 nm they lose their excimer features, dissociating into isolated molecular species or possibly electron-hole pairs still bound by the Coulombic attraction. In a typical aromatic excimer, the equilibrium distance r_0 amounts to about 0.33 nm.

The effect of intermolecular conformation on the emission spectrum is well illustrated by anthracene excimers, as shown in Fig. 5.

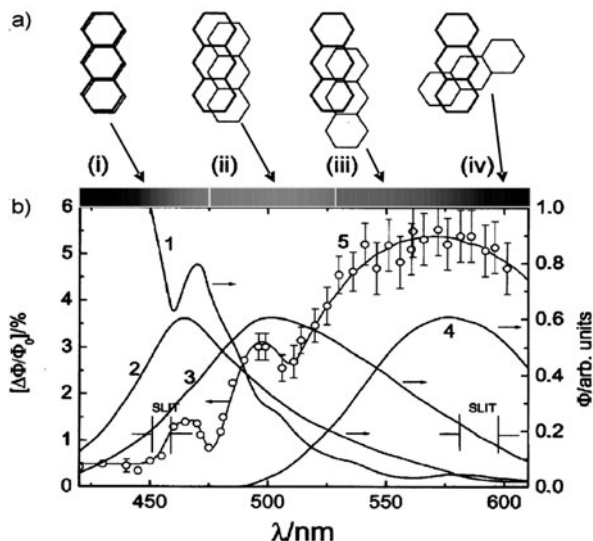


Fig. 5. Various excimer conformation PL spectra in solid anthracene, curves 1–4 [8–10]. The action spectrum of the PL quenching by injected holes in an anthracene single crystal is shown for comparison (points) [11]. For discussion see text

An incipient dimer formed by exact parallel overlapping of two molecules in anthracene single crystal: (1) gives an emission that is almost the same as the emission of slightly “slided” molecules; (2) from low-temperature evaporated films, both suggesting a large contribution from the “loc” excimer component, broad-band (3) originates from a molecular pair with molecules displaced by one benzene ring, and (4) two molecules turned around an axis perpendicular to their planes, as formed in the photocleavage of single di-anthracene crystal. The latter suggests the CT excimer to be dominating. Interestingly, all of these conformation emissions are reflected in photo-luminescence quenching by injected holes (points).

Electromers are defined by a separated, but coulombically-correlated, electron-hole pairs which can decay with a non-zero cross transition radiative rate constant. Therefore, their formation requires the intermolecular charge separation when excited

optically, or independent sources of holes and electrons that undergo bimolecular recombination in a luminescent material [6].

3.1. Generation by electron–hole recombination

Free electrons (e) and holes (h), introduced, e.g., at suitable electrodes, approach each other being able to form either excimer or molecular emissive states (Fig. 6). They, by definition, have to pass an intermediate stage of Coulombically-correlated electron–hole pairs (e...h). Due to spin statistics, three times more triplet $^3(e...h)$ than singlet $^1(e...h)$ pairs are created, that is their creation probabilities amount to $P_T=3/4$ and $P_S=1/4$, respectively.

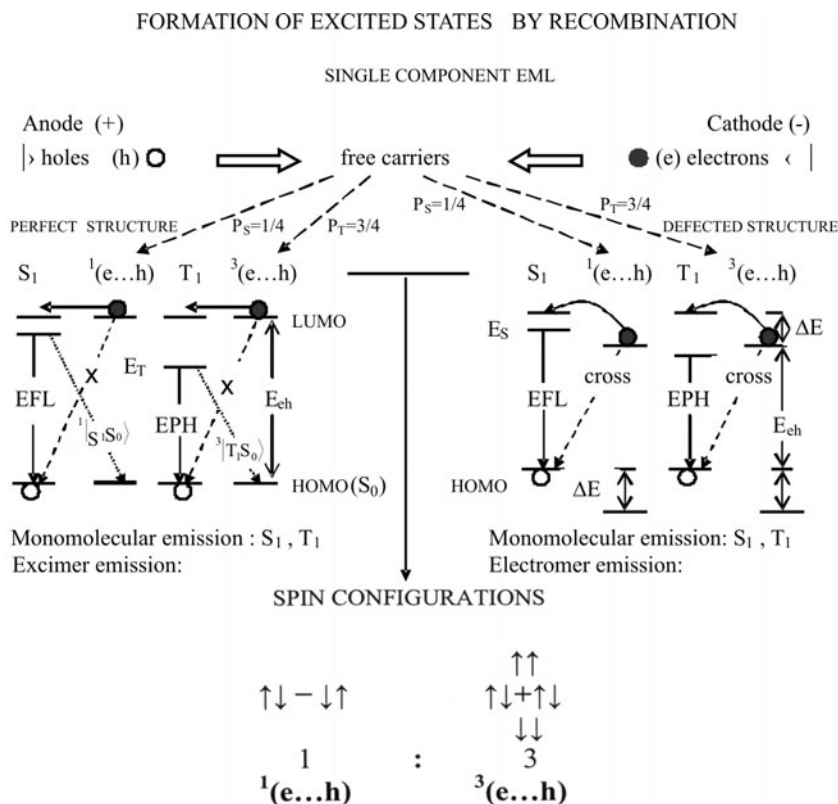


Fig. 6. Generation of excited states by electron–hole recombination in single-component emitters. The effect of defects on the recombination products is shown in the right-hand part of the figure (adapted from [12]). For explanations see text

Another important point is the structural quality of the luminescent material. In a perfect structure, the LUMOs (Lowest Unoccupied Molecular Orbitals) and HOMOs (Highest Occupied Molecular Orbitals) of all molecules are on the same level, the

charge motion is due to hopping over a barrier dependent only on the molecular structure and the intermolecular distance. Radiative electron–hole “cross transitions” between neighbour molecules are highly ineffective in competition with charge recombination on one molecule (it is indicated by bold crosses in the left-hand side of Fig. 6). Thus, the emission originates from molecular excitons (electrofluorescence or electrophosphorescence) and possibly from singlet and triplet excimers. In disordered structures with defects, the hopping time becomes much longer because, there, an additional barrier (ΔE) for charge hopping can appear due to local defects. Radiative cross transition may become detectable in the long-wavelength wing of the emission. Such “prepared” emissive electron–hole pairs have been named *electromers*. They can be observed in simple molecules of anthracene and in more complex molecules. Figure 7 compares PL and EL spectra from a 20% anthracene:polycarbonate blend.

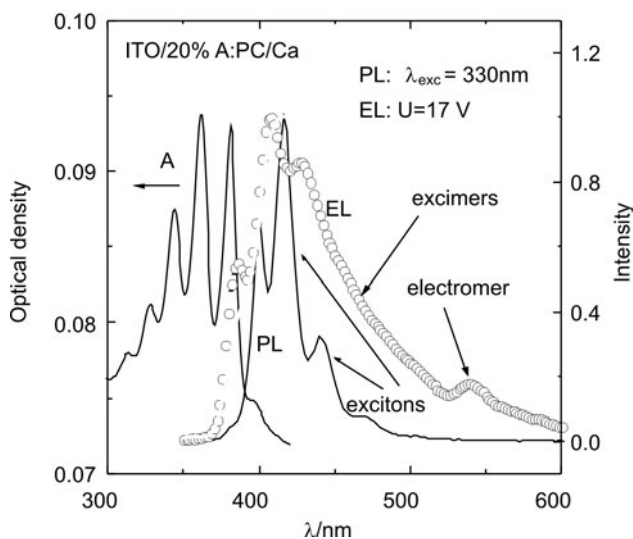


Fig. 7. Comparison of PL and EL from a 20% anthracene–polycarbonate blend emitter. EL originates from a single-layer LED with ITO and Ca provided anode and cathode, respectively. We note the differences between PL and EL spectra, caused by the apparent presence of B-M states (excimers and electromers) in the EL spectrum [7]

In PL, molecular emission is apparent with well-resolved, vibrational progression. In EL, a combination of emission from various types of excimers forms a long-wavelength tail of the emission spectrum. In addition, a well-resolved bump at about 530 nm can be seen. This feature has been ascribed to an electromer [7].

3.2. Excimer LEDs

Recall the idea of a simple, double-layer organic LED (Fig. 8). What is an organic light emitting device?

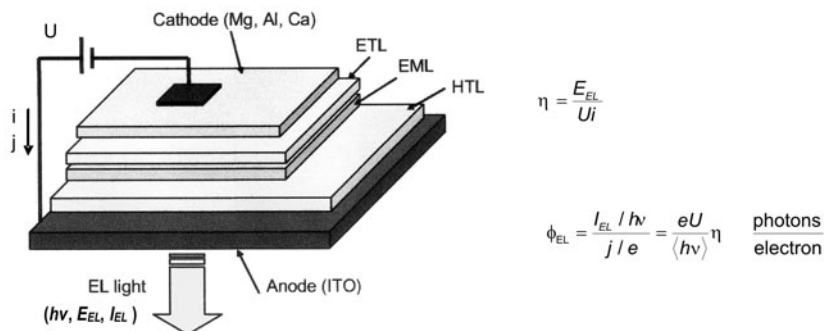


Fig. 8. Fundamental setup of a double layer (DL) organic LED: ETL– electron transport layer, EML – emission layer (20–100 nm), HTL – hole transport layer. Indium–tin oxide (ITO) covered glass (or quartz) substrate is used typically as a hole-injecting contact and a metal (usually Mg, Al, Ca) as an electron injecting electrode. Adapted from Ref. [12]

It consists of a system of thin organic layers provided with a transparent semiconductor hole-injecting anode (usually indium–tin oxide, ITO) and a metal electron-injecting cathode. Electron- and hole-transporting layers are marked by ETL and HTL, respectively. LED performance is characterized by the power conversion efficiency (η) and the quantum electroluminescence efficiency (ϕ_{EL}); the latter is defined as the ratio of the light quantal flux ($E_{EL}/h\nu$) and the electron stream (j/e) driving the device. The heart of an organic LED is its emitter layer (EML), containing a fluorescent or phosphorescent material. Depending on its emission spectrum, colour LEDs or white LEDs can be fabricated. In an EML, excimers can be formed and their emission observed through the transparent ITO anode.

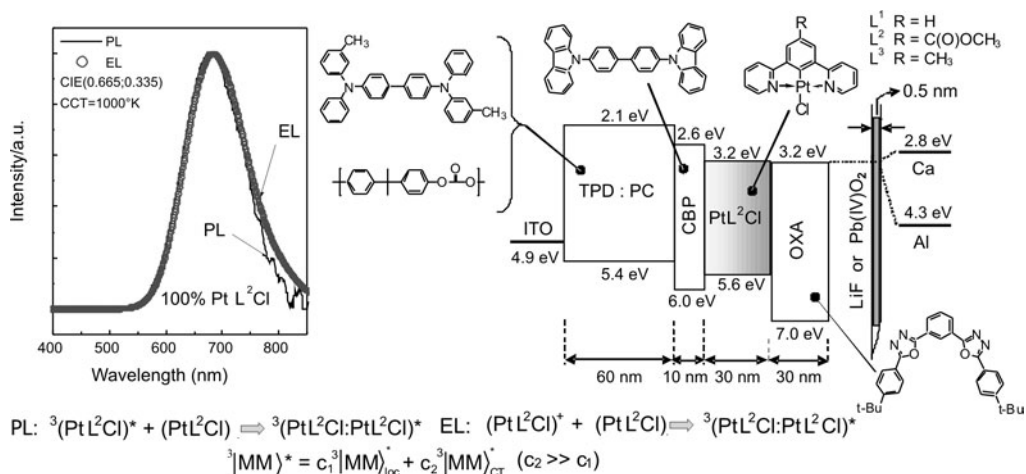


Fig. 9. Read/near-infrared excimer LEDs using Pt complexes with various substituents L^n (here a PtL^2Cl -based LED is demonstrated). Two different ways of the formation of excimer triplets in PL and EL are pointed out. The Commission Internationale de L'Eclairage (CIE) and Correlated Colour Temperature (CCT) of the emission are shown aside the PL and EL spectra. Adapted from Ref. [13]

An interesting class of excimer-forming molecules are flat platinum complex molecules. An example of such highly phosphorescent molecules (PtL^nCl) is shown in Fig. 9. Its neat film PL and EL spectra coincide, peaking at about 700 nm, and suggesting CT excimers dominating the emission. We note that the heavy Pt atom enhances the singlet-triplet intersystem crossing rate constant, thus leading to the formation of triplet excimers. As shown in Fig. 9, such films can form an emission layer in a four-layer LED; layers of CBP and OXA confine the recombination and emission to the emitter layer, due to their blocking function for particular charge carriers and triplet excitons. Changing the ligand allows the spectrum to be red shifted as illustrated in Fig. 10a.

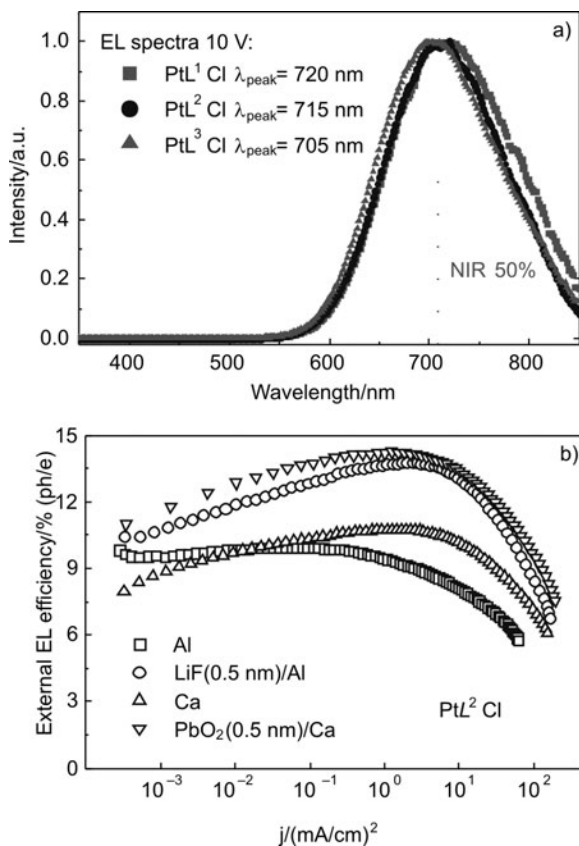


Fig. 10. EL emission spectra from neat films of PtL^nCl with various ligands (a) [14] as indicated in Fig. 9, and EL external quantum efficiency as a function of driving current of a LED (b) based on a neat film emitter of PtL^2Cl with different buffers at the cathode [13]. The LED architecture as given in Fig. 9

The emission maximum for a hydrogen atom as a ligand is located at about 720 nm, the NIR region, above 700 nm, covers roughly 50% of the whole spectrum, with still high quantum efficiency. These LEDs exhibit so far the highest quantum efficiencies in the NIR region, exceeding 9% ph/e for all buffer layers in front of the cathode, and reaching almost 15% ph/e for a lead (Pb) oxide buffer (Fig. 10b).

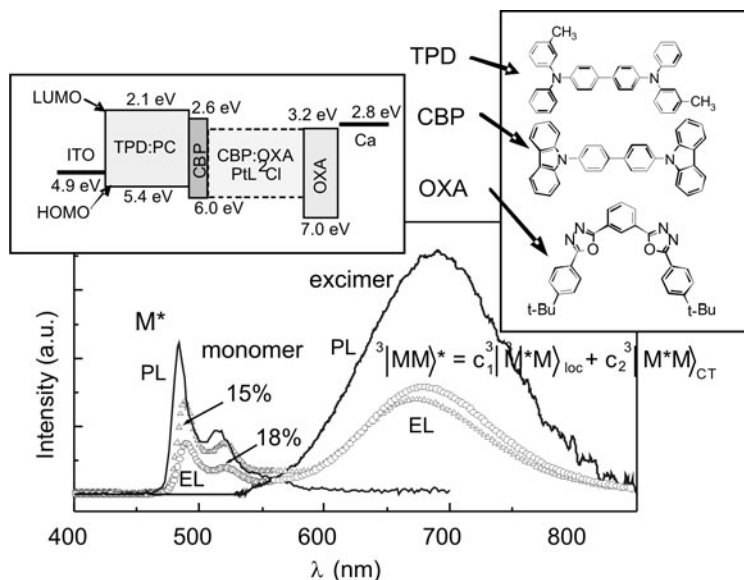


Fig. 11. EL emission spectra of PtL^2Cl -doped blend emitters (15 and 18 wt. %) from a four-layer LED depicted in the left upper inset compared with the PL spectra of a 5 wt. % -doped blend (monomer emission) and a 100% neat PtL^2Cl film (excimer emission). The molecular structures of some component materials used are given in the right-upper inset. Adapted from Ref. [15]

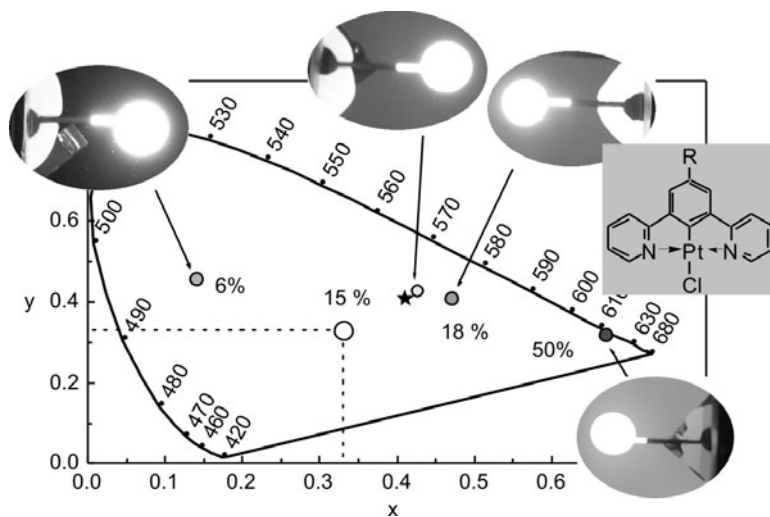


Fig. 12. Colour and white LEDs by manipulating the concentration of the complex concentration in blend emitters. Here, 6, 15, 18 and 50 wt. % of PtL^2Cl blended with a CBP:OXA emitter, all in the LED's architecture shown in Fig. 11. Taken from Ref. [15]

It must be pointed out that the emission spectrum of a low concentration (below 5 wt. %) complex solid solution displays a well-structured phosphorescence spectrum, as compared with a broad, structureless excimer spectrum peaking for L^2 ligand at

about 660 nm. From the data of Fig. 11, two emission bands (molecular triplet and excimer) are observed for 15% and 18% concentrations of the Pt complex in a blend with CBP and OXA. By adjusting the concentration, the monomer-to-excimer band ratio can be changed and the LED colour change follows (Fig. 12).

At a low concentration complex level, a blue emitting diode dominated by the monomer emission can be fabricated, a red shift is observed as the concentration increases from 15% up to 50%, an increase of the excimer emission largely dominates at high concentrations. For a certain concentration (here about 15 wt. %) the CIE chromaticity coordinates fall close to those characteristic of soft white light (star) from incandescent light sources. This provides a simple way to prepare white light emitting diodes.

3.3. Exciplex LEDs

In two-component blends composed of an electron donor (D) and an electron acceptor (A), the formation of bimolecular excited states by electron transfer from donor to acceptor molecules is highly facilitated. In analogy to single-component systems they are called *exciplexes* and *electroplexes* (see Fig. 13). An example is shown in Fig. 14.

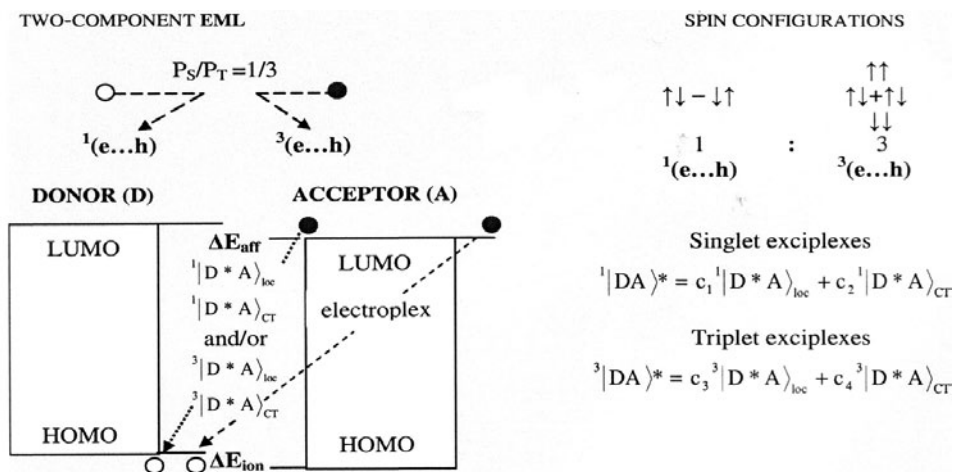


Fig. 13. The formation of bimolecular excited species (exciplex and electroplex) in two-component (electron donor (D) : electron acceptor (A)) organic solids [12]

Relatively narrow and structured spectra of individual donor (TPD) and acceptor (PBD) molecules switch to broader, structureless PL and EL spectra for their blends. In addition, a distinct difference between PL and EL spectra is apparent. The PL spectrum ascribed to the exciplex emission becomes more complex under electrical excitation. The EL spectrum at the photon energy scale can be decomposed into Gaussian profiles showing 4 different emissive species.

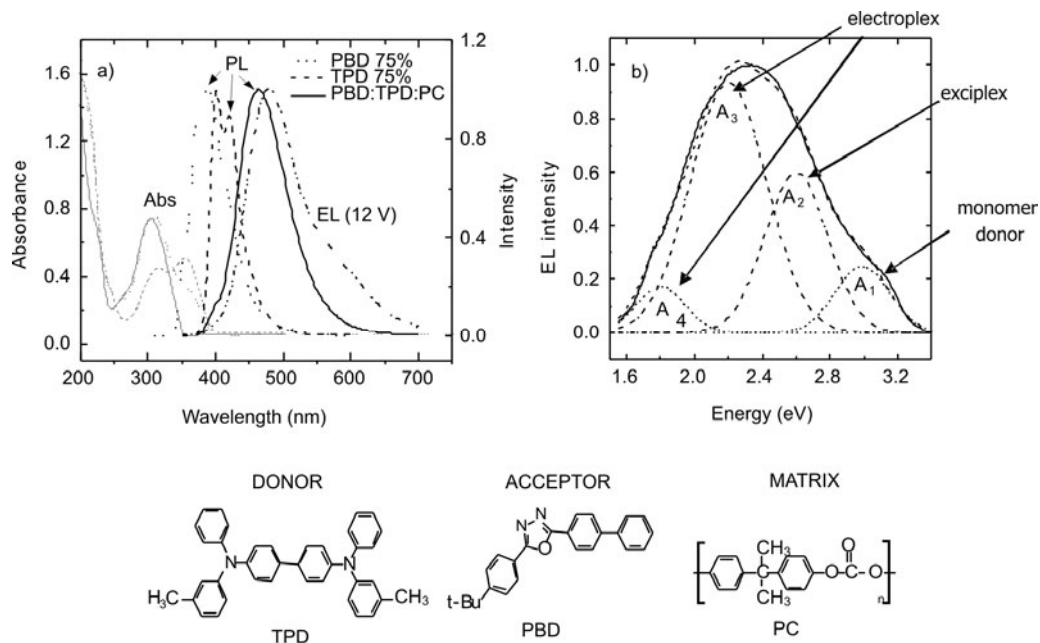


Fig. 14. (a) Emission spectra from an electron donor (TPD), electron acceptor (PBD) (PL) and from their blend in a neutral binder (PC), TPD:PBD:PC (PL and EL). (b) Photon energy representation of the broad EL spectrum of the blend from part (a). Its decomposition into Gaussian components shows the spectrum to be a combination of the emission from different types of the excited monomer and B-M states: monomer, exciplex and electroplex indicated respectively in the figure [16]

Besides of the maxima A_1 associated with monomer emission of the donor (D) and A_2 associated with the exciplex emission in both PL and EL spectra, two additional long-wavelength bands can be distinguished in the EL spectrum assigned to two different electroplexes due to cross transitions between two molecules with slightly different distances (one or two intermolecular spacings).

Like excimers, exciplexes can be formed as a result of both exciton and charge transfer resonances, a mixed type exciplex is composed of local (loc) and CT exciplexes (Fig. 15).

The emission maximum is determined here by a simple relation between the ionization potential of the donor (I_D), the electron-hole Coulombic attraction energy (E_C), and the electron affinity of the acceptor (A_A) (which is stabilized by E_C),

$$h\nu_{EX}^{\max} \approx I_D - A_A - E_C \quad (2)$$

$$E_c = \frac{e^2}{4\pi\epsilon_0\epsilon r} \quad (3)$$

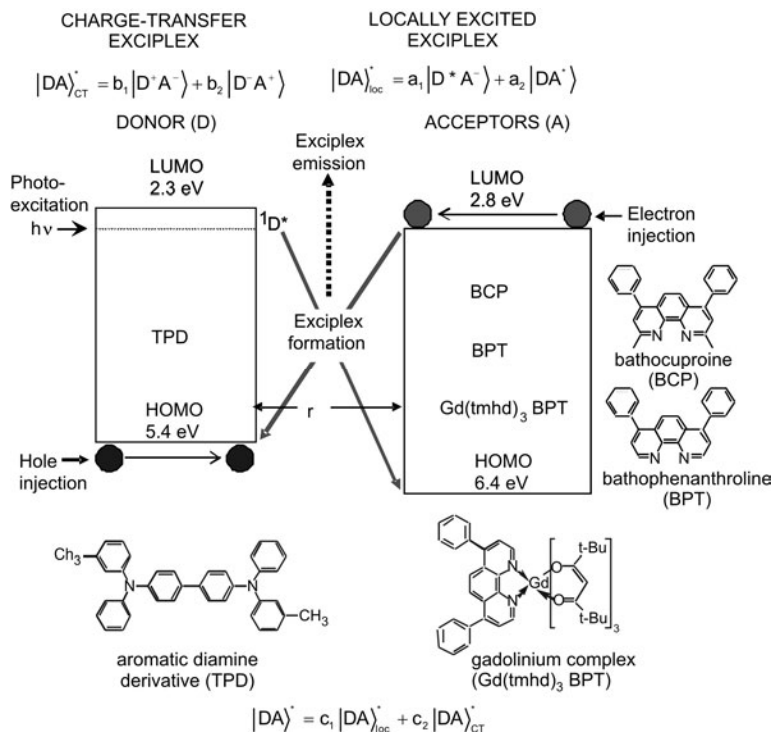


Fig. 15. Exciplex types and their formation mechanisms under optical ($h\nu$) and electrical ($e + h$) excitation for an electron donor (TPD) and three various acceptors (BCP, BPT, Gd(tmhd)₃BPT).

In general, the exciplexes are composed of a 'loc' and 'CT' components and can have either singlet or triplet character dependent on the acceptor (cf. Fig. 16)

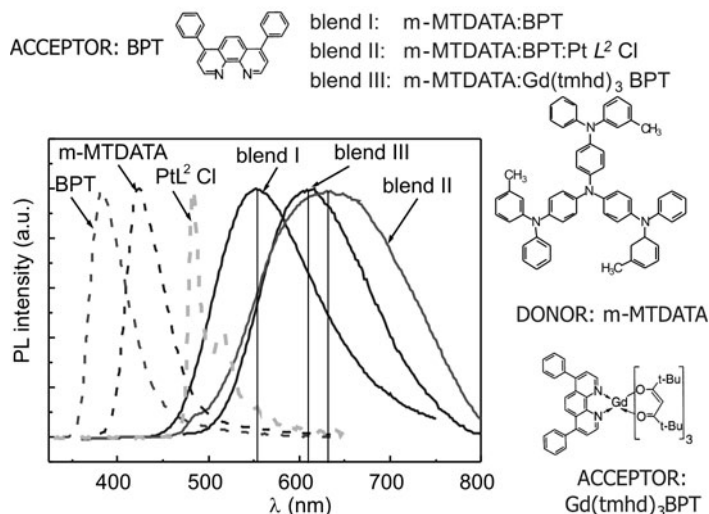


Fig. 16. PL spectra of exciplex emitter films with an electron donor m-MTDATA and two various acceptors BPT and Gd(tmhd)₃BPT incorporated in a PC binder. Adapted from Ref. [17]

Like in the case of excimers, stable exciplexes can be formed at distances below 0.4 nm. An interesting observation comes out from the exciplex spectra associated with various acceptors (Fig. 16). Again, we can see relatively narrow molecular emission spectra of individual components of various donor–acceptor blends, and broad, red-shifted spectra of the latter. Interestingly, replacing an acceptor BPT with its Gd-substituted derivative, shifts the exciplex emission spectrum to the red. An explanation is that in contrast to the donor–BPT system, where singlet exciplexes are formed, the same donor Gd substituted BPT leads to triplet exciplexes. The heavy gadolinium atom enhances singlet–triplet intersystem crossing transitions, resulting in the creation of triplet exciplexes. A similar effect is observed with the Pt complex blend, where exciplexes with the Pt complex dominate, showing its triplet character. Based on these properties, efficient exciplex LED structures have been fabricated (Fig. 17).

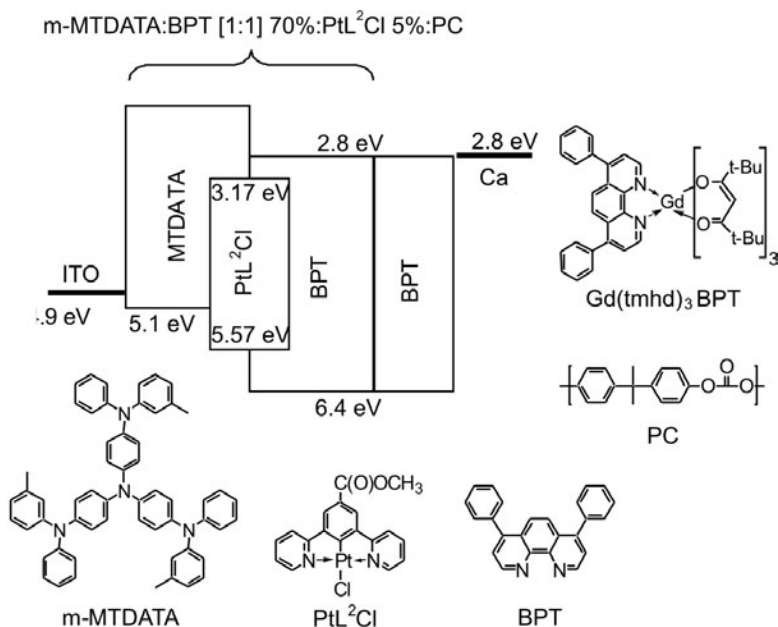


Fig. 17. An exciplex LED structure with an electron donor (m-MTDATA) and three various electron acceptors (BPT, Gd(tmhd)₃BPT, and PtL²Cl) incorporated in a PC binder [18]

These are double-layer LEDs composed of the ETL of BPT and the Pt complex-doped emitter layer (also, acting as HTL) with ITO-hole injecting anode and calcium-electron injection cathode. A time resolved study of the PL and EL from such LEDs with different blends, provided a strong evidence that different spin multiplicity occurs in emissive exciplexes. Interestingly, a difference between the emission spectra from blend I and blend III is clearly apparent, suggesting the first one to be underlain by singlet and the second to be underlain by triplet exciplexes. Indeed, as expected, the emission decay for triplets is an order of magnitude longer than that for singlets (Fig. 18).

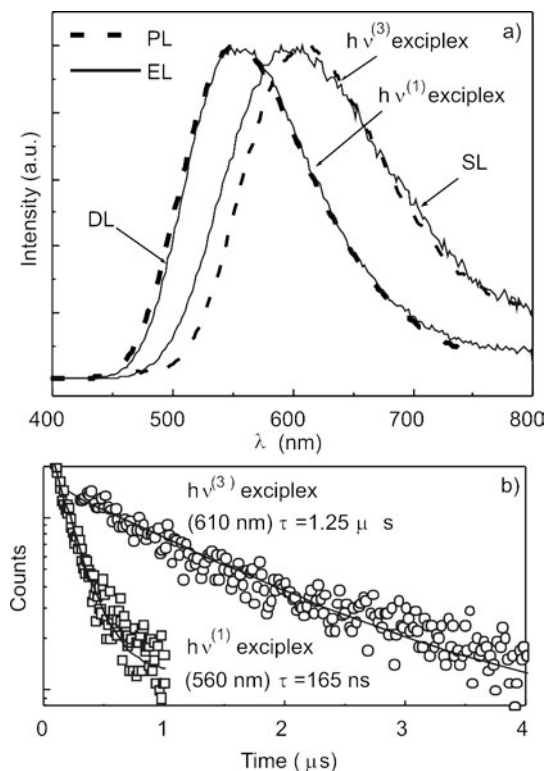


Fig. 18. Emission (PL and EL) spectra of the exciplex LED structures (a) depicted in Fig. 17. $h\nu^{(1)}$: blend I, m-MTDATA:BPT; $h\nu^{(3)}$: blend II, m-MTDATA:BPT:PtL²Cl and blend III, m-MTDATA:Gd(tmhd)₃BPT. The EL spectrum of a single-layer (SL) LED (ITO/m-MTDATA:BPT:PC/Ca) is shown for comparison; PL decay curves (b) at the maxima of the fluorescence (560 nm) and phosphorescence (610 nm) exciplex spectra excited at 336 nm under argon atmosphere. The decay time for $h\nu^{(3)}$ decreases by about 30% in the ambient air (not shown in the figure)

Now, let us recall our earlier conclusion that bimolecular excited states in PL and EL occur in opposite ways. While in PL a molecular excited state interacts with a ground state molecule, leading to a partial transfer of charge, in EL the primary stage is due to separated carriers. One of the consequences is that much more triplet states are formed under charge carrier recombination conditions. We should expect more triplet exciplexes to be formed, dominating triplet exciplex emission. In fact, in a TPD donor–BCP acceptor system two exciplex bands are observed in EL (Fig. 19): band G₁ belongs to singlet exciplexes, and band G₃ belongs to triplet exciplexes.

Only the G₁ band appears in the PL spectrum proving efficient formation of primary singlet excitons. The ratio of G₁-to-G₃ band emissions depends on the electric field. Using a gadolinium substituted complex as an acceptor makes the PL and EL spectra quasi-identical. In both cases, the production of molecular triplets dominates the primary generation process. A slight shift between PL and EL spectra for this sys-

tem may be attributed to a difference in amplitudes of loc and CT components of the mixed excimer, the CT component, understandably, contributing more in EL emission.

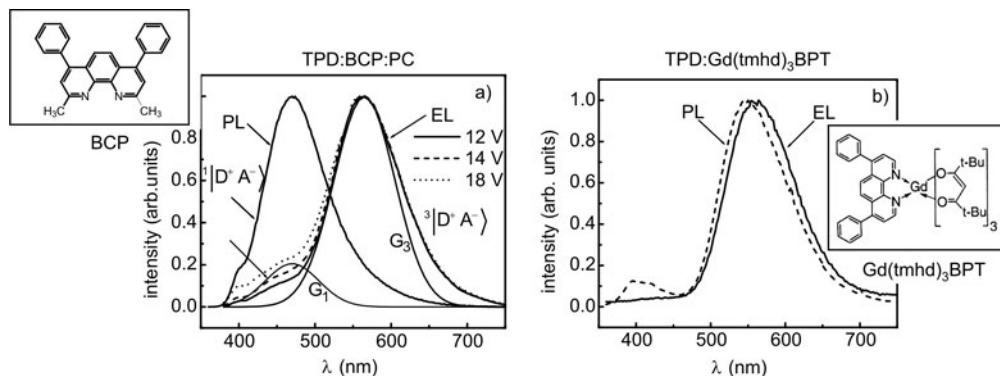


Fig. 19. PL versus EL exciplex spectra for an electron donor TPD and two electron acceptors BCP (a) and Gd(tmhd)₃BPT (b). While the singlet exciplex underlain PL spectrum and singlet-triplet mixture underlain EL spectrum (bands G₁ and G₃, respectively) for the BCP acceptor are observed, solely triplet exciplex underlain PL and EL emissions are revealed for the Gd(tmhd)₃BPT acceptor [19]

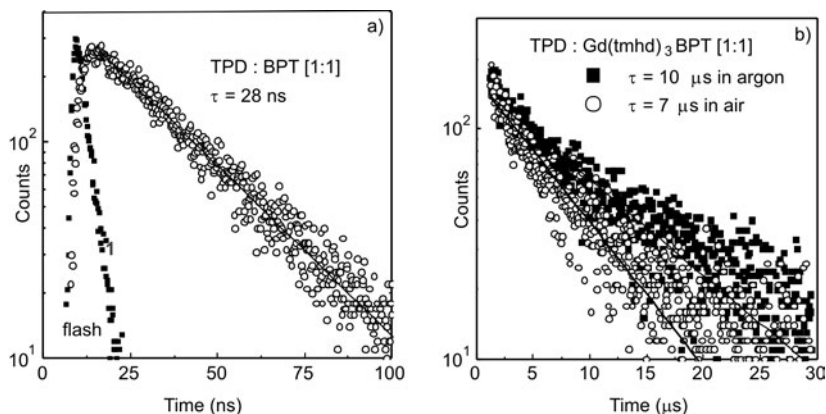


Fig. 20. Triplet versus singlet exciplexes: PL decays for G₁ (a) and G₃ (b) emission bands from Fig. 18.

While the G₁ band emission decay on the nanosecond scale is typical of singlet exciplex states, the G₃ band emission decay on the microsecond scale indicates its triplet character. The latter is strongly supported by a shortening of the lifetime when the sample is placed in ambient air [19]

Is there any other proof of the triplet character of the band G₃? The answer is yes. In Figure 20, we see photoluminescence decay profiles for bands G₁ and G₃. Clearly, the short time decay at band G₁ (ten nanosecond scale), independent of the ambient atmosphere, contradicts the much longer time for band G₃ (ten microsecond scale in argon), being reduced by about 30% in air, where triplet are quenched by oxygen.

Recently, we have shown [20] how white light emitting diodes can be improved, combining monomer, excimer and exciplex emissions all together within a single dopant emitter (Fig. 21).

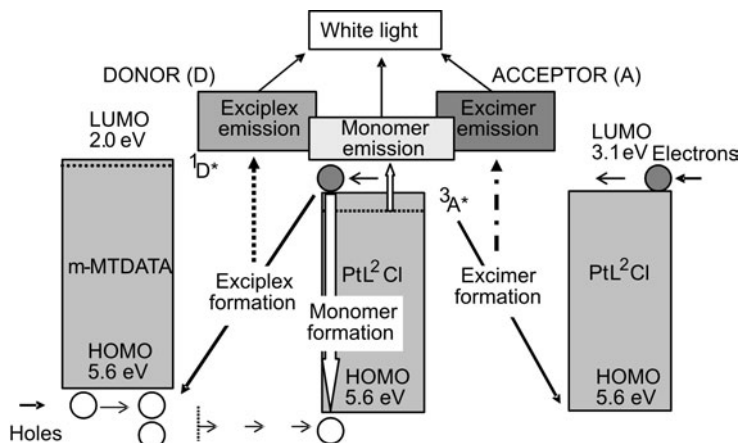


Fig. 21. Combining monomer, excimer and exciplex emissions a way to improve performance of white LEDs [20]. Copyright Wiley, VCH Verlag GmbH & Co. KGaA. Reproduced with permission

As a dopant we have chosen a phosphorescent Pt complex, also playing the role of the acceptor incorporated in a donor matrix of TPD or m-MTDATA. In this system, the Pt complex dopant can emit monomolecular phosphorescence, excimer phosphorescence and exciplex phosphorescence, the latter emanating from triplet exciplexes formed from donor–dopant interaction (Fig. 22).

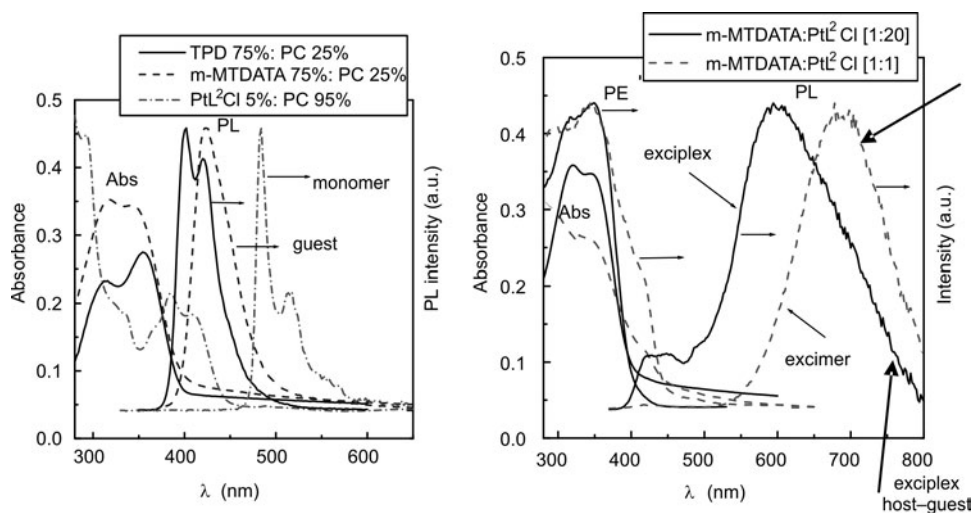
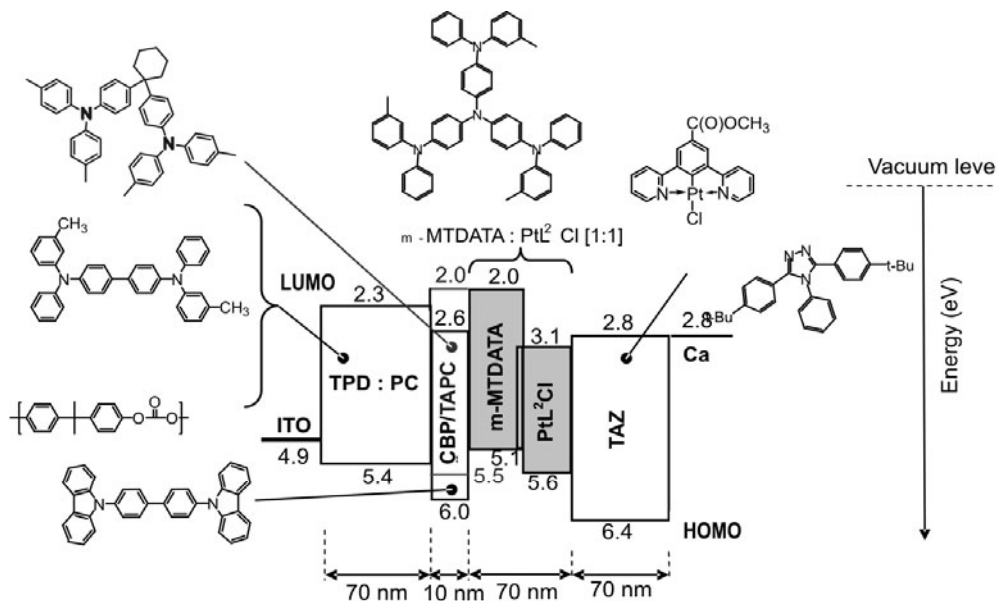


Fig. 22. PL spectra of TPD, m-MTDATA and PtL^2Cl , and their blends in PC, along with their absorption and photoexcitation (PE) spectra [20]. Molecular structures of the materials used are given in Fig. 23

An efficient white light emitting diode with a particular colour rendering index (CRI) has been fabricated [20]. Its architecture, along with the values of its most important performance parameters, is given in Fig. 23.



Selected performance characteristics of organic MEE LED

Structure	φ_{ext} [% ph/e]	η_p [lm/W] (L) [cd/m^2]	CIE*	CRI**
MEE LED	6.5	9.0 (500)	(0.46, 0.45)	90

*CIE – Commission Internationale de l'Éclairage; ideal white light CIE coordinates are ($x=0.33, y=0.33$) and those for warm incandescent lamp light are (0.41, 0.41).

** CRI – colour rendering index; for ideal white light CRI=100.

Fig. 23. Monomer : excimer : exciplex (MEE) white LED. Selected performance parameters are given below its schematic architecture [20]

It is a 4-layer LED of total thickness 220 nm, provided with an ITO hole injecting anode and an electron injecting calcium cathode. Its CIE coordinates are close to warm, incandescent lamp light (0.41, 0.41) and its CRI is as high as 90, as compared with the index of 100 for ideal, white light.

4. Exciplexes in electrophotoluminescence (EL-PL)

Electrophotoluminescence (EL-PL) comes into existence when optically excited film is subjected to injection of electrons and holes from suitable electrodes (Fig. 24). In Figure, 25 we see such a system with a hole injecting ITO and electron injecting calcium applied to exciplex emitting films of an electron donor (m-MTDATA) and an

electron acceptor of the Pt complex $Pt L^2Cl$, which has already been discussed. The total emission consists of PL and EL components. The electric field effect on the emission signal is shown in Fig. 26.

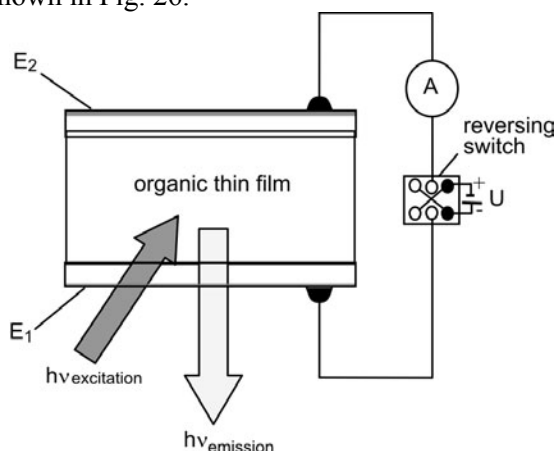


Fig. 24. How electrophotoluminescence comes into existence

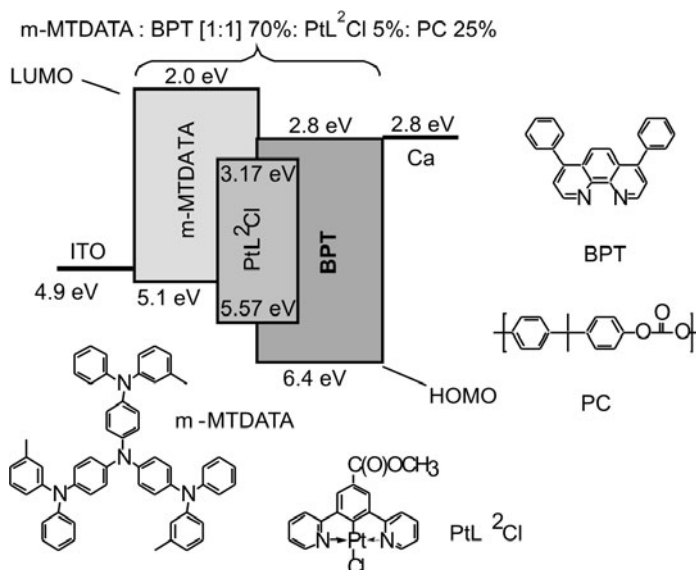


Fig. 25. The energy level scheme of materials forming the blend emitter of a single-layer (SL) LED with ITO and Ca injecting anode and cathode, respectively. After Ref. [5]

With the electrical polarization blocking charge injection (ITO^-), the PL signal is reduced, we observe only the quenching effect (δ -positive). For the forward polarization, the low-field quenching is followed by a signal increase (δ -negative quenching). Under a certain electric field, a reduction in the emission is compensated by the enhancement, the quenching of total emission diminishes to zero, no electric field effect

on the total emission is visible. It is understandable that the zero field effect is a function of the light excitation level, injection efficiency of electrodes and the phosphorescence efficiency of the exciplex [5].

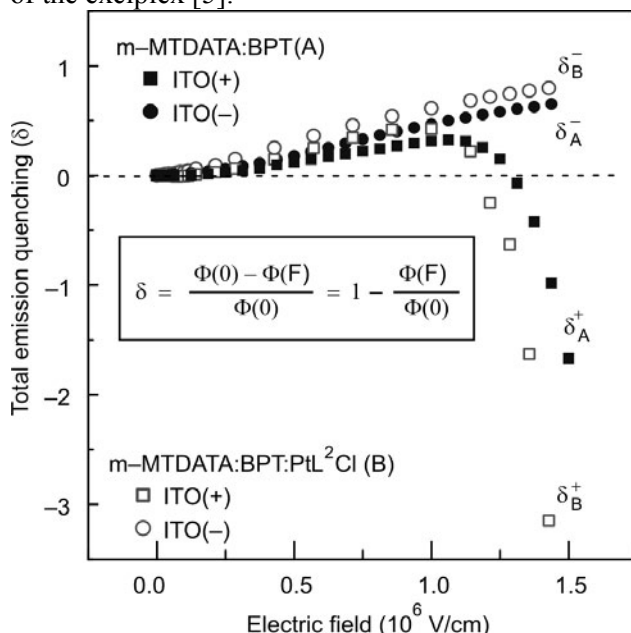


Fig. 26. Electric field effect on the total effective emission quenching (δ) defined by a relative change in the emission light flux (EL-PL) in the absence ($\Phi(0)$) and presence ($\Phi(F)$) of electric field (F) applied for two SL LEDs designated in the figure as devices (A) and (B). We note the effect to be positive ($\delta > 0$) reflecting the real quenching (a reduction in the light flux), negative quenching ($\delta < 0$) reflecting and enhancement of the light flux, and $\delta = 0$ for a certain electric field (reversing field) that is no change in the light flux at this field value [5]

A straightforward application of this phenomenon is mutual control of electrical and optical signals in various optoelectronic devices. For non-injecting electrodes (reversed bias), the considered film structures already function as luminescence attenuator devices. Charge injection (forward bias) into these films makes it possible to exploit them in devices that, upon voltage switching, can be changed from luminescence attenuators to luminescence amplifiers.

5. Concluding remarks

Bimolecular excited states, like excimers and exciplexes, can be efficiently produced in organic solids, especially under electrical excitation (recombination electroluminescence). These states essentially modify their electronic properties. This opens up the unusual possibility to tailor the performance parameters of organic optoelectronic devices.

We have seen numerous examples of organic light emitting diodes (LEDs): (i) organic material blends can be prepared to form thin film emitters for colour, white and near IR efficient LEDs; (ii) very high external quantum efficiency $> 16\%$ ph/e and $> 10\%$ ph/e have been achieved for white LEDs (WLEDs) and NIR LEDs, respectively, based on the diversity of excited states. Further improvements of WLEDs are expected, employing a combination of emissions from monomers, excimers and exciplexes formed by electron acceptor emitters and electron donor binder matrices. Further improvements of IR LEDs can be achieved by the application of more efficient electron injecting electrodes.

Bimolecular excited states enable mutual control of optically and electrically excited luminescence signals (EL-PL) in a way that allows for the manufacture of optoelectronic switches (electrical field switching from luminescence enhancing to luminescence attenuating devices).

Acknowledgements

The paper has been largely based on the results obtained in friendly and fruitful collaboration with my colleagues Drs. Massimo Cocchi, Piergiulio Di Marco, Valeria Fattori and Dalia Virgili at C.N.R. Bologna, Italy, and Drs. Stéphanie Develay, Lisa Murphy and J.A. Gareth Williams of the University of Durham, U.K. The author would like to dedicate this paper to Dr. Piergiulio Di Marco, the founder and protector of the Molecular Electronics Group at C.N.R. Bologna where the author initiated intensive studies on electroluminescence in thin organic films including light emitting diodes.

References

- [1] POPE M., SWENBERG C.E., *Electronic Processes in Organic Crystals*, Clarendon Press, Oxford, 1982.
- [2] KALINOWSKI J., *Organic Light Emitting Diodes: Principles, Characteristics and Processes*, Marcel Dekker, New York, 2005.
- [3] BIRKS J.B., *Photophysics of Aromatic Molecules*, Wiley, New York, 1970.
- [4] FÖRSTER T., *Excimers and Exciplexes*, [in:] *The Exciplex*, M. Gordon, W.R. Ware (Eds.), Academic Press, New York, 1975, p. 1.
- [5] KALINOWSKI J., COCCHI M., VIRGILI D., FATTORI V., WILLIAMS J.A.G., *Chem. Phys. Lett.*, 447 (2007), 279.
- [6] KALINOWSKI J., GIRO G., COCCHI M., FATTORI V., DI MARCO P., *Appl. Phys. Lett.*, 76 (2000), 2352.
- [7] KALINOWSKI J., GIRO G., COCCHI M., FATTORI V., ZAMBONI R., *Chem. Phys.*, 277 (2002), 387.
- [8] HOFMANN J., SEEFELD K.P., HOFBERGER W., BAESSLER H., *Mol. Phys.*, 37 (1979), 973.
- [9] FERGUSON A., MAU A.W.H., *Mol. Phys.*, 27 (1974), 377.
- [10] FERGUSON A., MAU A.W.H., *Mol. Phys.*, 28 (1974), 1467.
- [11] KALINOWSKI J., GODLEWSKI J., CHANCE R.R., *J. Chem. Phys.*, 64 (1976), 2389.
- [12] KALINOWSKI J., *Opt. Mater.*, 30 (2008), 792.
- [13] COCCHI M., KALINOWSKI J., VIRGILI D., WILLIAMS J.A.G., *Appl. Phys. Lett.*, 92 (2008), 113302.
- [14] COCCHI M., VIRGILI D., FATTORI V., WILLIAMS J.A.G., KALINOWSKI J., *Appl. Phys. Lett.*, 90 (2007), 023506.
- [15] COCCHI M., KALINOWSKI J., VIRGILI D., FATTORI V., DEVELAY S., WILLIAMS J.A.G., *Appl. Phys. Lett.*, 90 (2007), 163508.
- [16] GIRO G., COCCHI M., KALINOWSKI J., DI MARCO P., FATTORI V., *Chem. Phys. Lett.*, 318 (2002), 137.
- [17] KALINOWSKI J., COCCHI M., VIRGILI D., FATTORI V., WILLIAMS J.A.G., *Chem. Phys. Lett.*, 432 (2006), 110.

- [18] VIRGILI D., COCCHI M., FATTORI V., SABATINI C., KALINOWSKI J., WILLIAMS J.A.G., Chem. Phys. Lett., 433 (2006), 145.
- [19] COCCHI M., VIRGILI D., SABATINI C., KALINOWSKI J., Chem. Phys. Lett., 421 (2006), 351.
- [20] KALINOWSKI J., COCCHI M., VIRGILI D., FATTORI V., WILLIAMS J.A.G., Adv. Mater., 19 (2007), 4000.

Received 9 September 2008

Revised 8 January 2009

Photoelectric properties of WO₃/tetracene heterojunctions *

R. SIGNERSKI **, G. JAROSZ

Faculty of Applied Physics and Mathematics, Gdansk University of Technology,
Narutowicza 11/12, 80-952 Gdańsk, Poland

Photoelectric properties of ITO/tetracene (Tc)/Ag and ITO/WO₃/Tc/Ag sandwich systems have been reported. The system containing the WO₃/Tc heterojunction exhibits a higher current rectification in the dark and a stronger photovoltaic effect. Values of the open-circuit voltage exceeding 800 mV have been observed. The obtained results can be elucidated on the assumption that a downward band bending or an interface dipole at the WO₃/Tc heterojunction occurs.

Key words: *hybrid heterojunction; tetracene; tungsten trioxide*

1. Introduction

Hybrid heterojunctions, formed from inorganic semiconductor transporting electrons and organic dye or semiconductor applied as a material which both absorbs light and transports holes, presently attract a great deal of attention due to their potential applications in electronic devices, particularly in solar cells. In such heterojunctions, mostly TiO₂, CdS and CdSe are used as inorganic semiconductors, while polymers [1, 2], porphyrins and phthalocyanines are used as organic materials [3, 4].

The results of our research on the photoelectric properties of a planar heterojunction formed from WO₃/tetracene (Tc) are presented in this work. Tungsten trioxide (WO₃) is a wide band-gap ($E_g = 3.3$ eV) n-type semiconductor which attracts a great deal of attention due to possible application in electrochromic devices, gas sensors and as a photoanode material for photochemical hydrogen production [5, 6]. In organic systems, thin layers of WO₃ were applied as hole-injecting layers or as interlayers in tandem devices [7, 8]. Tetracene is also a wide band-gap semiconductor ($E_g = 3.1$ eV), however, its electric and photoelectric properties are mainly related to the transport of

*The paper presented at the 11th International Conference on Electrical and Related Properties of Organic Solids (ERPOS-11), July 13–17, 2008, Piechowice, Poland.

**Corresponding author, e-mail: ryszard@mif.pg.gda.pl

holes. The processes of injection, photogeneration and transport of charge carriers as well as photovoltaic and photoconductive properties of single crystals and polycrystalline tetracene layers, have been discussed in many works (e.g., [9–18]). On the other hand, only a few papers have been published dealing with heterojunction structures based on tetracene [19–21]. This work presents the results of research performed on the ITO/WO₃/Tc/Ag system which have been compared with the results obtained on the ITO/Tc/Ag systems.

2. Experimental

The investigated systems were obtained by vacuum evaporation (3×10^{-4} Pa, Auto 306 Turbo, Edwards) of the following materials: WO₃ (thickness 6 nm), Tc (thickness 455 nm) and Ag (thickness 40 nm), on a glass/ITO substrate (100 Ω /square, AWAT). The active surface of electrodes was equal to 6 mm². The average deposition rate was 0.1 nm/s. The apparatus applied for measurements was described in detail elsewhere [4].

The samples were illuminated through the ITO electrode. Measurements of current–voltage curves in the dark and under illumination as well as of the short-circuit current (j_{sc}) and the open-circuit voltage (U_{oc}) against wavelength (λ) and light intensity (I_0) were performed.

3. Results and discussion

Dark current–voltage curves of the investigated systems are presented in Fig. 1. Positive voltage refers to the higher potential on the ITO electrode.

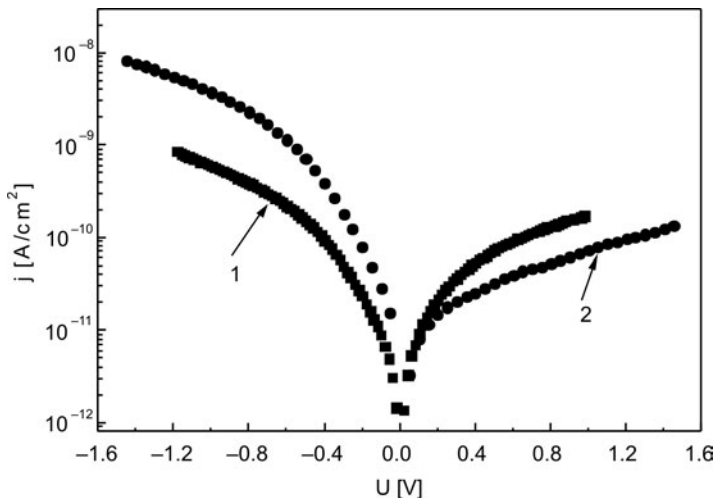


Fig. 1. Dark current–voltage curves of the investigated systems: curve 1 – ITO/Tc/Ag, curve 2 – ITO/WO₃/Tc/Ag

Curve 1 (the ITO/Tc/Ag system) exhibits little current rectification. The ratio of rectification is 3.3 at $U = 1$ V. As the work functions of ITO and Ag electrodes are high (higher than 4 eV) and the ionization energy and energy gap of tetracene equal 5.3 eV and 3.1 eV, respectively [10], we can notice that the electrode barriers for hole injection are much higher than for electron injection. Therefore, we can assume that the current flowing through Tc in the ITO/Tc/Ag system is a hole current, flowing independently of bias direction.

Curve 2 was obtained for the ITO/ WO_3 /Tc/Ag system. As the thickness of WO_3 in this system was merely 6 nm, we can presume that the applied voltage was equal to the voltage across the Tc layer (455 nm thick). The ITO/ WO_3 /Tc/Ag system exhibits a stronger current rectification: the ratio of rectification yields 50 at 1 V. This rectification can be interpreted on the assumption that the energy level shift resulting from transfer of electrons from Tc into WO_3 forms at the WO_3 /Tc interface. It is either a downward band bending, formed by space charge, or an interface dipole layer. In the presence of such an energy level shift, the barrier for hole injection from ITO into Tc is higher, while the barrier for electron injection is lower. This enables us to elucidate why, at the +ITO/−Ag polarization we observed a smaller hole current in the ITO/ WO_3 /Tc/Ag than in the ITO/Tc/Ag. On the other hand, the current flowing through the ITO/ WO_3 /Tc/Ag system at the −ITO/+Ag polarization is a sum of a hole current injected by Ag and an electron current injected by ITO/ WO_3 .

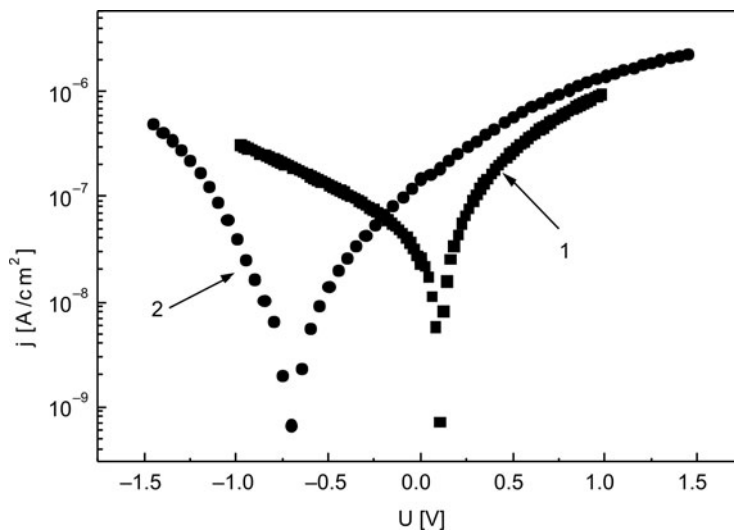


Fig. 2. Photocurrent–voltage curves of the ITO/Tc/Ag illuminated with light of 530 nm (curve 1) and of the ITO/ WO_3 /Tc/Ag illuminated with light of 515 nm (curve 2); $I_0 = 10^{15}$ ph/($cm^2 \cdot s$)

Figure 2 shows the photocurrent–voltage curves of the samples illuminated with monochromatic light of the intensity of 10^{15} ph/($cm^2 \cdot s$) and of the wavelength corresponding to maxima of photocurrent spectra presented in Fig. 3. The system of

ITO/Tc/Ag (curve 1) exhibits rather a small value of the open-circuit voltage ($U_{oc} = 80$ mV) whereas quite a high value of U_{oc} was observed for the system with the WO_3 layer, and it has the opposite direction ($U_{oc} = -700$ mV, curve 2). It can be explained if the energy level shift is assumed to occur at the WO_3 /Tc interface. This energy level shift, Δ , has to fulfil the following condition: $\Delta \geq \Delta W + eU_{ocmax}$, where ΔW is the difference between the work functions of the ITO and Ag electrodes.

The values of the photocurrent obtained for the highest applied voltages are several orders of magnitude higher than for dark current (cf. Fig. 1) and, with the increase of voltage, they tend towards saturation. The flux of excitons dissociating at the positively biased electrode determines the saturation photocurrent. Holes are injected into tetracene as a result of exciton dissociation [9, 13, 17]. This mechanism of photogeneration of charge carriers is confirmed by the spectrum of short-circuit current shown in Fig. 3.

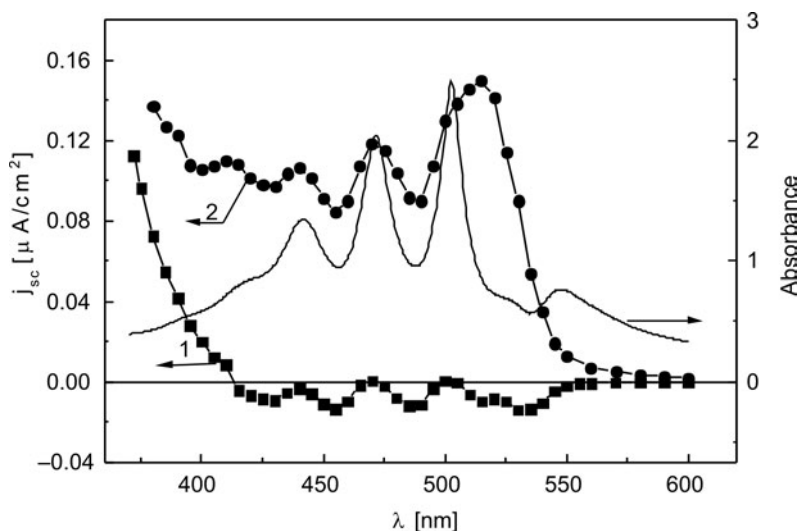


Fig. 3. Spectra of short-circuit current of the investigated systems (curve 1 – ITO/Tc/Ag, curve 2 – ITO/ WO_3 /Tc/Ag) and the absorbance spectrum of the Tc layer; $I_0 = 10^{15}$ ph/($cm^2 \cdot s$)

In the ITO/Tc/Ag system, the short-circuit current flows through the Tc layer from Ag to ITO (therefore we note that $j_{sc} < 0$) and is determined by the difference in fluxes of holes injected by excitons dissociating at both electrodes. The direction of short-circuit current is in agreement with the direction of the inner electric field resulting from the difference between the work functions of the electrodes ($W_{Ag} < W_{ITO}$). The current spectrum (curve 1) is antibatic to the absorption spectrum of the Tc layer [9, 13, 17]. It should be noticed that the absorption spectrum of the Tc layer 455 nm thick does not correlate well with the real absorption for $\lambda > 500$ nm. In particular, a single component of the Davydov splitting, which has the maximum at $\lambda = 520$ nm, is weakly noticeable in measurements of unpolarized light transmission. On the other

hand, the maximum of the absorption spectrum observed at 545 nm derives from the diffraction effect occurring in polycrystalline layers of Tc [22].

The spectral dependence of the short-circuit current of ITO/ WO_3 /Tc/Ag is presented as curve 2 in Fig. 3. The short-circuit current flows through the Tc layer from the ITO/ WO_3 electrode to Ag. This is the hole current generated as a result of exciton dissociation at the WO_3 /Tc interface. Its direction correlates with the inner electric field if we take into account the presence of an energy level shift at the WO_3 /Tc interface. Values of the short-circuit current are significantly higher than in the system without the WO_3 layer, and curve 2 correlates reasonably well with the absorption spectrum of tetracene (sympatric relation [9, 13, 17]).

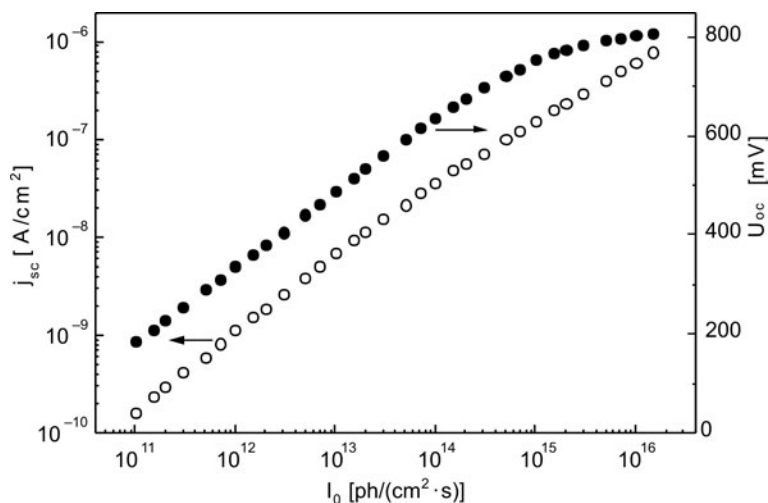


Fig. 4. Short-circuit current and open-circuit voltage against light intensity for the ITO/ WO_3 /Tc/Ag system illuminated with light of 515 nm

Figure 4 shows the dependences of the short-circuit current and the open-circuit voltage on light intensity for the ITO/ WO_3 /Tc/Ag system. The system was illuminated with monochromatic light of $\lambda = 515$ nm (the wavelength at which j_{sc} reaches its maximum, see Fig. 3). The $j_{sc}(I_0)$ relationship is sublinear and it can be approximated by $j_{sc} \propto I_0^m$, where $m = 0.8$ for $I_0 < 10^{14}$ $\text{ph}/(\text{cm}^2 \cdot \text{s})$ and $m = 0.6$ for higher values of light intensity.

The sublinear relation between photocurrent and light intensity has already been observed in other systems with Tc layers [12, 13, 17], and was interpreted as a result of charge carrier trapping or exciton quenching by charge carriers. The influence of these processes increases with the increase in the thickness of the organic layer. From the open circuit voltage–light intensity curve we can notice that U_{oc} increases by 150 mV/decade for $I_0 < 10^{14}$ $\text{ph}/(\text{cm}^2 \cdot \text{s})$ and for higher light intensity it reaches 0.8 V. Such a relation has not been observed for the systems with a Tc layer, according to the published data. Taking into account that $U_{oc\text{max}} = 0.8$ V and $\Delta W = 0.3$ eV (the differ-

ence between the work functions of the ITO and the Ag electrodes) we can estimate the energy level shift as $\Delta \geq 1.1$ eV.

It is worth emphasizing that in the investigated systems the photogeneration of charge carriers (holes) occurs at the ITO/Tc, WO₃/Tc and Tc/Ag interfaces as a result of exciton dissociation. The ITO/WO₃/Tc/Ag system shows an explicitly stronger photovoltaic effect in comparison with the ITO/Tc/Ag system. The obtained open-circuit voltage exceeded 800 mV. Our experimental results can be explained on the assumption that an energy level shift occurs at the hybrid heterojunction of WO₃/Tc.

Acknowledgement

This work has been supported by the Polish Ministry of Science and Higher Education with a Grant for the years 2006–2009 under the project No. 3T11B06530.

References

- [1] *Organic Photovoltaics*, S.-S. Sun, N.S. Sariciftci (Eds.), Taylor and Francis, Boca Raton, 2005.
- [2] BOUCLE J., RAVIRAJAN P., NELSON J., *J. Mater. Chem.*, 17 (2007), 3114.
- [3] OHMORI Y., ITOH E., MIYAIRI K., *Thin Solid Films*, 499 (2006), 369.
- [4] SIGNERSKI R., KOŚCIELSKA B., *Opt. Mater.*, 27 (2005), 1480.
- [5] HUTCHINS M.G., ABU-ALKHAIR O., EL-NAHASS M.M., ABDEL-HADY K., *J. Non-Cryst. Solids*, 353 (2007), 4137.
- [6] WEINHARD L., BLUM M., BÄR M., HESKE C., COLE B., MARSEN B., MILLER E.L., *J. Phys. Chem. C*, 112 (2008), 3078.
- [7] MEYER J., HAMWI S., BÜLOW T., JOHANNES H.-H., RIEDL T., KOWALSKY W., *Appl. Phys. Lett.*, 91 (2007), 113506.
- [8] JANSSEN G.F., RIEDL T., HAMWI S., JOHANNES H.-H., KOWALSKY W., *Appl. Phys. Lett.*, 91 (2007), 073519.
- [9] GEACINTOV N., POPE M., KALLMANN H., *J. Chem. Phys.*, 45 (1966), 2639.
- [10] SILINSH E.A., ČAPEK V., *Organic Molecular Crystals*, AIP Press, New York, 1994.
- [11] GHOSH K., FENG T., *J. Appl. Phys.*, 44 (1973), 2781.
- [12] GODLEWSKI J., KALINOWSKI J., *Phys. Stat. Sol. (a)*, 53 (1979) 161.
- [13] SIGNERSKI R., KALINOWSKI J., KOROPECKÝ I., NEŠPŮREK S., *Thin Solid Films*, 121 (1984), 175.
- [14] GUNDLACH D.J., NICHOLS J.A., ZHOU L., JACKSON T.N., *Appl. Phys. Lett.*, 80 (2002), 2925.
- [15] REYNAERT J., ARKHIPOV V.I., BORGHIS G., HEREMANS P., *Appl. Phys. Lett.*, 85 (2004), 603.
- [16] DE BOER R.W.I., JOCHEMSEN M., KLAPWIJK T.M., MORPURGO A.F., NIEMAX J., TRIPATHI A.K., PFLAUM J., *J. Appl. Phys.*, 95 (2004), 1196.
- [17] SIGNERSKI R., JAROSZ G., GODLEWSKI J., *Macromol. Symp.*, 212 (2004), 357.
- [18] DE BOER R.W.I., MORPURGO A.F., *Phys. Rev. B*, 72 (2005), 073207.
- [19] CHU C.-W., SHAO Y., SHROTRIYA V., YANG Y., *Appl. Phys. Lett.*, 86 (2005), 243506.
- [20] TSENG R.J., CHAN R., TUNG V.C., YANG Y., *Adv. Mater.*, 20 (2008), 435.
- [21] SIGNERSKI R., JAROSZ G., GODLEWSKI J., *Macromol. Symp.*, 212 (2004), 369.
- [22] HOFBERGER W., *Phys. Stat. Sol. (a)*, 30 (1975), 271.

Received 11 September 2008

Revised 25 February 2009

Photovoltaic properties of organic heterojunctions formed from tetracene and zinc hexadecafluorophthalocyanine*

R. SIGNERSKI**

Faculty of Applied Physics and Mathematics, Gdansk University of Technology,
Narutowicza 11/12, 80-952 Gdańsk, Poland

Experimental results obtained for the systems with a planar heterojunction of tetracene (Tc)/zinc perfluorophthalocyanine ($F_{16}ZnPc$) are presented in this work. The systems were prepared by vacuum evaporation of the following materials: MoO_3 , Tc, $F_{16}ZnPc$, bathocuproine (BCP) and Ag, onto glass/ITO substrates. Dark current–voltage and photocurrent–voltage relationships as well as spectral and light intensity dependences of short-circuit current are presented. The favourable effect of a buffer layer of BCP at the Ag electrode was observed.

Key words: *photovoltaic effect; organic heterojunction; tetracene; zinc perfluorophthalocyanine*

1. Introduction

Organic heterojunctions have been the subject of intensive investigations for twenty years due to their possible application in electronic devices, particularly in organic solar cells. Planar or bulk heterojunctions are most often formed from such materials as polymers, fullerenes, phthalocyanines and perylene dyes [1].

The preliminary investigations into photovoltaic properties of planar heterojunction formed from tetracene (Tc) and zinc hexadecafluorophthalocyanine ($F_{16}ZnPc$) have been presented in this work. Electric and photoelectric properties of monocrystals and polycrystalline layers of tetracene have been the subject of numerous analyses [2–11], however, there are only a few reports on heterostructures based on Tc [12–14]. Perfluorophthalocyanines and, in particular, $F_{16}ZnPc$, have also been intensively investigated, since they exhibit good chemical and thermal stability, strong light absorp-

*The paper presented at the 11th International Conference on Electrical and Related Properties of Organic Solids (ERPOS-11), July 13–17, 2008, Piechowice, Poland.

**Corresponding author, e-mail: ryszard@mif.pg.gda.pl

tion (up to 900 nm) and they transport electrons relatively well [15,16]. It is worth noting that the range of strong absorption of Tc (400–550 nm) covers the range of weak absorption of $F_{16}ZnPc$ existing between the Soret and Q bands. This means that the range of strong absorption of the Tc/ $F_{16}ZnPc$ bilayer system is quite wide.

This work presents experimental results obtained on the ITO/MoO₃/tetracene (Tc)/zinc hexadecafluorophthalocyanine ($F_{16}ZnPc$)/bathocuproine (BCP)/Ag systems, which were prepared by vacuum evaporation of successive layers onto glass/ITO substrates. A thin layer of MoO₃ has been applied in order to improve the injection properties of ITO [17,18]. The absorption of light by this layer is negligibly small. The layer of BCP should prevent the $F_{16}ZnPc$ layer from being damaged during Ag deposition [19, 20].

2. Experimental

The samples were obtained in vacuum (3×10^{-4} Pa, Auto 306 Turbo, Edwards) by evaporation of the following materials: MoO₃, Tc, $F_{16}ZnPc$, BCP, Ag, onto glass/ITO substrates (100 Ω /square, AWAT). All materials for evaporation were purchased from Aldrich. Tc and $F_{16}ZnPc$ were purified in advance by sublimation. The thicknesses of layers are given in Fig. 1. The active surfaces of electrodes were 6–8 mm² and the average deposition rate was 0.1 nm/s. The samples were illuminated through ITO. The apparatus used for measurements has been described elsewhere [21].

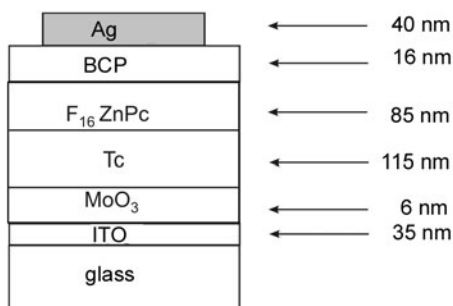


Fig. 1. The structure of the device

3. Results and discussion

Figure 2 presents the spectral dependence of short-circuit current of ITO/MoO₃/Tc/ $F_{16}ZnPc$ /Ag and the absorption spectrum of the Tc/ $F_{16}ZnPc$ system. The short-circuit current flows through the system from Ag to ITO, which is in agreement with the inner electric field resulting from the difference between work functions of electrodes ($W_{ITO/MoO_3} > W_{Ag}$). Within the absorption range of Tc (400–550 nm), the short-circuit current curve exhibits antibatic behaviour to absorbance, while outside this range we observe rather a symbatic behaviour. This means that, similarly as in many other bi-

layer planar heterojunctions, charge carriers are generated as a result of exciton dissociation at the interface of organic layers [1]. It can also be added that results obtained on the systems with other electrodes, namely on Al/F₁₆ZnPc/Tc/CuI, which are not discussed here, confirmed the above conclusion about the mechanism of charge carrier photogeneration.

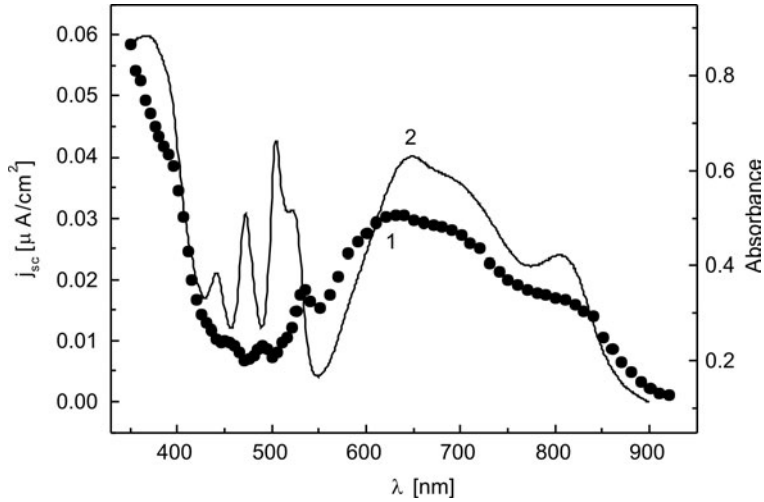


Fig. 2. Spectral dependence of the short-circuit current of the ITO/MoO₃/Tc/F₁₆ZnPc/Ag system (curve 1) illuminated with light of 10^{14} photons/(cm²·s) and the absorbance spectrum of the Tc/F₁₆ZnPc bilayer (curve 2)

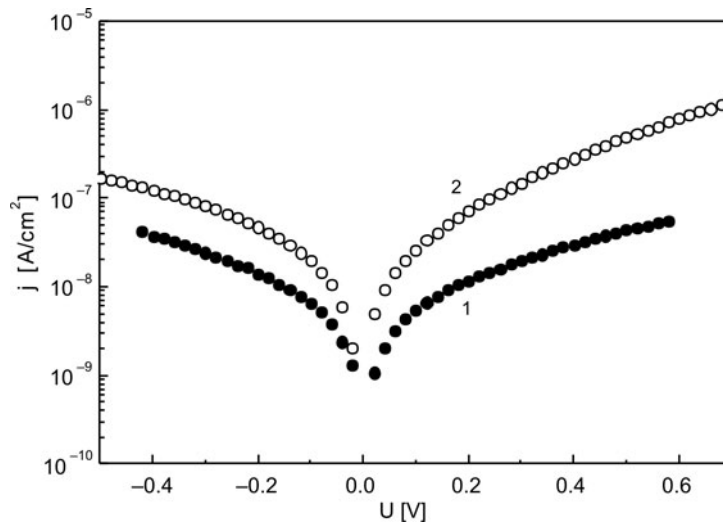


Fig. 3. Dark current–voltage curves of the investigated systems:
1 – ITO/MoO₃/Tc/F₁₆ZnPc/Ag, 2 – ITO/MoO₃/Tc/F₁₆ZnPc/BCP/Ag.
Positive values of voltage refer to the higher potential on ITO

The specific role of the Tc/F₁₆ZnPc interface is not observed in the measurement of dark current–voltage dependence (Fig. 3). Characteristic of the system without BCP (curve 1) is that it does not depend on the voltage polarization. In the case of the system including BCP (curve 2), we observed currents several time higher and the occurrence of a small rectification effect: at $U = 0.4$ V, the rectification ratio equals 2. These results indicate that Ag/F₁₆ZnPc is not an ohmic contact and the incorporation of the BCP layer reduces resistance of the contact (and the whole system as well).

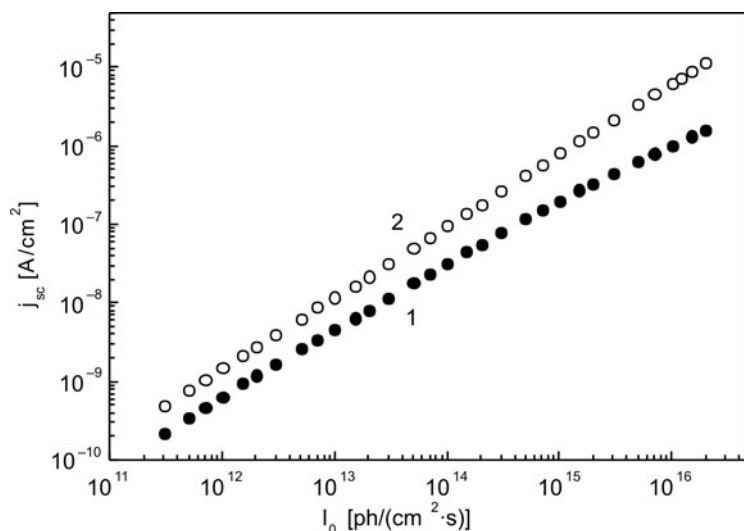


Fig. 4. Light intensity dependence of the short-circuit current of the investigated systems illuminated with light of 630 nm: 1 – ITO/MoO₃/Tc/F₁₆ZnPc/Ag, 2 – ITO/MoO₃/Tc/F₁₆ZnPc/BCP/Ag

Such a role of the BCP layer is also noticed in the relationship between short-circuit current and light intensity, as presented in Fig. 4. In both systems, with BCP or without BCP, photogeneration currents result from the same process (exciton dissociation at the Tc/F₁₆ZnPc interface), however the short-circuit current in the system with BCP is higher and almost proportional to light intensity, $j_{sc} \propto I_0^{0.9}$. It has to be borne in mind that in bilayer photovoltaic systems [1], the short-circuit current is a hole current in one layer (here it is Tc), while an electron current in the other one (here it is F₁₆ZnPc). Lower values of short-circuit current for the system without BCP, as well as sublinear dependence of $j_{sc}(I_0)$, indicate that the Ag/F₁₆ZnPc contact limits the transport of electrons through the system. A thin layer of BCP incorporated between Ag and F₁₆ZnPc can lead to the reduction in this limitation. Therefore, we suppose that the BCP prevents the F₁₆ZnPc layer from being damaged during Ag deposition and reduces the contact barrier.

Current–voltage relationship of the system with BCP illuminated with white light (Xe lamp, AMO Oriol filter) of 20 mW/cm² is presented in Fig. 5. The system exhibits a photovoltaic effect with the following parameters: short-circuit current $j_{sc} = 18.1$ μ A/cm²,

open-circuit voltage $U_{oc} = 0.41$ V, fill factor $FF = 0.25$. Small values of j_{sc} and FF as well as the shape of the curve (see inset) are indicative of high series resistance R_s and relatively small parallel resistance R_p of the systems [22, 23]. Their values can be estimated as $R_s = 21$ $\text{k}\Omega\cdot\text{cm}^2$ and $R_p = 24$ $\text{k}\Omega\cdot\text{cm}^2$. The main reason for high R_s is a too large thickness of the Tc and F_{16}ZnPc layers. Moreover, oxygen from the air adversely affects the electric conductivity of F_{16}ZnPc [16].

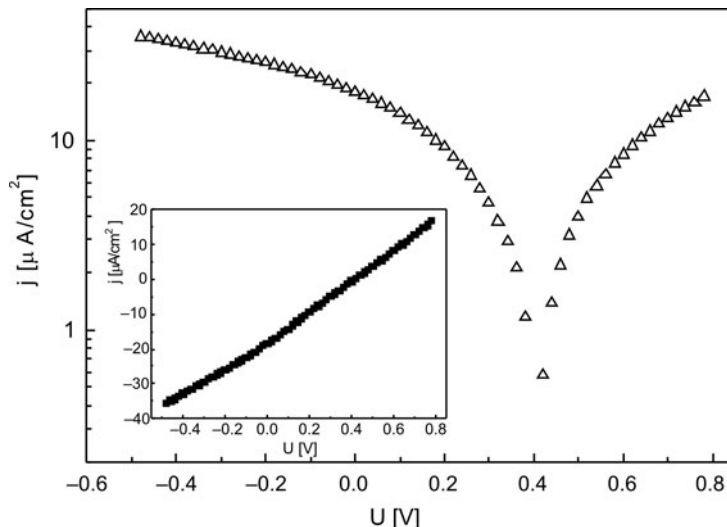


Fig. 5. Photocurrent–voltage curve of the ITO/MoO₃/Tc/F₁₆ZnPc/BCP/Ag system illuminated with white light of 20 mW/cm². Inset: the same curve in linear plot. Positive values of voltage refer to higher potential on ITO

The main factor limiting the value of the open-circuit voltage, U_{oc} , in organic heterojunctions is the difference Δ between the ionization energy I_h of a layer transporting holes and electron affinity energy A_e of the layer transporting electrons [24]. For Tc/F₁₆ZnPc, the value of Δ can be estimated as ca. 0.8 eV [3, 15], which means that the maximum value of U_{oc} should not exceed 0.8 V. The obtained value, $U_{oc} = 0.41$ V, fulfils this condition, even though it is not the maximum value. Measurements of U_{oc} indicate also that the value of U_{oc} does not depend on the presence of the BCP layer.

4. Summary

The systems with planar heterojunction of Tc/F₁₆ZnPc exhibit strong absorption of light within a wide range of wavelengths, from 350 nm up to 900 nm. The process of charge carrier photogeneration occurs at the Tc/F₁₆ZnPc interface as a result of dissociation of excitons excited in the Tc or F₁₆ZnPc layers, and diffusing towards this interface. Incorporation of the buffer layer of BCP improves the transport of electrons through the Ag/F₁₆ZnPc contact. The analysis of the current–voltage curve leads us to

the conclusion that it is strongly determined by parasite resistances, and in particular by high series resistance.

Acknowledgement

This work has been supported by the Polish Ministry of Science and Higher Education with a grant for the years 2006–2009 under the project No. 3T11B06530.

References

- [1] *Organic Photovoltaics*, S.-S. Sun, N. S. Saricicfci (Eds.), Taylor and Francis, Boca Raton, 2005.
- [2] GEACINTOV N., POPE M., KALLMANN H., *J. Chem. Phys.*, 45 (1966), 2639.
- [3] SILINSH E.A., ČAPEK V., *Organic Molecular Crystals*, AIP Press, New York, 1994.
- [4] GHOSH K., FENG T., *J. Appl. Phys.*, 44 (1973), 2781.
- [5] GODLEWSKI J., KALINOWSKI J., *Phys. Stat. Sol. (a)*, 53 (1979), 161.
- [6] SIGNERSKI R., KALINOWSKI J., KOROPECKÝ I., NEŠPŮREK S., *Thin Solid Films*, 121 (1984), 175.
- [7] GUNDLACH D.J., NICHOLS J.A., ZHOU L., JACKSON T.N., *Appl. Phys. Lett.*, 80 (2002), 2925.
- [8] REYNAERT J., ARKHIPOV V.I., BORGHS G., HEREMANS P., *Appl. Phys. Lett.*, 85 (2004) 603.
- [9] DE BOER R.W.I., JOCHEMSEN M., KLAPWIJK T.M., MORPURGO A.F., NIEMAX J., TRIPATHI A.K., PFLAUM J., *J. Appl. Phys.*, 95 (2004), 1196.
- [10] SIGNERSKI R., JAROSZ G., GODLEWSKI J., *Macromol. Symp.*, 212 (2004), 357.
- [11] DE BOER R.W.I., MORPURGO A.F., *Phys. Rev. B*, 72 (2005), 073207.
- [12] CHU C.-W., SHAO Y., SHROTRIYA V., YANG Y., *Appl. Phys. Lett.*, 86 (2005), 243506.
- [13] TSENG R.J., CHAN R., TUNG V.C., YANG Y., *Adv. Mater.*, 20 (2008), 435.
- [14] SIGNERSKI R., JAROSZ G., GODLEWSKI J., *Macromol. Symp.*, 212 (2004), 369.
- [15] PFEIFFER M., LEO K., KARL N., *J. Appl. Phys.*, 80 (1996), 6880.
- [16] BRINKMANN H., KELTING C., MAKAROV S., TSARYOVA O., SCHNURPFEL G., WÖHRLE D., SCHLETTWEIN D., *Phys. Stat. Sol.*, 205 (2008), 409.
- [17] REYNOLDS K.J., BARKER J.A., GREENHAM N.C., FRIEND R.H., FRAY G.L., *J. Appl. Phys.*, 92 (2002), 7556.
- [18] MATSUSHIMA T., KINOSHITA Y., MURATA H., *Appl. Phys. Lett.*, 91 (2007), 253504.
- [19] PEUMANS P., YAKIOMOV A., FORREST S.R., *J. Appl. Phys.*, 93 (2003), 3693.
- [20] VOGEL M., DOKA S., BREYER C., LUX-STEINER M.C., FOSTIROPOULOS K., *Appl. Phys. Lett.*, 89 (2006), 163501.
- [21] SIGNERSKI R., *J. Non-Cryst. Solids*, 352 (2006), 4319.
- [22] PETRITSCH K., *Organic Solar Cell Architectures*, PhD Thesis, TU Graz, 2000.
- [23] MOLITON A., NUNZI J.-M., *Polym. Int.*, 55 (2006), 583.
- [24] CHEYNS D., POORTMANS J., HEEREMANS P., DEIBEL C., VERLAAK S., RAND B.P., GENOE J., *Phys. Rev. B*, 77 (2008), 165332.

Received 11 September 2008

Revised 25 February 2009

Electrical conductivity in thin films fabricated from nanoparticles of a polymeric composite based on PEDOT*

D. RAIS^{1**}, J. HAIN², A. PICH², S. POCHKAILOV¹,
S. NEŠPŮREK¹, H.-J. P. ADLER², A. HAMÁČEK³, J. ŘEBOUN³

¹Institute of Macromolecular Chemistry, Academy of Sciences of the Czech Republic,
v. v. i., 162 06 Prague, Czech Republic

²Institute of Macromolecular Chemistry and Textile Chemistry,
Dresden University of Technology, Mommsenstr. 4, D-01062 Dresden, Germany

³The University of West Bohemia, Faculty of Electrical Engineering, 306 14 Pilsen, Czech Republic

A comparative study of electrical properties of films fabricated from a series of polymeric core shell particles and microgels is presented. The core shell particles consist of spherical polystyrene core covered by electrically conductive poly[3,4-(ethylenedioxy)thiophene] (PEDOT). Microgels are composed of PEDOT grains embedded into crosslinked, electrically insulating polymer bodies. The electrical resistivity of the films changes from 12 G Ω ·cm to 100 Ω ·cm; the value depends on the thickness of the shell cover and the type of oxidant used for PEDOT polymerization. Electrical conductivity in the films of core shell particles is thermally activated and obeys the inverse Meyer–Neldel rule, which indicates that the electrical conductivity is governed by a common transport mechanism. Electrical conductivity depends, among others, on the humidity in the surrounding environment. In films consisting of particles with a high PEDOT content (and thus high conductivity) the resistivity increases as the humidity increases. Conversely, when the films are formed from particles having a low PEDOT content, the humidity has a reverse effect. An explanation for this behaviour is proposed. The frequency dependences of ac conductivities of high conductivity “core shell” and “microgel” films suggest existence of hopping charge carrier transport mechanism for large humidity scale.

Key words: *core shell particles; microgel; polystyrene; humidity sensitivity; Meyer-Neldel rule*

*The paper presented at the 11th International Conference on Electrical and Related Properties of Organic Solids (ERPOS-11), July 13–17, 2008, Piechowice, Poland.

**Corresponding author, e-mail: david.rais@atlas.cz

1. Introduction

Investigations into conductive polymers have attracted great scientific interest because of their high application potential [1–3]. A well known example is poly [3,4-(ethylenedioxy)thiophene] (PEDOT) with a high thermal stability up to 280 °C [4]. Due to high conductivity and good environmental stability, this material seems to be a good candidate for use in electrodes, electromagnetic shielding, capacitors, sensors, antistatic and anticorrosion coatings, etc. [5, 6]. The lack of solubility in the majority of typical organic solvents is an aspect limiting the practical use of conducting polymers. One of the ways to make them more soluble is to prepare them in the form of colloidal dispersions [7] of core shell particles or microgels. In our study, we concentrate on the relationship between particle morphology and electrical properties under varying humidity and temperature conditions.

2. Experimental

Materials. The synthesis of the materials under study was described in our previous publication [8]. Here, we will only indicate some important details related to the present work. Core shell composites were synthesized by *in-situ* oxidative polymerization of 3,4-(ethylenedioxy)thiophene monomer (EDOT) in latex dispersion of poly(styrene-*co*-acetoacetoxyethyl methacrylate) (PS/PAAEM). The latex dispersion was composed of spherical polymer particles (of uniform diameters – either 520 or 110 nm, estimated by dynamic light scattering method (DLS)) in 30 mol % ethanol; the latex dispersion of small particles was stabilized by the addition of a surfactant – sodium dodecylsulphonate (SDS). The oxidant was added in equimolar ratio to the EDOT monomer. Variation of PEDOT content in the resulting composite was achieved by changing the weight ratio of EDOT to PS/PAAEM or by the use of a different oxidant. The reaction medium during EDOT polymerization was heated to 60 °C, except in the cases when H₂AuCl₄ was used as the oxidation agent (here, the temperature was 25 °C). The parameters of the synthesized core shell materials under study are summarized in Table 1, together with the estimated PEDOT contents as obtained from elemental analysis (the measurement of the sulphur element content) of the washed products.

The PEDOT inclusions were fabricated by *in-situ* oxidation of EDOT in the presence of the poly(*N*-vinylcaprolactam-*co*-acetoacetoxyethyl methacrylate) (PVCL/PAAEM) microgel particles (of the diameter 260 nm estimated by DLS at 20 °C) dispersed in 30 mol % ethanol. Oxidation agent (FeCl₃) was added in equimolar ratio to the EDOT monomer. To deposit various amounts of PEDOT into the polymer microgel, the amount of PVCL/PAAEM added to the reaction mixture was varied. Table 2 gives a summary of the parameters of the synthesis for each microgel material under study, together with estimations of their PEDOT contents, as obtained from elemental analysis of the washed products.

Table 1. Composite particles of the core shell type under study

Run	Oxidant for PEDOT	Latex core diameter D [nm]	EDOT: polymer ^a [g/g]	PEDOT [wt. %]	Resistivity ρ [$\Omega\cdot\text{cm}$]
CS1	FeCl ₃	110 ^c	1:1	0.6	1.0×10^{11}
CS2	FeCl ₃	520	5:1	2.0	3.1×10^8
CS3	FeCl ₃	520	10:1	4.7	7.3×10^7
CS4	FeCl ₃	520	1:2	7.3	6.7×10^7
CS5	FeCl ₃	520	10:1	35.6	5.3×10^4
CS6 ^b	HAuCl ₄	520	1:1	26.9	1.0×10^2
CS7 ^b	HAuCl ₄	110 ^c	1:1	18.5	3.5×10^2
CS8	Na ₃ Mo ₁₂ PO ₄₀	520	1:1	23.0	1.2×10^5
CS9	(NH ₄) ₂ S ₂ O ₈	520	1:1	^d 25.7	1.2×10^{10}

^aMass of EDOT related to pure mass of the empty microgel (PVCL/PAAEM).

^bTemperature of EDOT polymerization was 25 °C.

^cLatex polymer was (PS/PAAEM)/SDS.

^dIn this case, the PEDOT concentration is overestimated, because we used the measurements of sulphur element content (by the elemental analysis method) for the calculation of the PEDOT content. The method does not distinguish the sulphur in the PEDOT from the sulphur in the oxidant which remained in the material after washing.

Table 2. Composite materials of the microgel type under study

Run	Oxidant for PEDOT	EDOT : polymer ^a [g/g]	PEDOT [wt. %]	Resistivity ρ [$\Omega\cdot\text{cm}$]
MG1	FeCl ₃	1:10	0.5	3.5×10^{10}
MG2	FeCl ₃	1:5	0.6	4.4×10^9
MG3	FeCl ₃	1:1	4.6	1.7×10^8
MG4	FeCl ₃	5:1	5.3	9.5×10^7
MG5 ^b	FeCl ₃	5:1	30.8	6.1×10^2
MG6	HAuCl ₄	1:1	12.5	3.0×10^4

^aMass of EDOT related to pure mass of the Latex polymer (PS/PAAEM).

^bReaction medium was 60 mol % ethanol.

Electrical measurements. Thin films of both core shell particles and microgels for electrical measurements were fabricated by drop casting from 1 wt. % aqueous ethanol colloidal dispersion onto glazed ceramic substrates with interdigital gold electrode systems of the coplanar type. The resulting film thicknesses after drying were ca. 1 μm . The distance between the opposite electrodes was 50 μm , the thickness of the gold electrode was 1.1 μm . The electrical current was measured with a Keithley 6517A electrometer, which was also used as a voltage source. The resistances R were determined from the slopes of the current–voltage characteristics. Electrical resistivity ρ and conductivity σ were calculated from the expression $\rho = \sigma^{-1} RL/g$, where l/g is the electrode geometrical factor (l is the total length of the electrode width and g is the

electrode distance), L is the film thickness. The activation energies of the conductivities were determined from the temperature dependences in the temperature range 20–70 °C. These measurements were performed in a vacuum cryostat with temperature stabilization.

The influence of environmental humidity on ac conductivity was investigated with the sample placed in a chamber with continuous flow of nitrogen (the flow rate was 1000 sccm). The humidity of the flowing gas was changed by mixing wet and dry nitrogen. The flow rates in the branches (dry and wet N₂) were adjusted by mass flow regulators, in order to achieve the predetermined RH level. The response kinetics of the equivalent parallel resistance, R_p , were measured by repeating cycles of dry nitrogen flow (400 s) followed by flow of 50 % RH mixed nitrogen (400 s). The cycle was repeated at least 6 times, to evaluate the stability of the sample. ac conductivity parameters were measured with a HIOKI LCR 3532-50 HiTESTER; the testing frequency was 12 kHz, except where specified otherwise.

3. Results and discussion

3.1. dc conductivity

The values of electrical resistivities of the materials under study are presented in Tables 1 and 2. These values were determined from the current–voltage characteristics measured under normal air atmosphere at room temperature. The characteristics follow Ohm's law. As can be seen from the tables and from Fig. 1, the amount of PEDOT in the composites strongly influences the electrical resistivities.

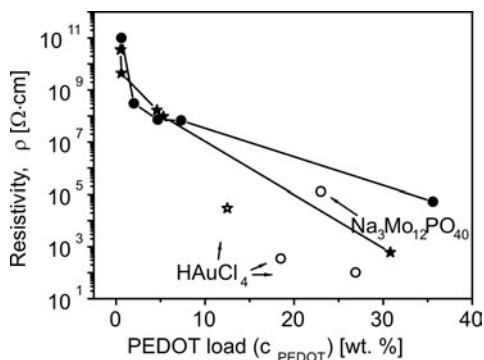


Fig. 1. The dependences of resistivities of thin films fabricated from core shell particles (full circles) and microgel composites (full stars) fabricated with FeCl₃ oxidant. Lines are added as visual guides. Hollow symbols not connected with lines (circles and stars), represent thin film of core shell or microgel, respectively. Resistivities of materials synthesized with other oxidants (indicated in the graph) suggest the influence of the oxidant

The dependences of the resistivities on the PEDOT contents in the films fabricated from the composite materials that had been synthesized using FeCl₃ oxidant are almost the same for both core shell and microgel structures, except for the samples fabricated with the highest PEDOT content (see the lines in Fig. 1). Our hypothesis for this similarity is the following: The electrically conductive component of the composites

(PEDOT) is polymerized in the form of grains lying either on the surface of the latex core, or in the swollen polymer chains of a microgel (cf. the micrographs (a) and (d) in Fig. 2). If the content of PEDOT does not reach a percolation threshold, the PEDOT grains are separated by insulating polymer chains (mostly the PAAEM part of the template copolymer). From the point of view of charge carrier transport, the situation is similar for both core shell and microgel morphologies. For the materials with higher PEDOT content, the percolation threshold is reached and conductivity increases; the film forming material capacity, which is better in the case of the microgels, might play an important role. The high resistivity of the core shell material CS9, which was oxidized with $(\text{NH}_4)_2\text{S}_2\text{O}_8$, does not agree with its apparently very high PEDOT content (cf. Table 1, note d).

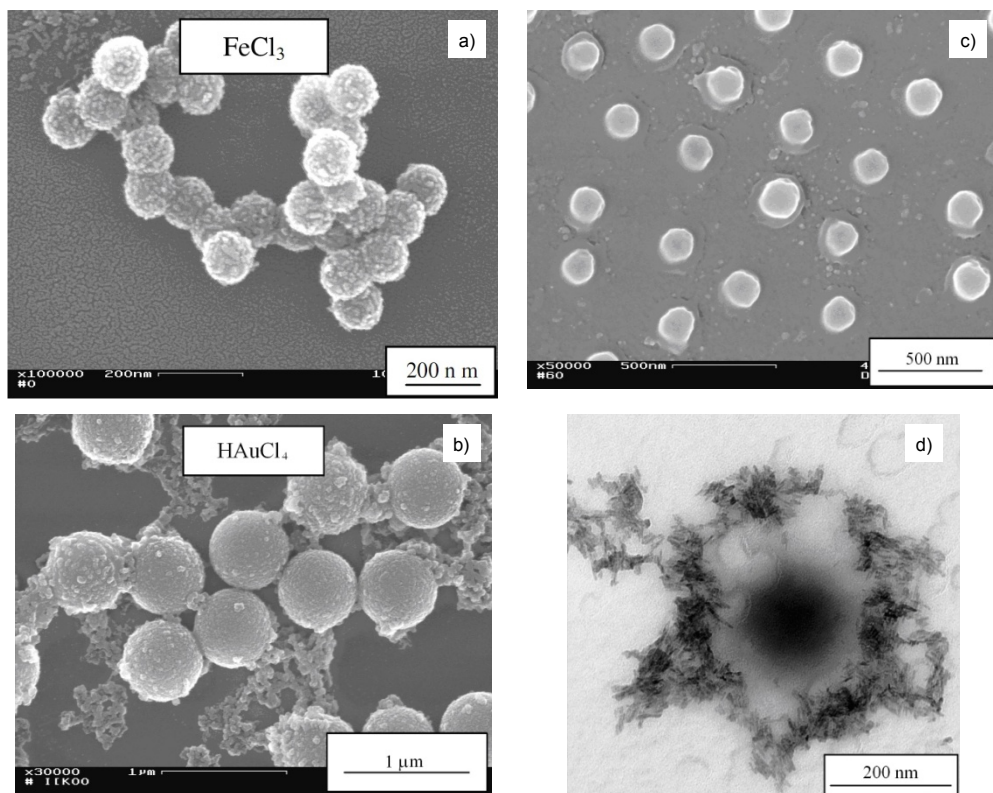


Fig. 2. Micrograph examples of the core shell and microgel composites: a) material CS1 with small diameter latex template (110 nm) and low PEDOT content; the rod-shaped grains of PEDOT on the PS/PAAEM particles are separated from each other, b) material CS6 with a large diameter latex template (520 nm) and high PEDOT content; the particles are covered by a compact PEDOT shell surrounded by additional PEDOT grains not attached to the latex particles; oxidant used for PEDOT polymerization is indicated in the photographs. Typical images of the microgel material (MG2 in this case): c) SEM of an array of particles, d) TEM of a single particle. The PEDOT inclusions in microgel can be distinguished in image (d) as dark, rod-shaped structures surrounding the particle

Figure 1 illustrates the influence of various oxidants used for the PEDOT polymerization on the properties of the material. The use of $\text{Na}_3\text{MoO}_4 \cdot 12\text{H}_2\text{O}$ yielded material (CS8), in which the resistivity and PEDOT content values are not far from the trend exhibited by the FeCl_3 oxidized core shell composites (full circles connected by a line in Fig. 1). When HAuCl_4 was used, lower resistivities at lower PEDOT content (in comparison with all the other oxidants) were observed in composites of both core shell and microgel morphologies. This is caused, among others, by more intensive creation of “secondary” PEDOT particles – not attached to the latex core, which were observed in CS6 composite (cf. the micrograph in Fig. 2b) and which enhance the electrical contacts among neighbouring latex particles in the thin film. Additionally, the high doping efficiency of the aurate and the presence of Au nanoparticles (AuNPs) formed by the reduction of aurate simultaneously with the EDOT polymerization (AuNPs presence was indicated by SEM, STM analysis, not shown here.) also enhances electrical contacts between the particles and, consequently, film resistivity decreases.

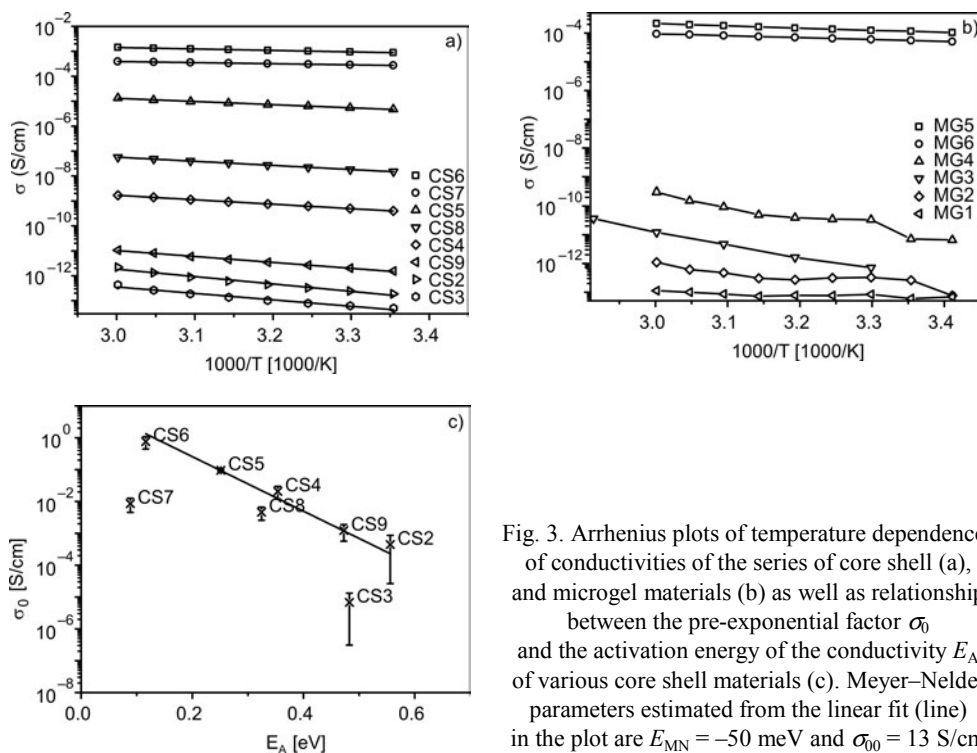


Fig. 3. Arrhenius plots of temperature dependences of conductivities of the series of core shell (a), and microgel materials (b) as well as relationship between the pre-exponential factor σ_0 and the activation energy of the conductivity E_A of various core shell materials (c). Meyer–Neldel parameters estimated from the linear fit (line) in the plot are $E_{MN} = -50$ meV and $\sigma_{00} = 13$ S/cm

We have studied the temperature dependences of dc conductivity in both core shell and microgel materials. The Arrhenius plots of conductivities the studied materials are presented in Fig. 3. All the materials under study are included, except the CS1, in which the high resistivity prevented us from the determination of temperature de-

pendence of conductivity in vacuum. It was found that the conductivities σ in the core shell materials show Arrhenius-type behaviour:

$$\sigma(T) = \sigma_0 \exp\left(-\frac{E_A}{kT}\right), \quad (1)$$

where T stands for temperature, σ_0 is the pre-exponential factor, k is the Boltzmann constant and E_A is the activation energy. Furthermore, the logarithm of σ_0 was correlated with the activation energy E_A (cf. Fig. 3c); thus, the group of materials conform to the anti-Meyer–Neldel rule [9] (also called the compensation law):

$$\ln \sigma_0 = \ln \sigma_{00} + \frac{E_A}{E_{MN}} \quad (2)$$

where σ_{00} and E_{MN} are the so-called Meyer–Neldel parameters (M–N prefactor and M–N characteristic energy). The M–N parameters in the Eq. (2) for the investigated materials were calculated to be $E_{MN} = -50$ meV and $\sigma_{00} = 13$ S/cm.

The M–N rule is a relation, which can be used for the description of thermally activated processes, e.g. charge carrier transport in microcrystalline and amorphous semiconductors [10–12]. When the M–N characteristic energy E_{MN} in Eq. (2) has a negative value, the phenomenon is called the inverse (or anti-) Meyer–Neldel rule. Up to now, there has been no universal explanation of the origin of the anti-M–N rule behaviour in materials. Several explanations were proposed: For example, Lucovsky and Overhof [13] have shown that this effect occurs in heavily-doped microcrystalline silicon as a result of statistical shift of a Fermi level into the tail states of the charge carrier transport band. Other researchers, Widenhorn, Rest and Bodegom [14] observed the occurrence of both regular and anti-M–N rule behaviour for dark currents in the CCD elements.

The appearance of this relationship in a group of the core shell materials (CS2, CS3 CS4, CS5, CS6, CS8 and CS9), depicted in Fig. 3c, indicates a common transport mechanism in these materials. The electric charge in the PEDOT is transported by a combination of microscopic processes, like tunnelling or hopping between localized sites on polymer chains (inter-chain hopping) and hopping among grains of PEDOT. As a result, the macroscopic dc conductivity is determined by the slowest process. The most favourable microscopic charge transport mechanism, limiting the conduction in the investigated materials with strongly varying contents of conductive grains of PEDOT, is hopping of the charge carriers (holes) between the grains. The frequency dependences of ac conductivity (discussed in a separate section) support this hypothesis. The parameters of materials designated CS7 and CS3 do not fit well with the linear relationship $\ln \sigma_0 \propto E_A$ fulfilled by the rest of the tested core shells (see. Fig. 3c). This may be due to a different morphology of the CS7 material which consists of smaller particles (110 nm) compared with the rest of the core shell samples (520 nm)

– see Table 1, and in the case of material CS3 due to a large experimental error with the estimation of activation energy E_A and pre-exponential factor σ_0 .

In microgels, the M–N rule-conforming behaviour was not recognized, due to the temperature dependence of the activation energy, which can be seen as non-linear characteristics in Arrhenius plot of some microgels (Fig. 3b). This is possibly a result of microgel insulating polymer template (PVCL/PAAEM) morphology change – the onset of the glass transition at about 30 °C [15].

3.2. Sensitivity of the ac electrical conductance to humidity

Table 3. Humidity sensing properties of selected materials under study

Material	R_p^{wet} at 50.5% RH [Ω]	R_p^{dry} at 3.5% RH [Ω]	Relative sensitivity ^a S [%]	R_p^{dry} relative drift ^b [%]
Core shell materials				
CS6	6.28×10^2	5.85×10^2	7.4	–0.07
CS7	1.19×10^3	1.11×10^3	7.3	0.05
CS5	3.28×10^5	3.09×10^5	6.1	0.32
CS3	2.4×10^5	2.5×10^8	–100	0.00
Microgel materials				
MG5	1.19×10^4	1.16×10^4	2.6	0.42
MG6	8.4×10^4	7.14×10^4	18	0.02
MG2	5.0×10^8	7.5×10^8	–33	0.06
MG4	4.3×10^8	7.2×10^8	–40	–0.01
MG1	6.2×10^8	8.3×10^8	–25	0.00

^aRelative change of R_p upon the transition from the dry to wet N_2 , as defined in Eq. (3).

^bChange of R_p^{dry} between two consecutive cycles of periodic RH change, as shown in Fig. 4a.

In order to further elucidate the microscopic charge conduction mechanism, we measured the dependence of ac conductivity (parameters: R_p – equivalent parallel resistance and G – conductance) on environmental humidity (water vapour content in nitrogen gas surrounding tested sample). We found that R_p of thin films changed as the humidity changed; both dependences, increase and decrease of R_p upon increasing the humidity, were found. The results are summarized in Table 3 (results of 6 cycles of changes of humidity from 3.5% to 50.5 % RH at room temperature and under normal pressure) and in Fig. 4. The time evolution of R_p in response to periodic humidity changes was measured for all composites listed in Table 3; a typical behaviour of the low resistivity material (MG6) is shown in Fig. 4a, where we also indicate how the values in Table 3 were obtained.

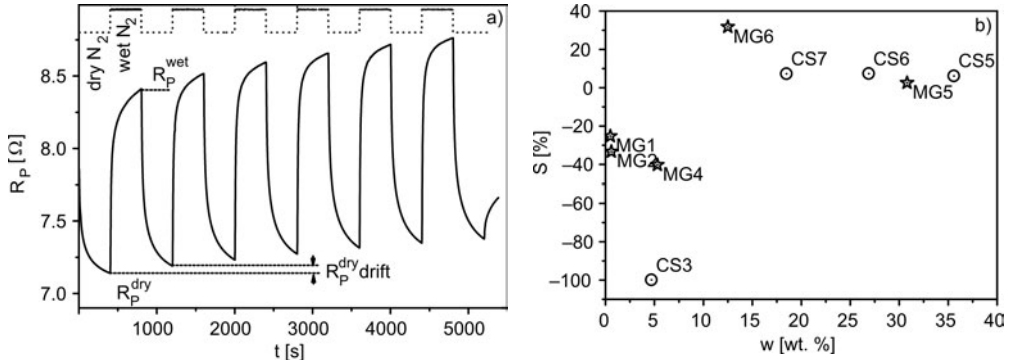


Fig. 4. A typical behaviour of equivalent parallel resistance R_p (solid lines) in response to periodic changes of humidity (dotted lines) from 3.5 to 50.5 % RH (a). The dashed lines indicate how the values of R_p^{wet} , R_p^{dry} and the drift of R_p^{dry} used for comparison of the materials in Table 3 were obtained from the periodic humidity change tests and sensitivities to humidity of selected materials (b) under study (stars for various microgels, circles for core shells). The data are combined from Tables 1–3

The relative sensitivity towards the humidity change was calculated from the measured values as follows:

$$S = \frac{R_p^{\text{wet}} - R_p^{\text{dry}}}{R_p^{\text{dry}}} \times 100 \quad (3)$$

where R_p^{dry} and R_p^{wet} represent the saturated values of ac resistances in dry and wet N₂ flow (humidity about 3.5% and 50.5% RH), respectively. In the case of core shell materials (CS5, CS6 and CS7) and microgel materials (MG5 and MG6) R_p increased as the RH increased, leading to the positive values of S . In the remaining materials under investigation, reverse behaviour was observed, yielding $S < 0$. The materials which have higher PEDOT contents and, consequently, smaller ac resistances R_p , exhibit the former type of response, while the samples with low PEDOT content and high R_p behave in the opposite manner. Thus, these materials can be assigned, depending on their PEDOT content, to one of two classes; corresponding to the two complementary types of humidity response, as can be seen in Fig 4b.

To explain the differences in the behaviour of humidity response, we concentrated on a more detailed study of two core shell materials CS6 and CS3 (highly and low conductive, respectively). R_p of the layers fabricated from these materials in function of relative humidity are given in Fig. 5. The equivalent parallel resistance, R_p , of the conductive layer of CS6 increases as the relative humidity increases at all tested temperatures (20, 30, 40 and 50 °C). This characteristic cannot be explained by the model of purely ionic conductivity but it can be assumed that intercalation of water molecules among the core shell particles takes place. Greater interparticle distances lead to a decrease in the probability of charge carrier transport and, consequently, to an electric current decrease, i.e., increase of impedance and resistance.

The weak dependence of R_p on RH suggests that polarons (electronic charges) are responsible for the electrical conductivity. Note that the higher temperature of the ambient atmosphere, the higher is the amount of water at a fixed RH. Therefore, R_p increases with temperature, consistently with its dependence on RH and low activation energy of the conductivity. A different behaviour was observed for low conductive material CS3. Here the R_p values decrease upon increasing RH for all temperatures. This behaviour can be explained by the presence of ionic conductivity and increased dissociation of the ionic species.

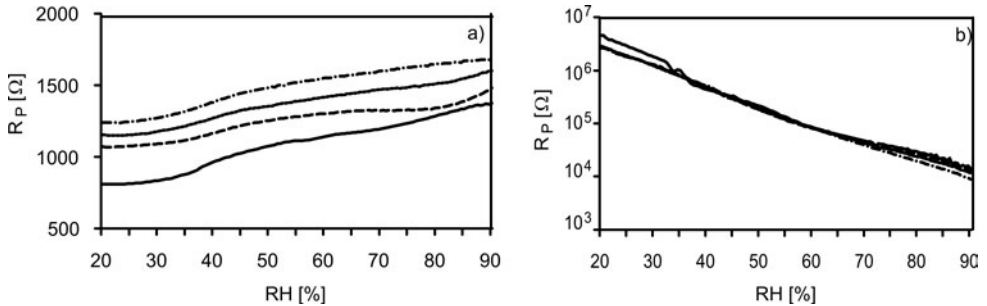


Fig. 5. Dependences of R_p of two core shell films on the relative humidity and temperature of the surrounding environment measured at ac frequency $f = 1$ kHz. Each graph shows measurement data at four various temperatures: 20 °C – full lines, 30 °C – dashed lines, 40 °C – dotted lines, and 50 °C – dash-and-dotted lines. Materials have substantially different response towards humidity change. Highly conductive CS6 (a) and low conductive CS3 (b)

In conclusion, we can say that both electronic and ionic conductivities participate in the charge carrier transport. In more conductive layers, polarons are mainly responsible for charge carrier transport. Polaron conductivity is strongly dependent on the distances among the particles – here water intercalation plays an important role. Ionic conductivity is lower due to lower charge carrier mobility. The electrical characteristics of less conductive films are typical for ionic conductors. The electronic (polaronic) conductivity is low and ionic transport prevails. The typical decrease of impedance with increasing humidity supports this idea. Charge dissociation plays an important role in this case.

Dependence of the ac conductance G on frequency f can be expressed with the following empirical equation, the so-called Jonscher expressions [16]:

$$G'(f) = G_0 \left(1 + \left(\frac{f}{f_0} \right)^\alpha \right) \quad (4)$$

where G_0 is the frequency independent part of the conductance, f_0 is a constant and $0 > \alpha > 1$ is a fractional exponent dependent on the transport mechanism. Figure 6 shows that the frequency dependent parts of the sample conductance, measured in a broad range of RH values (at room temperature), can be superimposed onto a master

curve (this is not valid for high relative humidity, 96 %, where water condensation can take place).

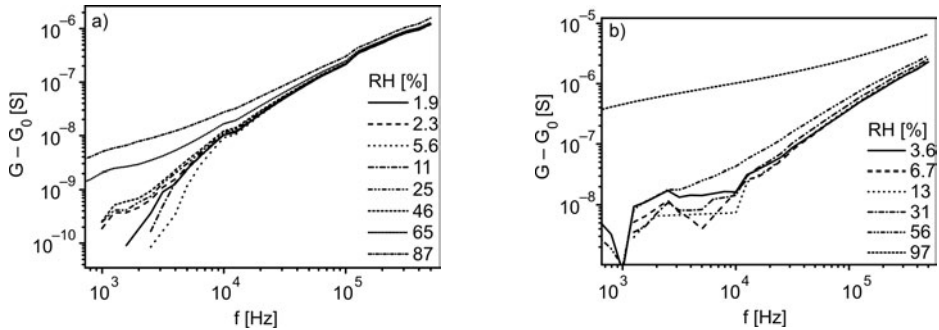


Fig. 6. Frequency dependences of corrected ac conductances in various levels of humidity in two materials having similar values of conductances: core shell CS5 (a) and microgel MG6 (b).

In the humidities around 90% RH, the humidity caused some condensation of water on the sample surfaces, changing their morphology

From these dependences we could estimate that the power law parameter α in Eq. (4) is close to 1. This supports the idea that polaron hopping plays an important role in charge carrier transport in materials with low resistivity in a broad range of relative humidity conditions.

4. Conclusions

Core shell composite particle systems exhibit the anti-Meyer–Neldel rule behaviour. This leads us to the conclusion that these systems have a common charge transport mechanism in vacuum. Microgel composites, on the other hand, do not show the simple Arrhenius behaviour in the investigated temperature range, possibly due to the morphology transition of their insulating polymer component.

Investigation of the influence of humidity on the electrical conduction in thin films of the composite particles has shown that there is a correlation between the material resistivity and the responsiveness of the material to humidity. The high resistivity materials exhibit decrease of their resistivities upon transition from dry to humid nitrogen atmosphere. This was attributed to the increase in ionic conductivity, due to the charge dissociation induced by adsorbed water molecules. The resistivities of the low resistivity materials increase when exposed to humidity. This could be explained by water intercalation among the grains of conducting polymer (PEDOT) thus weakening their electrical contacts. The frequency dependences of ac conductance in various levels of humidity show that there is practically no departure from the pure electron hopping transport mechanism, except in the highest humidities, where a strong water vapour condensation on the sample is expected.

Acknowledgements

This work was supported by the Ministry of Education, Youth and Sports of the Czech Republic (grant No. 1041/2006-32, COST) and by the Deutsche Forschungsgemeinschaft (DFG, research project SFB 287 *Reactive Polymers*).

References

- [1] SHIRAKAWA H., *Angew. Chem.*, 113 (2001), 2642.
- [2] MACDIARMID A.G., *Angew. Chem.*, 113 (2001), 2649.
- [3] HEEGER A.J., *Angew. Chem.*, 113 (2001), 2660.
- [4] WEI Z., XU J., HOU J., ZHOU W., PU S., *J. Mater. Sci.*, 41 (2006), 3923.
- [5] OUYANG J., CHU C.-W., CHEN F.-C., XU Q., YANG Y., *Adv. Funct. Mater.*, 15 (2005), 203.
- [6] ERDEN A., SAHIN E., GÜLLÜ M., TOPPARE L., *Eur. Polym. J.*, 42 (2006), 1866.
- [7] HENDERSON J.A.M., SAUNDERS J.M., MRKIC J., KENT P., GORE J., SAUNDERS B.R., *J. Mater. Chem.*, 11 (2001), 3037.
- [8] HAIN J., PICH A., ADLER H.-J., RAIS D., NEŠPŮREK S., *Macromol. Symp.*, 288 (2008), 61.
- [9] MEYER W., NELDEL H., *Z. Tech. Phys.*, 18 (1937), 588.
- [10] RAM S.K., KUMAR S., ROCA I CABARROCAS P., *J. Non-Cryst. Solids*, 354 (2008), 2263.
- [11] ABTEW T.A., ZHANG M., PAN Y., DRABOLD D.A., *J. Non-Cryst. Solids*, 354 (2008), 2909.
- [12] MEIJER E.J., MATTERS M., HERWIG P.T., DE LEEUW D.M., KLAPWIJK T.M., *Appl. Phys. Lett.*, 76 (2000), 3433.
- [13] LUCOVSKY G., OVERHOF H., *J. Non-Cryst. Solids*, 164–166 (1993), 973.
- [14] WIDENHORN R., REST A., BODEGOM E., *J. Appl. Phys.*, 91 (2002), 6524.
- [15] BOYKO V., LU Y., RICHTER S., ARNDT K.-F., PICH A., ADLER H.-J., *Polymer*, 44 (2003), 7821.
- [16] JONSCHER A.K., *Dielectric Relaxation in Solids*, Chelsea Dielectric Press, London, 1983.

Received 25 September 2008

Revised 3 March 2009

Electronic and gas sensing properties of soluble phthalocyanines*

S. POCHEKAILOV^{1,2**}, D. RAIS¹, S. NEŠPŮREK^{1,2}, J. RAKUŠAN³, M. KARÁSKOVÁ³

¹Institute of Macromolecular Chemistry AS CR, v. v. i., Heyrovský Sq. 2, 162 06 Prague 6, Czech Republic

²Faculty of Chemistry, Brno University of Technology, Purkyňova 118, 612 00 Brno, Czech Republic

³Research Institute for Organic Syntheses, Rybitví 296, 532 18 Pardubice, Czech Republic

Some optical and electrical properties of 3-diethylamino-1-propylsulfonamide substituted zinc and metal-free phthalocyanines are presented. These materials are sensitive to NO₂ even at concentrations as low as 0.1–2.5 ppm. Electrical conductivity and photoconductivity were used as the detection methods.

Key words: *substituted phthalocyanine; nitrogen dioxide sensor; optical properties; photoconductivity*

1. Introduction

Phthalocyanines (Pcs) are organic molecules consisting of a planar π -conjugated skeleton with a metal or two hydrogen atoms at the centre. They are solid under usual conditions, stable (up to 400 °C) organic semiconductors, used in many electronic and photonic applications, like photodetectors, gas sensors, transistors, solar cells, non-linear optical media, etc. [1]. Pcs are coloured, absorbing light mainly in two regions, 250–350 nm (Soret band) and 600–700 nm (Q-band) [2–4]; therefore, visible light can be used for photoelectronic applications [5]. Phthalocyanines have already been proposed as active layers for NO₂ detection. The majority of authors studied copper phthalocyanine sensitivity under various conditions. Cadmium, cobalt, aluminium [6, 7], plumbum [8] and lanthanide phthalocyanines [9] were also studied as NO₂ sensors. There is little information available about the use of Zn and metal-free Pcs for NO₂ sensor application.

*The paper presented at the 11th International Conference on Electrical and Related Properties of Organic Solids (ERPOS-11), July 13–17, 2008, Piechowice, Poland.

**Corresponding author, e-mail: sergey@imcm.cas.cz

Very often the method of vacuum evaporation is used for Pc thin film preparation. For non-soluble Pcs, vacuum evaporation seems to be one of the simplest methods for the deposition of homogeneous thin films of controlled thicknesses. This method has some shortcomings, among others the high cost for industrial applications. When exposed to NO_2 , the conductivity of such vacuum evaporated thin films increases. It is hard to compare absolute values of the increase, as presented by various authors, because of different deposition conditions, temperature, etc. Generally, according to the literature, responses are slow and not easily reproducible. The reverse part of the kinetic process is very often longer than 3 h [10, 11]. The increase in temperature improves the reversibility. Usually temperatures between 150 and 200 °C are necessary. However, this limits the application possibilities of the sensor.

Several approaches such as use of modified sample substrates have been applied to improve the sensor reaction speed and recovery, as well as to simplify the deposition conditions. The use of porous silicon with pores filled with Pc reduces the recovery time to 10 min [6], while the sensitivity to NO_2 remains the same. Another approach is to use substituted Pc as a sensing layer. These Pcs are often soluble, which makes it possible to use cold wet technologies for layer deposition, like spin coating, dipping, drop-casting and ink-jet printing. Although electronic properties of non-soluble phthalocyanines have been very well established, only limited information about substituted soluble derivatives is available. In this paper, we present some optical, photoelectrical and gas sensing properties of two soluble phthalocyanines, viz. 3-diethylamino-1-propylsulphonamide-Zn-phthalocyanine (ZnPcSu) and its metal-free (H_2PcSu) analogue. Sulfonamide substituent acts as a relatively strong electron acceptor; thus, a semiconductor of n-type is available [12]. Optical and electrical gas detection is discussed in the paper. In this paper, the terms “optical gas detection” and “electrical gas detection” mean the change of optical properties and electrical properties of the material under the influence of the studied gas, respectively.

2. Experimental

2.1. Materials

Two 3-diethylamino-1-propylsulphonamide substituted phthalocyanines were studied in this work: one with a Zn atom and the other with two hydrogen atoms at the centre of the Pc skeleton.

Synthesis of metal-free phthalocyanine (H_2Pc). Metal free phthalocyanine was prepared according to the US Pat. 3.297712. 300 g of 1,2-dicyanobenzene was suspended in 270 g of quinoline and subsequently heated under a hydrogen blanket in an autoclave (volume 2000 cm^3 , pressure 10 MPa, temperature 200 °C) for 8 h. After the reaction had been completed, the dark blue suspension was taken out from the autoclave and filtered.

The filtered cake was thoroughly washed with acetone and dried until a constant weight had been achieved. This way, 106,4 g of dark blue product was obtained.

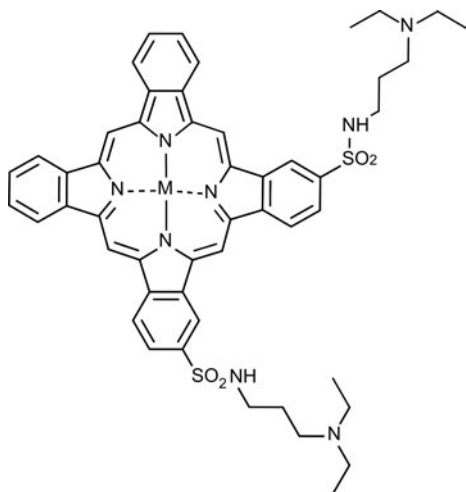
Synthesis of metal-free phthalocyanine sulfochloride. 10 g of H₂Pc was dissolved in 56 g of chlorosulfonic acid and heated in a 500 cm³ Keller flask, equipped with an agitator, thermometer, dropping funnel and reflux cooler, at the temperature of 100 °C for 30 min. The reaction mixture was cooled down to a temperature of 85 °C by agitating and subsequently 14.5 g of thionyl chloride was gradually added with a dropping funnel into the reaction mixture at the temperature between 80 and 85 °C. When thionyl chloride was charged, the reaction mixture was heated for 2 h at 100 °C. The reaction mixture was cooled down by agitating to the laboratory temperature and gradually added into the agitated mixture of 1000 g ice and 1500 cm³ water. Precipitated H₂Pc sulfochloride was filtered and washed with ice-water until the analytical test with BaCl₂ solution on sulfate anion was negative. 62 g of wet H₂Pc sulfochloride filter cake was obtained. Small sample, ca. 10 g of the wet filter cake, was dispersed in methanol, filtered, washed with methanol, filtered and dried. The hydrolysable chlorine content was determined by argentometric titration, after alkaline hydrolysis of the dry sample. The content of hydrolysable chlorine was found to be 11.2%. The average number of SO₂Cl groups on each H₂Pc molecule was 2.2. The rest of wet filter cake was kept in a freezer box at -18 °C.

Synthesis of metal-free phthalocyanine sulfonamide (H₂PcSu). 52 g of the frozen filter cake of H₂Pc sulfochloride was crushed and fully dispersed by agitation in 26 cm³ of water. The temperature of the mixture was 3 °C. After H₂Pc sulfochloride had been fully dispersed, 10 g of N,N-diethyl-1,3-propanediamine was added into the dispersion at once. The temperature of the mixture immediately reached 16 °C. The mixture was then subsequently agitated at 60 °C for 6 h. The reaction mixture was then filtered and the filter cake of sulfonamide was thoroughly washed with water and dried until a constant weight of 4.5 g of dry product had been obtained.

Synthesis of zinc phthalocyanine (ZnPc). 43 g 1,2-dicyanobenzene, 15.6 g anhydrous zinc chloride, 45 cm³ ethanol and 25 cm³ ethanolic solution of sodium ethanolate (0.01 g of Na per cm³) were placed in a 500 cm³ flask equipped with an agitator, thermometer, dropping funnel and a cooler. The mixture was agitated and heated in order to remove ethanol by distillation. Ethanol was gradually changed for 1-octanol, which was gradually added into the mixture through a dropping funnel. The reaction mixture was agitated at 175 °C for 3 h. Then the mixture was cooled down to 110 °C, the distillation cooler was changed for the reflux cooler and 250 cm³ of ethanol was added into the reaction mixture through the dropping funnel. The dark blue product was isolated by filtration, thoroughly washed with ethanol, water and dried to a constant weight. 36.4 g of zinc phthalocyanine was obtained this way. Its purity was 95.5 %, as estimated from the quantity of Zn, which was found to be 10.8 %.

Synthesis of zinc phthalocyanine sulfochloride. 20 g of ZnPc was dissolved in 112 g of chlorosulfonic acid and heated in 500 cm³ Keller flask, equipped with an agitator, thermometer, dropping funnel and reflux cooler, at 100 °C for 30 min. The reaction mixture was cooled by agitation to 85 °C and subsequently 20 g of thionyl chloride was gradually added through a dropping funnel into the reaction mixture at the temperature between 80 °C and 85 °C. After all the thionyl chloride had been used, the reaction mixture was heated for 2 h at 100 °C. The reaction mixture was then cooled by agitation to room temperature and gradually added into the agitated mixture of 1000 g ice and 1500 cm³ water. The precipitated ZnPc sulfochloride was filtered and washed with ice-water until the analytical test with BaCl₂ solution on sulfate anion was negative. 80 g of wet ZnPc sulfochloride filter cake was obtained. A small sample, ca. 10 g of wet filter cake, was dispersed in methanol, filtered, washed with methanol, filtered and dried. The hydrolysable chlorine content was determined by the argentometric titration, after alkaline hydrolysis of the dry sample. The content of hydrolysable chlorine was found to be 8.1 %. The average number of SO₂Cl groups on each ZnPc molecule was 1.5. The rest of the wet filter cake was kept in a freezer box at -18 °C.

Synthesis of zinc phthalocyanine sulfonamide (ZnPcSu). 70 g of frozen filter cake of ZnPc sulfochloride was crushed and fully dispersed by agitation in 40 cm³ of water. The temperature of the mixture was 3 °C. After the ZnPc sulfochloride had fully dispersed, 20 g of N,N-diethyl-1,3-propanediamine was charged into the dispersion at once. The temperature of the mixture immediately reached 28 °C. The mixture was then subsequently agitated at 60 °C for 6 h. The reaction mixture was then filtered and the filter cake of sulfonamide was thoroughly washed with water. The washed filter cake was dried until a constant weight had been achieved. 16 g of dry product was obtained. The chemical structures of Pcs under study are shown in Scheme 1.



Scheme 1. Structural formula of phthalocyanines under study. M = 2H or Zn

2.2. Samples

Samples with various structures were used in the experiments. UV-grade fused silica glass substrates were used for optical transmittance measurements. Samples for optical gas detection in transmittance mode were prepared using UV-grade fused silica spectroscopic cuvettes (Fig. 1).

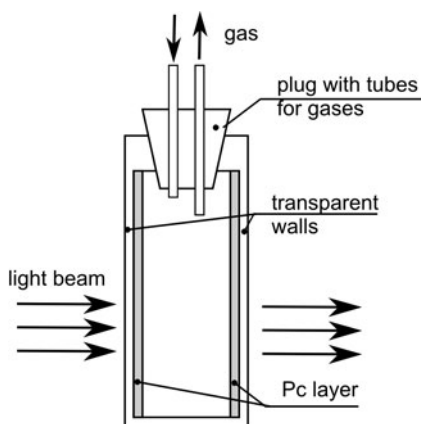


Fig. 1. Modified cuvette with Pc layer for optical gas sensitivity measurements

Thin films of Pcs were deposited on the inner sides of the cuvette from the solution by drop-casting. After drying, the cuvette was closed with a modified plug containing thin tubes for gas supply and gas extraction. The atmosphere inside the cuvette was controlled by the gas flowing through these tubes. The design of the cuvette allowed the measurements of optical spectra during the exposure of the samples to the analyte gas. For the electrical and photoelectrical measurements, ceramic substrates with interdigital gold electrodes were used. Pcs were deposited over the electrodes. The distance between electrodes was 30 μm . A schematic diagram of the substrates used in this study is shown in Fig. 2.

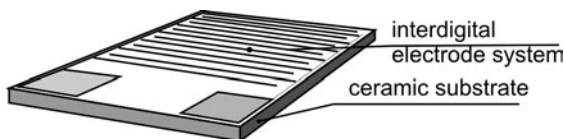


Fig. 2. Substrate with interdigital electrode system for electrical and gas sensitivity measurements

Substrates made of fused silica glasses were washed in hot peroxysulfuric acid for 15 min, then rinsed thoroughly with distilled water and dried. Ceramic substrates were cleaned in isopropanol vapours for 10 min and then dried. Thin films were deposited

by the spin-coating technique and by drop-casting from chloroform solution onto freshly cleaned substrates. The films were homogeneous; their thicknesses were approximately 20–30 nm. The thicknesses of the films were measured using a Taylor–Hobson Talystep profilometer .

2.3. Measurements

Optical absorption spectra were measured using a Perkin-Elmer Lambda 950 UV-VIS-NIR spectrometer. IR spectra were recorded with a Perkin-Elmer Paragon 1000PC FTIR spectrometer using a single-bounce, attenuated total reflection method.

Electrical measurements were performed in a dc regime, using a Keithley 6517A electrometer. Red light emitting diode ($\lambda = 670$ nm) or quartz tungsten halogen lamp equipped with a Corner Stone monochromator from Lot Oriel Gruppe Europa were used for the sample illumination in photoconductivity studies.

The electrical response to gas exposure was tested in a 62.8 cm³ sample chamber, made of stainless steel (Fig. 3). Gas exposure was realized using a continuous flow of a carrier gas mixed with the analyte in a predefined proportion and at a constant flow rate. Atmospheric air was used as a carrier gas, a 100 ppm mixture of NO₂ with synthetic air was used as the analyte gas. The presence of oxygen in the mixture prevents the transformation of NO₂ to other nitrogen oxides N_xO_y.

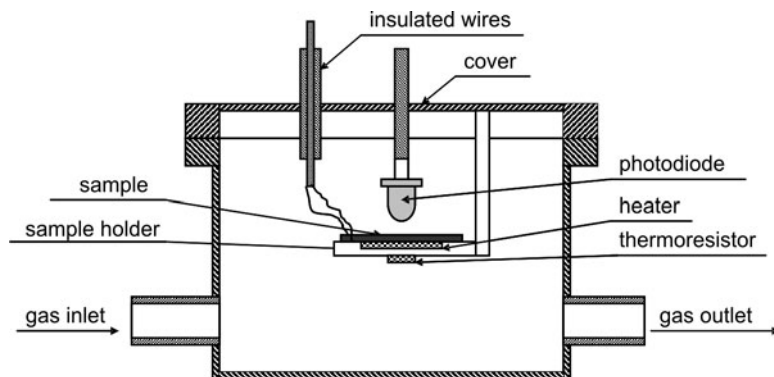


Fig. 3. Scheme of the chamber for gas sensing measurements

The amount of the gas passing through the sample chamber as well as the content of NO₂ were controlled by two gas mass flow controllers. Carrier gas flow was controlled using an Alicat Scientific MC 16 series flow controller, while the analyte gas flow was regulated by an Omega FMA3703 flow controller. Carrier and analyte gases were mixed and supplied to the sample chamber. All electrical gas sensing measurements were performed according to the following scenario: First, the chamber was purged with a pure carrier gas until the electrical current was stabilized. Then, the inflow of the mixture of a given concentration of NO₂ was applied for 50 min. After that

the sample was exposed to pure carrier gas for 50 min. The procedure was repeated for several NO₂ concentrations.

3. Results and discussion

3.1. Optical properties

Absorption spectra of ZnPcSu thin films (Fig. 4) are characterized by two main bands: the Soret or B-band with a maximum at 338 nm, and the Q-band with a maximum at 680 nm. The former band is related to d- π^* electronic transition, the latter one to π - π^* electronic transition of the phthalocyanine skeleton [13]. The spectrum of H₂PcSu thin film is also shown in Fig. 4 (curve 2). The character of the spectrum is similar to that of ZnPcSu. The Soret and Q-bands show maxima at 334 and 626 nm, respectively. Energy gaps E_g were determined from the low-energy onset of Q-band absorption in the $(h\nu\alpha)^2$ vs. $h\nu$ plot (α is the absorption coefficient, h is the Planck constant and ν is the wavenumber). For both Pcs, $E_g = 1.7$ eV. It is worth noting that the absorption coefficient of H₂PcSu is higher than that of ZnPcSu.

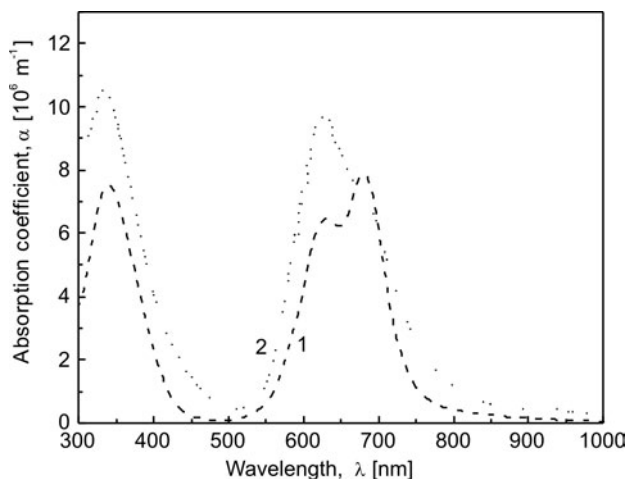


Fig. 4. Absorption spectra of ZnPcSu (curve 1) and H₂PcSu (curve 2) thin films

Infrared spectra of studied materials are shown in Fig. 5. The peaks at 3284 cm⁻¹ and 1016 cm⁻¹ (curve 2) can be assigned to central N-H stretching and bending vibrations, respectively. These bands are missing in the ZnPcSu spectrum (curve 1), which corresponds to the structural difference between ZnPcSu and H₂PcSu. All other peaks characteristic of non-substituted phthalocyanines [14, 15] are present in the spectra. There are unassigned peaks present in both spectra: 475(sh), 487(w), 500(w), 516(w), 552(m), 564(m), 576(sh), 611(w), 651(w), 661(sh), 720(vs), 807(m), 836(w), 849(w),

923(vw), 951(m), 1046(s), 1075(sh), 1137(s), 1185(m), 1254(s), 1387(s), 1451(s), 1653(w), 1714(w), 2549(m), 2806(m), 2965 cm^{-1} (s).

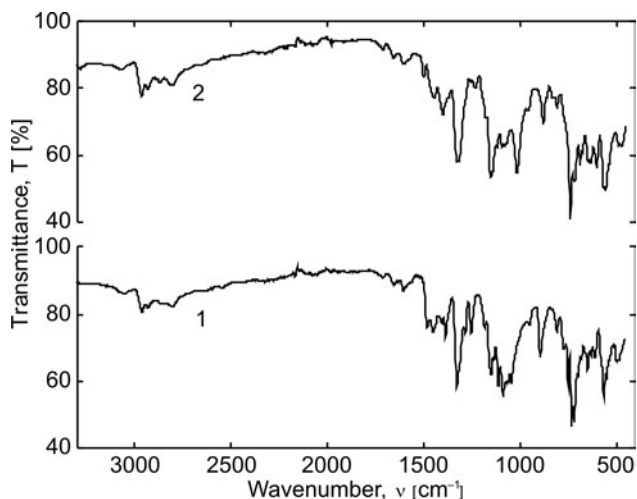


Fig. 5. Infrared spectra of ZnPcSu (curve 1) and H_2PcSu (curve 2)

3.2. Optical gas detection

We have found minor changes in the absorption spectrum of ZnPcSu during NO_2 exposure. The changes are presented in Fig. 6 in the form of the differential transmittance spectrum.

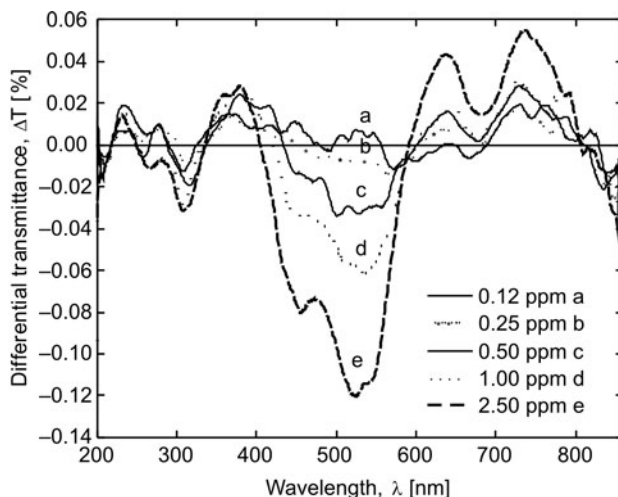


Fig. 6. Differential transmittance spectra of ZnPcSu thin film in the presence of NO_2 ; concentrations from 0.12 ppm to 2.50 ppm. The reference is the spectrum of neat ZnPcSu

The positive values in the picture correspond to increases in the transmittance, whereas negative values correspond to decreases in the transmittance upon exposure to NO_2 . The main changes are: the decrease in the absorption in the Q-band region, and the increase in the absorption around 500 nm. This increase of the absorption can be associated with an exciplex band. Some changes were also observed around 233, 307 and 380 nm, which is consistent with the reports of other authors [9, 16, 17].

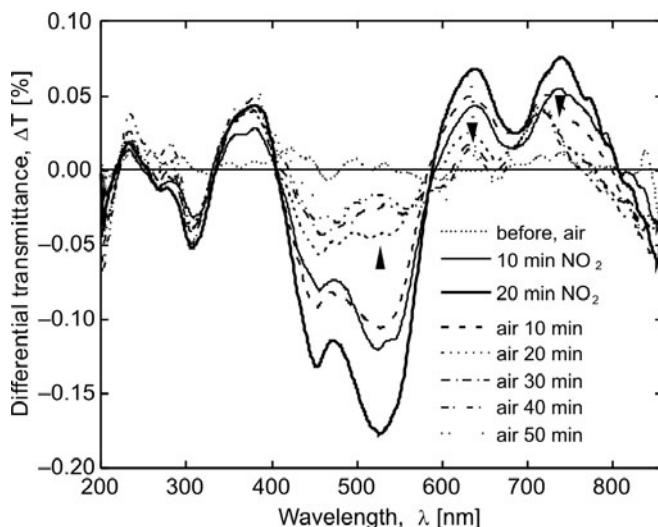


Fig. 7. Differential transmittance spectra of ZnPcSu after the NO_2 exposure (concentration 2.50 ppm, 10 and 20 min) and their relaxation on air

In order to investigate the reversibility of the changes described above, the cuvette previously filled with NO_2 mixture was purged with clean carrier gas for 1 h. During this time, the absorption spectra were measured at 10 min intervals (Fig. 7). It was found that the band in the region 400–600 nm almost disappeared after 1 h of purging (reversibility 92 %). The value of the Q-band differential transmittance also decreased, but the reversibility at 637 nm was only 85%.

There was no change in the absorption spectra of H_2PcSu under the NO_2 exposure.

3.3. Electrical properties

Dark current–voltage characteristics were ohmic for both the studied Pcs. The dark current of the ZnPcSu sample was 4 orders of magnitude lower than that of the H_2PcSu sample. The activation energy of the dark current, measured in the temperature range 15–80 °C, was 0.77 eV for both the phthalocyanines under study. These values are close to the halves of the energy gaps determined optically (see above), which suggests that there is practically no dopant present in the material.

Under illumination with monochromatic light at the maximum of photocurrent in the region of Q-band ($\lambda = 596$ nm for H_2PcSu and 598 nm for ZnPcSu , see Fig. 8), a strong current increase was observed; three orders of magnitude for ZnPcSu and 1.5 order of magnitude for H_2PcSu (photon flux $\phi = 0.76$ W/m^2). The spectrum of the photoelectrical response roughly followed the absorption spectrum (Fig. 8). The shift of the photoresponse maximum to the blue region, in the comparison with the absorption spectrum, could be caused by long-time processes (the spectra were recorded in the red to blue region).

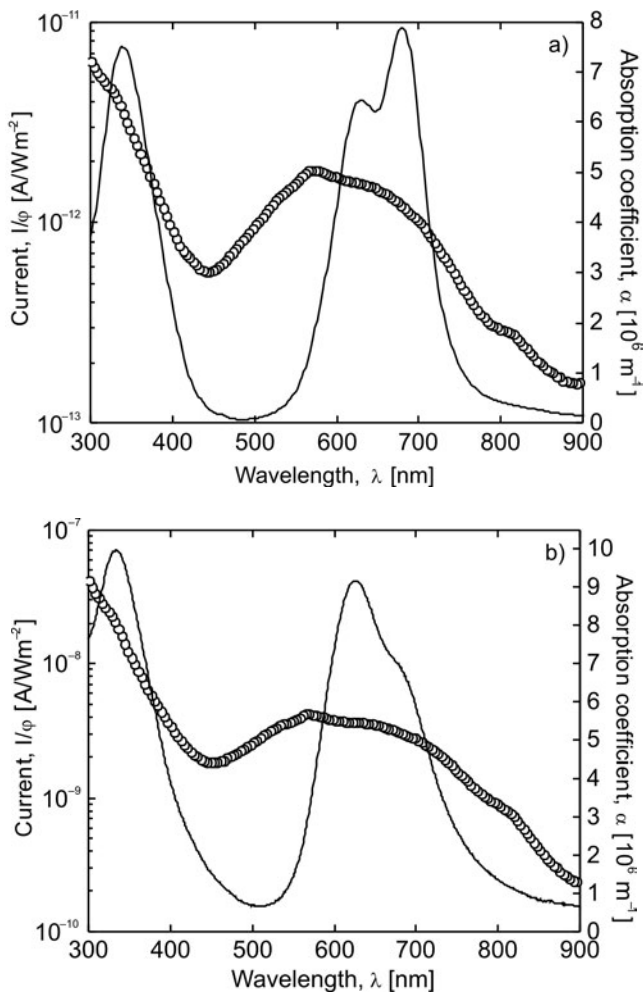


Fig. 8. Photoresponses and absorption spectra of thin films of phthalocyanines under study: a) spectra of ZnPcSu , b) spectra of H_2PcSu

The photocurrent kinetics showed a stable behaviour in the dark and under illumination (Fig. 9). Immediately after the sample illumination a quite fast current increase

was observed. However, the steady state conditions were not reached even after 30 min. After switching off the light, the current returned to the dark value after ca. 30 min for ZnPcSu and after a few hours for H₂PcSu.

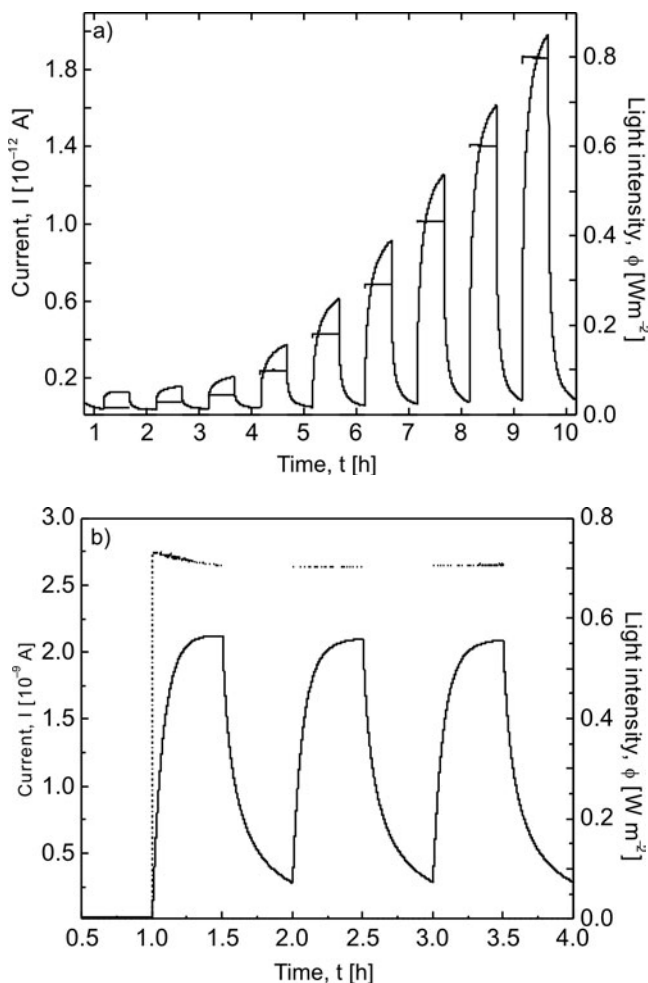


Fig. 9. Photocurrent kinetic of studied phthalocyanines: a) – ZnPcSu, b) – H₂PcSu. Light intensity scenario is plotted with thin curves, photoelectric response in thick ones

This behaviour seems to be unusual because the electrical conductivity of H₂PcSu is four orders of magnitude higher than that of ZnPcSu. One reason for this behaviour could be the formation of deep traps. This supposition is supported by the shape of the dependence of current I on the light intensity ϕ , which is of the type $I = \phi^n$, $n = 0.8$. This suggests the influence of traps on charge carrier transport. However, the shapes of long time kinetics do not show behaviour consistent with the space charge forma-

tion, i.e., the current decrease after the current saturation (see Fig. 9b). This behaviour, which is not important from the point of view of sensor design, needs additional study.

3.4. Electrical gas detection

Electrical sensitivity of ZnPcSu to NO₂ exposure is shown in Fig. 10. Electrical response could be detected even for concentrations of several hundred ppb at room temperature. At the concentration of 2.50 ppm, the dark current increase was already two orders of magnitude. The response consisted of a fast and a slow part. The signal did not reach saturation even after 40 min. However, the duration of the fast response could be estimated to be about 5 min. The characteristic time of the slow reverse process was much longer still. It explains the gradual increase of the current at the end of clean carrier gas exposure following each step of NO₂ exposure (shift of baseline). Under the NO₂ exposure, the photocurrent response shows behaviour similar to that of the dark current under the NO₂ exposure. However, the photocurrent sensitivity was significantly lower (see Fig. 10, curve 2).

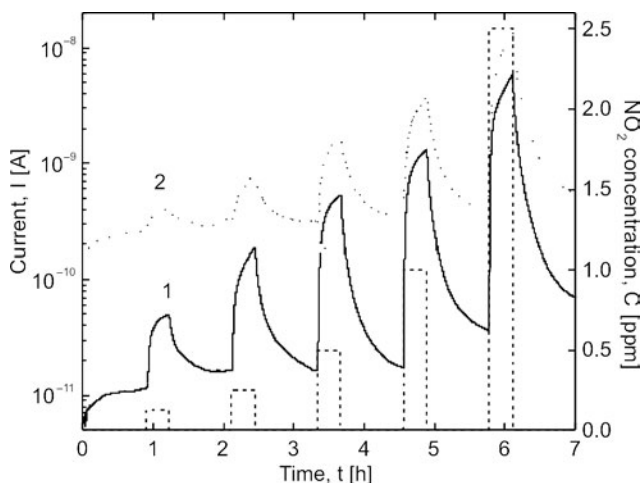


Fig. 10. Kinetics of the current of ZnPcSu thin film during NO₂ exposure of various concentrations: 1 – dark current, line 2 – photocurrent. The dashed line shows the scenario of the NO₂ exposure and concentration

A qualitatively different behaviour was found for H₂PcSu, investigated under the same conditions as ZnPcSu. Kinetic curves are shown in Fig. 11. The basic differences were: both dark and photocurrent response under the NO₂ exposure were opposite, i.e. the current decreased upon exposure to the gas. The dark current change was much smaller. The dark current responses were smaller at higher NO₂ concentrations. Conversely – with the sample under illumination, the photocurrent response during the NO₂ exposure was fast, the slow component was missing, and the response was fully

reversible. Photocurrent stabilization was achieved in about 15 min under the exposure to NO_2 , the reverse process was complete after about 15–20 min.

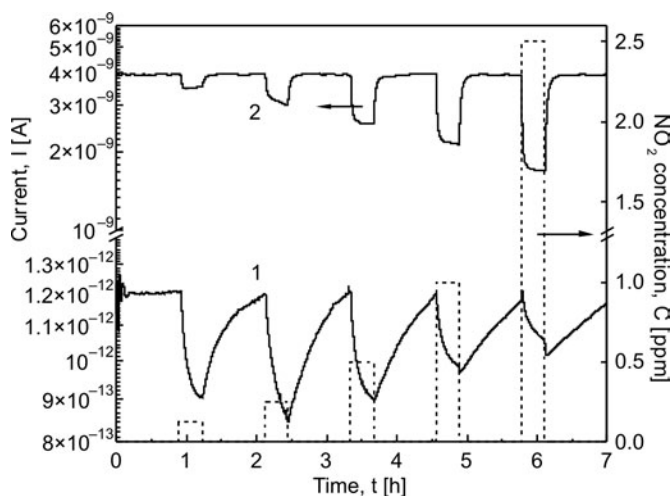


Fig. 11. Kinetics of the current change of H_2PcSu thin film during NO_2 exposure of various concentrations: 1 – dark current change, 2 – photocurrent change. The dashed lines show the history of the NO_2 exposure and its concentration

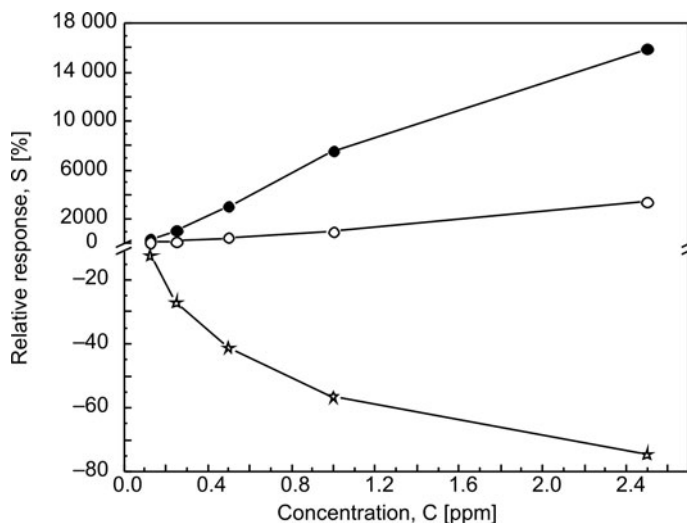


Fig. 12. Electrical sensitivity of ZnPcSu to NO_2 in the dark (filled dots), under illumination (empty dots), and of H_2PcSu to NO_2 under illumination (stars)

The comparison of the above described sensitivities to NO_2 for both investigated materials is shown in Fig. 12. The sensitivity curve of H_2PcSu in the dark has not been shown because of the instability of the response at higher NO_2 concentrations. The

response of H₂PcSu under illumination is quite stable and seems to be useful for practical applications. The relative response magnitude S here is defined as

$$S = \frac{R_{\text{exp}} - R_{\text{before}}}{R_{\text{before}}} \times 100 \quad [\%]$$

where R_{before} is the resistivity before the gas exposure, R_{exp} – resistivity during the exposure.

4. Conclusions

We have observed that sulfonamide substituted phthalocyanines have quite high absorption coefficients and photoconductivities. Photoconductivity relaxation is slow; it can be explained by charge carrier trapping in deep traps. The Pcs under study are prospective materials for NO₂ sensors, capable of operating even at room temperature. Transmittance optical spectroscopy can be also used as a detection method but responses are weak. The electrical response in the dark is higher but its reaction and recovery times are slow. This leads to the shift of the baseline between the successive exposures. This problem can be overcome by sample illumination during the detection. The photoelectrical responses of H₂PcSu thin films under the NO₂ exposure are stable, quite fast and fully reversible. The profiles of the current changes for H₂PcSu and ZnPcSu are completely different, which suggests different mechanisms of the sensitivity to NO₂.

Acknowledgements

This work was supported by the Grant Agency of the Academy of Sciences of the Czech Republic (grants No. KAN400720701 and KAN401770651).

References

- [1] FORREST S.R., *Nature*, 428 (2004), 911.
- [2] WALZER K., TOCCOLI T., PALLAORO A., VERUCCHI R., FRITZ T., LEO K., BOSCHETTI A., IANNOTTA S., *Surf. Sci.*, 573 (2004), 346.
- [3] POCHEKAILOV S., RAIS D., NEŠPŮREK S., RAKUŠAN J., KARÁSKOVÁ M., *J. Optoelect. Adv. Mat.*, 9 (2007), 479.
- [4] DJURIŠIĆ A.B., KWONG C.Y., LAU T.W., LIU Z.T., KWOK H.S., SZE L., LAM M., CHAN W.K., *Appl. Optics*, 42 (2003), 6382.
- [5] POCHEKAILOV S., NEŠPŮREK S., RAKUŠAN J., KARÁSKOVÁ M., *Mol. Cryst. Liq. Cryst.*, 468 (2007), 375.
- [6] CHAKANE S., GOKARNA A., BHORASKAR S., *Sensors Actuat. B*, 92 (2003), 1.
- [7] MALEYSSON C., BOUCHE-PILLON D., TOMAS O., BLANC J.P., DOGO S., GERMAIN J.P., PASSARD M., PAULY A., *Thin Solid Films*, 239 (1994), 161.
- [8] BOTT B., JONES T.A., *Sensors Actuat. B*, 5 (1984), 43.
- [9] DE SAJA J.A., RODRIGUEZ-MENDEZ M.L., *Adv. Colloid Interface Sci.*, 116 (2005), 1.

- [10] VIRICELLE J.P., PAULY A., MAZET L., BRUNET J., BOUVET M., VARENNE C., PIJOLAT C., *Mater. Sci. Eng. C*, 26 (2006), 186.
- [11] LEE Y.-L., CHANG C.-H., *Sensor Actuat. B*, 119 (2006), 174.
- [12] LIU G., KLEIN A., THISSEN A., JAEGERMANN W., *Surf. Sci.*, 37 (2003), 539.
- [13] BOHRER F.I., SHARONI A., COLESNIUC C., PARK J., SCHULLER I.K., KUMMEL A.C., TROGLER W.C., *J. Am. Chem. Soc.*, 129 (2007), 5640.
- [14] SEOUDI R., EL-BAHY G.S., EL SAYED Z.A., *J. Mol. Struct.*, 753 (2005), 119.
- [15] JIANG J., BAO M., RINTOUL L., ARNOLD D.P., *Coord. Chem. Rev.*, 250 (2006), 424.
- [16] BALDINI F., CAPOBIANCHI A., FALAI A., PENNESI G., *Sensor Actuat. B*, 51 (1998), 176.
- [17] BORTCHAGOVSKY E.G., KAZANTSEVA Z.I., KOSHETS I.A., NEŠPŮREK S., JASTRABIK L., *Thin Solid Films*, 460 (2004), 269.

Received 26 September 2008

Revised 29 March 2009

Modelling of charge carrier transport in conjugated polymers doped by polar additives*

P. TOMAN^{1**}, S. NEŠPŮREK^{1,2}, W. BARTKOWIAK³

¹Institute of Macromolecular Chemistry, Academy of Sciences of the Czech Republic, v.v.i.,
Heyrovský Sq. 2, 162 06 Prague 6, Czech Republic

²Faculty of Chemistry, Brno University of Technology,
Purkyňova 118, 612 00 Brno, Czech Republic

³Institute of Physical and Theoretical Chemistry, Wrocław University of Technology,
Wybrzeże Wyspiańskiego 27, 50-370 Wrocław, Poland

A theoretical model of the inter-chain charge carrier transport in poly[2-methoxy-5-(2'-ethylhexyloxy)-*p*-phenylene vinylene] doped with a photochromic polar additive is put forward. The model attributes to each polymer chain a set of charge states, in which charge carriers thermalize. These on-chain states are calculated by solving the Schrödinger equation with a tight binding Hamiltonian. The inter-chain transfer rates are determined using the Marcus formula. The model describes the effect of polar additives on charge carrier transport. The presence of the additives results in a decrease of charge mobility, because of the increase of the local energy disorder. A decrease of the inter-chain mobility by up to several orders of magnitude is found if the width of the local energy disorder is doubled. This finding confirms the possibility of constructing an optoelectrical switch based on a polymer doped with a photochromic polar additive.

Key words: *conjugated polymers; charge carrier transport; molecular electronics; Monte Carlo modeling*

1. Introduction

Inter-chain charge carrier transport in conjugated polymers is commonly considered as hopping within a geometrically and energetically disordered system. A classical model of charge transport in disordered organic solids was developed by Bäessler [1]. The model describes conjugated segments of the polymer chains as sites with Gaus-

*The paper presented at the 11th International Conference on Electrical and Related Properties of Organic Solids (ERPOS-11), July 13–17, 2008, Piechowice, Poland.

**Corresponding author, e-mail: toman@imc.cas.cz

sian distribution of energies reflecting an energy (diagonal) disorder. The jump rates among these sites are described by means of the Miller–Abrahams relation [2]. This relation is appropriate if the polaronic effects can be neglected but simultaneously the electron–phonon coupling is strong enough to ensure charge carrier thermalization. The inter-site coupling parameters are decomposed to site specific randomized ones. Consequently, the model considers a Gaussian geometric (off-diagonal) disorder with some correlation. The charge carrier motion is then solved numerically using a Monte Carlo simulation technique. A similar model was also used by Fishchuk et al. [3, 4] for an analytical solution of the charge carrier transport. If the polaronic effects cannot be neglected, it seems that the Marcus theory [5, 6] better describes the charge carrier transport.

The motivation of our paper is the verification of the idea to construct an optoelectrical switch based on a conjugated polymer doped with a polar photochromic additive, which significantly changes its dipole moment during its photochromic conversion. In our previous paper [7], we studied photoswitching of the on-chain hole transport in MEH–PPV doped with the photochromic additive 6-nitro-1',3',3'-trimethylspiro[2*H*-1-benzopyran-2,2'-indoline]. Upon irradiation with light of an appropriate wavelength, this molecule undergoes a ring opening reaction from the closed form (spiropyran (SP)) to the open form (merocyanine (MR)) [8]. A reversible $SP \longleftrightarrow MR$ transformation is accompanied by a charge redistribution, resulting in a significant increase in the dipole moment of the molecule. It was found that the introduction of polar species results in a broadening of the distribution of the local charge carrier site energies (local energy disorder), and consequently leads to a decrease in the on-chain hole mobility. The aim of this paper is to extend the model, taking into account the inter-chain charge carrier transport.

Unlike Bäessler and Fishchuk [1, 3, 4], we seek a more realistic description of the polymer charge carrier states participating in the transport. Charge carrier transport in conjugated polymers involves both the on-chain motion through the conjugated chain segments and hops either between two adjacent polymer chains or between two segments of a chain separated by a conjugation break. Thus, our model considers the conjugated polymer chains (or chain segments) as one-dimensional disordered rods, possessing many charge carrier states, instead of the point one state sites. The on-chain transfer integrals are randomized by the torsional disorder of the polymer chain. Simultaneously, the site energy disorder coming from the intermolecular interaction of the charge carrier with dispersed polar species is introduced. Thus, we separate the one-dimensional on-chain motion from the essentially two-dimensional inter-chain hopping, which is investigated in this paper. Since MEH–PPV is a hole-transporting material, only the hole transport is considered.

Although conjugated polymer repeat units can be treated as elementary localization sites possessing specific energies ε_n , their mutual interaction, resulting in energy level splitting, is typically stronger than the disorder of these site energies. While the on-chain transfer integrals between adjacent phenylene and vinylene units in MEH

–PPV are as high as 1.3 eV, the standard deviation $\sigma(\varepsilon_n)$ of the local site energy distribution can hardly exceed 0.4 eV, even in the case of a highly doped polymer. Moreover, due to the long-range character of the Coulombic interaction, adjacent site energies are highly correlated, and the difference of their values rarely exceeds 0.3 eV if these sites describe the repeat units of the same type. Consequently, the charge carrier states become delocalized on the conjugated chain segments. Such a system allows semi-coherent charge carrier motion, limited by the chain disorder. The segment charge carrier states can be described by a tight-binding Hamiltonian and calculated using a numerical solution of the Schrödinger equation.

The typical distance between repeat units located on different chains can be estimated from the envelope of the van der Waals atomic spheres to be about 7 to 10 Å in MEH–PPV. Thus, the inter-chain transfer integrals are several orders of magnitude smaller than the on-chain ones. For this reason, the charge carrier transport occurs mainly by hopping between states localized on the conjugated segments. The charge carrier thermalization, which occurs typically in times of several picoseconds, leads to a complete decoherence of the charge motion between any subsequent hops. Therefore, unlike the on-chain transport, it is appropriate to describe the inter-chain transport by means of quasi-classical master equations. Because the MEH–PPV conformation is rather soft, the presence of any additional charge carrier on the chain segment leads to the conformation distortion and polaron formation. For this reason, the inter-chain hopping is studied using Marcus charge transfer theory [5, 6]. Because the inter-chain transport is much slower than the on-chain motion, the slow inter-chain motion acts as a bottleneck determining the macroscopic charge carrier mobility, if the frequency of the external electric field is not too high.

2. Charge states

2.1. Model

The conjugated polymer chain segments are modelled as sequences of N sites corresponding to the repeat units, alternating phenylenes and vinylenes. The hole states on such a chain can be described within the tight-binding approximation by the Hamiltonian

$$H = \sum_{n=1}^N \left[\varepsilon_n a_n^+ a_n - b_{n,n+1} (a_{n+1}^+ a_n + a_n^+ a_{n+1}) \right] \quad (1)$$

where a_n and a_n^+ are the annihilation and creation operators for a hole located at the n -th site, ε_n is the energy of this hole, and $b_{n,n+1}$ is the on-chain transfer integral between the sites n and $n+1$. The distribution of transfer integrals $b_{n,n+1}$ is calculated according to the model of Grozema et al. [9].

In the absence of a polar additive, the site energies ε_n are essentially equal to the ionization potentials of the isolated polymer repeat units and can be calculated using standard quantum chemical methods. For materials doped by polar species, it was found that within the frozen orbital approximation, the local site energies are given by the formula [10]

$$\varepsilon_n = \varepsilon_n^{(0)} + \langle \text{HOMO} | \sum_i \Delta\varphi_i | \text{HOMO} \rangle \quad (2)$$

where $\varepsilon_n^{(0)}$ is the site energy of an isolated repeat unit and $\Delta\varphi_i$ are the electrostatic potentials describing the charge–dipole interactions of a hole located at the highest occupied molecular orbital |HOMO> of this unit with all surrounding polar species. Note that the |HOMO> orbitals are located on the phenylenes and vinylenes forming the main polymer chain, and not on their aliphatic substituents. Since the sizes of individual repeat units as well as additive molecules are much smaller than the distance of the additive molecules from the main chain, it is possible to treat them as points. Because the positions and orientations of the additive molecules with respect to the polymer chain are essentially random, their common effect results in the broadening of the distribution of local site energies ε_n . The most important parameter of this distribution is its half-width, proportional to the standard deviation $\sigma(\varepsilon_n)$ of the site energies from its average value. It should be remarked that we define $\sigma(\varepsilon_n)$ as just the standard deviation of the distribution of the second term on the right side of Eq. (2), regardless of the different values $\varepsilon_n^{(0)}$ of phenylenes and vinylenes. Another very important characteristic of this distribution, influencing the charge transport, is the site to site energy correlation, which effectively reduces $\sigma(\varepsilon_n)$. There is a strong correlation between sites that are no more than about ten sites apart from each other. This fact can be explained by the long-range character of the charge–dipole interactions. It was shown in our previous paper [7] that the additive photochromic reaction SP \longleftrightarrow MR is accompanied by a significant change in the dipole moment resulting in ca. twofold change in the standard deviation $\sigma(\varepsilon_n)$ of the polymer chain local site energies.

Using the Hamiltonian (1) with the molecular parameters ε_n and $b_{n,n+1}$ and taking the stationary states $|\varphi_i\rangle$ as superpositions of states $|n\rangle$ located at individual sites

$$|\varphi_i\rangle = \sum_{n=1}^N c_{i,n} |n\rangle \quad (3)$$

the time-independent Schrödinger equation can be solved

$$H|\varphi_i\rangle = E_i|\varphi_i\rangle \quad (4)$$

This approach leads to the same time evolution of the wave function

$$|\psi(t)\rangle = \sum_{i=1}^N k_i e^{-iE_i t/\hbar} |\varphi_i\rangle \quad (5)$$

where the time-independent coefficients k_i can be found from the initial conditions, as an alternative approach based on the direct numerical integration of the time-dependent Schrödinger equation, performed in our previous paper [7]. However, the solution of the eigenstate problem provides also the charge carrier states $|\phi_i\rangle$ and their energies E_i .

2.2. Results and discussion

The on-chain hole states were calculated for polymer chains (conjugated segments) consisting of 180 phenylene vinylene units, i.e. $N = 360$ centres. This length was suggested by Grozema et al. [9] as an effective conjugation length, at which the calculated on-chain hole mobility reproduces the experimental mobility measured for MEH-PPV by the microwave technique.

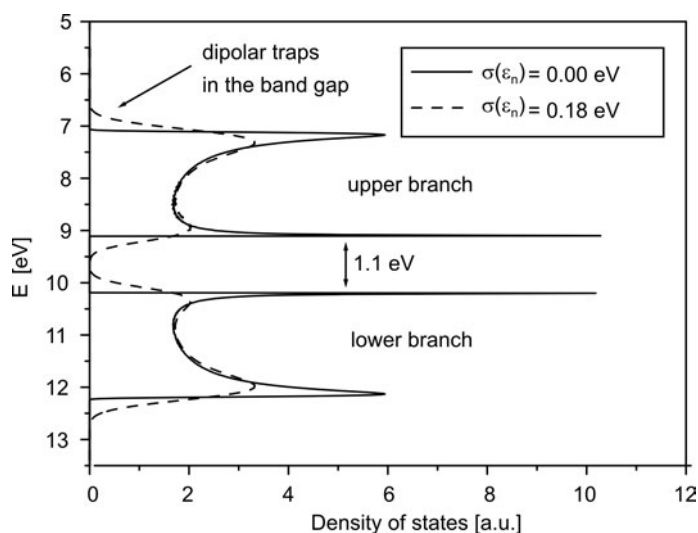


Fig. 1. Diagram of the MEH-PPV valence band consisting of two branches. The value of the local energy disorder is indicated by the standard deviation $\sigma(\epsilon)$. Solid lines corresponds to the pristine polymer, dashed lines to the polymer doped with a polar additive

Figure 1 shows a diagram of the valence band of the pristine and doped polymer. The valence band of the pristine polymer is split into two branches, which correspond to two types of repeat units, phenylenes and vinylenes, in the main chain. The 1.1 eV gap between these two branches is equal to the difference between phenylene and vinylene ionization potentials (local site energies ϵ_n). An increasing local energy disorder $\sigma(\epsilon_n)$ leads to the broadening of the originally sharp valence band edge and formation of the tail states in the gap. These states, owing to their relatively low density and consequently weak connectivity, behave as shallow hole traps. Furthermore, the

valence states in the doped polymer are less delocalized along the polymer chain than the states in the pristine polymer, which limits inter-chain hopping.

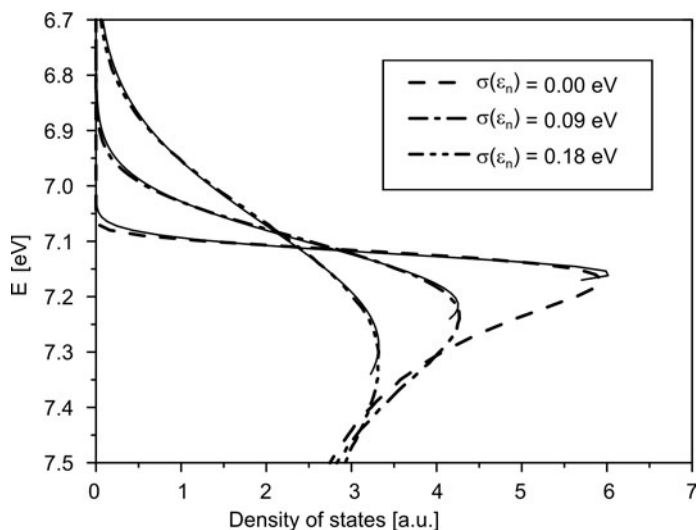


Fig. 2. Detailed drawing of the band edge for various values of the local site energy disorder $\sigma(\epsilon)$. Solid lines show the fitting of the band edge slope by a Gaussian curve

Figure 2 displays a detailed drawing of the band edge region for various local energy disorders $\sigma(\epsilon_n) = 0.00, 0.09, \text{ and } 0.18 \text{ eV}$. Tiny lines show that the band edge slope can be well fitted by a Gaussian curve. The fitted standard deviations $\sigma(E_i)$ of hole state energies E_i are listed in Table 1. Note that due to the transfer integral disorder there is also a small non-zero standard deviation $\sigma(E_i)$ of hole state energies for the pristine polymer, which possesses no local energy disorder ($\sigma(\epsilon_n) = 0$).

Table 1. Centres E_{\max} of the peaks and standard deviations $\sigma(E_i)$ of the Gaussian fits of the density of states on the valence band edge slope calculated for various values of the local site energy disorder $\sigma(\epsilon_n)$ at 293 K. All values are given in eV

$\sigma(\epsilon_n)$	E_{\max}	$\sigma(E_i)$
0.000	7.158	0.034
0.045	7.179	0.061
0.090	7.216	0.110
0.135	7.250	0.161
0.180	7.289	0.215

It should be pointed out that our model takes into account only the highest molecular orbitals (HOMO) of individual repeat units. Thus, the band diagram of a real polymer should consist of more mutually overlapped bands. However, only the charge carrier states near the valence band edge can participate in charge carrier transport.

Since the transfer integrals between lower orbitals of phenylene and vinylene are much smaller than the transfer integrals between HOMOs, lower orbitals do not contribute to the density of states near the band edge. Hence, for our purpose it is sufficient to calculate only the highest occupied band.

3. Charge carrier transport

3.1. Model

The description of the charge carrier transport in polymers is complicated, due to the absence of any well-ordered crystal structure typical of molecular single crystals and crystalline inorganic semiconductors. Our inter-chain hopping model assumes a simplified three-dimensional polymer structure, schematically depicted in Fig. 3.

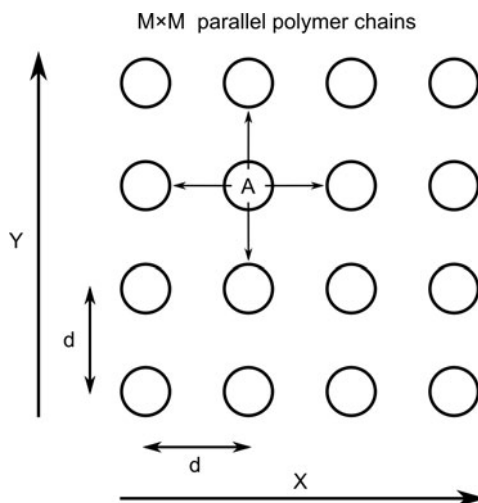


Fig. 3. Simplified polymer chain alignment considered in the inter-chain hole mobility modelling. The possible charge carrier hops from a given chain A are denoted by arrows

The polymer chains of a given length N form a regular, equidistant matrix. Additive molecules, which are not shown in the figure, are placed randomly among them. While the on-chain motion proceeds in a one-dimensional space, the inter-chain hopping takes place in the two remaining perpendicular directions X and Y . The geometric (off-diagonal) disorder is introduced by the Gaussian distribution of the transfer integrals $J_{\alpha\beta}$ between the corresponding repeat units of adjacent chains (see Fig. 4). The distribution is centred at zero and its standard deviation is $\sigma(J_{\alpha\beta}) = 10^{-3}$ eV. This value, which just acts as a multiplication factor in the Marcus equation, was set to reproduce the experimental mobility of the pristine MEH-PPV (ca. 10^{-5} cm²/(V·s) [11]) at room temperature. We believe that the shape of the transfer integral distribution has no signifi-

cant influence on the results. Each polymer chain possesses disorder in local energies ε_n and on-chain transfer integrals $b_{n,n+1}$ resulting in a unique set of the on-chain charge carrier states, i.e. hole energies E_i and expansion coefficients $c_{i,\alpha}$ (see Eq. 3). No correlation among chains is assumed.

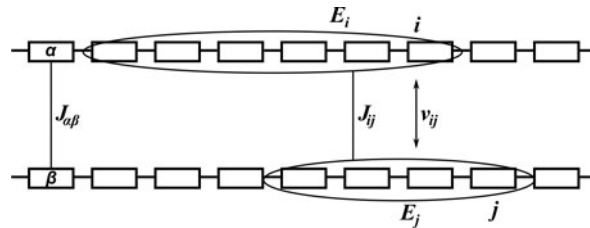


Fig. 4. Two adjacent polymer chains A and B . Letters α and β denote repeating units, i and j are the on-chain hole states

The model considers full charge carrier thermalization over all states of the given chain A between two subsequent hops. Hence, the charge carrier transport consists of the following steps: hole movement to any possible state on the chain A , thermalization of the hole over all its possible states on the chain A , and finally a hop of the hole to any possible state on one of the nearest neighbouring chains B . The more distant hops can be safely omitted due to the negligibly small transfer integrals.

Although fermions generally follow the Fermi–Dirac statistic, under usual experimental conditions it is very improbable that there is more than one free charge carrier on a given conjugated segment. Thus, in the case of one-particle approximation, the position of the Fermi level is not important and a simpler Boltzmann distribution can be used. Hence, if the hole hops to a given chain A , the occupation probability of its state i at temperature T will be

$$p_i(E_i) = \frac{\exp\left(\frac{-E_i}{kT}\right)}{Z(T)} \quad (6)$$

where E_i is the energy of state i , and $Z(T)$ is the partition function over all states of the chain A .

MEH–PPV chain conformation is relatively soft and undergoes a significant deformation (polaron formation) in the presence of an additive charge. For this reason, using the Marcus concept is more appropriate than using the Miller–Abrahams formula. Hence, the rate of hole hopping between an initial state i with the energy E_i on the chain A and a final state j with the energy E_j on an adjacent chain B can be calculated as [6]

$$v_{i \rightarrow j} = \frac{J_{ij}^2}{\hbar} \sqrt{\frac{\pi}{\lambda_j kT}} \exp\left(\frac{-(E_i - E_j - \lambda_j)^2}{4\lambda_j kT}\right) \quad (7)$$

where λ_{ij} is the charge carrier reorganization energy and J_{ij} is the effective charge transfer integral.

The reorganization energy λ_{ij} can be separated into an inner (molecular) and an outer (solvent) part. The solvent reorganization energy is often important in solutions [12]. On the other hand, in the solid state environment the phonon-like modes are sufficiently stiff that local vibronic coupling should dominate [13]. Thus, only the inner reorganization energy is considered. It can be calculated, in principle, using standard quantum chemical methods. However, such a calculation takes too much cpu time to be repeated many thousands times for all considered Monte Carlo realizations of the chain disorder. Therefore, we have roughly estimated its value, from the calculations of short regular oligomers, to be about $\lambda_{ij} = \lambda = 0.4$ eV. This value is consistent with the values determined by Prins et al. [14] for similar phenylene–vinylene derivatives.

The transfer integral J_{ij} between states i and j located on two different chains A and B is determined from the transfer integrals $J_{\alpha\beta}$ between the repeat units α and β using known expansion coefficients $c_{i,\alpha}$ as

$$J_{ij} = \sum_{\alpha,\beta} c_{i,\alpha} c_{j,\beta} J_{\alpha\beta} \delta_{\alpha\beta} \quad (8)$$

where $\delta_{\alpha\beta}$ is the Kronecker delta function, and summation runs through all polymer repeat units. Note that besides the hole energies E_i , the expansion coefficients $c_{i,\alpha}$ are also strongly dependent on the distribution of local site energies ε_n .

Determination of the inter-orbital transfer rates $v_{i \rightarrow j}$ and the thermalized occupation probability p_i of the initial state makes it possible to calculate the charge transfer rates $v_{A \rightarrow B}$ between two adjacent chains A and B

$$v_{A \rightarrow B} = \sum_{\substack{i \in A \\ j \in B}} p_i(E_i) v_{i \rightarrow j} \quad (9)$$

where summation runs through all states of the respective chain. Finding the inter-chain transfer rates $v_{A \rightarrow B}$ makes it possible to write the master equation describing the hole motion

$$\frac{dP_A(t)}{dt} = \sum_B v_{A \rightarrow B} P_B(t) \quad (10)$$

where $P_A(t)$ and $P_B(t)$ are the probabilities of finding the hole on the chains A and B , respectively, at time t . By analogy to the time-dependent Schrödinger equation for the on-chain motion, the master equation (Eq. (10)) is solved either by means of direct numerical integration, or by using the eigenstates. However, note that the matrix $\mathbf{v}_{A \rightarrow B}$ is not symmetric and its eigenstates are not the stationary states. They involve at least one time-independent eigenstate corresponding to the thermal equilibrium, whereas all other eigenstates decay, due to negative real parts of their respective eigenvalues.

At $t = 0$, the hole is assumed to be localized on a single chain, i.e., $P_0(t = 0) = 1$ and all other P_A are equal to zero. It is important to select this initial hole localization randomly with regard to the thermal equilibrium occupational probabilities $P_A(t \rightarrow \infty)$.

Once the time evolution of $P_A(t)$ is found, the mean-square displacement $\Delta^2(t)$ of the hole can be calculated as

$$\Delta^2(t) = \sum_A i_A^2 d^2 P_A(t) \quad (11)$$

with d being the interchain distance and the product $i_A d$ being the projection of the distance of the chains A and 0 to the direction of the electric field. This quantity was averaged over 500 different Monte Carlo realizations of the disordered polymer chains to achieve numerical stability. The mean-square displacement $\Delta^2(t)$ is related to the frequency dependent mobility by the Kubo formula [15]

$$\mu(\omega) = \frac{-e\omega^2}{2kT} \operatorname{Re} \left[\int_0^\infty \Delta^2(t) \exp(-i\omega t) dt \right] \quad (12)$$

where e is the elementary charge, k is the Boltzmann constant, T is the temperature, and $\omega = 2\pi f$ is the radian frequency of the external field.

3.2. Room temperature results

The modelling of hole mobility presented in this paper was performed with the following parameters: The size of the array of the polymer chains (Fig. 3) was $M = 601$. Each of these chains consisted of $N = 360$ repeat units. The estimated inter-chain distance was $d = 1$ nm.

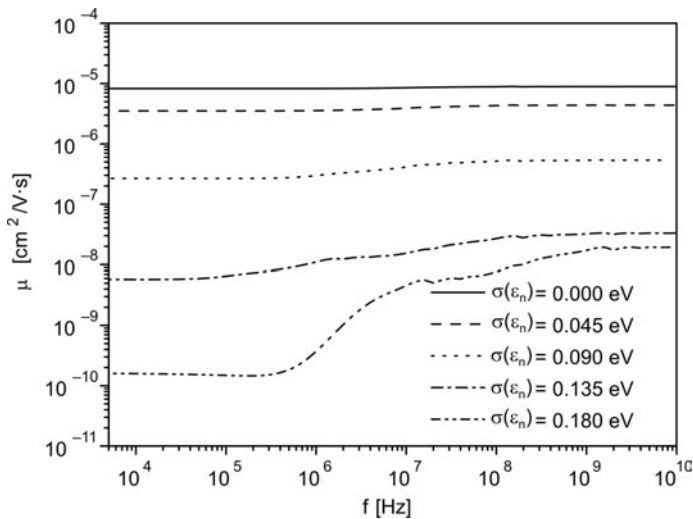


Fig. 5. Frequency dependence of the hole mobility $\mu(f)$ calculated for various values of the local energy disorder $\sigma(\epsilon_n)$

The frequency dependent mobility calculated for the different levels of the local energy disorder $\sigma(\epsilon_n)$ is presented in Fig. 5. While the mobility in the polymer with

a low value of the local energy disorder is frequency-independent, for higher values of $\alpha(\varepsilon_n)$ there is a certain increase of the mobility with the frequency. The explanation of this effect is based on the fact that at higher external field frequencies each charge carrier oscillates in a small region containing few polymer chains. Also at greater values of $\alpha(\varepsilon_n)$, it may happen that there are rather high transfer rates among such a small number of chains. Consequently, the charge carrier will find a path on which its motion is weakly influenced by the energy disorder. If the external field frequency is low, the charge carrier is surrounded by barriers and cannot follow the oscillating field direction. A typical energy landscape, in which the hole moves, is depicted in Fig. 6.

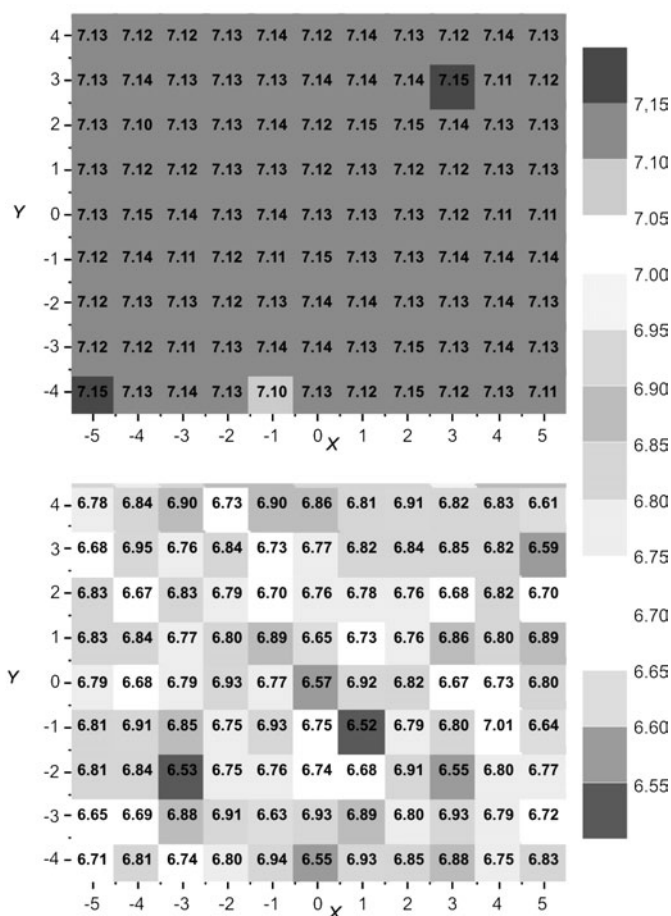


Fig. 6. Map of the average energy (in eV) of the thermalized hole located on particular polymer chains calculated for the pristine (upper, $\alpha(\varepsilon_n) = 0$) and doped (lower, $\alpha(\varepsilon_n) = 0.18$ eV) polymer, respectively. Polymer chains are depicted as gray squares. Coordinates X and Y show the chain positions.

Polymer chains, aligned perpendicular to the plane, are symbolized by gray squares. The intensity of the gray colour and number indicate an average energy of

a hole located on a given chain. Coordinates X and Y show the chain positions. For the pristine polymer (Fig. 6, upper diagram), there are no significant barriers among the chains. On the other hand, for a doped polymer (Fig. 6, lower diagram), there are several rather isolated chains possessing low energy and hence acting as traps. However, if there are more chains with lower energy next to each other, like the pair in the centre of the picture, and the external field frequency is sufficiently high, the charge can oscillate in this small region. A similar phenomenon has been already reported by Hilt et al. [16]. They investigated the charge transport in one-dimensional disordered systems and concluded that the mobility is frequency dependent, if the charges hops over barriers, but it is frequency independent, if the charges hop out of wells.

Figure 5 shows a very significant dependence of the inter-chain hole mobility on the local energy disorder $\sigma(\varepsilon_n)$. At low frequencies, the inter-chain mobility decreases by several orders of magnitude if the standard deviation of the energy distribution is doubled from $\sigma(\varepsilon_n) = 0.09$ to 0.18 eV. Such a change of $\sigma(\varepsilon_n)$ can be achieved by the change of the additive dipole moment connected with the photochromic reaction $SP \rightarrow MR$ at experimentally reasonable additive concentrations.

3.3. Temperature dependence of mobility

Using our model, the temperature dependence of mobility was calculated in the range from 100 K to 600 K. Temperature influences the chain torsional disorder, which determines the on-chain transfer integral $b_{n,n+1}$ distribution, hole thermalization, and transfer rates given by the Marcus formula (Eq. (7)).

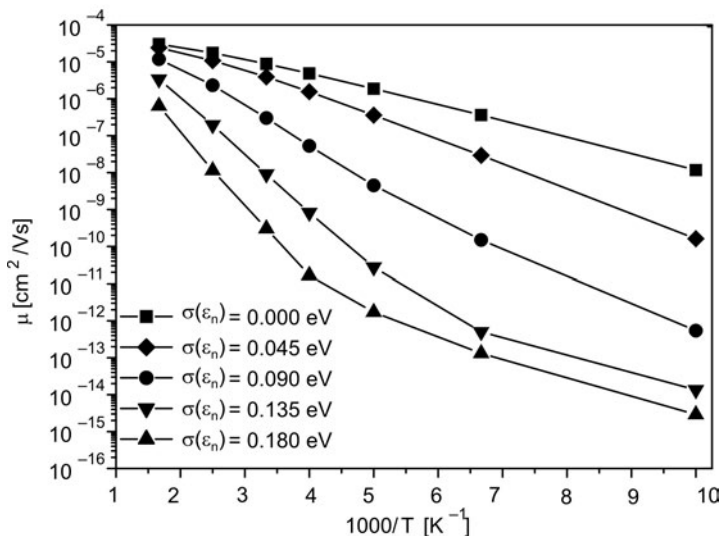


Fig. 7. Arrhenius plot of the temperature dependence of mobility calculated for various values of the local energy disorder $\sigma(\varepsilon_n)$ at the external field frequency 100 kHz. Results obtained for the temperature dependent polymer conformation

Temperature dependence of hole mobility (at 100 kHz) calculated for several values of the local energy disorder $\sigma(\varepsilon_n)$ is shown in Fig. 7. It should be noticed that at low temperatures the chain torsional disorder may be underestimated using the Grozema model [9], due to the relatively greater importance of the conformational mistakes and chemical defects. For this reason, to distinguish the influence of the temperature change of the chain torsional disorder on mobility, the calculation was repeated with the on-chain hole states calculated at room temperature (293 K), i.e., temperature dependence of the chain torsional disorder was in the latter case neglected (frozen conformation results). The results obtained with the temperature-dependent and frozen conformation are compared in Fig. 8. It is obvious that the temperature change of the conformation causes only a slight decrease in the mobility as the temperature increases, which can be explained by a shorter effective conjugation length and thus greater localization of the on-chain hole states at higher temperatures. Thus, possible underestimation of the chain torsional disorder should not significantly affect the results shown in Fig. 7.

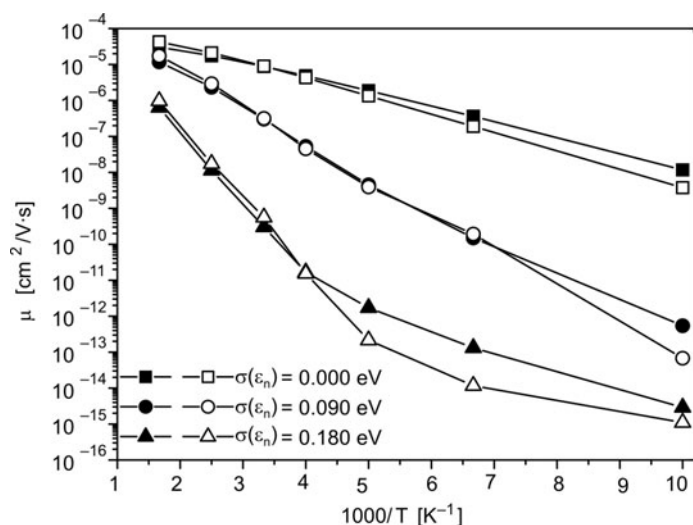


Fig. 8. Mobilities of the temperature dependent polymer conformation (solid symbols) and for the room temperature (frozen) conformation (open symbols). In the latter case, the on-chain hole states were calculated at the constant temperature 293 K, while the mobility modeling was performed at the temperature T . The external field frequency was 100 kHz

We compared our calculated data with the analytical model of hopping mobility proposed by Fishchuk et al. [4]. He suggests, that using Marcus transfer rates at low carrier concentrations leads to the approximate relation

$$\ln(\mu) = -\frac{E_p}{kT} - k_2 \left(\frac{\sigma(E_i)}{kT} \right)^2 + \text{const} \quad (13)$$

where $E_p = \lambda/4$ is the polaron activation energy, $\sigma(E_i)$ is the standard deviation of the on-chain hole states, and the coefficient $k_2 = 0.12$. This model was derived with the limitation $\sigma(E_i) \ll E_p$ and under the assumption of three-dimensional hopping among point centres, each possessing only one energy state. It does not consider any influence of temperature on the molecular conformation. Relation (13) shows that polaron formation eventuate in Arrhenius-type temperature dependence of mobility, while the energy disorder of the charge carrier states is responsible for sub-Arrhenius dependence. Our mobility data calculated for the pristine polymer ($\sigma(\epsilon_n) = 0$, $\sigma(E_i) = 0.034$ eV) can be fitted using Eq. (13) over the whole temperature range, as is shown in Table 2. The parameters of the fit obtained for the frozen conformation roughly match the expected values $E_p = \lambda/4 = 0.1$ eV and $\sigma(E_i) = 0.034$ eV (see Table 1). On the other hand, mobility calculated for doped polymers cannot be approximated by this relation due to the mobility saturation at low temperatures. Note that in this case $\sigma(E_i)$ (see Table 1) is comparable or higher than the polaron activation energy $E_p = 0.1$ eV and therefore relation (13) cannot be applied.

Table 2. Fitting of the calculated temperature dependence of mobility according to Eq. (13) for the pristine polymer ($\sigma(\epsilon_n) = 0$). Results obtained for the temperature dependent polymer conformation are compared with the frozen conformation results. All values are given in eV

Conformation	E_p	$\sigma(E_i)$
Temperature dependent	0.062	0.036
Frozen	0.083	0.030

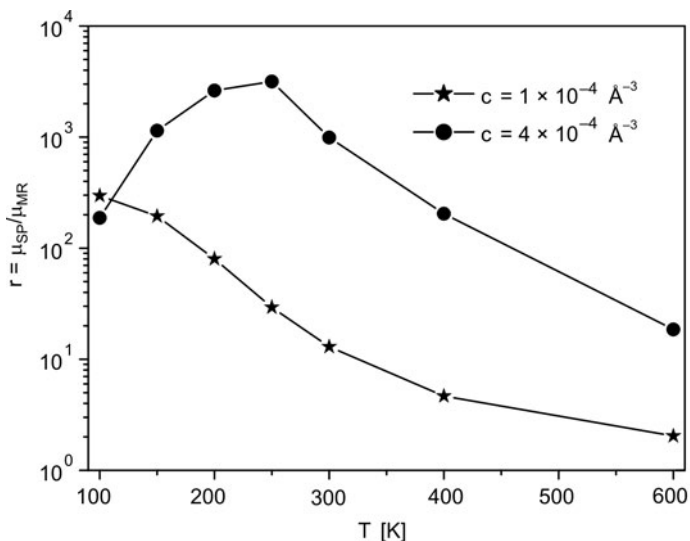


Fig. 9. Temperature dependence of the switching ratio of mobility ($f = 100$ kHz) during the photochromic SP \leftrightarrow MR reaction calculated for the low and high additive concentration c

If the reaction field of the dipoles is not taken into account, the MR molecules with the dipole moment 12 D and a high but experimentally achievable concentration $c = 4 \times 10^{-4} \text{ \AA}^{-3}$ (ca. 20 wt. %) would produce disorder in local energies with the $\sigma(\epsilon_n) = 0.37 \text{ eV}$ [7]. If the relative permittivity is about 3 (a typical value for organic materials), the dipole reaction field decreases the local energy disorder by about 50 % (see Ref. [17] for details). Thus, the disorder in local energies can be estimated to be about $\sigma(\epsilon_n) = 0.18 \text{ eV}$. Because our model neglects mutual interaction of the additive molecules, the local energy disorder is proportional to the additive dipole moment and the square root of the additive concentration c . It follows that SP molecules with dipole moment 6 D and the same concentration cause disorder in local energies for $\sigma(\epsilon_n) = 0.09 \text{ eV}$. Figure 9 shows the temperature dependence of the switching ratio $r = \mu_{\text{SP}}/\mu_{\text{MR}}$ of the hole mobilities in the polymer doped by spiropyran and merocyanine, respectively, at low ($1 \times 10^{-4} \text{ \AA}^{-3}$) and high ($4 \times 10^{-4} \text{ \AA}^{-3}$) additive concentrations. The switching ratio generally decreases as the temperature increases. However for high concentration, there is a saturation and decrease if the temperature decreases below 250 K. This effect corresponds to the low-temperature saturation of the mobility at high energy disorder (see Fig. 7). Except for the lowest temperatures, the results show a strong dependence of the switching ratio on the additive concentration.

4. Conclusion

The proposed model of the inter-chain hopping predicts a strong dependence of the hole mobility in MEH-PPV on the local energy disorder. Doubling the local energy disorder causes a decrease in the inter-chain hole mobility, by up to several orders of magnitude. These results confirm the possibility of constructing an efficient optoelectrical switch based on a polymer doped with a photochromic polar additive. It should be noted that the magnitudes of the calculated mobilities are relative only; however the scaling does not affect the ratio of the mobilities of the pristine and the doped material. The calculated temperature dependence of the mobility shows essentially Arrhenius type behaviour, with a moderate sub-Arrhenius deviation at a low energy disorder and the low-temperature saturation at a high energy disorder. The switching ratio is significantly dependent on the additive concentration and the temperature.

Acknowledgement

This work was supported by the Ministry of Science and Higher Education of Poland (grant No. 3 T08E 084 30), by the Czech Science Foundation (grant No. 203/06/0285), by the Grant Agency of the Academy of Sciences of the Czech Republic (grant No. KAN400720701), and by the Ministry of Education, Youth, and Sports of the Czech Republic and the Polish Ministry of Science and Higher Education (Czech-Polish cooperation Project MEB 050815 – 2008/CZ-5). The work was also supported by the European Commission through the Human Potential programme (Marie Curie RTN BIMORE, Grant No. MRTN-CT- 2006-035859). The access to the META Centrum supercomputing facilities provided under the research intent MSM6383917201 as well as to the servers Luna/Apollo in the Institute of Physics of the AS CR, v.v.i., Prague is highly appreciated.

References

- [1] BÄSSLER H., *Phys. Stat. Sol. (b)*, 175 (1993), 15.
- [2] MILLER A., ABRAHAMS E., *Phys. Rev.*, 120 (1960), 745.
- [3] FISHCHUK I.I., KADASHCHUK A., BÄSSLER H., NEŠPŮREK S., *Phys. Rev. B*, 67 (2003), 224303.
- [4] FISHCHUK I.I., ARKHIPOV V.I., KADASHCHUK A., HEREMANS P., BÄSSLER H., *Phys. Rev. B*, 76 (2007), 045210.
- [5] MARCUS R.A., *Rev. Mod. Phys.*, 65 (1993), 599.
- [6] MAY V., KÜHN O., *Charge and Energy Transfer Dynamics in Molecular Systems*, Wiley, Berlin, 2000.
- [7] TOMAN P., NEŠPŮREK S., WEITER M., VALA M., SWORAKOWSKI J., BARTKOWIAK W., MENŠÍK M., *Polym. Adv. Technol.*, 17 (2006), 673.
- [8] BROO A., *Int. J. Quant. Chem.*, 77 (2000), 454.
- [9] GROZEMA F.C., VAN DUIJNEN P.T., BERLIN Y.A., RATNER M.A., SIEBBELES L.D.A., *J. Phys. Chem. B*, 106 (2002), 7791.
- [10] TOMAN P., BARTKOWIAK W., NEŠPŮREK S., SWORAKOWSKI J., ZALEŠNÝ R., *Chem. Phys.*, 316 (2005), 267.
- [11] CHUA L.L., ZAUMSEIL J., CHANG J.F., OU E.C.W., HO P.K.H., SIRRINGHAUS H., FRIEND R.H., *Nature*, 434 (2005), 194.
- [12] TAVERNIER H.L., FAYER M.D., *J. Chem. Phys.*, 114 (2001), 4552.
- [13] HUTCHISON G.R., RATNER M.A., MARKS T.J., *J. Am. Chem. Soc.*, 127 (2005), 2339.
- [14] PRINS P., SENTHILKUMAR K., GROZEMA F.C., JONKHEIJM P., SCHENNING A.P.H.J., MEIJER E.W., SIEBBELES L.D.A., *J. Phys. Chem. B*, 109 (2005), 18267.
- [15] KUBO R., *J. Phys. Soc. Japan*, 12 (1957), 570.
- [16] HILT O., SIEBBELES L.D.A., *Chem. Phys. Lett.*, 269 (1997), 257.
- [17] BÖTTCHER C.J.F., *Theory of Electric Polarization*, Elsevier, Amsterdam, 1952.

Received 10 September 2008

Revised 26 October 2008

Liquid crystalline phases in DNA and dye-doped DNA solutions analysed by polarized linear and nonlinear microscopy and differential scanning calorimetry*

J. OLESIAK^{1**}, K. MATCZYSZYN¹, H. MOJZISOVA²,
M. ZIELINSKI², D. CHAUVAT², J. ZYSS²

¹Group of Physics and Chemistry of Molecular Materials, Institute of Physical and Theoretical Chemistry, Wrocław University of Technology, Wybrzeże Wyspiańskiego 27, 50-370 Wrocław, Poland

²Laboratoire de Photonique Quantique et Moléculaire, Ecole Normale Supérieure de Cachan, 61 avenue du Président Wilson, 94235 Cachan, Cedex, France

The contribution reports on an investigation of liquid crystalline phases in salmon (ca. 2000 bp) and herring (ca. 50 bp) roe DNA solutions in water. DNA aqueous solutions exhibit lyotropic liquid crystal (LLC) properties. To characterize LLC phases in DNA solutions, specially prepared LC cells as well as drying droplets were observed under a polarized light microscope (PLM). Differential scanning calorimetry (DSC) was used to determine the temperatures of phase transitions. The preliminary results are discussed and several structures of LLC in DNA aqueous solutions are presented as a function of temperature, concentration and DNA contour length. Apart from pure DNA solutions, a host-guest system was fabricated, with DNA doped with 4-(4-Nitrophenylazo)aniline – an azobenzene derivative, known as Disperse Orange 3 (DO3). In such a system, liquid crystalline phases were observed differing from the phases formed in pure DNA solutions of similar concentrations of matter. To study the mutual orientation of DNA chains and small dye molecules, polarization sensitive nonlinear microscopy was applied. DNA dissolved in water and doped with azobenzene was found to produce a two-photon fluorescence signal. From polarization analysis, a partial ordering of DO3 molecules in DNA matrix was observed.

Key words: *DNA liquid crystal phases; calorimetry; polarized light microscopy; Disperse Orange 3; two photon fluorescence; nonlinear polarimetry analysis*

1. Introduction

The very first observations of liquid crystalline phases in DNA solutions in water or buffers were described in the 1950s [1]. It was assumed that ordering of DNA

*The paper presented at the 11th International Conference on Electrical and Related Properties of Organic Solids (ERPOS-11), July 13–17, 2008, Piechowice, Poland.

**Corresponding author, e-mail: joanna.olesiak@pwr.wroc.pl

chains has a profound impact on their function as well as their configuration in a cellular environment. The following decades brought new data on the lyotropic liquid crystalline (LLC) phases in DNA aqueous solutions. The relation between the creation of LLC and numerous parameters was investigated: dependence on temperature, DNA concentration, ionic strength of a solution and occurring counterions [2]. The features of the double helix, i.e. its length, topology, the sequence of bases, were also found to influence the observed phases [3, 4].

A number of fluorescent dyes and NLO chromophores can be doped to DNA matrix. They can intercalate into a DNA helix, bind to DNA grooves or just weakly interact with double strands in a solution. Mutual interactions affect optical properties of dyes and increase photoluminescence intensity, which has robust applications. It is commonly used to stain DNA for microscopy, and is exploited in diverse methods of gel-based nucleic acid separation, with the use of ethidium bromide, acridine orange or Hoechst stain [5]. It can also be applied to the detection of mismatched sites in double-stranded DNA, with the use of destabilizing agents, e.g. octahedral rhodium(III) complexes [6]. Furthermore, it is applied to sensing in DNA microarrays [7] as well as biosensor devices.

DNA modified with a cationic surfactant and doped with photoactive dyes is a promising material for applications in photonics because of its exceptional structure and excellent optical properties [8, 9]. Azobenzenes are suitable dopants for DNA-based photoactive materials, as their optical and photochemical properties are well known and widely applied in combination with liquid crystals [10–13]. To date, only a few studies have been reported on azobenzene–DNA interactions [14] and the nature of binding is still in debate.

We propose to apply linear and nonlinear microscopy as well as differential scanning calorimetry to investigate arrangements of azobenzene molecules and DNA. More specifically, we observe polymorphism of DNA configuration in order to find the specific range of temperature and concentration where individual phases exist. We characterize DNA matrix doped with 4-(4-nitrophenylazo)aniline (Disperse Orange 3) by polarized light microscopy and differential scanning calorimetry and compare to pure DNA solutions. Then, nonlinear microscopy allows us to extract further information about the mutual orientation of long chains of DNA and the molecules of the dopant.

2. Materials and methods

Sample preparation. Marine-based DNA isolated from salmon and herring roe was purchased from Sigma-Aldrich. According to the information provided by the supplier, salmon DNA contains approximately 2000 base pairs (bp), with MW around 1.3×10^6 . The melting temperature (T_m) is about 87.5 °C. To confirm the exact size of strands, electrophoresis was performed in agarose gel (70 V and 0.5 A, $t = 20$ min). Lambda DNA/PstI Marker was used, which covers the range 15–11501 bp. Visualized

fringes of salmon DNA spread as one smear from 260 bp (very low intensity) to ca. 6000 bp. The purity of DNA was confirmed, the results indicate, however, that the length of individual chains are distributed over a very broad range. Herring DNA oligonucleotides are 50 bp long.

4-(4-Nitrophenylazo)aniline, an azobenzene derivative known as Disperse Orange 3 (DO3), was bought from Sigma-Aldrich. According to the information sheet provided, the absorbance maximum of the *trans* form is at 443 nm. Absorption spectra of DNA, DO3 and DNA doped with DO3 were recorded and the maxima of absorption were established. For pure DNA (concentration ca. 0.2 mg/cm³) $\lambda_{\max} = 260$ nm, for DO3 aqueous solution $\lambda_{\max} = 403$ nm. Absorption spectra of DNA and DO3 solutions in water show two separate maxima, one related to DNA absorption and the other one, around λ_{\max} of DO3. The presence of the latter one is an indication that this particular dye does not intercalate into the DNA chains (Fig. 1).

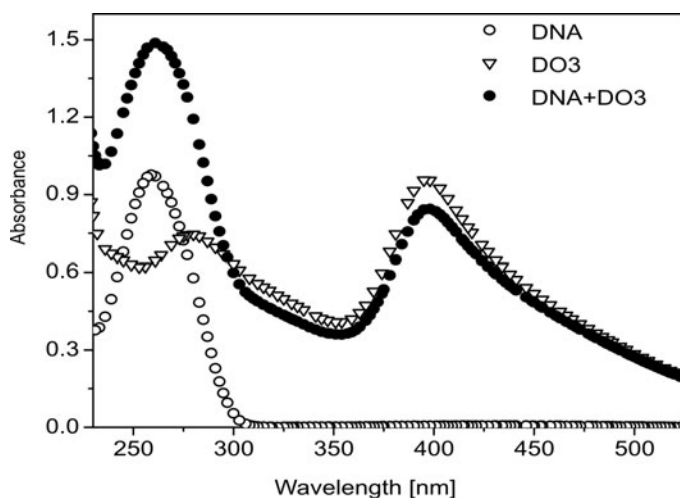


Fig. 1. Absorption spectra of pure DNA solution, DO3 solution and DNA-DO3 solution

Polarized light microscopy (PLM). Prior to PLM analysis, both salmon and herring DNA were dissolved in water and sodium salt solutions were obtained in a concentration range from $c_{\text{DNA}} = 3$ mg/cm³ to 120 mg/cm³. DO3 aqueous solutions were obtained after several hours of sonication, followed by filtration. DNA solutions and DNA solutions doped with DO3 were deposited atop glass plates and several kinds of samples were prepared: droplets of the volume 5–15 μl and cells built of two glass plates with Teflon spacers of the thickness of 6 μm , 70 μm and 1 mm. PLM photographs were taken under an Olympus 60BX microscope equipped with a hot stage, under a crossed polarizer condition.

Differential scanning calorimetry (DSC). DSC measurements were performed with a Perkin Elmer DSC7 at a scan rate of 1 or 2 $^{\circ}\text{C}/\text{min}$. Each sample was heated from the room temperature to almost 100 $^{\circ}\text{C}$ and then cooled down to 25 $^{\circ}\text{C}$.

Two photon fluorescence (TPF) microscopy. Nonlinear optical properties of DNA and DO3 were investigated by nonlinear microscopy combined with polarimetric detection [15]. The source of light was a Ti:Sa laser (100 fs, 80 MHz repetition rate) with the incident wavelength in the range 680–1020 nm. The laser beam, after passing through a Glan–Taylor prism polarizer, passed through an achromatic half-wave plate mounted on a motorized rotation stage, in order to continuously vary the polarization direction of the incident light. Then the beam was focused on the sample through a high numerical aperture oil immersion objective ($\times 100$, $NA = 1.4$). The sample was mounted on an xyz piezoelectric scanning system which was moved in its plane with a scan step of 20 nm or greater. The spot size was about 350 nm. The TPF emission was collected in epifluorescence mode through the same high numerical aperture objective and split by a polarizing beam splitter. That resulted in orthogonally polarized signals, which were recorded by two avalanche photodiodes operating in the photon counting regime.

3. Results and discussion

DNA strands in aqueous solutions exhibit wide polymorphism and lyotropic liquid crystalline (LLC) properties. To establish a critical concentration required to create LLC phases, solutions of salmon and herring DNA were prepared and observed as droplets under PLM. The first anisotropic phase in salmon DNA samples appeared for $c_{\text{DNA}} < 3 \text{ mg/cm}^3$.

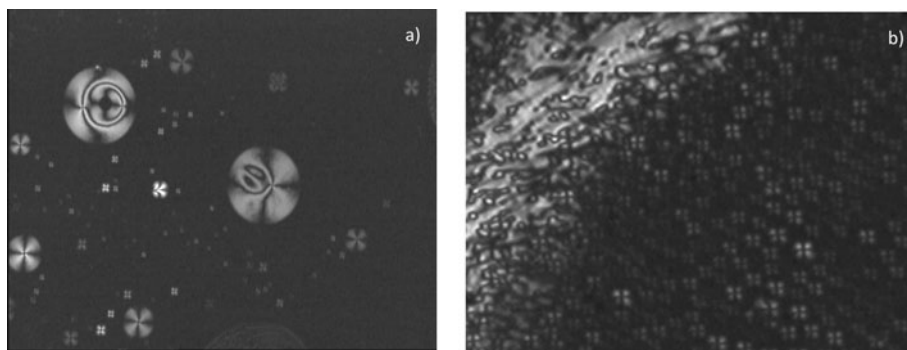


Fig. 2. Nematic extinction brushes in salmon DNA solution (a), $c_{\text{DNA}} < 3 \text{ mg/cm}^3$ and LLC phases in herring DNA solution (b), $c_{\text{DNA}} = 70 \text{ mg/cm}^3$

In these conditions, Schlieren textures, characteristic of nematics, were observed, as is shown in Fig. 2a. The critical concentration required to form LLC phases in shorter, herring DNA strands was significantly higher. In this case, LLC lamellar phases were obtained in aqueous solutions with $c_{\text{DNA}} > 70 \text{ mg/cm}^3$ (Fig. 2 b). After these preliminary results with herring DNA, all the subsequent experiments were conducted with salmon DNA solutions. In the following paragraphs, we describe the most

characteristic phases observed in specific ranges of salmon DNA concentration and temperature, for both, pure and dye-doped DNA.

3.1. Drying droplets

In drying droplets of DNA solution with low concentration of DNA ($10 \text{ mg/cm}^3 < c_{\text{DNA}} < 20 \text{ mg/cm}^3$) characteristic zig-zag forms are created, described previously by Smalyukh et al. [16] (Fig. 3a). They result from competition between the radial stress

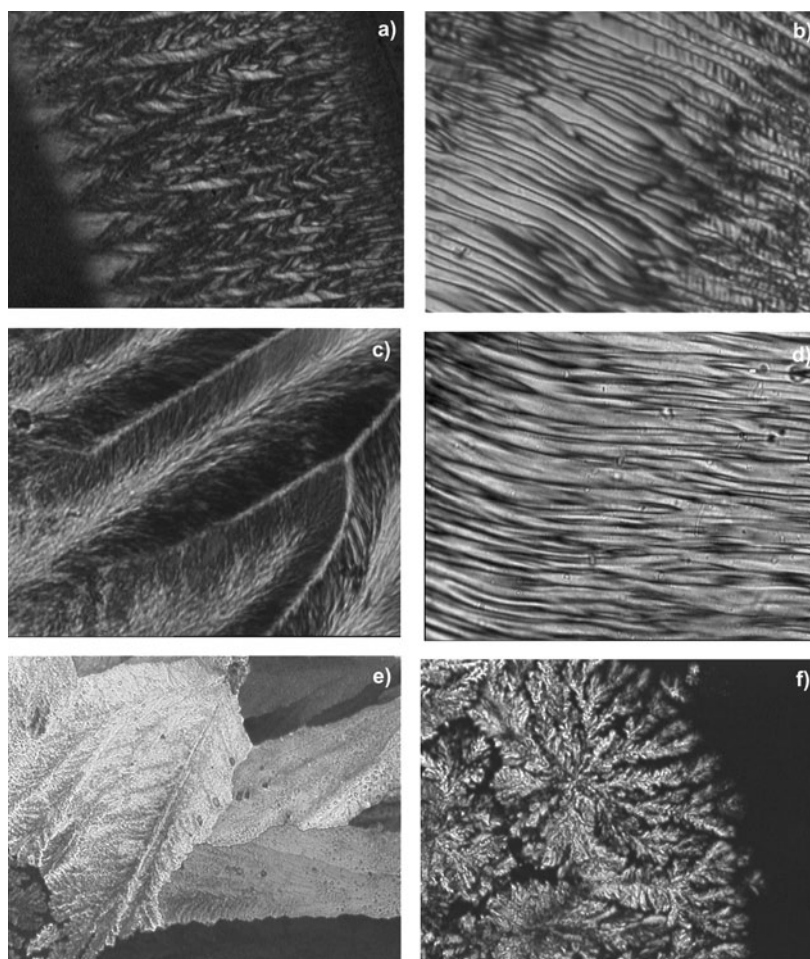


Fig. 3. Zig-zag pattern in drying droplet of DNA solution, $c_{\text{DNA}} = 13 \text{ mg/cm}^3$, $h = 176 \text{ }\mu\text{m}$ (a), columnar structure in DNA drying droplet, $c_{\text{DNA}} = 27 \text{ mg/cm}^3$, $h = 157 \text{ }\mu\text{m}$ (b), undulating columnar phase in DNA-DO3 drying droplet, $c_{\text{DNA}} = 15 \text{ mg/cm}^3$, $h = 90 \text{ }\mu\text{m}$ (c), striped texture in drying DNA-DO3 droplet, $c_{\text{DNA}} = 20 \text{ mg/cm}^3$, $h = 235 \text{ }\mu\text{m}$ (d), and centres of a droplet of DNA-DO3 solution with $c_{\text{DNA}} = 10 \text{ mg/cm}^3$ (e) and $c_{\text{DNA}} = 15 \text{ mg/cm}^3$ (f), respectively, h is the overall height of the image

tending to stretch DNA strands along the radius of a droplet, and the LC elasticity that aligns DNA parallel to the contact line. For higher DNA concentrations ($c_{\text{DNA}} > 20 \text{ mg/cm}^3$) a kind of columnar phase is created, shown in Fig. 3b.

A similar behaviour is observed in DNA-DO3 drying droplets ($10 \text{ mg/cm}^3 < c_{\text{DNA}} < 18 \text{ mg/cm}^3$). PLM images present several zones, with the zig-zag texture nearby the contact line, followed by undulating columnar hexagonal phase (Fig. 3c). However, in the centre of the droplet, dendrimeric phases are formed, not observed in pure DNA solutions (Figs. 3e, f). This spatial distribution of phases can be related to the dispersion of DNA lengths as well as the process of migration of DNA strands. Some portion of DNA molecules accumulate by the contact line of a droplet and form the outermost thick ring. The remaining DNA chains are deposited as the inner rings, and are separated by the black areas which presumably consist of cholesteric phases. The mechanism of dendrimeric phase formation in DNA-DO3 droplets is under investigation. In DNA-DO3 solutions with $c_{\text{DNA}} > 20 \text{ mg/cm}^3$, a striped pattern is observed, as shown in Fig. 3d. It can be related to the columnar phase observed in pure DNA solution.

3.2. LC cells

LC cells were prepared with concentrated solutions of DNA and DNA-DO3. For $c_{\text{DNA}} = 15 \text{ mg/cm}^3$ birefringent phases were hardly visible, as the evaporation of a solvent was constricted by the cover glass and the spacer. For $c_{\text{DNA}} = 30 \text{ mg/cm}^3$ and 60 mg/cm^3 , cholesteric liquid crystals were obtained for both, pure and doped DNA.

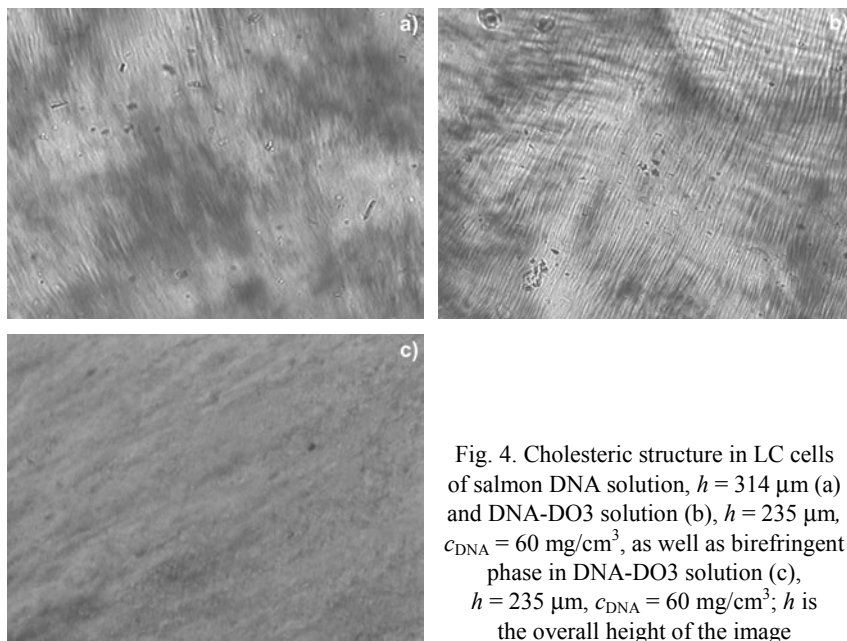


Fig. 4. Cholesteric structure in LC cells of salmon DNA solution, $h = 314 \mu\text{m}$ (a) and DNA-DO3 solution (b), $h = 235 \mu\text{m}$, $c_{\text{DNA}} = 60 \text{ mg/cm}^3$, as well as birefringent phase in DNA-DO3 solution (c), $h = 235 \mu\text{m}$, $c_{\text{DNA}} = 60 \text{ mg/cm}^3$; h is the overall height of the image

Figure 4 presents their characteristic fingerprint patterns. However, in some concentrated samples, domains of birefringent phase could be observed without stripes specific of cholesteric phase. We assume that they are related to DNA molecules unidirectionally aligned, otherwise without any higher ordering or rotation between the planes in which the molecules are aligned (Fig. 4c).

Pure DNA and DNA-DO3 solutions, observed in heated LC cells under PLM, exhibit two main transitions. Considering pure DNA, the first, less profound transition is observed at 66–70 °C. At ca. 84 °C, a black image corresponding to the order-disorder phase transition begins to appear. The uniformly black area, indicating an isotropic solution, is obtained at 86 °C. In the case of DNA doped with DO3, the cholesteric pattern of DNA-DO3 solution vanishes at 50–53 °C, and a plain, birefringent phase is observed. The order–disorder transition starts at ~58 °C and ends at ~68 °C. Both processes are reversible and a clearly visible, birefringent area appears upon cooling.

3.3. DSC measurements

DSC runs were carried out in the same temperature range just as for the PLM images (from 25 °C to 100 °C) for several samples with various concentrations of salmon DNA. Relative changes in the heat flow were very small and difficult to observe in more diluted solutions ($c_{\text{DNA}} < 30 \text{ mg/cm}^3$). The positions of the peaks evaluated with the use of DSC software are presented in Table 1.

Table 1. DSC peaks positions in salmon DNA samples of various concentrations, pure or doped with DO3 molecules

Solution	dry DNA	120 mg/cm ³ DNA	60 mg/cm ³ DNA	30 mg/cm ³ DNA	15 mg/cm ³ DNA
DNA	92.85 °C	75.78 °C	74.77 °C 93.10 °C	70.44 °C 93.08 °C	poorly resolved peak ca. 73 °C
DNA + DO3	–	–	71.28 °C 93.12 °C	70.53 °C 93.11 °C	poorly resolved peak ca. 77 °C

Analysing DSC plots, we can distinguish two main processes; one around 70–75 °C and the other at 93 °C (Fig. 5a). $T_m = 93 \text{ °C}$ is the melting temperature of DNA strands, which is confirmed by DSC measurement in dry DNA. Denaturation does not depend on DNA concentration. However, a temperature shift is observed for a DNA-DO3 system, as plotted in Fig. 5b. DO3 molecules may destabilize DNA chains, thereby resulting in a lower denaturation temperature and the occurrence of an order–disorder transition already at ca. 68 °C. The other, broad peak corresponds to a change in the cholesteric structure, similar to the transition observed by Kagemoto et al. at 70 °C [17]. Differences in temperature evaluated from DSC and PLM observations may exist due to different conditions of sample preparation and investigation.

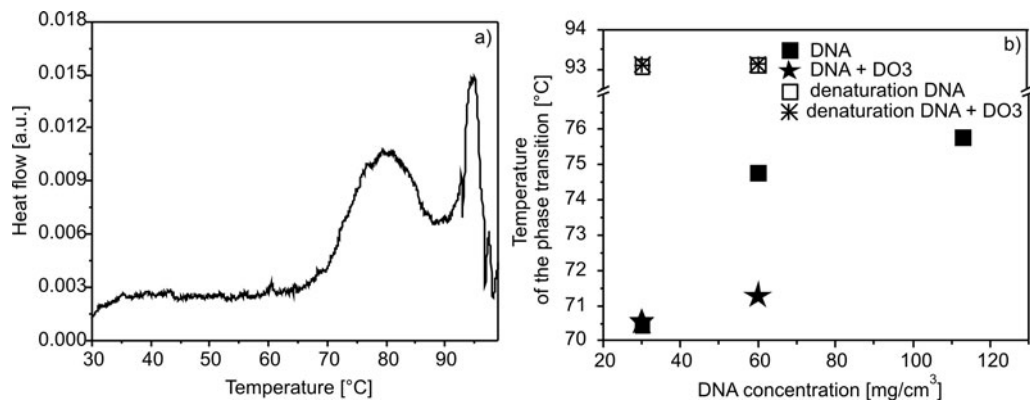


Fig. 5. DSC plot of DNA solution doped with DO3, $c_{\text{DNA}} = 60 \text{ mg/cm}^3$ (a) and the dependence of temperatures of two main phase transitions in pure DNA and doped DNA solutions on the DNA concentration (b)

Material sealed in DSC vessels is isolated from the environment, thus drying, evaporation of a solvent and non-uniform heating in the cell volume do not affect the measurement.

3.4. Nonlinear polarimetry analysis

Since the absorption and the fluorescence emission processes are sensitive to the polarization of the excitation light, nonlinear optical polarimetry was considered to be a valuable technique to determine the local ordering of sample molecules [15, 18, 19]. If a solution of randomly oriented absorbing molecules is irradiated with polarized light, the average absorption is independent of the incident polarization. However, if the absorbing molecules are at least partly oriented, the absorption will occur preferentially along the polarization direction parallel to the absorbing transition dipoles. Similarly, the fluorescence emission occurs in a clearly identifiable axis, parallel to the axis of the emission dipole of the ordered molecules. Therefore, detection of fluorescence intensity at various incident polarizations allows us to determine the orientation of emission dipoles projection in a macroscopic XY coordinate system.

DO3 is a rod-like molecule with a central conjugated system and a couple of electron donor and acceptor groups on the extremities. In a rough approximation, it was assumed that the absorption and emission dipoles are parallel to the long molecular axis.

As a first attempt to apply the nonlinear microscopy to dye-doped DNA liquid crystal we chose one of the above mentioned sample configurations, i.e., DNA-DO3 in a closed cell with $c_{\text{DNA}} = 60 \text{ mg/cm}^3$. The structure of the sample is presented in Fig. 4c.

DO3 molecules were excited at 810 nm, equivalent to 405 nm for one photon excitation, and the emitted fluorescence was recorded in the spectral range between 400 nm and 650 nm. The maximum light intensity incident on the sample was

800 μW . In these experimental conditions, the intrinsic DNA two-photon fluorescence signal is found to be negligible compared with the DO3 emission.

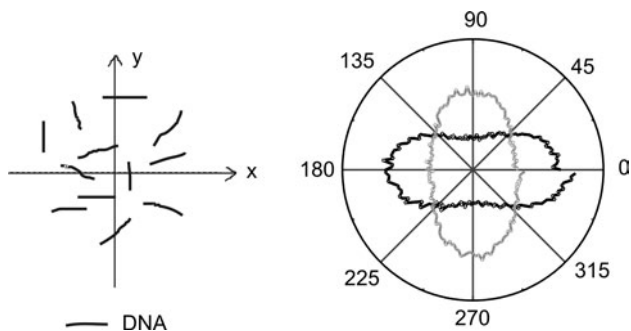


Fig. 6. Polar graphs of the isotropic solution of DNA-DO3

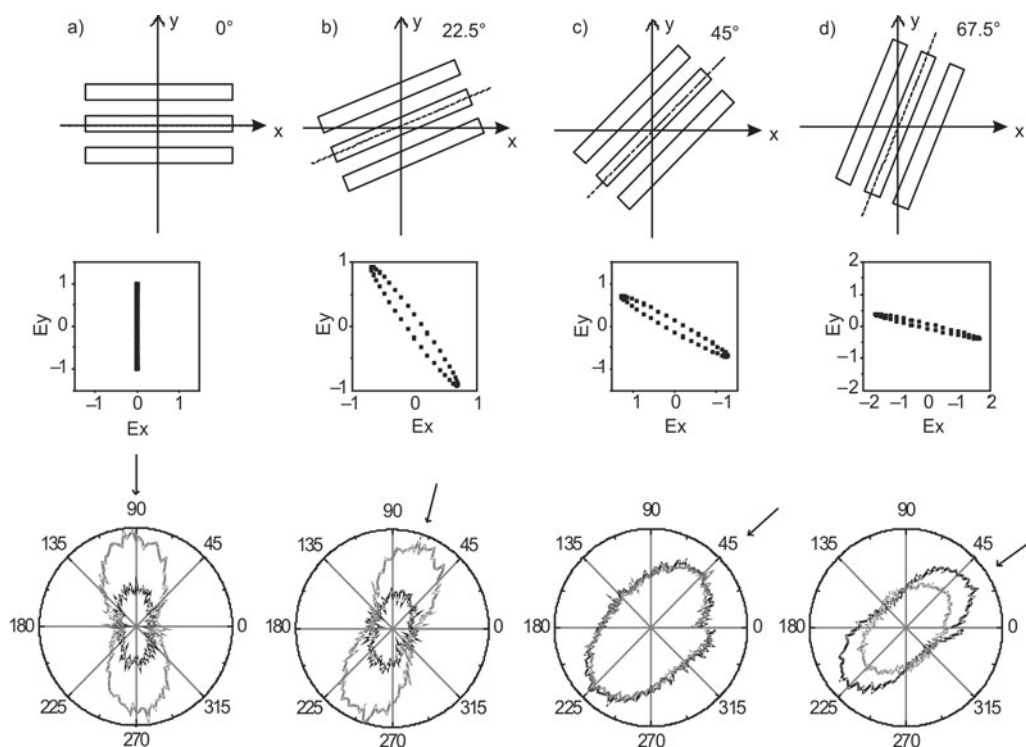


Fig. 7. Rotation of the sample in the XY framework: 1st row: scheme of the orientation of DNA domains. The dashed line represents the long axis of the domain. 2nd row: theoretical modelling of the deformation of the incident linear polarization at angles corresponding to the maximum TPF intensity for every polar graph (denoted by arrows). 3rd row: polar graphs of TPF emitted by DO3 in a DNA liquid crystal

First, we consider a reference sample where DNA-DO3 solution is isotropic liquid phase. Figure 6 shows typical polar graphs of fluorescence intensity of X and Y polari-

zation components emitted by DO3. The crossed pattern indicates a random orientation of the emitting dipoles. Conversely, Figure 7a represents polar graphs recorded in samples where DNA has an ordered distribution in liquid crystal domains. The two X and Y components are aligned parallel to each other and their orientation refers to the orientation of DO3 linked to DNA strands. Clearly, the alignment of DO3 molecules appears to be perpendicular to the alignment of the DNA strands. In order to confirm that this orientation is imposed by DNA strands, and to avoid any light-induced alignment of DO3 molecules, the sample was rotated in the XY plane and the polarimetric measurements were taken at a few different positions. The orientation of liquid crystalline texture and the corresponding polar graphs are shown in Figs. 7b–d.

Care has to be taken in analysis of a few data, since the actual light polarization on the sample depends on some optical parameters of the setup such as the birefringence of the optical elements and namely of the dichroic mirror. More specifically, the incident polarization is shown in Fig. 7. If we consider the angle of the maximum fluorescence intensity, we observe that it corresponds to an elliptic incident polarization, which is roughly oriented at 90° to the DNA texture. Therefore this sample rotation and corresponding analysis confirm the orientation of DO3 at about 90° relative to the DNA LC pattern. A more detailed mathematical analysis will be published elsewhere.

4. Conclusions

DNA dissolved in water forms lyotropic liquid crystalline phases (nematic, cholesteric, columnar) depending on DNA length, concentration and temperature, which were observed by polarized light microscopy. Similar liquid crystalline phases are created in LC cells filled with DNA solutions doped with 4-(4-Nitrophenylazo)aniline (DO3). However, phase transitions in the DNA-DO3 system occur at temperatures lower than those in pure DNA solutions. Moreover, in drying droplets of DNA-DO3 additional dendrimeric phases appear in the centre of a droplet, apart from the zig-zag pattern and columnar phases observed at the rim of the droplet in both, pure DNA and DNA-DO3 solutions. According to nonlinear polarimetry analysis, DO3 is oriented by DNA strands. The relative angle between liquid crystalline textures of DNA and the long axis of the DO3 molecule is approximately 90° . Nonlinear polarimetry thus appears as a useful tool to analyze the relative orientation of a dye and DNA molecules, and could be applied locally to understand, for instance, the additional dendrimeric and columnar phases found in dye-doped DNA solutions. This work is currently in progress in our laboratory.

Acknowledgements

This work was supported by the European Commission through the Human Potential Programme (Marie-Curie RTN BIMORE, Grant No. MRTN-CT-2006-035859), grant no. N50713231/3302 and IMFOVIR Project ANR-06-PCVI-0015 as well as through the Wrocław University of Technology. We express our gratitude to Prof. Juliusz Sworakowski for helpful discussions.

References

- [1] LUZZATI V., NICOLAIEFF A., *J. Mol. Biol.*, 1 (1959), 127.
- [2] LIVOLANT F., LEFORESTIER A., *Prog. Polym. Sci.*, 21 (1996), 1115.
- [3] KASSAPIDOU K., JESSE W., VAN DIJK J.A.P.P., VAN DER MAAREL J.R.C., *Biopolymers*, 46 (1998), 31.
- [4] MERCHANT K., RILL R.L., *Biophys. J.*, 73 (1997), 3154.
- [5] LI Y., DICK W.A., TUOVINEN O.H., *Biol. Fertil. Soils*, 39 (2004), 301.
- [6] JUNICKE H., HART J.R., KISKO J., GLEBOV O., KIRSCH I.R., BARTON J.K., *Proc. Natl Acad. Sci. USA*, 100 (2003), 3737.
- [7] LEE N.H., SAEED A.I., *Methods Mol. Biol.*, 353 (2007), 265.
- [8] HE G.S., ZHENG Q., PRASAD P.N., GROTE J.G., HOPKINS F.K., *Opt. Lett.*, 31 (2006), 359.
- [9] GROTE J.G., DIGGS D.E., NELSON R.L., ZETTS J.S., HOPKINS F.K., OGATA N., HAGEN J.A., HECKMAN E., YANEY P.P., STONE M.O., DALTON L.R., *Mol. Cryst. Liq. Cryst.*, 426 (2005), 3.
- [10] NATANSOHN A., ROCHON P., *Chem. Rev.*, 102 (2002) 4139.
- [11] YESODHA S.K., SADASHIVA PILLAI C.K., TSUTSUMI N., *Prog. Polym. Sci.*, 29 (2004), 45.
- [12] MATCZYSZYN K., SWORAKOWSKI J., *J. Phys. Chem. B*, 107 (2003), 6039.
- [13] MATCZYSZYN K., CHWIALKOWSKA A., SWORAKOWSKI J., *Thin Solid Films*, 516 (2008), 8899.
- [14] SNYDER R.D., MCNULTY J., ZAIROV G., EWING D.E., HENDRY L.B., *Mut. Res.*, 578 (2005), 88.
- [15] BRASSELET S., LE FLOC'H V., TREUSSART F., ROCH J.-F., ZYSS J., BOTZUNG-APPERT E., IBANEZ A., *Phys. Rev. Lett.*, 92 (2004), 207401.
- [16] SMALYUKH I., ZRIBI O.V., BUTLER J.C., LAVRENTOVICH J.D., WONG G.C.L., *Phys. Rev. Lett.*, 96 (2006), 177801-1.
- [17] KAGEMOTO A., NAKAZAKI M., KIMURA S., MOMOHARA Y., UENO K., BABA Y., *Thermochim. Acta*, 284 (1996), 309.
- [18] LE FLOC'H V., BRASSELET S., ROCH J.-F., ZYSS J., *J. Phys. Chem. B*, 107 (2003), 12403.
- [19] BRASSELET S., ZYSS J., *Compt. Rend. Phys.*, 8 (2007), 165.

Received 26 October 2008

Revised 8 January 2009

High temperature impedance spectroscopy study of non-stoichiometric bismuth zinc niobate pyrochlore

K. B. TAN^{1*}, C. C. KHAW², C. K. LEE³, Z. ZAINAL¹, Y. P. TAN¹, H. SHAARI¹

¹Faculty of Science, Universiti Putra Malaysia, 43400 Serdang, Selangor, Malaysia

²Faculty of Engineering and Science, Universiti Tunku Abdul Rahman, 53300 Kuala Lumpur, Malaysia

³Academic Science Malaysia, 902-4 Jalan Tun Ismail, 50480 Kuala Lumpur, Malaysia

Single phase non-stoichiometric bismuth zinc niobate, $\text{Bi}_3\text{Zn}_{1.84}\text{Nb}_3\text{O}_{13.84}$, was fabricated by a conventional solid state method. The sample was refined and fully indexed on the cubic system, space group $Fd\bar{3}m$ (No. 227), $Z = 4$ with $a = 10.5579(4)$ Å. Electrical characterisation was performed using an ac impedance analyser over the temperature range of 25–850 °C and frequency range of 5 Hz–13 MHz. Typical dielectric response is observed in $\text{Bi}_3\text{Zn}_{1.84}\text{Nb}_3\text{O}_{13.84}$ with a high relative permittivity, low dielectric loss and a negative temperature coefficient of capacitance, with the values of 147, 0.002 and –396 ppm/°C, at 100 kHz at ambient temperature, respectively. This material is highly resistive, with a conductivity of $1 \times 10^{-21} \Omega^{-1} \cdot \text{cm}^{-1}$ and a high activation energy of ca. 1.59 eV.

Key words: *activation energy; bismuth zinc niobate; dielectric response; impedance spectroscopy; pyrochlore*

1. Introduction

Ceramic materials have been used in a wide range of industrial applications such as electrical and electronic components, superconductors, catalyst and automobile components [1–3]. The study of advanced ceramic materials involves many disciplines, including chemistry, physics, mechanical engineering, materials science and metallurgy. Both electroceramics and structural ceramics are classified as advanced ceramics, and they have different applications. Applications of electroceramics involve electrical and magnetic properties, whereas those of structural ceramics are mainly based on its mechanical behaviour [4].

One of the promising candidates in electroceramics is bismuth pyrochlore [5]. Pure bismuth oxides are highly reactive, volatile and thermally unstable with poly-

*Corresponding author, e-mail: tankb@science.upm.edu.my

morphic transitions in which monoclinic α - Bi_2O_3 transforms to a defect fluorite δ - Bi_2O_3 above 729 °C, and then followed by the formation of two metastable phases, tetragonal β - Bi_2O_3 and body-centred cubic γ - Bi_2O_3 upon cooling [6]. However, bismuth derivatives are suitable and cost effective for various commercial applications, particularly in microwave and radio frequency applications, due to their low firing temperatures of miniaturisation with passive integration using multilayer ceramic technology whereby active or passive components are laminated and co-fired at low temperature. In general, pyrochlore materials have the formula, $\text{A}_2\text{B}_2\text{O}_7$ indicating the existence of two different crystallographic sites, namely a relatively larger 8-coordinate A site and a smaller 6-coordinate B site within the structure. These sites are commonly occupied by a combination of A^{3+} and B^{4+} cations, A^{2+} and B^{5+} cations or other combinations with required average mixed valency [7]. By far the most extensively studied Bi-based dielectrics are the cubic pyrochlore $\text{Bi}_{3/2}\text{ZnNb}_{3/2}\text{O}_7$ ($k' = 150$, $t_k = -400$ ppm/°C) and the monoclinic zirconolite phase ($k' = 80$, $t_k = 200$ ppm/°C, k' is the relative electric permittivity, and t_k stands for the temperature coefficient of capacitance). With the opposite signs for the temperature dependence of permittivity, they are considered a good pair that provides temperature compensated dielectric properties when mixed together [8].

An “ideal” composition for a pyrochlore phase in the Bi_2O_3 – ZnO – Nb_2O_5 (BZN) system could be $\text{Bi}_3\text{Zn}_2\text{Nb}_3\text{O}_{14}$, referred to as P, in which the expectation is that part of Zn and all Bi would be disordered over the large, 8-coordinate A sites; the remainder of Zn, together with Nb, would be disordered over the octahedral B sites. However, it has been shown that the material of the composition $\text{Bi}_3\text{Zn}_2\text{Nb}_3\text{O}_{14}$ contains excessive ZnO as a second phase and lies outside the BZN subsolidus solid solution area [9–13]. The pure-phase composition was confirmed to be ZnO deficient by electron probe microanalysis and a combination study of electron, neutron and X-ray diffraction.

Work since the 1990's has clarified many of the fundamental aspects of BZN materials. However, there are inconsistencies and discrepancies in the literature regarding the characterization of BZN materials. In particular, estimates of the electric relative permittivities, as reported from different researchers working on multiphase samples, can vary anywhere in the 80–120 range [9–13]. Preliminary electrical studies on Bi_2O_3 – ZnO – Nb_2O_5 ternary system indicate that these materials are highly insulating and their conductivities are not likely to be determined at temperatures below 500 °C. However, it is possible to measure permittivities at high frequencies at ambient temperatures and above. An overall objective of electrical characterisation is to investigate the effects of composition and temperature on bulk permittivity, i.e. variation of bulk permittivity with composition and whether the permittivity varies, positively or negatively with temperature. Investigation of various possible sources of error and variations in permittivity measurement are therefore indispensable before a firm conclusion can be drawn in correlating permittivity with density, sintering temperature and electrodes. The electrical data were collected on samples whose sintering conditions have been optimised with respect to capacitance value, bismuth loss and pellet density. The focus of this paper is on the high temperature electri-

cal behaviour of optimised $\text{Bi}_3\text{Zn}_{1.84}\text{Nb}_3\text{O}_{13.84}$ via a systematic impedance spectroscopy study.

2. Experimental

Cubic pyrochlore $\text{Bi}_3\text{Zn}_{1.84}\text{Nb}_3\text{O}_{13.84}$ was prepared via conventional solid state reactions using Bi_2O_3 , ZnO , and Nb_2O_5 as starting materials (all Alfa Aesar, 99.99%). ZnO and Nb_2O_5 were dried at 600 °C while Bi_2O_3 was dried at 300 °C, for 3 h prior to weighing. Stoichiometric quantities of the oxides were weighted and mixed with acetone in an agate mortar to ensure the homogeneity of the mixture. The resulting powder was transferred into a gold boat and pre-fired at 700 °C for 24 h (below Bi_2O_3 melting point of ca. 825 °C) in a Carbolite muffle furnace. Subsequently, the mixture was fired at 800 °C and 950 °C for 24 h with intermediate regrinding. The phase purity of the sample was examined at room temperature by X-ray diffraction using a Shimadzu X-ray powder diffractometer XRD-6000 equipped with a diffracted-beam graphite monochromator, with CuK_α radiation (1.5418×10^{-10} m). Pellets of a single phase sample were prepared using a stainless steel die measuring 8 mm in diameter. A sufficient amount of powder was added, cold pressed uniaxially, and sintered at 1050 °C in order to increase the mechanical strength and to reduce the intergranular resistance in the pellets. Gold paste (Engelhard) was smeared and hardened onto parallel faces of the ceramics.

The pellets with gold electrode attached were placed on a conductivity jig and inserted in a horizontal tube furnace. The pellets were characterised using an ac impedance analyser, Hewlett Packard LF HP4192A over the frequency range 5– 1.3×10^7 Hz with the applied voltage of 100 mV. Conductivity measurements were carried out over the temperature range ca. 28–850 °C on heating and cooling cycles each at 50 °C interval. The samples were allowed to equilibrate at each temperature for 30 minutes prior to measurement. Most measurements were made in air, and where necessary in oxygen free nitrogen (OFN) at the flow rate of 80 cm³/min for reducing atmosphere study. The nitrogen gas was supplied to a sealed tube furnace for 1 h in order to create a nitrogen atmosphere prior to measurement.

3. Results and discussion

Electrical properties of optimised $\text{Bi}_3\text{Zn}_{1.84}\text{Nb}_3\text{O}_{13.84}$ pellets with the density of ca. 90%, sintered at 1050 °C, were determined by ac impedance spectroscopy over the frequency range of 5 Hz–13 MHz in air. The measured impedance data are represented in the Nyquist form with a typical complex plane plot (Z'' vs Z'). The impedance is normalised by the geometric factor and represented in the form, $\rho^* = Z^*(S/d) = \rho' + j\rho''$ where ρ^* is the complex resistivity and S/d is the geometric factor. The parameters S and d represent the area and the separation of the electrodes [14, 15], re-

spectively. Perfect semicircles are only observed in the Cole–Cole plots of cubic pyrochlore $\text{Bi}_3\text{Zn}_{1.84}\text{Nb}_3\text{O}_{13.84}$ above 550 °C (Fig. 1).

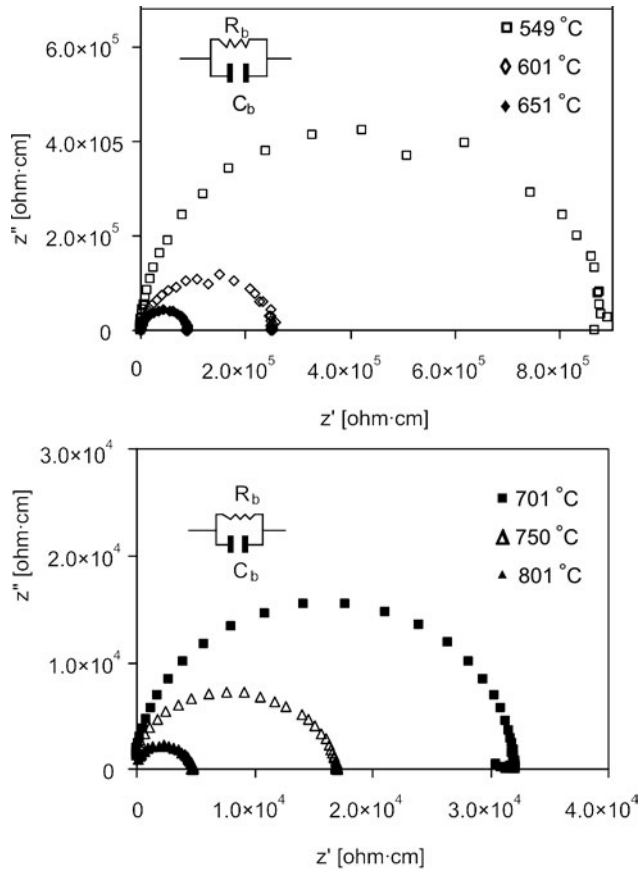


Fig. 1. Cole–Cole plots of $\text{Bi}_3\text{Zn}_{1.84}\text{Nb}_3\text{O}_{13.84}$ measured at various temperatures; $C_{\text{max}} = 1.19 \times 10^{-11} \text{ F}\cdot\text{cm}^{-1}$

The impedance data can be represented by the equivalent circuit shown in the inset of Fig. 1. The circuit consists of parallel R and C elements of the bulk material and the total impedance Z^* for the circuit is given by:

$$Z^* = \frac{1}{j\omega C + \frac{1}{R}} = \frac{R}{1 + j\omega CR} = Z' - jZ'' \quad (1)$$

An associated capacitance of $1.19 \times 10^{-11} \text{ F}\cdot\text{cm}^{-1}$ (after correction for jig) is obtained at 549 °C and this corresponds to the bulk properties of the material. The corresponding bulk resistivities, R_b of ca. 8.3×10^5 to ca. $2 \times 10^3 \Omega\cdot\text{cm}$ over the temperature range 550–850 °C are obtained from the intercept on the real part of impedance. This

could be associated with the increase in thermally activated drift mobility of electric charge carriers according to the hopping conduction mechanism. In addition, the resistivity falls as the temperature increases, because the probability of carriers being promoted into the conduction band, or being transferred from one defect to another is governed by thermal fluctuations described by the Boltzmann statistics [16]. On the other hand, higher dielectric polarisation may result in higher electric permittivities and higher dielectric losses as the temperature increases [17].

For a highly resistive material, the Nyquist diagram is not completely defined as the data fitting may lead to a gross error. Hence, the capacitance and permittivity value can be extracted based on the electrical response in a high frequency range 10^5 – 10^7 Hz using the equation $-Z'' = 1/(jC_b \times 2\pi f)$ where Z'' is the imaginary part of impedance, $j = (-1)^{1/2}$ and ω is the angular frequency. The capacitance C_b of the bulk material can be determined from the slope of the plot $-Z''$ vs. $1/2\pi f$. A bulk capacitance of 1.19×10^{-11} F·cm $^{-1}$ (after correction for stray capacitance from the empty jig) is obtained for $\text{Bi}_3\text{Zn}_{1.84}\text{Nb}_3\text{O}_{13.84}$ at 549 °C (Fig. 2) which agrees reasonably well with that obtained from the Cole–Cole plot ($\omega RC_b = 1$).

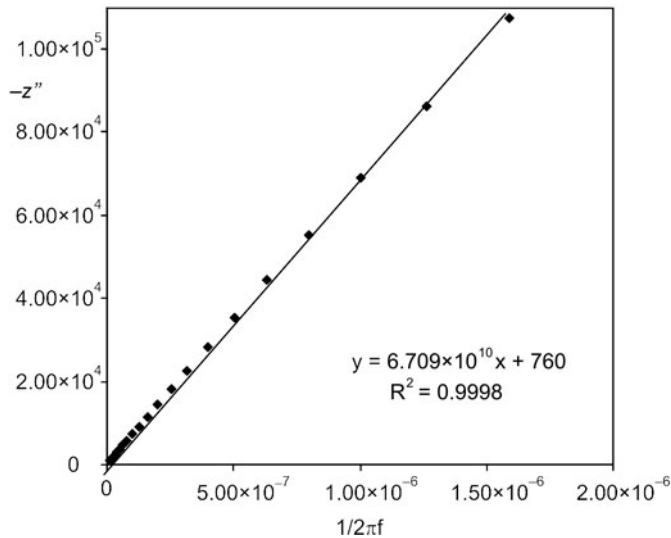


Fig. 2. Imaginary part of impedance, Z'' as a function of the reciprocal angular frequency at 549 °C

The impedance data of the material are further examined using the combined spectroscopic plots of imaginary components of the complex impedance, Z'' and electric modulus, M'' . The frequency maxima of Z'' and M'' should be coincident, and the full width at half maximum (FWHM) should be equal to 1.14 decades for an ideal Debye response representing bulk properties. There appears to be no grain boundary effect as two overlapping peaks with FWHM value of ca. 1.15 decades are obtained (Fig. 3), indicating that the material is homogeneous.

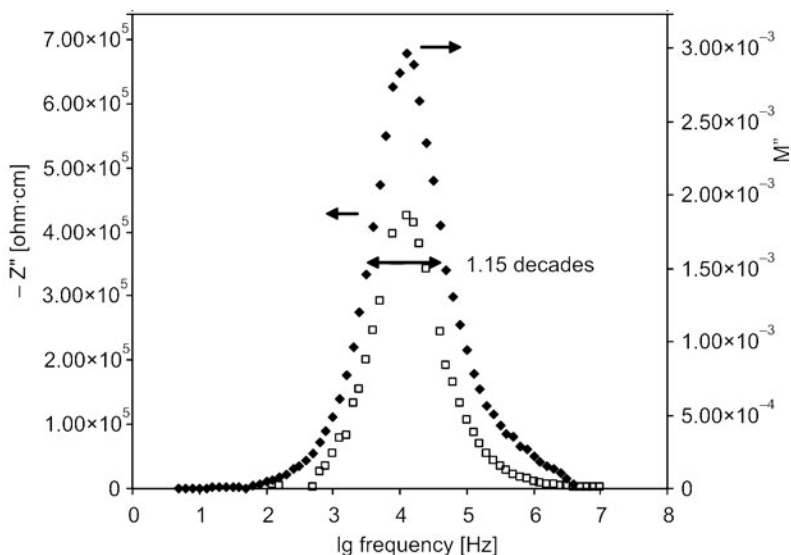


Fig. 3. Combined Z'' and M'' spectroscopic plots for cubic pyrochlore $\text{Bi}_3\text{Zn}_{1.84}\text{Nb}_3\text{O}_{13.84}$ at $549\text{ }^\circ\text{C}$

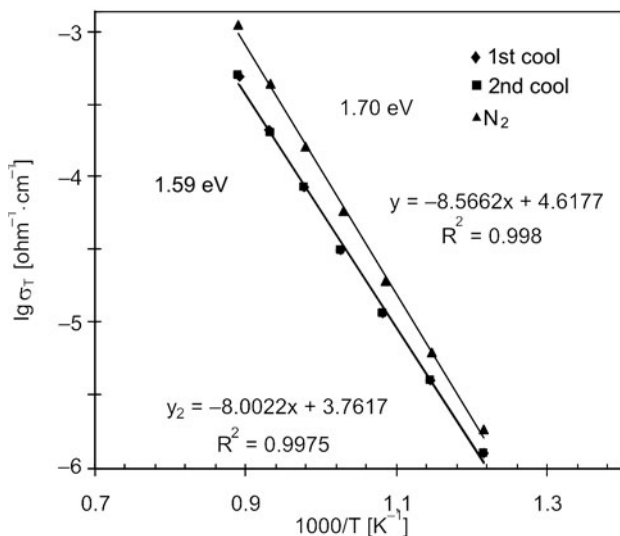


Fig. 4. Conductivity Arrhenius plots of cubic pyrochlore, $\text{Bi}_3\text{Zn}_{1.84}\text{Nb}_3\text{O}_{13.84}$

Figure 4 shows the electrical conductivity of the material as a function of temperature. The Arrhenius law is applied in order to correlate the observed behaviour with a general relation, $\sigma = \sigma_0 \exp(-E_a/kT)$ where σ_0 represents a pre-exponential factor, E_a is the apparent activation energy of the conduction process, k is Boltzmann's constant and T is the absolute temperature. The conductivity data are reproducible and reversible in heat-cool cycles with a high activation energy of ca. 1.59 eV. Usually, high

activation energy is required for the occurrence of a hopping type electronic mechanism, especially with the presence of defects of the oxygen vacancy in the pyrochlore structure [14, 15]. The conductivity at room temperature is determined by data extrapolation. Cubic pyrochlore, $\text{Bi}_3\text{Zn}_{1.84}\text{Nb}_3\text{O}_{13.84}$, exhibits conductivity which is an order of magnitude lower than that of bismuth zinc antimonite (BZS) material with the value of $1 \times 10^{-21} \Omega^{-1} \cdot \text{cm}^{-1}$ at room temperature. The high resistivity of Bi based pyrochlores has been noted in literature and these materials are mainly used for dielectric applications [18].

Oxides are susceptible to oxygen loss with creation of anion vacancies and associated reduction at high temperature, especially under reducing atmosphere where a process, $2\text{O}^{2-} \rightarrow \text{O}_2 + 4e^-$ takes place. In a nitrogen atmosphere, $\text{Bi}_3\text{Zn}_{1.84}\text{Nb}_3\text{O}_{13.84}$ exhibits n-type conduction behaviour with higher conductivity and the activation energy of 1.70 eV (Fig. 4). This may be considered as evidence that cation disordered pyrochlores (A \leftrightarrow B exchange) exhibit a high level of intrinsic oxygen Frenkel disorder ($48f \rightarrow 8b$). It was suggested by Clayton et al. [19] that $\text{Bi}_3\text{Zn}_2\text{Nb}_3\text{O}_{14}$ pyrochlore disclosed an n- to p-type behaviour as a function of temperature and partial pressure of oxygen. The p-type conductivity dominated at high pressure of oxygen, under oxidizing conditions and n-type conductivity dominated at low p_{O_2} with considerable ionic contribution to the conductivity, due to the presence of the shallow minimum in conductivity measurements.

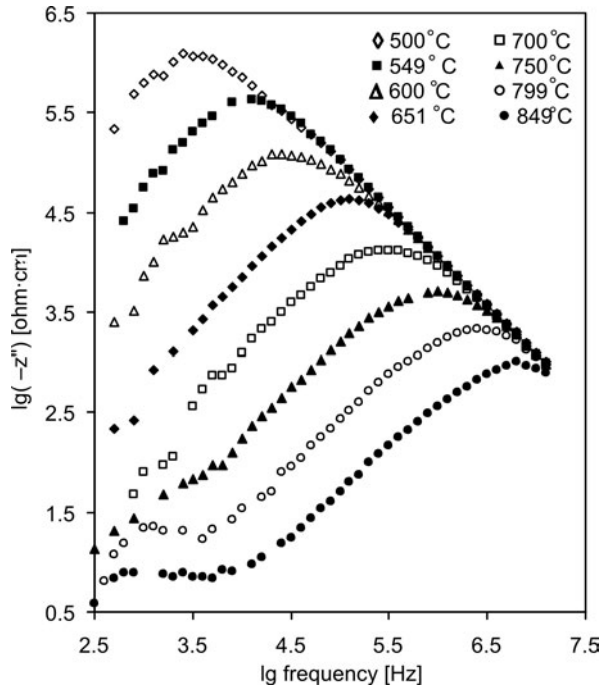


Fig. 5. Imaginary part of impedance as a function of frequency for cubic pyrochlore, $\text{Bi}_3\text{Zn}_{1.84}\text{Nb}_3\text{O}_{13.84}$ at various temperatures

A dispersion of imaginary impedance, Z'' as a function of frequency is shown in Fig. 5. The maxima of the curves shift towards a higher frequency region as the measuring temperature increases; this indicates the presence of a polarisation process in the dielectric material.

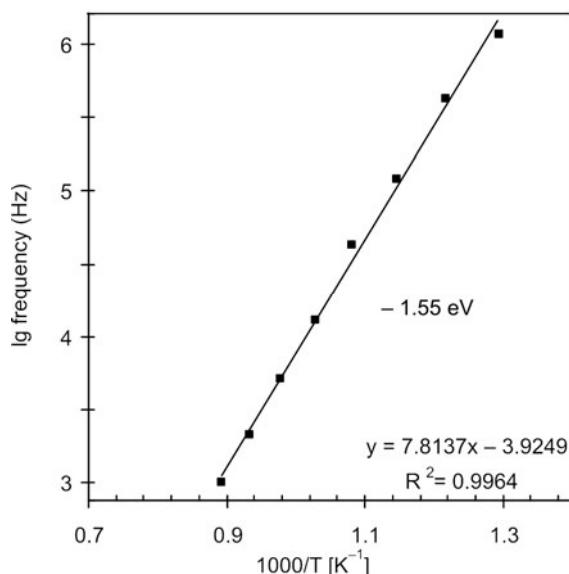


Fig. 6. Arrhenius plot for peak frequency of cubic pyrochlore, $\text{Bi}_3\text{Zn}_{1.84}\text{Nb}_3\text{O}_{13.84}$

Peak frequencies in Fig. 6 are used in the Arrhenius plot (peak frequency type) to show its dependence on temperature. Figure 6 shows the evolution of the peak frequency that follows the Arrhenius law with an apparent activation energy of 1.55 eV. This value is in good agreement with the activation energy calculated from the conductivity Arrhenius plot, i.e. 1.59 eV. This suggests strongly that the electrical behaviour of cubic pyrochlore, $\text{Bi}_3\text{Zn}_{1.84}\text{Nb}_3\text{O}_{13.84}$ is influenced by the polarisation phenomenon in the crystalline lattice and that the conduction mechanism is of the hopping type [14, 15].

The electric modulus is inversely proportional to the capacitance C . The peak heights of the modulus plots (Fig. 7) are independent of temperature, indicating that $\text{Bi}_3\text{Zn}_{1.84}\text{Nb}_3\text{O}_{13.84}$ does not exhibit ferroelectric properties in the temperature range studied. Similarly, the dielectric relaxation behaviour of ideal BZN cubic pyrochlore, $\text{Bi}_3\text{Zn}_2\text{Nb}_3\text{O}_{14}$ has been studied and it was suggested that the material is neither a dipolar glass nor a relaxor ferroelectric [20]. The complex dielectric response of $\text{Bi}_3\text{Zn}_2\text{Nb}_3\text{O}_{14}$ between 100 Hz and 100 kHz revealed a dielectric relaxation below the polar phonon frequencies. Relaxation at room temperature was observed at the frequency of 10^8 Hz, and the high frequency limit of relaxation frequencies was nearly temperature independent. The relaxation was postulated to be associated with hopping

of disordered Bi and Zn atoms at A sites (each of the A atoms occupy one of 6 equivalent, closely spaced positions) and hopping of O' atoms among 12 sites [20].

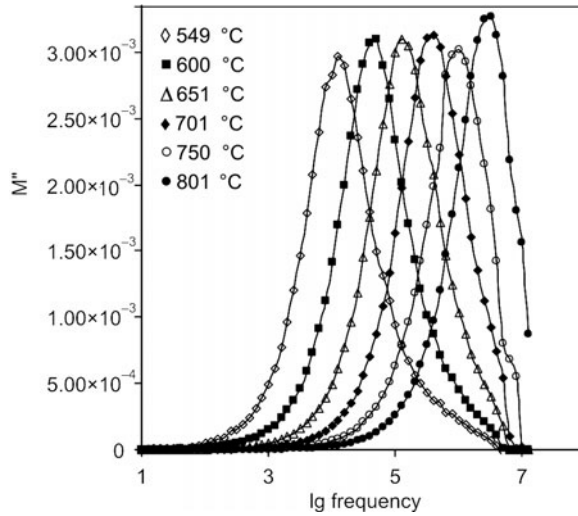


Fig. 7. Imaginary part of electrical modulus as a function of frequency

The complex electric permittivity ϵ^* can be expressed as a complex number

$$\epsilon^* = \epsilon'(\omega) - j\epsilon''(\omega) \tag{2}$$

where ϵ' and ϵ'' are the real and imaginary parts of the complex permittivity.

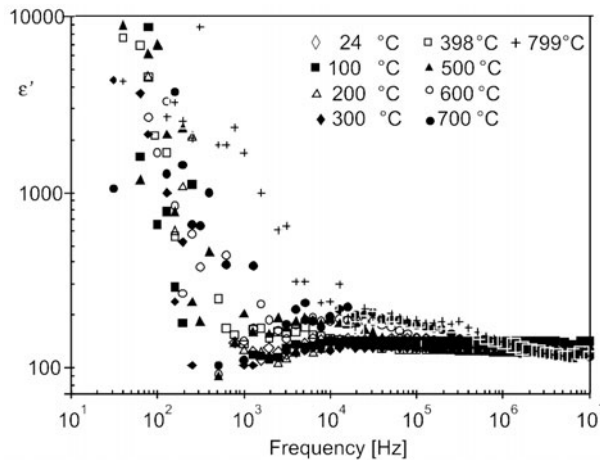


Fig. 8. Permittivity, ϵ' , as a function of frequency at various temperatures

Figure 8 illustrates the relative permittivity of $\text{Bi}_3\text{Zn}_{1.84}\text{Nb}_3\text{O}_{13.84}$ as a function of frequency. High dispersion characteristics in the curves at frequencies lower than

1 kHz could be attributed to the dielectric material behaviour where a conduction mechanism of the hopping type is present [14, 15]. This is probably due to the atomic defects in cubic pyrochlores where intrinsic oxygen vacancies are present. On the other hand, permittivity depends on the concentration of defects and on the extent to which the internal field is raised above the applied field. Occurrence of a continuous flow of the current rather than a limited oscillation between sites is noted to be due to high concentration of defects and/or high probability of hopping events. This contribution to the permittivity is small while the resistivity remains at a sufficiently high level for the dielectric to be of practical interest [16]. The degree of dispersion decreases as the frequency increases. In the frequency range of 10–10³ kHz, a frequency-independent response is observed over the entire temperature range studied (Fig. 8). This may be attributed to the inherent characteristic of dielectric materials as the oscillating system cannot follow the resonant frequency or jumping frequency, ω_r , in an applied field.

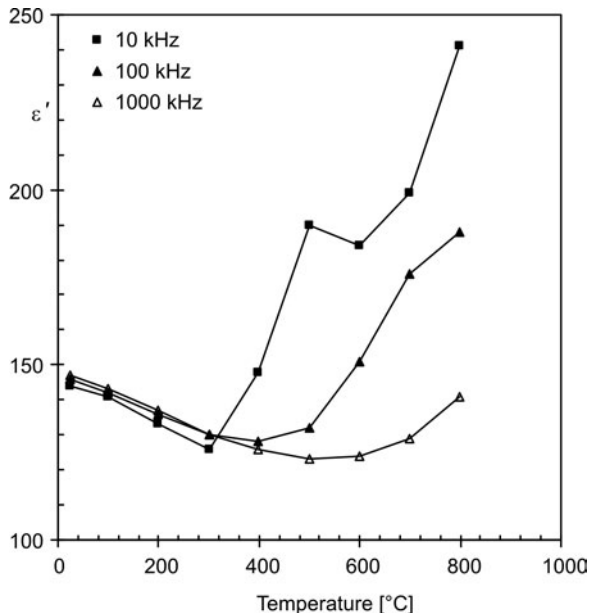


Fig. 9. Real part of complex permittivity as a function of temperature at several frequencies

Figure 9 illustrates the temperature dependence of the real part of the complex permittivity at several frequencies. The decline in permittivity in the temperature range 25–400 °C (100–1000 kHz) indicates a negative temperature coefficient of permittivity of ca. 396 ppm/°C which is comparable to the reported value –400 ppm/°C [21, 22].

The dielectric loss can be expressed as

$$\tan \delta = \frac{\varepsilon''(\omega)}{\varepsilon'(\omega)} \quad (3)$$

A dense and pore free structure is a prerequisite for a low loss dielectric, as the pores may take up moisture which results in a higher dielectric loss, particularly if soluble ions are leached from the solid phase.

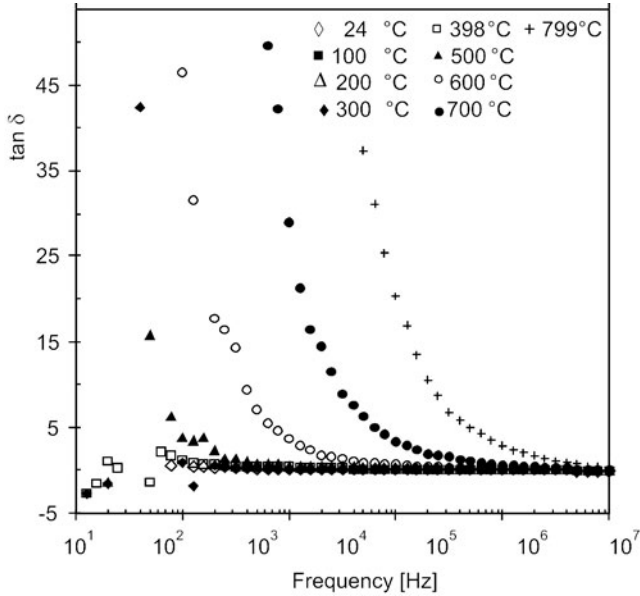


Fig. 10. Dielectric losses, $\tan\delta$, as a function of frequency at several temperatures

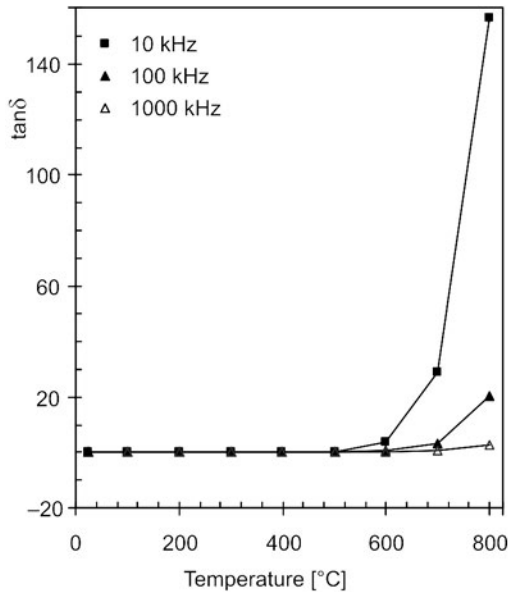


Fig. 11. Dielectric losses, $\tan\delta$, as a function of temperature at several frequencies

Dielectric losses at various temperatures are shown in Fig. 10. All the curves display a similar frequency independent behaviour below 500 °C. Above 500 °C, an appreciable increase in the dielectric losses is observed. Dielectric losses are strongly dependent on frequencies, i.e., lower losses are observed at higher frequencies (Fig. 11). The behaviour below 500 °C could be associated with the frequency independence of dielectric loss (above kilohertz region) of BZN cubic pyrochlore with hopping conduction mechanism mentioned earlier. High dielectric loss at low frequencies is possibly due to time availability for the displacement of defects. Energy is lost through the movement of the screening charge (adjustment of surrounding ions relative to their state when the defect is absent) against the applied field. The ratio of energy lost, W_L to energy stored, W_S in each hopping transition is represented by $W_L/W_S = (1 - \zeta)/\zeta$ where ζ is the restraint of screening imposed by the lattice [16]. On the other hand, increase in temperature (above 500 °C) may increase the number of thermally activated charge carriers (defects) and this will lead to displacement of defects. $\text{Bi}_3\text{Zn}_{1.84}\text{Nb}_3\text{O}_{13.84}$ possesses the highest value of relative permittivity and the lowest dielectric loss in comparison with two analogous systems, $\text{Bi}_3\text{Zn}_2\text{M}_3\text{O}_{14}$, (M = Ta and Sb). There is a decrease in the relative permittivity and increase in the dielectric loss going from Nb to Sb system with the values of ca. 148, 48 and 0.002, 0.006, respectively [22–24]. This could be associated with the substitution of less polarisable Sb^{5+} or Ta^{5+} cation.

4. Conclusion

The cubic pyrochlore, $\text{Bi}_3\text{Zn}_{1.84}\text{Nb}_3\text{O}_{13.84}$ exhibits a typical dielectric behaviour in the frequency and temperature ranges studied. High dispersion of permittivity and high dielectric loss at low frequencies, and frequency-independent permittivity and dielectric loss at high frequencies (> 100 kHz) with much lower permittivity and dielectric loss are observed. These phenomena could be attributed to the dielectric behaviour of the material, where a conduction mechanism of a hopping type is present. In general, the sample is highly resistive with a high activation energy of ca. 1.59 eV; a high relative permittivity value, 147 and low dielectric loss, 0.002, making it a potential candidate in multilayer ceramic capacitors.

Acknowledgements

Financial support from Ministry of Science, Technology and Innovation (MOSTI) is gratefully acknowledged. Special thanks are extended to Prof. A.R. West for his constructive suggestions and comments on impedance study.

References

- [1] HEYWANG W., THOMANN H., *Positive Temperature Coefficient Resistors*, [In:] B.C.H Steele (Ed.), *Electronic Ceramics*, Elsevier, Amsterdam, 1991, p. 29.

- [2] RAO C.N.R., GOPALAKRISHNAN J., *New Direction in Solid State Chemistry*, 2nd Ed., Cambridge University Press, Cambridge, 1997.
- [3] MUKTHA B., DARRIET J., GIRIDHAR MADRAS., GURU ROW T.N., *J. Solid State Chem.*, 179 (2006), 3919.
- [4] SEGAL D.L., *Powders for Electronics*, [In:] B.C.H. Steele (Ed.), *Electronic Ceramics*, Elsevier, Amsterdam, 1991, p. 185.
- [5] CANN D.P., RANDALL C.A., SHROUT T.R., *Solid State Commun.*, 100 (1996), 529.
- [6] ZHOU W., *J. Solid State Chem.*, 101 (1992), 1.
- [7] SUBRAMANIAM M.A., ARAVAMUDAN G., SUBBA RAO G.V., *Progr. Solid State Chem.*, 15 (1983), 55.
- [8] VALANT M., SUROROV J. *Am. Ceram. Soc.*, 88 (2005), 2540.
- [9] NINO J.C., LANAGAN M.T., RANDALL C.A., *J. Mater. Res.*, 16 (2001), 1460.
- [10] WITHERS R.L., WELBERRY T.R., LARSSON A-K., LIU Y., NOREN L., RUNDLOF H., BRINK F.J., *J. Solid State Chem.*, 177 (2004), 231.
- [11] TAN K.B., LEE C.K., ZAINAL Z., MILES G.C., WEST A.R., *J. Mater. Chem.*, 15 (2005), 3501.
- [12] VANDERAH T.A., LEVIN I., LUFASO M.W., *Eur. J. Inorg. Chem.*, (2005), 2895.
- [13] LEVIN I., AMOS T.G., VANDERAH T.A., RANDALL C.A., LANAGAN M.T., *J. Solid State Chem.*, 168 (2002), 69.
- [14] NOBRE M.A.L., LANFREDI S., *Mater. Lett.*, 47 (2001), 362.
- [15] NOBRE M.A.L., LANFREDI S., *Appl. Phys. Lett.*, 81 (2002), 451.
- [16] HERBERT J.M., *Ceramics Dielectrics and Capacitors*, [In:] D.S. Campbell (Ed.), *The Properties of Dielectrics*, Gordon and Breach, New York, 1985, p. 9.
- [17] DU H.L., YAO X., WANG H., *Ferroelectrics*, 262 (2001), 89.
- [18] RANDALL C.A., NINO J.C., BAKER A., YOUN H-J., HITOMI A., THAYER R., EDGE L.E., SOGABE T., ANDERSON T.D., SHROUT T.R., TROLIER-MCKINSTRY S., LANAGAN M.T., *Am. Ceram. Soc. Bull.*, (2003), 9101.
- [19] CLAYTON J., TAKAMURA H., METZ R., TULLER H.L., WUENSCH B.J., *J. Electroceramic*, 7 (2001), 113.
- [20] KAMBA S., POROKHONSKY V., PASHKIN A., BOVTUN V., PETZELT J., *Phys. Rev. B.*, 66 (2002), 054106.
- [21] NINO J.C., LANAGAN M.T., RANDALL C.A., *J. Applied. Phys.*, 89 (2001), 4512.
- [22] WANG X.L., WANG H., YAO X. *J. Am. Ceram. Soc.*, 80 (1997), 2745.
- [23] YOUN H.J., SOGABE T., RANDALL C.A., SHROUT T.P., LANAGAN M.T., *J. Am. Ceram. Soc.*, 84 (2001), 2557.
- [24] DU H.L., YAO X., *Mater. Electr.*, 15 (2004), 13.

Received 12 May 2008
Revised 31 October 2008

Electrostriction and electromechanical coupling in elastic dielectrics at nanometric interfaces

O.P. THAKUR, A. KUMAR SINGH*

School of Applied Sciences, Netaji Subhas Institute of Technology, Sector-3,
Dwarka, New Delhi-110078, India

Electrostrictive coefficients, expressed in terms of dielectric parameters and elastic constants, are obtained for elastic dielectrics. In most of the recent experiments concerning determination of electrostrictive parameters in elastic dielectrics, several researchers used incorrect equations without considering the contribution from the edge effect, the shear stresses and suitable boundary conditions. This led to wrong predictions of experimental results particularly for materials with high Poisson ratios. Errors in the estimation of induced strains, varying from an underestimation of 202% to an overestimation of 168%, have been pointed out in the case of polycarbonate (PC). However, the contribution from the boundary conditions is very difficult to predict correctly and hence it is still unresolved. The electromechanical properties of the nanometric interface are also discussed. Due to significant electrostrictive and piezoelectric characteristics of the nanometric interface, PC has a great potential for electromechanical applications as electromechanical transducers, sensors and actuators.

Key words: *nanodielectric; electrostriction; elastomer*

1. Introduction

The objective of this work is to provide a clear understanding of the possible mechanism involving various dielectric and mechanical parameters for electric field induced strains in elastic dielectrics. The elastic deformation of a dielectric material under the forces exerted by electrostatic fields is called electrostriction. The mechanical deformation (stresses and strains) induced in a dielectric material (generally non piezoelectric) under the influence of an electric field occurs in two processes. The Maxwell stress effect occurs due to variation in the electric field distribution under strain, and the phenomena of electrostriction occur due to variation in the dielectric properties of the material under strain. The deformed material is no longer isotropic,

*Corresponding author, e-mail: opthakur@yahoo.com

and the scalar permittivity (ϵ) becomes a dielectric tensor (ϵ_{ij}) due to anisotropic dielectric properties, in the case of an elastic dielectric material.

In equilibrium, the total forces, i.e. the total internal body forces F_{int} and the total external forces F_{ext} such as forces due to a gravitational field, in every volume element of elastic dielectrics must be balanced to a zero value [1]:

$$F_{\text{int}} + F_{\text{ext}} = 0 \quad \text{or} \quad \sum_{j=1}^3 \frac{\partial T_{ij}}{\partial x_j} + \rho g_i = 0 \quad (1)$$

where $F_{\text{ext}} = \rho g_i$ is an external force due to a gravitational field g_i in a vertically downward direction Γ and T_{ij} is the mechanical stress tensor. If there is another external force instead of a gravitational force, then the vector ρg_i on the right hand side of above Eq. (1) must be replaced accordingly. But in the absence of external field, we have

$$\sum_{j=1}^3 \frac{\partial T_{ij}}{\partial x_j} = 0 \quad (2)$$

The strain tensor, S_{ij} , describes the state of an elastic dielectric material subjected to a small deformation, and is given as

$$S_{ij} = S_{ji} = \frac{1}{2} \left(\frac{\partial s_i}{\partial x_j} + \frac{\partial s_j}{\partial x_i} \right) \quad \text{for} \quad i \neq j \quad (3)$$

where \mathbf{s} is a displacement vector.

As the deformation is extremely small, only the first order terms in S_{ij} have been considered in the variation of components of the dielectric tensor ϵ_{ij} and the dielectric tensor is given as

$$\epsilon_{ij} = \epsilon^0 \delta_{ij} + a_1 S_{ij} + a_2 S_{kk} \delta_{ij} \quad (4)$$

where ϵ^0 is the permittivity of the undeformed body, and a_1 and a_2 are two parameters describing the variation in the dielectric properties of the material under shear and bulk deformations, respectively. The general form of the dielectric tensor, ϵ_{ij} , for the deformed material is

$$\epsilon_{ij} = \epsilon_{ij}^0 + a_{ijkl} S_{kl} \quad (5)$$

where a_{ijkl} is a constant tensor of rank four.

For linear and anisotropic dielectric under small deformation, the variation in the dielectric tensor ϵ_{ij} is given as

$$\delta\epsilon_{ij} = \sum_{k=1}^3 \sum_{l=1}^3 a_{ijkl} \delta S_{kl} \quad (6)$$

and the coefficients

$$a_{ijkl} = \frac{\partial \epsilon_{ij}}{\partial S_{kl}} \quad (7)$$

represent a tensor of rank four characteristic of dielectrics, and also have different values at different points in an inhomogeneous dielectric medium. However, all but two classes of coefficients are approximately zero, namely the body strain coefficients a_{iiii} and a_{ijij} and the shear strain coefficients a_{ijij} [1].

Electromechanical phenomena have been observed in several macroscopic systems such as polycrystalline ceramics, ceramic polymer composites, several organic polymers, biopolymers, single crystals, systems with a liquid component, etc. However, this effect is very small in the case of solid dielectrics. Experimental data on the subject are not abundant, and the researchers [2, 3] frequently used an incorrect formula in the derivation of elastic strain with respect to the Maxwell stress effect, particularly in the case of polyurethane elastomer (a cross-linked polymer), assuming various unrealistic approximations [4]. A linear electromechanical effect does not exist in the case of elastomers and Hooke's law based on thermodynamic consideration (Helmoholtz free energy and Gibbs free energy concept) should not be applied for elastomers up to a large extent due to its nonlinear elastic behaviour. Electromechanical coupling effects in the case of non-piezoelectric material such as polyurethane elastomers have been exploited in the areas of fundamental sensors and actuators [5, 6]. Due to potential applications in sensing and actuation, the electrostrictive response is very important [7].

The coupling between electrical and mechanical fields at the nanometric scale has been poorly exploited up to now. The interface between two dissimilar macroscopic phases in mutual contact has invariably different properties from the bulk on the either side in continuum. The electric fields at the interface induce a mechanical stress in addition to influencing polarization and conduction phenomena. The exploitation of the interface as electromechanical transducers is the real challenge in the development of nanometric dielectrics.

2. Electrostriction in elastic dielectrics: A theoretical approach

Fundamental assumptions of the theoretical approach to electrostriction in elastic dielectrics are as follows:

- A. In unstrained state, electric and elastic properties are assumed to be isotropic.
- B. On application of an electric field, variations in permittivity are dependent on the components of strain and as a result, the material becomes electrically anisotropic .
- C. In static equilibrium, the elastic forces induced during deformations will balance the mechanical forces induced by the static field.

D. The relation between the mechanical stress (T_{ij}) and the strain (S_{ij}) is governed by Hook's law.

E. Deformation is extremely small.

F. The dependence of D on E is linear even in an anisotropic dielectric and D and E are parallel only along preferred axes, i.e.

$$D_i = \epsilon_0 \sum_{j=1}^3 \epsilon_{ij} E_j$$

where ϵ_0 is the permittivity of a free space.

The Maxwell stress tensor [8] results from a force produced by the electric field and is given as

$$T_{ij} = T_{ij}^0 + \frac{\epsilon_0}{2} (2\epsilon^0 - a_1) E_i E_j - \frac{\epsilon_0}{2} (\epsilon^0 + a_2) E^2 \delta_{ij} \quad (8)$$

where T_{ij}^0 is the stress tensor in the absence of an electric field. Generally we tend to neglect T_{ij}^0 in isotropic dielectrics but in the case of a dielectric interface, the presence of a significant number of point defects introduces distortion in the interfacial region. In the case of a size difference of two particles from two phases, elastic stress and strains are created. A larger atom introduces compressive stress and the corresponding strain around it, while a smaller interacting atom creates a tensile stress-strain field. An interstitial atom also produces strain around the void it occupies.

If the direction of the electric field is assumed to be along the X_3 axis (k direction) in the Cartesian coordinate system, the principal stresses induced electrically are

$$T_{33} = T_{33}^0 - \frac{1}{2} \epsilon_0 \epsilon^0 E^2 \left(1 - \frac{a_1 + a_2}{\epsilon^0} \right) \quad (9)$$

$$T_{11} = T_{22} = T_{11}^0 + \frac{1}{2} \epsilon_0 \epsilon^0 E^2 \left(1 + \frac{a_2}{\epsilon^0} \right) \quad (10)$$

Where $a_1 = \partial\epsilon/\partial S_1 = \partial\epsilon/\partial S_2$, due to strain in the X_1X_2 plane, and $a_2 = \partial\epsilon/\partial S_3$, expresses the increment in the field direction, i.e. along the X_3 axis. T_{11}^0 and T_{33}^0 are the stresses even in the absence of an external field, however these stresses are independent of the direction in the case of isotropic dielectrics, and it should not be neglected at the interface having a significant number of point defects. However, it is very difficult to evaluate T_{ij}^0 precisely.

For a linear elastic dielectric material (described by Hooke's law), the electrically induced stresses will also generate elastic stress and strain in equilibrium condition and the elastic stress tensor T_{ij} [9] is given in terms of the elastic strain tensor, S_{ij} , Young modulus Y and Poisson's ratio, σ , by

$$T_{ij} = \frac{Y}{1+\sigma} \left(S_{ij} + \frac{\sigma}{1-2\sigma} S_{kk} \delta_{ij} \right) \quad (11)$$

conversely

$$S_{ij} = \frac{1}{Y} \left[(1+\sigma) T_{ij} - \sigma T_{kk} \delta_{ij} \right] \quad (12)$$

If the force acts only along the X_3 direction, i.e. along the direction of the electric field E , then we have $S_{11} = S_{22} = 0$, and if the sides of dielectric material are also fixed (Fig. 1), we have $S_{32} = S_{31} = 0$.

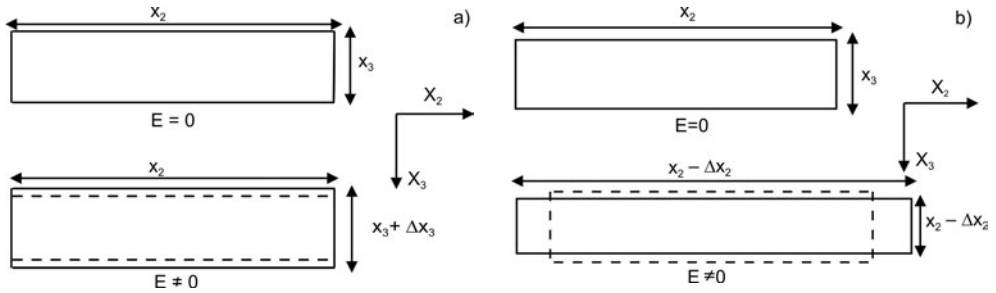


Fig. 1. Schematic diagrams illustrating the effect of electric field E (acting along the X_3 direction) on the elastic dielectric material enclosed between two parallel rigid electrodes: a) sides of a dielectric slab are rigidly fixed as a result of this; no expansion in a lateral direction takes place, i.e., $S_{31} = S_{32} = 0$, b) sides of slab are open and a longitudinal compressive strain S_{33} acts along the X_3 direction, whereas the shear strains, $S_{31} = S_{32}$, act along the X_1 and X_2 directions

For such a unilateral deformation, the principal elastic stresses and strains are

$$T_{11} = T_{22} = \frac{Y}{(1+\sigma)(1-2\sigma)} S_{33} \quad (13)$$

$$T_{33} = \frac{Y(1-\sigma)}{(1+\sigma)(1-2\sigma)} S_{33} \quad (14)$$

$$S_{33} = \frac{p(1+\sigma)(1-2\sigma)}{Y(1-\sigma)} \quad (15)$$

where $T_{33} = p$ is a compressive force, i.e. pressure. On substituting the principal value of the Maxwell stress tensor (assuming $T_{11}^0 = T_{33}^0 = 0$) from Eqs. (9) and (10) into Eq. (12), we can express the principal elastic strains as

$$S_{11} = S_{22} = \frac{1}{2} \epsilon_0 \epsilon^0 E^2 \left(1 - \frac{\sigma a_1}{\epsilon^0} + \frac{(1-2\sigma) a_2}{\epsilon^0} \right) Y^{-1} \tag{16}$$

$$S_{33} = -\frac{1}{2} \epsilon_0 \epsilon^0 E^2 \left((1+2\sigma) - \frac{a_1 + (1-2\sigma) a_2}{\epsilon^0} \right) Y^{-1} \tag{17}$$

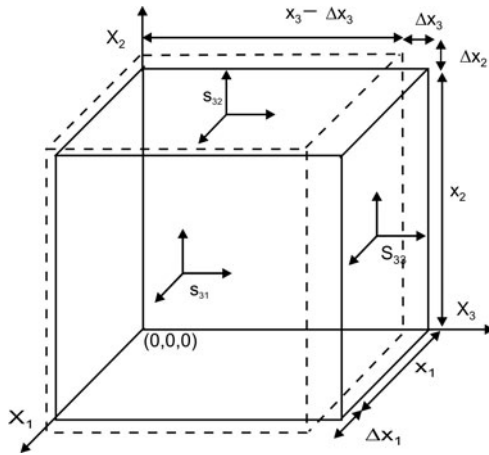


Fig. 2. Schematic diagram illustrating an elastic dielectric subjected to one normal electrical stress along the X_3 direction, causing compressive longitudinal strain S_{32} and two tensile shear strains, S_{31} and S_{32} along the X_1 and X_2 directions, respectively, as the electric field has only one component along the X_3 direction. If E also has other components, then there are other principal strains $S_{11} = S_{22} \neq 0$

The principal elastic strain, S_{33} , represents the relative change in thickness of the interface, whereas the strain, S_{11} or S_{22} , represents the relative change in the diameter of the capacitor, as described in [4], which is not correct in the case of a parallel plate capacitor in which S_{31} or S_{32} actually represent the lateral change in dimension, as E has only a component along X_3 (Fig. 2), i.e. only one normal component of stress, T_{33} , along with its two shearing components, T_{31} or T_{32} . On comparing Eqs. (16) and (17) with a general equation for electrostriction

$$S_{ij} = \gamma_{ijkl} E_k E_l \tag{18}$$

we get

$$S_{11} = S_{22} = \gamma_{31} E^2, \quad S_{33} = -\gamma_{33} E^2 \tag{19}$$

where γ_{31} and γ_{33} are the electrostrictive coefficients. A negative sign for the strain S_{33} indicates that it is a contraction along X_3 and S_{11} and S_{22} are tractions, so causing expansion along the X_1 and X_2 directions.

3. Interface as an electromechanical transducer

Macroscopic electromechanical behaviour arises from interactions occurring at the nanometric interface. At the nanodielectric interface between two phases, the segregation of charge clusters and double layer polarization are responsible for producing

electrostriction in the presence of a non-uniform electric field. If the electric field E is changed to $E + \Delta E$, the change in S_{33} becomes

$$\Delta S_{33} = -2\lambda_{33}E_0\Delta E = \mu_{33}\Delta E \tag{20}$$

where μ_{33} is the piezoelectric coefficient. Similarly, the coefficient μ_{31} and μ_{32} can be found along the X_1 and X_2 directions. The piezoelectric transverse coefficients have been frequently used [10] in piezoelectric thin film devices. The average value of compressive elastic strain induced along the X_3 direction is

$$K \int_0^\lambda \Delta S_{33} dx_3 \tag{21}$$

where λ is the Debye–Hückel length. Similarly, the expression for the tensile strains (ΔS_{32} and ΔS_{31}) along the X_1 and X_2 directions can be obtained.

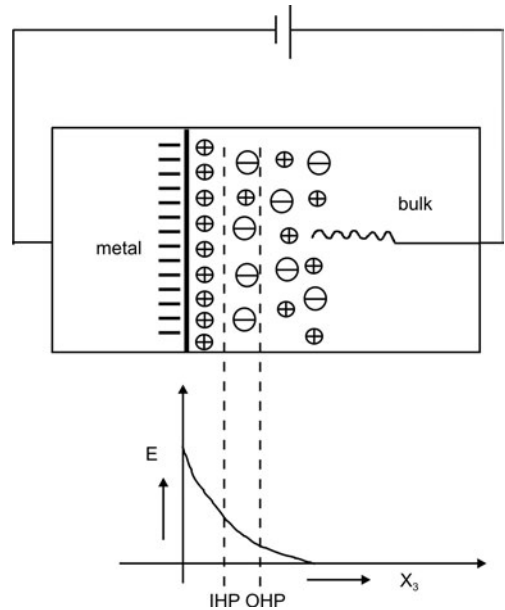


Fig. 3. Schematic diagram showing the formation of electric double layer formed due to segregation of charge clusters at an electrode–electrolyte interface. The distribution of a nonuniform electric field in noncentrosymmetric interface is also shown

At the electrode–electrolyte interface (Fig. 3) having decaying electric fields from the electrode surface, the only modification required for the calculation of E^2 is

$$\overline{E^2} = \frac{1}{\lambda} \int_0^\lambda E^2(x_3) dx_3 \tag{22}$$

The integration is over the thickness of the double layer, i.e. the Debye–Hückel length λ .

If E has only one component along the X_3 direction, we should consider the longitudinal component S_{33} and the transverse components S_{32} and S_{31} , and neglect the prin-

principal strains, S_{11} and S_{22} , as E has no components along the X_1 and X_2 direction but the actual boundary conditions satisfied (after deformations) at the interface between an electrode and dielectric are the points of main concern, and it is very difficult to correctly predict the contributions from boundary conditions. If E has small components along the X_1 and X_2 directions, we should not neglect the principal elastic strains S_{11} and S_{22} .

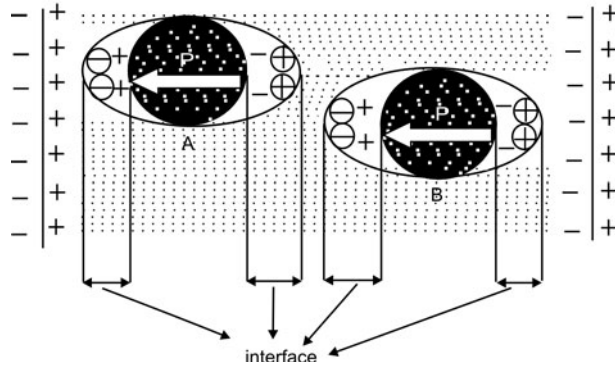


Fig. 4. Schematic diagram illustrating polycrystalline material exhibiting strong piezoelectric properties: a) for $E = 0$, dipoles are randomly oriented and double layers do not form, b) for $E \neq 0$, the material is subjected to the resulting poling process, and a number of interfaces have been formed inside the material. The interface with the double layer formation and the polarization strongly support the existence of piezoelectric characteristic

Recently piezoelectric properties have been created in a polycrystalline or composite material by using poling process. That is why an exfoliated laminar polymer (polypropylene) showed significant piezoelectric properties upon poling [11]. In micro sensor applications of PZT ceramic $\text{Pb}(\text{ZrTiO}_3)$, it has been observed that polycrystalline films with many internal interfaces exhibit a greater piezoelectric response [10, 12], whereas the epitaxial films with two electrode interfaces show a weak response. A number of nanometric structures (rings, helices, bolts etc.) in the ZnO system exhibit ordered polar non-centrosymmetry and most of them can be exploited in a wide range of piezoelectric nanometric electromechanical systems (NEMS) [13]. The above examples point to the interfacial origin of the piezoelectric effect, and these materials have many nanometric interfaces (Fig. 4) with a tremendous potential for electromechanical applications [14].

4. Discussion and comparison with previous experimental results

Errors are often committed in the derivation of suitable expressions for the interpretation of experimental results.

4.1. Contributions from shear stresses

The electromechanical response of the polyurethane elastomer (Dow 2103-80AE) has been obtained and the relative change in the thickness of a dielectric slab between the electrodes of a capacitor has been experimentally determined [3] without considering lateral stresses, the edge effect, boundary conditions and the tensor form of permittivity. The equation used may be written as:

$$\frac{\Delta x_3}{x_3} = \frac{1}{2Y} \epsilon_0 \epsilon^0 E^2 = S_{33} \quad (23)$$

However the correct mathematical expression can be seen from Eq. (17), which indicates that neglecting the lateral stress and the Poisson ratio leads to underestimation of $\Delta x_3/x_3$. Similarly, another researcher [2] used Maxwell's principal stress (Eq. (9)) for the determination of relative change in the thickness of a dielectric slab, neglecting the contributions from lateral elastic stresses and the edge effect. Here, the expression used was

$$\frac{\Delta x_3}{x_3} = -\frac{1}{2Y} \epsilon_0 \epsilon^0 E^2 \left(1 - \frac{a_1 + a_2}{\epsilon^0} \right) \quad (24)$$

Equation (17) gives the correct representation of the expression for elastic dielectrics. In particular, the elastomers, which undergo recoverable deformations of a few hundred percent, do not exhibit linear elastic behaviour (Fig. 5) and do not follow Hooke's law, in contrast to an ordinary elastic material. Thus the experimental results [2, 3] for the cross linking elastomers cannot be correctly predicted from the actual induced strain response using Eqs. (23) and (24).

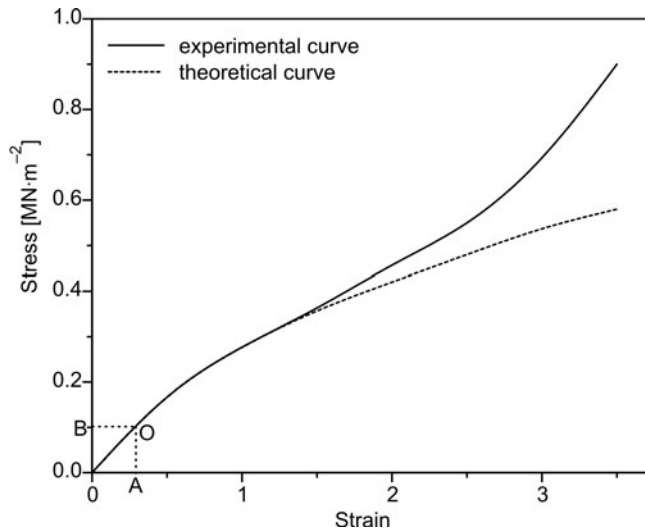


Fig. 5. Nonlinear stress–strain characteristic which does not follow Hooke's law, however, Hooke's law is considered for very small deformation up to the point *O*

Theoretically, Poisson's ratio (σ) varies from -1 to 0.5 but in practice no material is available with $\sigma < 0$ [9]. Poisson's ratio for polymers has been found to be ca. 0.5 [15]. Neglect of lateral stresses, particularly in the case of elastic dielectrics or polymers with high Poisson's ratio, and using Eq. (9) leads to incorrect estimation of the electrically induced strain. On putting $\sigma = 0.5$ in Eq. (17), we get

$$S_{33} = -\frac{1}{2} \varepsilon_0 \varepsilon^0 E^2 \left[2 - \frac{a_1}{\varepsilon_0} \right] Y^{-1} \quad (25)$$

and this is quite different from Eq. (9), in the sense that the contribution from the term a_2 has been cancelled due to the presence of the $(l - 2\sigma)$ term in Eq. (17). Actually the longitudinal principal strain S_{33} calculated from Eq. (25) is twice the value of the strain calculated in [3] from Eq. (23) for a material with $\sigma = 0.5$ and $a_1 = 0$. Errors in the estimations of induced strains can be pointed out in the case of polycarbonate (PC). The following data for polycarbonate are given [16]: $|a_1| = 1.404$, $|a_2| = 2.6$, $|a_2| = 2.6$, $\varepsilon^0 = 2.9^*$ at 1 MHz, $\sigma = 0.37$ at 1 MHz.

Comparing Eqs. (23) and (24) with Eq. (17), after substituting the above data, an overestimation of 168% and an underestimation of 202%, respectively, have been found.

The use of the correct Eq. (17) is necessary, particularly for the material having a high Poisson's ratio. Using the dielectric constant and the elastic compliance data, the contribution of the Maxwell stress to the total strain response can be determined.

If the sides of the dielectric slab/interface are rigidly fixed, the effective stiffness (T_{33}/S_{33}) is governed by Eq. (14). The dielectric parameters, a_1 and a_2 , are experimentally obtained [16] by determining $d\varepsilon_{33}/dS_{33}$ in constrained and unconstrained conditions, and using Eq. (4). However, the linearity of the theory of electrostriction fails if the deformations are not quadratic in the applied field, particularly at a higher field strength.

In the case of dielectrics with a non-uniform field, e.g. cylindrical capacitor and nanometric interface, we should use either Eq. (22) or deal with the problem separately to evaluate $\overline{E^2}$ for the situation. In the presence of a non-uniform electric field with a high field strength, the phenomenon of dielectrophoresis takes place. However, it is in general a weak effect, particularly in the case of a solid dielectric.

4.2. Contributions from edge effects

Due to free edges of plates of a capacitor, the distribution of charge over them is not uniform. Hence a correction due to edge effects [8] is very much required for all practical purposes in which the thickness of the dielectric slab is comparable to its

*www.matweb.com.

lateral dimension i.e., $\Delta x_3 \approx (\text{cross sectional area of plate})^{1/2}$. However, this correction may be neglected in the case of a thin film capacitor and a nanometric interface having a lateral dimension that is much greater relative to its thickness (typically of order a few nm).

4.3. Contribution from boundary conditions

For experimental study [3, 16], a parallel plate capacitor with a dielectric film/slab has been considered, due to its simple, symmetrical geometry. However, due to electrostrictive deformation, the permittivity of different regions (Fig. 1 shows two regions, one with an air gap and other with a dielectric medium) is different, thus the solution to the field or potential must be different although having the same general form of solution (to the Laplace equation). Appropriate electrical boundary conditions must be satisfied at the interface between the two regions.

For the mechanical boundary conditions, Eq. (1) must be satisfied in equilibrium, i.e. the external forces on the boundary may be regarded as a continuation of the internal stress distribution.

However, it is very difficult to predict exact boundary conditions at the interface between electrodes and the dielectric or between two regions with different permittivities. If the field is applied exactly along the X_3 direction, the strain components, S_{33} (normal/bulk strain along X_3), and S_{31} and S_{32} (shear strains along the X_1 and X_2 directions) play the major role in the electromechanical phenomena exhibited by the interface in nanometric dielectrics [17].

5. Conclusion

In elastic dielectrics, shear and lateral stresses play a major role in the correct estimation of induced elastic strain. Thus neglecting the contribution from lateral and shear stresses leads to overestimation or underestimation of the results. However, the boundary conditions at the interface between electrode and the dielectrics are the points of main concern, as it is very difficult to predict exact mechanical and electrical boundary conditions in deformed dielectrics. It has also been pointed out that nanometric dielectric interfaces, which are non-centrosymmetric systems, have tremendous potential for electromechanical applications. A lot of work has to be done, particularly in the field of biology, cellular polymers, biopolymers, intercellular biomembranes, etc. at the nanoscale level, in order to exploit nanometric interfaces for various applications as sensors, actuators and transducers.

References

- [1] STRATTON J.A., *Electromagnetic Theory*, McGraw-Hill, New York, 1941.
- [2] SHKEL Y.M., KLINGENBERG D.J., *J. Appl. Phys.*, 80 (1996), 4567.

- [3] ZHANG Q.M., SU J., KIM C.H., TING R., CAPPS R., J. Appl. Phys., 81 (1997), 2770.
- [4] KRAKOVSKÝ L., ROMIJN T., POSTHUMA DE BOER A., J. Appl. Phys., 85 (1999), 628.
- [5] LADABAUM I., KHURI-YAKUB B.T., SPOLIANSKY D., Appl. Phys. Lett., 68 (1996), 7.
- [6] HERBERT J.M., *Ferroelectric Transducers and Sensors*, Gordon and Breach, New York, 1982.
- [7] *Electroactive Polymer (EAP) Actuators as Artificial Muscles: Reality, Potential and Challenges*, 2nd Ed., Y. Bar-Cohen (Ed.), SPIE Press, Bellingham, WA, Vol. PM 136, 2004.
- [8] LANDAU L.D., LIFSHITZ L.M., *Electrodynamics of Continuous Media*, 2nd Ed., Pergamon Press, Oxford, 1984.
- [9] LANDAU L.D., LIFSHITZ L.M., *Theory of Elasticity*, Pergamon Press, Oxford, 1970.
- [10] KANNO I., KOTERA H., WASA K., Sensors Act. A, 107 (2003), 68.
- [11] MONTANARI G.C., IEEE Trans. DEI, 10 (2003), 615.
- [12] KANNO I., FUJII S., KAMADA T., TAKAYAMA R., Appl. Phys. Lett., 70 (1997), 1378.
- [13] WANG Z.L., Materials Today (2004), 26.
- [14] LEWIS T.J., J. Phys. D: Appl. Phys., 38 (2005), 202.
- [15] FERRY J.D., *Viscoelastic Properties of Polymers*, Wiley, New York, 1980.
- [16] LEE H.Y., PENG Y., SHKEL Y.M., J. Appl. Phys., 98 (2005), 074104.
- [17] THAKUR O.P., SINGH A.K., *Electromechanical Phenomena at the Interface in Nanometric Dielectrics*, Proc. 2nd Int. Conf. on Sensing Technology, ICST, Palmerston North, New Zealand, pp. 188–192, 2007.

Received 16 May 2008
Revised 28 November 2008

Thermal degradation of solvent-borne water soluble acrylic acid–butyl acrylate copolymers

Z. CZECH*, R. PELECH

Institute of Chemical Organic Technology, Szczecin University of Technology,
Pułaskiego 10, 70-322 Szczecin, Poland

Thermal degradation of water soluble copolymers synthesized from acrylic acid and butyl acrylate, used as water soluble self-adhesives, especially for bonding of different kinds of paper, was investigated at 250 °C using pyrolysis-gas chromatography. The thermal degradation process and the kind and amounts of the pyrolysis products provide relevant information about the thermal resistance of water soluble acrylic adhesives. It was observed that during the pyrolysis of acrylic acid–butyl acrylate copolymers main breakdown products as carbon dioxide, butene-1, butanol-1, butyl acrylate and butyl methacrylate were formed.

Key words: *adhesion; pressure-sensitive adhesive; thermal resistance; thermal degradation products*

1. Introduction

Solvent-borne water soluble polymers, used as pressure sensitive adhesives (PSAs), are still something of a speciality. They are applied as one-sided and double-sided tapes or as transfer films for web splicing in the paper industry. A challenging area of water soluble PSA application is their use for water-dispersible labels, medical devices, such as surgical tapes and bioelectrodes [1]. Solvent-based water soluble PSAs can be synthesized using a water-insoluble monomer, such as butyl acrylate (BA), and soluble monomers, such as acrylic acid (AA) or β -acryloyloxy propionic acid (PAA) [2].

Times of dissolution in water of acrylic copolymers based on unsaturated acrylic acid or β -acryloyloxy propionic acid and butyl acrylate at various pH values (4, 7 and 11) are shown in Fig. 1 [3]. It is evident from the figure that the increase in pH value improves the water solubility of acrylic PSAs containing hydrophilic acids in the polymer structure. A shorter dissolving time was observed for polymers containing

*Corresponding author, e-mail: psa_czech@wp.pl

acrylic acid. In the manufacture, coating and printing of various paper types, the continuous production methods used in the paper industry require paper reels to be spliced by joining the end of one reel to the beginning of the next. Similarly, paper reels must be spliced back together after blemishes and defects have been cut out. For this purpose either double-sided, single-sided or transfer adhesive tapes are used, depending on the individual application. These tapes containing water soluble acrylic copolymers are characterised by aggressive bonding strength on the paper surface.

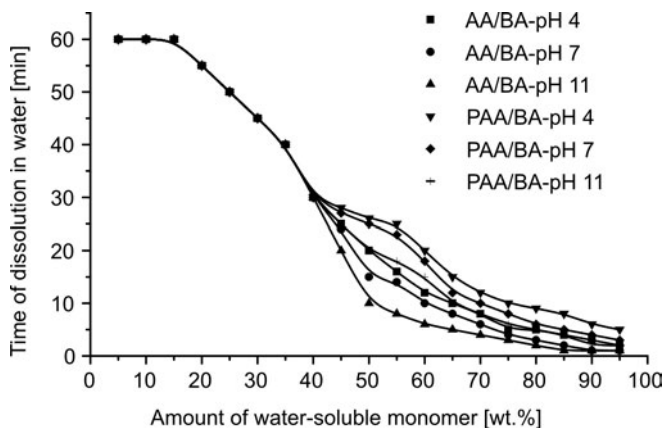


Fig. 1. Times of dissolution in water of PSAs at various pH values and various concentrations of unsaturated acid monomers

Since many processes in the paper industry require high temperatures (180–240 °C), reliable adhesion at these temperatures must be ensured by appropriate thermal shear strength of the splicing tape. In the interest of recycling, the splices which are cut out are not discarded, but are recovered for reprocessing and, therefore, the pressure-sensitive adhesives used in the manufacture of splicing tapes must be completely water soluble under production conditions [4]. A goal of this investigation was the testing of the thermal resistance and the thermal degradation of water soluble acrylic PSAs, based on acrylic acid–butyl acrylate copolymers using thermogravimetry and gas chromatography for the pyrolysis products.

2. Experimental

Water soluble acrylic PSAs under investigation were synthesized in acetone using acrylic acid (AA) and butyl acrylate (BA) in the presence of 0.1 wt. % radical starter AIBN at 56 °C. All components were purchased from BASF Germany in Ludwigshafen. The polymerization process was conducted with a 1 h dosage time and a 5 h post reaction. The synthesized water soluble acrylic PSAs having ca. 50 wt. % polymer content, dependent on the initial composition, are characterized through viscosity at 20 °C measured with a Rheomat RM 189 from Rheometric Scientific (spindle No. 3)

(Table 1). Thermal acrylic polymer stability was assessed by thermogravimetry (TGA) using a TA Instruments Inc. model 2950 TGA unit interfaced with the TA Instruments Thermal Analyst 2100 control unit. All samples, ca. 10 mg, were placed in a platinum sample pan and the TGA cell was swept with nitrogen at 60 cm³/min during the degradation process. The temperature was ramped at 5 °C/min.

Table 1. Viscosity of the synthesized PSA

PSA	Acrylic acid [wt. %]	Butyl acrylate [wt. %]	Viscosity [Pa·s]
WS-PSA 1	97	3	29.6
WS-PSA 2	95	5	20.3
WS-PSA 3	93	7	12.7
WS-PSA 4	90	10	7.6
WS-PSA 5	85	15	4.4

The thermal degradation experiments were performed by pyrolysis gas chromatography and pyrolysis gas chromatography/mass spectrometry techniques with the following parameters: Unicam 610, capillary column (QC2/BP1) 25 m×0.25 mm (100% dimethyl polysiloxane), carrier gas He, 80 kPa, detector FID 250 °C, injector temperature 250 °C, oven – temperature program from 50 °C (0 min) to 230 °C at 10 °C/min (32 min), sample 0.3 µl and pyrolysis gas chromatography/mass spectrometry techniques.

3. Results and discussion

The thermal resistance testing of the water soluble acrylic PSA synthesized from acrylic acid and butyl acrylate using the thermogravimetry method is shown in Fig. 2.

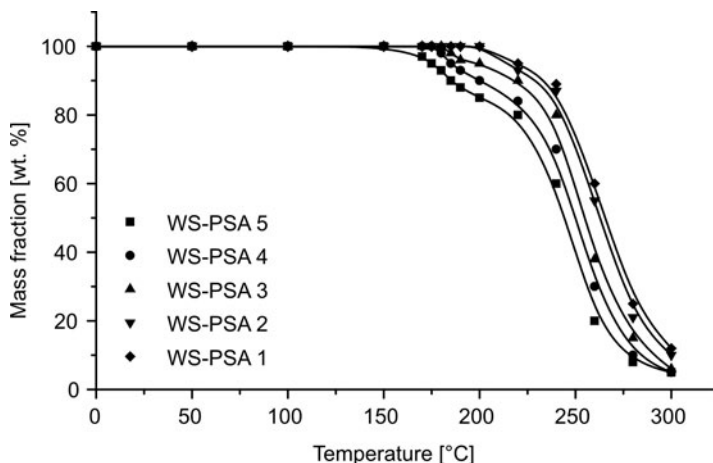


Fig. 2. Thermal degradation of water soluble copolymers from acrylic acid and butyl acrylate

The rate of thermal degradation of water soluble acrylic copolymers containing acrylic acid and butyl acrylate depends on their composition. More acrylic acid into polymeric backbone means *de facto* improvement to the thermal resistance. All the evaluated water soluble polymers were stable up to about 160 °C. Water soluble copolymers WS-PSAs 1–2 with 95 and 97 wt. % of acrylic acid (Table 1) are thermally stable to about 210 °C. At higher temperatures, their thermal decomposition begins, and depends on the concentration of acrylic acid in the copolymers. The gaseous and liquid thermal decomposition products of water soluble copolymer PSA 2 are listed in Table 2.

Table 2. Thermal degradation products of water soluble acrylic PSA containing 95 wt. % of acrylic acid and 5 wt. % of butyl acrylate as a function of pyrolysis time

Products of pyrolysis	Products of thermal degradation of WS-PSA 2 wt. %					
	1 min	2 min	4 min	8 min	16 min	32 min
Residue (soluble)	86.0	80.0	70.3	41.9	34.9	18.0
Liquid products	12.2	16.3	12.0	9.5	3.1	2.3
butyl acrylate	10.4	13.2	7.1	5.4	2.5	1.9
butyl methacrylate	1.6	2.2	3.1	3.0	0.4	0.3
butanol-1	0.2	0.9	1.8	1.1	0.2	0.1
Condensable gases	1.7	3.4	17.2	47.8	61.0	78.6
carbon dioxide	1.6	3.2	16.6	47.4	60.7	78.5
butene-1	0.1	0.2	0.4	0.4	0.3	0.1
Non condensable gases	0.0	0.2	0.4	0.7	0.9	1.0
Total volatiles	13.9	19.9	29.6	58.0	65.0	81.9
Total products	99.9	99.9	99.9	99.9	99.9	99.9

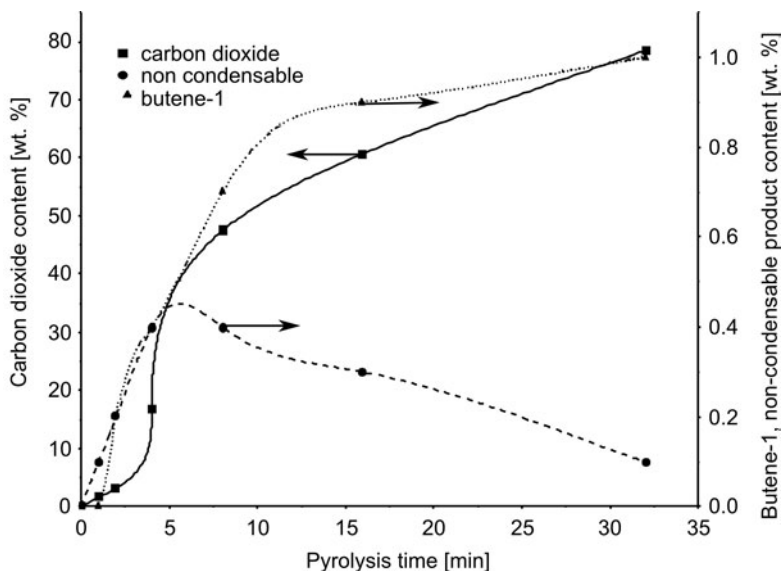


Fig. 3. Formation of carbon dioxide, butene-1 and non condensable products during pyrolysis of water-based acrylic PSA based on copolymer obtained from acrylic acid and butyl acrylate

The main decomposition gasses (Table 2) were carbon dioxide, butene-1 and non condensable products. An olefin, butene-1, corresponded to the butyl ester side groups in the synthesized copolymers. The olefin, being less volatile, in this case appears among the liquid products. The formation process of gaseous pyrolysis products is shown in Fig. 3. The amounts of carbon dioxide, ranging between 1.6 and 78.5 wt. % after 32 min pyrolysis time, were not comparable with the amounts of butene-1 (0.1–0.4 wt. %) and the amounts of non condensable pyrolysis products (between 0.2 and 1.0 wt. %) produced during the pyrolysis of acrylic acid–butyl acrylate-copolymer.

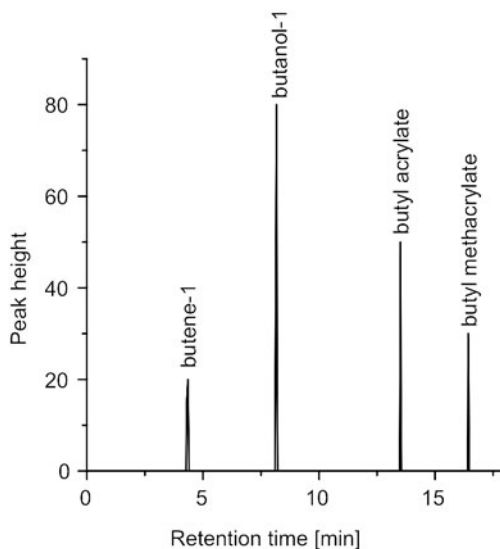


Fig. 4. Pyrolysis chromatogram of water soluble copolymer synthesized from acrylic acid and butyl acrylate

Figure 4 shows the pyrolysis chromatogram of water soluble acrylic acid–butyl acrylate-copolymer PSA 2. It contains four principal peaks. The first one corresponds to butene-1 and the second to butanol-1 from butyl acrylate. The presence of these peaks in the pyrolysis chromatogram at higher pyrolysis temperatures is possibly due to the thermal degradation of acrylate groups in the side chain. The other peaks correspond to butyl acrylate and to butyl methacrylate from the thermal decomposition of the main chain acrylic copolymer. The elimination of water in the presence of carboxylic groups from acrylic acid is necessary for anhydride formation. The probability of anhydride formation is also minimized by the space concentration of carboxylic groups along the copolymer backbone. It was observed that the dehydration and decarboxylation are the first order reactions, the latter being much slower than the former one. It was also found that water and carbon dioxide were the only volatile pyrolysis products in the range between 170 and 240 °C [5].

4. Conclusions

Water soluble acrylic copolymers synthesized with concentrated acrylic acid (ca. 95 wt. %) are characterized by their excellent thermal resistance at high temperatures between 180 and 240 °C and can be used for the manufacture of splicing tapes for the paper industry and water dispersible labels. The composition of their breakdown products at high temperatures, determined by the pyrolysis method, includes butene-1, butanol-1, butyl acrylate and butyl methacrylate. One may reasonably presume that butene-1 and butanol-1 are formed in quite distinct ester decomposition processes. Butene-1 formation almost inevitably involves the formation of carboxyl groups or carboxyl radicals whose decomposition could yield carbon dioxide. A comparable pyrolysis reaction of the tested water soluble acrylic copolymer would produce butyl acrylate and butyl methacrylate. Butyl acrylate is formed in rather greater amounts than butyl methacrylate and probably arises by depropagation from an acrylate terminated polymer radicals, although this is known to be only a very minor reaction in acrylics.

References

- [1] MILKER R., CZECH Z., *New trends and applications for water soluble PSAs*, Conference AFERA, Brussels, Belgium, 2002.
- [2] MILKER R., CZECH Z., *Adhäsion*, 6 (1989), 20.
- [3] MILKER R., CZECH Z., *Coating*, 7 (2004), 275.
- [4] D'HAESE F.C., LILLY J.V., Int. Patent WO 93/06184, *Pressure-sensitive adhesion composition which is repulpable under acidic pH-conditions*, 3M, 1992.
- [5] LATTIMER R.P., *J. Anal. Appl. Pyrolysis*, 68–69 (2003), 3.

Received 28 May 2008

Magnetic properties of mechanically milled nanosized Mn

X.J. WU^{1*}, X.W. XU¹, X.S. SUN²

¹Material Science & Technology College, Shenyang Ligong University, Shenyang 110168, China

²College of Materials & Metallurgy, Northeastern University, Shenyang 110006, China

Nanosized Mn powders were fabricated by milling Mn flakes in pure ethyl alcohol followed by homogenization. XRD analysis confirms single-phase characterization of the product and shows it has a grain size of 40 nm. The ZFC and FC magnetizations exhibit a large irreversibility with onset of about 60 K. The fit of the Curie–Weiss relation indicates strong AFM interaction in the considered system. A large coercive field and shifted hysteresis loops, i.e. $H_e = 83.6$ kA/m, are observed at 5 K in the 2 T field cooling case. The analysis indicates that surface anisotropy can lead to the occurrence of large exchange bias.

Key words: *nanosized powder; exchange bias; antiferromagnetism; surface anisotropy*

1. Introduction

Antiferromagnetic nanoparticles (AFN) have recently received increased attention due to their potential for exhibiting magnetization reversal by quantum tunnelling [1, 2]. Large surface to volume ratios of AFN make it reasonable to correlate their magnetic behaviours with surface effects. AFN such as NiO and CuO exhibited the exchange bias effect (EB) and a hysteresis loop, which indicates the existence of strong inter-particle interactions [3, 4]. Typically, these effects occur when the ferromagnetic (FM)–antiferromagnetic (AFM) interface is cooled through the Néel temperature (T_N) of the AFM in the field-cooled case. Besides, the exchange bias is known to enhance the coercivity and the shift of the hysteresis loop along the field axis [5]. Meiklejohn and Bean observed exchange anisotropy in core-shell Co/CoO nanoparticles, where the FM Co core was oxidized to produce an AFM CoO shell [6]. On the other hand, AFN can serve as a natural candidate material for the study of exchange bias, in which the core is AFM and the shell is FM, based on its high concen-

*Corresponding author, e-mail: wu_xiaojuan@yahoo.com.cn

tration of surface defects. The occurrence of the exchange bias field in CuO AFN was ascribed to the exchange interaction between surface defects, resulting from the increase in the surface area of the nanoparticles upon size reduction, and the AFM core [7]. If the presence of defects has a role in exchange bias, further enhancement in the exchange bias field is possible via mechanical milling, i.e. the process which introduces large defects on the surface of the particles from plastic deformation and size reduction.

Among the 3d transition metal elements, Mn can be considered as the most complex of all metallic elements. Due to possessing a moment as high as 5 μB , Mn and various structures containing Mn are expected to exhibit a variety of magnetic properties. In the past two decades, considerable interest in Mn nanostructures has been devoted to theoretical studies and experimental investigations [8]. Irrespective of the fact that nanosized particles of other transition metals have been extensively studied [9], reports on Mn nanoparticles are comparatively rare.

In this work, nanosized Mn powders were prepared successfully by milling Mn flakes for 50 h in a pure ethyl alcohol medium, followed by homogenization. The structure and magnetic properties of the powders were investigated in detail.

2. Experimental

Mn flakes (–22 mesh, 99.99%) were milled for 50 h in a home-made planetary ball mill, with a powder-to-ball weight ratio of 1:14, and at the spin rate of 400 rpm. The powders were milled in a tungsten carbide bowl in a pure ethyl alcohol medium using tungsten carbide balls. The as-milled powders were annealed at 673 K in a high vacuum for 30 min. X-ray diffraction (XRD) patterns were obtained with a Philips PW-1404 diffractometer using $\text{CuK}\alpha$ radiation. The Williamson–Hall relationship was used to calculate the effect of the grain size. The temperature and magnetic field variation of the magnetization M for the sample were measured with a vibrating sample magnetometer (VSM). In the zero-field-cooled (ZFC) case, the sample was cooled to 5 K in a zero field; a measuring field was then applied, followed by data acquisition as the temperature was increased. In the field-cooled (FC) case, the sample was cooled in a field, followed by the data acquisition as described above.

3. Results and discussion

Figure 1 represents XRD patterns of the as-annealed Mn powders. Obviously, Mn single phase is indexed with a space group of $I\bar{4}3m$. The lattice parameter a calculated from the (444) diffraction peak equals 0.8910 nm, basically consistent with the standard value of $a = 0.8912$ nm (Card Number: 89-4252). Moreover, all the diffraction peaks exhibit broadening, which reveals the presence of nanocrystallites. In addition,

tion, from the half-width of the XRD peaks of the pattern, the grain size is estimated as 40 nm for the nanosized Mn powders.

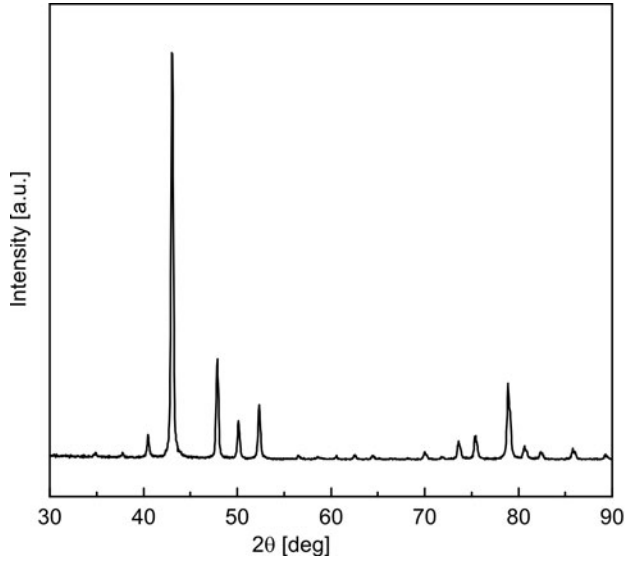


Fig. 1. XRD patterns of the nanosized Mn powders

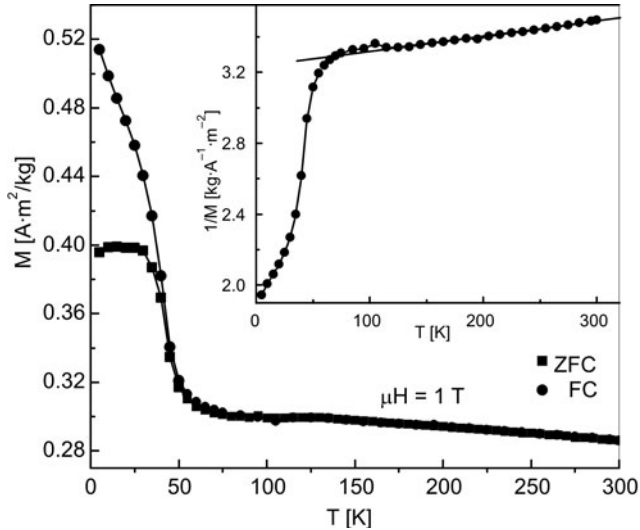


Fig. 2. Temperature dependences of zero-field cooled and field cooled magnetizations of nanosized Mn powders. Inset: Temperature dependence of reciprocal magnetization $1/M$ measured in the FC process with the field of 1 T, and the line shows that $1/M$ is fitted to the Curie–Weiss dependence for the data of $T > 50$ K.

The ZFC and FC magnetizations of nanosized Mn powders, as functions of temperature under the magnetic field of 1 T, are shown in Fig. 2. The inset in this figure

shows the temperature dependence of the reciprocal magnetization, $1/M$, as measured in the FC process with the field of 1 T. As temperature is lowered from room temperature, a very sharp step at about 30 K is observed in the M_{ZFC} curve with the field of 1 T, while a gradual increase of M_{FC} appears, especially, below 50 K. Namely, an increasingly large irreversibility is observed between M_{ZFC} and M_{FC} , with the onset of about 60 K. The maximum in the ZFC curve, at about 30 K, is usually ascribed to the average blocking temperature of the magnetic moment T_B , corresponding to the largest particles in the size distribution. Assuming the measured moments are due to uncompensated surface spins, Néel [10] suggested that the spin lattice of the particle could reverse coherently and randomly under thermal activation, and that the net moment of the uncompensated surface spins would fluctuate accordingly, i.e., superparamagnetism, with a blocking temperature below which spin systems are stable. Furthermore, the fit of the Curie–Weiss relation, i.e. $\chi = C/(T - \Delta)$, as shown in the inset, gives $\Delta = 3796$ K, which reveals very strong antiferromagnetism of the nanosized Mn powders.

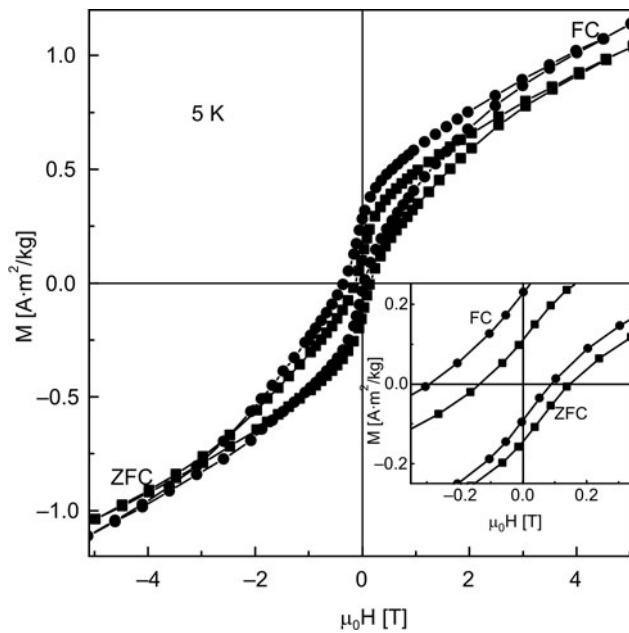


Fig. 3. The hysteresis loops of nanosized Mn powders under the ZFC and FC cases. The inset shows the same loops in a larger magnification

The hysteresis loops of the nanosized Mn powders at 5 K were measured in magnetic fields up to 5 T before and after field cooling at 2 T, as shown in Fig. 3. Its inset shows the same dependences in a larger magnification. Obviously, the ZFC loop is almost symmetric around the origin, whereas the 2 T field is strongly displaced from the origin and even broadened. The value of the displacement defines directly the EB

field H_e . A large coercive field and shifted hysteresis loops, including vertical and horizontal directions, are observed after cooling in a 2 T field. Commonly, the ZFC isofield curve of the AFN can be expressed by the equation

$$M(H) = M_{\text{FM}}(H) + \chi_{\text{AF}}H$$

where χ_{AF} is the antiferromagnetic susceptibility of the core and N_{FM} denotes the magnetization due to uncompensated surface spins.

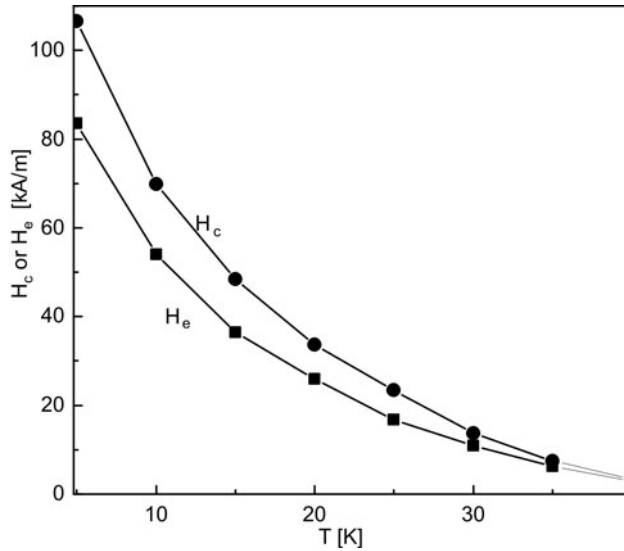


Fig. 4. Temperature dependences of exchange bias and coercive field of nanosized Mn powders

For the FC case, the temperature dependences of coercive (H_c) and exchange bias fields (H_e) are shown in Fig. 4. A maximum $H_e = 83.6$ kA/m can be observed at 5 K. Furthermore, both H_c and H_e decrease with the increase in temperature and both almost disappear above 50 K, the bifurcation temperature in Fig. 2a.

According to Néel [10], weak ferromagnetic behaviour from very fine antiferromagnetic particles can be attributed to the uncompensated spins on the surfaces of the particles, which has verified for a lot of AFN, such as MnO [11], Co_3O_4 [12] and CuO [13], etc. Kodama et al. [14] suggested that the reduced coordination of surface spins, resulting from the finite size effect, can cause a fundamental change in the magnetic order, which leads to large coercivity and loop shifts. In addition to surface spin canting and surface spin disorder via the synthesis techniques of ball milling, the change of coordination of the surface atoms, especially in oxides due to broken exchange bonds [15], can also render surface spin disorder. This indicates that surface anisotropy is present in the system. Moreover, nanosized particles/powders are often enclosed by a thin oxide layer, when they are exposed to air [16].

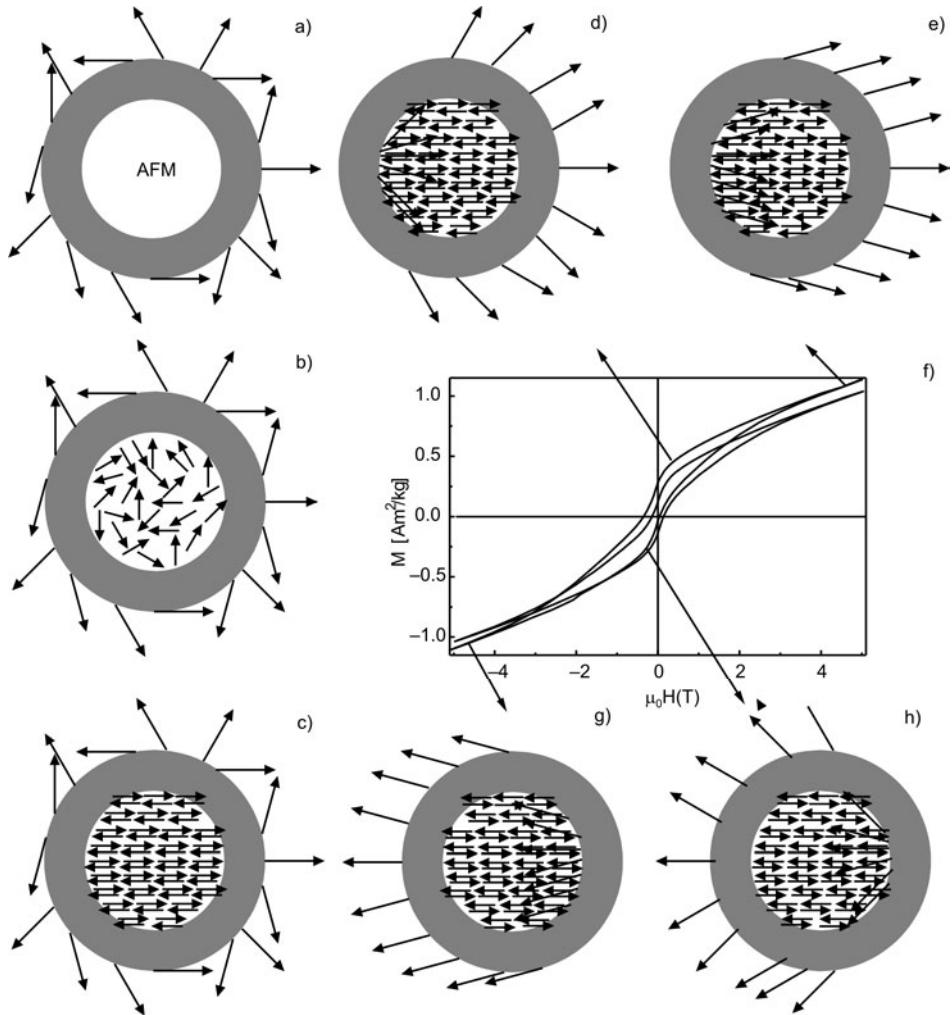


Fig. 5. The schematic diagram of the spin configurations in the nanosized Mn powders at various magnetization stages. Details in the text

A simple phenomenological model has been constructed based on the aforementioned findings to illustrate the spin configurations in the nanosized EB system (Fig. 5) [17]. Mn can form several types of oxides depending on the Mn to O ratio, which is usually controlled by the diffusion of oxygen. Therefore, we can refer to the oxide layer as Mn(O), shown as the gray loop in Fig. 5a. Above the Néel temperature of Mn, 107 K, both shell and core are in a paramagnetic state (Fig. 5b). Decreasing the temperature below 107 K will result in the AFM ordering of Mn, while the shell remains random (Fig. 5c). As the temperature is lowered below 60 K, the uncompensated surface spins play an increasingly important role. After lowering the temperature of nanosized Mn powders to 5 K, in the FC case, the spins on the surface of the Mn(O)

should lie almost parallel to each other along the field direction (Fig. 5e). With the decreased field strength, the surface spin becomes disordered again (Fig. 5d). After the magnetic field is reversed, the spins on the Mn(O) surface start to rotate in the opposite direction. Due to the strong surface anisotropy of surface spins, a microscopic torque will occur for the surface spins of the Mn(O), trying to keep them in their original positions. Therefore, the magnetic field required to completely reverse the magnetization in the surface spins will be higher than that in normal state, i.e., an extra magnetic field will be required to overcome the microscopic torque exerted by the spins in the AFM. As a result, the coercive field in the negative field branch increases (Fig. 3). Conversely, when the magnetic field is reversed back to positive values, the rotation of surface spins along the initial direction will be easier than in the opposite direction, since the interaction with the spins in the AFM will now favour the magnetization reversal, i.e., the AFM will exert a microscopic torque in the same direction as the applied magnetic field (Fig. 5h). Therefore, the coercive field in the positive field branch will be reduced. The total effect will be a shift of the hysteresis loop along the magnetic field axis, H_e . Therefore, the surface spins play an important role in the considered system.

4. Conclusions

By means of milling Mn flakes in pure ethyl alcohol followed by homogenization, the nanosized Mn powders were fabricated. The X-ray diffraction measurement reveals its single-phase character, besides the broadening of diffraction peaks. The ZFC and FC magnetizations exhibit a large irreversibility with the onset of about 60 K. The fit of the Curie-Weiss law reveals a strong AFM interaction in the considered system. A large coercive field and shifted hysteresis loops, i.e. $H_e = 83.6$ kA/m, are observed at 5 K, after cooling in a 2 T field. The analysis of a simple phenomenological model illustrates that surface anisotropy plays an important role in the large exchange bias field of the considered system.

References

- [1] IBRAHIM M.M., DARWISH S., SEEHRA M., Phys. Rev. B, 51 (1995), 2955.
- [2] GIDER S., AWSCHALOM D.D., MANN S., CHAPARALA M., Science, 268 (1995), 77.
- [3] MISHRA S.R., DUBENKO I., LOSOBY J., GHOSH K., KHAN M., ALI N., J. Nanosci. Nanotechnol., 5 (2005), 2076.
- [4] MAKHLOUF S.A., AL-ATTAR H., KIDAMA R.H., Solid State Commun., 145 (2008), 1.
- [5] BODKER F., HANSEN M.F., BENDER K.C., MORUP S., J. Magn. Magn. Mater., 221 (2000), 32.
- [6] MEIKLEJOHN W.H., BEAN C.P., Phys. Rev., 102 (1965), 1314.
- [7] PUNNOOSE A., MAGNONE H., SEEHRA M.S., BONEVICH J., Phys. Rev. B, 64 (2001), 174420.
- [8] DEMANGEAT C., PARLEBAS J.C., Rep. Prog. Phys., 65 (2002), 1679.
- [9] DONG X.L., ZHANG Z.D., ZHAO X.G., CHUANG Y.C., JIN S.R., SUN W.M., J. Mater. Res., 14 (1999), 1782.

- [10] NEEL L., *Low Temperature Physics*, Gordon and Beach, New York, 1962.
- [11] MORALES M.A., SKOMSKI R., FRITZ S., SHELBURNE G., SHIELD J.E., YIN M., O'BRIEN S., LESLIE-PELECKY D.L., *Phys. Rev. B*, 75 (2007), 134423.
- [12] MAKHLOUF S.A., *J. Magn. Magn. Mater.*, 246 (2002), 184.
- [13] PUNNOOSE A., SEEHRA M.S., *J. Appl. Phys.*, 91(10) (2002), 7766.
- [14] KODAMA R.H., MAKHLOUF S.A., BERKOWITZ A.E., *Phys. Rev. Lett.*, 79 (1997), 1393.
- [15] KODAMA R.H., BERKOWITZ A.E., *Phys. Rev. B*, 59 (1999), 6321.
- [16] REDDY B.V., DEEVI S.C., REUSE F.A., KHANNA S.N., *Phys. Rev. B*, 64 (2001), 132408.
- [17] NOGUES J., SORT J., LANGLAIS V., SKUMRYEV V., SURINACH S., MUNOZ J.S., BARO M.D., *Physics Report*, 422 (2005), 65.

Received 1 June 2008
Revised 20 August 2008

Microstructure and properties of Ti–45Al–5V intermetallic alloy

S. DYMEK¹, M. WRÓBEL^{1*}, Z. WITCZAK², M. Blicharski¹

¹AGH University of Science and Technology, al. Mickiewicza 30, 30-059 Cracow, Poland

²Institute of High Pressure Physics of the Polish Academy of Sciences,
ul. Sokołowska 29/37 01-142 Warsaw, Poland

An alloy of the chemical composition Ti-45Al-5V (at. %) was synthesized by mechanical alloying in a Szegvari-type attritor from elemental powders of high purity. The powders were further consolidated by hot isostatic pressing and hot isostatic extrusion. The resulting material was composed of a mixture of TiAl- and Ti₃Al-based phases. However, no lamellar microstructure, typical of such alloys, was observed. The alloys exhibited exceptionally high yield strength, together with satisfactory ductility and fracture toughness. The high strength was unequivocally due to grain refinement and the presence of oxide dispersoid.

Key words: *intermetallics; mechanical alloying; TiAl; Ti₃Al*

1. Introduction

TiAl-based alloys are promising materials for high temperature applications, especially for industrial and aviation turbines as well as for the aerospace and automobile industries. Their advantageous properties include low density, high melting point, good oxidation and burn resistance, completed with high yield strength and high elastic modulus, which is retained at elevated temperatures. The disadvantages of the TiAl-based intermetallic materials, consequently limiting their application, are brittleness at room temperature and a rapid loss of mechanical properties at temperatures above 700 °C [1].

Various approaches have been attempted to improve the properties of TiAl-based alloys. For example, greater ductility and fracture toughness were obtained by modifying the chemical composition, by alloying with substitutional elements such as vanadium [2]. Another alternative for enhancing the properties of TiAl-based alloys is the application of novel processing methods, by achieving accurate control of size and

*Corresponding author, e-mail: mwrobel@agh.edu.pl

distribution of constituent phases (in particular refinement of the lamellar microstructure) as well as by refining the grain size [3].

This research was aimed at processing TiAl-based materials, modified by the addition of small amounts of vanadium. Mechanical alloying (MA) was selected as the processing route. MA has the advantage of enabling grain size refinement down as far as the nanoscale; another advantage is the possible generation of non-equilibrium and amorphous phases. Also, the controlled oxygen level in the milling chamber produces oxide dispersoid, which is believed to contribute to the retention of strength and creep resistance at elevated temperatures, regardless of how fine-grained the microstructure is.

2. Experimental

An alloy with the composition Ti-45Al-5V (at. %) was synthesized in a Szegvari laboratory attritor mill. The excess titanium, with respect to stoichiometry in the alloy, was included in order to ensure that the alloy would exhibit a two-phase microstructure (near γ). The alloy was fabricated by mechanical milling of high purity elemental powders. All the powder particles had an average diameter lower than 44 μm (325 mesh). Mechanical alloying was carried out in an argon atmosphere: the controlled oxygen level was reduced to about 3–5 ppm. The controlled amount of oxygen was believed to produce oxide dispersoid, and consequently it was expected to improve the strength of the final material. A slight positive pressure (ca. 20 kPa) was maintained inside the mill in order to prevent air entering the mill during the milling process. The milling was carried out in a 1400 cm^3 sealed stainless steel tank with a 3.63 kg of 4.76 mm (3/16") stainless steel balls. The ball to powder ratio (by weight) was about 11:1. The first stage of milling (2 h) was carried out at cryogenic temperatures, using liquid nitrogen as a coolant. The liquid nitrogen prevents relatively ductile powder particles from agglomerating on the tank walls, shaft arms and balls, and also promotes the initial cold fracture. During the next milling stages, water cooling was applied. The powder was sampled periodically (after 2, 10, 50 and 100 h) during the milling, allowing characterization of the powder morphology and the progress of the mechanical alloying process. The amount of powder produced in one run of the mill was usually 200–300 g. The changes in the particle morphology during milling were examined by scanning electron microscopy. X-ray diffraction (XRD) was used for evaluation of the lattice parameters, lattice strains and the X-ray crystallite sizes.

The powders collected at the end of milling were sieved through a 44 μm mesh and consolidated by hot isostatic pressing (HIP) at 1100 $^\circ\text{C}$ and 1200 $^\circ\text{C}$ under 1.4 GPa for 14 h. An additional sample was compacted by hot isostatic extrusion (HIE) at 1000 $^\circ\text{C}$ with reduction 4:1 (true strain about 1.4) and at a strain rate of 10^2 s^{-1} . All powders were degassed before consolidation. The samples after both HIP and HIE were in the form of cylinders 10 mm in diameter. The compacted materials were subjected to XRD analysis, light microscopy, transmission and scanning electron micros-

copy (TEM and SEM) as well as mechanical tests. X-ray crystallite size and the lattice strain were determined from peak broadening according to the method proposed by Williamson and Hall [4]. The electron microscopy investigation was supplemented by chemical analysis performed by energy dispersive spectroscopy (EDS) – both in SEM and TEM. Thin foils were prepared by the ion milling method.

Mechanical tests comprised hardness and compression tests at room temperature, determination of elastic constants and evaluation of fracture toughness K_{Ic} . For this purpose, samples in the shape of parallelepipeds ($2.0 \times 2.8 \times 5.0 \text{ mm}^3$) were cut out from the central part of the consolidated samples. The non-square base was selected intentionally since, prior to mechanical tests, the elastic constants were evaluated on the samples using a resonant ultrasound spectroscopic method. The compression tests were carried out at a strain rate of $3 \times 10^{-3} \text{ s}^{-1}$. The assessment of fracture toughness K_{Ic} was performed from microcracks propagating from Vickers indentation corners on the prepolished sample surfaces. For this purpose, the Palmquist [5] model of microcrack formation and the mathematical analysis proposed by Niihara et al. [6] were adopted.

3. Results and discussion

The mechanical alloying process proceeded in a manner typical for milling ductile powders [7]. The powder particle morphology, after selected milling times, is shown in Fig. 1.

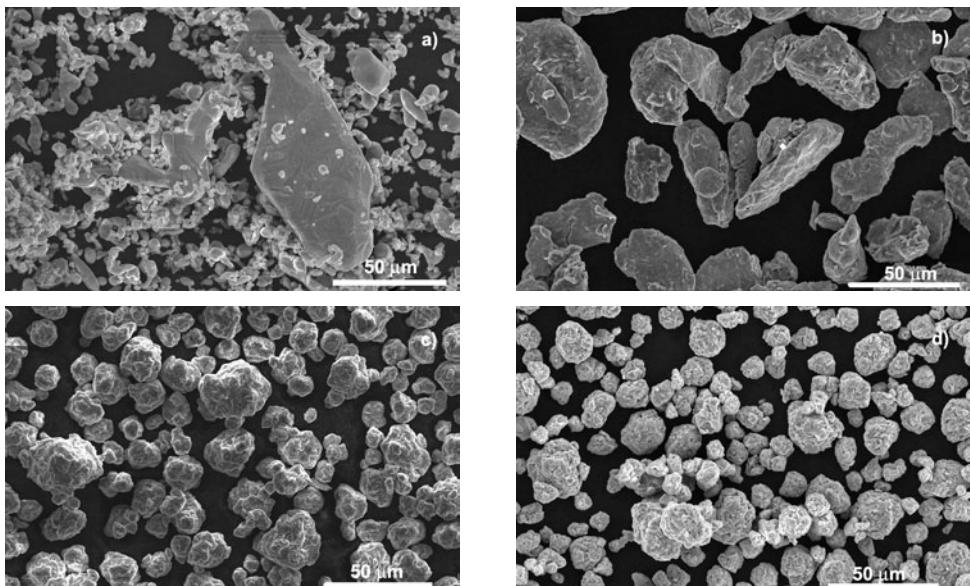


Fig. 1. SEM image of powder particles after: a) 0 h, b) 2 h, c) 50 h and d) 100 h of milling

Initially, an increase in the particle size, and their flattening was observed. This was due to the predominance of welding over fracturing occurring in relatively soft particles. Many particles had sizes approaching 500 μm , though considerable size variation was observed. The particle shapes became more spheroidal with the milling time. After 50 h of milling, the particles became much finer, indicating the predominance of fracturing over welding, but rough particle surface showed that welding was still in progress (Fig. 1). 100 h of milling produced a uniform powder with almost spherical particles having smooth surfaces. The average size of a powder particle (after sieving through a 45 μm mesh) was about 10 μm . The chemical composition of individual powder particles, measured by EDS, was uniform throughout the particle volume and corresponded to the starting composition of the powder blend.

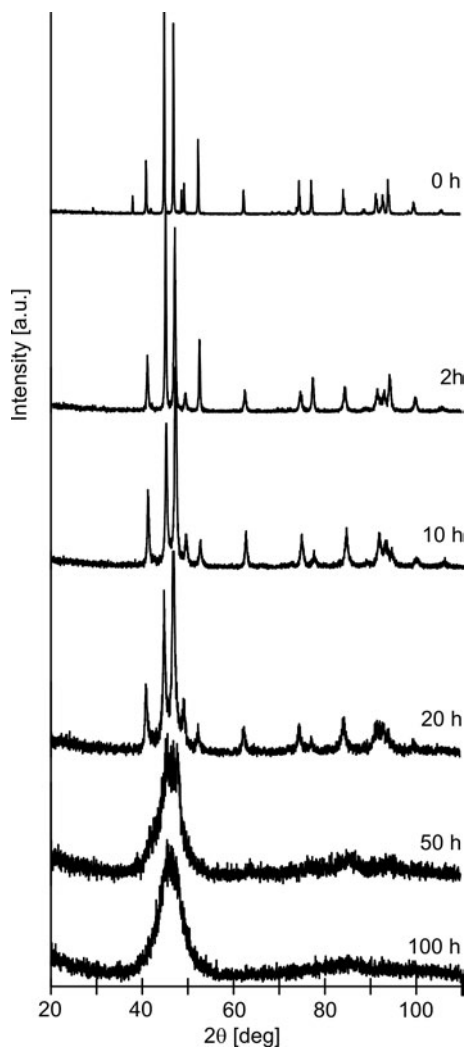


Fig. 2. XRD patterns of milled powders showing progress of mechanical alloying

X-ray diffractograms revealed clear dependences on the milling time (Fig. 2). In general, the powder behaviour during milling was typical of the mechanical alloying when solid solutions are formed [7]. The peaks became broader, their intensities decreased and most of them finally vanished as the mechanical alloying process progressed. A significant broadening of peaks suggested the formation of an amorphous phase, fine crystallite grains and/or high density of defects. The change in X-ray crystallite sizes and lattice strain for all alloys occurred in a typical manner, i.e. the crystallite sizes decreased and lattice strain increased with the milling time (Table 1).

Table 1. Crystallite sizes and lattice strains for Ti peaks

Milling time, h	0	2	10	50	100
Crystallite size, nm	819	215	165	31	18
Lattice strain, %	0.11	0.32	0.49	3.48	5.83

The peak positions changed a little with the milling time, i.e. only a slight shift to higher values of 2θ was observed. This indicated a little alteration of the lattice parameters of the processed alloy with the milling time. The direction of this shift was expected, since atom diameters of dissolved elements in Ti (Al, V) are smaller than the diameter of Ti atoms. Minor differences exist between Ti and Al atom radii (145 pm vs. 143 pm) and these two elements are basic constituents of the alloy. That is why such a small shift in peak positions occurred in the X-ray diffractograms. A broad peak at a 2θ position around 45° after 100 h of milling can be associated with reflections belonging to either pure alloy constituents (such as Al, Ti), compound TiAl or the formation of an amorphous phase. Similar effects were observed by Dutkiewicz et al. in mechanically alloyed TiAl–V alloy [8]. The XRD patterns show that vanadium dissolves easily in titanium or turns into an amorphous form.

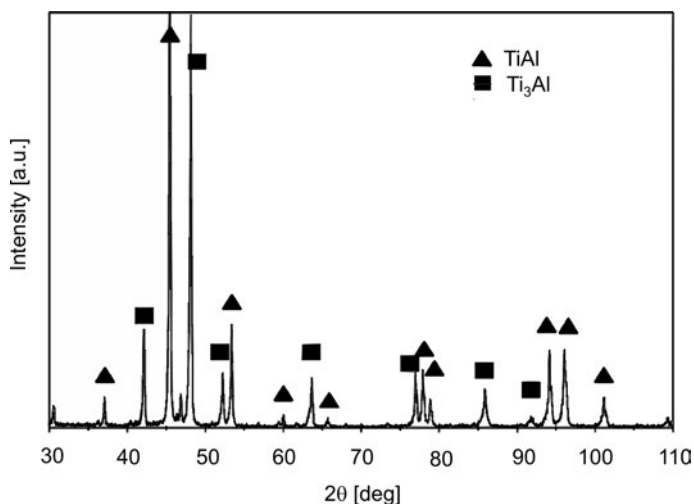


Fig. 3. Typical XRD pattern from the consolidated material; HIP at 1100 °C

The consolidation of mechanically alloyed powders produced solids of the required quality. XRD patterns from all consolidated materials were similar and showed the presence of TiAl and Ti₃Al-based phases (Fig. 3). An unexpected result was, however, a relatively large width of the diffraction peaks. This might have happened due to a probable presence of a fine grained microstructure and stresses arising from different coefficients of thermal expansion of particular phases.

Optical microscopy allowed the distribution of large oxide particles to be revealed. The distribution was fairly uniform throughout each HIP and HIE sample. A typical microstructure is presented in Fig. 4.

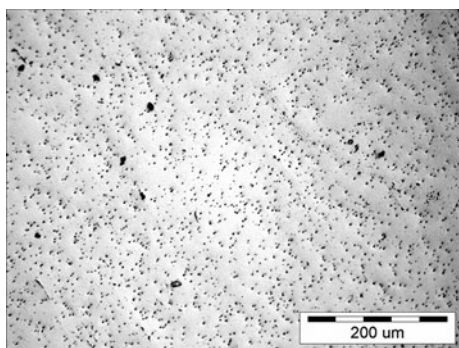


Fig. 4. Optical microstructure of the alloy consolidation by HIP at 1100 °C; not etched sample

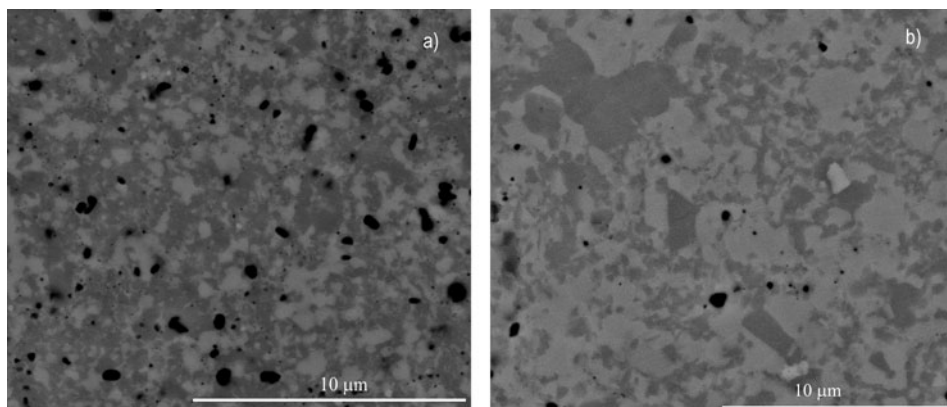


Fig. 5. Typical microstructures of the alloy consolidated by HIE (a) and HIP at 1100 °C (b); SEM BSE, contrast Z

The phases detected by X-ray analysis were also revealed in SEM images formed by backscattered electrons with utilization of Z contrast (Fig. 5). Such images are particularly useful in determining the size and distribution of constituent phases. The black particles in Fig. 5 contained mainly aluminum and oxygen (with at. % ratio 2/3) and thus were identified as Al₂O₃. SEM investigation confirmed that the distribution of oxides in all samples was more or less uniform. Beside oxides, the microstructure was composed of areas having different degree of grayness: brighter areas contained more Ti than Al, while in the darker ones the Ti and Al contents were similar. Taking

into account X-ray phase analysis, the brighter and darker areas were identified as phases based on Ti_3Al and $TiAl$ compounds, respectively. The interesting discovery in the present research was that the produced alloys did not exhibit a lamellar microstructure, which is typical of the two-phase γ - $TiAl$ based alloys having similar chemical compositions but synthesized by other methods [1].

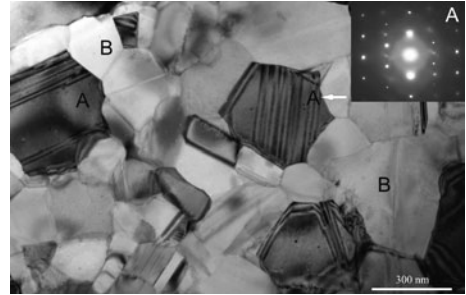


Fig. 6. TEM micrograph of the alloy consolidated by HIP at 1100 °C

A typical microstructure of the synthesized alloys, revealed by TEM, is shown in Fig. 6. TEM investigation, along with selected area diffraction pattern analysis, confirmed that the examined alloys consisted of a mixture of Ti_3Al -based and $TiAl$ -based phases, regardless of the consolidation route and temperature. The two phases could be easily recognized by numerous stacking faults which occurred in the Ti_3Al -based as opposite to the $TiAl$ -based phase. Both phases were built of colonies of small grains ($<1 \mu m$), however, the chemical compositions varied in particular grains belonging to the same phase. The content of V was partitioned evenly into both phases and its content was near the targeted value of 5 at. %. This unequivocally shows that vanadium diffuses easily into $TiAl$ and Ti_3Al solid solutions. The Ti:Al atomic ratio in the $TiAl$ based phase was close to 1. On the other hand, the chemical composition of the Ti_3Al based phase was far from stoichiometric, with Ti content ranging from 57 to 67 at. %. The presence of the Al-rich Ti_3Al based phase is detrimental to the mechanical properties of these alloys since it is considered as a primary source of brittleness at room temperature [9]. Density and elastic constants of consolidated materials, together with their mechanical properties, are listed in Table 2.

Table 2. Physical and mechanical properties of the MA Ti-45Al-5V alloy at room temperature

Property	Consolidation method		
	HIE 1000 °C	HIP 1100 °C	HIP 1200 °C
Density, g/cm^3	3.99	3.99	4.00
Young modulus, GPa	180	175	179
Poisson ratio	0.20	0.26	0.26
Yield strength, MPa	2500	2500	1800
Hardness, HV	590	630	613
K_{Ic} , $MPa \cdot m^{0.5}$	4	6	no microcraks at indent corners

The yield strengths of all examined materials were significantly higher than in other γ -TiAl alloys having similar chemical compositions, which is usually in the range of 360–450 MPa, depending on the alloy microstructure [1]. The higher strength of the material described in the present paper was unequivocally a result of grain refinement and the presence of oxide dispersoid. It was found that the physical and mechanical properties depended to some degree on the consolidation method. Higher ductility was observed for HIP-ed materials which increased with the consolidation temperature (Fig. 7). However, the ductility was not accompanied by any considerable strain hardening. Samples consolidated at 1000 °C and 1100 °C showed an exceptionally high yield stress of about 2500 MPa. Samples compacted at 1200 °C exhibited a lower yield stress but their ductility was much better.

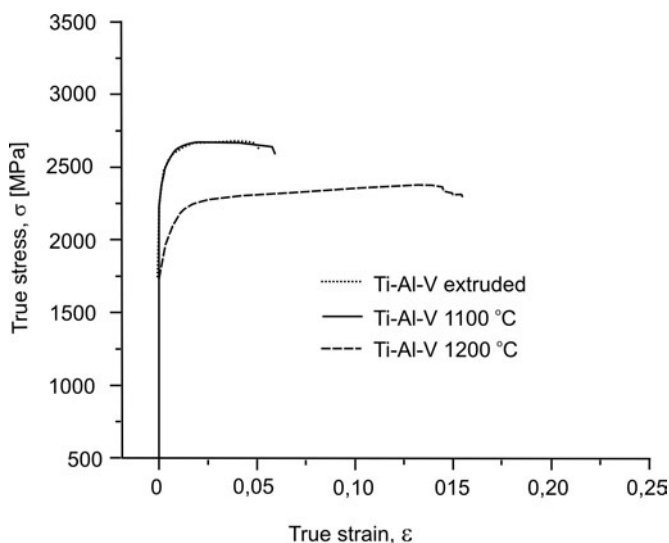


Fig. 7. Stress–strain curves for the alloys deformed at room temperature

A similarly high level of strength in TiAl-based alloys was also reported by Bohn et al. [10] for a Ti-48Al alloy with a grain size of around 130 nm, and by Calderon et al. [11] for a nanocrystalline Ti-46Al-4Cr alloy, also produced by mechanical milling but consolidated by spark plasma sintering – the method which makes it possible to obtain a nanostructure in bulk materials, due to short processing times. It is worth noting that the present Ti-45Al-5V alloy, consolidated by HIP or HIE, shows extremely high flow stresses without having a lamellar microstructure, which is usually considered for achieving the highest strength among all γ -type alloys [1]. The high yield strengths obtained in the present research are certainly associated with the alloying with vanadium, the fine grain size as well as the presence of oxide dispersoid.

The hardness of the examined materials varied with the method of consolidation and cannot be correlated with yield strength. A similar conclusion may be drawn about the fracture toughness, which depends mainly on the consolidation temperature.

4. Conclusions

The applied processing route (i.e., mechanical alloying followed by hot isostatic pressing or hot isostatic extrusion of powders) can be successfully used for the production of TiAl-based alloys having exceptionally high yield strength, together with some ductility and satisfactory fracture toughness.

The high strength of the produced intermetallic alloy was unequivocally a result of grain size refinement and the presence of oxide dispersoid.

The produced alloys are composed mostly of TiAl- and Ti₃Al-based phases, however no lamellar microstructure, typical for TiAl-based intermetallic, was observed.

Vanadium partitioned equally into both TiAl- and Ti₃Al-based phases.

Acknowledgements

The work was supported by EU Network of Excellence, project Knowledge-based Multicomponent Materials for Durable and Safe Performance (KMM-NoE) under the contract No. NMP3-CT-2004-502243.

References

- [1] FROES F.H., SURYANARAYANA C., *Titanium Aluminides*, [in:] *Physical Metallurgy and Processing of Intermetallic Compounds*, N.S. Stoloff, V.K. Sikka (Eds.), Chapman and Hall, 1996, p. 297.
- [2] HISHINUMA A., TABUCHI M., SAWAI T., *Intermetallics*, 7 (1999), 875.
- [3] JOVANOVIĆ M.T., DIMČIĆ B., BOBIĆ I., ZEC S., MAKSIMOVIĆ V., J. Mater. Proc. Techn., 167 (2005), 14.
- [4] WILLIAMSON G.K., HALL W.H., *Acta Metall.*, 1 (1953), 22.
- [5] PALMQUIST S., *Jernkontorets Ann.*, 141 (1957), 300.
- [6] NIIHARA K., MORENA R., HASSELMAN D.P.H., *J. Amer. Ceram. Soc.*, 65 (1982), C-116.
- [7] SURYANARAYANA C., *Prog. Mater. Sci.*, 46 (2001), 1.
- [8] DUTKIEWICZ J., MAZIARZ W., *Solid State Phenom.*, 101–102 (2005), 117.
- [9] HAO Y.L., YANG R., CUI Y. Y., LI D., *J. Mater. Sci. Technol.*, 15 (1999), 536.
- [10] BOHN R., KLASSEN T., BORMANN R., *Acta Mater.*, 49 (2001), 299.
- [11] CALDERON H.A., GARIBAY-FEBLES V., UMEMOTO M., YAMAGUCHI M., *Mater. Sci. Eng.*, A329–331 (2002), 196.

Received 3 July 2008

Revised 8 November 2008

Effect of milling time and addition of alumina powder on the structural properties and fracture surface of nanocrystalline Al

S.S. RAZAVI TOUSI, R.YAZDANI RAD^{*}, E. SALAHI, M. RAZAVI

Ceramic Department, Materials and Energy Research Center, P.O. Box 31787/316, Karaj, Iran

The effects of milling time and the addition of alumina reinforcement on the structural evolution of Al matrix were investigated. By analysing the cross section of powder, cold welding mechanism for both monolithic and composite powders was studied. Results show that presence of the alumina powder has a marked effect on variation of apparent density, preferred orientation, impurity content and thus lattice parameter of Al by milling time. The reduction of the grain size to the nanometric scale changes the fracture mechanism of Al particles completely, from dimpled into intergranular, though alumina addition does not seem to have notable influence on the fracture mechanism.

Key words: *ball milling; nanostructured materials; fracture surface*

1. Introduction

In order to predict the final properties of samples produced by ball milling, an accurate investigation into the structural evolution, dependent on the milling time, should be considered. With regard to the effect on the structural properties, addition of small amounts of ceramic phases into a ductile matrix has been studied in several works [1–6]. However, the addition of higher volume proportions (e.g., up to 20 wt. %) of ceramic phase has not been considered much up to now [7]. Fracture and welding are known to be the two major mechanisms affecting structural evolution during mechanical alloying (MA) [8]. For both brittle and ductile components, the systems do not reach the steady state as long as one of these mechanisms prevails [9]. Bearing this in mind, fracture and welding in monolithic Al and Al–Al₂O₃ systems will be studied.

Ceramic powder affects cold welding and fracture mechanism of the matrix. Thus, time necessary to reach the steady state, porosity and orientation of crystallites change in comparison with the monolithic ductile metal [2, 3].

^{*}Corresponding author, e-mail: ryazdani5@gmail.com

As crystallite size is reduced to less than 100 nm, metals change from ductile to brittle [10]. Nevertheless, dimpled fracture surfaces have been observed in many nanocrystalline materials [11–15]. As will be discussed, in spite of the appearance of a fracture surface of nano-grained metals, cracks propagate along the grain boundaries (GBs) and the fracture surface is completely intergranular [16, 17].

2. Experimental

Monolithic Al powder (Merck, Art. No: 1056) and a mixture of Al–20 wt. % Al₂O₃ powder (Martinswerk, MR70, d_{50} : 0.5–0.8 μm) with 3 wt. % of stearic acid as the process control agent (PCA) were milled in a P5 planetary mill for various periods of time, up to 25 h. The milling atmosphere was Ar and the product sampling was performed in a glow box, to prevent oxidation. Samples were examined under an optical microscope (OM) and a Cambridge scanning electron microscope (SEM) operating at a voltage of 30 kV. A Philips CM 200 FEG transmission electron microscope (TEM) was used to investigate the grain size and dispersoids. The X ray diffraction (XRD) patterns were taken using a Siemens X ray diffractometer (30 kV and 25 mA).

Grain size changes during the milling stages were calculated by the Williamson–Hall method for at least three peaks [18]:

$$B \cos \theta = \frac{0.9\lambda}{D} + 2\eta \sin \theta \quad (1)$$

where B , λ , θ , D and η are FWHM, the wave length, peak position, crystallite size and lattice strain, respectively.

In order to minimize errors caused by aberration of 2θ variation, the Nelson–Riely method was used to calculate the lattice parameter of Al for at least three peaks, using Eq. (1) [19].

$$F(\theta) = 0.5 \left(\frac{\cos^2 \theta}{\sin^2 \theta} + \frac{\cos^2 \theta}{\theta} \right) \quad (2)$$

The minor errors caused by peak position displacement and peak shape deformation were reduced by the following procedure: peak position of each peak assigned to the middle of three $P_{x/y}$ with x/y equal to 0.6, 0.8 and 1, the final peak position was obtained by averaging these values. Full details of this method have been described elsewhere [20].

The powders were then pressed with an isostatic press (1 GPa) and sintered at 640 °C for 30 min. Fracture testing was carried out at a 3.3×10^{-2} (s⁻¹) strain rate at room temperature, and neither etching nor particular preparation were induced on fracture surfaces.

3. Results and discussion

3.1. Structural evaluation

In the first 5 h of milling, Al particles are deformed into lamellae and weld together, creating secondary particles (Fig. 1a). Upon further milling, the thickness of the lamellae decreases to such an extent that it cannot be distinguished by optical microscopy (Fig. 1b). After 20 h, the morphology changes from plate-like into equiaxed form (Fig. 1c). Comparing Fig. 1c and Fig. 1d (Al milled for 25 h), it seems that the system reached a steady state after 20 h of milling. It must be noted that the layered structure of Al remains after achieving the steady state but it has no preferred orientation (Fig. 1e). Indeed, the laminated initial Al particles are thinner than anything that can be observed by OM [1].

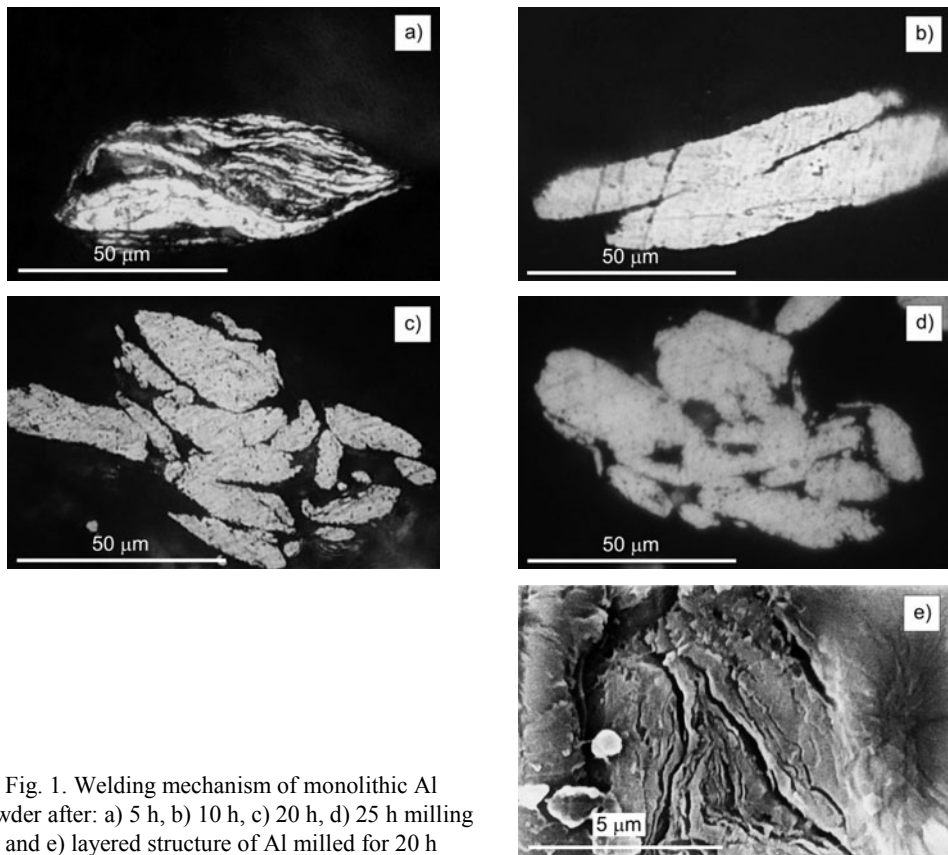


Fig. 1. Welding mechanism of monolithic Al powder after: a) 5 h, b) 10 h, c) 20 h, d) 25 h milling and e) layered structure of Al milled for 20 h

In the case of the Al–Al₂O₃ system, the presence of alumina particles prevents any formation of Al, flake-like particles after 5 h of milling (Fig. 2a). Indeed, before deforming into a flaky shape, Al particles are torn by Al₂O₃ particles and thus, micro-welding occurs among spherical, rather than plate-like, particles. Comparing the composite powders milled for 15 h and 20 h (Figs. 2b, c), it is obvious that welding and

fracture have reached a steady state after 15 h milling. High plastic deformation in the vicinity of alumina particles increases the work hardening rate of Al matrix, thus the fracture and welding mechanism achieve equilibrium in a shorter time [4].

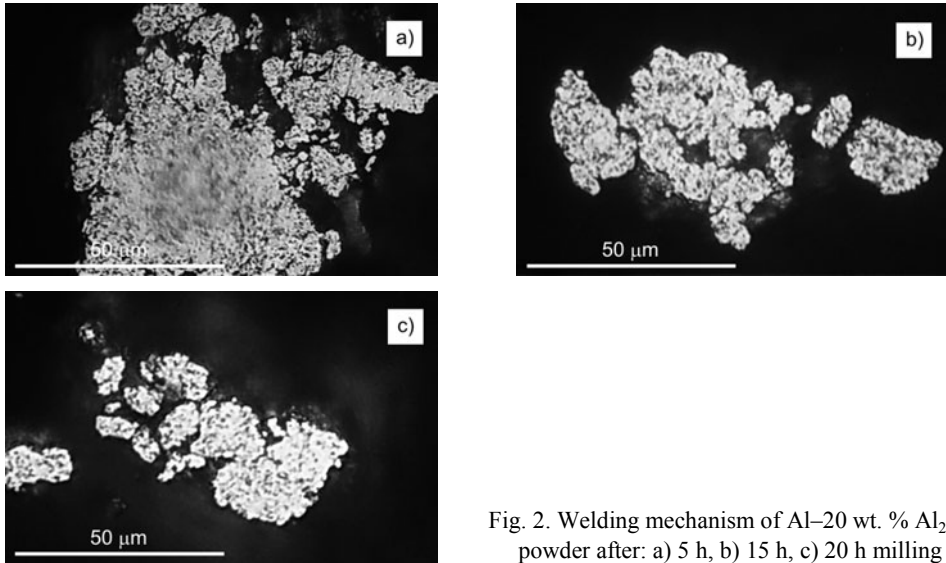


Fig. 2. Welding mechanism of Al-20 wt. % Al_2O_3 powder after: a) 5 h, b) 15 h, c) 20 h milling

Two types of porosity can be distinguished in the milled powder: pores of about 5–10 μm (Fig. 1d) caused by cold welding of the powder and pores existing only in the composite powder, caused by the Al_2O_3 particles penetrating into the Al matrix, resulting in fine pores distributed uniformly among the matrix (Fig. 2b). The formation of any types of pores decreases the apparent density of the powder (Fig. 3). A slight increase in the apparent density of the composite powder after 25 h of milling is attributed to the presence of Fe debris caused by the abrasion of balls and vial, thereby increasing the density of the powder.

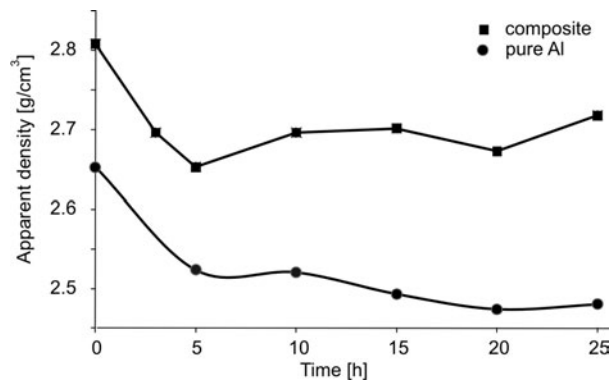


Fig. 3. Time dependence of the apparent density of monolithic and composite powders

Fe content in the monolithic Al powder increases by 0.4% after completion of the milling process (Table 1). Presence of the alumina particles in the composite system increases the abrasion so that Fe amount in the reinforced powder is larger than in monolithic powders (Table 2).

Table 1. The composition of as-received and 25 h milled monolithic Al

Sample	Zn	Ni	Cr	Fe	Ti	Cu	Mn
As received Al [%]	0.021	0.003	<0.004	0.42	0.008	0.0007	<0.01
Milled monolithic Al [%]	0.017	0.092	<0.004	0.87	0.01	0.046	0.128

Table 2. Effect of milling time on the Fe amount of the reinforced powder

Milling time [h]	0	5	10	15	20	26
Fe [%]	0.42	1.49±0.53	1.786±0.35	2.01±0.4	2.48±0.17	2.65±0.47

In order to evaluate the nature of the Fe phase, whether it is in the form of a solid solution or a particulate, the Nelson–Riely method was used to estimate the Al lattice parameter [19]. Results show that the lattice parameter increased immediately after 5 h of milling and then it decreased after further milling, for both the monolithic and the composite powder (Table 3).

Table 3. Effect of milling time on the lattice parameter of Al in the monolithic and composite powder

Milling time [h]	0	5	10	15
Composite powder	4.047	4.048	4.047	4.046
Monolithic powder	4.047	4.049	4.048	4.048

Decomposition of the PCA by a mechanochemical process, followed by solid solution of C and O atoms in the Al lattice, is responsible for the abrupt increase in the first 5 h [21]. Two different mechanisms can be considered for the decrease in the lattice parameter. In the case of pure Al, due to surface tension of grains, the lattice parameter decreases with the grain size reduction [22, 23].

In the case of the composite powder, the lower lattice parameter of Al is ascribed to dissolution of Fe debris into Al [24]. The smaller atomic radius of Fe (0.126 nm) compared with that of Al (0.143 nm) reduced the lattice parameter. However, after the annealing process, the dissolved Fe atoms react with Al to form Fe–Al intermetallic (the needle-like white particles in Fig. 4).

High plastic deformation produces too many imperfections in the Al lattice such as GBs and dislocations. The more imperfections created in the matrix, the more evident peak broadening can be seen in the XRD pattern.

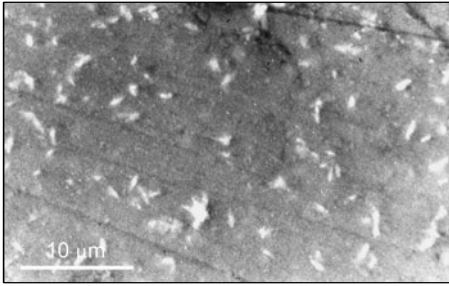


Fig. 4. Al-Fe intermetallic in the annealed composite sample milled for 20 h

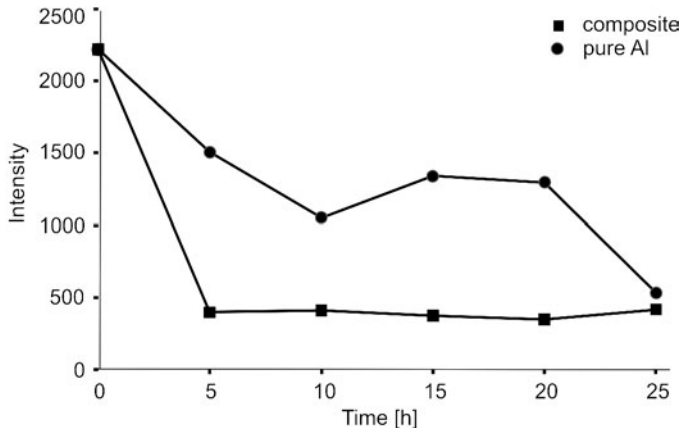


Fig. 5. Dependence of the intensity of the (111) peak of Al for monolithic and composite powders on the milling time

Figure 5 shows that the intensity of the (111) reflection for Al in the composite powder decreases faster compared with the monolithic Al. As mentioned before, the presence of Al_2O_3 particles assists work hardening, thus saturation of imperfection and consequently steady state takes place in a shorter time [4, 25]. For pure Al, it is at least 10 h milling. This can be understood by considering the anisotropy in the elastic module of Al single crystal. Therefore, grains within a powder particle are deformed into thin layers in the 'soft' direction, perpendicular to the direction in which the powder particles were flattened by the milling ball. When the sample is prepared, in order to perform the powder XRD analysis, this flattened powder and its (200) planes are arranged parallel to the sample holder, i.e., I_{200} increases whereas I_{111} decreases [26]. With further milling, the flattened particles are fractured and divided to equiaxial particles. Therefore particles lose their preferred orientation, and their planes of reflection are randomly arranged again and I_{111} recovers its significance. In a different manner, I_{111} of the reinforced Al has an abrupt reduction after 5 h of milling without any considerable change afterwards. This confirms lack of any lamination of the Al particles in the presence of alumina.

3.2. Fractography

As a determinant criterion, prior knowledge of the structural traits is essential for fractography. Grain size estimates for the sintered samples, obtained by XRD, and the Williamson–Hall equation [18] show that in spite of time and temperature, the grains did not grow markedly during heating and had a constant diameter of about 80 nm. The presence of nanometric carbide and oxide particles created by the decomposition of PCA results in the Zener pinning mechanism, and so grain growth ceases [27].

On the other hand, GB energy can be decreased by the accumulation of Fe atoms in the GB region, thus the presence of Fe impurity in the form of solid solution can retard the grain growth mechanism [28, 29]. By migration of the boundaries, the concentration of Fe atoms in the boundary regions increases and thus driving force for boundary migration, i.e. GB energy reduces. Accordingly, grain growth is suppressed at the early stages of annealing [30, 31].

Hardness is inversely proportional to the grain size, according to the Hall–Petch formula (Eq. (3)) [32, 33], thus a fracture surface different from the usual one is anticipated for the milled product samples.

$$H = H_0 + KD^{-1/2} \quad (3)$$

where H_0 is the hardness of the annealed coarse grained sample, K is a constant and D is the size of a crystallite.

In the case of monolithic Al sample (Fig. 6a), microvoid coalescence and hence dimple rupture is known as the main fracture mechanism. In the absence of any inclusion or second phase particles, prior particle boundaries act as the proper sites for nucleation of dimples (Fig. 6b). Such elongated dimples, arranged in the same direction, indicate that the fracture surface results from tear [34].

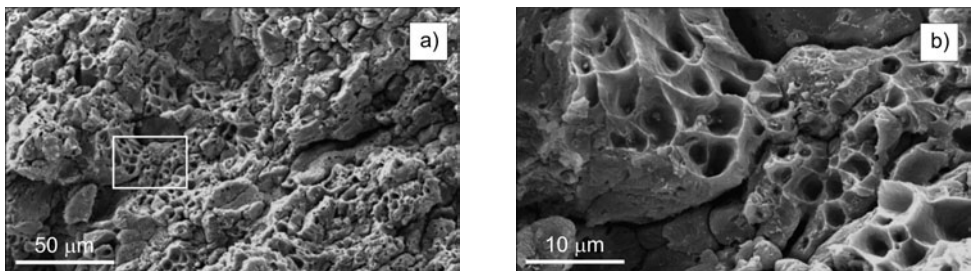


Fig. 6. Fracture surface of monolithic Al without milling

There is a different fracture surface of Al milled for 25 h (Fig. 7a). The fracture surface is covered with microvoids of different shapes compared with one produced by microvoid coalescence (Fig. 7b). Indeed, the presence of the alumina layer on the surface of initial Al particles reduces the cohesive strength of the material at the particle boundaries and promotes decohesive rupture mechanism (Fig. 7c).

On the other hand, due to the presence of a high volume proportion of the GB phase, another suitable region for crack propagation must be considered [17]. In the

nanocrystalline (NC) regime, the spatial confinement of the grains below several tens of nanometres inhibits the operation of dislocation sources inside grains, limiting the plastic deformation [12, 15].

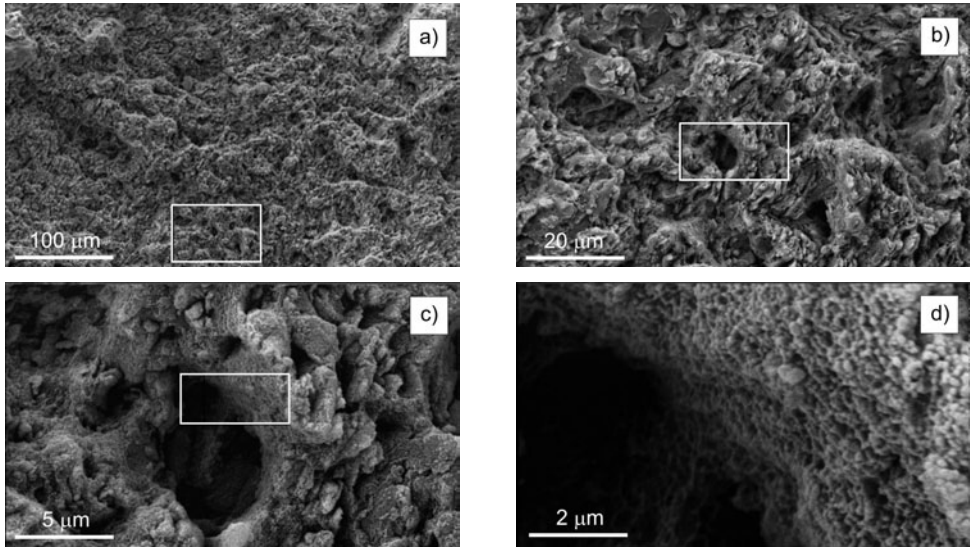


Fig. 7. Fracture surface of monolithic Al milled for 25 h at various magnifications

It is expected that in NC plastic deformation can be accommodated by the GBs. Rotation of grains, together with GB sliding, creates nanometric pores along the GBs acting as thresholds of crack propagation. Since GB have the lowest melting point of an alloy system and are easy paths for diffusion and sites for segregation, cracks propagate along the GBs and thus an intergranular fracture is anticipated in nanocrystalline materials [16]. Figure 7d shows that creation of dimples proceeded along the GBs, resulting in a different mode of intergranular fracture accompanied by decohesive rupture.

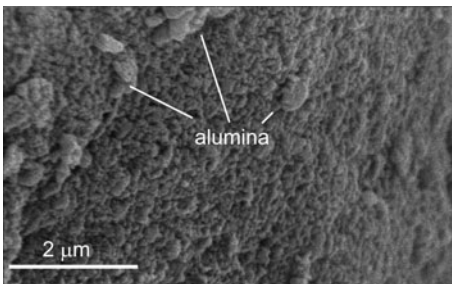


Fig. 8. Fracture surface of composite sample fabricated by 20 h milling

Addition of 20 wt. % of alumina powder has no considerable effect on the fracture surface of milled samples (Fig. 8). Since GBs are more accessible than alumina particles, microvoids tend to propagate along the GBs rather than along the mismatch be-

tween the Al–Al₂O₃ phases. Despite the presence of alumina particles (marked with in the picture), fracture surface is completely intergranular.

4. Conclusion

High energy milling of monolithic Al and Al–20 wt. % Al₂O₃ was studied in terms of its structural evolution. Addition of 20 wt. % of Al₂O₃ to the Al powder changed the cold welding mechanism and hence the preferred orientation and porosity in the Al matrix. The presence of alumina powder caused Fe impurity, which dissolved in the matrix during milling. This changes the Al lattice parameter, and also produces an Al–Fe intermetallic after annealing. In the case of a milled powder, grain boundary sliding and decohesion of initial particles are known to be the two mechanisms that cause fracture, therefore, a combination of intergranular and decohesive rupture is observed in the fracture surface.

References

- [1] FOGOGNOLO J.B., VELASCO F., ROBERT M.H., TORRALBA J.M., *Mater. Sci. Eng. A*, 342 (2003), 131.
- [2] RAZAVI HESABI Z., SIMCHI A., SEYED REIHANI S.M., *Mater. Sci. Eng. A*, 428 (2006), 159.
- [3] FOGOGNOLO J.B., ROBERT M.H., TORRALBA J.M., *Mater. Sci. Eng. A*, 426 (2006), 85.
- [4] FOGOGNOLO J.B., RUIZ-NAVAS ELISA M., ROBERT M.H., TORRALBA J.M., *Mater. Sci. Eng. A*, 355 (2003), 50.
- [5] ZEBARJAD S.M., SAJJADI S.A., *Mater. Design*, 28 (2007), 2113.
- [6] RUIZ-NAVAS E.M., FOGAGNOLO J.B., VELASCO F., FROYN L., *Composites A*, 37 (2006), 2114.
- [7] PRABHU B., SURYANARAYANA C., AN L., VAIDYANATHAN R., *Mater. Sci. Eng. A*, 425 (2006), 192.
- [8] RODIGUEZ A., GALLARDO J.M., HERRERA E.J., *J. Mater. Sci.*, 32 (1997), 3535.
- [9] SURYANARAYANA C., *Prog. Mater. Sci.*, 46 (2001), 1.
- [10] HONGQI L., EBRAHIMI F., *Adv. Mater.*, 17 (2005), 1969.
- [11] DALLA TORRE F., VAN SWYGENHOVEN H., VICTORIA M., *Acta Mater.*, 50 (2002), 3957.
- [12] KUMAR K.S., SWYGENHOVEN H.V., SURESH S., *Acta Mater.*, 53 (2003), 5743.
- [13] MEYERS M.A., MISHRA A., BENSON D.J., *Prog. Mater. Sci.*, 51 (2006), 427.
- [14] MUKAIA T., KAWAZOEB M., HIGASHI K., *Nanostruct. Mater.*, 10 (1998), 755.
- [15] IWASAKI H., HIGASHI K., NIEH T.G., *Scripta Mater.*, 50 (2004), 395.
- [16] LI H., EBRAHIMI F., *Acta Mater.*, 54 (2006), 2877.
- [17] HASNAOUI A., VAN SWYGENHOVEN H., DERLET P., *Science*, 300 (2003), 1550.
- [18] WILLIAMSON G.K., HALL W.H., *Acta Metal.*, 1 (1953), 22.
- [19] NELSON J.B., RIELY D.P., *Proc. Phys. Soc. (London)*, 57 (1945), 160.
- [20] HAROLD P.K., ALEXANDER L.E. *X Ray Diffraction Procedure*, Wiley, New York, 1954.
- [21] XIA Z.P., LI Z.Q., LU C.J., ZHANG B., ZHOU Y., *J. Alloys Comp.*, 399 (2005), 139.
- [22] KORCHEF A., CHAMPION Y., NJAH N., *J. Alloys Comp.*, 427 (2007), 176.
- [23] LIU M., SHI B., GUO J., CAI X., SONG H., *Scripta Mater.*, 49 (2003), 167.
- [24] ORTIZ A.L., SHAW L., *Acta Mater.*, 52 (2004), 2185.
- [25] FOGOGNOLO J.B., ROBERT M.H., TORRALBA J.M., *Mater. Sci. Eng. A*, 426 (2006), 85.
- [26] AMADOR D.R., TORRALBA J.M., *J. Mater. Proc. Tech.*, 143–144 (2003), 776.
- [27] ZENER C., *Trans. AIME*, 175 (1948), 15.
- [28] KIRCHHEIM R., *Acta Mater.*, 50 (2002), 413.

- [29] LIU F., KIRCHHEIM R., *Acta Mater.*, 51 (2004), 521.
- [30] LIU F., YANG G., KIRCHHEIM R., *J. Crystal Growth*, 264 (2004), 392.
- [31] LIU K.W., MUCKLICH F., *Acta Mater.*, 49 (2001), 395.
- [32] HALL E., *Proc. Phys. Soc. B*, (1951), 747.
- [33] PETCH N., *J. Iron Steel Inst.*, 174 (1953), 25.
- [34] DAVIS J.R., *Aluminum and Aluminum Alloys*, ASM International, Almere, 1993.

Received 29 July 2008
Revised 7 November 2008

Effect of growth time on the morphologies of vapour grown carbon fibres and a suggested mechanism of growth

H. ZHANG^{1,2}, J. SHI¹, Y. SONG¹, J. ZHAO¹, K. WANG^{1,2}, Q. GUO¹, G. ZHAI¹, L. LIU^{1*}

¹Key Laboratory of Carbon Materials, Institute of Coal Chemistry,
Chinese Academy of Sciences, Taiyuan, Shanxi, 030001, PR China

²Graduate University of Chinese Academy of Sciences, Beijing, 100049, PR China

The microstructure of vapour grown carbon fibres is two-double layered. This paper addresses the question of morphology transformation of vapour grown carbon fibres. Special attention is given to developing understanding of the growth mechanism of the outer layer of the fibres. The influence of growth time on the morphologies of as-prepared carbon fibres was investigated using scanning electron microscopy. Results showed that with the prolongation of reaction time, their morphology changed from linear fibres to carbon micro-bead chains and then again to thicker linear fibres, which led to the increase of the carbon fibres diameters from 200 nm to several micrometers. Furthermore, several kinds of carbon fibres with special morphology such as carbon micro-beads, chains, etc., could be obtained by adjusting the growth time. A growth mechanism, henceforth referred to as *fibre-bead-thicker fibre*, for the outer layer of vapour grown carbon fibres is proposed.

Key words: *vapour grown carbon fibres; vapour deposition; electron microscopy; microstructure*

1. Introduction

Vapour grown carbon fibres (VGCF) have attracted much attention in recent years, due to their desirable properties and potential applications [1–4]. Chemical vapour deposition (CVD) is a widely used method to prepare VGCF based on the deposition of hydrocarbons or other gaseous carbon sources over small metal particles such as iron, cobalt, nickel or their alloys [5–8]. It is well known that the deposition process plays an important role in the morphology and structure of VGCF. It is very important to understand clearly the growth mechanisms of VGCF in further technical improvements and innovations for large-scale synthesis and structural controls. Up to now, the

*Corresponding author, e-mail: liulang@public.ty.sx.cn

structure of VGCF is two-double layers [9, 10]: the inner layer is the core structure of VGCF formed of oriented carbon layers, while the outer layer is made of decomposed carbon. The most popular mechanism of catalytic growth of VGCF has two stages, as follows: in the first stage, metal-catalytic growth of the core structure occurs, and then, in the second stage, deposition growth of the outer layer of VGCF occurs. The growth mechanism of the metal-catalytic growth of the core structure of VGCF has been extensively studied. The adsorption–diffusion–precipitation (ADP) model developed by Baker et al. [11] has been widely accepted [12–15]. In this model, C_n species are first adsorbed on the surface of a metal particle, then they diffuse through the metal particle, and finally they precipitate in a crystalline tubular form. However, little information about the growth of the outer layer of VGCF in the second stage has been reported in the published literature.

The aim of this work was to obtain VGCF synthesized at various growth times, in order to clarify the growth mechanism of the outer layer of VGCF.

2. Experimental

VGCF was synthesized through the catalytic pyrolysis of methane. A graphite substrate was merged in a catalyst-contained solution, dried at room temperature for at least 8.0 h and then heated in an oven at 383 K for 2.0 h. The catalytic decomposition of methane was carried out in a flow reactor under the atmospheric pressure. The graphite substrate was placed in the centre of the reactor tube (inner diameter 36 mm, length 800 mm). A methane/hydrogen gas mixture (volume ratio 1:1) was introduced into the reactor when the temperature was raised to 1373 K. The growth time was varied from 0.5 h to 6.0 h. Subsequently the as-prepared VGCFs were examined by the scanning electron microscopy (SEM).

3. Results and discussion

3.1. Morphology evolution of VGCF at prolonged growth time

The morphologies of VGCF, synthesized at various times from 0.5 h to 6 h are shown in Fig. 1. Figure 1a shows that the linear and smooth carbon fibres coexist with rough fibres when the reaction time is 0.5 h. The diameter of smooth carbon fibres is about 200 nm, while the diameter of rough fibres is about 300 nm. When the reaction time is prolonged to 1.0 h, the morphology of carbon fibre transforms from linear carbon fibres to carbon micro-bead chains (Fig. 1b). In addition, the surface of carbon micro-beads is rough, while the surface of the segment 1 beside carbon micro-beads is relatively smooth and the diameter of this part is about 200 nm. This implied a transitional morphology of carbon micro-beads having diameters of approximately 200 nm.

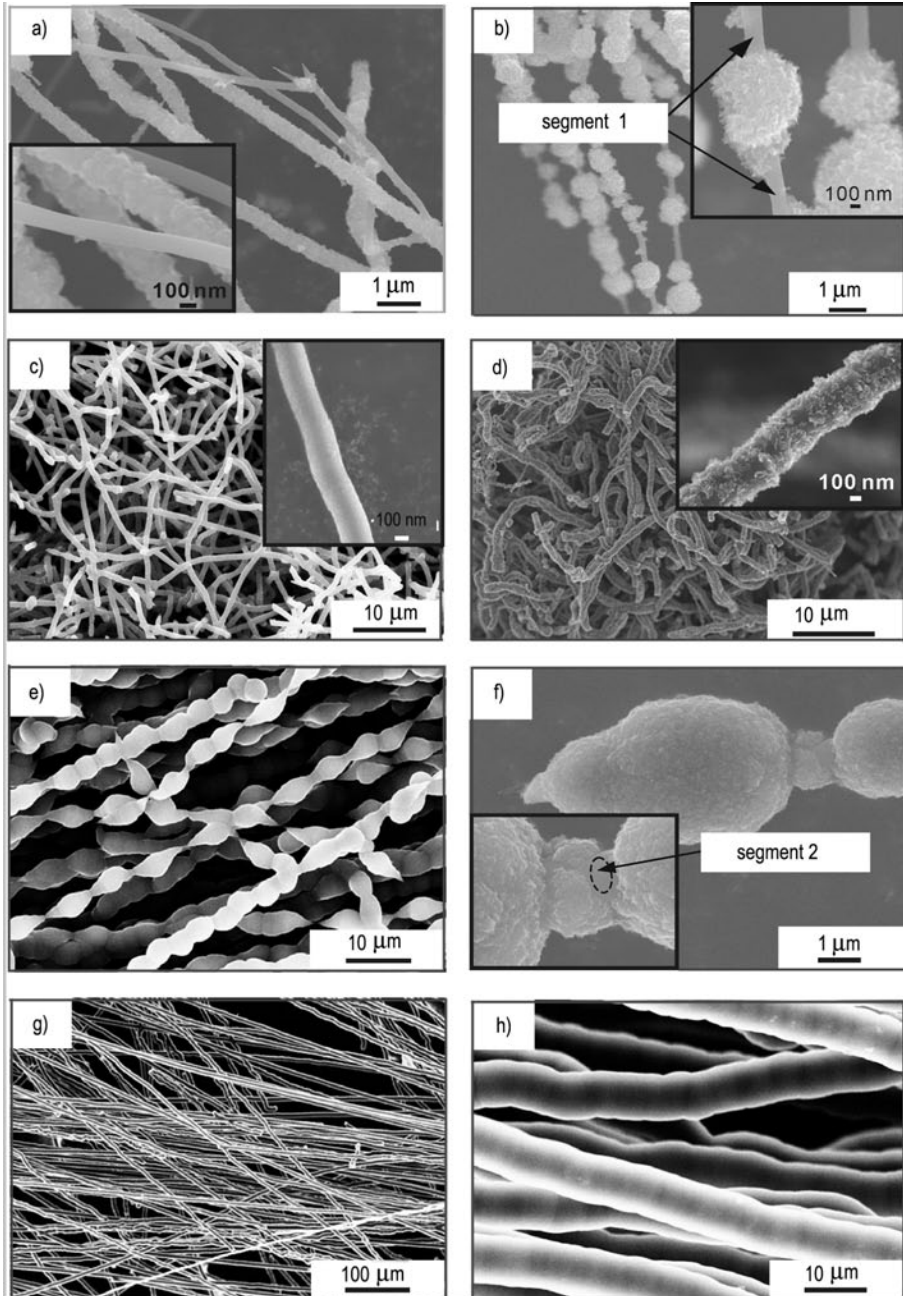


Fig. 1. Effect of growth time on morphologies of VGCF:
 a) 0.5 h, b) 1.0 h, c) 2.0 h, d) 2.5 h, e, f) 4.0 h and g, h) 6.0 h

As shown in Fig. 1c, the diameter of as-prepared fibres at 2.0 h is about 2 μm and most of them are straight and smooth. Figure 1d shows that when the reaction time is

prolonged to 2.5 h, the carbon fibres of the diameters of ca. 2 μm are rough. The morphology of carbon fibres changes from linear fibres to carbon micro-bead chains again, when the reaction time is prolonged to 4.0 h (Figs. 1e, f). The carbon micro-beads on the fibres are homogeneous and the distance between the centres of two adjacent micro-beads is about 5–7 μm . Figure 1f shows that the surface of carbon micro-beads is rough, while the surface of the segment 2 between two adjacent carbon micro-beads is relatively smooth and the diameter of this part is about 2 μm , indicating that carbon micro-bead chains transformed from linear fibres approximately 2 μm in diameter

When the growth time is prolonged to 6.0 h, as-prepared carbon fibres having diameters of ca. 6 μm are straight and smooth (Figs. 1g, h). It is noticed that there are some indistinct protuberances, just like the shadow of carbon beads among carbon fibres, as shown in Fig. 1h. This suggested that these carbon fibres were obtained from carbon micro-bead chains.

Gradual enlargement of fibre diameters is not the only feature characterizing the morphological evolution of VGCF as a function of prolonged reaction time: linear carbon fibres change to carbon micro-bead chains and then to thicker linear fibres.

3.2. Growth mechanism of the outer layer of VGCF

Based on the SEM observations, a simple growth mechanism of the outer layer of VGCF is proposed, and henceforth referred to as fibre–bead–thicker fibre (Fig. 2).

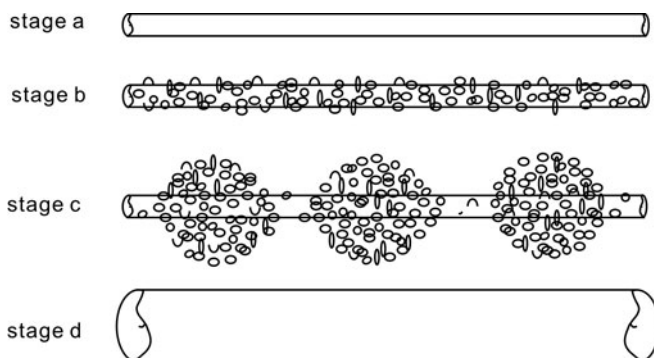


Fig. 2. Two-dimensional scheme of the proposed growth mechanism of the outer layer of VGCF

First, the linear and smooth carbon nanofibres appear (stage a). Secondly, the carbon nanoparticles pyrolyzed from methane precipitate on the surface of VGCF symmetrically, and then carbon fibres with rough surfaces form the stage b. Thirdly, with the prolongation of the reaction time, more and more carbon nanoparticles precipitate on the surface of the fibres formed earlier, and, at the same time, they self-assemble to shape micro-beads. The carbon fibres look like the carbon micro-bead chains (stage c).

Finally, carbon nanoparticles precipitate continuously and fill in the interstice between the adjacent carbon beads, and therefore thicker, linear and smooth fibres appear (stage d).

In stage c, it is reasonable to ask the following question: why should carbon-bead chains appear? It is presumed that at high temperature carbon nanoparticles from carbon source have high surface energy. If these nanoparticles precipitate on the former fibres symmetrically, they will have higher surface areas and higher energies. It is known that conglobulations possess the lowest surface area and the surface energy. A new microstructure-like sphericity may form, which has simultaneously lower surface area and lower surface energy, thus nanoparticles self-assemble to form carbon micro-beads. In stage d, the indentations on carbon micro-bead chains might have higher energy and higher surface areas. With the prolongation of the growth time, the carbon nanoparticles pyrolyzed from methane are adsorbed in the interstice between the adjacent carbon beads, and then carbon fibres with many protuberances appear. Because the least energy principle governs the growth process at all times, thicker, linear and smooth carbon fibres can be finally obtained with the continuous deposition of carbon nanoparticles.

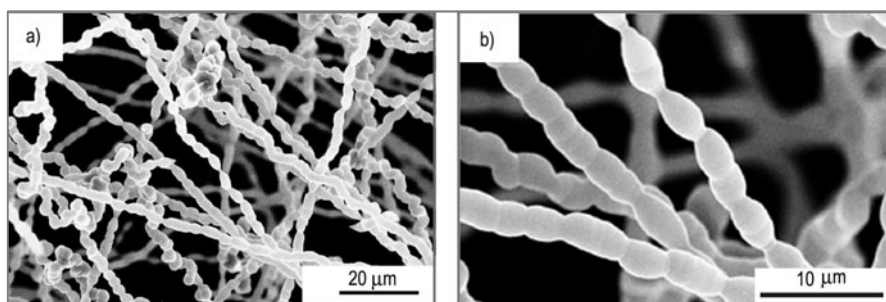


Fig. 3. SEM of as-prepared carbon fibres at 5.0 h

To test this model, an additional experiment with the reaction time 5.0 h was carried out and as-prepared carbon fibres were examined (Fig. 3). Figure 3a shows many protuberances on the carbon fibres. In Figure 3b the distance between the centres of two adjacent protuberances is 5–7 μm, which corresponds to the distance between the centres of two adjacent carbon micro-beads (Figs. 1e, f). This suggests that carbon fibres with many protuberances were representative of the transitional morphology from carbon micro-bead chains to linear carbon fibres. This result is consistent with the growth process fibre–bead–thicker-fibre.

4. Conclusions

The growth time has a significant influence on the morphologies of VGCF synthesized through the catalytic pyrolysis of methane. As the syntheses of VGCF proceed,

the morphology of VGCF changes from linear carbon fibres to carbon micro-bead chains, and then to thicker linear fibres, the diameters of VGCF increase from 200 nm to several micrometers. Furthermore, some kinds of VGCF with unusual morphology, such as carbon micro-bead chains etc. can be obtained by adjusting the reaction time. The growth mechanism of outer layers of VGCF fibre–bead–thicker fibre is proposed: first, growth of linear and smooth carbon nanofibres occurs, then decomposed carbon deposits on a smooth surface and assembly into carbon micro-bead chains occurs: lastly, pyrolytic carbon continuously precipitates in the interstice between adjacent carbon beads and thicker, linear and smooth fibres form.

Acknowledgements

This work was performed in the Key Laboratory of Carbon Materials, Institute of Coal Chemistry, Chinese Academy of Sciences and supported by the National 863 Programs of China.

References

- [1] SHIBUYA M., SAKURAI M., TAKAHASHI T., *Comp. Sci. Techn.*, 67 (2007), 3338.
- [2] LEE B.J., SIVAKKUMA S.R.R., KO J.M., KIM J.H., JO S.M., KIM D.Y., *J. Power Sources*, 168 (2007), 546.
- [3] ZHU H., LI X., XU C., WU D., *Mater. Res. B.*, 37 (2002), 177.
- [4] CHOI Y.K., SUGIMOTO K., SONG S.M., GOTOH Y., OHKOSHI Y., ENDO M., *Carbon*, 43 (2005), 2199.
- [5] REN X., ZHANG H., CUI Z.L., *Mater. Res. B.*, 42 (2007), 2202.
- [6] MÉNDEZ A., FREITAS M.M.A., FIGUEIREDO J.L., *Carbon*, 44 (2006), 2350.
- [7] BENISSAD-AISSANI F., AÏT-AMAR H., SCHOULER M.C., GADELLE P., *Carbon*, 42 (2004), 2163.
- [8] SCHLÜTER O.F.K., WEHNER B.I., HU D., XIA W., QUANDT T., MARGINEAN G., BRANDL W., MUHLER M., *Appl. Catal. A*, 274 (2004), 71.
- [9] TIBBETTS G.G., *Carbon*, 27(1989), 745.
- [10] TING J.M., HUANG N.Z., *Carbon*, 39 (2001), 835.
- [11] BAKER R.T.K., BARBER M.A., HARRIS P.S., FEATES F.S., WAITE R.J., *J. Catal.*, 26 (1972), 51.
- [12] SNOECK J.W., FROMENT G.F., FOWLES M., *J. Catal.*, 169 (1997), 250.
- [13] DUPUIS A.C., *Prog. Mater. Sci.*, 50 (2005), 929.
- [14] LEE C.J., PARK J., *J. Phys. Chem. B*, 105 (2001), 2365.
- [15] LIU L., FAN S.S., *J. Am. Chem. Soc.*, 123 (2001), 11502.

Received 3 September 2008

Relaxor characteristics of ferroelectric BaZr_{0.2}Ti_{0.8}O₃ ceramics

C. FU^{1,2*}, F. PAN¹, W. CAI^{1,2}, X. DENG², X. LIU²

¹School of Materials Science and Engineering, Chongqing University, Chongqing 400030, China

²School of Metallurgical and Materials Engineering,
Chongqing University of Science and Technology, Chongqing 401331, China

The crystalline microstructure, surface morphology, and the dielectric properties of BaZr_{0.2}Ti_{0.8}O₃ (BZT) ceramics are investigated. From the X-ray diffraction pattern, it is found that the *c*-axis lattice parameter of the BZT ceramics is greater than the *a*-axis one. The temperature dependence of the electric permittivity indicates that there exists a diffuse transition in BZT ceramics. According to a modified Curie-Weiss law, it is calculated that the diffuseness constant (γ) equals 1.93. From the hysteresis loops, it is found that the remanent polarization ($2P_r$) and the coercive field ($2E_C$) of BZT ceramics both increase as the applied maximum voltage increases.

Key words: barium zirconium titanate; ceramics; diffuse phase transition; hysteresis loop

1. Introduction

Barium titanate (BaTiO₃) ceramics have been used extensively as capacitor dielectrics for decades. Pure BaTiO₃ undergoes a paraelectric-to-ferroelectric phase transition at 130 °C, appearing as a sharp peak in the permittivity curve. Isovalent dopants, such as strontium and zirconium, are often employed to shift the Curie point for particular applications. The Ba_xSr_{1-x}TiO₃ (BST) has a high electric permittivity, low leakage current and low dielectric dispersion against frequency [1–3]. However, the leakage current often abruptly shoots up by several orders of magnitude as the applied field exceeds a critical value of several hundred kV/cm, and breakdown occurs at a field around 2MV/cm [2, 3]. Recently, BaZr_xTi_{1-x}O₃ (BZT) has been chosen as an alternative to BST in the fabrication of ceramic capacitors. The Zr⁴⁺ ion (0.087 nm) is chemically more stable than Ti⁴⁺ (0.068 nm) and has a larger ionic size to expand the lattice. Therefore, the conduction by electron hopping between Ti⁴⁺ and Ti³⁺ would be reduced by the substitution of Ti by Zr [4].

*Corresponding author, e-mail: chlflu@126.com

In past years, some preliminary results on the preparation, microstructure and properties of BZT ceramics have been reported [5-11]. For example, BZT powders were synthesized through a hydrothermal reaction by using amorphous $\text{BaZr}_x\text{Ti}_{1-x}$ -peroxo-hydroxide and there is diffuse transition in $\text{BaZr}_{0.2}\text{Ti}_{0.8}\text{O}_3$ ceramics [5]. Moreover, a relaxor ferroelectric characteristic was observed for $\text{BaZr}_{0.2}\text{Ti}_{0.8}\text{O}_3$ ceramics [5-7]. However, descriptions of the relaxor characteristics of $\text{BaZr}_{0.2}\text{Ti}_{0.8}\text{O}_3$ ceramics by the conventional mixed-oxide method have not been found in the literature.

In this paper, the crystalline microstructure, surface morphology, relaxor characteristics and hysteresis loops of $\text{BaZr}_{0.2}\text{Ti}_{0.8}\text{O}_3$ ceramics are investigated by the conventional mixed-oxide method.

2. Experimental

The starting chemicals were 99.5% BaCO_3 , ZrCO_3 and TiO_2 powders used as received. A series of samples of $\text{BaZr}_{0.2}\text{Ti}_{0.8}\text{O}_3$ ceramics were prepared by the conventional mixed oxide method. The raw material was weighed in stoichiometric proportions, ball-milled in water, dried and then calcined at 1200 °C for 2 h. The obtained powders were pressed at 20 MPa into disks 10.0 mm in diameter, 1.5 mm thick prior to sintering at 1350 °C for 4 h. After sintering, X-ray diffraction (XRD) with $\text{CuK}\alpha$ radiation ($\lambda = 0.1541$ nm) was used to examine the phase composition of the specimens at room temperature. The morphology of $\text{BaZr}_{0.2}\text{Ti}_{0.8}\text{O}_3$ ceramics was investigated by the scanning electron microscopy (SEM). Before measurements of electric capacitances, polished samples were covered with silver paste and fired at 830 °C for 15 min. Then a HIOKI 3532-50 LCR at 1 V/mm was used while the samples were heated from -55 °C to 200 °C at the rate of 0.5 °C/min. The electric permittivity was calculated based on the capacitance from the equation:

$$\varepsilon = C \frac{d}{\varepsilon_0 A} \quad (1)$$

where C is the capacitance (F), ε_0 the free space electric permittivity (8.85×10^{-12} F/m), A the capacitor area (m^2) and d the thickness (m) of the ceramics. The polarization–electric voltage (P – V) hysteresis characteristics were determined using a radiant precision LC material analyzer.

3. Results and discussion

3.1. Crystal structure

The X-ray diffraction pattern of $\text{BaZr}_{0.2}\text{Ti}_{0.8}\text{O}_3$ ceramics is shown in Fig. 1. It is evident that the ceramics are of perovskite crystal structure. No other phases are ob-

served in the spectra. The lattice constants of BZT ceramics were calculated from the following equation:

$$d_{hkl} = \left[\left(\frac{h}{a} \right)^2 + \left(\frac{k}{a} \right)^2 + \left(\frac{l}{c} \right)^2 \right]^{-1/2} \quad (2)$$

where d_{hkl} is the interplanar distance, h , k and l are the crystallographic indices. The c axis lattice parameter ($c = 0.4107$ nm) of the BZT ceramics is greater than the a axis one ($a = 0.4101$ nm), the ratio c/a being 1.001. It is suggested that the crystal structure of the ceramics belongs to tetragonal phase and is close to cubic phase.

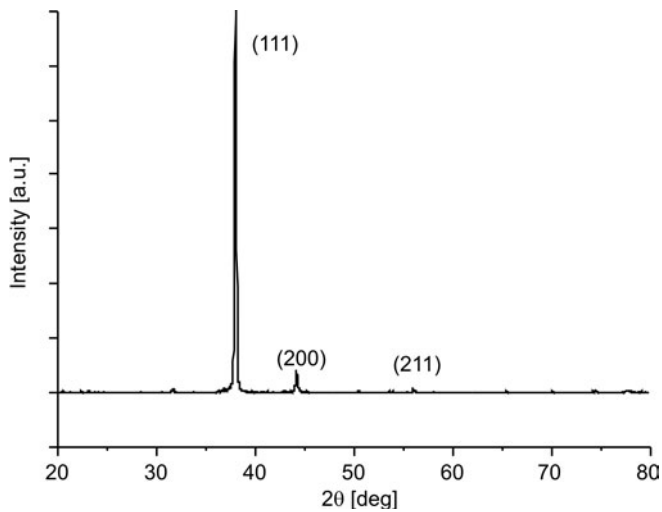


Fig. 1. XRD pattern of BaZr_{0.2}Ti_{0.8}O₃ ceramics

3.2. Surface morphology

Figure 2 shows a typical SEM micrograph of BaZr_{0.2}Ti_{0.8}O₃ ceramics. It is seen that it is very dense and crack-free. The average grain size of the ceramics is ca. 45 μ m.

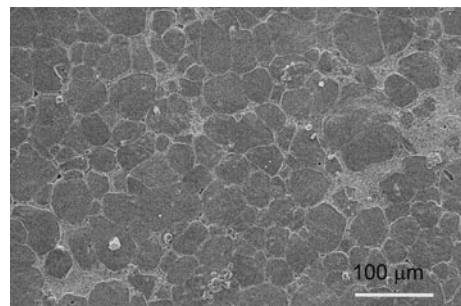


Fig. 2. Scanning electron micrograph of BaZr_{0.2}Ti_{0.8}O₃ ceramics

3.3. Temperature dependence

The temperature dependence of the electric permittivity of $\text{BaZr}_{0.2}\text{Ti}_{0.8}\text{O}_3$ ceramics is shown in Fig. 3. The maximum value of the electric permittivity occurs at 50 °C.

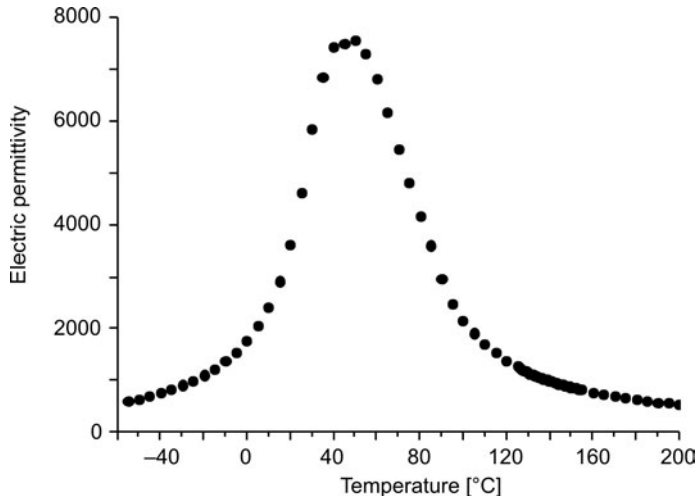


Fig. 3. Temperature dependence of the electric permittivity of $\text{BaZr}_{0.2}\text{Ti}_{0.8}\text{O}_3$ ceramics at 1 kHz

Compared with BST ceramics [12], the electric permittivity of BZT ceramics exhibited broad peaks indicating occurrence of a diffuse phase transition from ferroelectric to paraelectric phase.

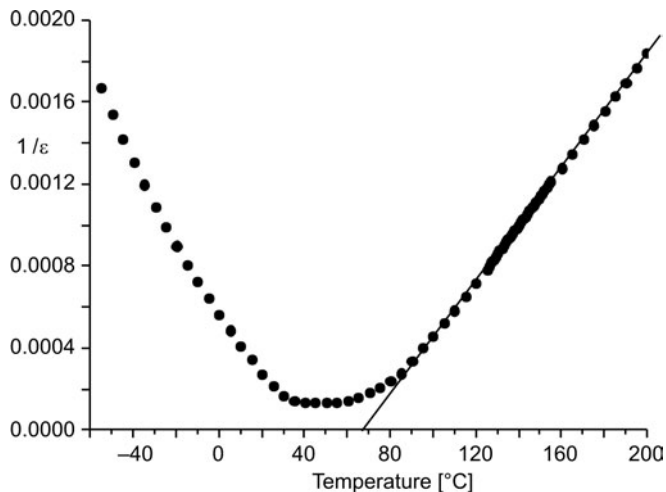


Fig. 4. Temperature dependence of the reciprocal value of the permittivity for $\text{BaZr}_{0.2}\text{Ti}_{0.8}\text{O}_3$ ceramics at 1 kHz

For a normal ferroelectric, at a temperature T above T_C , the dielectric behaviour follows the Curie–Weiss law:

$$\frac{1}{\varepsilon} = \frac{T - T_0}{C} \quad (3)$$

where T_0 is the Curie–Weiss temperature and C the Curie–Weiss constant. The temperature dependence of the reciprocal of the electric permittivity is shown in Fig. 4. It can be seen that the dielectric behaviour does not completely follow the Curie–Weiss law at temperatures above T_C . The Curie–Weiss temperature can be obtained from linear extrapolation of the reciprocal values of the electric permittivities in the high-temperature range.

A modified Curie–Weiss law was proposed to describe the diffuseness of the ferroelectric phase transition [6, 7]:

$$\frac{1}{\varepsilon} - \frac{1}{\varepsilon_m} = \frac{(T - T_m)^\gamma}{C_1} \quad (4)$$

where ε_m and T_m represent the maximum of electric permittivity and the corresponding temperature. Here, γ and C_1 are assumed to be constant. The parameter γ provides information about the character of the phase transition: for $\gamma = 1$, the normal Curie–Weiss law is followed, whereas $\gamma = 2$ describes a complete diffuse phase transition.

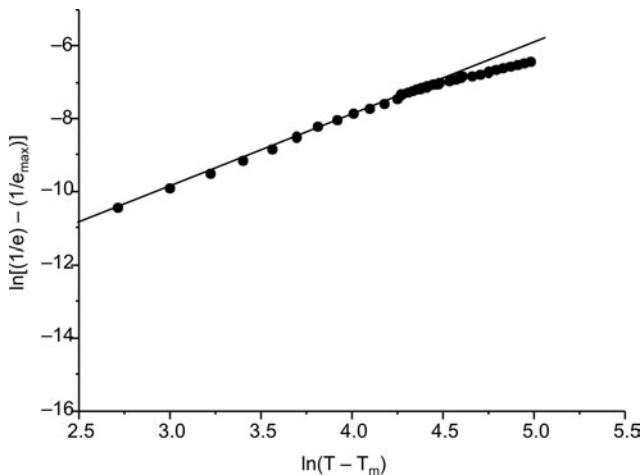


Fig. 5. Dependence of $\ln(1/\varepsilon - 1/\varepsilon_m)$ on $\ln(T - T_m)$ at 1 kHz

T_m and $1/\varepsilon_m$ of BaZr_{0.2}Ti_{0.8}O₃ ceramics are 50 °C and 1.325×10^{-4} . The dependence of $\ln(1/\varepsilon - 1/\varepsilon_m)$ on $\ln(T - T_m)$ is shown in Fig. 5. According to Eq. (4), the slope of the curve gives the diffuseness constant γ . A nearly linear relationship is observed and the γ value equals 1.93. It implies that the BaZr_{0.2}Ti_{0.8}O₃ ceramics exhibits a strong diffuse phase transition, which may be due to the high Zr content.

3.4. Hysteresis loop

Figure 6 shows the polarization curves of the same ceramics with various applied maximum voltages at the frequency of 1 kHz. Typical hysteresis loops can be observed. This suggests that at room temperature the crystal structures are in the ferroelectric phase, which is consistent with the XRD patterns and the temperature dependence of the relative permittivity. Moreover, it is found that the remanent polarization ($2P_r$) and the coercive field ($2E_C$) of $\text{BaZr}_{0.2}\text{Ti}_{0.8}\text{O}_3$ ceramics both increased as the applied maximum voltage increased. As the applied maximum voltage increased from 500 V to 1000 V and 1500 V, the remanent polarization increased from $1.69 \mu\text{C}/\text{cm}^2$ to $3.10 \mu\text{C}/\text{cm}^2$ and $3.60 \mu\text{C}/\text{cm}^2$.

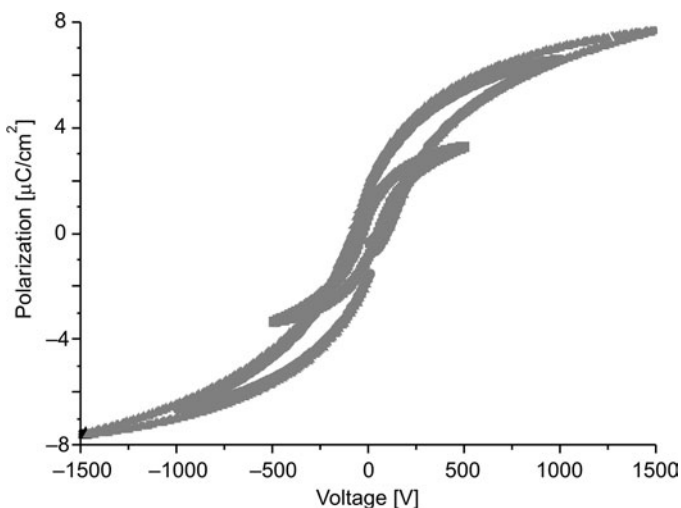


Fig. 6. Hysteresis loops for $\text{BaZr}_{0.2}\text{Ti}_{0.8}\text{O}_3$ ceramics with various applied maximum voltages at 1 kHz

Furthermore, the coercive field increased from $0.88 \text{ kV}/\text{cm}$ to $1.19 \text{ kV}/\text{cm}$ and $1.35 \text{ kV}/\text{cm}$. The number of ferroelectric domains along the direction of the applied electric field increased as the applied voltage increased. Therefore, the remanent polarization increased gradually. Accordingly, under reverse bias, the number of reversal domains increased. Consequently, the coercive field increased gradually.

4. Conclusions

The microstructures and dielectric properties of $\text{BaZr}_{0.2}\text{Ti}_{0.8}\text{O}_3$ ceramics were investigated. The c axis lattice parameter ($c = 0.4107 \text{ nm}$) of the BZT ceramics is greater than the a axis one ($a = 0.4101 \text{ nm}$). It was found that the crystal structure of the ceramics belongs to tetragonal phase and is close to cubic phase. There is a diffuse tran-

sition in BaZr_{0.2}Ti_{0.8}O₃ ceramics, and the diffuseness constant γ equals 1.93. It is found that the remanent polarization ($2P_r$) and the coercive field ($2E_C$) of BaZr_{0.2}Ti_{0.8}O₃ ceramics both increased as the applied maximum voltage increased.

Acknowledgements

This work is supported by the National Science Foundation for Post-doctoral Scientists of China (Grant No. 20070410774), the Natural Science Foundation of Chongqing, China (Grant No. CSTC2007BB4212) and the Research Foundation of the Education Bureau of Chongqing, China (Grant No. KJ071401 and No. KJ081411).

References

- [1] IOACHIM A., TOACSAN M.I., BANCIU M.G., NEDELICU L., VASILIU F., ALEXANDRU H.V., BERBECARU C., STOICA G., Prog. Solid State Chem., 35 (2007), 513.
- [2] FU C., PAN F., CHEN H., CAI W., YANG C., J. Mater. Sci. Mater. Electron., 18 (2007), 453.
- [3] LEE S.Y., CHIOU B.S., Jpn. J. Appl. Phys., 46 (2007), 6550.
- [4] CHOI W.S., JANG B.S., LIM D.G., YI J., HONG B., J. Cryst. Growth, 237–239 (2002), 438.
- [5] LEE B.W., CHO S.-B., J. Eur. Ceram. Soc., 25 (2005), 2009.
- [6] TANG X.G., CHEN K.H., CHAN H.L.W., Acta Mater., 52 (2004), 5177.
- [7] TANG X.G., WANG J., WANG X.X., CHAN H.L.W., Solid State Commun., 131(2004), 163.
- [8] CHOU X., ZHAI J., YAO X., J. Am. Ceram. Soc., 90 (2007), 2799.
- [9] LIANG R.H., DONG X.L., CHEN Y., CAO F., WANG Y.L., Ceram. Int., 33 (2007), 957.
- [10] SHAN D., QU Y.F., SONG J.J., Solid State Commun., 141 (2007), 65.
- [11] CAO W., XIONG J., SUN J., Mater. Chem. Phys., 106 (2007), 338.
- [12] FU C., YANG C., CHEN H., WANG Y. HU L., Mater. Sci. Eng. B, 119 (2005), 185.

Received 9 September 2008

Revised 13 November 2008

The sorption of copper ions by gyrolite in alkaline solution

A. BANKAUSKAITE, K. BALTAKYS*

Department of Silicate Technology, Kaunas University of Technology,
Radvilenu 19, LT – 50270 Kaunas, Lithuania

Sorption of copper ions by synthetic pure gyrolite ($\text{CaO/SiO}_2 = 0.66$; 96 h; 200 °C) in alkaline solutions was examined. When the initial concentration of Cu^{2+} ions is 1 g/dm³, the cation exchange capacity of the gyrolite is 100 mg Cu^{2+} /g after 360 min of sorption at 25 °C. It has been proved that the cation exchange capacity of gyrolite depends on the concentration of copper ions in the $\text{Cu}(\text{NO}_3)_2$ solution, because a five-fold increase of the concentration (from 1.0 to 5.0 g/dm³) reduces the duration of the ion exchange reaction by a factor of three (from 15 min to 5 min). In solutions with higher initial concentrations of Cu^{2+} ions (10.0 and 20.0 g/dm³), the sorption proceeds more intensively and all the copper ions are adsorbed in 1 min. It should be noted that the cation exchange reactions are reversible in alkaline solution, because nearly 90% of the copper ions are adsorbed in a physical process, while the remaining part of the cation exchange process takes place in a chemical reaction. Furthermore, the crystal structure of gyrolite is stable in alkaline solution. The products of sorption were characterized by X-ray diffraction, thermogravimetry–differential scanning calorimetry and Fourier-transform infrared spectroscopy methods.

Key words: *gyrolite; cation exchange; calcium silicate hydrate; X-ray diffraction*

1. Introduction

Greater urbanisation and ever-growing populations have accelerated the problem of collecting and disposing both solid and liquid wastes. The world has to face one of the biggest disasters – pollution. Manmade chemicals, many of them very toxic, can be difficult to recycle and expensive to destroy [1]. Most wastes, hazardous or not, are simply dumped together at the nearest available government-owned land or even thrown into the water. Consequently, it is very important to find a way to minimize the damage. One way to do this is to develop new effective sorption materials [2–7].

The first time calcium silicate hydrates were used for ion exchange almost three decades ago [8–11]. These compounds created a new family of inorganic cation ex-

*Corresponding author, e-mail: kestutis.baltakys@ktu.lt

changers. The ion exchange capacity of calcium silicate hydrates depends on their chemical composition as well as on the structure of their crystalline lattice. Both, naturally occurring and synthetic, unsubstituted calcium silicate hydrates are noted for their low ion exchange capacity, predetermined by the fact that Ca^{2+} ions in these compounds are inserted between separate layers and connected by a chemical bond with oxygen atoms [12–15]. Extraneous ions may interfere only if this bond is broken up. Importantly, additives increase the capacity of calcium silicate hydrates to extract heavy metal ions from water solutions [9–12, 16–19].

Supposedly, gyrolite can adsorb more chemical elements, because the interlayer sheets, with a thickness of about 2.2 nm (one of the largest in all the calcium silicate hydrates group) in the case of gyrolite, are available for the intercalation of a new guest by controlling the charge of the host [20–22].

Recently, the cation uptake reactions have been studied [23] of the transition metal ions (Mn^{2+} , Fe^{2+} , Co^{2+} , Ni^{2+} , Cu^{2+} , Zn^{2+} , Pb^{2+} , Cs^+ , Cd^{2+} , Hg^{2+}) with some synthetic crystalline calcium silicates such as xonotlite, gyrolite and β -wollastonite. The total amounts of ions uptaken by these solids have been found in a descending order: xonotlite – gyrolite – β -wollastonite. Moreover, the quantities of Fe^{2+} , Co^{2+} and Ni^{2+} ions taken up by xonotlite and wollastonite were found to be higher than those of the other cations. On the other hand, gyrolite showed a low selectivity towards different elements.

It should be underlined that the reaction of xonotlite and β -wollastonite with Fe^{2+} , Pb^{2+} , Cd^{2+} and Hg^{2+} leads to the precipitation of goethite [$\text{FeO}(\text{OH})$], hydrocerussite [$\text{Pb}_3(\text{CO}_3)_2(\text{OH})_2$], otavite [CdCO_3] and $\text{HgCO}\cdot 2\text{HgO}$ phases. Meanwhile, reaction of Cu^{2+} and Zn^{2+} ions with β -wollastonite or gyrolite leads to the precipitation of gerhardite [$\text{Cu}_2(\text{OH})_3\text{NO}_3$] and zincate [$\text{CaZnO}_2\cdot x\text{H}_2\text{O}$] phases [23].

However, in all papers quoted no detailed data can be found on the dependence of the stability of the crystal structures of calcium silicate hydrates on pH of a solution. Moreover, it is very important to identify the influence of pH on the parameters governing the ion exchange reaction.

The objectives of the present work were to explore the cation exchange capacity of gyrolite for Cu^{2+} ions in an alkaline solution, and to evaluate the potential for its application as a new, effective sorption material. The cation exchange reaction mechanism is presented.

2. Experimental

Pure gyrolite was synthesized after 96 h at 200 °C from a stoichiometric composition ($\text{CaO}/\text{SiO}_2 = 0.66$) of calcium oxide (CaO was produced by burning calcium oxide at 950 °C for 0.5 h, specific surface area $S_a = 548 \text{ m}^2/\text{kg}$, evaluated by Blaine's method) and fine-grained $\text{SiO}_2\cdot n\text{H}_2\text{O}$ (ignition losses 21.28%, $S_a = 1155 \text{ m}^2/\text{kg}$) mixture. The dry primary mixture was mixed with water in stainless steel vessels (water/solid ratio of the suspension $W/S = 10.0$). The product was filtered off, dried at

50 ± 5 °C and sieved (the mesh size was 50 μm). Such conditions of the synthesis were chosen according to the previously published data [24, 25].

Ion exchange experiments were carried out at 25 °C in a Grant SUB14 thermostatic adsorber by stirring 1 g of gyrolite in 100 cm^3 of $\text{Cu}(\text{NO}_3)_2$ aqueous solution, containing 1, 5, 10, 20 g/dm^3 of Cu^{2+} ions, for 360 min. Different amounts of NH_4OH aqueous solution ($c = 10\%$) were used to prevent $\text{Cu}(\text{OH})_2$ precipitation and to maintain the alkalinity of the solution. The initial concentration of Cu^{2+} ions and the pH value of the solution are shown in Table 1.

Table 1. Initial concentration of Cu^{2+} ions and pH of solutions

Cu^{2+} ions concentration in the solution [g/dm^3]	pH of solution	The amount of NH_4OH [cm^3]
1	10.38	5.5
5	9.79	8
10	9.69	13
20	9.62	25

The percentage of exchange was determined using a Perkin-Elmer Analyst 4000 spectrometer based on the changes of the concentrations of the cations in the solution and the cations in the gyrolite. The pH value was measured with a Hanna instrument (Hi 9321, microprocessor pH meter).

The X-ray powder diffraction (XRD) data were collected with a DRON-6 X-ray diffractometer, endowed with the Bragg-Brentano geometry, using Ni-filtered CuK_α radiation and a graphite monochromator, operating at a voltage of 30 kV and an emission current of 20 mA. The scan-step covered the angular range $2-60^\circ$ (2θ) in steps of 0.02° .

Simultaneous thermal analysis (STA) comprising both differential scanning calorimetry (DSC) and thermogravimetry (TG) was also employed for measuring the thermal stability of gyrolite at a heating rate of 15 °C/min; the temperature ranged from 30 °C up to 1000 °C, under air atmosphere. The test was carried out on a Netzsch STA 409 PC Luxx instrument. Ceramic sample handlers and Pt-Rh crucibles were used.

FT-IR spectra were obtained with the aid of a Perkin Elmer FT-IR Spectrum X system. The specimens were prepared by mixing of 1 mg of a given sample with 200 mg of KBr. Spectral analyses were performed in the range of $4000-400$ cm^{-1} with the spectral resolution of 1 cm^{-1} . The specific surface area of the raw materials was determined by Blaine's method with an air permeability apparatus (Model 7201, Toni Technik Baustoffprüfsysteme GmbH).

3. Results and discussion

Synthetic gyrolite was characterized by XRD, STA, and FT-IR spectroscopy to evaluate its purity (Fig. 1). XRD analysis showed that in the $\text{CaO-SiO}_2 \cdot n\text{H}_2\text{O-H}_2\text{O}$

system pure gyrolite within 96 h at 200 °C was formed. The most characteristic peak of gyrolite (d spacing 2.2390 nm), not characteristic of other calcium silicate hydrates, was identified. Moreover, in the X-ray diffraction patterns, the peaks were determined by d spacings equal to 0.1262, 0.8371, 0.4197, 0.3732, 0.3511, 0.2803, 0.2141 nm, which are also typical of gyrolite (Fig. 1a). The results of XRD were confirmed by other analyses. On the DSC curve, a broad endothermic peak at 145 °C reflects the loss of physisorbed and interlayer water from the crystal structure of gyrolite (Fig. 1b). The other exothermic peak at 853 °C is associated with recrystallization of this compound into wollastonite. The shape of the absorption bands of the FT-IR spectrum, its multiplicity and width also are characteristic of gyrolite (Fig. 1c).

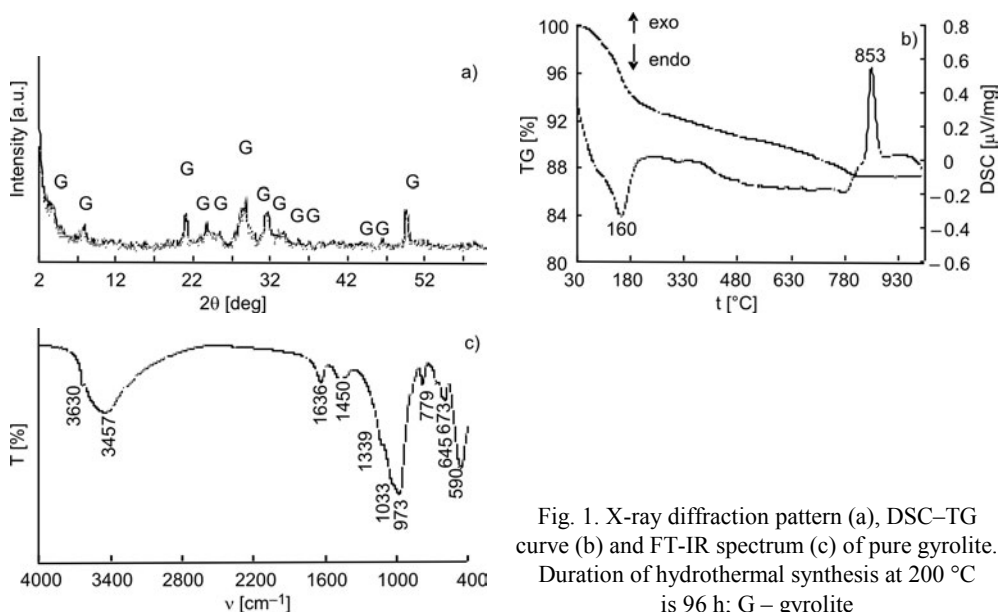


Fig. 1. X-ray diffraction pattern (a), DSC-TG curve (b) and FT-IR spectrum (c) of pure gyrolite. Duration of hydrothermal synthesis at 200 °C is 96 h; G – gyrolite

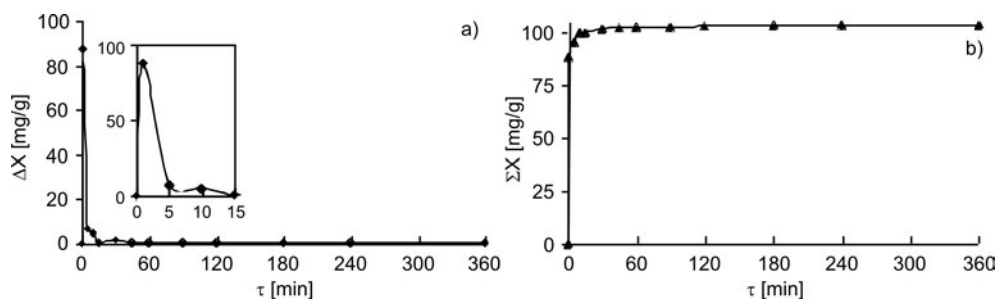


Fig. 2. Differential (a) and integral (b) kinetic curves of Cu^{2+} ions adsorption from $\text{Cu}(\text{NO}_3)_2$ solution at the initial concentration of Cu^{2+} ions of 1.0 g/dm^3 , at 25 °C

The results of ion exchange experiments showed that the cation exchange capacity of gyrolite depends on the concentration of copper ions in the $\text{Cu}(\text{NO}_3)_2$ solution. It

was noticed that the cation exchange reaction proceeds rapidly in the first minute of the adsorption process. The amount of adsorbed Cu^{2+} ions in the crystal lattice of gyrolite is equal to 88 mg Cu^{2+}/g at the initial concentration of Cu^{2+} ions of $1 \text{ g}/\text{dm}^3$ (Fig. 2a). Upon prolonging the duration of the sorption process, the concentration of Cu^{2+} ions in the solution slightly decreases, and after 15 min all the Cu^{2+} ions are incorporated into the crystal structure of gyrolite (100 mg Cu^{2+}/g) (Fig. 2b).

It should be noted that the cation exchange capacity of gyrolite increases greatly in the $5.0 \text{ Cu}^{2+} \text{ g}/\text{dm}^3$ solution. The amount of adsorbed copper ions in the crystal lattice of gyrolite is equal to 450 mg Cu^{2+}/g after 1 min (Fig. 3a). In this case, all the Cu^{2+} ions in the solution were incorporated in the adsorbent structure after 5 min of sorption (Fig. 3b).

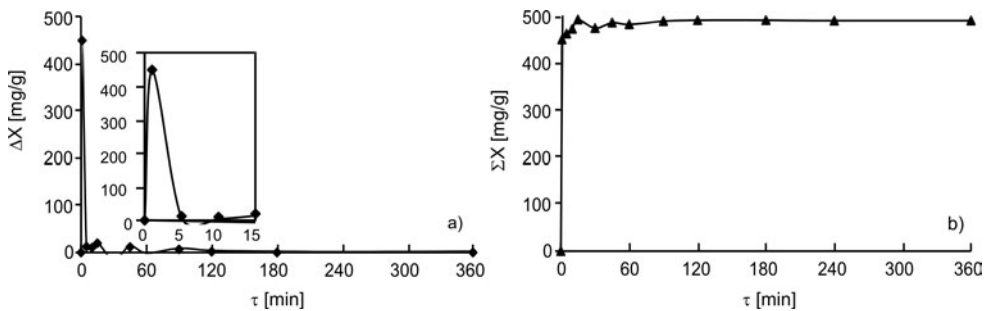


Fig. 3. Differential (a) and integral (b) kinetic curves of adsorption Cu^{2+} ions from $\text{Cu}(\text{NO}_3)_2$ solution at the initial concentration of Cu^{2+} ions of $5.0 \text{ g}/\text{dm}^3$ at 25°C

Thus, the five-fold increase in the Cu^{2+} ion concentration (from 1.0 to $5.0 \text{ g}/\text{dm}^3$) shortens the duration of the ion exchange reaction by a factor of 3 (from 15 min to 5 min). As expected, in the solutions having higher initial concentrations (10.0 and $20.0 \text{ g}/\text{dm}^3$), the sorption proceeds more rapidly and all copper ions are adsorbed in 1 min.

Several authors [8–11, 18] reported that the partial exchange $\text{Ca}^{2+} \leftrightarrow \text{M}^{2+}$ proceeds at the same time in both directions, i.e. the cation exchange reaction of these ions is reversible. Meanwhile, our results have shown that the partial exchange $\text{Ca}^{2+} \leftrightarrow \text{Cu}^{2+}$ is not in equilibrium, though the character of the desorption kinetic curves is close to that of the adsorption curves (Figs. 4–7). Most of the Ca^{2+} ions are released from the crystal lattice of gyrolite in the first minutes of sorption, and their concentration remains more or less the same, even when the process is prolonged. However, all Cu^{2+} ions were incorporated in the crystal lattice of gyrolite after 1–15 min (depending on the initial concentration of the solution), meanwhile the desorption of Ca^{2+} ions began only after 15 min, when the initial concentration of the solution was 1.0 , $5.0 \text{ g Cu}^{2+}/\text{dm}^3$ (Figs. 4, 5).

Furthermore, calcium ions are released into the solution only when all the copper ions are incorporated into the crystal lattice of gyrolite. It is presumed that the Cu^{2+} ions are intercalated in the interlayer sheets at the beginning of the sorption process, when the d spacing of this compound (2.2000 nm) is important. Calcium ions are re-

leased from the crystal lattice of gyrolite into the solution when the charge of the host is changed in order to maintain its neutrality.

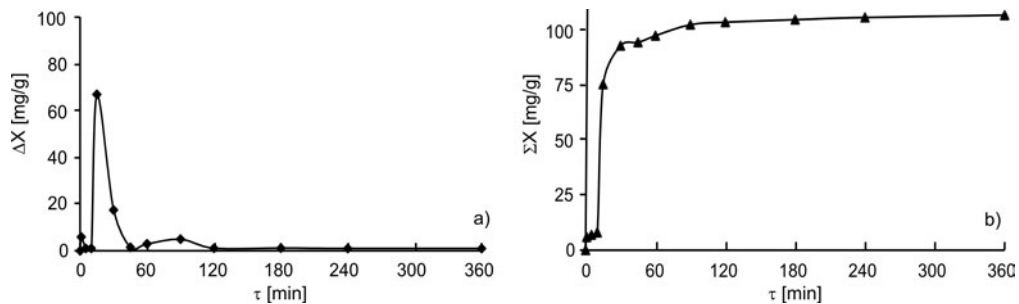


Fig. 4. Differential (a) and integral (b) kinetic curves of Ca^{2+} ions concentration in $\text{Cu}(\text{NO}_3)_2$ solution at the initial concentration of Cu^{2+} ions of 1.0 g/dm^3

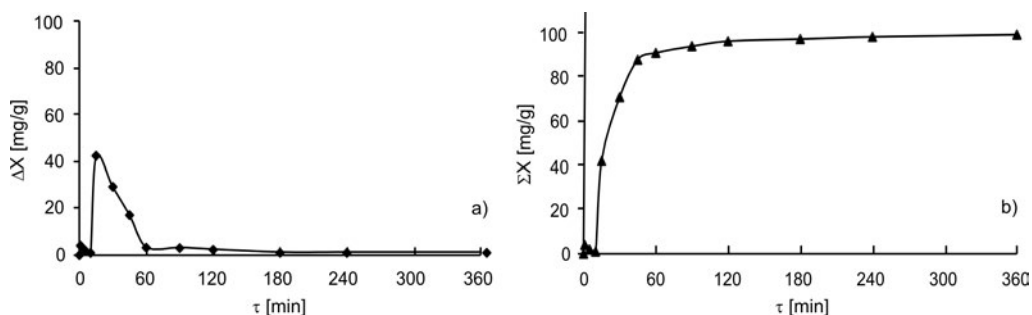


Fig. 5. Differential (a) and integral (b) kinetic curves of Ca^{2+} ions concentration in $\text{Cu}(\text{NO}_3)_2$ solution at the initial concentration of Cu^{2+} ions of 5.0 g/dm^3

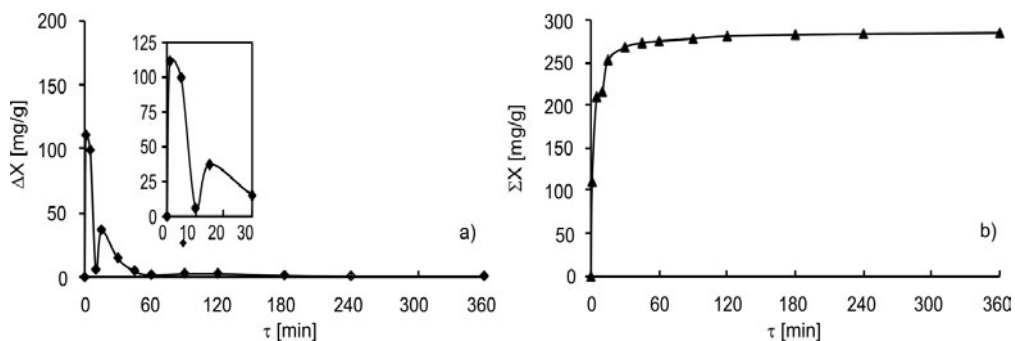


Fig. 6. Differential (a) and integral (b) kinetic curves of Ca^{2+} ions concentration in $\text{Cu}(\text{NO}_3)_2$ solution at the initial concentration of Cu^{2+} ions of 10.0 g/dm^3

Notably, an increase in the concentration of the copper ions in the solution accelerated the desorption of calcium ions. The concentration of released Ca^{2+} ions in the solution was greater than $100 \text{ mg Ca}^{2+}/\text{g}$ after 1 min, when $c_{\text{Cu}^{2+}}$ was equal to

10.0 g/dm^3 (Fig. 6a). The desorption process of calcium ions terminated after 60 min (275 mg Ca^{2+}/g) because the concentration of ions was almost the same when the duration of sorption was prolonged, and after 6 h their concentration was equal to 284 mg Ca^{2+}/g .

Unexpected results were obtained with 20 g $\text{Cu}^{2+}/\text{dm}^3$ because the concentration of desorbed Ca^{2+} ions in the solution was 20 mg Ca^{2+}/g (Fig. 7). The main reason might be the alkalinity of the solution. In this case, the pH was over 10 during the ion exchange experiment.

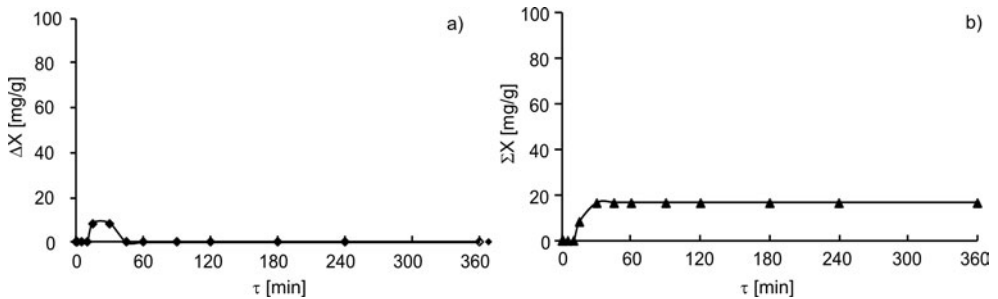


Fig. 7. Differential (a) and integral (b) kinetic curves of Ca^{2+} ions concentration in $\text{Cu}(\text{NO}_3)_2$ solution at the initial concentration of Cu^{2+} ions of 20.0 g/dm^3

The amounts of Cu^{2+} ions adsorbed from the solutions of various concentrations are listed in Table 2.

Table 2. The amount of adsorbed Cu^{2+} ions

$c_{\text{Cu}^{2+}}$ in the solution [g/dm^3]	The amount of adsorbed Cu^{2+} ions [mg/g], at 25 °C after 6 h of the sorption		
	Calculated from the data of differential and integral kinetic curves [mg/g]	Determined in the adsorbent [mg/g]	Average [mg/g]
1	100	100	100
5	500	490	495
10	1000	1000	1000
20	2000	1998	1999

As far as we know, this is the first time that cation exchange reactions have been seen to be reversible in alkaline solution. It has been proven that Cu^{2+} ions are released from the crystal lattice of gyrolite into solution during desorption. Nearly 90% of the copper ions were physisorbed, while the remaining ions took part in the chemical reaction. Thus, the sorption process in gyrolite is similar to the same process in clay minerals or zeolites. The amount of Cu^{2+} desorbed in the solution is given in Table 3.

Table 3. The amount of Cu^{2+} desorbed in solution

$c_{\text{Cu}^{2+}}$ in the solution [g/dm ³]	The amount of adsorbed Cu^{2+} ions from Table 2	The amount of desorbed Cu^{2+} ions [mg/g] at 25 °C after 60 min of desorption		
		[mg/g]	[%]	Average [%]
1	100	91	91	90
5	495	445.5	90	
10	1000	900	90	
20	1999	1779.1	89	

In order to identify the stability of gyrolite, the products of sorption were characterized by numerous methods of instrumental analysis. The X-ray powder diffraction analysis showed that the structure of gyrolite did not change during the sorption. In the X-ray diffraction pattern, the most characteristic peak (d spacing 2.2000 nm) of gyrolite was identified. This principal reflection did not change over the duration of the cation exchange reaction (Fig. 8).

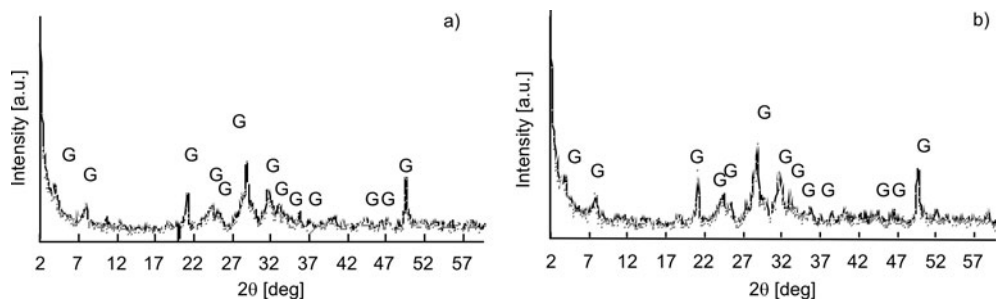


Fig. 8. X-ray diffraction patterns of gyrolite after adsorption (25 °C, 360 min) at the concentration of Cu^{2+} ions: a) 1.0 g/dm³, b) 5.0 g/dm³

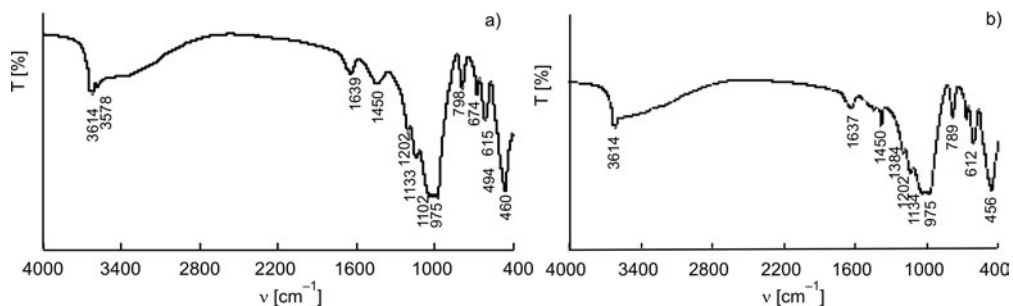


Fig. 9. FT-IR spectra of gyrolite after adsorption (25 °C, 360 min) at the concentration of Cu^{2+} ions: a) 1.0 g/dm³, b) 5.0 g/dm³

The results of XRD were confirmed by FT-IR spectroscopy. The presence of a very weak, sharp band at about 3630 cm^{-1} confirms the presence of OH^- groups

bound in the structure, while the presence of a broad band, located at 3457 cm^{-1} , and of a weak one, at 1636 cm^{-1} , may be due to the physically adsorbed water. Also, FT-IR spectroscopy data show that after the sorption process the intensities of absorption bands characteristic of gyrolite at about 1450 , 1339 and 1033 cm^{-1} are the highest (Fig. 9).

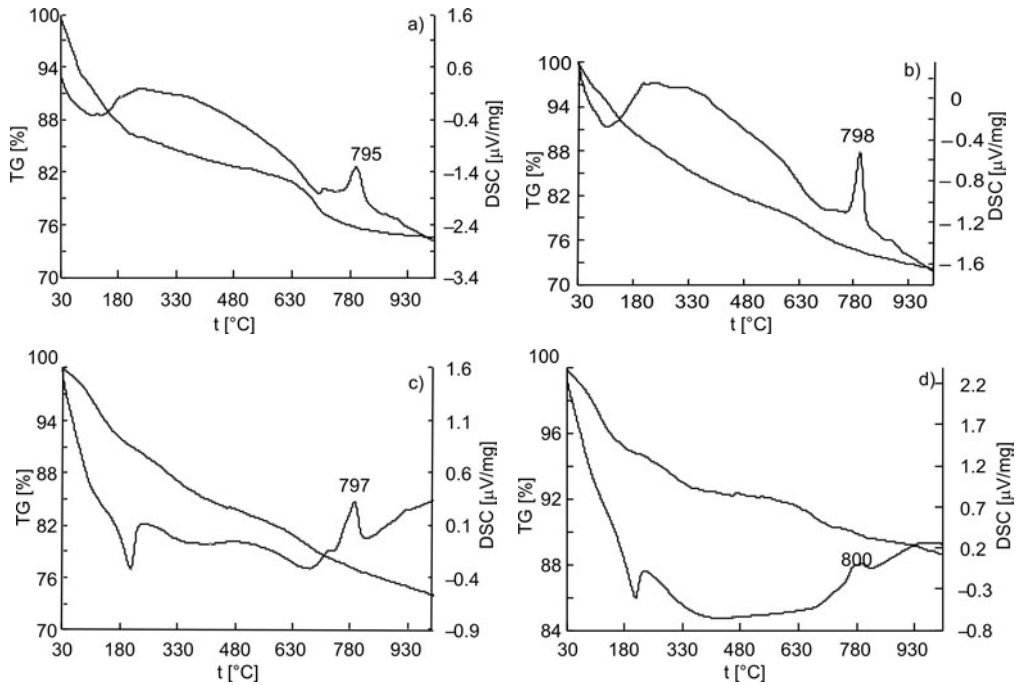


Fig. 10. DSC–TG curves of gyrolite after adsorption (25 °C, 360 min); concentration of Cu^{2+} ions, g/dm^3 : a) 1.0, b) 5.0, c) 10.0, d) 20.0

After the sorption process, the same thermal effects as in pure gyrolite (water dehydration and recrystallization to wollastonite) were identified. However, the temperature of the exothermic effect (853 °C) decreases by about 50 °C after the cation exchange reaction, as was identified in the DSC curve at the temperature range of $795\text{--}800\text{ °C}$ (Fig. 10).

4. Conclusions

The cation exchange capacity of gyrolite depends on the initial concentration of copper ions in the $\text{Cu}(\text{NO}_3)_2$ solution, because a five-fold increase in the concentration (from 1.0 to 5.0 g/dm^3) shortens the duration of the ion exchange reaction by a factor of three (from 15 min to 5 min). In the solutions having higher initial concentrations

(10.0, 20.0 g/dm³), the sorption proceeds more intensively and all copper ions are adsorbed in 1 min.

The cation exchange reactions are reversible in alkaline solutions, because nearly 90% of the copper ions are physically adsorbed, while the remaining ions take part in the chemical reaction.

During the sorption process, the crystal structure of synthetic pure gyrolite is stable in alkaline solution, when pH is at most 9.5. Meanwhile, the temperature of an exothermic effect, typical of recrystallization into wollastonite, decreases by about 50 °C after the cation exchange reaction.

References

- [1] HAK-SU K., Ministerial Conference on Environment and Development in Asia and the Pacific 2000 *Pollution and Waste*, Japan (2000).
- [2] ZHANG Q.R., DU W., PAN B.C., PAN B.J., ZHANG W.M., ZHANG Q.J., XU Z.W., ZHANG Q.X., *J. Hazard. Mater.*, 152 (2008), 469.
- [3] NABI S. A., NAUSHAD MU., INAMUDDIN, *J. Hazard. Mater.*, 142 (2007), 404.
- [4] NABI S.A., SHALLA A. H., KHAN A. M., GANIE S. A., *Coll. Surf. A: Physicochem. Eng. Aspects*, 302 (2007), 241.
- [5] NABI S. A., NAUSHAD MU., *Coll. Surf. A: Physicochem. Eng. Aspects*, 293 (2007), 175.
- [6] WANG S., WU H., *J. Hazard. Mat.*, 136 (2006), 482.
- [7] KASPERAVICIUTE V., BALTAKYS K., SIAUCIUNAS R., *Ceram. Sil.*, 52 (2008), 95.
- [8] LABHESTWAR N., SHRIVASTAVA O. P., *J. Mater. Sci.*, 24 (1989), 4359.
- [9] KOMARNENI S., ROY D. M., *J. Mater. Sci.*, 24 (1985), 2930.
- [10] KOMARNENI S., ROY D. M., *Nature*, 221 (1983), 647.
- [11] KOMARNENI S., TSUJI M., *J. Am. Ceram. Soc.*, 72 (1989), 1668.
- [12] MICHIIHIRO M., MASAKI I., TAKASHI S., HIROYUKI K., TAKESHI M., *J. Com. Am. Cer. Soc.*, 73 (1990), 3524.
- [13] SABRY A., EL-KORASHY S.A., *Monats. Chemie*, 133 (2002), 333.
- [14] AL-WAKEEL E. I., EL-KORASHY S. A., EL-HEMALY S. A., RIZK M. A., *J. Mater. Sci.*, 36 (2001), 2405.
- [15] SIAUCIUNAS R., JANICKIS V., PALUBINSKAITE D., IVANAUSKAS R., *Ceram. Sil.*, 48 (2004), 76.
- [16] SHRIVASTAVA O. P., KOMARNENI S., *Cem. Concr. Res.*, 24 (1994), 573.
- [17] KOMARNENI S., ROY R., ROY D. M., *Cem. Concr. Res.*, 12 (1982), 773.
- [18] TSUJI M., KOMARNENI S., *J. Mat. Sci.*, 4 (1989), 698.
- [19] EL-KORASHY S. A., AL-WAKEEL E. I., EL-HEMALY S. A., RIZK M. A., *Egypt. J. Chem.*, 45 (2002), 723.
- [20] MERLINO S., *Mineral. Mag.*, 52 (1988), 377.
- [21] MEYER J. W., JAUNARAJ S. K. L., *Am. Mineral.*, 46 (1961), 913.
- [22] SHAW S., HENDERSON C. M. B., CLARK S. M., *Am. Mineral.*, 87 (2002), 533.
- [23] EL-KORASHY S. A., AL-WAKEEL E. I., EL-HEMALY S. A., RIZK M. A., *Egypt. J. Chem.*, 46 (2003), 27.
- [24] BALTAKYS K., SIAUCIUNAS R., *J. Mater. Sci.*, 41 (2006), 4799.
- [25] BALTAKYS K., SIAUCIUNAS R., *Cem. Concr. Res.*, 34 (2004), 2029.

Received 16 September 2008

Revised 8 December 2008

Fabrication of mesoporous mixed oxides containing copper and cerium by using substituted anionic clays as precursors

G. CARJA*, S. DRANCA, G. CIOBANU, E. HUSANU, I. BALASANIAN

Faculty of Chemical Engineering and Environmental Protection,
Technical University "Gh. Asachi" of Iasi, Iasi 700554, Romania

Copper and cerium partially substituted anionic clay was synthesized by the coprecipitation method. The XRD analysis and N₂ adsorption at 77 K indicated that calcination destroys the layered matrix of the clay, giving rise to mixed oxides having a high surface area and mesoporous characteristics; SEM analysis showed that the new formed mixed oxides consist of ensembles of highly agglomerated, interconnected nanoparticles. It results from XPS that copper and cerium both contribute to establish the specific redox properties on the surface.

Key words: *copper; cerium; mixed oxides; mesoporosity; textural characteristics*

1. Introduction

Nowadays, continuous efforts have been made to develop new and superior catalytic systems for removing toxic environmental pollutants, CO being one of the most dangerous of such pollutants. A selective oxidation seems to be the simplest way to remove it [1]. Recently, reported results show that a cost effective and promising catalytic system for the selective oxidation of CO is based on copper–cerium mixed oxides [2]. Not only the composition but also textural and surface properties are important to establish the catalytic performance of mixed oxides containing copper and cerium; the specific ensembles of the catalyst nanoparticles, more precisely their shape, size and the configuration pattern giving rise to tailored nanoporous properties and high surface areas are important for the practical applications of these materials [3]. Represented by a general formula $[M^{II}_{1-x}M^{III}_x(OH)_2]^{x+} [A^{m-}_{x/m} \cdot nH_2O]^{x-}$, layered double hydroxides anionic clays (LDHs) are built up of sheets of edge sharing metal octahedra, where in

*Corresponding author, e-mail: carja@uaic.ro

comparison with brucite $M(OH)_2$, part of the M^{II} is replaced by M^{III} metal cations; the excess positive charge is counterbalanced by exchangeable anions A^{m-} , located as water molecules, in the interlayer space [4]. The large variety of compositions that can be developed by altering the nature of the divalent and trivalent cations (M^{II} , M^{III}), the interlayer anions (A^{m-}) and the stoichiometric coefficient (x), give rise to a large diversity of layered, anionic, clay like structures, [5]. The thermal decomposition of hydrotalcite-like materials around 773 K gives rise to stable homogeneous and highly dispersed mixed metal oxides with a high surface area and specific acid–base/redox and textural properties with well known applications as catalysts [6–8]. Based on this data, we have synthesized copper and cerium partially substituted hydrotalcite-like anionic clays and further used them as precursors to obtain, for the first time to our knowledge, copper and cerium containing mixed oxides of specific mesoporous properties. We also present here the textural and surface properties of the new material.

2. Experimental

Sample syntheses. The hydrotalcite like samples were synthesized by the coprecipitation method in low saturation conditions [9], at 313 K, under a bubbling, constant flow of nitrogen and under vigorous stirring.

CuCeLDH: the precipitants NaOH, Na_2CO_3 and metal salts used as precursors: $Mg(NO_3)_2 \cdot 6H_2O$ (0.015 mol), $Al(NO_3)_3 \cdot 9H_2O$ (0.005 mol), $Cu(NO_3)_2 \cdot 3H_2O$ (0.015 mol), $CeNO_3 \cdot 6H_2O$ (0.005 mol) were added dropwise together in such a way that the pH of the synthesis medium was kept at a constant level of 8.9 ± 0.2 . The resulting light blue precipitate was aged at 305 K for 8 h under mild stirring, separated by centrifugation, washed extensively with warm, deionized water until sodium free, and dried under vacuum at 338 K. The CuCeLDH sample was calcined in air at 723 K (the temperature was raised at $8 K \cdot min^{-1}$ to 723 K, maintained there for 7 h and then cooled slowly in nitrogen) is denoted as cCuCeLDH.

MgAlLDH: 100 cm³ of aqueous solution of $Mg(NO_3)_2 \cdot 6H_2O$ (0.03 mol), $Al(NO_3)_3 \cdot 9H_2O$ (0.01 mol) and aqueous solution of the precipitants NaOH, Na_2CO_3 were added dropwise together in such a way that the pH remained constant (pH = 9.5). The resulting white precipitate was aged at 338 K for 24 h under stirring, separated by centrifugation, washed extensively with warm deionized water until sodium free and then dried under vacuum at 338 K.

Characterization. The chemical compositions of the synthesized samples were determined by X-ray fluorescence spectroscopy (Rigaku RIX2000 sequential X-ray fluorescence spectrometer).

XRD: X-ray powder diffraction patterns were recorded with a Philips PW 1840 diffractometer using monochromatic CuK_{α} radiation ($\lambda = 0.154$ nm), operating at 40 kV and 30 mA over a 2θ range from 4 to 70 degree. N_2 adsorption isotherms were measured on a Coulter SA 3100 automated gas adsorption system. Prior to the measurements,

the samples were heated under vacuum at 383 K for 5 h in order to expel the interlayer water molecules. Microcomputer processing controlled the analysis. The BET specific surface area (S_{BET}) was calculated by the standard Brunauer, Emmett and Teller method based on adsorption data [10]. Pore size distributions were calculated from the desorption branches of the isotherms by the Barret, Joyner and Halenda method [11] and the corrected Kelvin equation. Pore volume (V_p) values were determined by the De Boer t-plot method [12]. X-ray photoelectron spectra (XPS) were recorded using a Perkin Elmer model 5500-MT (ESCA/MC/SAM) surface science instrument equipped with a magnesium anode (1253.6 eV) operating at 15 kV and 20 mA. A microcomputer processor controlled the spectra acquisition and data handling. Samples were analyzed as powders dusted onto a double sided sticky tape in an analysis chamber, typically operating at 10^{-9} Torr. All binding energy values were determined with respect to the C 1s line (284.6 eV) of the carbon overlayer, and the standard deviation of the peak position was within ± 0.1 eV. The surface (XPS) concentration of each element, expressed as surface atomic ratios, was calculated from the corresponding peak areas using specific atomic sensitivity factors, with the integral subtraction of the background noise [13]. A Hitachi S-800 scanning electron microscope was utilized for scanning electron microscopy (SEM).

3. Results and discussion

The results of chemical analyses of the samples are given in Table 1; the experimental XRD results are coincident, within experimental errors, with those of the starting mixed aqueous solutions.

Table 1. Chemical compositions, lattice parameters and porosity characteristics of the studied samples

Sample	Lattice parameters [\AA]		Molar fraction				S_{BET} [m^2/g]	C_{BET}	V_p [cm^3/g]	% μpA
	a	c	Mg	Cu	Ce	Al				
MgAlLDH	3.059	23.37	0.74	-	-	0.25	94.5	27.9	0.431	-
CuCeLDH	3.067	22.79	0.37	0.34	0.14	0.15	69.3	16.7	0.177	-
cCuCeLH	-	-	0.34	0.35	0.17	0.14	134.4	401.9	0.381	14

Figure 1 shows the powder XRD patterns of the as-synthesized and also thermally treated (723 K and 1173 K) copper and cerium containing layered double hydroxides. For CuCeLDH, the diffraction peaks are typical of a double layered hydroxide structure [4] with sharp and symmetric reflections of the basal (003), (006), and (009) planes and broad, less intense, asymmetric reflections for the nonbasal (012), (015) and (018) planes; the XRD reflections were indexed using a hexagonal cell with a rhombohedral symmetry ($R\bar{3}m$), commonly used as a description of the LDH structure. The parameter a , calculated as $2d(110)$, is a function of the metal-metal distance within the layers, pointing out the cations stacking in (003) planes, while the c param-

ter, calculated as $3d(003)$, is a function of the average charge of the metal cations, the nature of the interlayer anions and the water content of the hydrotalcite like sample.

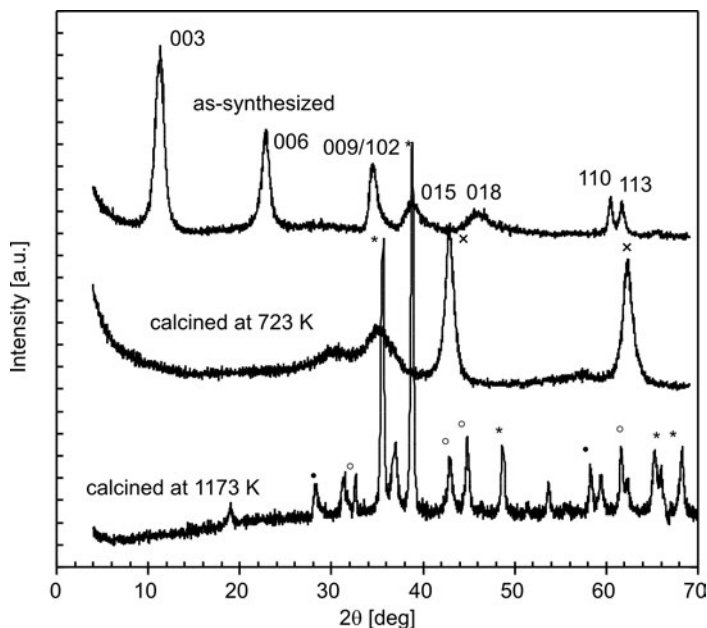


Fig. 1. The XRD patterns of CuCeLDH: * - cooper oxide, • - cerium oxide, ◦ - $MgAl_2O_4$ spinel like phase, × - MgO

The XRD parameters are shown in Table 1. The value of the lattice parameter a is equal to 3.059 \AA for MgAILDH, but the corresponding value increases to 3.067 \AA for CuCeLDH. The increase in the parameter a for CoCeLDH indicates that Ce^{3+} ions replace Al^{3+} ions in the brucite-like layers, and that is because the ionic radius of Ce^{3+} (Shannon ionic radius 1.01 \AA [14]) is larger than the ionic radius of Al^{3+} (Shannon ionic radius 0.53 \AA), while a correspondence exists between the ionic radius of Cu^{2+} hexacoordinate (Shannon ionic radius 0.73 \AA) and the ionic radius of Mg^{2+} hexacoordinate (Shannon ionic radius 0.72 \AA). The decrease in the c parameter can be attributed to the modified electrostatic interactions between the layer and the interlayer network when copper and cerium ions are introduced in the LDH layer. After calcination at 723 K , the hydrotalcite structure completely collapses and the new reflections indicate the presence of poorly crystallized mixed oxides, characteristic of the LDHs calcined at this temperature [1, 3]. The XRD pattern of the samples, calcined at 1173 K for 8 h, gives information about the evolution of the newly formed mixed oxides; the corresponding XRD pattern (see Fig. 1) shows strong peaks characteristic of a well defined phase of CuO (JCPDS file 5-0661) and also low intensity peaks characteristic of the CeO_2 phase [15].

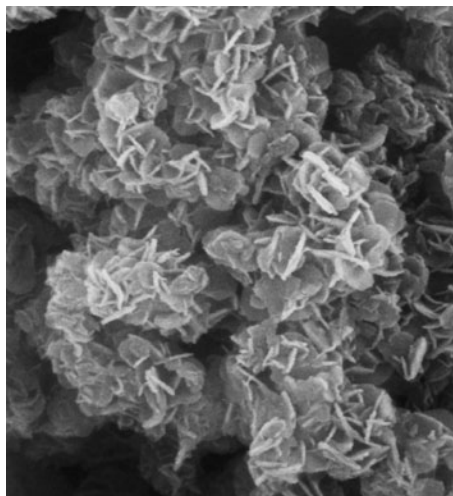


Fig. 2. The SEM image of cCuCeLDH

The SEM image of the cCuCeLDH is presented in Fig. 2. It indicates a high crystalline material formed by enough uniform and highly interconnected particles with an average diameter equal to 110 nm. The nitrogen adsorption isotherms of CuCeLDH and cCuCeLDH are shown in Fig. 3. Their different appearances suggest differences in the porosity characteristics after thermal treatment. For the CuCeLDH a type IV isotherm with a type H₃ hysteresis loop and no limiting adsorption at p/p_0 values close to unity is obtained. The broadness of the hysteresis loop reveals highly non-uniform pore-size and/or shape. This result indicates that Cu and Ce containing LDH consists of aggregates of plates or edged particles forming slit shaped pores, which are characteristics of LDH like materials.

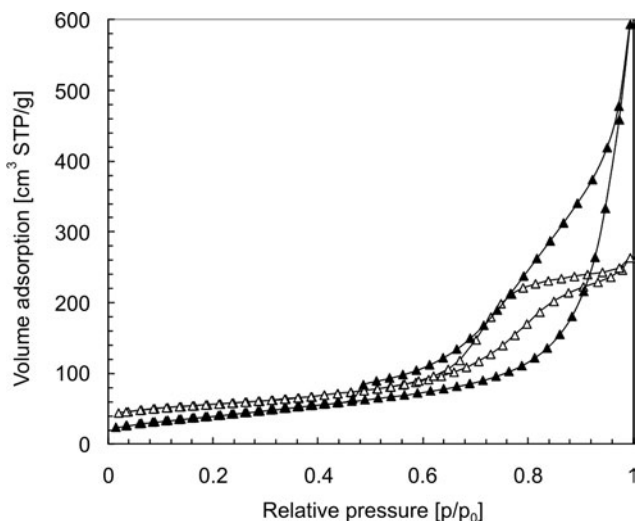


Fig. 3. N₂ adsorption-desorption isotherms of:
 ▲ – CuCeLDH and Δ – cCuCeLDH

For cCuCeLDH, the multilayer adsorption at p/p_0 values close to zero, as well as for a high value of the C constant in the BET equation (see Table 1) indicate that some microporosity features developed in the sample [16]; furthermore, a much lower adsorption value at p/p_0 close to unity shows that larger mesopores and macropores are absent in this sample. In general, in the LDHs, mesopore formation is through interparticle packing, while the distribution of pores is influenced by the crystallite size and packing arrangement of crystallites [17, 18]. In the case of the mixed oxides, obtained after subjecting the LDHs to thermal treatment at 723 K, the loss of interlayer water and interlayer anions (e.g., CO_3^{2-} , NO_3^-) by a cratering mechanism during calcination [9] allows the formation of micropores and gives rise to an important increase in the surface area and pore volume, as results from Table 1.

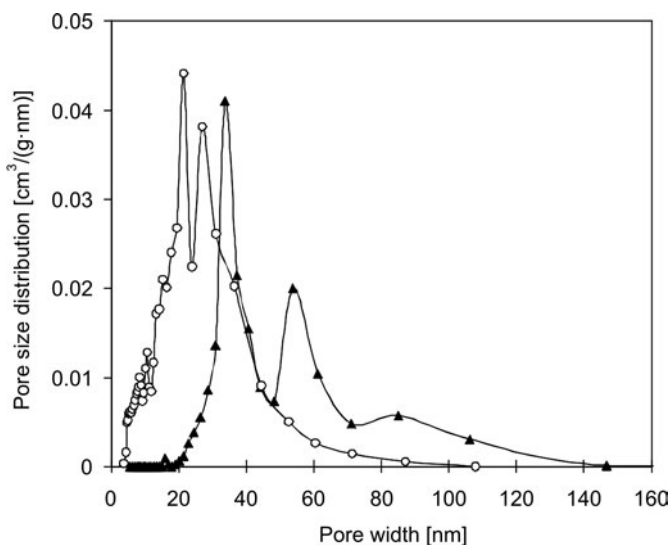


Fig. 4. Pore size distributions of: ▲ – CuCeLDH and ○ – cCuCeLDH

Pore size distribution (PSD) is further used to study the sample porosity. The PSD curves presented in Fig. 4 also indicate the change in the porous features of CuCeLDH after thermal treatment. The PSD curve of CuCeLDH is defined by two maxima at 34 and 57 nm. For cCuCeLDH, the PSD curve is shifted to the left with two maxima at 21 and 27 nm, thus indicating clearly the decrease in the pore sizes after the thermal treatment. This behaviour is characteristic of hydrotalcite like materials [17, 18]. The data of Table 1 reveal that the S_{BET} value of MgAILDH reaches $94.5 \text{ m}^2/\text{g}$, though the corresponding value for CuCeLDH is equal to $69.3 \text{ m}^2/\text{g}$. Calcination gives rise to a slight increase in the S_{BET} value, to $134.4 \text{ m}^2/\text{g}$, for cCuCeLDH, though the corresponding value of the calcined MgAILDH reaches $167 \text{ m}^2/\text{g}$. Pore volume (V_p) decreases after Cu and Ce were introduced in the layered clay, reaching $0.381 \text{ cm}^3/\text{g}$ for cCuCeLDH, in comparison with $0.483 \text{ cm}^3/\text{g}$ for the calcined MgAILDH.

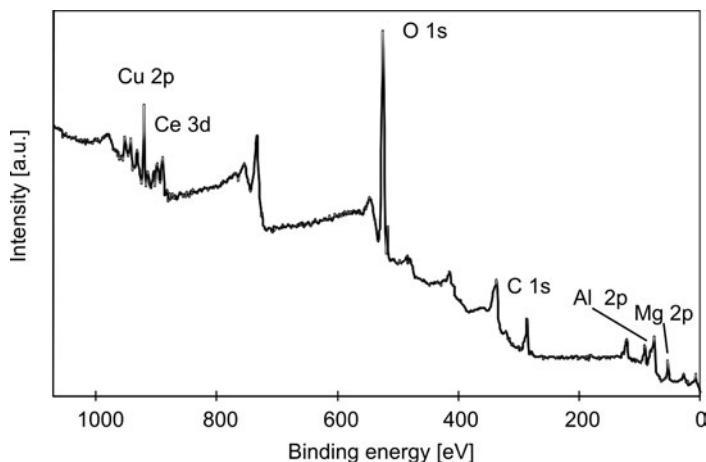


Fig. 5. XPS pattern of cCuCeLDH

The nature of the active species present on the surface is important for establishing the properties of the catalytic samples. Taking this into account, XPS analysis was performed in order to obtain information about the surface composition of the Cu–Ce mixed oxides derived from copper and cerium substituted hydroxalcalite-like samples.

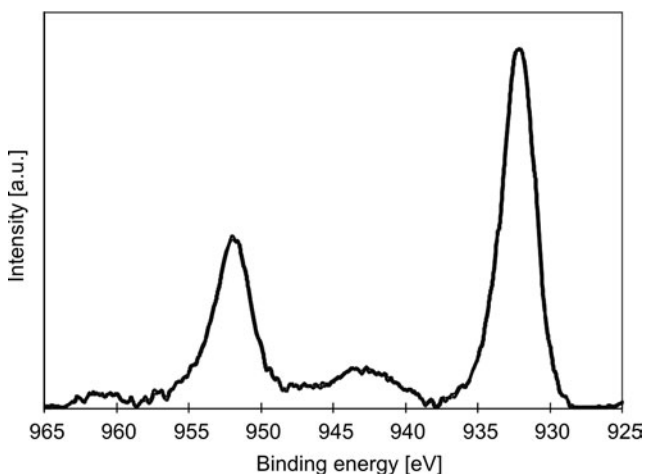


Fig. 6. Cu 2p XPS spectra in cCuCeLDH sample

The corresponding XPS pattern of cCuCeLDH, presented in Fig. 5, shows that all the elements are present on the sample surface. A closer look at the Cu 2p XPS spectra (Fig. 6) reveals the presence of shake-up satellite features for both Cu 2p_{3/2} and Cu 2p_{1/2}, thus indicating that Cu²⁺ ions [19] are present on the surface of cCuCeLDH. The pattern characteristic of the Ce 3d XPS spectra (Fig. 7) suggests that a redox couple Ce⁴⁺/Ce³⁺ [20, 21] is present on the sample surface; the state of the surface copper

together with the different contribution of the surface Ce^{4+} and Ce^{3+} point to specific surface features of mixed oxides obtained from LDH containing copper and cerium.

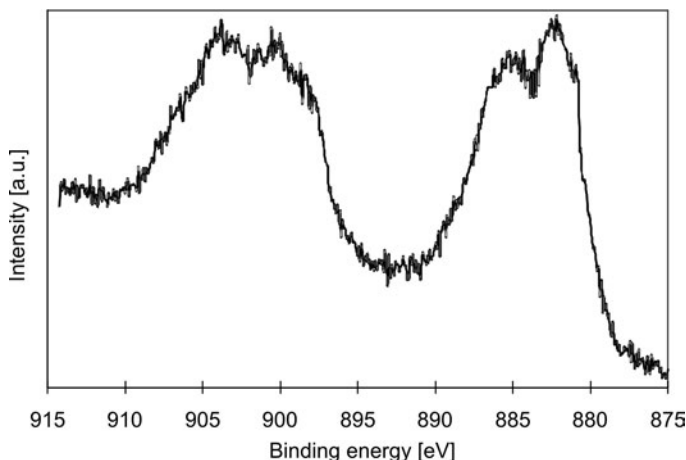


Fig. 7. Ce 3d XPS spectra in cCuCeLDH sample

4. Conclusions

Copper and cerium substituted layered double hydroxides were used as precursors for obtaining mixed oxides with specific textural and surface properties. XRD analysis demonstrates the formation and evolution of an LDH layered structure, after the thermal treatment, to the mesoporous mixed oxides. The SEM image shows the formation of overlapped, highly agglomerated nanoparticles, irregular in size and/or shape and with an average diameter equal to 110 nm. The presence of Cu^{2+} and the redox couple $\text{Ce}^{4+}/\text{Ce}^{3+}$ on the surface contribute to design-specific surface properties for the newly formed mixed oxides. Further works aim to test this material as a catalyst in CO selective oxidation.

Acknowledgement

This research was partially supported by the PNCDI II contracts NATOEPA 71-020/2007 and LACAFIA 134 CPI/2007.

References

- [1] AVGOUROPOULOS G., IOANNIDES T., *Appl. Catal.*, B, 67 (2006), 11.
- [2] ZHENG X.C., WANG S.P., WANG S.R., ZHANG S.M., HUANG W.P., WU S.H., *Mater. Sci. Eng.*, C, 25 (2005), 516.
- [3] RIVES V., *Layered Double Hydroxides: Present and Future*, Nova Sci. Pub. Inc., New York, 2001.
- [4] CAVANI F., TRIFIRO F., VACCARI A., *Catal. Today*, 11 (1991), 173, and references therein.
- [5] ARCO M., GUTIERREZ S., MARTIN C., RIVES V., ROCHA J., *J. Solid State Chem.*, 177 (2004), 3954.

- [6] VACCARI A., *Appl. Clay Sci.*, 14 (1999), 161.
- [7] CARJA G., NAKAMURA R., AIDA T., NIYAMA H., *J. Catal.*, 218 (2003), 104.
- [8] KANNAN S., DUBEY A., KNOZINGER H., *J. Catal.*, 2312 (2005), 381.
- [9] REICHLER W.T., YANG S.Y., EVERHARDT S.D., *J. Catal.*, 10 (1986), 352.
- [10] BRUNAUER S., EMMETT P.H., TELLER E., *J. Am. Chem. Soc.*, 60 (1938), 309.
- [11] SING K.S.W., EVERETT D.H., HAUL R.A.W., MOSCOU L., PIEROTTI R.A., ROUQUEROL J., SIEMIENIEWSKA T., *Pure Appl. Chem.*, 57 (1985), 603.
- [12] GREGG S.J., SING K.S.W., *Adsorption, Surface Area and Porosity*, 2nd Ed., Academic Press, London, 1982.
- [13] DEFFOSE C., [in:] *Chemical Industries*, F. Dellany (Ed.), Marcel Dekker, New York, 1984, p. 225.
- [14] SHANNON R.D., *Acta Crystallogr., Sect. A: Found. Crystallogr.*, 32 (1976), 751.
- [15] MOGENSEN M., SAMMES N.M., TOMPSETT G.A., *Solid State Ionics*, 129 (2000), 63.
- [16] ZARĘBA-GRODŹ I., MIŚTA W., SIKORA A., GOTSZALK T., STRĘK W., HERMANOWICZ K., MARUSZEWSKI K., *Mater. Sci.*, 23 (2005), 147.
- [17] HUTSON N.D., *Chem. Mater.*, 16 (2004), 4135.
- [18] TAKEHIRA K., KAWABATA T., SHISHIDO T., MURAKAMI K., OHI T., SHORO D., HONDA M., TAKAKI K., *J. Catal.*, 231 (2005), 92.
- [19] CARJA G., NAKAMURA R., NIYAMA H., *Microporous Mesoporous Mater.*, 83 (2005), 147.
- [20] WAGNER C.D., RIGGS W.N., DAVIS L.E., MOULDER J.F., MUILENBERG G.E., *Handbook of X-Ray Photoelectron Spectrometry*, Perkin-Elmer, Eden Prairie, 1979.
- [21] LAACHIR A., PERRICHON V., BADRI A., LAMOTTE J., CATHERINE E., LAVALLEY J.C., FALLAH J., HILAIRE L., NORMAND F., QUEMERE E., SAUVION G.N., TOURET O.J., *J. Chem. Soc., Faraday Trans.*, 87 (1991), 1601.
- [22] GROEN J.C., PEPPER L.A.A., PEREZ-RAMIREZ J., *Microporous Mesoporous Mater.*, 60 (2003), 1.

Received 2 October 2008

Revised 19 January 2009

Quasicrystalline phase formation in the conventionally solidified Al–Cu–Fe system

M. GÖĞEBAKAN^{1*}, B. AVAR¹, O. UZUN²

¹Department of Physics, Faculty of Art and Science, Kahramanmaraş Sutcu Imam University,
Kahramanmaraş 46100, Turkey

²Department of Physics, Faculty of Art and Science, Gaziosmanpaşa University, Tokat 60240, Turkey

Structural characteristics and thermal behaviour of the conventionally solidified Al–Cu–Fe alloys with nominal compositions of $\text{Al}_{70}\text{Cu}_{20}\text{Fe}_{10}$, $\text{Al}_{65}\text{Cu}_{20}\text{Fe}_{15}$ and $\text{Al}_{63}\text{Cu}_{25}\text{Fe}_{12}$ were investigated by X-ray diffraction, scanning electron microscopy, and differential thermal analysis techniques. Results show that a single quasicrystalline phase forms in a conventionally solidified $\text{Al}_{65}\text{Cu}_{20}\text{Fe}_{15}$ alloy, being thermodynamically stable without phase transition up to the melting point. A cubic $\text{AlFe}(\text{Cu})$ solid solution, identified as β phase, and a cubic $\text{AlCu}(\text{Fe})$ solid solution, identified as τ phase, were observed with quasicrystalline phase for $\text{Al}_{63}\text{Cu}_{25}\text{Fe}_{12}$ alloy. Conventional solidification of $\text{Al}_{70}\text{Cu}_{20}\text{Fe}_{10}$ alloy does not result in quasicrystalline phase formation. However, the formation of quasicrystalline phase in conventionally solidified $\text{Al}_{70}\text{Cu}_{20}\text{Fe}_{10}$ alloy was observed after additional annealing at elevated temperature. SEM micrographs for $\text{Al}_{70}\text{Cu}_{20}\text{Fe}_{10}$ and $\text{Al}_{63}\text{Cu}_{25}\text{Fe}_{12}$ alloys after annealing at 700 °C for 4 h revealed the formation of pentagonal dodecahedrons in the quasicrystalline phase, with an edge size of about 30 μm .

Key words: *quasicrystals; conventional solidification; heat treatment, Al–Cu–Fe*

1. Introduction

Quasicrystals are a new class of materials characterized by quasi-periodic order. These materials can be manufactured by mechanical alloying, rapid or conventional solidification, physical vapour deposition and plasma processing. Quasicrystals have many attractive properties, such as high hardness [1–3], low electrical and thermal conductivities [4], low surface energy [5], accompanied by a low coefficient of friction [5, 6], reasonable oxidation and strong corrosion resistance [7], and unusual optical properties [8, 9] which have not been observed for crystalline alloys. Such proper-

*Corresponding author, e-mail: gogebakan@ksu.edu.tr or mgogebakan27@hotmail.com

ties of quasicrystalline materials have been exploited for catalyst and coating applications. So far, a number of quasicrystals have been obtained in several binary, ternary and multicomponent systems. Usually, quasicrystalline phases form in systems based on Al, Mg, Zr, Ti, Zn and Cu. As the variety of base metallic elements forming quasicrystalline phases is wide, the spectrum of alloying elements is even wider. However, the alloying elements are often toxic, not easily available or very costly. Al–Cu–Fe alloys are an exception; they are interesting due to their lack of toxicity, easy availability, and reasonable costs of purchasing their alloying elements. Therefore, in the last two decades, quasicrystalline Al–Cu–TM (TM are Fe, Co, Ni) alloy systems have been intensively studied [10–14]. Most of these alloys form metastable quasicrystals which turn irreversibly into regular crystals upon heating. It has been reported that the quasicrystal phase formed in the conventionally solidified $\text{Al}_{65}\text{Cu}_{20}\text{Fe}_{15}$ alloy is thermodynamically stable and does not undergo phase transformation up to the melting point, at 1135 K [10]. Therefore, the discovery of thermodynamically stable quasicrystalline phase in $\text{Al}_{65}\text{Cu}_{20}\text{Fe}_{15}$ alloy has opened a new avenue for its experimental investigations. After the discovery, the number of alloy systems, in which quasicrystals are formed by rapid or conventional solidification, has steadily increased. The preparation, properties, structure and application of these quasicrystalline alloys have been the main topics of interest in the field of alloy science.

The structural characteristics, morphological features and thermal behaviour of the conventionally solidified $\text{Al}_{70}\text{Cu}_{20}\text{Fe}_{10}$, $\text{Al}_{65}\text{Cu}_{20}\text{Fe}_{15}$ and $\text{Al}_{63}\text{Cu}_{25}\text{Fe}_{12}$ alloys were investigated in the present study, using X-ray diffraction (XRD), scanning electron microscopy (SEM) and differential thermal analysis (DTA) techniques.

2. Experimental

The samples in this study were obtained by a conventional solidification. Three different Al–Cu–Fe alloy ingots with nominal compositions (expressed in at. %) of $\text{Al}_{70}\text{Cu}_{20}\text{Fe}_{10}$, $\text{Al}_{65}\text{Cu}_{20}\text{Fe}_{15}$ and $\text{Al}_{63}\text{Cu}_{25}\text{Fe}_{12}$ were prepared by induction melting of appropriate proportions of 99.99% purity Al, 99.9% purity Cu and 99.9% purity Fe in a graphite crucible under an argon atmosphere. The ingots were re-melted several times in order to achieve homogeneity. Then the ingots were left to cool in air to allow slow cooling. The master ingots were annealed at 700 °C for 4 h under vacuum. phase identification and microstructural examination of as-cast and heat-treated alloy specimens were carried out using X-ray diffraction (XRD) and scanning electron microscopy (SEM). The XRD examination was performed using a Philips X'Pert PRO diffractometer with CuK_{α} radiation with the wavelength of 0.154 nm. For phase identification, measurements were taken for a wide range of diffraction angles (2θ) ranging from 20° to 120° with a scanning rate of 5 deg/min. SEM analysis was performed with a JEOL JSM 5400 scanning electron microscope at an acceleration voltage of 20 kV after the specimen had been coated with a vacuum-deposited gold layer in order to enhance

contrast. Thermal properties of the master ingot alloys were analysed by differential thermal analysis (DTA) using a Perkin-Elmer's Diamond TG/DTA thermal analyser at 20 K/min heating rate under flowing N₂.

3. Results and discussion

Figure 1 shows the XRD patterns for conventionally solidified Al₇₀Cu₂₀Fe₁₀, Al₆₅Cu₂₀Fe₁₅ and Al₆₃Cu₂₅Fe₁₂ alloys. The XRD trace of the Al₇₀Cu₂₀Fe₁₀ alloy (curve a) shows the presence of cubic β -AlFe(Cu) solid solution phase (β phase), tetragonal θ -Al₂Cu phase (θ phase) and a small amount of tetragonal ω -Al₇Cu₂Fe phase (ω phase).

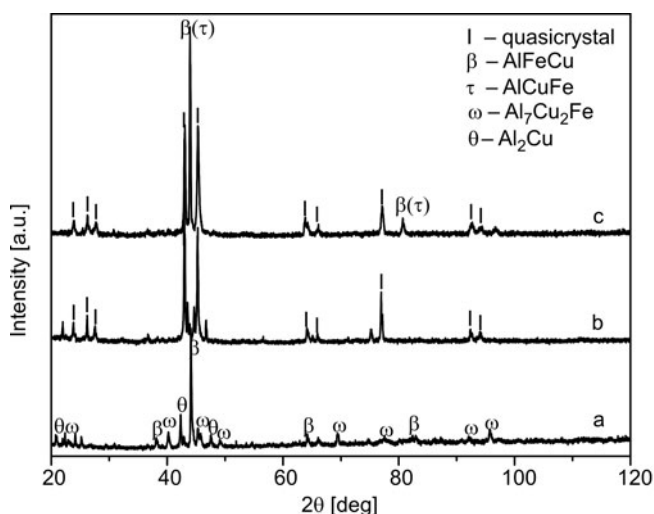


Fig. 1. XRD patterns for conventionally solidified Al–Cu–Fe alloys: a) Al₇₀Cu₂₀Fe₁₀, b) Al₆₅Cu₂₀Fe₁₅ and c) Al₆₃Cu₂₅Fe₁₂

It is clear from the peak intensities that β is the major phase for this alloy composition. However, the present result indicated that iron concentration in Al₇₀Cu₂₀Fe₁₀ alloy is too low to form quasicrystalline phase by a conventional solidification. For the Al₆₅Cu₂₀Fe₁₅ alloy (curve b), only the icosahedral quasicrystalline phase (I phase) was distinguished in the XRD pattern. In the XRD curve of the Al₆₃Cu₂₅Fe₁₂ alloy (curve c), mainly the peaks associated with I phase, the cubic β phase and cubic τ -AlCu(Fe) solid solution phase (τ phase) were observed. As shown in Fig. 1 (curve c), the diffraction peaks of τ phase exactly overlap with the diffraction peaks of β phase, owing to the same crystal structure of CsCl type cubic and a very similar lattice parameter, approximately 0.293 nm [15]. However, these results indicated that the single quasicrystalline phase is formed only in the conventionally solidified Al₆₅Cu₂₀Fe₁₅ alloy.

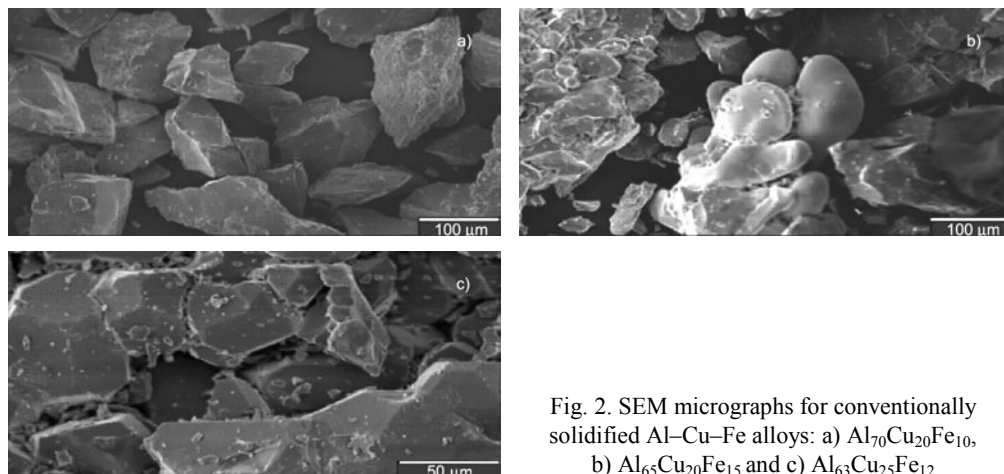


Fig. 2. SEM micrographs for conventionally solidified Al–Cu–Fe alloys: a) $\text{Al}_{70}\text{Cu}_{20}\text{Fe}_{10}$, b) $\text{Al}_{65}\text{Cu}_{20}\text{Fe}_{15}$ and c) $\text{Al}_{63}\text{Cu}_{25}\text{Fe}_{12}$

With the aim of examining the compositional dependence of the microstructure for conventionally solidified Al–Cu–Fe alloys in more detail, the alloys were also examined by SEM. Figure 2 shows the SEM micrographs for conventionally solidified $\text{Al}_{70}\text{Cu}_{20}\text{Fe}_{10}$, $\text{Al}_{65}\text{Cu}_{20}\text{Fe}_{15}$ and $\text{Al}_{63}\text{Cu}_{25}\text{Fe}_{12}$ alloys. These micrographs showed different microstructural features. For $\text{Al}_{70}\text{Cu}_{20}\text{Fe}_{10}$ alloy, no appreciable quasicrystals were observed, in agreement with the XRD results. This is probably because the composition of this alloy is very different from that of quasicrystalline phase. The morphology of this alloy is diverse and some particles exhibited faceted morphology, as shown in Fig. 2a. The SEM micrograph of the $\text{Al}_{65}\text{Cu}_{20}\text{Fe}_{15}$ alloy reveals the formation of the ‘cauliflower’ morphology observed in previous studies [16, 17]. The grain size of this quasicrystal ranges from 20 to 80 μm . However, for the $\text{Al}_{63}\text{Cu}_{25}\text{Fe}_{12}$ alloy, typical pentagonal dodecahedral crystals were clearly observed, as seen in Fig. 2c. Therefore, it is emphasized that a slight change in the compositions would cause a significant difference in the microstructural evolution during metallurgical processing.

In order to investigate the structural change that occurs during heat treatment of Al–Cu–Fe alloys, the samples were annealed for 4 h at 700 °C and then cooled rapidly to freeze the microstructure for subsequent XRD and SEM analysis. Figure 3 shows the XRD patterns for conventionally solidified Al–Cu–Fe alloys after annealing for 4 h at 700 °C. The XRD pattern of the $\text{Al}_{70}\text{Cu}_{20}\text{Fe}_{10}$ alloy consisted of a mixture of I, β and ω phases. Therefore, the icosahedral quasicrystalline phase (I phase) in conventionally solidified $\text{Al}_{70}\text{Cu}_{20}\text{Fe}_{10}$ alloy was observed after heat treatment at 700 °C for 4 h. At this processing stage, the peak intensity of ω phase increased.

As seen in Fig. 3b, the XRD patterns of an $\text{Al}_{65}\text{Cu}_{20}\text{Fe}_{15}$ alloy in as-solidified state and heated state at 700 °C were quite similar. No appreciable differences, even in the peak position and peak intensity, were observed in either cases. All the diffraction peaks were identified as I phase. This result clearly indicated that I phase is formed as a thermodynamically stable phase in $\text{Al}_{65}\text{Cu}_{20}\text{Fe}_{15}$ alloy. This is in good agreement with the results for the conventionally solidified $\text{Al}_{65}\text{Cu}_{20}\text{Fe}_{15}$ reported earlier by Tsai

et al. [10]. On the other hand, XRD patterns of the $\text{Al}_{63}\text{Cu}_{25}\text{Fe}_{12}$ alloy after additional annealing for 4 h at 700 °C showed a considerable increase in the diffraction intensities corresponding to I phase.

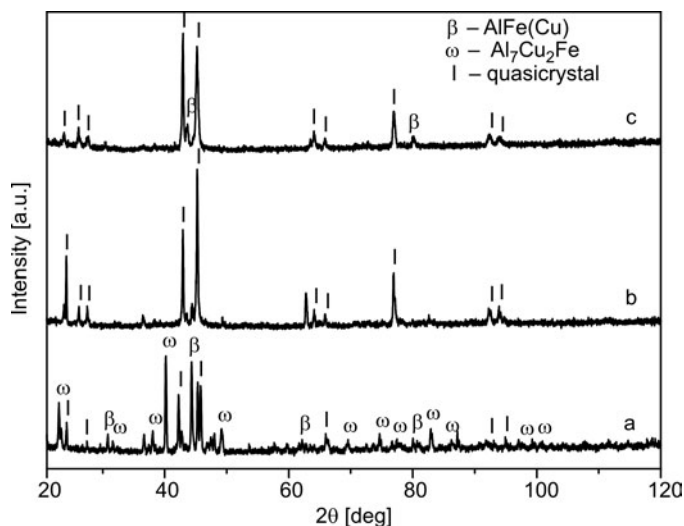


Fig. 3. XRD patterns for conventionally solidified Al–Cu–Fe alloys annealed for 4 h at 700 °C: a) $\text{Al}_{70}\text{Cu}_{20}\text{Fe}_{10}$, b) $\text{Al}_{65}\text{Cu}_{20}\text{Fe}_{15}$ and c) $\text{Al}_{63}\text{Cu}_{25}\text{Fe}_{12}$

As is seen in Fig. 3c, the τ phase completely disappears at this stage. It has been reported that the τ phase is a metastable one, containing less Fe with a lower melting temperature and the β phase is a stable phase, containing more Fe with a higher melting temperature [18]. Thus, the present investigation demonstrates that during the heat treatment of $\text{Al}_{63}\text{Cu}_{25}\text{Fe}_{12}$ alloy, the τ phase melted and peritectic reaction occurred between liquid and β phases. It is therefore reasonable to assert that the I phase in $\text{Al}_{63}\text{Cu}_{25}\text{Fe}_{12}$ alloy formed as the result of a peritectic reaction. This is in agreement with other results [15, 19, 20]. Therefore, the XRD pattern of the $\text{Al}_{63}\text{Cu}_{25}\text{Fe}_{12}$ alloy after additional annealing for 4 h at 700 °C consists of I phase and the β phase.

Figure 4 shows SEM micrographs for conventionally solidified Al–Cu–Fe alloys after additional annealing for 4 h at 700 °C. High magnification SEM results for the $\text{Al}_{70}\text{Cu}_{20}\text{Fe}_{10}$ and $\text{Al}_{63}\text{Cu}_{25}\text{Fe}_{12}$ alloys after annealing for 4 h at 700 °C revealed the formation of pentagonal dodecahedrons in the quasicrystalline phase with the edge size of about 30 μm as shown in Fig. 4a and c. The icosahedral quasicrystal particles, in the shape of dodecahedrons, for conventionally solidified Al–Cu–Fe alloy have been previously reported [10, 15, 21]. However, the SEM micrograph of $\text{Al}_{65}\text{Cu}_{20}\text{Fe}_{15}$ alloy after annealing for 4 h at 700 °C shows an array of the pentagonal dodecahedral crystals in the shape of a cauliflower, as seen in Fig. 4b. Therefore the SEM micrographs of $\text{Al}_{65}\text{Cu}_{20}\text{Fe}_{15}$ alloy in as-solidified state and after heat treatment, at 700 °C for 4 h, were quite similar.

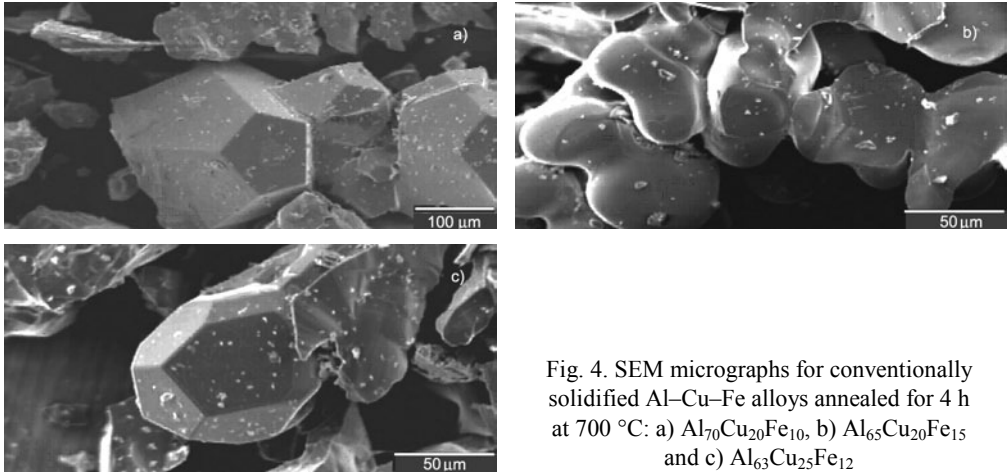


Fig. 4. SEM micrographs for conventionally solidified Al–Cu–Fe alloys annealed for 4 h at 700 °C: a) $\text{Al}_{70}\text{Cu}_{20}\text{Fe}_{10}$, b) $\text{Al}_{65}\text{Cu}_{20}\text{Fe}_{15}$ and c) $\text{Al}_{63}\text{Cu}_{25}\text{Fe}_{12}$

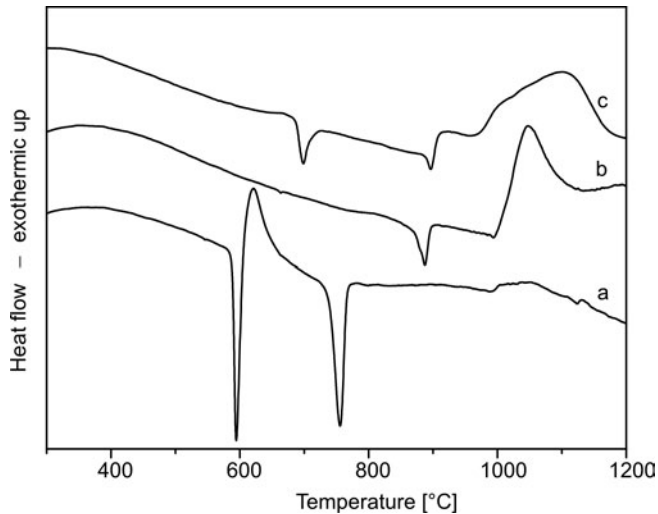


Fig. 5. DTA curves for conventionally solidified Al–Cu–Fe alloys: a) $\text{Al}_{70}\text{Cu}_{20}\text{Fe}_{10}$, b) $\text{Al}_{65}\text{Cu}_{20}\text{Fe}_{15}$ and c) $\text{Al}_{63}\text{Cu}_{25}\text{Fe}_{12}$ alloy

Figure 5 shows the DTA curves for conventionally solidified $\text{Al}_{70}\text{Cu}_{20}\text{Fe}_{10}$, $\text{Al}_{65}\text{Cu}_{20}\text{Fe}_{15}$ and $\text{Al}_{63}\text{Cu}_{25}\text{Fe}_{12}$ alloys. The DTA traces for $\text{Al}_{70}\text{Cu}_{20}\text{Fe}_{10}$ alloy showed two major endothermic peaks at around 595 °C and 750 °C, respectively, during heating up to 1200 °C. The pseudo-binary Al_3Fe – Al_2Cu phase diagram indicated that the melting points of θ and ω phases are 591 °C and 740 °C, respectively [22]. Thus, it is clear that the endothermic peaks around 595 °C and 750 °C correspond to the melting of the θ phase and ω phase. In addition, the DTA traces of the $\text{Al}_{70}\text{Cu}_{20}\text{Fe}_{10}$ alloy also showed an exothermic effect at around 615 °C. This exothermic effect is attributed to formation of the ω phase. This result is consistent with XRD observation. As men-

tioned above, the XRD patterns of the Al₇₀Cu₂₀Fe₁₀ alloy indicated the presence of the β and θ phases, a small amount of ω phase, and after the sample had been heated to 700 °C for 4 h, the peak intensity of the ω phase increased.

On the other hand, the DTA curve of the Al₆₅Cu₂₀Fe₁₅ alloy showed only one endothermic peak, around 890 °C, corresponding to the fusion. This result indicated that the quasicrystal has a melting point at 890 °C, and is a stable phase without phase transition up to the melting point. Furthermore, the endothermic peak corresponding to the fusion takes places at a single stage; no splitting in the peak was observed, indicating that the Al₆₅Cu₂₀Fe₁₅ quasicrystal is mostly composed of a single phase. This is again consistent with XRD results, since XRD patterns of the Al₆₅Cu₂₀Fe₁₅ alloy annealed up to 700 °C for 4 h showed no significant difference, even in the peak position and peak intensity. However, this DTA result is quite similar to the earlier one reported for the Al₆₅Cu₂₀Fe₁₅ by Tsai et al. [10]. The DTA trace of Al₆₃Cu₂₅Fe₁₂ alloy shows mainly two endothermic peaks at around 700 °C and 896 °C, respectively. The first endothermic peak at around 700 °C is considered to correspond to the dissolution of the τ phase. This observation is consistent with the conclusion obtained from Fig. 3c, where no τ phase was observed after the sample had been heated to 700 °C for 4 h. The second endothermic peak at around 896 °C corresponds to the melting of I phase.

4. Conclusions

In the present study, the formation of icosahedral quasicrystalline phase in conventionally solidified Al–Cu–Fe alloys has been investigated.

The microstructure of the as-solidified Al₇₀Cu₂₀Fe₁₀ alloy consisted of a mixture of β , θ and ω phases. However, for this alloy, the formation of the I phase was observed after additional annealing at elevated temperatures. A single quasicrystalline phase was observed in the conventionally solidified and annealed Al₆₅Cu₂₀Fe₁₅ alloy.

SEM micrographs of this alloy in as-solidified state and after heat treatment at 700 °C for 4 h, showed an array of the pentagonal dodecahedral crystals in the shape of a cauliflower.

The DTA curve of the Al₆₅Cu₂₀Fe₁₅ alloy showed only one endothermic peak around 890 °C corresponding to the fusion. The DTA result indicated that the Al₆₅Cu₂₀Fe₁₅ quasicrystal is mostly composed of a single phase, and is a thermodynamically stable phase without phase transition up to melting point.

As-solidified Al₆₃Cu₂₅Fe₁₂ alloy exhibited I phase together with β phase and τ phase. After annealing at 700 °C for 4 h, the τ phase completely disappeared and the sample consisted of I phase and β phase.

SEM micrographs for the Al₇₀Cu₂₀Fe₁₀ and Al₆₃Cu₂₅Fe₁₂ alloys annealed for 4 h at 700 °C revealed the formation of pentagonal dodecahedrons in the quasicrystalline phase.

Acknowledgements

This work was supported by The Scientific and Technological Research Council of Turkey (TUBITAK), Project No. 106 T 701.

References

- [1] KOSTER U., LIU W., HERTZBERG H., MICHEL M., *J. Non-Cryst. Solids*, 153/154 (1993), 446.
- [2] WOLF B., BAMBAUER K.O., PAUFLER P., *Mater. Sci. Eng. A*, 298 (2001), 284.
- [3] HUTTUNEN-SAAIRIVIRTA E., *J. Alloys Compds.* 363 (2004), 150.
- [4] RAPP O., *Mater. Sci. Eng. A*, 294–296 (2000), 458.
- [5] DUBOIS J.M., *Mater. Sci. Eng. A*, 294–296 (2000), 4.
- [6] BRUNET P., ZHANG L.M., SORDELET D.J., BESSER M., DUBOIS J.M., *Mater. Sci. Eng. A*, 294–296 (2000), 74.
- [7] CHANG S.L., CHIN W.B., ZHANG C.M., JENKS C.J., THIEL P.A., *Surf. Sci.*, 337 (1995), 135.
- [8] HOMES C.C., TIMUSK T., WU X., ALTOUNIAN Z., SAHNOUNE A., STROM-OSLEN J.O., *Phys. Rev. Lett.*, 13 (1991), 2694.
- [9] EISENHAMMER T., MAHR A., HAUGENEDER A., ASSMANN W., *Sol. Energy Mater. Sol. Cells*, 46 (1997), 53.
- [10] TSAI A.P., INOUE A., MASUMOTO T., *Japan. J. Appl. Phys.*, 26 (1987), L1505.
- [11] BOJARSKI Z., BOGDANOWICZ W., *Arch. Nauk. Mater.*, 19 (1998), 215.
- [12] BOJARSKI Z., BOGDANOWICZ W., GIGLA M., LELATKO J., SUROWIEC M., *Arch. Nauk. Mater.*, 18 (1997), 237.
- [13] BOGDANOWICZ W., *J. Cryst. Growth*, 240 (2002), 255.
- [14] BOGDANOWICZ W., *Mater. Sci. Eng. A*, 346 (2003), 328.
- [15] LEE S.M., KIM B.H., KIM S.H., FLEURY E., KIM W.T., KIM D.H., *Mater. Sci. Eng. A*, 294–296 (2000), 93.
- [16] CHEUNG Y.L., CHAN K.C., ZHU Y.H., *Mater. Charact.*, 47 (2001), 299.
- [17] ROSAS G., REYES-GASGA J., PEREZ R., *Mater. Charact.*, 58 (2007), 765.
- [18] KIM B.H., KIM S.H., KIM W.T., KIM D.H., *Phil. Mag. Lett.*, 81 (2001), 483.
- [19] LEE S.M., KIM W.T., KIM D.H., *Mater. Sci. Eng. A*, 294–296 (2000), 99.
- [20] LEE S.M., JEON H.J., KIM B.H., KIM W.T., KIM D.H., *Mater. Sci. Eng. A*, 304–306 (2001), 871.
- [21] HOLLAND-MORITZ D., SCHROERS J., GRUSHKO B., HERLACH D.M., URBAN K., *Mater. Sci. Eng. A*, 226–228 (1997), 976.
- [22] FAUDOT F., QUIVY A., CALVAYRAC Y., GRATIAS D., HARMELIN M., *Mater. Sci. Eng. A* 133 (1991), 383.

Received 17 October 2008

Revised 5 December 2008

Contents

11th International Conference on Electrical and Related Properties of Organic Solids (ERPOS-11)

W. Bartkowiak, From the Guest Editor.....	617
I. Olejniczak, B. Barszcz, A. Graja, J.A. Schlueter, Optical study of β'' -(bis(ethylenedithio)-tetrathiafulvalene) ₂ SF ₅ CH ₂ SO ₃ . Activation of intramolecular modes.....	619
A. Eilmes, Stabilization energies in charged tetracene clusters. Quantum chemical and microelectrostatic calculations.....	629
R. W. Munn, A. Eilmes, S. Scarle, M. Sterzel, Simulation of ion transport through poly(ethyleneoxide) loaded with lithium perchlorate.....	637
O. Salyk, P. Bednář, M. Vala, J. Vyňuchal, Sensoric properties of aromatic and heterocyclic compounds with conjugated bonds.....	649
P. Uznański, J. Kurjata, E. Bryszewska, Modification of gold nanoparticle surfaces with pyrenedisulfide in ligand-protected exchange reactions.....	659
M. Menšík, K. L Král, Nonradiative electron and energy transfer. Explicit estimation of the influence of coherent and dephasing processes in a vibrational bath on electronic dynamics.....	671
J. Cabaj, A. Chyla, J. Sołoducho, G. Olszowa, Thin protein LB films as functional components within biosensors.....	685
Ł. Pietrzak, J. K. Jeszka, Gold nanoparticles grown on multiwall carbon nanotubes.....	693
M. Koszykowska, M. Tokarek, S. Kucharski, Synthesis and photochromic properties of poly [<i>N</i> -vinyl-2-(phenylazo)-imidazole] derivatives in the near UV range.....	699
T. Manaka, M. Nakao, E. Lim, M. Iwamoto, Ambipolar injection into pentacene field effect transistor observed by time-resolved optical second harmonic generation imaging.....	709
Y. Ohshima, H. Kohn, E. Lim, T. Manaka, M. Iwamoto, Observation of electron injection in an organic field-effect transistor with electroluminescence.....	719
H. Kohn, M. Fukada, Y. Ohshima, T. Manaka, M. Iwamoto, Circular dichroism and electroluminescence of poly(diacetylene) film with chirality.....	727
J. Kalinowski, Excimers and exciplexes in organic electroluminescence.....	735
R. Signerski, G. Jarosz, Photoelectric properties of WO ₃ /tetracene heterojunctions.....	757
R. Signerski, Photovoltaic properties of organic heterojunctions formed from tetracene and zinc hexadecafluorophthalocyanine.....	763
D. Rais, J. Hain, A. Pich, S. Pochekailov, S. Nešpůrek, H.-J. P. Adler, A. Hamáček, J. Řeboun, Electrical conductivity in thin films fabricated from nanoparticles of a polymeric composite based on PEDOT.....	769
S. Pochekaylov, D. Rais, S. Nešpůrek, J. Rakušan, M. Karásková, Electronic and gas sensing properties of soluble phthalocyanines.....	781
P. Toman, S. Nešpůrek, W. Bartkowiak, Modelling of charge carrier transport in conjugated polymers doped by polar additives.....	797
J. Olesiak, K. Matczyszyn, H. Mojzisoava, M. Zielinski, D. Chauvat, J. Zyss, Liquid crystalline phases in DNA and dye-doped DNA solutions analysed by polarized linear and nonlinear microscopy and differential scanning calorimetry.....	813

Regular papers

K. B. Tan, C. C. Khaw, C. K. Lee, Z. Zainal, Y. P. Tan, H. Shaari, High temperature impedance spectroscopy study of non-stoichiometric bismuth zinc niobate pyrochlore.....	825
O. P. Thakur, A. Kumar Singh, Electrostriction and electromechanical coupling in elastic dielectrics at nanometric interfaces.....	839

Z. Czech, R. Pelech, Thermal degradation of solvent-borne water soluble acrylic acid-butyl acrylate copolymers.....	851
X. J. Wu, X.W. Xu, X.S. Sun, Magnetic properties of mechanically milled nanosized Mn.....	857
S. Dymek, M. Wróbel, Z. Witczak, M. Blicharski, Microstructure and properties of Ti-45Al-5V intermetallic alloy.....	865
S. S. Razavi Tousi, R.Yazdani Rad, E. Salahi, M. Razavi, Effect of milling time and addition of alumina powder on the structural properties and fracture surface of nanocrystalline Al.....	875
H. Zhang, J. Shi, Y. Song, J. Zhao, K. Wang, Q. Guo, G. Zhai, L. Liu, Effect of growth time on the morphologies of vapour grown carbon fibres and a suggested mechanism of growth.....	885
C. Fu, F. Pan, W. Cai, X. Deng, X. Liu, Relaxor characteristics of ferroelectric BaZr _{0.2} Ti _{0.8} O ₃ ceramics.....	891
A. Bankauskaite, K. Baltakys, The sorption of copper ions by gyrolite in alkaline solution.....	899
G. Carja, S. Dranca, G. Ciobanu, E. Husanu, I. Balasanian, Fabrication of mesoporous mixed oxides containing copper and cerium by using substituted anionic clays as precursors.....	909
M. Göğebakan, B. Avar, O. Uzun, Quasicrystalline phase formation in the conventionally solidified Al-Cu-Fe system.....	919

GUIDELINES FOR AUTHORS

Manuscripts can be sent by conventional mail or by e-mail. Submission of a manuscript to *Materials Science-Poland* implies that it is not being considered for the publication elsewhere, and the authors have a necessary authorization to publish the material contained in the paper. **The manuscripts should conform to the formal standards of the Journal which may be found in the first issue of each volume and on the web page.**

Authors are encouraged to submit electronic versions of the manuscript by e-mail, to the address of the Journal. A single PDF file should be sent, containing text, references, figures, tables etc. Alternatively, the authors can submit the manuscript by conventional mail, sending a CD with the PDF file mentioned above, to the Editor-in-Chief at his address given below.

Each submitted manuscript will be reviewed, the final decision concerning its acceptance resting with the editors. Upon acceptance, the corresponding author will be requested to submit the following material (via e-mail or by conventional mail, on CD)

- A DOC or RTF file containing the final version of the text, references, tables and figure captions. The content of the file should be identical with that of the hard copy, and should exactly match the version seen and accepted by the referee(s).

- File(s) in appropriate formats containing figures. The required formats of the drawings (plots, schemes of technological processes) must be vector files such as XLS, OPJ, cdr (Excel, Origin, Corel-Draw) which may also be exported as EPS, EMF or WMF files. Drawings submitted in tiff or jpg formats (bitmaps, raster graphics), even if exported as EPS, EMF or WMF files, will not be accepted. **Bitmaps are acceptable only in the case of photographs.** The photographs (only in grayscale) should have the resolution not lower than 300 dpi (estimated for the size in which they are expected to be reproduced).

- A PDF file containing the complete manuscript (text, literature, tables, figures, etc). The file should be carefully checked as it will serve as a hard copy in case of doubts. **The contents of the PDF file should exactly match the material in other files.**

Irrespective of whether the final version is submitted by e-mail or by conventional mail, the authors should also send **via conventional mail** a signed copy of the Copyright Transfer Agreement (available on the web page of the Journal).

For detailed information consult the first issue of each volume or the web page of the Journal.

The mail should be addressed to:

Professor Juliusz Sworakowski
Editor-in-Chief, Materials Science-Poland
Politechnika Wrocławska, W-3
Wybrzeże Wyspiańskiego 27
50-370 Wrocław, Poland

Electronic correspondence should be sent to: MatSci@pwr.wroc.pl

Web page of Materials Science-Poland: www.MaterialsScience.pwr.wroc.pl

The Publisher reserves the right to make necessary alterations to the text. Each corresponding author will be supplied with one free copy of the journal. Orders for additional offprints can be placed with the Publisher.